elektronisches
dokument
ULB Sachsen-Anhalt

# Beiträge zur Theorie der Elektronenspektroskopie: Anwendungen der relativistischen Vielfachstreutheorie

Habilitationsschrift

zur Erlangung des akademischen Grades
Dr. rer. nat. habil.

vorgelegt der

Mathematisch-Naturwissenschaftlich-Technischen Fakultät
der Martin-Luther-Universität Halle-Wittenberg

von

Herrn Dr. rer. nat. Jürgen Henk
geb. am 23. September 1960 in Plön

Gutachter:
1. Gutachter: Prof. Dr. Patrick Bruno
2. Gutachter: Prof. Dr. Peter Dederichs
3. Gutachter: Prof. Dr. Hubert Ebert

Halle (Saale), den 17. Dezember 2004

**urn:nbn:de:gbv:3-000009330**
[http://nbn-resolving.de/urn/resolver.pl?urn=nbn%3Ade%3Agbv%3A3-000009330]

# Inhaltsverzeichnis

**Dank**

**Eidesstattliche Erklärung**

**Lebenslauf**

# Kurzfassung/*Abstract*

Electron spectroscopy provides access to fundamental properties of solids, such as the geometric, electronic, and the magnetic structure. The latter are necessary for the understanding of a variety of basic but nevertheless important effects. The present work outlines recently developed theoretical approaches to electron spectroscopies. Most of the collected results rely on first-principles calculations, as formulated in multiple-scattering theory, and are contrasted with experimental findings. One topic involves spin- and angle-resolved photoelectron spectroscopy which is addressed for magnetic surfaces and ultrathin films. Exemplary results comprise magnetic dichroism in both valence-band and core-level photoemission as well as the temperature dependence of magnetic properties of ultrathin films. Another topic is spin-dependent ballistic transport through planar tunnel junctions, focusing here on the zero-bias anomaly. In most of the cases, spin-orbit coupling (SOC) is an essential ingredient and, hence, favors a relativistic description. Prominent effects of SOC are illustrated by means of the electronic structure of rare gases adsorbed on a substrate and by the splitting of surface states on Au(111). Concerning magnetism, the magnetic anisotropy of Ni films on Cu(001) is discussed, focusing in particular on the spin reorientation transition induced by lattice distortions in ultrathin films.

*Science consists of two parts – experiment and theory – which are in constant interplay with each other. It is hardly possible to carry out a meaningful experiment, unless one has a specific idea or theory in mind, and a scientific theory is worthless unless it is based on experimental observations.*

Per-Olov Löwdin (1916–2000)

# 1. Einführung

**electron spectroscopy** – method of determining the energy with which electrons are bound in chemical species by measuring the kinetic energies of the electrons emitted upon bombardment of the species with X-ray or ultraviolet radiation. Details of the structure may be inferred from the results because differences in the arrangements of the atoms affect the amount of energy required. [...] Ref.: *Encyclopædia Britannica* [1]

Die Definition der Elektronenspektroskopie, wie sie die *Encyclopædia Britannica* gibt, bezieht sich in erster Linie auf optische Messmethoden und erscheint aus heutiger Sicht recht eng gefasst. Um aktuelle Methoden der Festkörperphysik unter Elektronenspektroskopien subsumieren zu können, muss die Definition weiter gefasst werden, beispielsweise als Antwort der Probe auf eine äußere Störung, wobei die gemessene Größe von einem kontinuierlich variierten Parameter abhängt.

In der Elektronenspektroskopie, so wie sie in dieser Arbeit definiert wird, besteht die Antwort aus dem elektrischen Strom, der von der Probe emittiert wird. Im Falle der Photoelektronenspektroskopie ist die Störung die auf die Probe einfallende elektromagnetische Strahlung, deren Energie und Einfallsrichtung verändert werden. Jedoch fallen auch Streuexperimente unter diese Definition: bei der Streuung langsamer Elektronen [*Low-energy electron diffraction* (LEED)] wird die Probe durch einen einfallenden Elektronenstrahl, dessen kinetische Energie, Spinpolarisation und Einfallsrichtung gewählt werden können, angeregt. Auch die Messung des elektrischen Stroms, der durch eine Probe aufgrund einer angelegten Spannung fließt, stellt in diesem Sinne eine elektronenspektroskopische Methode dar.

Die Wahl der spektroskopischen Methode richtet sich in erster Linie nach der Fragestellung. Je nach Art der applizierten Störung lassen sich gezielt Informationen über die gewählte Probe gewinnen. Da die Eigenschaften der kondensierten Materie in hohem Ausmaße von Elektronen nahe der Fermi-Energie bestimmt werden, bieten sich Elektronen als Testobjekte geradezu an. So lassen sich strukturelle Eigenschaften vorzugsweise mittels LEED bestimmen, während die Photoelektronenspektroskopie vorwiegend zur Analyse der elektronischen Struktur herangezogen wird.

Elektronen besitzen neben ihrer Ladung auch Drehimpuls, den Spin. Ihre Wellenfunktionen enthalten somit einen räumlichen Anteil und einen Spinanteil. In Atomen und Festkörpern sind beide Anteile nicht voneinander unabhängig, sondern durch die Spin–Bahn-Kopplung (SBK) miteinander verflochten. Daher ist es möglich, bei Detektion eines Anteils Aussagen über den anderen zu erhalten, also einen Informationsgewinn zu bekommen.

Die elektronischen Eigenschaften von Festkörpern, sowie die mit diesen eng verbundenen strukturellen und magnetischen Eigenschaften, können zuverlässig und genau aus ersten Prinzipien berechnet werden. Diese *Ab–initio*-Rechnungen basieren meist auf der Dichtefunktionaltheorie (DFT) und ihren Näherungen, wie zum Beispiel die lokale Spindichtenäherung. Zugänglich sind somit Grundzustandseigenschaften wie Zustandsdichte, Bandstruktur, magnetisches Moment und magnetische Anisotropie. Letztere sind in der Regel Experimenten nicht direkt zu entnehmen, sondern müssen aus den aufgenommenen Spektren abgeleitet werden: die Informationen werden quasi in den Spektren kodiert. Der Vergleich von theoretisch berechneten mit experimentell gemessenen Größen ist demnach *indirekt*. Diese Lücke lässt sich allerdings schließen — oder zumindest verringern —, wenn die Theorie dahingehend erweitert wird, dass Spektren auf der Grundlage der verlässlichen DFT berechnet werden. Somit wird ein *direkter* Vergleich der Messgrößen ermöglicht. Die Grundzustandsrechnungen der DFT werden also für angeregte Systeme erweitert und erlauben daher Aussagen darüber, wie sich Grundzustandsgrößen in der jeweiligen Spektroskopie widerspiegeln. Als Beispiel dienen in dieser Arbeit *Quantum–size*-Effekte in der Photoemission von dünnen Filmen und die Temperaturabhängigkeit der Photoemission von magnetischen Filmen.

Der obige Aspekt ist insbesondere dann wichtig, wenn die Messung selbst die interessierende Größe signifikant verändert. Wichtige Beispiele für diese fundamentale Einschränkung des Messprozesses beruhen auf der Spin–Bahn-Kopplung. So erzeugt letztere in der Photoelektronenspektroskopie spinpolarisierte Photoelektronen, auch wenn die Grundzustandselektronen nicht spinpolarisiert sind. Der naive Schluss von der Spinpolarisation der Photoelektronen auf die der Grundzustandselektronen führt offensichtlich in die Irre. Dieser SBK-Effekt ist insbesondere bei der Untersuchung von magnetischen Systemen mittels spinaufgelöster Photoemission zu beachten.

Das Vorhergehende unterstreicht, dass der theoretischen Berechnung von Messgrößen eine große Bedeutung zukommt. Weiterhin ist zu bemerken, dass der erwähnte SBK-Effekt die interessierende Observable nicht nur verschleiert, sondern selbst durch seine Ausnutzung zu weitergehenden Erkenntnissen führen kann. Als Beispiel mag hier der Magnetische Dichroismus (MD) in der spinintegrierten Photoemission dienen. Da, wie man theoretisch zeigen kann, der MD dann groß sein sollte, wenn elektronische Zustände aufgrund der SBK miteinander hybridisieren, lassen sich mit seiner Hilfe Bandstrukturen von Ferromagneten detailliert untersuchen. Diese Genauigkeit ist mit konventioneller, d. h. nichtdichroischer, Photoemission nur schwer zu erreichen.

Wurde als prominentes Beispiel die Photoemission für eine Spektroskopie angeführt, in der die orbitalen Freiheitsgrade und die Spinfreiheitsgrade der Elektronen eng miteinander verknüpft sind, so mag der spinabhängige Transport von Elektronen dazu dienen, den Einfluss des Spinfreiheitsgrades auf eine Observable (hier: des elektrischen Stroms durch die Probe) zu illustrieren. Denn in diesem Falle ist die Kopplung der beiden elektronischen Freiheitsgrade von minderer Bedeutung. Ein weiterer Unterschied zur Photoelektronenspektroskopie besteht darin, dass diese meist zur Untersuchung von paradigmatischen Systemen herangezogen wird, beispielsweise von Oberflächen und dünnen Filmen, und eher auf deren inhärente Eigenschaften abzielt. Im Gegensatz dazu befasst sich der spinabhängige Transport mit zusammengesetzten Systemen, wie zum Beispiel Tunnelkontakten, und weist somit von der Grundlagenforschung in Richtung der Angewandten Physik. Auch werden für das System charakteristische Observable untersucht, die mit dessen jeweiliger Realisierung (Probe) variieren können. Um den Unterschied zu verdeutlichen: die elektrische Leitfähigkeit ist eine Materialgröße, der Leitwert hingegen eine Systemgröße.

Zur Berechnung der elektronischen Struktur von Festkörpern existiert eine Vielzahl diverser Methoden, die oftmals für bestimmte Systeme und Fragestellungen besonders geeignet erscheinen. Neben der Genauigkeit und der numerischen Effizienz erlangt die Flexibilität der Verfahren zunehmende Bedeutung, insbesondere in dem Maße, wie die zu untersuchenden Systeme komplexer werden. Eine Methode ist in dieser Hinsicht besonders vielversprechend: die KKR-Methode [Korringa–Kohn–Rostoker (KKR)]. Diese basiert auf der Vielfachstreutheorie (VST) und ist durch die Trennung von geometrischer und elektronischer Information gekennzeichnet. Die einzelnen Streuzentren, aus denen die Probe zusammengesetzt gedacht ist, bewahren einerseits die geometrische Information (Ort), andererseits die elektronische Information (Streumatrix) und bestimmen in ihrer Gesamtheit die Eigenschaften des Systems. Das hohe Maß an Flexibilität wird dadurch erreicht, indem mit Hilfe der Dyson-Gleichung das zu untersuchende System mit einem einfacher zu behandelnden Referenzsystem verknüpft wird. Daher sind der KKR-Methode kaum Grenzen in Bezug auf die geometrische Anordnung der Streuzentren gesetzt.

Neben der gewöhnlichen KKR, die die Streuzentren als fundamentales Objekt verwendet, hat sich die LKKR-Methode [*Layer*-KKR (LKKR)] für Systeme mit Schichtstruktur etabliert. Hier dienen Schichten von Streuzentren als Basisobjekt, was einerseits Vorteile gegenüber der KKR bietet, andererseits die Flexibilität geringfügig einschränkt. Die überwiegende Anzahl von Resultaten, die in der vorliegenden Arbeit präsentiert werden, wurden mit dem Computerprogrammpaket `omni` berechnet, in dem eine relativistische Version der LKKR implementiert ist. Die Spin–Bahn-Kopplung ist somit vollständig berücksichtigt (Dirac-Gleichung). Da das Hauptaugenmerk des Programmpakets auf der Berechnung von Elektronenspektroskopien liegt, werden die Potentiale der Streuzentren daher meist mit Hilfe anderer Computerprogramme selbstkonsistent berechnet, ohne dass Abstriche an der Genauigkeit der Ergebnisse hingenommen werden müssen. Als sehr ergiebige Quelle ist hier das KKR-Programm von Arthur Ernst hervorzuheben.

Die vorliegende Arbeit ist wie folgt aufgebaut. Nach einer Einführung in die Vielfachstreutheorie (Kap. 2) wird der Einfluss der Spin–Bahn-Kopplung auf die elektronische und magnetische Struktur von Festkörpern exemplarisch behandelt (Kap. 3). Mit Aspekten der Photoelektronenspektroskopie befasst sich Kapitel 4, wobei das Hauptaugenmerk auf Spineffekten liegt. Im abschließenden Kapitel 5 werden Beispiele für spinabhängigen ballistischen Transport von Elektronen vorgestellt. Zuletzt wird eine Methode zur Untersuchung dünner magnetischer Filme vorgestellt, die die spinaufgelöste Photoemission und den spinabhängigen Transport miteinander verbindet (Abschn. 5.5). Im Anhang sind Publikationen dokumentiert, in denen die in den vorangegangenen Kapiteln skizzierten Beispiele umfassender diskutiert sind.

# 2. Elemente der Vielfachstreutheorie

Die meisten theoretischen Resultate, die in dieser Arbeit dargestellt und dokumentiert sind, wurden durch *Ab–initio*-Rechnungen im Rahmen der Vielfachstreutheorie (VST) gewonnen. Daher werden in diesem Kapitel deren Grundlagen skizziert, zum ersten die Dichtefunktionaltheorie (DFT), zum zweiten die Korringa–Kohn–Rostoker-Methode (S. 6ff).

## 2.1. Grundlagen der Dichtefunktionaltheorie

Wegen der großen Zahl von Elektronen in ausgedehnten Systemen, wie große Moleküle oder Festkörper, kann die Wechselwirkung der Elektronen miteinander nicht exakt behandelt werden. Man ist deshalb auf Näherungen angewiesen. Eine der erfolgreichsten ist die DFT in der lokalen Dichtenäherung (*Local density approximation*, LDA).[1] Moderne Rechnungen zur elektronischen Struktur basieren auf dieser Näherung oder einer ihrer Erweiterungen.

**Die Hohenberg–Kohn-Theoreme.** Der Hamilton-Operator $H$ eines $N$-Teilchensystems lautet $H = T + U + V$, worin $T$ der Operator der kinetischen Energie, $U$ die Coulomb-Wechselwirkung zwischen den Elektronen und $V$ das externe Potential bedeuten. Die Gesamtenergie ist dann durch den Erwartungswert $E = \langle\Psi|H|\Psi\rangle$ bezüglich der $N$-Teilchenwellenfunktion $|\Psi\rangle$ gegeben. Aus Letzterer lässt sich ein Dichteoperator gemäß $N(\boldsymbol{r}) = \Psi^\star(\boldsymbol{r})\Psi(\boldsymbol{r})$ konstruieren. Die Hohenberg–Kohn-Theoreme besagen, dass *(i)* der Grundzustand $|\Phi\rangle$ des $N$-Elektronensystems ein Funktional der Dichte $n(\boldsymbol{r}) = \langle\Phi|N(\boldsymbol{r})|\Phi\rangle$ ist, $|\Phi[n]\rangle$, und dass *(ii)* das Energiefunktional $E[n]$ für die Grundzustandsdichte minimal ist.

Um magnetische Systeme beschreiben zu können, wurde die Spindichtefunktionaltheorie entwickelt [2, 3]. Unter der Annahme, dass das externe Potential nur an die Spinfreiheitsgrade koppelt, tritt der zusätzliche Beitrag $\int \boldsymbol{B}(\boldsymbol{r}) \cdot \boldsymbol{m}(\boldsymbol{r})\,\mathrm{d}r^3$ im Hamilton-Operator auf. Hier ist

$$\boldsymbol{m}(\boldsymbol{r}) = \sum_{\tau\tau'} \langle\Phi|\Psi^\star_\tau(\boldsymbol{r})\boldsymbol{\sigma}_{\tau\tau'}\Psi_{\tau'}(\boldsymbol{r})|\Phi\rangle\,, \quad \tau,\tau' = \pm, \tag{2.1}$$

die Spindichte, mit dem Vektor $\boldsymbol{\sigma}$ der Pauli-Matrizen. Die Summe läuft über die Spinindizes $\tau$. Die Hohenberg–Kohn-Theoreme besagen dann, dass der Grundzustand ein Funktional der Dichten $n(\boldsymbol{r})$ und $\boldsymbol{m}(\boldsymbol{r})$ ist. Die Gesamtenergie $E[n,m]$ ist minimal für die Grundzustandsdichten. Da das externe Potential nur an den Spin koppelt, wird orbitaler Magnetismus nicht in der Spindichtefunktionaltheorie beschrieben. Dieses ist jedoch innerhalb der Stromdichtefunktionaltheorie möglich [4, 5].

**Die Kohn–Sham-Gleichungen.** Nach der allgemeinen Formulierung wird nun eine Lösung des Problems entwickelt, also eine „Rechenvorschrift“. Diese führt zu effektiven Einteilchengleichungen, den Kohn–Sham-Gleichungen. Das „universale“ Hohenberg–Kohn-Funktional $F[n] = T[n] + E_\mathrm{H}[n] + E_\mathrm{xc}[n]$ wird in die Coulomb-Wechselwirkung $U(\boldsymbol{r},\boldsymbol{r}') = 1/|\boldsymbol{r}-\boldsymbol{r}'|$ (Hartree-Beitrag),

$$E_\mathrm{H}[n] = \frac{1}{2}\int\int n(\boldsymbol{r})\,U(\boldsymbol{r},\boldsymbol{r}')\,n(\boldsymbol{r}')\mathrm{d}r^3\mathrm{d}r'^3, \tag{2.2}$$

und in die kinetische Energie $T[n]$ des wechselwirkungsfreien Elektronengases mit Dichte $n(\boldsymbol{r})$ zerlegt: $F[n] = \langle\Phi[n]|T + U|\Phi[n]\rangle$. Der Restbeitrag $E_\mathrm{xc}[n]$ subsumiert die Austausch- und die

---

[1] Englische Abkürzungen werden an Stelle deutscher verwendet, wenn sie die gebräuchlicheren sind.

Korrelationsenergie. Die Grundzustandsdichte $n$ minimiert die Gesamtenergie $E[n] = F[n] + \int V(\boldsymbol{r})\, n(\boldsymbol{r})\, \mathrm{d}r^3$. Die Erhaltung der Teilchenzahl wird mittels eines Lagrange-Parameters $\mu = \delta T[n]/\delta n(\boldsymbol{r}) + V_{\text{eff}}[n(\boldsymbol{r})]$ garantiert, der mit dem chemischen Potential identifiziert wird. Die Definition des effektiven Potential

$$V_{\text{eff}}(\boldsymbol{r}) = V_{\text{H}}[n(\boldsymbol{r})] + V_{\text{xc}}[n(\boldsymbol{r})] + V(\boldsymbol{r}) \tag{2.3}$$

und die Einführung einer orthonormalen Einteilchenbasis $\{|\Phi_i\rangle\}$ resultiert im Gleichungssystem

$$0 = \{T + V_{\text{eff}}[n] - \epsilon_i\}\, |\Phi_i\rangle\,, \tag{2.4a}$$

$$n(\boldsymbol{r}) = \sum_{i=1}^{N} |\, \langle \boldsymbol{r}|\Phi_i\rangle\, |^2, \tag{2.4b}$$

welches selbstkonsistent zu lösen ist ($V_{\text{xc}}[n] = \delta E_{\text{xc}}[n]/\delta n$). Vernachlässigt man in den Kohn–Sham-Gleichungen (2.4) das Austausch-Korrelationspotential $V_{\text{xc}}$, so sind sie mit den Hartree-Gleichungen identisch, und die Einteilchenzustände erzeugen die Slater-Determinanten.

Bei der Generalisierung auf magnetische Systeme nimmt man an, dass das externe Potential spinabhängig ist. Mit der $z$-Achse als Spinquantisierungsachse braucht nur die $z$-Projektion der spinabhängigen Dichten $n^{\pm}(\boldsymbol{r})$ betrachtet zu werden. Die Elektronendichte $n = n^+ + n^-$ und die Spindichte $m = n^+ - n^-$ treten als unabhängige Variable auf, und anstelle eines einzigen Satzes von Kohn–Sham-Gleichungen liegt nun ein Satz für jede Spinprojektion $\tau$ vor: $0 = \{T + V^{\tau}_{\text{eff}}[n] - \epsilon^{\tau}_i\}\, |\Phi^{\tau}_i\rangle$, $\tau = \pm$. Gewöhnlich führt man ein spingemitteltes Austausch-Korrelationspotential $V_{\text{xc}}[n^+, n^-] = \delta E_{\text{xc}}[n, m]/\delta n$ und ein „magnetisches“ Austausch-Korrelationspotential $B_{\text{xc}}[n^+, n^-] = \delta E_{\text{xc}}[n, m]/\delta m$ ein. Mit diesen lässt sich das effektive Einteilchenpotential als

$$V^{\tau}_{\text{eff}}(\boldsymbol{r}) = V_{\text{H}}[n(\boldsymbol{r})] + V_{\text{xc}}[n(\boldsymbol{r}), m(\boldsymbol{r})] + \tau\{B(\boldsymbol{r}) + B_{\text{xc}}[n(\boldsymbol{r}), m(\boldsymbol{r})]\} \tag{2.5}$$

schreiben.

Für eine relativistische Beschreibung wird in Analogie zum Vorherstehenden angenommen, dass das wechselwirkende Elektronensystem auf ein wechselwirkungsfreies abgebildet werden kann, welches die Grundzustandsdichte reproduziert. Vernachlässigt man den orbitalabhängigen Beitrag zur Stromdichte, ist die Austausch-Korrelationsenergie ein Funktional der Elektronen- und der Spindichte, wie im nichtrelativistischen Fall auch. Zu lösen sind somit die Dirac–Kohn–Sham-Gleichungen

$$\left[c\boldsymbol{\alpha} \cdot \boldsymbol{p} + \beta c^2 + V_{\text{eff}} - \epsilon_i\right] |\Phi_i\rangle = 0, \tag{2.6}$$

mit $V_{\text{eff}} = V + V_{\text{H}} + V_{\text{xc}} + \beta\boldsymbol{\sigma} \cdot (\boldsymbol{B} + \boldsymbol{B}_{\text{xc}})$. Die Matrizen

$$\boldsymbol{\alpha} = \begin{pmatrix} 0 & \boldsymbol{\sigma} \\ \boldsymbol{\sigma} & 0 \end{pmatrix} \text{ und } \beta = \begin{pmatrix} 1 & 0 \\ 0 & -1 \end{pmatrix} \tag{2.7}$$

lassen sich durch die Pauli-Matrizen

$$\sigma_x = \begin{pmatrix} 0 & 1 \\ 1 & 0 \end{pmatrix}, \sigma_y = \begin{pmatrix} 0 & -\mathrm{i} \\ \mathrm{i} & 0 \end{pmatrix} \text{ und } \sigma_z = \begin{pmatrix} 1 & 0 \\ 0 & -1 \end{pmatrix} \tag{2.8}$$

ausdrücken.

**Lokale Näherungen für das Austausch-Korrelationsfunktional.** Weil das Austausch-Korrelationsfunktional nicht bekannt ist, muss man Näherungen finden, die für bestimmte Modellsysteme exakt und außerdem für Rechnungen praktikabel sind. Die einfachste Näherung für spinpolarisierte Systeme ist die lokale Spindichtenäherung [*Local spin-density approximation* (LSDA)]. Im Falle einer geringfügig variierenden Dichte ist eine naheliegende Näherung, das Austausch-Korrelationsfunktional des homogenen Elektronengases zu verwenden. Dazu wertet man die Dichte am aktuellen Aufpunkt $\boldsymbol{r}$ aus und berechnet für diese das Austausch-Korrelationspotential.

Während der Austauschbeitrag zu $E_{\mathrm{xc}}$ des homogenen Elektronengases bekannt ist, muss der Korrelationsbeitrag numerisch für Modellsysteme ausgewertet und parametrisiert werden. Populär sind Parametrisierungen von von-Barth und Hedin [2], Vosko, Wilk und Nusair [7] sowie von Perdew und Wang [8]. Über die LSDA hinaus gehen die *Generalized gradient approximation* (GGA) [9] und die *Self-interaction correction* (SIC). Während diese Erweiterungen parameterfrei bleiben, führt man in der LDA+$U$ die Coulomb-Energie $U$ auf den einzelnen Gitterplätzen als frei zu variierende Größe ein. Diese Abbildung auf ein Hubbard-Modell ist also im strikten Sinne nicht mehr *ab initio*. Allerdings ist meist nur ein Wert von $U$ mit diversen physikalischen Größen verträglich.

## 2.2. Elemente der Korringa–Kohn–Rostoker-Methode

Die Vielfachstreutheorie, wie sie im Folgenden skizziert wird, kann auf die Arbeiten von Korringa [10] sowie von Kohn und Rostoker [11], die sie für dreidimensionale Systeme formulierten, zurückgeführt werden [12]. Die Methode wird daher auch als KKR bezeichnet (nach Korringa, Kohn und Rostoker). Eine speziell an Oberflächen und planare Grenzflächen angepasste Formulierung ist als *Layer*-KKR (LKKR) bekannt. Hier ist das wesentliche Objekt eine Schicht von Streupotentialen, im Gegensatz zu einzelnen Streuzentren in der „dreidimensionalen" KKR [13]. In der vorliegenden Arbeit kann nur ein kurzer Überblick der VST gegeben werden. Umfassende Darstellungen finden sich bei Mertig *et al.* [14], Weinberger [15] und Gonis [16].

Im Gegensatz zu einer kinematischen Streutheorie umfasst eine dynamische Theorie die Vielfachstreuung der Elektronen innerhalb des Festkörpers [17]. Die Hauptaufgabe einer VST besteht darin, die Streueigenschaften des Gesamtsystems zu bestimmen. In der LKKR-Methode wird dieses durch sukzessive Berechnung der Streueigenschaften der Konstituenten erreicht: beginnend beim einzelnen Streupotential, einer einzelnen Schicht von Streupotentialen, Schichtenstapeln und schließlich vom gesamten System. Diese Schritt-für-Schritt-Prozedur gewährleistet somit ein hohes Maß an Flexibilität in der räumlichen Anordnung der streuenden Potentiale. Damit einhergehend ist die VST, insbesondere in der LKKR-Formulierung, durch einen Darstellungswechsel gekennzeichnet (Drehimpulsdarstellung ↔ ebene Wellen).

### Streuung an einem Gitterplatz

Der erste Schritt in einer VST-Rechnung ist die Bestimmung der Streueigenschaften der einzelnen, auf Gitterplätzen lokalisierten Potentiale $V_i$. Das Gesamtpotential $V$ des Systems wird als Summe von Einzelpotentialen angenommen, $V(\boldsymbol{r}) = \sum_i V_i(\boldsymbol{r} - \boldsymbol{R}_i)$. Gewöhnlich besitzen die Potentiale sphärische Symmetrie und haben MT-Form [*Muffin tin* (MT)],

$$V_i(\boldsymbol{r}_i) = \begin{cases} V_i(r) & r \leq r_{\mathrm{mt}i} \\ 0 & \text{sonst} \end{cases}, \tag{2.9}$$

wobei die MT-Kugeln mit Radius $r_{\mathrm{mt}i}$ disjunkt sind. Ferner nimmt man reguläre Potentiale an [$\lim_{r\to 0} r^2 V(r) = 0$; [15]]. Selbstverständlich existieren Verallgemeinerungen für nichtsphärische sowie für raumfüllende Potentiale [18, 19].

Prinzipiell verfährt man bei der relativistischen Behandlung der Gitterplatzstreuung wie im nichtrelativistischen Fall. Die Dirac-Gleichung für ein Streupotential mit effektivem Magnetfeld $\boldsymbol{B}(\boldsymbol{r})$ lautet [Gl. (2.6)]

$$\left[c\boldsymbol{\alpha} \cdot \boldsymbol{p} + \beta c^2 + v(\boldsymbol{r}) + \beta \boldsymbol{\sigma} \cdot \boldsymbol{B}(\boldsymbol{r})\right] \Psi(\boldsymbol{r}) = E \Psi(\boldsymbol{r}). \tag{2.10}$$

Die Streulösungen werden als

$$\langle \boldsymbol{r} | \Psi \rangle = \frac{1}{r} \sum_{\Lambda} \begin{pmatrix} f_{\Lambda}(r) \, \langle \widehat{\boldsymbol{r}} | \chi_{\Lambda} \rangle \\ \mathrm{i} g_{\Lambda}(r) \, \langle \widehat{\boldsymbol{r}} | \chi_{\overline{\Lambda}} \rangle \end{pmatrix} = \sum_{\Lambda} \begin{pmatrix} \Psi_{\Lambda}(r) \, \langle \widehat{\boldsymbol{r}} | \chi_{\Lambda} \rangle \\ \mathrm{i} \Phi_{\Lambda}(r) \, \langle \widehat{\boldsymbol{r}} | \chi_{\overline{\Lambda}} \rangle \end{pmatrix}, \tag{2.11}$$

angesetzt, mit $\Psi_\Lambda(r) = f_\Lambda(r)/r$ und $\Phi_\Lambda(r) = g_\Lambda(r)/r$. Die relativistischen „Partner" $\chi_\kappa^\mu$ der Kugelflächenfunktionen erhält man durch Kopplung von $\boldsymbol{l}$ und $\boldsymbol{s}$ zum Gesamtdrehimpuls $\boldsymbol{j} = \boldsymbol{l} + \boldsymbol{s}$ [20],

$$\chi_\kappa^\mu = \sum_{\tau=\pm 1/2} C(l\frac{1}{2}j; \mu - \tau, \tau) Y_l^{\mu-\tau} \chi^\tau. \tag{2.12}$$

Diese sind Eigenfunktionen von $\boldsymbol{\sigma}\cdot\boldsymbol{l}+1$ zum Eigenwert $\kappa = (j+\frac{1}{2})^2 - l(l+1)$. Die Koeffizienten $C$ in Gl. (2.12) sind die bekannten Clebsch–Gordan-Koeffizienten. Für $j = l+\frac{1}{2}$ ($j = l-\frac{1}{2}$) ist $\kappa = -l-1$ ($\kappa = l$). Wenn möglich, werden die Drehimpulsquantenzahlen zusammengefasst, $L = (l, m)$ im nichtrelativistischen und $\Lambda = (\kappa, \mu)$ im relativistischen Fall. Ferner werden $S_\kappa = \kappa / \mid \kappa \mid$, $\overline{l} = l - S_\kappa$ sowie $\overline{\Lambda} = (-\kappa, \mu)$ definiert.

Wird die $z$-Achse als Spinquantisierungsachse gewählt, so resultiert daraus das Gleichungssystem

$$c\partial_r f_\Lambda = -c\frac{\kappa}{r} f_\Lambda + (E + c^2 - v) g_\Lambda + B \sum_{\Lambda'} \langle \chi_{\overline{\Lambda}} | \sigma_z | \chi_{\overline{\Lambda'}} \rangle \, g_{\Lambda'}, \tag{2.13a}$$

$$c\partial_r g_\Lambda = c\frac{\kappa}{r} g_\Lambda - (E - c^2 - v) f_\Lambda + B \sum_{\Lambda'} \langle \chi_\Lambda | \sigma_z | \chi_{\Lambda'} \rangle \, f_{\Lambda'}. \tag{2.13b}$$

Im nichtmagnetischen Fall ($B = 0$) hängen $f_\Lambda$ und $g_\Lambda$ nicht von $\mu$, sondern nur von $\kappa$ ab.

Die Matrixelemente von $\sigma_z$ in Gl. (2.13) koppeln die Lösungen zu $l$ und $l + 2$. Ackermann hat gezeigt, dass diese aufgrund der fehlenden Singularität von $B(r)$ vernachlässigt werden dürfen [21]. Somit erhält man ein System von vier gekoppelten Differentialgleichungen erster Ordnung, in dem Partialwellen mit Drehimpulsen $\kappa$ und $-\kappa - 1$ gekoppelt sind.

Die regulären und irregulären Lösungen verhalten sich asymptotisch wie

$$\langle \boldsymbol{r} | \Psi_\Lambda^{\mathrm{reg}} \rangle \to \sum_{\Lambda'} \begin{pmatrix} [j_l(kr)\delta_{\Lambda'\Lambda} + h_{l'}^{+}(kr) t_{\Lambda'\Lambda}] \, \langle \widehat{\boldsymbol{r}} | \chi_{\Lambda'} \rangle \\ \mathrm{i}\; S_{\kappa'} \frac{ck}{E+c^2} [j_{\overline{l}}(kr)\delta_{\Lambda'\Lambda} + h_{\overline{l'}}^{\pm}(kr) t_{\Lambda'\Lambda}] \, \langle \widehat{\boldsymbol{r}} | \chi_{\overline{\Lambda'}} \rangle \end{pmatrix}, \tag{2.14a}$$

$$\left\langle \boldsymbol{r} \middle| \Psi_\Lambda^{\mathrm{irr}} \right\rangle \to \sum_{\Lambda'} \begin{pmatrix} h_{l'}^{+}(kr) \, \langle \widehat{\boldsymbol{r}} | \chi_{\Lambda'} \rangle \\ \mathrm{i}\; S_{\kappa'} \frac{ck}{E+c^2} h_{\overline{l'}}^{\pm}(kr) \, \langle \widehat{\boldsymbol{r}} | \chi_{\overline{\Lambda'}} \rangle \end{pmatrix} \delta_{\Lambda'\Lambda}, \tag{2.14b}$$

für $r \to \infty$. Hier bezeichnen $j_l$ und $h_l^\pm$ sphärische Bessel- bzw. Hankel-Funktionen. Die einfallende Partialwelle ist durch

$$\langle \boldsymbol{r} | J_\Lambda \rangle = \begin{pmatrix} j_l(kr) \, \langle \widehat{\boldsymbol{r}} | \chi_\Lambda \rangle \\ \mathrm{i}\; S_\kappa \frac{ck}{E+c^2} j_{\overline{l}}(kr) \, \langle \widehat{\boldsymbol{r}} | \chi_{\overline{\Lambda}} \rangle \end{pmatrix} \tag{2.15}$$

gegeben. Mit

$$\left\langle \boldsymbol{r} \middle| H_\Lambda^{(\pm)} \right\rangle = \begin{pmatrix} h_l^\pm(kr) \, \langle \widehat{\boldsymbol{r}} | \chi_\Lambda \rangle \\ \mathrm{i}\; S_\kappa \frac{ck}{E+c^2} h_{\overline{l}}^\pm(kr) \, \langle \widehat{\boldsymbol{r}} | \chi_{\overline{\Lambda}} \rangle \end{pmatrix} \tag{2.16}$$

ergibt sich für die Gesamtwellenfunktion $\langle \boldsymbol{r} | \Psi \rangle = \sum_\Lambda (A_\Lambda \langle \boldsymbol{r} | J_\Lambda \rangle + B_\Lambda \left\langle \boldsymbol{r} \middle| H_\Lambda^{(+)} \right\rangle)$, wobei die Koeffizienten $A_\Lambda$ (einfallend) und $B_\Lambda$ (auslaufend) durch die Gitterplatzstreumatrix $t$ miteinander verknüpft sind, $B_\Lambda = \sum_{\Lambda'} t_{\Lambda\Lambda'} A_{\Lambda'}$. Letztere kann entweder durch stetig-differenzierbares Anpassen der Lösungen am MT-Radius oder mittels Wronski-Determinanten bestimmt werden [15, 22]. Für sphärische Potentiale sind nur diejenigen Elemente von $t$ von Null verschieden, die zu gekoppelten Partialwellen gehören; also $t_{\Lambda\Lambda'} = 0$ falls $\kappa' \notin \{\kappa, -\kappa - 1\}$ oder $\mu' \neq \mu$. Im nichtmagnetischen Fall ist die $t$-Matrix diagonal und hängt nur von $\kappa$ ab.

Viele Effekte in der Elektronenspektroskopie beruhen auf dem gleichzeitigen Vorhandensein von Magnetismus und Spin–Bahn-Kopplung. In der numerischen Problembehandlung ist es daher wünschenswert, beide Faktoren in ihrer Stärke variieren zu können. In nichtrelativistischen Theorien lässt sich die entsprechende Kopplungskonstante leicht skalieren. In relativistischen Theorien erhöht man die als Parameter auftretende Lichtgeschwindigkeit $c$, mit dem unerwünschten Nebeneffekt, dass alle relativistischen Effekte (Massenterm, Darwin-Term) ebenfalls verändert werden. Ausgehend von der skalar-relativistischen Näherung [23–25], lässt sich allerdings eine Methode entwickeln, die zwischen der relativistischen Dirac-Gleichung und der skalarrelativistischen Schrödinger-Gleichung interpoliert und nur die SBK skaliert [26–28].

### Streuung an Schichten

**Streuung an einer einzelnen Schicht.** Nachdem die Streuung an einem einzelnen Potential behandelt wurde, werden die Streueigenschaften einer einzelnen Schicht, dem wesentlichen Objekt der *Layer*–KKR-Methode, berechnet.

Für jeden Strahl,[2] der durch den zweidimensionalen reziproken Gittervektor $\boldsymbol{g}$ charakterisiert ist, definiert man den Wellenvektor

$$\boldsymbol{k}_{\boldsymbol{g}}^{\pm} = \begin{pmatrix} \boldsymbol{k}_{\parallel} + \boldsymbol{g} \\ \pm\sqrt{k^2 - (\boldsymbol{k}_{\parallel} + \boldsymbol{g})^2} \end{pmatrix} . \tag{2.17}$$

Das Vorzeichen $+$ $(-)$ steht für ebene Wellen, die entlang der $+z$-Richtung $(-z$-Richtung) propagieren oder gedämpft sind. Die auf die Schicht einfallenden $(\Psi_{\text{inc}})$ und von der Schicht auslaufenden $(\Psi_{\text{out}})$ Wellenfelder werden damit als

$$\Psi_{\text{inc}}(\boldsymbol{r}) = \sum_{\boldsymbol{g}\tau} \left[ u_{\boldsymbol{g}\tau}^{+} \exp(\mathrm{i}\boldsymbol{k}_{\boldsymbol{g}}^{+} \cdot \boldsymbol{r}) + u_{\boldsymbol{g}\tau}^{-} \exp(\mathrm{i}\boldsymbol{k}_{\boldsymbol{g}}^{-} \cdot \boldsymbol{r}) \right] \chi^{\tau}, \tag{2.18a}$$

$$\Psi_{\text{out}}(\boldsymbol{r}) = \sum_{\boldsymbol{g}\tau} \left[ v_{\boldsymbol{g}\tau}^{+} \exp(\mathrm{i}\boldsymbol{k}_{\boldsymbol{g}}^{+} \cdot \boldsymbol{r}) + v_{\boldsymbol{g}\tau}^{-} \exp(\mathrm{i}\boldsymbol{k}_{\boldsymbol{g}}^{-} \cdot \boldsymbol{r}) \right] \chi^{\tau} \tag{2.18b}$$

geschrieben. Fasst man die Koeffizienten $u_{\boldsymbol{g}\tau}^{\pm}$ und $v_{\boldsymbol{g}\tau}^{\pm}$ in Spaltenvektoren zusammen, so ist deren Beziehung untereinander durch die Streumatrix $M$ der Schicht gegeben (Abb. 2.1),

$$\begin{pmatrix} \boldsymbol{v}^{+} \\ \boldsymbol{v}^{-} \end{pmatrix} = \begin{pmatrix} M^{++} & M^{+-} \\ M^{-+} & M^{--} \end{pmatrix} \begin{pmatrix} \boldsymbol{u}^{+} \\ \boldsymbol{u}^{-} \end{pmatrix} . \tag{2.19}$$

Um $M$ zu berechnen, werden alle Beiträge von sphärischen Streuwellen addiert, die am Referenzgitterplatz einfallen. Dieses Wellenfeld ist also durch das von außerhalb der Schicht einfallende und das innerhalb der Schicht gestreute Feld gegeben, da die einfallende Welle mehrfach an jedem Gitterplatz der Schicht gestreut wird. Das an einem Gitterplatz $\boldsymbol{R}_j$ einfallende Feld ist mit dem zugehörigen von $\boldsymbol{R}_j$ auslaufenden durch die $t$-Matrix verknüpft. Letzteres kann anschließend vermöge sogenannter Strukturkonstanten in ein am Referenzplatz einlaufendes umgerechnet werden [16, 29]. Nach Rücktransformation der sphärischen in ebene Wellen sind die einzelnen Blöcke der $M$-Matrix schließlich bestimmt.

**Streuung an einer Oberflächenbarriere.** Eine Oberflächenbarriere, also der Übergang des Potentials im Inneren des Festkörpers zum Vakuum, lässt sich einerseits durch MT-Potentiale beschreiben. Andererseits werden in der Spektroskopie, insbesondere in der LEED und in der Photoemission, stetige Potentialübergänge verwendet. Diese „weichen“ Barrierenformen erfüllen in der Regel die Asymptotik der klassischen Bildladung an einer Metalloberfläche, $V(z) \approx 1/(4z)$ [30].

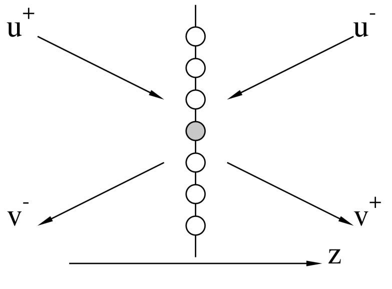

**Abbildung 2.1.** Streuung an einer einzelnen Schicht von Streuzentren (schematisch). Das Referenzstreuzentrum ist durch den grauen Kreis repräsentiert. Einfallende (auslaufende) Strahlen $u^{\pm}$ $(v^{\pm})$ werden nach ihrer Propagationsrichtung $(\pm z)$ indiziert.

---

[2] Die Bezeichnungen „Strahl“ und „ebene Welle“ werden synonym verwendet. Als historische Begründung kann die Anwendung der LKKR-Methode zur Berechnung von LEED-Spektren herangezogen werden.

Die JJJ-Barriere interpoliert zwischen dem Bildladungspotential und dem konstanten inneren Potential $V_0$ des Festkörpers (*Muffin-tin zero*) und wurde von Jones, Jennings und Jepsen [31] eingeführt (daher der Name JJJ). Neben der einfachen Integration der Schrödinger-Gleichung in der Oberflächenregion mittels numerischer Standardverfahren wurden fortgeschrittene Methoden angewendet und entwickelt, um das Oberflächenpotential, insbesondere seine Korrugation, zu behandeln [32–35].

**Streuung an Schichtenstapeln.** Sind die Streueigenschaften aller Schichten im System bekannt, lassen sich mit Hilfe einer geringen Zahl von Basisalgorithmen diejenigen einer beliebigen Stapelung von Schichten berechnen, was die Flexibilität der VST unterstreicht. Die einzig essentielle Bedingung ist die Translationsinvarianz innerhalb der Schichten: alle Schichten des Systems müssen die gleiche Periodizität besitzen.

Die $M$-Matrix einer Doppelschicht erhält man zum Beipiel, indem über alle Vielfachstreuereignisse summiert wird, die durch Reflexion an jeder der Schichten auftreten (*Layer stacking*, Abb. 2.2). Die Propagation zwischen den Schichten wird durch $P^{\pm}_{\boldsymbol{g}\tau,\boldsymbol{g}'\tau'} = \exp(\mathrm{i}\boldsymbol{k}^{\pm}_{\boldsymbol{g}} \cdot \boldsymbol{d})\, \delta_{\boldsymbol{g}\boldsymbol{g}'}\, \delta_{\tau\tau'}$ beschrieben, wobei der Translationsvektor $\boldsymbol{d}$ äquivalente Gitterplätze der Schichten $1$ und $2$ verbindet.

Die obige Prozedur ermöglicht es, die Reflexionsmatrix $R^{-+}_{\mathrm{bulk}}$ des Volumens, also eines unendlich oft wiederholten Arrangements von identischen Schichten oder von identischen Schichtenstapeln, zu berechnen (*Layer doubling*). Desweiteren kann die komplexe Bandstruktur $k_{\perp}(E, \boldsymbol{k}_{\|})$ aus der Streumatrix mit Hilfe der Bloch-Wellenmethode gewonnen werden. Dabei geht man von identischen Schichten $1$ und $2$ aus. Die ein- und auslaufenden ebenen Wellen auf der linken Seite von $1$ und von $2$ unterscheiden sich gemäß dem Floquet'schen Theorem nur durch einen Faktor $\lambda$: $\boldsymbol{u}^{-} = \lambda \boldsymbol{v}^{-}$ und $\boldsymbol{v}^{+} = \lambda \boldsymbol{u}^{+}$. Eine kurze Rechnung ergibt ein Standardeigenwertproblem der Form $Q\boldsymbol{c}_n = \lambda_n \boldsymbol{c}_n$, wobei die Blöcke der Matrix $Q$ sich aus der Streumatrix $M$ einer einzelnen Schicht berechnen lassen. Die Eigenwerte $\lambda_n$ sind im allgemeinen komplex, und $\boldsymbol{c}_n$ ist ein $(4\,N_{\boldsymbol{g}})$-Vektor und umfasst die $(2\,N_{\boldsymbol{g}})$-Vektoren $\boldsymbol{u}^{+}$ und $\boldsymbol{v}^{-}$ ($N_{\boldsymbol{g}}$ ist die Anzahl der in der numerischen Rechnung berücksichtigten Strahlen). Aus $\lambda_n = \exp(\mathrm{i}\boldsymbol{k}_n \cdot \boldsymbol{d})$ ergibt sich dann die komplexe Wellenzahl $k_{n,\perp}$ zu $k_{n,\perp} = -\mathrm{i}\left(\ln \lambda_n - \mathrm{i}\boldsymbol{k}_{\|} \cdot \boldsymbol{d}_{\|}\right)/d_{\perp}$. Die Reflexionsmatrix $R^{-+}_{\mathrm{bulk}}$ des Volumens lässt sich ebenfalls aus den Eigenvektoren erhalten.

Um die reflektierten Intensitäten in LEED zu berechnen, benötigt man die Reflexionsmatrix des gesamten halbunendlichen Systems, das sich aus den identischen Schichten des Volumens und den sich davon unterscheidenden oberflächennahen Schichten zusammensetzt. Diese Reflexionsmatrix kann schrittweise mittels der oben beschriebenen Algorithmen bestimmt werden.

### Green-Funktion und Streupfadoperator

In diesem Abschnitt werden die grundlegenden Eigenschaften der KKR-Green-Funktionen rekapituliert. Da die Energie $E$ komplex sein darf, und somit der Hamilton-Operator nicht mehr hermitesch ist, muss mit links- (Superskript L, $\left\langle \Psi^{\mathrm{L}} \right| H = E \left\langle \Psi^{\mathrm{L}} \right|$) und rechtsseitigen (Superskript R, $H \left| \Psi^{\mathrm{R}} \right\rangle = E \left| \Psi^{\mathrm{R}} \right\rangle$) Wellenfunktionen gearbeitet werden [36].

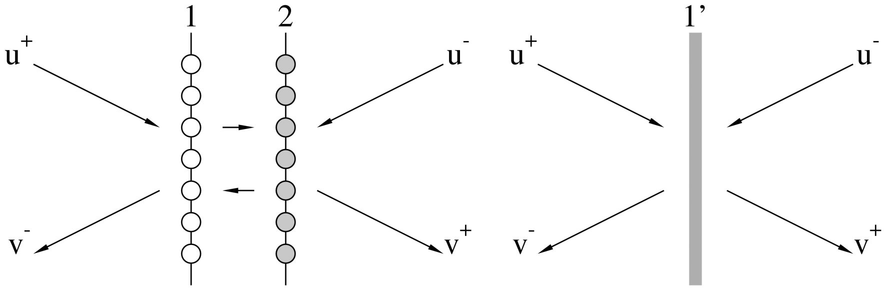

**Abbildung 2.2.** Streuung an einer Doppelschicht (schematisch). Der Stapel zweier Schichten (1 und 2, links) kann durch eine effektive Schicht (1′, rechts) ersetzt werden.

Analog zur vorgehend beschriebenen sukzessiven Berechnung der Streueigenschaften geht man bei der Berechnung der Green-Funktion (GF) des gesamten Systems vor. Zunächst wird die GF in Anwesenheit eines einzelnen Potentials $V$, die Gitterplatz-Green-Funktion

$$G_1^+(\boldsymbol{r},\boldsymbol{r}') = -\mathrm{i}k \sum_{\Lambda} \begin{cases} \left\langle \boldsymbol{r} \middle| J_\Lambda^{\mathrm{R}} \right\rangle \left\langle H_\Lambda^{\mathrm{L}(+)} \middle| \boldsymbol{r}' \right\rangle, & r < r' \\ \left\langle \boldsymbol{r} \middle| H_\Lambda^{\mathrm{R}(+)} \right\rangle \left\langle J_\Lambda^{\mathrm{L}} \middle| \boldsymbol{r}' \right\rangle, & r > r' \end{cases}, \tag{2.20}$$

berechnet [16]. Anschließend wird aus dem Gesamtsystem eine Schicht entfernt und deren GF $G_{\mathrm{EL}}^+$ bestimmt. Dabei werden die Randbedingungen, also die Bloch-Bedingung $G_{\mathrm{EL}}^+(\boldsymbol{r}_i + \boldsymbol{R}, \boldsymbol{r}_i') = \exp(\mathrm{i}\boldsymbol{k}_\parallel \cdot \boldsymbol{R})\, G_{\mathrm{EL}}^+(\boldsymbol{r}_i, \boldsymbol{r}_i')$ parallel zu den Schichten und die Reflexionseigenschaften der „gefüllten" Schichtenstapel links und rechts der leeren Schicht ($\boldsymbol{R}$ bezeichnet eines Gittervektor der Schicht), berücksichtigt. Durch Lösung der Dyson-Gleichung für die „leere" Schicht erhält man dann die GF

$$G^+(\boldsymbol{r}_i, \boldsymbol{r}_i') = G_1^+(\boldsymbol{r}_i, \boldsymbol{r}_i') + \sum_{\Lambda\Lambda'} \left\langle \boldsymbol{r}_i \middle| J_\Lambda^{i\mathrm{R}} \right\rangle U_{\Lambda\Lambda'}^{ii} \left\langle J_{\Lambda'}^{i\mathrm{L}} \middle| \boldsymbol{r}_i' \right\rangle \tag{2.21}$$

der gefüllten Schicht $i$. Durch Zerlegung in ein- und auslaufende ebenen Wellen lassen sich auch die Matrizen $U^{ij}$ für alle Schichten $i$ und $j$ des Systems berechnen. Wieder spielen die oben beschriebenen Basisalgorithmen für die Berechnung der Streueigenschaften eine profunde Rolle.

Die regulären Lösungen des Gitterplatzproblems erfüllen die Lippmann–Schwinger-Gleichung für das Potential $V_i(\boldsymbol{r})$,

$$\left\langle \boldsymbol{r}_i \middle| J_\Lambda^{i\mathrm{R}} \right\rangle = \left\langle \boldsymbol{r}_i \middle| j_\Lambda^{\mathrm{R}} \right\rangle + \int_{\Omega_i} G_0^+(\boldsymbol{r}_i, \boldsymbol{r}_i') V_i(\boldsymbol{r}_i') \left\langle \boldsymbol{r}_i' \middle| J_\Lambda^{i\mathrm{R}} \right\rangle \mathrm{d}{r_i'}^3 \tag{2.22}$$

($G_0$ Green-Funkton freier Elektronen), womit sich die *Single-site-$t$*-Matrix als

$$t_{\Lambda\Lambda'}^{i\mathrm{R}} = -\mathrm{i}k \int_{\Omega_i} \left\langle j_\Lambda^{\mathrm{L}} \middle| \boldsymbol{r}_i \right\rangle V_i(\boldsymbol{r}_i) \left\langle \boldsymbol{r}_i \middle| J_{\Lambda'}^{i\mathrm{R}} \right\rangle \mathrm{d}{r_i}^3 \tag{2.23}$$

ergibt. Desweiteren gilt $t_{\Lambda'\Lambda}^{i\mathrm{L}} = t_{\Lambda\Lambda'}^{i\mathrm{R}}$.

**Streupfadoperator und Streulösungen.** Bestimmte Größen in der VST lassen sich vorteilhafter formulieren, wenn man anstelle der bisher verwendeten Streulösungen solche mit anderer Asymptotik benutzt: $\left|Z_\Lambda^{\mathrm{R}}\right\rangle = \sum_{\Lambda'} \left|J_{\Lambda'}^{\mathrm{R}}\right\rangle (t^{\mathrm{R}})_{\Lambda'\Lambda}^{-1}$ und $\left\langle Z_\Lambda^{\mathrm{L}}\right| = \sum_{\Lambda'} (t^{\mathrm{L}})_{\Lambda\Lambda'}^{-1} \left\langle J_{\Lambda'}^{\mathrm{L}}\right|$ (Tab. 2.1) [37]. Beim Darstellungswechsel werden die Matrizen $U^{ij}$ durch Streupfadoperatoren (SPO) $\tau^{ij}$ ersetzt, $U^{mn} = (t^{m\mathrm{R}})^{-1}(\tau^{mn} - t^{m\mathrm{R}}\delta_{mn})(t^{n\mathrm{L}})^{-1}$ [14–16] und

$$G(\boldsymbol{r}_n, \boldsymbol{r}_n') = \left\langle \boldsymbol{r}_n \middle| Z^{n\mathrm{R}} \right\rangle \tau^{nn} \left\langle Z^{n\mathrm{L}} \middle| \boldsymbol{r}_n' \right\rangle - \mathrm{i}k \left\langle \boldsymbol{r}_n \middle| Z^{n\mathrm{R}} \right\rangle \left\langle \tilde{J}^{n\mathrm{L}} \middle| \boldsymbol{r}_n' \right\rangle. \tag{2.24}$$

Die Matrizen $\tau^{ij}$ sind rekursiv durch $\tau^{ij} = t^i \delta_{ij} + \sum_{k \neq i} t^i\, G_0\, \tau^{kj}$ definiert und transformieren eine einlaufende Welle in der Zelle $j$ in eine auslaufende in der Zelle $i$, wobei alle Streupfade von $j$ nach $i$ berücksichtigt werden. Die Streupfadoperatoren $\tau^{ij}(\epsilon)$ sind die *On–the–energy–shell*-Matrixelemente des Übergangsoperators $T$, $T(\epsilon) = \sum_{ij} \tau^{ij}(\epsilon)$.

Der Imaginärteil der GF lässt sich damit kompakt durch $\langle \boldsymbol{r}_n | \Gamma(E) | \boldsymbol{r}_m' \rangle = 2\mathrm{i} \sum_{\Lambda\Lambda'} \langle \boldsymbol{r}_n | Z_\Lambda^n \rangle \operatorname{Im}(\tau_{\Lambda\Lambda'}^{nm}) \langle Z_{\Lambda'}^m | \boldsymbol{r}_m' \rangle$ ausdrücken, wobei die Symmetrie $\tau_{\Lambda\Lambda'}^{nm} = \tau_{\Lambda'\Lambda}^{mn}$ ausgenutzt wurde. Ein Nachteil ist allerdings mit dem Auftreten der inversen $t$-Matrix verbunden, da für $t = 0$ singuläre Terme auftreten können. In der Darstellung mit $|J\rangle$ und $|H\rangle$ erhielte man einen zusätzlichen Beitrag vom gitterplatzdiagonalen Anteil.

**Tabelle 2.1.** Asymptotisches Verhalten der Streulösungen.

| Funktion | Verhalten für $r \to 0$ | Verhalten für $r \to \infty$ |
|---|---|---|
| $\lvert J\rangle$ | regulär | $\lvert j\rangle + \lvert h\rangle\, t$ |
| $\lvert H\rangle$ | irregulär | $\lvert h\rangle$ |
| $\lvert Z\rangle$ | regulär | $\lvert j\rangle\, t^{-1} + \lvert h\rangle$ |
| $\lvert \tilde{J}\rangle$ | irregulär | $\lvert j\rangle$ |

***Screened* KKR.** Im Gegensatz zu KKR-Methoden, die auf der *Screened* KKR beruhen [38, 39], ist in LKKR *Screening* nicht notwendig, da die Berechnung der schichtdiagonalen GF schon ein $\mathrm{O}(N)$-Verfahren ist. Ferner kann *Screening* nicht für höhere Energien angewendet werden, da die GF nicht hinreichend lokalisierbar ist. Für Photoemissionsrechnungen ist *Screened* KKR demnach nicht geeignet.

### Defekte und Unordnung

**Green-Funktion einzelner Defekte.** Ersetzt man das Potential $V_0(\boldsymbol{r})$ am Gitterplatz $0$ durch $\widetilde{V}_0(\boldsymbol{r})$ (Abb. 2.3), so lautet die GF des Defektsystems

$$\widetilde{G}_{ij}(\boldsymbol{r}_i, \boldsymbol{r}'_j) = \widetilde{G}^{+}_{i}(\boldsymbol{r}_i, \boldsymbol{r}'_i)\delta_{ij} + \sum_{\Lambda\Lambda'} \left\langle \boldsymbol{r}_i \middle| \widetilde{J}^{i}_{\Lambda} \right\rangle \widetilde{U}^{ij}_{\Lambda\Lambda'} \left\langle \widetilde{J}^{j}_{\Lambda} \middle| \boldsymbol{r}'_j \right\rangle . \tag{2.25}$$

Die regulären Streulösungen $\left|\widetilde{J}^{i}_{\Lambda}\right\rangle$ sind hier durch $\left|\widetilde{J}^{i}_{\Lambda}\right\rangle = \left|\widetilde{J}^{0}_{\Lambda}\right\rangle \delta_{i0} + \left|J^{0}_{\Lambda}\right\rangle (1-\delta_{i0})$ und entsprechenden Ausdrücken für die irregulären Lösungen $\left|\widetilde{H}^{i}_{\Lambda}\right\rangle$ definiert. Die Dyson-Gleichung bzgl. der GF des Wirtsgitters führt zu $\widetilde{U}^{00} = \Delta^{\mathrm{L}} U^{00}$, $\widetilde{U}^{0j} = \Delta^{\mathrm{L}} U^{0j}$, $\widetilde{U}^{i0} = U^{i0}\Delta^{\mathrm{R}}$ und $\widetilde{U}^{ij} = U^{ij} - \frac{1}{\mathrm{i}k} U^{i0}(\widetilde{t}^{0} - t^{0})\Delta^{\mathrm{L}} U^{0j}$, wobei die „Defektmatrizen“ durch $\Delta^{\mathrm{L}} = \left[1 + U^{00}(\widetilde{t}^{0} - t^{0})/(\mathrm{i}k)\right]^{-1}$ und $\Delta^{\mathrm{R}} = \left[1 + (\widetilde{t}^{0} - t^{0})U^{00}/(\mathrm{i}k)\right]^{-1}$ gegeben sind. Die Matrizen $\widetilde{U}^{ij}$ hängen insbesondere von der Differenz der Streumatrizen $\widetilde{t}^{0}$ und $t^{0}$ ab [14]. Die Green-Funktion für ein System mit mehreren Defekten kann durch die sukzessive Anwendung der obigen Gleichungen berechnet werden.

***Coherent Potential Approximation.*** Die einfachsten Möglichkeiten, die Unordnung von binären substitutionellen Legierungen $\mathrm{A}_c\mathrm{B}_{1-c}$ zu beschreiben, sind die *Virtual crystal approximation* (VCA) und die *Averaged t-matrix approximation* (ATA). Im ersten Fall wird das Potential an jedem Gitterplatz $i$ durch $V_i = cV_{\mathrm{A}} + (1-c)V_{\mathrm{B}}$ ($c$ Konzentration) ersetzt, und es können daher Standardmethoden zur Berechnung der elektronischen Struktur verwendet werden. In der ATA ersetzt man nicht das Potential, sondern die Gitterplatz-Streumatrizen $t$. Da innerhalb der ATA nur die Wellenfunktionen der defektfreien Systeme A ($c = 1$) und B ($c = 0$) bekannt sind, erfordert die Berechnung von Größen, die die Wellenfunktionen enthalten (Zustandsdichte, Photostrom), eine Behandlung wie in der *Coherent potential approximation* (CPA).

In der CPA fixiert man die Eigenschaften eines ausgewählten Gitterplatzes und führt die Konfigurationsmittelung an den restlichen Gitterplätze aus (bedingter Mittelwert). Somit wird ein effektives Medium durch die Forderung bestimmt, dass dieses dieselben Streueigenschaften besitzt wie die mit den Konzentrationen gewichteten Defektsysteme. Dieses führt zur CPA-Bedingung $\widetilde{\tau}^{00}_{\mathrm{C}} = c\tau^{00}_{\mathrm{A}} + (1-c)\tau^{00}_{\mathrm{B}}$ in der *Single-site approximation* für die Streupfadoperatoren $\widetilde{\tau}_{\mathrm{C}}$ des effektiven Mediums. Die Defektsysteme werden duch die gitterplatzdiagonalen Streupfadoperatoren $\tau^{00}_{\mathrm{A}}$ und $\tau^{00}_{\mathrm{B}}$ beschrieben. Hier befindet sich ein Defekt vom Typ A bzw. B am Gitterplatz $0$ eingebettet im effektiven Medium C (Abb. 2.3). Die CPA-Bedingung erfordert also eine selbstkonsistente Bestimmung des effektiven Mediums, die in die *Ab–initio*-Berechnung der elektronischen Struktur eingefügt werden kann. „Fluktuationsartige“ Beiträge, wie die Differenz einer Größe von ihrem Mittelwert, werden vernachlässigt, und der Einfluss kurzreichweitiger Ordnung wird nicht erfasst.

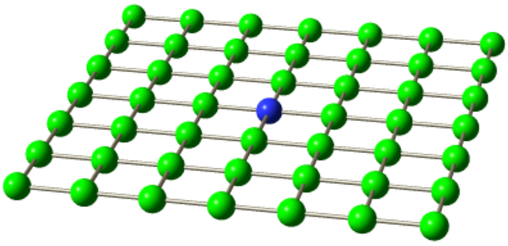

**Abbildung 2.3.** Defekt in einer Schicht von Streuzentren (schematisch). Ein einzelner Defekt (blaue Kugel), beschrieben durch das Potential $\widetilde{V}_0(\boldsymbol{r})$, ist in einer Schicht von Streuzentren (grüne Kugeln) mit den Potentialen $V_0(\boldsymbol{r})$ eingebettet.

**Beschreibung des Magnetismus bei endlichen Temperaturen — Das Bild der ungeordneten lokalen Momente.** Das Verschwinden der Magnetisierung eines ferromagnetischen Systems oberhalb der kritischen Temperatur lässt sich anschaulich auf zwei Weisen im Bild lokalisierter magnetischer Momente verstehen. Bei der Temperatur $T = 0$ sind alle lokalen magnetischen Momente parallel ausgerichtet (entlang der Magnetisierungsrichtung $\boldsymbol{M}$).[3] Im einen Szenario nimmt das magnetische Moment an jedem Gitterplatz mit wachsender Temperatur ab, sodass oberhalb der kritischen Temperatur $T_\mathrm{C}$ das Gesamtsystem, wie auch jedes Teilvolumen, nichtmagnetisch wird. Im anderen Szenario bleiben die lokalen Momente endlich, ihre Ausrichtung jedoch fluktuiert zunehmend. Oberhalb $T_\mathrm{C}$ sind die Fluktuationen so stark, dass keine Vorzugsrichtung der Momente mehr existiert und das Gesamtsystem somit paramagnetisch wird, wobei endliche Teilvolumina magnetisch bleiben können.

Das zweite Modell kann offensichtlich im Rahmen der CPA behandeln werden. Die Idee der ungeordneten lokalen Momente [*Disordered local moment* (DLM)] bildet die Unordnung auf eine binäre substitutionelle Legierung $\mathrm{A}_c\mathrm{B}_{1-c}$ ab, in der die Spezies A und B lokale Momente darstellen, die entlang der Magnetisierungsrichtung $\boldsymbol{M}$ und entlang $-\boldsymbol{M}$ für $T = 0$ ausgerichtet sind. Bei der Konzentration $c = 0$ liegt der ferromagnetische Fall vor ($T = 0$), während $T_\mathrm{C}$ bei $c = 0.5$ erreicht wird. Das DLM-Bild eignet sich besonders für Systeme nahe der kritischen Temperatur. Eine Realisierung des DLM erhält man, indem die spinabhängigen Potentiale $V(r)$ für die Spezies A und B komplementär gewählt werden: $v_{\mathrm{A}+} = v_{\mathrm{B}-} = v + B$ und $v_{\mathrm{A}-} = v_{\mathrm{B}+} = v - B$. Somit lässt sich die Temperaturabhängigkeit der elektronischen Struktur und der Spektroskopien, insbesondere der Photoemission, behandeln (vgl. Publikation 8 auf S. P80ff).

### Das Programmpaket OMNI

Die meisten der hier vorgestellten Resultate wurden mit dem Programmpaket OMNI berechnet. Ausgehend von einer Implementierung der relativistischen LKKR-Methode dient es zur Berechnung einer Vielzahl von Elektronenspektroskopien. Das Paket OMNI hat seinen Ursprung in der Arbeitsgruppe von Feder (Duisburg). In den letzten Jahren wurde die C++-Version von mir erheblich erweitert. Als Meilensteine können die Implementierung der CPA und des ballistischen Transport angeführt werden. Fominykh programmierte die Zweielektronenphotoemission ($\gamma$,2e).

Die strikte Befolgung des objektorientierten Ansatzes von C++ erlaubt die Abstrahierung von fundamentalen Datentypen, sodass mit den Objekten der LKKR-Methode direkt gearbeitet werden kann (Atome, Schichten, Kristalle, Wellenfunktionen, Zustände). Rekursive Algorithmen, Überladen von Operatoren und strikte Kompatibilitätsprüfung erleichtern die Entwicklung und Wartung des Codes. Das Kennenlernen des umfangreichen Codes ist durch den strukturierten Aufbau relativ einfach, insbesondere da LKKR-Gleichungen quasi eins-zu-eins kodiert werden können. Der Preis für die erzwungene Konsistenz ist das gegenüber einer FORTRAN-Version schlechtere Laufzeitverhalten.

---

[3] Als lokales magnetisches Moment kann das über eine Einheitszelle oder über eine MT-Kugel integrierte Spinmoment aufgefasst werden.

# 3. Spin–Bahn-Kopplung und elektronische Struktur

In diesem Kapitel wird exemplarisch gezeigt, wie die Spin–Bahn-Kopplung (SBK) elektronische und magnetische Eigenschaften von niedrigdimensionalen Systemen beeinflusst. Im folgenden Abschnitt 3.1 wird die Aufspaltung der elektronischen Valenzzustände von Edelgasketten auf einer strukturierten Pt-Oberfläche diskutiert. Neben der Aufspaltung kann die SBK zur Spinpolarisation von Oberflächenzuständen führen, in Analogie zur Rashba–Bychkov-Wechselwirkung in zweidimensionalen Elektronengasen, wie anhand der Au(111)-Oberfläche gezeigt wird (S. 15). Eine weitere Manifestation der SBK ist die magnetokristalline Anisotropie. Hier dienen dünne Ni-Filme auf Cu(001), die einen ungewöhnlichen Spinreorientierungsübergang zeigen, als prototypisches Beispiel (S. 19).

## 3.1. Energetische Aufspaltung elektronischer Zustände

Energetische Niveaus von Atomen können neben der Hauptquantenzahl $n$ durch die Drehimpulsquantenzahl $l$ klassifiziert werden. Sie sind bezüglich der $z$-Projektion $m$ des Drehimpulses $\boldsymbol{l}$ und bezüglich des Elektronenspins $\boldsymbol{s}$ entartet. Der relativistische Effekt der Spin–Bahn-Kopplung lässt sich im Rahmen der $\boldsymbol{ls}$-Kopplung (auch mit Russell–Saunders-Kopplung bezeichnet) oder, wie im Falle schwerer Atome, durch die $\boldsymbol{jj}$-Kopplung verstehen. Die Spin–Bahn-Kopplung hebt die Entartung auf, und die Niveaus müssen durch die Quantenzahl $j$ des Gesamtdrehimpulses $\boldsymbol{j} = \boldsymbol{l} + \boldsymbol{s}$ klassifiziert werden, $j = l \pm 1/2$. Wird die Rotationssymmetrie des Systems gebrochen, findet eine Aufspaltung in Subniveaus statt. Im Falle magnetischer Atome kann dann die $z$-Projektion $m_j$ des Gesamtdrehimpulses zur Klassifizierung dienen. Denn die Spin–Bahn-Kopplung koppelt Subniveaus mit gleichem $m_j$, aber verschiedenem $j$ [40]. Dominiert die Stärke der SBK gegenüber der Austauschaufspaltung, wie zum Beispiel in tiefliegenden Rumpfniveaus, ergeben sich zwei Gruppen von Niveaus, die deutlich voneinander getrennt sind. Die erste zu $j = l - 1/2$ enthält die Subniveaus zu $m_j = l - 1/2, \ldots, -l + 1/2$ und ist durch eine große energetische Lücke von der zweiten getrennt (ca. $12$ eV im Falle von Fe-$2p$). Die letztere Gruppe mit $j = l + 1/2$ umfasst die Subniveaus zu $m_j = -l - 1/2, \ldots, l + 1/2$. Für relativ schwach gebundene Rumpfniveaus, wie zum Beispiel Fe-$3p$, in denen die Stärke der SBK vergleichbar mit der Austauschaufspaltung ist, beoachtet man diese eindeutige energetische Trennung nicht.

Als eine weitere Ursache für die Brechung der Rotationssymmetrie kommt die geometrische Struktur des Systems in Frage. Eine starke Störung der sphärischen Symmetrie tritt in linearen Ketten von Edelgasatomen auf, die auf der strukturierten Pt(110)-Oberfläche adsorbiert sind. Die Pt(110)-Oberfläche zeigt eine 1×2-Rekonstruktion, in der jede zweite Reihe von Pt-Atomen fehlt, die sogenannte *Missing-row reconstruction*. Dadurch wird eine Vorzugsrichtung bei der Adsorption vorgegeben, die die Formierung linearer Ketten endlicher Länge bevorzugt (Abb. 3.1). Im Falle von Xenon können sich zwei Spezies von Ketten auf der reinen Pt-Oberfläche ausbilden, was allerdings durch Modifikation der Oberfläche mit Wasserstoff verhindert werden kann. Es liegt dann nur eine Xe-Spezies vor. Deren genauer Adsorptionsplatz, entweder in den Gräben (wie in Abb. 3.1 dargestellt) oder auf den äußersten Pt-Atomreihen dazwischen, spielt für die folgenden Betrachtungen keine Rolle, da die Wechselwirkung des Edelgases mit dem Substrat vernachlässigbar ist.

Die elektronische Struktur der Edelgasketten wird im Valenzbandbereich durch $p$-Zustände bestimmt, bei Krypton durch die $4p$- und bei Xenon durch die $5p$-Zustände. Diese spalten vermöge der SBK in Niveaus mit $j = 1/2$ und $j = 3/2$ auf. Im Folgenden werden Xe-Ketten auf wasserstoffmodifiziertem Pt(110)-1×2-H diskutiert. Die lineare Anordnung der Edelgasatome lässt Orbitale benachbarter Xe-Atome innerhalb einer Kette überlappen, was zur Ausbildung der Dispersion der

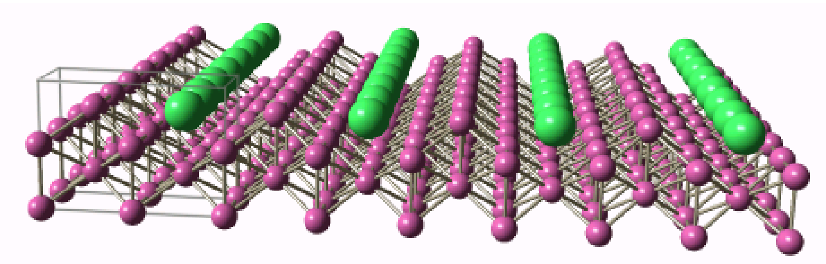

**Abbildung 3.1.** Adsorbierte Edelgasketten auf Pt(110)-1×2. In der äußersten Schicht der (110)-Oberfläche fehlt jede zweite Reihe von Pt-Atomen (magenta), sodass sich die sogenannte *Missing-row reconstruction* ausbildet. In die entstandenen Gräben können Edelgasatome (grün) adsorbieren und lineare Ketten bilden. Es sind nur die vier äußersten Pt-Schichten dargestellt.

elektronischen Zustände in Kettenrichtung führt (Abb. 3.2a). Die Dispersion in Richtung senkrecht zu den Ketten verschwindet (Abb. 3.2b), da der Überlapp der Orbitale benachbarter Ketten sehr gering ist. Zusätzlich beobachtet man eine Aufspaltung der Zustände mit $j = 3/2$ [Publikation 1 (S. P2ff)] [41–43]. Theoretische Rechnungen im Rahmen eines semi-empirischen *Tight-binding*-Modells, das auf DFT-Rechnungen für den Xe-Volumenkristall basiert, zeigen, dass nicht, wie man in Analogie zu hexagonalen Xe-Schichten erwarten dürfte, das $5p_{3/2}^{\pm 1/2}$-Niveau stärker als das $5p_{3/2}^{\pm 3/2}$-Niveau gebunden ist, sondern die umgekehrte energetische Anordnung vorliegt. Verstehen lässt sich dieser Effekt mit Hilfe des Quadrupolmoments der Xe-Ladungsverteilung.

Die beobachtete energetische Anordnung kann in Beziehung zum elektrischen Feldgradienten (EFG) $V_{xy} = \mathrm{d}^2V/\mathrm{d}x\mathrm{d}y$, der aufgrund der Ladungsverteilung benachbarter Atome entsteht, gebracht werden. In sphärisch symmetrischen Systemen ist die Wahl der Quantisierungsachse (etwa die $z$-Achse) willkürlich. Beim Vorliegen einer quadrupolaren Aufspaltung wird diese Wahlfreiheit genommen und die Quantisierungsachse durch die Quadrupolwechselwirkung diktiert. Die $5p_{3/2}$-Zustände sind nämlich nur dann Eigenzustände des Hamilton-Operators, wenn die $z$-Achse entlang der größten Hauptachse des EFG-Tensors (mit Tensorkomponente $V_{zz}$ ) ausgerichtet ist und die planare Asymmetrie $\eta = (V_{xx} - V_{yy})/V_{zz}$ verschwindet. In diesem Falle, der auf die hier behandelten linearen Xe-Ketten sowie auf zweidimensionale Xe-Schichten bei $\boldsymbol{k}_{\|} = 0$ zutrifft,[1] beobachtet man die besagte Aufspaltung. Deren Größe $6\,\omega_{\mathrm{q}}$ ist durch das Quadrupolmoment $Q$ der Ladungsverteilung bestimmt, $\omega_{\mathrm{q}} = QV_{zz}/2$. Der elektrische Feldgradient $V_{zz}$ kann aus der

---

[1] In beiden Fällen muss die Wechselwirkung der Xe-Atome mit dem Substrat vernachlässigbar sein, was aufgrund der Edelgasnatur des Adsorbats in sehr guter Näherung erfüllt ist.

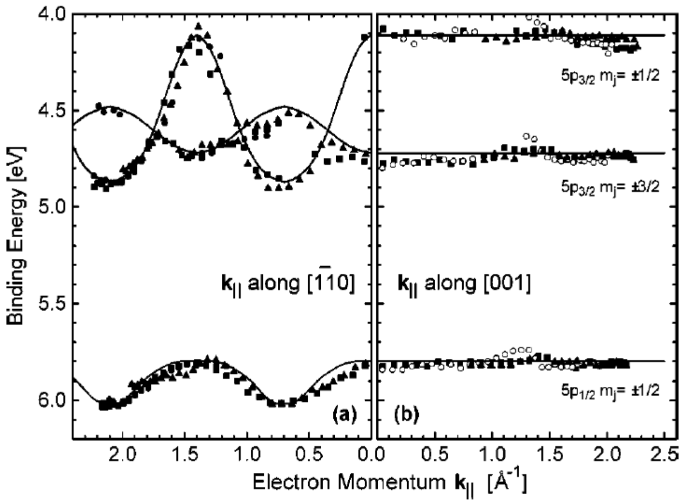

**Abbildung 3.2.** Elektronische Struktur von Xe-Ketten auf der wasserstoff-modifizierten Pt(110)-1×2-Oberfläche. (a) Mittels Photoelektronenspektroskopie bestimmte Dispersion der Xe-$5p$-Zustände entlang der Kettenrichtung (Dreiecke; $\boldsymbol{k}_{\|}$ parallel der [$\bar{1}$10]-Richtung des Pt-Substrats). (b) Wie (a), jedoch $\boldsymbol{k}_{\|}$ senkrecht zu den Xe-Ketten (entlang der [001]-Richtung des Pt-Substrats). Die Dispersion aus einem semi-empirischen *Tight-binding*-Modell ist vermöge durchgezogener Linien dargestellt. Aus Ref. [43].

Ladungsverteilung $\rho(\boldsymbol{r})$ an den Xe-Plätzen ermittelt werden,

$$V_{zz} = \frac{1}{4\pi\epsilon_0}\int \frac{3\cos^2\vartheta - 1}{r^3}\rho(\boldsymbol{r})\,\mathrm{d}r^3. \tag{3.1}$$

Für eine zweidimensionale Xe-Schicht liegt die Quantisierungsachse ($z$-Achse) normal zur Schicht, und der Hauptbeitrag zum EFG kommt von Winkeln nahe $\vartheta = \pi/2$. Damit ist $V_{zz}$ negativ. Für eine Xe-Kette hingegen fallen $z$-Achse und Kettenausrichtung zusammen, sodass der Hauptbeitrag zu $V_{zz}$ von Winkeln nahe $\vartheta = 0$ stammt und $V_{zz}$ positiv ist. Die verschiedenen Vorzeichen von $V_{zz}$ korrespondieren daher mit den unterschiedlichen energetischen Anordnungen der $5p_{3/2}^{\pm 1/2}$- und $5p_{3/2}^{\pm 3/2}$-Niveaus in ein- und zweidimensionalen Adsorbatsystemen.

## 3.2. Spinpolarisation elektronischer Oberflächenzustände

Neben der energetischen Aufspaltung kann die Spin–Bahn-Kopplung zu einer Spinpolarisation elektronischer Zustände führen. Ein eindrucksvolles Beispiel liefern die Oberflächenzustände von Edelmetallen, die sich in der Bandlücke um die $\Gamma$–$\Lambda$–L-Richtung der Volumen-Brillouin-Zone ausbilden. Die beigefügte Publikation 2 (S. P6ff) dokumentiert eine detaillierte theoretische und experimentelle Analyse dieser Zustände an der Au(111)-Oberfläche. In diesem Abschnitt werden die wesentlichen Aspekte der Theorie dargestellt.

Da die Geometrie der Au(111)-Oberfläche für das Verständnis der Effekte wichtig ist, wird zunächst das verwendete Koordinatensystem beschrieben. Dessen $x$- und $y$-Achse fallen mit den kristallographischen $[1\bar{1}0]$- und $[\bar{1}\bar{1}2]$-Richtungen zusammen, die $z$-Achse zeigt entlang der Oberflächennormalen in Richtung des Vakuums. Die $yz$-Ebene bildet somit eine Spiegelebene des Systems (Abb. 3.3a). Im reziproken Raum liegt die $k_x$-Achse entlang der $\overline{\mathrm{K}}$–$\overline{\Gamma}$–$\overline{\mathrm{K}}$-Richtung der zweidimensionalen Brillouin-Zone (2BZ), wogegen die $k_y$-Achse entlang $\overline{\mathrm{M}}$–$\overline{\Gamma}$–$\overline{\mathrm{M}}$ (Abb. 3.3b) weist.

Die Zeitumkehrsymmetrie erzwingt $E(\boldsymbol{k}) = E(-\boldsymbol{k})$ für die Energien der elektronischen Zustände (Kramers' Entartung) und $\boldsymbol{P}(\boldsymbol{k}) = -\boldsymbol{P}(-\boldsymbol{k})$ für deren Spinpolarisation. Für Systeme mit Inversionssymmetrie gilt zusätzlich $\boldsymbol{P}(\boldsymbol{k}) = \boldsymbol{P}(-\boldsymbol{k})$, und im Volumen kubischer Systeme verschwindet daher die Spinpolarisation. An der Oberfläche hingegen ist die Inversionsinvarianz zwangsläufig gebrochen. Da nur noch $\boldsymbol{k}_{\|}$ eine „gute Quantenzahl“ ist, im Gegensatz zu $\boldsymbol{k}$ im Volumen, wird nur $\boldsymbol{P}(\boldsymbol{k}_{\|}) = -\boldsymbol{P}(-\boldsymbol{k}_{\|})$ erzwungen. Oberflächenzustände dürfen somit spinpolarisiert sein, das Spinmoment des gesamten Systems bleibt aber weiterhin Null.

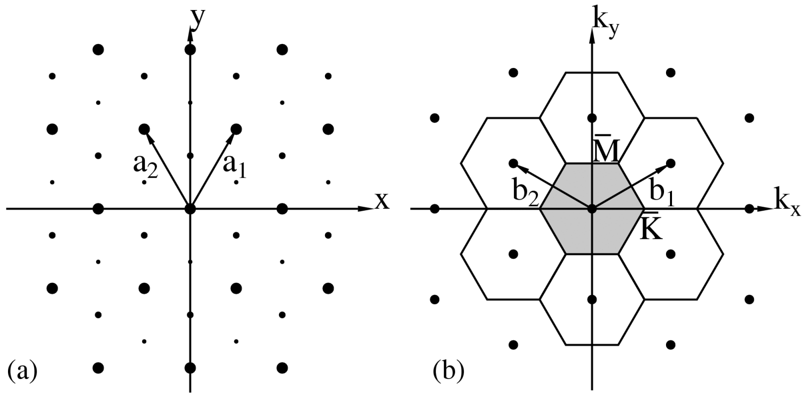

**Abbildung 3.3.** Geometrische Struktur der Au(111)-Oberfläche. (a) Aufsicht auf die Oberfläche, die durch die drei äußersten Atomlagen (große Punkte: erste Schicht; mittlere: zweite Schicht; kleine: dritte Schicht) repräsentiert wird. Die Basisvektoren $\boldsymbol{a}_1$ und $\boldsymbol{a}_2$ spannen das hexagonale Gitter der atomaren Schichten auf. (b) Reziprokes Gitter mit Basisvektoren $\boldsymbol{b}_1$ und $\boldsymbol{b}_2$. Die zentrale zweidimensionale Brillouin-Zone (2BZ) ist grau unterlegt. Die Symmetriepunkte $\overline{\mathrm{M}}$ und $\overline{\mathrm{K}}$ bezeichnen eine Kantenmitte und eine Ecke des Randes der 2BZ.

Der nichtrelativistische Hamilton-Operator der SBK lautet

$$H_{\mathrm{SBK}} = \frac{1}{2c^2}\boldsymbol{\sigma} \cdot [\boldsymbol{\nabla} V(\boldsymbol{r}) \times \boldsymbol{p}], \tag{3.2}$$

worin $\boldsymbol{\sigma}$ den Vektor der Pauli-Matrizen und $\boldsymbol{p}$ den Impulsoperator bezeichnen.[2] Die Spin–Bahn-Kopplung ist dort groß, wo sich das Potential $V(\boldsymbol{r})$ stark ändert, also insbesondere in der Nähe des Kerns schwerer Atome. Ein zweiter Beitrag zur SBK kann der Oberfläche zugeordnet werden. Diese bricht die Symmetrie des Volumensystems und kann daher als Quelle einer strukturellen Asymmetrie angesehen werden, die in einem zusätzlichen Beitrag zur SBK resultiert. Dieser Effekt ist ganz analog zur Rashba–Bychkov-Wechselwirkung in zweidimensionalen Elektronengasen [44] und zur Dresselhaus-Wechselwirkung in Volumensystemen mit gebrochener Inversionssymmetrie [45]. Explizit formuliert: ein zweidimensionales Elektronengas (2DEG) ist an der Grenzfläche zweier verschiedener Halbleiter (z. B. GaAs und GaAlAs) lokalisiert. Ein Oberflächenzustand in der (111)-Oberfläche eines Edelmetalls ist ebenfalls asymmetrisch räumlich beschränkt: in Richtung Vakuum durch das Potential der Oberflächenbarriere, in Richtung des Kristallinneren durch die Bandlücke des Volumens. Die Stärke des „atomaren“ Beitrags der SBK übertrifft den der Oberfläche erheblich [46]. Jedoch führt letzterer zur Aufspaltung und Spinpolarisation des L–Lücken-Oberflächenzustandes von Au(111).

Da der L–Lücken-Oberflächenzustand den Charakter freier Elektronen trägt, bietet sich eine Beschreibung mittels ebener Wellen an. Der Hamilton-Operator eines isotropen zweidimensionalen Elektronengases inklusive Rashba–Bychkov-SBK ist durch

$$H = \frac{1}{2}\boldsymbol{k}_{\parallel}^2 + \gamma\,(\sigma_x k_y - \sigma_y k_x) \tag{3.3}$$

gegeben. Der „atomare“ Beitrag der SBK tritt in dieser Formulierung nicht explizit auf. Die Eigenfunktionen obigen Operators lassen sich in einen inneren $(+)$ und einen äußeren $(-)$ Zustand klassifizieren (für $\gamma > 0$), deren Dispersionsrelationen durch

$$E_{\pm}(\boldsymbol{k}_{\parallel}) = \frac{1}{2}\boldsymbol{k}_{\parallel}^2 \pm \gamma|\boldsymbol{k}_{\parallel}| \tag{3.4}$$

gegeben sind. Die Impulsverteilung besteht somit aus zwei konzentrischen Kreisen, deren Radien sich um ca. $2\gamma$ unterscheiden. Die Größe $\gamma$ beschreibt die Stärke der strukturellen Asymmetrie, die im wesentlichen durch $\partial_z V$ bestimmt ist [47].

Mit der energetischen Aufspaltung geht eine vollständige Spinpolarisation $\boldsymbol{P}$ der Zustände einher. Letztere steht senkrecht auf $\boldsymbol{k}_{\parallel} = (\cos\varphi_{\mathrm{e}}, \sin\varphi_{\mathrm{e}})$,

$$P_{\pm}^{x}(\boldsymbol{k}_{\parallel}) = \alpha_{\pm}\sin\varphi_{\mathrm{e}}, \tag{3.5a}$$

$$P_{\pm}^{y}(\boldsymbol{k}_{\parallel}) = -\alpha_{\pm}\cos\varphi_{\mathrm{e}}, \tag{3.5b}$$

mit $\alpha_{\pm} = \pm 1$. Die $z$-Komponente von $\boldsymbol{P}_{\pm}$ verschwindet für ein isotropes 2DEG. Für die weitere Diskussion ist es vorteilhaft, $\boldsymbol{P}_{\pm}$ in radiale und tangentiale Komponenten. Offenbar rotiert die Spinpolarisation des äußeren Zustands im Uhrzeigersinn, die des inneren entgegen dem Uhrzeigersinn ($\gamma > 0$) [48].

Die Oberflächennormale von Au(111) ist eine dreizählige Rotationsachse des Gitters, die zu einer radialen strukturellen Asymmetrie führt. Der Hamilton-Operator erhält daher weitere Beiträge zur Rashba–Bychkov-SBK, die eine nicht verschwindende $z$-Komponente der Spinpolarisation erlauben. Wie die hier dokumentierten DFT-Rechnungen zur elektronischen Struktur gezeigt haben [47], sind die Abweichungen der Impulsverteilung von der zirkularen Form vernachlässigbar klein, sodass $\boldsymbol{P}$ weiterhin nach Zirkularfunktionen in $\varphi_{\mathrm{e}}$ entwickelt werden kann. Die führenden Beiträge von $P_{\pm}^{x}$ und $P_{\pm}^{y}$ verbleiben wie in Gl. (3.5), jedoch lautet $P_{\pm}^{z}$ nunmehr

$$P_{\pm}^{z}(\boldsymbol{k}_{\parallel}) = \beta_{\pm}\cos 3\varphi_{\mathrm{e}}. \tag{3.6}$$

---

[2] In atomaren Hartree-Einheiten, $e = m = \hbar = 1$, $c \approx 137$.

Das Vorhandensein einer nicht verschwindenden $z$-Komponente erfordert Komponenten des Potentialgradienten innerhalb der Oberflächenebene. Ein Beitrag zu $P^z_\pm$ stammt daher von der Korrugation, also der oberflächenparallelen Asymmetrie der Oberflächenbarriere. Da diese klein im Vergleich zu den anderen SBK-Beiträgen ist, kann $|\beta_\pm| \ll 1$ erwartet werden. Die $yz$-Spiegelebene erzwingt, dass die Spinpolarisation $\boldsymbol{P}_\pm$ für $\varphi_\mathrm{e} = 90^\circ$ entlang der $x$-Achse ausgerichtet ist. Das System verbleibt aufgrund der Zeitumkehrsymmetrie nichtmagnetisch.

Die Dispersion der L–Lückenzustände mit $\boldsymbol{k}_\|$ lässt sich aus den Maxima der lagen-und spinaufgelösten Spektraldichte entnehmen (Abb. 3.4). Wie die Analogie mit einem 2DEG nahelegt, ist das Verhalten zu dem freier Elektronen mit Rashba–Bychkov-SBK sehr ähnlich. Die effektive Masse $m^\star$ von $0.203$ zeigt, dass die Dispersion im Vergleich zum Experiment zu groß ist, wie die Fermi-Wellenzahlen belegen: $k_{+\mathrm{F}} = 0.079/\mathrm{Bohr}$ und $k_{-\mathrm{F}} = 0.091/\mathrm{Bohr}$ in der Theorie sowie $k_{+\mathrm{F}} = 0.091/\mathrm{Bohr}$ und $k_{-\mathrm{F}} = 0.104/\mathrm{Bohr}$ im Experiment [49]. Die Bindungsenergie von $0.51$ eV bei $\boldsymbol{k}_\| = 0$ hingegen korrespondiert gut mit dem experimentellen Wert von $0.49$ eV. Die Stärke $\gamma$ der SBK ist ca. drei- bis fünfmal größer als in typischen zweidimensionalen Elektronengasen in Halbleiter-Heterostrukturen: in GaAs-GaAlAs beträgt sie ca. $0.8 \cdot 10^{-9}$ eV cm, für Au(111) hingegen $4.4 \cdot 10^{-9}$ eV cm [47].

Gibt die analytische Theorie für ein isotropes 2DEG eine Spinpolarisation mit $\alpha_\pm = \pm 1$ und $\beta_\pm = 0$, so wird für die Au(111)-Oberfläche die parallele Komponente der Spinpolarisation aufgrund der dreizähligen Symmetrie auf $\alpha_+ = 0.967$ bzw. $\alpha_- = -0.926$ reduziert. Die Normalkomponente ist, wie erwartet, klein und beträgt $\beta_+ = 0.014$ und $\beta_- = -0.013$.

Obwohl die Aufspaltung der L-Lückenzustände schon in der ersten experimentellen Arbeit korrekt durch die SBK erklärt wurde [48], fehlte ein direkter experimenteller Nachweis der Spinpolarisation (Publikation 2 auf S. P6). Als Methode der Wahl bietet sich die spin- und winkelaufgelöste Photoelektronenspektroskopie an. Da die SBK zu spinpolarisierten Photoelektronen von nichtmagnetischen Oberflächen führen kann (Abschn. 4.3), ist zunächst fraglich, ob dieser Photoemissi-

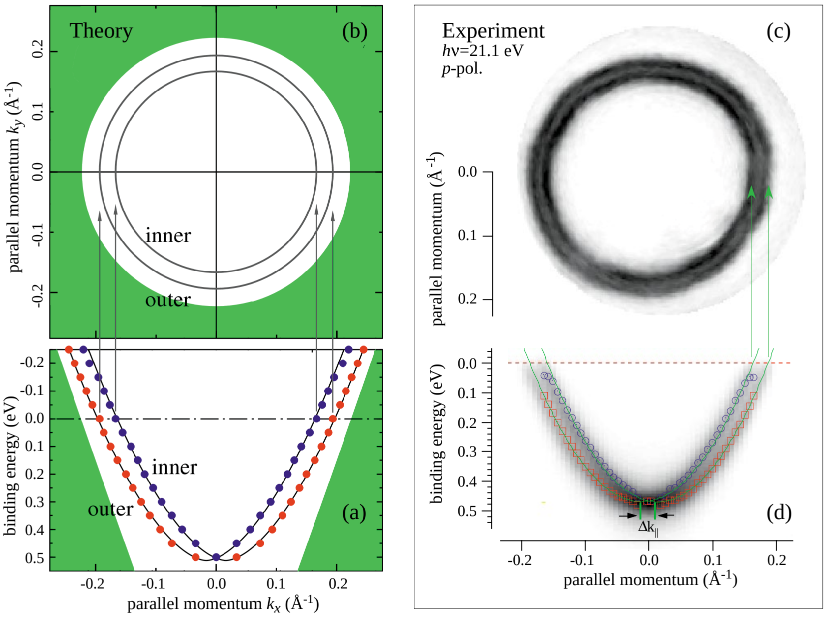

**Abbildung 3.4.** Oberflächenzustände in Au(111). (a) Berechnete Dispersion des „inneren“ (blaue Symbole) und „äußeren“ (rot) L-Lückenzustands entlang $\overline{\mathrm{K}}$–$\overline{\Gamma}$–$\overline{\mathrm{K}}$ ($k_x$). Der Bereich der Volumenzustände ist grün dargestellt. (b) Berechnete Impulsverteilung der beiden Oberflächenzustände an der Fermi-Energie $E_\mathrm{F}$. In (c) und (d) sind korrespondierende Resultate aus Photoemissionsexperimenten gezeigt. Nur das Zentrum der 2BZ ist gezeigt. Aus Publikation 2 auf S. P6.

onseffekt es erlaubt, Rückschlüsse von der Spinpolarisation der Photoelektronen auf die der Oberflächenzustände zu ziehen. Die durch den Anregungsprozess vermittelte Spinpolarisation könnte so groß sein, dass die des Anfangszustands quasi überdeckt, verschleiert wird. Wählt man allerdings die Messgeometrie geschickt dergestalt, dass der Photoelektronenspin entlang der erwarteten Spinpolarisation des Anfangszustands orientiert ist, gelingt der experimentelle Nachweis der Spinpolarisation der L-Lückenzustände dennoch, wie in der Gruppe von Jürg Osterwalder an der Universität Zürich gezeigt wurde. Deren Resultate stimmen sehr gut mit korrespondierenden Photoemissionsrechnungen überein. Es zeigt sich nämlich, dass die durch die Photoemission selbst erzeugte Spinpolarisation bei der gewählten Anregungsenergie klein ist.

Die Abbildung 3.5 fasst die experimentellen und theoretischen Befunde in spinaufgelösten Impulsverteilungen exemplarisch zusammen. Die Tangentialkomponente von $\boldsymbol{P}_{\pm}$ zeigt genau das analytisch und numerisch vorhergesagte Verhalten [Abb. 3.5a und Abb. 3.5d]. Nur die Extremalwerte im Experiment sind im Vergleich zur Theorie deutlich geringer, ein typisches Merkmal, welches durch die Auflösung und durch Lebensdauereffekte in der Photoemission erklärt werden kann. Auch die Normalkomponente $P^{z}_{\pm}$ [Abb. 3.5c und Abb. 3.5e] stimmt mit der Theorie gut überein: im Experiment liegt sie unterhalb des Detektionslimits von 5 %, in der Theorie bei maximal $4$ Prozent und ist somit wesentlich geringer als die oberflächenparallele Komponente.

Wie in Kapitel 4 gezeigt wird, ist die SBK eine Ursache für die Spinpolarisation von Photoelektronen. Abhängig von der Messgeometrie können spinpolarisierte Elektronen von nichtmagnetischen Oberflächen, genauer: von nichtspinpolarisierten elektronischen Zuständen, emittiert werden (Abschn. 4.3). Dieser Effekt ruft bei magnetischen Systemen den Magnetischen Dichroismus, also die Änderung des Photostroms unter Umkehr der Magnetisierungsrichtung hervor (Abschn. 4.4). Ein weiterer wesentlicher Effekt der SBK in magnetischen Systemen ist die magnetokristalline Anisotropie, die im Folgenden für dünne magnetische Filme behandelt wird.

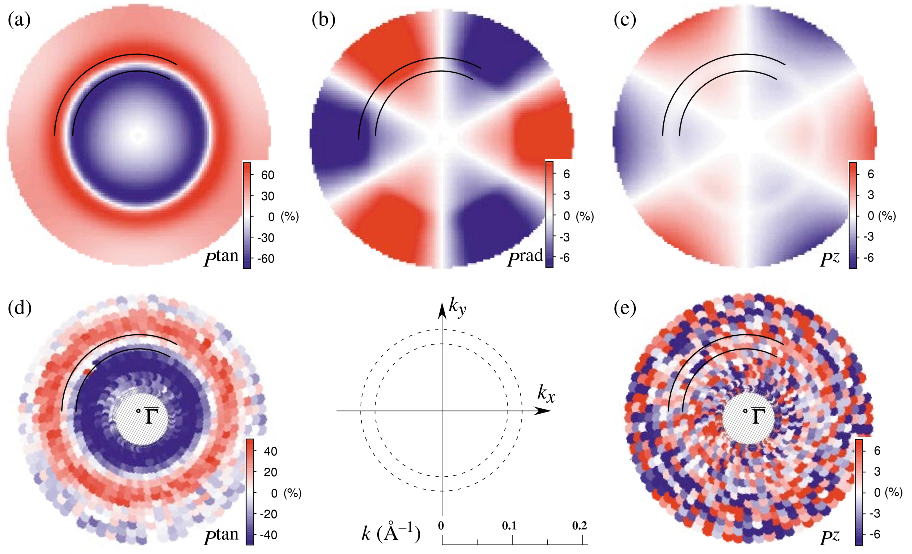

**Abbildung 3.5.** Spin- und winkelaufgelöste Photoelektronenspektroskopie von Au(111). Obere Reihe: Theoretische Resultate für die Tangentialkomponente $P^{\mathrm{tan}}$ (a), die Radialkomponente $P^{\mathrm{rad}}$ (b) und die Normalkomponente $P^{z}$ (c) der Spinpolarisation des „inneren“ und des „äußeren“ L-Lückenzustands im Zentrum der 2BZ (rot: positive Werte, blau: negative Werte; vgl. Abb. 3.4). Untere Reihe: Experimentell ermittelte Tangentialkomponente $P^{\mathrm{tan}}$ (d) und Normalkomponente $P^{z}$ (e). Die Positionen der Oberflächenzustände in der 2BZ sind durch Kreisbögen markiert. Die Bindungenergie beträgt $170\ \mathrm{meV}$. Die experimentellen Resultate wurden in Jürg Osterwalders Gruppe (Universität Zürich) aufgenommen.

## 3.3. Magnetokristalline Anisotropie dünner Filme

Mit magnetokristalliner Anisotropie [*Magneto-crystalline anisotropy* (MCA)] bezeichnet man die Ausrichtung der Magnetisierung $\boldsymbol{M}$ bezüglich ausgezeichneter kristalliner Achsen. Im Falle ferromagnetischer Systeme bei $T = 0$ bedeutet dieses, dass alle lokalen magnetische Momente parallel zur „leichten Achse“ ausgerichtet sind. Es sind jedoch auch nichtkollineare Anordnungen der magnetischen Momente möglich.

Die magnetokristalline Anisotropie erfordert die Kopplung der elektronischen Freiheitsgrade an die Spinfreiheitsgrade, was durch die SBK vermittelt wird. Die Spin–Bahn-Kopplung hebt Entartungen in der Bandstruktur $E(\boldsymbol{k})$ auf, jedoch in Abhängigkeit von der Magnetisierungsrichtung an unterschiedlichen Orten in der Brillouin-Zone (BZ). In weiten Teilen der BZ ergeben sich hingegen keine signifikanten Änderungen in der Bandstruktur. Die Magnetisierung wird die Konfiguration mit der geringsten Gesamtenergie einnehmen. Um die Gesamtenergien für verschiedene Magnetisierungsrichtungen genau zu bestimmen, sind deshalb sehr genaue Rechnungen auf einem sehr feinen Netz in der BZ notwendig (*Special points* [50]).

In Volumensystemen beträgt der Energiegewinn bei Änderung der Ausrichtung der Magnetisierung von der „harten“ in die „leichte“ Achse aufgrund der hohen Symmetrie lediglich einige $\mu$eV pro Atom. In dünnen Filmen hingegen ist durch die geringere Symmetrie der Energiegewinn zwischen der senkrechten Anisotropie (Ausrichtung der magnetischen Momente entlang der Oberflächennormalen) und der planaren Anisotropie (Ausrichtung innerhalb von zur Oberfläche koplanaren Ebenen) um einige Ordnungen größer und liegt im Bereich von $\mathrm{meV}$/Atom. Der Energiegewinn bei Ausrichtung entlang der leichten Achse innerhalb der Oberflächenebene ist wiederum deutlich kleiner.

Die Anisotropieenergie wird gewöhnlich durch Konstanten $K_i$ parametrisiert, indem man die Magnetisierungsrichtung in sphärischen Koordinaten $(\vartheta, \varphi)$ ausdrückt. Für ein tetragonal verzerrtes System erhält man beispielsweise für die Freie-Energiedichte

$$\begin{aligned} E(\vartheta, \varphi) = & - K_{2\perp} \cos^2(\vartheta) - K_{2\|} \cos(2\varphi) \sin^2(\vartheta) \\ & - \frac{1}{2} K_{4\perp} \cos^4(\vartheta) - \frac{1}{8} K_{4\|} [3 + \cos(4\varphi)] \sin^4(\vartheta) + \cdots . \end{aligned} \tag{3.7}$$

Einen wichtigen experimentellen Zugang zu den nicht einheitlich definierten Konstanten $K_i$ liefert die ferromagnetische Resonanz (FMR) [51]. Da die Orbitalmomente mit der Anisotropieenergie korrespondieren [53, 54], ist der Röntgenzirkulardichroismus in der Absorption von Rumpfniveaus [*X-ray magnetic circular dichroism* (XMCD) [55]] eine weitere, oft genutzte Methode, da mit ihm Orbitalmomente über die Summenregeln bestimmt werden können [56]. Im Volumenkristall ist das Orbitalmoment unterdrückt (sphärische Ladungsverteilung) und somit die Anisotropie klein, während in dünnen Filmen ein großes Orbitalmoment mit einer großen Anisotropie einhergeht. Mit wachsender Filmdicke $d$ bleibt der Volumenbeitrag $K_{i\mathrm{V}}$ der Anisotropie $K_i$ konstant. Die Grenzflächenbeiträge $K_{i\mathrm{S}}^{(\mathrm{surf})}$ von der Oberfläche und $K_{i\mathrm{S}}^{(\mathrm{if})}$ von der Film–Substrat-Grenzfläche nehmen relativ zur Gesamtanisotropie gemäß $K_i(d) = K_{i\mathrm{V}} + (K_{i\mathrm{S}}^{(\mathrm{surf})} + K_{i\mathrm{S}}^{(\mathrm{if})})/d$ ab.

Für große Filmdicken überwiegt der magnetostatische Dipolbeitrag, und die für geringe Filmdicken vorliegende senkrechte Anisotropie geht bei einer kritischen Dicke in die planare über. Dieses ist z. B. für Fe- und Co-Filme auf Cu(001) der Fall. Im Gegensatz dazu zeigen Ni-Filme auf Cu(001) ein komplementäres Verhalten. Diese sind bei geringen Filmdicken planar magnetisiert ($d < 7$ ML), zeigen dann allerdings einen Übergang zur senkrechten Anisotropie [*Spin-reorientation transition* (SRT)]. Für sehr dicke Filme ($d > 35$ ML) erzwingt der Dipolbeitrag wieder die planare Anisotropie. Um dieses ungewöhnliche Verhalten zu verstehen, wurden Gesamtenergierechnungen für verschiedene Gitterverzerrungen im Ni-Film durchgeführt (S. 20). Bevor deren Ergebnisse diskutiert werden, werden deren theoretische Grundlagen rekapituliert.

Für die Bestimmung der magnetokristallinen Anisotropie ist das *Force theorem* von essentieller Bedeutung [57–59]. Es erlaubt die Berechnung der magnetokristallinen Anisotropieenergie

(MAE) im Rahmen der lokalen Spindichtenäherung [*Local spin-density approximation* (LSDA)] und besagt, dass die durch die SBK hervorgerufene magnetokristalline Anisotropie durch die Differenz der relativistisch berechneten Bandenergien, die für zwei Richtungen $\boldsymbol{m}_1$ und $\boldsymbol{m}_2$ der Magnetisierung mit demselben skalar-relativistischen Potential berechnet wurden, gegeben ist: $E_{\mathrm{bnd}} = \sum_i^{\mathrm{occ}} \sum_{\boldsymbol{k}} [\epsilon_i(\boldsymbol{m}_1, \boldsymbol{k}) - \epsilon_i(\boldsymbol{m}_2, \boldsymbol{k})]$.

Der zweite Beitrag zur MAE ist die magnetostatische Energie $E_{\mathrm{dip}}$ der Magnetisierungsdichte $\boldsymbol{m}(\boldsymbol{r})$,

$$E_{\mathrm{dip}} = \frac{1}{c^2} \int \int \left[ \frac{\boldsymbol{m}(\boldsymbol{r}) \cdot \boldsymbol{m}(\boldsymbol{r}')}{|\boldsymbol{r} - \boldsymbol{r}'|^3} - 3 \frac{[(\boldsymbol{r} - \boldsymbol{r}') \cdot \boldsymbol{m}(\boldsymbol{r})]\,[(\boldsymbol{r} - \boldsymbol{r}') \cdot \boldsymbol{m}(\boldsymbol{r}')]}{|\boldsymbol{r} - \boldsymbol{r}'|^5} \mathrm{d}\boldsymbol{r}\, \mathrm{d}\boldsymbol{r}' \right]. \tag{3.8}$$

Der interatomare Beitrag des Moments für den Drehimpuls $l = 0$, der aus einer Multipolentwicklung von $\boldsymbol{m}(\boldsymbol{r})$ resultiert, ist nur bedingt konvergent und wird mittels Ewald-Technik berechnet. Durch die lange Reichweite der Dipol–Dipol-Wechselwirkung hängt die magnetostatische Energie von der Gestalt der Probe ab und führt somit zur Formanisotropie (*Shape anisotropy*). Bei dünnen Filmen zwingt der Dipolbeitrag die magnetischen Momente in die Filmebene.

Die Hauptaufgabe bei der numerischen Bestimmung der MAE dünner magnetischer Filme im Rahmen der LKKR-Methode ist die Berechnung der Bandenergie. Letztere lässt sich mit Hilfe der lagenaufgelösten Zustandsdichte $N_l(\epsilon)$ als $E_{\mathrm{bnd}}(\boldsymbol{M}) = \sum_l \int_{-\infty}^{E_{\mathrm{F}}} \epsilon\, N_l(\epsilon; \boldsymbol{M})\, \mathrm{d}\epsilon$ schreiben, wobei die Summe über alle magnetischen Schichten $l$ läuft, also auch über solche des Substrats, in denen ein Moment durch den magnetischen Film induziert wird. Die Energieintegration wird effizient als Konturintegral in der komplexen Ebene ausgeführt (Publikation 3 auf S. P23 [60]).

Um die Anisotropierechnungen interpretieren zu können, ist es hilfreich, die einzelnen Beiträge zur Bandenergie nach atomaren Schichten aufzulösen. Damit ergeben sich sog. Bandenergieprofile, die man sich näherungsweise aus einem Oberflächenbeitrag [$E_{\mathrm{bnd,L}}(\boldsymbol{M}, l)$] und einem Grenzflächenbeitrag [$E_{\mathrm{bnd,R}}(\boldsymbol{M}, l)$] superponiert vorstellen kann, von dem der Volumenbeitrag [$E_{\mathrm{bnd,B}}(\boldsymbol{M})$] subtrahiert wird (Abb. 3.6). Explizit formuliert,

$$E_{\mathrm{bnd}}(\boldsymbol{M}, l) \approx E_{\mathrm{bnd,L}}(\boldsymbol{M}, l) + E_{\mathrm{bnd,R}}(\boldsymbol{M}, l) - E_{\mathrm{bnd,B}}(\boldsymbol{M}). \tag{3.9}$$

Diese Näherung lässt sich mit Hilfe von Green-Funktionen für die konstituierenden Teilsysteme herleiten [60], in denen die SBK als Störung eingeführt wird. Vernachlässigt werden in obiger Gleichung Beiträge, die durch Reflexion der elektronischen Zustände an den beiden Grenzflächen den Ni-Films entstehen (Vakuum–Ni-Film und Ni-Film–Cu-Substrat in Abb. 3.6). Man könnte diese Beiträge als Quantentrogbeiträge bezeichnen. Für die schichtaufgelöste Magnetisierung $\boldsymbol{M}(l)$, also für das Magnetisierungsprofil, erhält man entsprechend $\boldsymbol{M}(l) \approx \boldsymbol{M}_{\mathrm{L}}(l) + \boldsymbol{M}_{\mathrm{R}}(l) - \boldsymbol{M}_{\mathrm{B}}$.

Wie erwähnt, zeigen Ni-Filme auf Cu(001) ein ungewöhnliches Verhalten in Bezug auf die magnetokristalline Anisotropie. Schon erste theoretische Arbeiten für tetragonal verzerrte Ni-Volumenkristalle gaben Hinweise darauf, dass die erste SRT durch die Gitterstruktur des Ni-Films erklärt werden könne [61]. Allerdings erlaubten diese Rechnungen keine Aussagen über die kritische Filmdicke, bei der die SRT stattfindet. Solche sind nur durch Anisotropierechnungen für

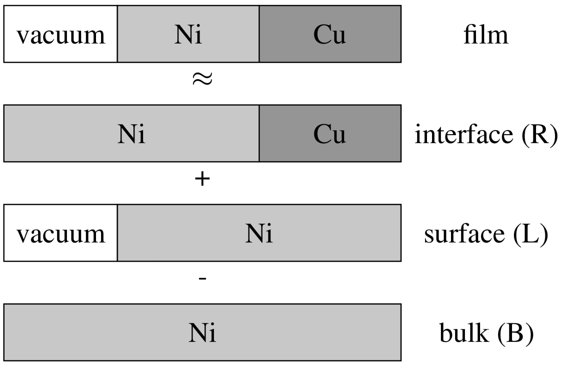

**Abbildung 3.6.** Konstruktion eines Ni-Films auf Cu(001). Ausgehend vom Ni-Volumenkristall (hellgrau; *Bulk*, B) werden die zwei Grenzflächen des Ni-Films (*Film*) durch Austausch von halbunendlichen Teilkristallen erzeugt: durch Vakuum (weiß) und durch Cu (dunkelgrau). Das erste ergibt das Oberflächensystem (*Surface*, L), das zweite das Grenzflächensystem (*Interface*, R). Die mathematischen Zeichen $\approx$, $+$ und $-$ beziehen sich auf Gl. (3.9).

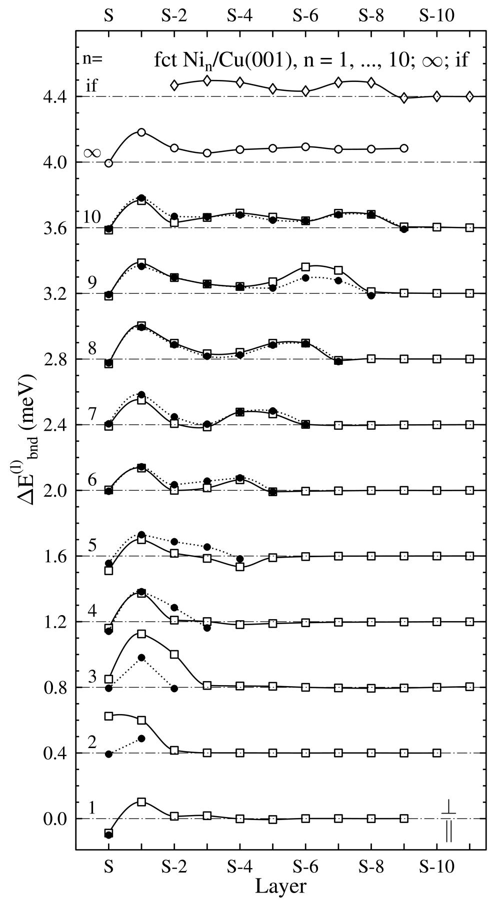

**Abbildung 3.7.** Bandenergiebeiträge zur magnetokristallinen Anisotropieenergie von tetragonal verzerrten Ni-Filmen auf Cu(001) mit Dicken von $n = 1$ bis $10$ ML. Das Profil für einen halbunendlichen Ni-Kristall ist mit $\infty$ gekennzeichnet, das einer Ni–Cu-Grenzfläche mit „if“. Ergebnisse aus *Ab–initio*-Rechnungen sind durch Quadrate dargestellt, während aus dem Superpositionprinzip [Gl. (3.9)] gewonnene durch ausgefüllte Kreise repräsentiert werden. Die atomaren Schichten sind mit S, S$-1$, S$-2$, …, bezeichnet, wobei S die äußerste Ni-Schicht markiert.

halbunendliche Ni/Cu(001)-Systeme möglich, in denen sowohl die Ni-Filmdicke variiert als auch die Gitterverzerrung in den Ni-Filmen berücksichtigt werden [60]. Der zweite, graduelle Spinreorientierungsübergang wurde durch Anpassungen an die Gitterstruktur des Ni-Volumens und durch Inselwachstum erklärt. Da diese Phänomene Rechnungen aus ersten Prinzipien nur schwer zugänglich sind, beschränkte man sich auf die erste und wichtigere SRT [62].

Der Spinreorientierungsübergang lässt sich anhand der Bandenergieprofile für den tetragonal verzerrten Ni-Film (fct-Fall) diskutieren. Hier wurden die Abstände aller Ni-Schichten um $6.9$ % im Vergleich zum Cu-Schichtabstand des Volumens reduziert, um das Atomvolumen wie im Ni-Volumenkristall zu erhalten. Abbildung 3.7 zeigt die lagenaufgelösten Bandenergiedifferenzen $\Delta E^{(l)}_{\mathrm{bnd}} = E^{(l)}_{\mathrm{bnd}}(\boldsymbol{M}^{(\|)}) - E^{(l)}_{\mathrm{bnd}}(\boldsymbol{M}^{(\perp)})$. Die Magnetisierungsrichtungen $\boldsymbol{M}^{(\|)}$ und $\boldsymbol{M}^{(\perp)}$ liegen entlang der kristallographischen [100]- und der [001]-Richtung. Insbesondere für dicke Filme sind die Beiträge von der Oberfläche („$\infty$“ in Abb. 3.7) und der Ni–Cu-Grenzfläche („if“) gut wiederzuerkennen. Im Vergleich zum unrelaxierten Ni-Film (fcc-Fall; hier nicht gezeigt) verschiebt sich die Bandenergiedifferenz zu positiven Werten, favorisiert also senkrechte Ansiotropie.[3] Der Volumenbeitrag der uniaxialen Anisotropie beträgt hier $K_{\mathrm{V}} = 0.081$ meV pro Atom und stimmt gut mit experimentellen und anderen theoretischen Werten überein. Ebenfalls zu positiven Werten verschieben sich der Oberflächen- und der Grenzflächenbeitrag. Ersterer ist im fcc-Fall in der äußersten Schicht S negativ, bevorzugt demnach planare Anisotropie.

Die Bandenergiedifferenzen aus dem Superpositionsprinzip zeigen im Allgemeinen qualitative Übereinstimmung mit den Resultaten der *Ab–initio*-Rechnungen. Nur bei sehr dünnen Filmen (etwa für Filmdicken $n \leq 3$) ergeben sich relevante Abweichungen, die auf das Fehlen der Quantisierungsbeiträge im Superpositionsmodell zurückzuführen sind. Das Profil für den Grenzflächenfall oszilliert weit in den vom Ni ausgefüllten Halbraum hinein. Damit wird unterstrichen, dass Ansätze, die sowohl den Grenzflächen- als auch den Oberflächenbeitrag auf eine fixierte Anzahl von

---

[3] Im Volumen von fcc-Ni verschwindet dieser Beitrag aufgrund der Symmetrie.

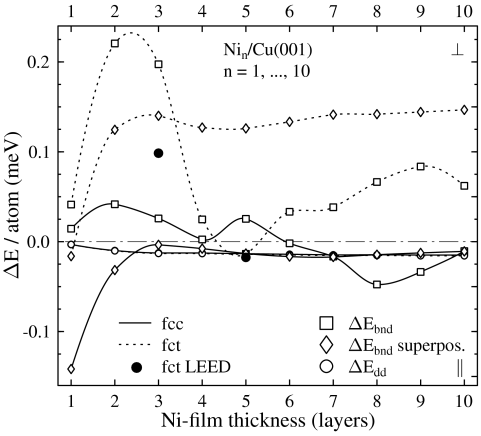

**Abbildung 3.8.** Magnetische Anisotropieenergien pro Ni-Atom in Ni-Filmen auf Cu(001). Bandenergiedifferenzen sind durch Quadrate ($\Delta E_{\mathrm{bnd}}$), Dipol-Dipol-Beiträge durch Kreise ($\Delta E_{\mathrm{dd}}$) dargestellt. Diamanten kennzeichnen Bandenergiebeiträge, die mit dem Superpositionsverfahren gewonnen wurden ($\Delta E_{\mathrm{bnd}}$ superpos.). Durchgezogene Linien verbinden die Werte für den fcc-Fall, gepunktete solche für den fct-Fall. Ausgefüllte Kreise für 3 und 5 ML zeigen Bandenergien für inhomogen verzerrte Ni-Filme („fct LEED“). Positive Werte bedeuten senkrechte Anisotropie, negative planare Anisotropie.

Schichten beschränken, dem Problem nicht vollständig gerecht werden. Das Superpositionsverfahren ist hier überlegen.

Wie Abbildung 3.8 zeigt, ist der magnetostatische Dipolbeitrag (Kreise in Abb. 3.8) von geringer Bedeutung für den Spinreorientierungsübergang. Die Dipolenergiedifferenzen $\Delta E_{\mathrm{dd}}^{(l)} = E_{\mathrm{dip}}^{(l)}(\boldsymbol{M}^{(\|)}) - E_{\mathrm{dip}}^{(l)}(\boldsymbol{M}^{(\perp)})$ sind deutlich kleiner (in absoluten Werten) als die Bandenergiebeiträge. Der Spinreorientierungsübergang lässt sich somit allein aus der Änderung des Bandenergiebeitrags bei Gitterverzerrungen erklären. In der Tat ist für den fct-Fall mit homogener Verzerrung ein Vorzeichenwechsel zwischen 5 und 6 ML zu erkennen, also ein Umklappen der Magnetisierung von der planaren in die senkrechte Ausrichtung, wie im Experiment gefunden wurde. Der fcc-Fall (unverzerrte Filme) hingegen zeigt auch für dicke Filme einen planare Ausrichtung ($\Delta E_{\mathrm{bnd}} < 0$). Das Ergebnis für den verzerrten Fall wird durch Rechnungen für 3 und 5 ML unterstützt, in denen Ni-Schichtabstände verwendet wurden, die aus LEED-Analysen stammen („fct LEED“). In diesen Fällen ist die Gitterverzerrung inhomogen.

Die Rechnungen für sehr dünne Filme, also für 1 und 2 ML Dicke, zeigen eine senkrechte Anisotropie, die im Experiment nicht gefunden wurde. Die hier diskutierten Rechnungen wurden für perfekte Grenzflächen und für die Temperatur 0 K durchgeführt. Es gibt dagegen experimentelle und theoretische Hinweise darauf, dass im ersten Stadium des Filmwachstums Ni-Atome nicht *auf* der Cu(001)-Oberfläche verbleiben, sondern *in* die ersten Schichten des Cu-Substrats diffundieren und somit eine Oberflächenlegierung bilden. Daraus resultiert eine Reduktion der MAE. Rechnungen im Rahmen der VCA bestätigen diese durch die strukturelle Unordung hervorgerufene Reduktion der Bandenergiedifferenzen (hier nicht gezeigt). Desweiteren sollte die Curie-Temperatur dieser dünnen Filme klein gegenüber der des Volumens sein und unterhalb der Raumtemperatur liegen. Daher könnten Fluktuationen der lokalen magnetischen Momente, die in der hier vorgestellten Theorie nicht enthalten sind, eine wesentliche Rolle spielen und die MAE ebenfalls reduzieren (vgl. in Hinblick auf Magnetismus dünner Filme bei endlichen Temperaturen auch Abschn. 4.6 auf S. 38ff).

Wie in Abbildung 3.7 gezeigt, ermöglicht das Superpositionsprinzip eine qualitative Analyse der Bandenergieprofile. Es erlaubt jedoch keine quantitive Bestimmung der kritischen Filmdicke des Spinreorientierungsübergangs, wie Abb. 3.8 belegt. Die Abweichungen zwischen den *Ab–initio*-Resultaten und denen der Superposition sind erheblich. Besonders deutlich wird dieses für den fct-Fall, für den die superponierten Bandenergien keinen Spinreorientierungsübergang zeigen ($\Delta E_{\mathrm{bnd}} > 0$ für $n \geq 2$). Dieser Befund ist ein Hinweis darauf, dass die Quantisierung der elektronischen Zustände im Ni-Film wichtig für die SRT ist.

## Resümee

In diesem Kapitel wurde anhand dreier Beispiele gezeigt, wie der relativistische Effekt der Spin–Bahn-Kopplung die elektronischen und magnetischen Eigenschaften von niedrigdimensionalen Systemen (atomaren Ketten, Oberflächen und magnetischen dünnen Filmen) beeinflussen kann. Ferner spielen geometrische und elektronische Struktur zusammen, insbesondere im Falle der Edelgasketten auf Pt(110)-1×2 und in Ni/Cu(001). Rechnungen, die auf ersten Prinzipien basieren, sind in der Lage, die experimentellen Befunde zu reproduzieren und zu erklären.

# 4. Photoelektronenspektroskopie

Nach einer Einführung in die Theorie der Photoemission (S. 25) wird in diesem Kapitel an ausgewählten Beispielen dargestellt, wie die Theorie im Zusammenspiel mit dem Experiment zu neuen Erkenntnissen führen kann. Die Spin–Bahn-Kopplung spielt eine wesentliche Rolle in der Erklärung der Spinpolarisation der Photoelektronen (S. 28), die von nichtmagnetischen Oberflächen emittiert werden, und beim Magnetischen Dichroismus (S. 29). Die Quantisierung elektronischer Zustände in dünnen Filmen wirkt sich in spezifischen Modulationen in den Photoemissionsspektren aus (S. 35), und die magnetische Struktur dünner Filme wird hinsichtlich ihrer Temperaturabhängigkeit untersucht (S. 38). Schließlich ermöglicht die Photoemission korrellierter Elektronenpaare die Abbildung der Elektron–Elektron-Wechselwirkung an Oberflächen (S. 41).

## 4.1. Einführung

Nachdem zahlreiche grundlegende Arbeiten verfasst wurden (siehe Ref. [63] für historische Details), gelang es erst in den sechziger Jahren des letzten Jahrhunderts, den photoelektrischen Effekt als spektroskopische Methode zu nutzen. Als Höhepunkt der frühen Arbeiten darf Einsteins Einführung der Photonen gelten, für die er 1921 den Nobelpreis erhielt [64]. Bahnbrechend waren die Arbeiten Siegbahns, der mittels Röntgenstrahlung die elektronische Struktur der inneren Schalen von Atomen untersuchte, eine Methode die heutzutage als *X-ray photoelectron spectroscopy* (XPS) bekannt ist [65]. Die Untersuchung der Valenzbandstruktur von Festkörpern erfordert typischerweise Photonen mit Energien im Vakuum-Ultraviolettbereich [*Vacuum ultraviolet* (VUV)] und eine winkelaufgelöste Detektion der Photoelektronen [66]. Wurden zunächst Gasentladungslampen eingesetzt, um monochromatisches Licht zu erhalten, wird heute vorwiegend Synchrotronstrahlung verwendet [67–69]: Beschleunigerringe stellen bei hoher Intensität hochgradig polarisiertes Licht in einem großen Energiebereich zur Verfügung. Wie LEED ist die VUV-Photoemission oberflächensensitiv, d. h., dass die Spektren Beiträge von der Oberfläche und vom Volumen enthalten.

Ein Photoemissionsexperiment ist durch eine Vielzahl von Parametern charakterisiert (Abb. 4.1 links). Das einfallende Licht wird durch seine Einfallsrichtung, seine Energie $\omega$ und seine Polarisation beschrieben. Die Photoelektronen werden hinsichtlich ihrer kinetischen Energie, der Austrittsrichtung (winkelaufgelöste Photoemission) und ihrer Spinpolarisation (spinaufgelöste Photoemission) analysiert.

Im Energie–Ort-Schema wird deutlich, dass sich der Photoemissionsprozess in drei Stufen darstellen lässt (Abb. 4.1 rechts) [70]. Anfangs sind die elektronischen Zustände bis zur Fermi-Energie $E_\mathrm{F}$ besetzt. Ein einfallendes Photon mit Energie $\omega$ regt ein Elektron in einen unbesetzten Zustand an. Letzteres bewegt sich zur Oberfläche und kann den Festkörper in Richtung des Detektors verlassen, falls seine Energie größer als das Vakuumniveau $E_\mathrm{vac}$ ist. Zurück bleibt ein Festkörper mit einem Loch. Die Mindestphotonenenergie, um Elektronen zu detektieren, ist durch die Austrittsarbeit $\Phi = E_\mathrm{vac} - E_\mathrm{F}$ gegeben und beträgt typischerweise etwa $5\ \mathrm{eV}$.

Im Allgemeinen werden Photoemissionsexperimente dergestalt durchgeführt, dass eine der involvierten Energien (Anfangszustands-, Endzustands- oder Photonenenergie) konstant gehalten wird. Im EDC-Modus (*Energy distribution curve*) ist die Photonenenergie konstant. Einer Variation der kinetischen Energie $E_\mathrm{kin}$ entspricht demnach eine Änderung der Anfangszustandsenergie. In den Modi *Constant initial-state* (CIS) und *Constant final-state* (CFS) wird hingegen die Photonenenergie variiert, während die Anfangszustandsenergie (CIS) oder die kinetische Energie (CFS) konstant gehalten wird.

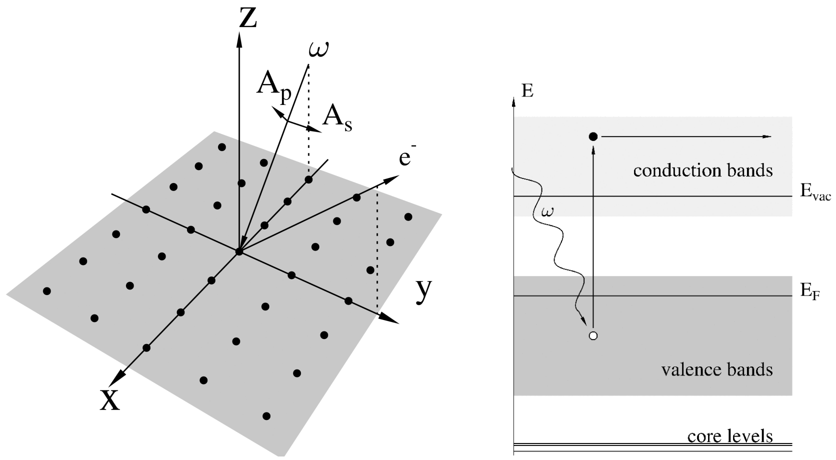

**Abbildung 4.1.** Schema der Photoemission. Links: Licht mit der Photonenenergie $\omega$ fällt auf eine Festkörperoberfläche (grau; Punkte repräsentieren Oberflächenatome). Die Komponenten seiner Polarisation sind $A_s$ und $A_p$. Die Austrittsrichtung der Photoelektronen ist durch $e^-$ gegeben (hier: in der $yz$-Ebene). Rechts: Ein Elektron (ausgefüllter Kreis) wird in einen Zustand oberhalb des Vakuumniveaus $E_{\mathrm{vac}}$ angeregt und lässt ein Loch (leerer Kreis) unterhalb der Fermi-Energie $E_{\mathrm{F}}$ zurück. Das Elektron, welches entweder aus dem Valenzbandbereich (*Valence bands*, grauer Bereich) oder aus den Rumpfniveaus (*Core levels*, horizontale Linien) stammt, verlässt den Festkörper und wird anschließend detektiert.

Eine einfache theoretische Beschreibung der Photoemission basiert auf Fermis Goldener Regel. Die Übergangswahrscheinlichkeit $w_{fi}$ zwischen dem Anfangszustand $|\Psi_i\rangle$ mit der Energie $E_i$ und dem Endzustand $\left|\Phi(\boldsymbol{k}_\parallel, E_f)\right\rangle$ mit der Energie $E_f = E_i + \omega$ und Impuls $\boldsymbol{k}_\parallel$ ist durch

$$w_{fi} = \left|\left\langle \Phi(\boldsymbol{k}_\parallel, E_f) \middle| \Delta \middle| \Psi_i \right\rangle\right|^2 \delta(E_f - E_i + \omega) \tag{4.1}$$

gegeben. Der Übergang wird durch den Dipoloperator $\Delta$ vermittelt. Den Photostrom $j$ zur kinetischen Energie $E_{\mathrm{kin}}$ und $\boldsymbol{k}_\parallel$ erhält man durch Summation über alle Anfangszustände, $j \sim \sqrt{E_{\mathrm{kin}}} \sum_i w_{fi}$. Die Detektionswinkel $\vartheta_{\mathrm{e}}$ und $\varphi_{\mathrm{e}}$ sowie die kinetische Energie bestimmen die Impulskomponenten $\boldsymbol{k}_\parallel$ der Photoelektronen parallel zur Oberfläche,

$$\boldsymbol{k}_\parallel = \sqrt{2E_{\mathrm{kin}}} \begin{pmatrix} \cos\varphi_{\mathrm{e}} \\ \sin\varphi_{\mathrm{e}} \end{pmatrix} \sin\vartheta_{\mathrm{e}}. \tag{4.2}$$

Heutzutage ist die winkelaufgelöste Photoemission [*Angle-resolved photoelectron spectroscopy* (ARPES)] mit VUV-Licht eine der erfolgreichsten Methoden, um die elektronische Struktur im Valenzbandbereich eines Festkörpers zu untersuchen [63, 71–73]. Allerdings kann die Interpretation der experimentellen Spektren fehl gehen, insbesondere im populären Modell der direkten Übergänge. Eine tiefergehende Analyse der Resultate erfordert daher Unterstützung seitens der Theorie, die im folgenden Abschnitt dargestellt wird. Sie bildet die Grundlage der in diesem Kapitel diskutierten Beispiele.

## 4.2. Einteilchentheorie der Photoemission

Die theoretischen Grundlagen der Photoemission als spektroskopische Methode wurden in den sechziger und siebziger Jahren des letzten Jahrhunderts gelegt. Als bahnbrechend kann die Arbeit von Pendry angesehen werden, der eine Vielfachstreutheorie der Photoemission entwickelte [74]. Diese enthält alle wesentlichen Zutaten für eine erfolgreiche Beschreibung der Experimente: elektronische Struktur, Übergangsmatrixelemente sowie Oberflächeneffekte [75–77].

Relativistische Effekte wurden vornehmlich von Feders [21] und Borstels [78–80] Forschergruppen untersucht. Befasste sich letztere vorwiegend mit *Optical orientation* [81, 82], also der Ausrichtung des Photoelektronenspins parallel oder antiparallel zur Einfallsrichtung des zirkular polarisierten Lichts, sagte erstere voraus, dass sogar linear polarisiertes Licht spinpolariserte Photoelektronen erzeugen kann [83–85]. Alle Vorhersagen wurden von Heinzmanns Gruppe experimentell bestätigt [86–88].

Die Erweiterung der relativistischen Photoemissionstheorie auf spinpolarisierte Systeme ermöglichte die Erklärung des Magnetischen Dichroismus (MD), d. i. die Änderung des Photostroms bei Umkehr der Magnetisierungsrichtung des ferromagnetischen Festkörpers [89]. Basierend auf einer gruppentheoretischen Analyse (Publikation 4 auf S. P34ff), konnten detaillierte Aussagen zur elektronischen Struktur von Ferromagneten getroffen werden (Publikationen 6 und 7 auf S. P59ff und S. P69ff) [90–92]. Somit wurde der Magnetische Dichroismus auch in der Valenzbandphotoemission etabliert, nachdem er schon in der Photoemission von Rumpfniveaus sehr erfolgreich eingesetzt wurde [55]. Summenregeln, die die Spin- und Orbitalmomente in Beziehung zu den integrierten Intensitäten bringen, existieren hingegen für die Valenzbandphotoemission nicht [56]. Desweiteren konnte die Photoemission von Ferromagneten bei endlichen Temperaturen beschrieben werden (Publikation 8 auf S. P80ff [93]).

**Formalismus der Einteilchentheorie der Photoemission.** Die Photoemissonstheorie, die die Grundlage für die meisten heutzutage verwendeten Implementationen in Computerprogrammen darstellt, wurde von Feibelman und Eastman [94] formuliert. Den Ausgangspunkt bilden Ergebnisse von Caroli *et al.* [95], die Keldyshs Green-Funktionsformalismus für Nichtgleichgewichtssysteme auf den Photoemissionsprozess anwendeten.

Ein halbunendlicher Festkörper, dessen Elektronen als voneinander unabhängig angenommen werden, wird mit monochromatischem Licht bestrahlt. Der Hamilton-Operator für das gesamte System lautet

$$H(t) = \frac{1}{2}\left[\boldsymbol{p} + \frac{1}{c}\boldsymbol{A}(\boldsymbol{r}, t)\right]^2 + V(\boldsymbol{r}), \tag{4.3}$$

worin $V(\boldsymbol{r})$ das Festkörperpotential ist. Die Stromdichte $j$ an der Position $\boldsymbol{R}$ des Detektors wird mittels zeitabhängiger Störungstheorie berechnet, wobei das Vektorpotential $\boldsymbol{A}$ adiabatisch eingeschaltet wird. Vernachlässigt man den diamagnetischen Anteil $\boldsymbol{A}^2/(2c^2)$ des Dipoloperators $\Delta$, und beachtet, dass Terme, in denen der Stromdichteoperator auf gebundene Zustände wirkt, keinen Beitrag zum Photostrom geben, bleibt genau ein Term übrig, der die Anregung von Zuständen mit der Energie $E$ in solche mit $E + \omega$ beschreibt. Ausgedrückt mittels Green-Funktionen lautet dann der Ausdruck für den Photostrom

$$j \sim -\sqrt{2(E+\omega)}\,\left\langle \Phi_0^{\star} \middle| G^{-}(E+\omega)\,\Delta\,\mathrm{Im}\,G^{+}(E)\,\Delta^{\dagger}\,G^{+}(E+\omega) \middle| \Phi_0^{\star} \right\rangle, \tag{4.4}$$

worin $|\Phi_0^{\star}\rangle$ eine ebene Welle an der Detektorposition ist. Diese Gleichung wird durch das Feynman-Diagramm in Abb. 4.2 beschrieben und kann wie folgt gedeutet werden. Zuerst wird der Photoelektronenzustand $|\Phi_0^{\star}\rangle$ mit der Energie $E{+}\omega$ mittels der retardierten GF $G^{+}$ vom Detektor ins Festkörperinnere propagiert. Anschließend bewirkt der Dipoloperator $\Delta^{\dagger}$ eine Abregung in einen Anfangszustand mit der Energie $E$ (beschrieben durch $\mathrm{Im}\,G^{+}$). Zuletzt erfolgt die Anregung in den auslaufenden Zustand $\langle\Phi_0^{\star}|\,G^{-}$ mittels $\Delta$. Diagramme höherer Ordnung werden im allgemeinen nicht berücksichtigt, d. h., man nimmt an, dass das Photoelektron nicht mit den verbleibenden Elektronen und dem Photoloch wechselwirkt (*Sudden approximation* [96–98]).

Inelastische Prozesse lassen sich mittels der Selbstenergie $\Sigma$ beschreiben [99]. In erster Näherung ist $\Sigma$ lokal und homogen und wird dann als optisches Potential bezeichnet. Ihr Realteil verschiebt die Energien der Quasiteilchen. Der Imaginärteil beschreibt die Lebensdauer und führt zu einer Verbreiterung der Strukturen in den Photoemissionsspektren, die der spektralen Dichte $A(E) = -\mathrm{Im}\,\mathrm{Tr}\,G(\boldsymbol{r}, \boldsymbol{r}; E)/\pi$ wie folgt zugeschrieben werden kann:

$$A(E) = \sum_m \begin{cases} \delta(E - E_m) & \text{relle Energie } E \\ \frac{\Gamma}{\pi}\frac{1}{(E-E_m)^2+\Gamma^2} & \text{komplexe Energie } E + \mathrm{i}\Gamma\ . \\ \frac{\mathrm{Im}\,\Sigma(E_m)}{[E-E_m-\mathrm{Re}\Sigma(E_m)]^2+[\mathrm{Im}\,\Sigma(E_m)]^2} & \text{allg. Fall} \end{cases} \tag{4.5}$$

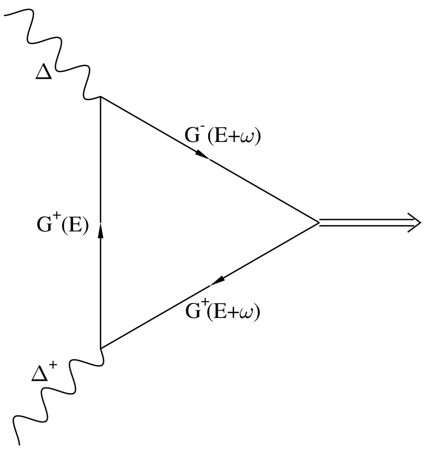

**Abbildung 4.2.** Feynman-Diagramm der Photoemission entsprechend Gl. (4.4). Die Doppellinie repräsentiert den Detektorzustand $|\Phi_0^\star\rangle$ mit der Energie $E+\omega$ und Impuls $\boldsymbol{k}_\parallel$. Die Green-Funktionen $G^\pm$ werden durch Pfeile dargestellt, Photonen durch Wellenlinien.

Die Energieabhängigkeit des optischen Potentials wird i. d. R. heuristisch modelliert.

**Der Endzustand der Photoemission.** Der Zusammenhang zwischen LEED und Photoemission wird am zeitumgekehrten Endzutand $|\Phi\rangle$ deutlich. Dieser erfüllt

$$\Phi(\boldsymbol{R}, E+\omega) = \exp(\mathrm{i}\boldsymbol{k}\cdot\boldsymbol{R}) + \int G^+(\boldsymbol{R},\boldsymbol{r}'; E+\omega)\, V(\boldsymbol{r}')\, \exp(\mathrm{i}\boldsymbol{k}\cdot\boldsymbol{r}')\,\mathrm{d}r'^3, \tag{4.6}$$

$[k = \sqrt{2(E+\omega)}]$ und entspricht der Superposition einer einlaufenden ebenen Welle $\langle\boldsymbol{R}|\Phi_0\rangle = \exp(\mathrm{i}\boldsymbol{k}\cdot\boldsymbol{R})$ [Gl. (4.4)] und auslaufenden Wellen, letztere beschrieben durch das Integral. Die retardierte Green-Funktion propagiert die Elektronen vom Inneren des Festkörpers zum Detektor. Kurz, $|\Phi\rangle$ ist ein zur Beschreibung von LEED geeigneter Zustand, und $|\Phi^\star\rangle$ wird daher als zeitumgekehrter LEED-Zustand bezeichnet.

In Vielfachstreutheorie formuliert, erhält man den Ausdruck

$$\begin{aligned}\Phi_\tau^{\mathrm{LEED}}(\boldsymbol{r}_n; E, \boldsymbol{k}) = {} & \exp(\mathrm{i}\boldsymbol{k}\cdot\boldsymbol{R}_n)\sum_\Lambda \left\langle\boldsymbol{r}_n\middle|J_\Lambda^{\mathrm{R}}\right\rangle a_{\Lambda\tau}(\widehat{\boldsymbol{k}}) \\ & + \frac{\mathrm{i}}{k}\sum_m \exp(\mathrm{i}\boldsymbol{k}\cdot\boldsymbol{R}_m) \sum_{\Lambda\Lambda'\Lambda''} \left\langle\boldsymbol{r}_n\middle|J_{\Lambda'}^{\mathrm{R}}\right\rangle U_{\Lambda'\Lambda''}^{nm}\, t_{\Lambda''\Lambda}^{\mathrm{L}}\, a_{\Lambda\tau}(\widehat{\boldsymbol{k}})\end{aligned} \tag{4.7}$$

für die Wellenfunktion am Gitterplatz $\boldsymbol{R}_n$ [$a_{\Lambda\tau}(\widehat{\boldsymbol{k}})$ stammt von der sphärischen Entwicklung der ebene Welle]. Noch kompakter ist die Darstellung mit Hilfe des Streupfadoperators (SPO) $\tau^{nm}$: $\Phi_\tau^{\mathrm{LEED}}(\boldsymbol{r}_n; E, \boldsymbol{k}) = \frac{\mathrm{i}}{k}\sum_m \exp(\mathrm{i}\boldsymbol{k}\cdot\boldsymbol{R}_m)\sum_{\Lambda\Lambda'} \left\langle\boldsymbol{r}_n\middle|Z_\Lambda^{\mathrm{R}}\right\rangle \tau_{\Lambda\Lambda'}^{nm}\, a_{\Lambda\tau}(\widehat{\boldsymbol{k}})$.

**Übergangsmatrixelemente und spinpolarisierter Photostrom.** Einen wichtigen Beitrag zur korrekten Beschreibung der Intensitäten bilden die Übergangsmatrixelemente zwischen dem Anfangs- und dem Endzustand. Die Wechselwirkung eines Elektrons mit dem einfallenden, monochromatischen Licht der Energie $\omega$ und dem Wellenvektor $\boldsymbol{q}$ wird relativistisch durch $H'(\boldsymbol{r},t) = \boldsymbol{\alpha}\cdot\boldsymbol{A}(\boldsymbol{r},t) = \boldsymbol{\alpha}\cdot\boldsymbol{A}_0\,\mathrm{e}^{\mathrm{i}\boldsymbol{q}\cdot\boldsymbol{r}-\omega t}$ beschrieben. Gewöhnlich zerlegt man den elektrischen Feldvektor $\boldsymbol{A}$ in Anteile, die links- und rechtszirkular sowie linear polarisiertes Licht beschreiben $[\boldsymbol{A} = (A_+, A_-, A_z)]$.

Die Übergangsmatrixelemente an einem bestimmten Gitterplatz erhält man durch Integration über die MT-Kugeln. Die Winkelintegration ergibt dann die bekannten „atomaren" Auswahlregeln: $\Delta l = \pm 1$ sowie $\Delta m = 0$ für linear und $\Delta m = \pm 1$ für zirkular polarisiertes Licht. Die radiale Integration enthält einerseits Matrixelemente zwischen regulären Lösungen, die zu

$$M_{i\Lambda'\Lambda}^{(1)} = \int_0^{R_{\mathrm{mt}}} \langle J_{\Lambda'}(E+\omega)|r\rangle\, \alpha_i A_i\, \langle r|J_\Lambda(E)\rangle\,\mathrm{d}r, \quad i = \pm, z, \tag{4.8}$$

führen. Der gitterplatz-diagonale Beitrag der GF $G^{+}(E)$ ergibt eine zweifache Integration aufgrund der irregulären Lösungen (mit Matrixelementen $M^{(2)}_{i\Lambda'\Lambda}$).

Setzt man die auslaufende ebene Welle als Pauli-Spinor an (mit Komponenten $\Phi^{\star}_{0\tau}$), so erlaubt die Spindichtematrix

$$\rho_{\tau\tau'} \sim \left\langle \Phi^{\star}_{0\tau} \middle| G^{-}(E+\omega)\Delta \operatorname{Im} G^{+}(E)\, \Delta^{\dagger}\, G^{+}(E+\omega) \middle| \Phi^{\star}_{0\tau'} \right\rangle, \quad \tau, \tau' = \pm, \tag{4.9}$$

des Photoelektrons die Berechnung des Photostroms $I = \mathrm{tr}(\rho)$ und der Spinpolarisation $\boldsymbol{P} = \mathrm{tr}(\boldsymbol{\sigma}\rho)/\mathrm{tr}(\rho)$. Die Symmetrie des Endzustands ermöglicht bei bekannter Lichtpolarisation eine detaillierte gruppentheoretische Analyse der Photoemission von magnetischen und nichtmagnetischen Oberflächen [100, 101]. Im besonderen zeigt diese, welche Dipolübergänge für bestimmte Anfangszustände erlaubt sind, welche Komponenten der Spinpolarisation ungleich Null sind und, im Fall magnetischer Systeme, ob Magnetischer Dichroismus auftreten kann [102].

## 4.3. Spinpolarisation in der Photoemission von nichtmagnetischen Oberflächen

Neben der Aufspaltung von Energieniveaus (Publikation 2 auf den S. P6ff; vgl. [41]) ist eine weitere wichtige Manifestation der Spin–Bahn-Kopplung (SBK) die Erzeugung von spinpolarisierten Photoelektronen in der Photoemission von nichtmagnetischen Oberflächen. Obwohl für Atome diese Spinpolarisationseffekte bereits bekannt waren [103], war man der Ansicht, dass für Festkörperoberflächen vergleichbare Effekte nicht aufträten [104]. Die Vorhersage der Feder'schen Gruppe (Universität Duisburg) von drei Effekten in der normalen Emission, die von der Heinzmann-Gruppe (Universität Bielefeld) experimentell bestätigt wurden, eröffneten der spinaufgelösten Photoemission neue Möglichkeiten. Man beachte in diesem Zusammenhang, dass der Dipoloperator nur auf die orbitalen Anteile der Zustände wirkt. Die Spin–Bahn-Kopplung ist demnach unabdingbar, da sie die orbitalen Freiheitsgrade der Elektronen an deren Spinfreiheitsgrade koppelt.

Die „optische Orientierung“, d. i. die Ausrichtung des Photoelektronenspins an der Helizität des einfallenden, zirkular polarisierten Lichts, lässt sich bildhaft so erklären, dass der Photonenspin auf das Photoelektron übertragen wird. Für linear polarisiertes Licht, dass sich als Linearkombination von links- und rechtszirkular polarisiertem Licht darstellen lässt, ist ein ähnlich anschauliches Bild schwer zu finden. Dass linear polarisiertes Licht in der Tat spinpolarisierte Photoelektronen erzeugt, kann auf dreierlei Wegen plausibel gemacht werden: (i) Symmetriebetrachtungen erlauben Aussagen darüber, welche Komponenten der Spinpolarisation für einen Messaufbau[1] von Null verschieden sind. (ii) Analytische Rechnung im Rahmen der Gruppentheorie ergeben die Abhängigkeit der Spinpolarisation vom einfallenden Licht (Einfallswinkel und Polarisation) für jede Darstellung der Anfangs- und Endzustände. (iii) Letztendlich geben numerische Rechnungen Aufschluss über die Größe der Spinpolarisation. Diese drei Ansätze liefern ein konsistentes Bild, bedürfen allerdings der Überprüfung durch das Experiment.

Als ein analytisches Beispiel diskutiere ich die Spinpolarisation von (110)-Oberflächen kubischer Festkörper. Die relevante Punktgruppe im Fall normaler Emission ($\boldsymbol{k}_{\parallel} = 0$) ist $2mm$ ($C_{2v}$ in Schönflies-Notation), die die Elemente $1$, $m_{xz}$, $m_{yz}$ und $c_{2z}$ umfasst (Tab. 4.1). Da $\boldsymbol{A}$ quadratisch in den Ausdruck für den Photostrom eingeht, sind Terme für $\boldsymbol{A}$ und $-\boldsymbol{A}$ äquivalent. Für in der $yz$-Ebene einfallendes s-polarisiertes Licht ($A_y = A_z = 0$) folgt $\boldsymbol{P} = 0$. Verwendet man stattdessen p-polarisiertes Licht ($A_x = 0$), darf $P_x$ ungleich Null sein. Eine Änderung des Azimuts um $180^{\circ}$ ergibt weiterhin $P_x(A_y, A_z) = -P_x(-A_y, A_z)$. Ein nicht verschwindendes $P_z$ erhält man zum Beispiel für s-polarisiertes Licht, das nicht in einer der Spiegelebenen einfällt.

Die gruppentheoretische Analyse ergibt Ausdrücke für die Spinpolarisation in Abhängigkeit vom Einfallsazimut $\varphi$ des Lichts (Publikation 4 auf S. P34ff [101]). Dazu werden zunächst sym-

---

[1] Unter Messaufbau ist die Gesamtheit der konstituierenden Ingredienzen zu verstehen, also Oberfläche, Polarisation und Einfallsrichtung des Lichts sowie die Detektionsrichtung der Photoelektronen.

| Operation | Feldvektor | | | Spinpolarisation | | |
|---|---|---|---|---|---|---|
| $1$ | $A_x$ | $A_y$ | $A_z$ | $P_x$ | $P_y$ | $P_z$ |
| $m_{xz}$ | $A_x$ | $-A_y$ | $A_z$ | $-P_x$ | $P_y$ | $-P_z$ |
| $m_{yz}$ | $-A_x$ | $A_y$ | $A_z$ | $P_x$ | $-P_y$ | $-P_z$ |
| $c_{2z}$ | $-A_x$ | $-A_y$ | $A_z$ | $-P_x$ | $-P_y$ | $P_z$ |

**Tabelle 4.1.** Symmetrieanalyse der normalen Photoemission von (110)-Oberflächen kubischer Festkörper. Die Operationen der Punktgruppe $2mm$ wirken auf den elektrischen Feldvektor $\boldsymbol{A} = (A_x, A_y, A_z)$ des einfallenden Lichts und die Spinpolarisation $\boldsymbol{P} = (P_x, P_y, P_z)$ des Photoelektrons. Die Oberflächennormale ist die $z$-Achse.

metrie-adaptierte Wellenfunktionen bestimmt. Die Einfachgruppe $2mm$ besitzt vier Darstellungen $(\Sigma^{(1)}, \ldots, \Sigma^{(4)})$, die in der zugehörigen Doppelgruppe $\overline{2mm}$ zu einer Darstellung zusammenfallen $(\Sigma_5)$. Die Wellenfunktionen lassen sich daher schematisch als

$$|\Psi_{5\pm}\rangle = \left|\Sigma_5^{(1)}\right\rangle \chi^{\pm} + \left|\Sigma_5^{(2)}\right\rangle \chi^{\pm} + \left|\Sigma_5^{(3)}\right\rangle \chi^{\mp} + \left|\Sigma_5^{(4)}\right\rangle \chi^{\mp} \tag{4.10}$$

schreiben, wobei die Raum–Winkel-Anteile gemäß den Darstellungen der Einfachgruppe klassifiziert werden. Die räumlichen Anteile sind im Fall nichtmagnetischer Systeme für jedes Kramers-Doublett gleich. Nur die Spin–Winkel-Anteile unterscheiden sich und lassen sich mit Hilfe des Zeitumkehroperators $T$ ineinander überführen. Die Spindichtematrix wird dann aus allen erlaubten Übergängen zwischen den Kramers-Doubletts des Anfangs- und des Endzustands bestimmt. Für die Spinpolarisation im Fall s-polarisierten Lichts ergibt sich

$$P_z(\varphi) = -\frac{1}{I(\varphi)} \sin 2\varphi \, \mathrm{Im}[M^{(3)} M^{(4)\star}], \tag{4.11}$$

wobei die Intensität durch

$$I(\varphi) = \sin^2 \varphi \mid M^{(3)} \mid^2 + \cos^2 \varphi \mid M^{(4)} \mid^2 \tag{4.12}$$

gegeben ist. Die Übergangsmatrixelemente $M^{(3)}$ und $M^{(4)}$ tragen als Index die Einfachgruppen-Darstellung des Anfangszustands (Der totalsymmetrische Endzustand gehört zur Darstellung $\Sigma^{(1)}$ [100]). Im obigen Ausdruck für $P_z$ ist der Einfluss der SBK sofort auszumachen: ohne sie gäbe es keine Hybridisierung der $\Sigma^{(3)}$- und $\Sigma^{(4)}$-Wellenfunktionen und damit kein Produkt von Matrixelementen verschiedener Darstellungen der Einfachgruppe. $P_z$ verschwände somit. Die Messung von $P_z$ erlaubt daher detaillierte Aussagen über die orbitale Zusammensetzung der Anfangszustände, insbesondere in Gebieten der Bandstruktur $E(\boldsymbol{k})$, in denen Anfangszustände miteinander hybridisieren. Denn die aus diesen emittierten Photoelektronen sollten erwartungsgemäß eine große Spinpolarisation aufweisen.

Numerische Vorhersagen, die im Rahmen der hier skizzierten relativistischen Photoemissionstheorie gewonnen wurden, finden sich in Publikation 5 (S. P53ff) für die rekonstruierte Pt(110)-1×2-Oberfläche. Die experimentelle Bestätigung erfolgte durch die Heinzmann-Gruppe [88]. Wie zu erwarten, ist $P_z$ an den Stellen in der Bandstruktur beträchtlich, an denen $\Sigma^{(3)}$- und $\Sigma^{(4)}$-Wellenfunktionen aufgrund der SBK hybridisieren.

## 4.4. Magnetischer Dichroismus

Mit Dichroismus in der Photoemission wird die Änderung der Intensität in Abhängigkeit eines einstellbaren Parameters bezeichnet. So ist der Zirkulardichroismus in der winkelaufgelösten Photoemission [*Circular dichroism in angular distribution* (CDAD)] die Variation des Photostroms bei Umkehr der Helizität des zirkular polarisierten Lichts. Dieser tritt in chiralen Messaufbauten oder in der Spektroskopie chiraler Moleküle auf und basiert auf der Symmetriebrechung aufgrund der Chiralität.

Eine wichtige Eigenschaft magnetischer Systeme ist die Richtung der Magnetisierung $\boldsymbol{M}$. Als Magnetischen Dichroismus (MD) bezeichnet man daher die Änderung der Photoemissionsintensität

$I$ bei Umkehr der Magnetisierungsorientierung ($\boldsymbol{M} \to -\boldsymbol{M}$), während alle anderen Parameter fixiert bleiben [$I(\boldsymbol{M}) \neq I(-\boldsymbol{M})$]. Offensichtlich erfordert die Beschreibung des MD die Einbeziehung der SBK, da der Dipoloperator nur auf die räumlichen Anteile der beteiligten Zustände wirkt. Letzterer muss jedoch an den Elektronenspin, und somit an die Magnetisierung, gekoppelt werden. Daraus folgt ein unmittelbarer Zusammenhang mit den im vorigen Abschnitt skizzierten Spinpolarisationseffekten in der Photoemission von nichtmagnetischen Oberflächen: Die Intensitätsänderung resultiert aus der Symmetriebrechung durch die Magnetisierung.

Um diesen Zusammenhang zu verdeutlichen, betrachte ich die Photoemission einer senkrecht magnetisierten (110)-Oberfläche, in Analogie zum vorigen Beispiel. In diesem Fall ist die Entartung der Kramers-Doubletts $|\Psi_{5\pm}\rangle$ aufgehoben (Austauschaufspaltung), und die räumlichen Anteile der Zustände unterscheiden sich:

$$|\Psi_{5\pm}\rangle = \left|\Sigma_5^{(1\pm)}\right\rangle \chi^{\pm} + \left|\Sigma_5^{(2\pm)}\right\rangle \chi^{\pm} + \left|\Sigma_5^{(3\pm)}\right\rangle \chi^{\mp} + \left|\Sigma_5^{(4\pm)}\right\rangle \chi^{\mp}. \tag{4.13}$$

Es gilt daher *nicht* mehr $T\,|\Psi_{5+}\rangle = |\Psi_{5-}\rangle$ und $T\,|\Psi_{5-}\rangle = -\,|\Psi_{5+}\rangle$. Eine Rechnung analog zum nichtmagnetischen Fall ergibt für die Spinpolarisation

$$\begin{aligned} P_z(\varphi) = \Big\{ &\sin^2\varphi \left(|\,M^{(3+-)}\,|^2 - |\,M^{(3-+)}\,|^2\right) + \cos^2\varphi \left(|\,M^{(4+-)}\,|^2 - |\,M^{(4-+)}\,|^2\right) \\ &- \sin 2\varphi \left[\mathrm{Im}(M^{(3-+)}M^{(4-+)\star}) + \mathrm{Im}(M^{(3+-)}M^{(4+-)\star})\right]\Big\} / I(\varphi), \end{aligned} \tag{4.14}$$

wobei die Intensität durch

$$\begin{aligned} I(\varphi) = &\sin^2\varphi \left(|\,M^{(3+-)}\,|^2 + |\,M^{(3-+)}\,|^2\right) + \cos^2\varphi \left(|\,M^{(4+-)}\,|^2 + |\,M^{(4-+)}\,|^2\right) \\ &- \sin 2\varphi \left(\mathrm{Im}(M^{(3-+)}M^{(4-+)\star}) - \mathrm{Im}(M^{(3+-)}M^{(4+-)\star})\right) \end{aligned} \tag{4.15}$$

gegeben ist. Der nichtmagnetische Fall folgt unmittelbar aus der Gleichheit der Matrixelemente, d. i. $M^{(i\pm\pm)} = M^{(i\mp\mp)}$ aufgrund der Entartung der dann vorliegenden Kramers-Doubletts. Die Spinpolarisation besteht aus zwei Anteilen: dem durch den Austausch induzierten ($|\,M^{(3+-)}\,|^2 - |\,M^{(3-+)}\,|^2$ und $|\,M^{(4+-)}\,|^2 - |\,M^{(4-+)}\,|^2$) und einem durch die SBK hervorgerufenen [$\mathrm{Im}(M^{(3-+)}M^{(4-+)\star}) + \mathrm{Im}(M^{(3+-)}M^{(4+-)\star})$]. Nur letzterer bleibt im Grenzübergang zum nichtmagnetischen System von Null verschieden.

Die Umkehrung der Magnetisierung vertauscht die Zeitumkehrindizes der Zustände, $M^{(i\pm\pm)} \to M^{(i\mp\mp)}$. Der Dichroismus $A(\varphi) = I(\varphi, \boldsymbol{M}) - I(\varphi, -\boldsymbol{M})$ enthält gerade diejenigen Matrixelemente, die auch den SBK-Anteil der Spinpolarisation ergeben:

$$A(\varphi) = \sin 2\varphi \left[[\mathrm{Im}(M^{(3-+)}M^{(4-+)\star}) - \mathrm{Im}(M^{(3+-)}M^{(4+-)\star})\right]. \tag{4.16}$$

Der direkte Zusammenhang des MD mit den Spinpolarisationseffekten in der Photoemission von nichtmagnetischen Systemen ist somit offenkundig. Die hier skizzierten Analysen lassen sich folglich zur Grundregel für das Vorhandensein vom MD zusammenfassen:

> Magnetischer Dichroismus tritt dann auf, wenn im Grenzfall des nichtmagnetischen Systems eine Komponente der Spinpolarisation entlang der Magnetisierung aus Symmetriegründen ungleich Null ist.

Diese Aussage wurde durch eine Vielzahl von analytischen und numerischen Rechnungen, von denen einige in den beigefügten Publikationen dokumentiert sind, vollauf bestätigt.

Magnetischer Dichroismus wurde als Ersatz für spinaufgelöste Messungen angesehen. Die obigen Resultate zeigen jedoch, dass diese Vermutung nicht gerechtfertigt ist. Die Spinpolarisation lässt sich in einen Austausch- und in einen Spin–Bahn-Anteil zerlegen: $P_z(\boldsymbol{M}) = P_z^{\mathrm{ex}}(\boldsymbol{M}) + P_z^{\mathrm{soc}}(\boldsymbol{M})$. Für ersteren gilt $P_z^{\mathrm{ex}}(\boldsymbol{M}) = -P_z^{\mathrm{ex}}(-\boldsymbol{M})$ [vgl. die ersten beiden Terme in Gl. (4.14)], während für letzteren $P_z^{\mathrm{soc}}(\boldsymbol{M}) = P_z^{\mathrm{soc}}(-\boldsymbol{M})$ [vgl. den letzten Term in Gl. (4.14)] gilt. Der Dichroismus $A(\varphi)$

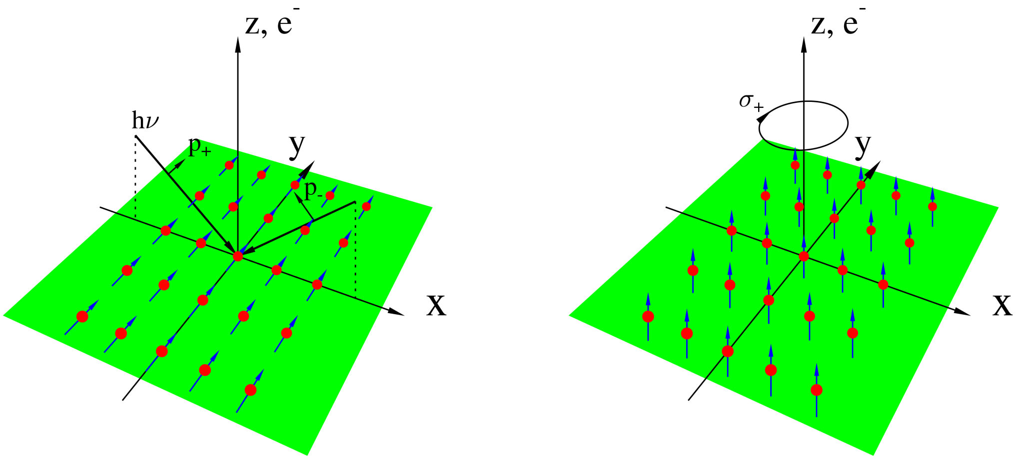

**Abbildung 4.3.** Standardmessaufbau für Magnetischen Dichroismus in normaler Emission. Links: Magnetischer Lineardichroismus (MLD). P-polarisiertes Licht mit der Energie $h\nu$ fällt unter nichtnormaler Inzidenz auf die Probenoberfläche (grün). Sein elektrischer Feldvektor ($p_+$ oder $p_-$) steht senkrecht auf der Magnetisierung $\boldsymbol{M}$, die durch blaue Pfeile an den Gitterplätzen (rot) symbolisiert ist. Rechts: Magnetischer Zirkulardichroismus (MCD). Zirkular polarisiertes Licht ($\sigma_+$) fällt unter normaler Inzidenz auf die Probenoberfläche. Die Probenmagnetisierung $\boldsymbol{M}$ ist ebenfalls parallel zur Probennormale ausgerichtet.

enthält jedoch die Matrixelemente des SBK-induzierten Anteils des Spinpolarisation, und nicht die vom Austausch induzierten. Ist die Stärke der SBK gering im Vergleich zum Austausch, was für die Übergangsmetalle Fe, Co und Ni der Fall ist, so würde eine spinaufgelöste Messung im Wesentlichen $P_z^{\mathrm{ex}}$ detektieren, und nicht $P_z^{\mathrm{soc}}$. Desweiteren lässt sich als Gegenargument anführen, dass der MD auf kleine „Bereiche“ in der elektronischen Struktur konzentriert ist, nämlich auf die aufgehobenen Kreuzungspunkte in der Bandstruktur $E(\boldsymbol{k})$, in denen die beteiligten Zustände aufgrund der SBK hybridisieren. Im Gegensatz dazu umfasst die Austauschaufspaltung die gesamte Bandstruktur. Zusammenfassend kann man sagen, dass eine vollständige Analyse der elektronischen Struktur MD *und* Spinpolarisation umfassen sollte, sich beide Messgrößen also ergänzen.

**Magnetischer Lineardichroismus: Fe(110).** Der Standardmessaufbau für Magnetischen Lineardichroismus [*Magnetic linear dichroism* (MLD)] ist geeignet, Systeme zu untersuchen, deren Magnetisierung in der Oberflächenebene liegt. Hierbei fällt p-polarisertes Licht unter nichtnormaler Inzidenz auf die Probenoberfläche. Die Spin–Bahn-Kopplung erzeugt somit eine Komponente der Photoelektronenspinpolarisation, die normal zur Streuebene (aufgespannt durch Probennormale und Einfallsrichtung des Lichts) liegt. Gemäß der Grundregel tritt MD dann auf, wenn die Magnetisierung senkrecht zur Streuebene ausgerichtet ist (Abb. 4.3 links). Die Änderung des Photostroms lässt sich entweder durch Umkehrung der Magnetisierungsorientierung ($\boldsymbol{M}$ entlang $+\boldsymbol{y}$ oder $-\boldsymbol{y}$) oder durch Änderung des Azimuts des Lichteinfalls erreichen ($p_+$ oder $p_-$). Da die Magnetisierung der meisten magnetischen Systeme innerhalb der Oberflächenebene liegt, ist MLD also die Methode der Wahl. Als Alternative böte sich Magnetischer Zirkulardichroismus [*Magnetic ciruclar dichroism* (MCD)] an, wobei zirkular polarisiertes Licht unter nichtnormaler Inzidenz auf die Probe fällt und die Magnetisierung innerhalb der Streuebene liegt. Als Beispiele für MLD dient in dieser Arbeit eine Untersuchung an Fe(110) (Publikation 7 auf S. P69ff).

Die Intensitäten für beide Magnetisierungsorientierungen, $I(+\boldsymbol{M})$ und $I(-\boldsymbol{M})$, wurden für verschiedene Photonenenergien experimentell bestimmt (A. Rampe *et al.*, RWTH Aachen). Im Bild der direkten Übergänge, in dem angenommen wird, dass die Normalkomponente $k_\perp$ des Wellenvektors $\boldsymbol{k}$ bei der Anregung erhalten bleibt, kann aus der Dispersion der Maxima die Bandstruktur ermittelt werden. Der Vergleich mit theoretischen Bandstrukturrechnungen gibt dann die Darstellung der beteiligten Zustände (Abb. 4.4).

Die gute Übereinstimmung der theoretischen Spektren (rechts in Abb. 4.4) mit den experimentellen (links) ermöglicht, die orbitale Zusammensetzung der Anfangszustände genau zu analysieren (Abb. 5 in Publikation 7). Beispielsweise lassen sich Bereiche in der Bandstruktur $E(\boldsymbol{k})$ genau

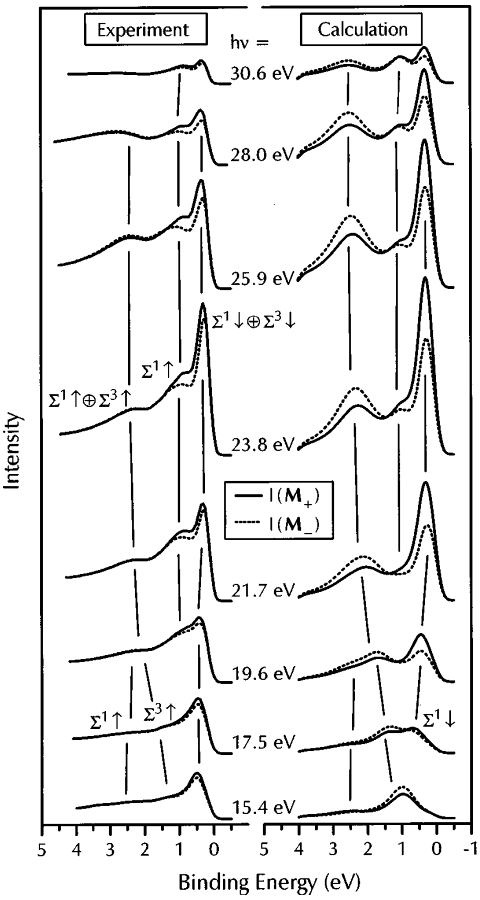

**Abbildung 4.4.** Magnetischer Lineardichroismus von Fe(110). Für normale Emission sind experimentelle (links) und theoretische Spektren (rechts) für verschiedene Photonenenergien $h\nu$ gegenübergestellt. Vertikale Markierungen weisen auf direkte Übergänge aus Anfangszuständen der angegebenen Darstellungen hin.

bestimmen, in denen die SBK zu Hybridisierungsbandlücken führt. Erfolgt die Anregung der Elektronen gerade aus den zugehörigen Anfangszuständen, so sollte gemäß der analytischen Theorie der MLD besonders groß sein. Zur Untersuchung trägt man die Summe $S^{\mathrm{MLD}} = I(+\boldsymbol{M}) + I(-\boldsymbol{M})$ und die Differenz $D^{\mathrm{MLD}} = I(+\boldsymbol{M}) - I(-\boldsymbol{M})$ der beiden Photoströme über der Photonenenergie bei fester Bindungsenergie auf (CIS-Modus). Der direkte Übergang manifestiert sich dann als Maximum in der Summenintensität $S^{\mathrm{MLD}}$. In Abbildung 4.5 (links) ist die Bindungsenergie mit $0.5$ eV gerade so gewählt, dass der direkte Übergang aus den $\Gamma_{25'}$-Minoritätszuständen stammt. Die Spin–Bahn-Kopplung erzeugt dort eine kleine Energielücke, die neben dem Summenmaximum einen maximalen Dichroismus erzeugt. In anderen Worten, die Maxima in $S^{\mathrm{MLD}}$ und $D^{\mathrm{MLD}}$ treten bei derselben Photonenenergie auf (hier: $23.8$ eV). Dieses Beispiel zeigt, wie es der MD im erfolgreichen Zusammenspiel von Theorie und Experiment erlaubt, detaillierte Aussagen über die elektronische Struktur zu erhalten, ohne die Nachteile einer spinaufgelösten Messung in Kauf nehmen zu müssen. Es sei noch bemerkt, dass eine Spinauflösung wenig neue Information geliefert hätte, da beide Zustände, die im $\Gamma_{25'}$-Punkt hybridisieren, Minoritätscharakter besitzen.

Ein andere Frage betrifft die optische Antwort eines magnetischen Systems. Im einfachsten Fall wird das elektrische Feld des einfallenden Lichts vom Vakuum in den Festkörper unmodifiziert fortgesetzt. Einen Schritt weiter geht die Modellierung gemäß der Fresnel'schen Formeln und Snellius' Gesetz, in der das elektrische Feld im Vakuum abrupt in das im Festkörper übergeht, jedoch gebrochen wird. Um zu untersuchen, ob eine Beschreibung im Rahmen der klassischen Brechung ausreichend ist, wurde im Experiment der Polarwinkel des Lichteinfalls variiert. Die so erhaltenen Intensitätsverläufe für feste Photonen- und Bindungsenergie sind in Abb. 4.5 (rechts) gezeigt. Dort werden ebenfalls die zu erwartenden Winkelabhängigkeiten gezeigt, die sich aus der analytischen Theorie ergeben: einerseits ohne, andererseits mit Berücksichtigung der Fresnel'schen Theorie. Hier dienen die Übergangsmatrixelemente als anzupassende Parameter. Zusätzlich sind die numerischen Resultate aus den entsprechenden *Ab–initio*-

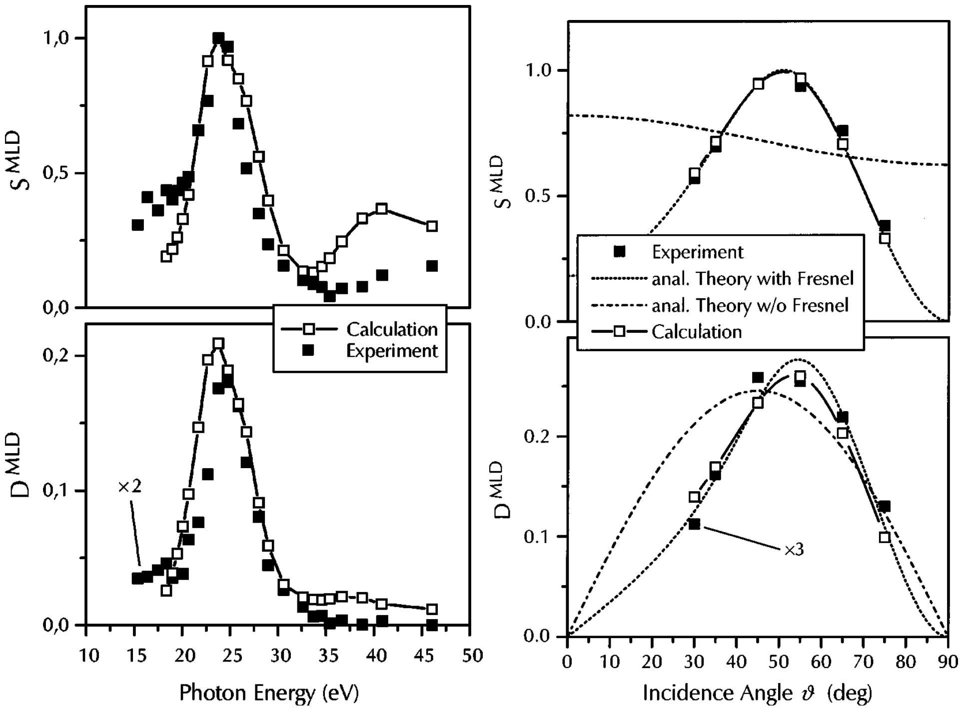

**Abbildung 4.5.** Magnetischer Lineardichroismus von Fe(110). Links: Abhängigkeit des MLD von der Photonenenergie. Für die gewählte Bindungsenergie von 0.5 eV sind die Summen (oben) und Differenzen (unten) der experimentellen und theoretischen Photoströme dargestellt. Rechts: Abhängigkeit des MLD vom Polarwinkel des einfallenden Lichts (Photonenenergie 25.9 eV, Bindungsenergie 0.5 eV). Zusätzlich zu den experimentellen Daten sind theoretische Winkelverläufe gezeigt: analytische Abhängigkeiten mit (*anal. Theory with Fresnel*) und ohne Berücksichtigung (*anal. Theory w/o Fresnel*) der Fresnel'schen Theorie, sowie numerische Daten der Photoemissionsrechnungen inkl. Fresnel-Theorie (*Calculation*).

Photoemissonsrechnungen dargestellt. Wie zu erwarten, geht die Beschreibung ohne Brechung an der Oberfläche vollständig fehl. Hingegen scheint die Fresnel-Theorie das Experiment gut zu beschreiben. Man kann demnach schließen, dass im hier skizzierten Fall das elektrische Feld an der Oberfläche das gleiche wie im Volumen des Festkörpers ist.

**Magnetischer Zirkulardichroismus: Ni/Cu(001).** Ein prominentes Beispiel für Systeme mit senkrechter magnetokristalliner Anisotropie sind dünne Ni-Filme auf Cu(001): bei einer Filmdicke von etwa 7 ML findet ein Spinreorientierungsübergang statt, wobei unterhalb von 7 ML die Magnetisierung in der Oberflächenebene liegt, oberhalb 7 ML jedoch senkrecht ausgerichtet ist. Dieses untypische Verhalten kann durch die tetragonale Verzerrung der Ni-Filme erklärt werden, wie Berechnungen der Anisotropieenergien für diverse Gitterverzerrungen bestätigen (Abschn. 3.3 und Publikation 3 auf S. P23ff). Um die elektronische Struktur von Ni/Cu(001) zu analysieren, bietet sich der Standardmessaufbau des Magnetischen Zirkulardichroismus an [*Magnetic ciruclar dichroism* (MCD)]. In diesem fällt zirkular polarisiertes Licht normal auf die Probenoberfläche, wodurch vermöge „optischer Orientierung" eine Komponente der Spinpolarisation entlang der Einfallsrichtung erzeugt wird (Abb. 4.3 rechts). Als Beipiel für eine gemeinsame experimentelle und theoretische Untersuchung ist die Publikation 6 (S. P59ff) in dieser Arbeit enthalten [90].

Das Zustandekommen des MCD in normaler Emission von Ni/Cu(001) lässt sich anhand der Ni-Bandstruktur für die Γ–Δ–X-Richtung erläutern. Die Punktgruppe ist in diesem Fall $4mm$ ($C_{4v}$), die die zweidimensionalen Doppelgruppendarstellungen $\Delta_6$ und $\Delta_7$ besitzt. Durch die Austauschaufspaltung wird die Zeitumkehrsymmetrie gebrochen, sodass diese Darstellungen jeweils in zwei eindimensionale zerfallen: $\Delta_6\pm$ und $\Delta_7\pm$. Das angefügte Vorzeichen symbolisiert das Verhalten der zugehörigen Basisfunktionen $|\Delta_i\pm\rangle$ unter Zeitumkehr, $T\,|\Delta_i\pm\rangle = \pm\,|\Delta_i\mp\rangle$. Neben der Spinauflösung in Majoritäts- und Minoritätsbänder lassen sich die Bänder gemäß dieser

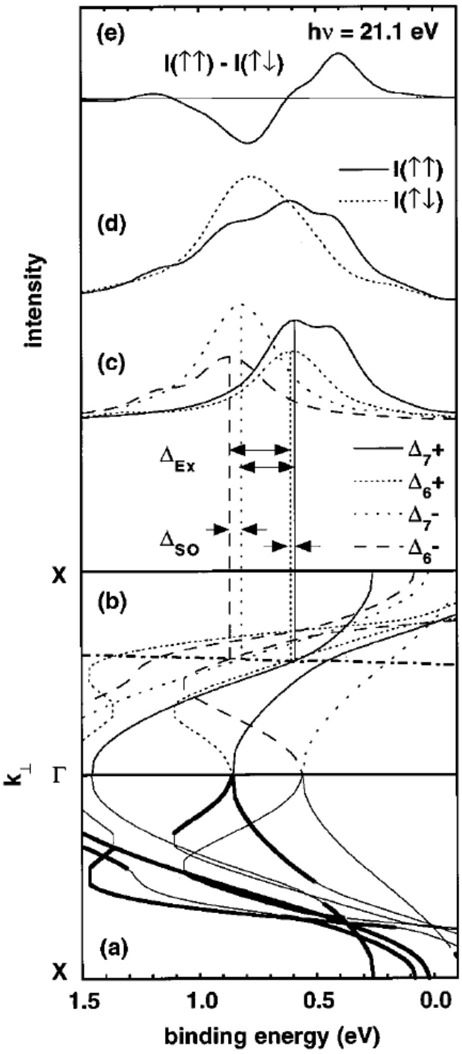

**Abbildung 4.6.** Magnetischer Zirkulardichroismus von Ni/Cu(001). (a) Spinaufgelöste Bandstrukur von Ni entlang der Γ–Δ–X-Richtung. Majoritätsbänder sind durch dicke, Minoritätsbänder durch dünne Linien dargestellt. (b) Bandstruktur von Ni aufgelöst nach Darstellungen der Doppelgruppe $4$ ($C_4$). Die Linientypen sind in (c) definiert. Direkte Übergänge in das für die Photonenenergie von 21.1 eV relevante Endzustandsband sind durch vertikale Linien gekennzeichnet. Diese führen zu den in (c) gezeigten spinaufgelösten theoretischen Photoemissionsspektren. Die Austausch- und die Spin–Bahn-Aufspaltung $\Delta_{\mathrm{Ex}}$ und $\Delta_{\mathrm{SO}}$ sind durch horizontale Pfeile markiert. (d) Spinintegrierte Photoemissionsspektren für parallele [$I(\uparrow\uparrow)$] und antiparallele [$I(\uparrow\downarrow)$] Konfiguration von Magnetisierung und Lichthelizität. (e) Differenz der in (d) gezeigten dichroischen Spektren.

Darstellungen klassifizieren (Abb. 4.6a und b).

Die gruppentheoretische Analyse der Photoemission ergibt, dass für rechtszirkular polarisiertes Licht ($\sigma_+$) nur Anfangszustände der Darstellungen $\Delta_6-$ und $\Delta_7+$ angeregt werden können, für linkszirkulares Licht ($\sigma_-$) hingegen nur solche der Darstellungen $\Delta_6+$ und $\Delta_7-$. Kehrt man die Orientierung der Magnetisierung im Ni-Film um ($\boldsymbol{M} \rightarrow -\boldsymbol{M}$), werden die Darstellungen vertauscht ($\Delta_i\pm \ \rightarrow \ \Delta_i\mp$) und somit die Relation $I(\sigma_\pm, \boldsymbol{M}) = I(\sigma_\mp, -\boldsymbol{M})$ für die Photoströme etabliert. Die Spektren für eine Helizität (oder eine Magnetisierungsorientierung) setzen sich demnach aus jeweils zwei Einzelspektren zusammen (Abb. 4.6c und d). Der Dichroismus, hier genommen als Differenz der Summenspektren in Abb. 4.6d, zeigt einen typischen Vorzeichenwechsel.

Die gemäß der Gruppentheorie erlaubten direkten Übergänge sind in Abb. 4.6b und c eingetragen. Anhand deren energetischer Position lassen sich die Austauschaufspaltung $\Delta_{\mathrm{Ex}}$ und die Spin–Bahn-Aufspaltung $\Delta_{\mathrm{SO}}$ ablesen. Da die Magnetisierung für die Zerlegung der Darstellungen $\Delta_i$ in $\Delta_i\pm$ verantwortlich zeichnet, sind die zugehörigen Zustände also um $\Delta_{\mathrm{Ex}}$ gegeneinander verschoben. Die Spin–Bahn-Kopplung ist die Ursache für das Vorliegen der zweidimensionalen Darstellungen $\Delta_6$ und $\Delta_7$, womit die Zustände zu $\Delta_i+$ und $\Delta_i-$ um $\Delta_{\mathrm{SO}}$ gegeneinander verschoben sind. Für Nickel ist $\Delta_{\mathrm{Ex}} \gg \Delta_{\mathrm{SO}}$, wie Abb. 4.6c zu entnehmen ist.

Die durch die SBK hervorgerufene Bandlücke in den $\Delta_7+$-Bändern bei ca. $0.5$ eV Bindungsener-

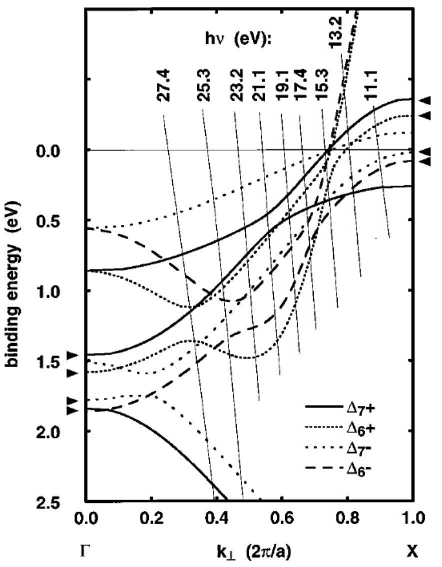

**Abbildung 4.7.** Symmetrieaufgelöste Valenzbandstruktur von Ni entlang der $\Delta$-Richtung. Die Linientypen entsprechen denen aus Abb. 4.6. Waagerechte Pfeile weisen auf Bänder mit überwiegendem $\Delta^5$-Anteil hin. Die stark dispersiven Bänder repräsentieren das um die Photonenenergie nach unten verschobene relevante Endzustandsband hin. Schnittpunkte mit den Valenzbändern ergeben dann direkte Übergänge.

gie führt zu der Doppelstruktur im zugehörigen Photoemissionsspektrum (Abb. 4.6c). Wird die Photonenenergie variiert, so werden im Modell der direkten Übergänge die Schnittpunkte des Endzustandsbandes mit den Anfangszustandsbändern verschoben (Abb. 4.7). Die Intensitätsmaxima verschieben sich dann entsprechend (strichpunktiert in Abb. 4.6b).

Wie im Fall von Fe(110) lassen sich durch die Untersuchung der Abhängigkeit von der Photonenenergie SBK-induzierte Bandlücken finden. Die Asymmetrie der Photoströme $I(\uparrow\uparrow)$ und $I(\uparrow\downarrow)$ ist in Abb. 4.8 rechts gezeigt. Wie oft ist die theoretische Asymmetrie erheblich größer als die im Experiment gemessene, was in dem hier diskutierten Beispiel im Wesentlichen an der zu großen Lebensdauer der Anfangszustände liegt. Rechnungen mit verbesserten Lebensdauern weisen dieses Manko nicht mehr auf [105].

Auffallend ist ein Minimum (durch die gestrichelten Linien gekennzeichnet), das mit zunehmender Photonenenergie zu höheren Bindungsenergien dispergiert und durch Zustände der Darstellung $\Delta_7+$ erzeugt wird. Die zugehörigen Bänder (durchgezogen in Abb. 4.7) zeigen bei etwa 0.5 eV Bindungsenergie eine SBK-induzierte Bandlücke ($k_\perp \approx 0.55 \cdot 2\pi/a$), aus der direkte Anregungen mit 21.1 eV Photonenenergie möglich sind. Die geringe energetische Aufspaltung der Bandlücke ist den Intensitäten nur schwer direkt zu entnehmen (vertikale Linien in Abb. 4.8 links), tritt jedoch in der Asymmetrie deutlich hervor. Dieses Beispiel offenbart erneut das Potential des Magnetischen Dichroismus bei der detaillierten Untersuchung elektronischer Strukturen, insbesondere im Zusammenwirken von Experiment und Theorie.

## 4.5. *Quantum–size*-Effekte in der Photoemission von dünnen Filmen

Ultradünne Filme und Vielfachschichtsysteme werden intensiv untersucht, weil an ihnen grundlegende, aber auch neue Phänomene studiert werden können. Eine wichtige Rolle spielen dabei sogenannte Quantentrogzustände [*Quantum–well state* (QWS)] in ultradünnen Filmen, die auf ein Substrat aufgebracht wurden. Elektronische Zustände des Filmmaterials, die energetisch in einer Bandlücke des Substrats liegen, werden im Film lokalisiert: an der Vakuum–Film-Grenzfläche durch die Oberflächenbarriere, an der Film–Substrat-Grenzfläche durch die erwähnte Bandlücke, da Zustände des Substrats für die Propagation der Elektronen ins Volumen nicht zur Verfügung stehen. Daraus resultiert eine energetische Quantisierung, sodass Filme als paradigmatische Realisierung des in Textbüchern behandelten Problems des eindimensionalen Quantentrogs oder -topfes verstanden werden können [106].

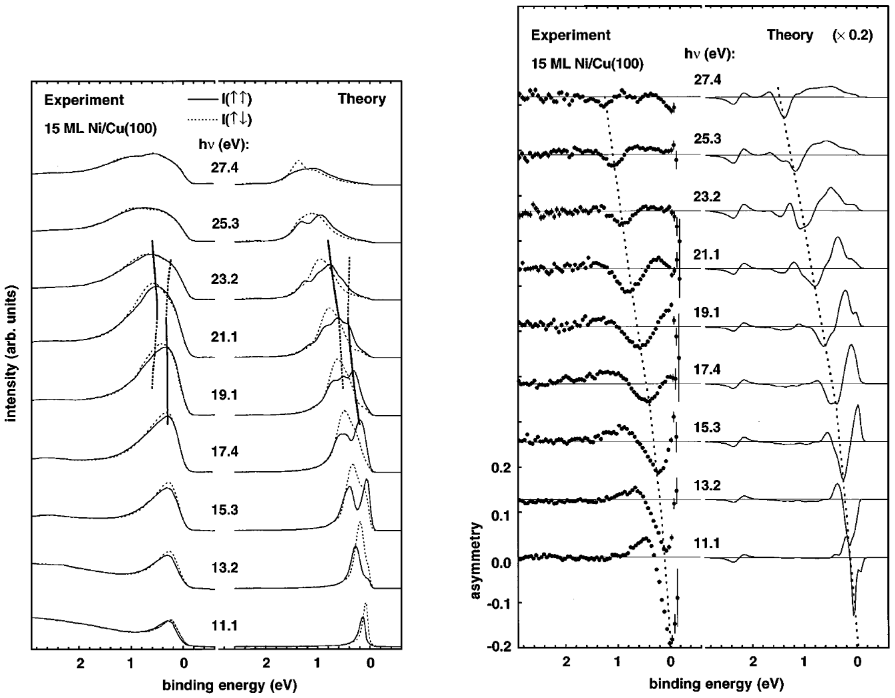

**Abbildung 4.8.** Magnetischer Zirkulardichroismus von Ni/Cu(001). Ganz links: Die experimentellen (links) und theoretischen (rechts) Intensitäten sind für verschiedene Photonenenergien (Mitte) gezeigt: $I(\uparrow\uparrow)$ für parallele Konfiguration von Magnetisierung und Lichthelizität, $I(\uparrow\downarrow)$ für die antiparallele Konfiguration. Die vertikalen Linien bei 21.1 eV Photonenenergie kennzeichnen die im Text diskutierte Bandlücke. Ganz rechts: Asymmetrie der links gezeigten Spektren, definiert gemäß $[I(\uparrow\uparrow) - I(\uparrow\downarrow)]/[I(\uparrow\uparrow) + I(\uparrow\downarrow)]$. Die gestrichelten Linien kennzeichnen ein markantes Minimum.

Die Quantentrogzustände besitzen Eigenschaften der Bloch-Zustände des Filmmaterials, erfahren jedoch durch die Lokalisierung spezifische Änderungen. Insbesondere ihre Wellenfunktion wird dahingehend modifiziert, dass sie durch eine Einhüllende moduliert wird [107, 108]. Diese Modulation manifestiert sich in ausgeprägten Oszillationen des CIS-Photostroms, woraus sich auf die Lokalisierung der Wellenfunktionen schließen lässt. Im Rahmen eines eindimensionalen TB-Modells können die fundamentalen Effekte verstanden werden (Publikation 9 auf S. P97ff). Eindimensionale Ketten mit $n$ Gitterplätzen und einem Orbital pro Gitterplatz besitzen $n$ Eigenzustände. Die CIS-Intensitäten von diesen Quantentrogzuständen zeigen ein Hauptmaximum genau bei der Energie, bei der auch die unendliche Kette maximale Intensität hervorrufen würde, d. i. bei einem direkten Übergang. Bei letzterem sind die Wellenvektoren von Anfangs- und Endzustand identisch und erlauben die Bestimmung der Volumenbandstruktur. Dünne Filme eignen sich demnach in besonderer Weise wegen der $k_\perp$-Quantisierung zur Bandstrukturbestimmung (*Band mapping*) [109]. In der Abbildung 4.9 für Ketten mit $n = 10$ (a) und $n = 5$ (b) Gitterplätzen folgen die Maxima der direkten Übergänge exakt der Dispersionsrelation $E(k) = \epsilon + 2t\cos(ka)$ (Hier bezeichnen die Gitterplatzenergie $\epsilon$ und das *Hopping*-Matrixelement $t$ die Parameter des TB-Modells). Ein weiteres typisches Merkmal sind Intensitätsoszillationen mit der Photonenenergie (repräsentiert durch $k_{\mathrm{fz}}a$ in Abb. 4.9). Neben den Hauptmaxima treten Nebenmaxima auf, deren Anzahl proprotional zur Kettenlänge ist, was auf die Filmdicke schließen lässt.

In geradezu paradigmatischer Weise lassen sich die am simplen TB-Modell studierten Quantisierungseffekte an QWS in Cu-Filmen auf fcc-Co(001) nachweisen. Im Zentrum der 2BZ ($\boldsymbol{k}_\parallel = 0$) zeigt das Co-Substrat eine Bandlücke im Bereich der $\Delta^1$-Minoritätselektronen, die sich von $-2.10$ eV bis $-0.65$ eV erstreckt (hellgrau unterlegter Bereich in Abb. 4.10a links). Das stark dispersive $sp$-Band des Kupfers (c), das zur $\Delta^1$-Darstellung gehört, wird in $k_\perp$ quantisiert und erzeugt in der lagen- und spinaufgelösten Zustandsdichte zwei Maxima (b). Die zugehörigen Quantentrogzustände sind mit A und B bezeichnet. Die Lokalisierung auf den Cu-Film ist spinabhängig, weil nur Minoritätselektronen durch eine Bandlücke im Kobalt betroffen sind. Die Majoritätselektro-

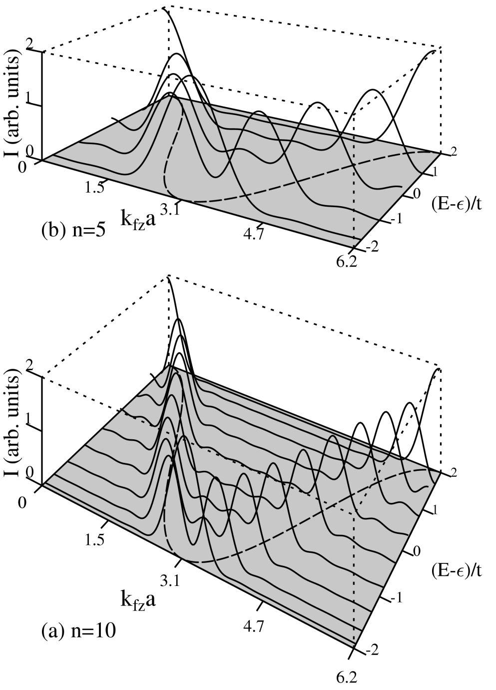

**Abbildung 4.9.** Photoemission von eindimensionalen endlichen Ketten mit $n = 10$ (a) und $n = 5$ (b) Gitterplätzen. Die Intensitätshauptmaxima folgen der Volumenbandstruktur $E(k_{\mathrm{fz}}) = \epsilon + 2t\cos(k_{\mathrm{fz}}a)$.

nen des $sp$-Cu-Bandes hingegen hybridisieren mit Co-Zuständen und werden nicht lokalisiert. Die sehr schwach ausgeprägte Struktur C ist ebenfalls mit den Co-Zuständen hybridisiert. Ihr Verhalten in der Photoemission, wie auch ihre Spinpolarisation, unterscheidet sich deutlich von dem der QWS A und B.

Wie im TB-Modell folgen die Photoemissionsintensitäten der Quantentopfzustände A und B generell denen des halbunendlichen Cu-Kristalls (Cu-Oberfläche ohne Co-Substrat). Der Einfluss der Cu-Filmdicke hingegen zeigt sich, wenn man die CIS-Photoemission von QWS betrachtet, die in etwa die gleiche Bindungenergie besitzen. Solche Quantentrogzustände treten zum Beispiel in Cu-Filmen der Dicken $9$, $14$ (vgl. A), $19$, $24$ und $29$ ML auf. Für dünne Filme, etwa $n = 9$, zeigt die Intensität neben dem Hauptmaximum bei ca. $12.5$ $\mathrm{eV}$ Photonenenergie deutliche Oszillationen (Abb. 4.10 rechts). Deren Wellenlänge (in der Photonenenergie) nimmt mit wachsender Dicke ab (vgl. die gestrichelten Linien). Im Limes unendlicher Dicke verschwindet die Quantisierungsoszillation. Die Oszillationen des QWS B zeigen das gleiche Verhalten wie die von Zustand A. Die Resonanz C hingegen unterscheidet sich signifikant, einerseits in den Wellenlängen und andererseits in den Amplituden der Modulationen. Dass überhaupt ihre Intensität moduliert wird, ist auf die geringe Reflexion an der Cu–Co-Grenzfläche zurückzuführen.

Zusammenfassend bietet die CIS-Photoemission die Möglichkeit, Aussagen über die Filmdicke und über den Grad der Lokalisierung der elektronischen Zustände zu erhalten. Das System Cu/fcc-Co(001) ist insofern prototypisch, dass die QWS strikt auf den sozusagen inerten Cu-Film eingeschränkt sind. Die deutliche Manifestation derjenigen Effekte, die aus dem TB-Modell gewonnen wurden, überrascht daher nicht. Ein signifikant abweichendes Verhalten zeigen dagegen QWS in Ag-Filmen auf V(001) [110]. Die Quantentrogzustände stammen, wie bei Cu, vom dispersiven $sp$-Band und bilden sich in der $\Delta^1$-Bandlücke des bcc-V-Substrats aus. Allerdings findet an der Ag–V-Grenzfläche ein Ladungsübertrag von den Ag–$d$-Zuständen in die Bandlücke des Vanadiums statt. Die Quantentopfzustände des Silbers hybridisieren mit diesen Elektronen und sind nicht mehr räumlich scharf auf den Film beschränkt (Abb. 4.11b). Die CIS-Oszillationen weichen daher beträchtlich vom modellhaften Verhalten ab (Abb. 4.11a).

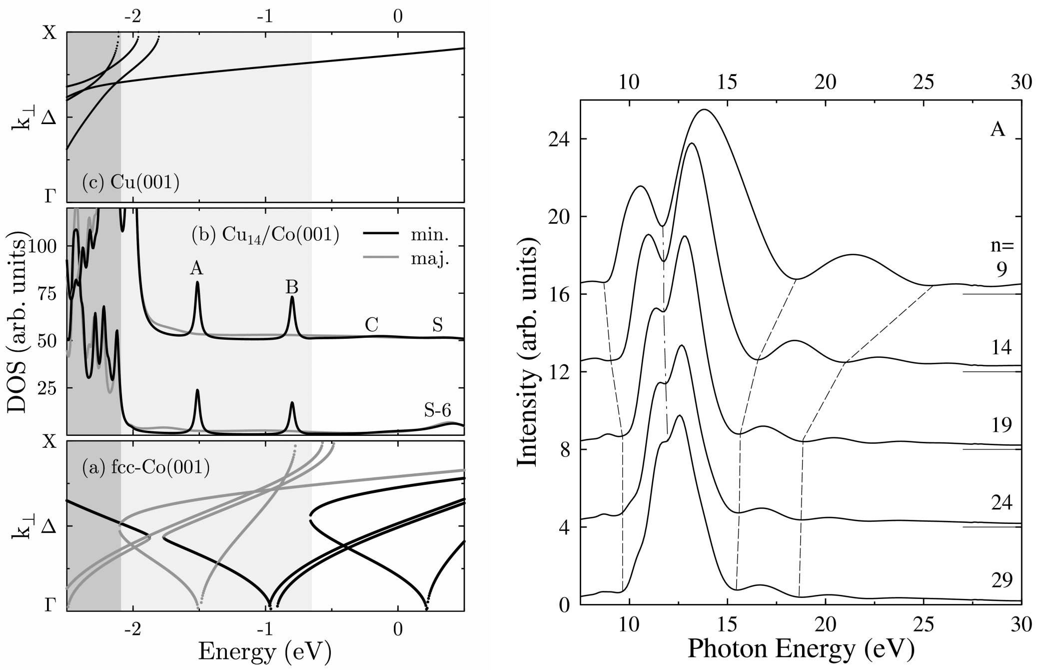

**Abbildung 4.10.** Quantentrogzustände in Cu/fcc-Co(001). Links: QWS in 14 ML Cu/Co für $\boldsymbol{k}_{\|} = 0$. (a) Spinaufgelöste Bandstruktur von Co (Minorität schwarz, Majorität grau). Die Bandlücke der zur $\Delta^1$-Darstellung gehörenden Minoritätselektronen ist durch den hellgrauen Bereich gekennzeichnet. (b) Spin- und lagenaufgelöste Spektraldichte von 14 ML Cu/fcc-Co(001) für die äußerste (S) und eine zentrale (S−6) Atomlage des Cu-Films. Die mit A und B bezeichneten Maxima gehören zu QWS, die Struktur C zu einer Resonanz. (c) Bandstruktur von Cu. Die Energieskala bezieht sich auf die Fermi-Energie des Substrats. Rechts: *Constant-initial-state*-Photoemission aus QWS für Cu-Filmdicken $n$ von 9, 14, 19, 24 und 29 Schichten. Die Bindungsenergien der QWS entspricht der von Zustand A für $n = 14$.

## 4.6. Temperaturabhängige Photoemission von dünnen magnetischen Filmen

Die Temperatur wird in Photoemissionsrechnungen im Allgemeinen nicht berücksichtigt. Ausnahmen bilden die Elektron–Phonon-Kopplung, die Eingang in die Gitterplatzstreumatrizen mittels Debye–Waller-Faktoren findet, und die „Aufweichung" der Fermi–Dirac-Verteilung in der Nähe des Fermi-Niveaus. Magnetische Systeme zeigen eine ausgeprägte Temperaturabhängigkeit, die sich zum Beispiel im Curie–Weiss-Gesetz manifestiert. Die kritische Temperatur $T_c$, oberhalb der die globale Magnetisierung verschwindet, ist für ausgedehnte Systeme jedoch so hoch, dass Messungen, die bei Raumtemperatur vorgenommen wurden, gut mit Rechnungen für $T = 0$ verglichen werden können. Bei dünnen Filmen sinkt $T_c$ allerdings in die Nähe der Raumtemperatur (oder sogar darunter), sodass die reduzierte Magnetisierung in der Theorie berücksichtigt werden sollte. Eine wichtige Frage ist demnach, in welchem Modell diese Reduktion beschrieben werden muss.

Im Stoner-Bild geht die Temperaturerhöhung mit einer Reduktion der lokalen magnetischen Momente (LMM), und damit mit einer Reduktion der Austauschaufspaltung, einher (*Rigid-band model*). Oberhalb der kritischen Temperatur $T_c$ ist das Gesamtsystem, wie auch jedes Teilsystem, nicht mehr magnetisch. Desweiteren existieren Modelle, die auf Fluktuationen der LMM beruhen. Bei $T = 0$ sind alle LMM entlang der globalen Magnetisierung $\boldsymbol{M}$ ausgerichtet und erzeugen somit die maximale Magnetisierung. Mit zunehmender Temperatur weicht die Orientierung einzelner LMM von dieser Richtung ab, was zu einer Reduktion der globalen, mittleren Magnetisierung führt. Oberhalb $T_c$ sind die Fluktuationen so stark, dass keine Vorzugsrichtung der Magnetisierung mehr existiert. Die globale Magnetisierung verschwindet, endliche Teilsysteme können jedoch magnetisch bleiben. Haines und Heine haben ein Modell entwickelt, dass die Verteilung der Fluktuationen der LMM parametrisiert [111–113]. Die Moment–Moment-Korrelationsfunktion wird als

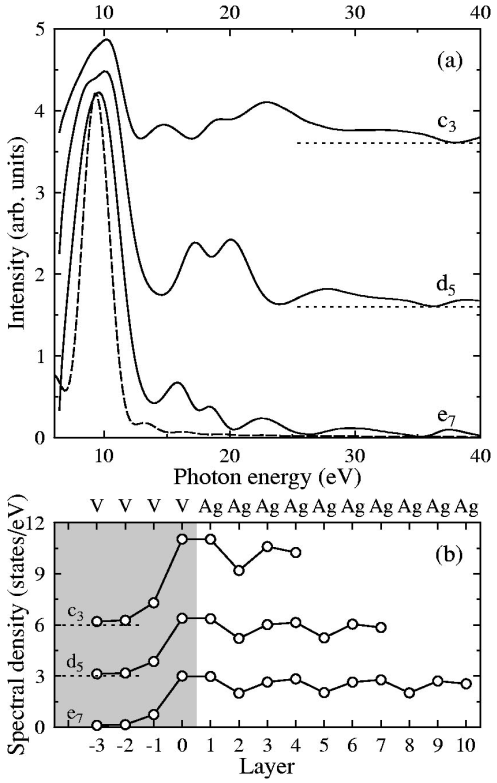

**Abbildung 4.11.** *Constant-initial-state*-Photoemission aus Quantentopfzuständen in Ag-Filmen auf V(001) für Filmdicken $n$ von 4 (Zustand $c_3$), 7 ($d_5$), und 10 ($e_7$) Schichten. Die Bindungsenergien der QWS ist nahezu identisch. (a) Photoemissionsintensitäten der QWS im Vergleich zu der von halbunendlichem fct-Ag(001) (gestrichelt). (b) Lagenaufgelöste Spektraldichte der QWS. Der Bereich der V-Substratschichten ist grau unterlegt. Die Oberflächenschichten tragen die Indices 4 ($c_3$), 7 ($d_5$) und 10 ($e_7$).

gauss-verteilt angenommen, sodass benachbarte LMM mit größerer Wahrscheinlichkeit gleich orientiert sind als weit voneinander entfernte. Die elektronische Struktur erhält man durch Mittelung über alle magnetischen Konfigurationen, die mit den vorgegebenen Parametern kompatibel sind. Für 2 ML fcc-Co/Cu(001) zeigen TB-Rechnungen, dass dieses Modell Photoemissionsexperimente gut beschreibt [114].

Das Bild der ungeordneten lokalen Momente [*Disordered local moment* (DLM)] unterscheidet sich vom Haines–Heine-Modell im wesentlichen dadurch, dass die Nahordnung vernachlässigt wird. Somit kann eine numerische Behandlung des Problems im Rahmen der CPA erfolgen (S. 11). Die Unordnung wird auf eine binäre substitutionelle Legierung $\mathrm{A}_x\mathrm{B}_{1-x}$ abgebildet, in der die Spezies A und B lokale magnetische Momente darstellen, die entlang $\boldsymbol{M}$ und $-\boldsymbol{M}$ ausgerichtet sind. Bei der Konzentration $x = 0$ liegt der ferromagnetische Fall vor ($T = 0$), während bei $x = 0.5$ $T_\mathrm{c}$ erreicht wird. Eine Realisierung der DLM erhält man durch komplementäre Wahl der spinabhängigen Potentiale für die Spezies A und B: $v_{\mathrm{A}+} = v_{\mathrm{B}-} = v + B$ und $v_{\mathrm{A}-} = v_{\mathrm{B}+} = v - B$. Somit lässt sich die Temperaturabhängigkeit der elektronischen Struktur und der Spektroskopien im Rahmen der VST behandeln (Publikation 8 auf S. P80ff).

Im Folgenden wird die Photoemissionstheorie für binäre Legierungen, wie sie von Durham entwickelt wurde, skizziert [115, 116]. Größen, die an einem einzelnen Gitterplatz $i$ ausgewertet werden, sind durch die mit der Konzentration $x$ gewichteten Größen für die Konstituenten A und B gegeben. Für die Übergangsmatrixelemente ergibt sich $M^i = xM^i_\mathrm{A} + (1-x)M^i_\mathrm{B}$. Aufgrund der Vielfachstreuung treten Terme auf, die zwei Gitterplätze miteinander verknüpfen, z. B. $\langle M^i \tau^{ij} M^{j\star}\rangle$, wobei $\langle \cdots \rangle$ den Konfigurationsmittelwert bezeichnet. Im Falle $i = j$ erhält man $\langle M^i \tau^{ii} M^{i\star}\rangle = xM^i_\mathrm{A}\langle\tau^{ii}_A\rangle {M^i_\mathrm{A}}^\star + (1-x)M^i_\mathrm{B}\langle\tau^{ii}_B\rangle {M^i_\mathrm{B}}^\star$. Sind die Gitterplätze $i$ und $j$ voneinander verschieden, so folgt

$$\begin{aligned}\langle M^i \tau^{ii} M^{j\star}\rangle =& x^2 M^i_\mathrm{A}\langle\tau^{ij}_\mathrm{AA}\rangle {M^j_\mathrm{A}}^\star + x(1-x)M^i_\mathrm{A}\langle\tau^{ij}_\mathrm{AB}\rangle {M^j_\mathrm{B}}^\star \\ &+ x(1-x)M^i_\mathrm{B}\langle\tau^{ij}_\mathrm{BA}\rangle {M^j_\mathrm{A}}^\star + (1-x)^2 M^i_\mathrm{B}\langle\tau^{ij}_\mathrm{BB}\rangle {M^j_\mathrm{B}}^\star.\end{aligned} \tag{4.17}$$

Die Konfigurationsmittelwerte der Streupfadoperatoren können im Rahmen der CPA durch den SPO $\tau_\mathrm{c}$ des kohärenten Systems und durch die Defektmatrizen $D^i_\mathrm{A}$ ausgedrückt werden [117]: $\langle\tau^{ij}\rangle = \tau^{ij}_\mathrm{c}$, $\langle\tau^i_\mathrm{A}\rangle = D^{i\mathrm{L}}_\mathrm{A}\tau^i_\mathrm{c} = \tau^i_\mathrm{c} D^{i\mathrm{R}}_\mathrm{A}$ und $\langle\tau^{ij}_\mathrm{AB}\rangle = D^{i\mathrm{L}}_\mathrm{A}\tau^{ij}_\mathrm{cB}D^{j\mathrm{R}}_\mathrm{B}$ (S. 11).

Der Photostrom zerfällt in zwei Anteile: den intra-atomaren Beitrag $I^i_{\mathrm{atom}}$, der durch die gitterplatzdiagonale GF $G^{ii}$ hervorgerufen wird, und in den inter-atomaren Beitrag. Letzterer enthält alle Terme, in die zwei verschiedene Gitterplätze involviert sind. Mit der Definition $M^i_{\mathrm{c}} = xM^i_{\mathrm{A}} D^{i\mathrm{R}}_{\mathrm{A}} + (1-x) M^i_{\mathrm{B}} D^{i\mathrm{R}}_{\mathrm{B}}$ der effektiven Übergangsmatrixelemente kann der Photostrom als

$$\begin{aligned}\langle I\rangle = & \sum_i \langle I^i_{\mathrm{atom}}\rangle - \frac{1}{\pi}\mathrm{Im}\sum_{ij} M^i_{\mathrm{c}}\tau^{ij}_{\mathrm{c}} M^{j\star}_{\mathrm{c}} \\ & - \frac{1}{\pi}\mathrm{Im}\sum_i \left( x M^i_{\mathrm{A}}\tau^{ii}_{\mathrm{A}} M^{i\star}_{\mathrm{A}} + (1-x) M^i_{\mathrm{B}}\tau^{ii}_{\mathrm{B}} M^{i\star}_{\mathrm{B}} - M^i_{\mathrm{c}}\tau^{ii}_{\mathrm{c}} M^{i\star}_{\mathrm{c}} \right)\end{aligned} \tag{4.18}$$

ausgedrückt werden. Der intra-atomare Beitrag $I^i_{\mathrm{atom}}$ vom Gitterplatz $i$ ist hier durch $\langle I^i_{\mathrm{atom}}\rangle = xI^i_{\mathrm{A}} + (1-x)I^i_{\mathrm{B}}$ gegeben. Die obere Zeile in Gl. (4.18) enthält nur Größen des kohärenten Gitters und besitzt somit die Symmetrie eines geordneten Systems. Dieser kohärente Beitrag erzeugt die $\boldsymbol{k}_{\parallel}$-Abhängigkeit des Photostroms. Die Interpretation der unteren Zeile als inkohärenten Beitrag folgt aus der CPA-Gleichung $\tau^{ii}_{\mathrm{c}} = x\tau^{ii}_{\mathrm{A}} + (1-x)\tau^{ii}_{\mathrm{B}}$. Damit lautet dieser Beitrag

$$\begin{aligned}I_{\mathrm{inkoh}} = & -\frac{1}{\pi}\mathrm{Im}\sum_i x \left( M^i_{\mathrm{A}}\tau^{ii}_{\mathrm{A}} M^{i\star}_{\mathrm{A}} - M^i_{\mathrm{c}}\tau^{ii}_{\mathrm{A}} M^{i\star}_{\mathrm{c}} \right) \\ & -\frac{1}{\pi}\mathrm{Im}\sum_i (1-x) \left( M^i_{\mathrm{B}}\tau^{ii}_{\mathrm{B}} M^{i\star}_{\mathrm{B}} - M^i_{\mathrm{c}}\tau^{ii}_{\mathrm{B}} M^{i\star}_{\mathrm{c}} \right).\end{aligned} \tag{4.19}$$

Während $\tau^{ii}_{\mathrm{c}}$ im Wesentlichen die ($\boldsymbol{k}_{\parallel}$-abhängige) Bloch'sche Spektraldichte widerspiegelt, korrespondieren $\tau^{ii}_{\mathrm{A}}$ und $\tau^{ii}_{\mathrm{B}}$ eher mit der lokalen Zustandsdichte. Die Winkelabhängigkeit von $I_{\mathrm{inkoh}}$ ist durch die der Übergangsmatrixelemente selbst gegeben.

**Anwendung auf dünne Co-Filme auf Cu(001).** Die Curie-Temperatur von 2 ML Co auf Cu(001) liegt etwa bei Raumtemperatur, sodass spin- und winkelaufgelöste Photoemissionexperimente nur eine geringe Spinpolarisation detektierten. Ferner zeigen die Spektren statt ausgeprägter Maxima breite Strukturen (Abb. 4.12, unterstes Spektrum), die sich nur schwer im Rahmen des *Band mapping* für $T = 0$ interpretieren ließen.

Für $T = 0$ berechnete Spektren (Abb. 4.12, $x = 0$) zeigen in der Tat kaum Übereinstimmung mit dem Experiment, denn es finden sich ausgeprägte Maxima mit großer Spinpolarisation. Eine Erhöhung der Temperatur, ausgedrückt durch die Konzentration $x$, erzeugt zwei wesentliche Effekte: eine Verbreiterung der Maxima, die durch die CPA-Selbstenergie hervorgerufen wird [15], und eine energetische Verschiebung der Maxima. Letztere verschieben zu geringeren Energien für Anfangszustände mit Minoritätsspinorientierung und zu höheren Energien für solche mit Majoritätsspinorientierung, was im Einklang mit dem *Rigid-band model* steht. Für $T = T_{\mathrm{c}}$ ($x = 0.5$) laufen austauschaufgespaltene Partnermaxima allerdings nicht zusammen (vgl. A und C in Abb. 4.12), sondern bleiben getrennt — sofern man bei der großen Verbreiterung noch von Maxima sprechen möchte. Einige Strukturen, zum Beispiel D, zeigen keine Verschiebung mit der Temperatur, was durch ihren Ursprung im Cu-Substrat erklärt wird. Während A und C von elektronischen Anfangszuständen im Co-Film stammen, und daher vollständig dem Einfluss der magnetischen Unordnung unterliegen, wird D durch Anfangszustände im Cu erzeugt, deren Photoelektronen durch den Co-Film transmittiert werden. Nur dieser spinabhängige Transfer unterliegt der Temperaturabhängigkeit und kann somit keine Energieverschiebung des Maximums hervorrufen.

Der Unterschied im Temperaturverhalten der individuellen Maxima offenbart sich auch in der Spinpolarisation der Photoelektronen (Abb. 4.13). Diejenige der aus dem Substrat stammenden Struktur D hängt linear von der Konzentration $x$ ab, während die Maxima A und C das typische Verhalten der Magnetisierung zeigen. Für $T = T_{\mathrm{c}}$ ($x = 0.5$) verschwindet die Spinpolarisation.[2]

Die Übereinstimmung der theoretischen Spektren für $x = 0.45$ mit dem Experiment zeigt, dass das DLM-Bild die Temperaturabhängigkeit dünner Co-Filme auf Cu(001) korrekt beschreibt. Die

---

[2] Für die gewählte Messgeometrie manifestiert sich die SBK aufgrund der Symmetrie nicht in einer von Null verschiedenen Spinpolarisation der Photoelektronen.

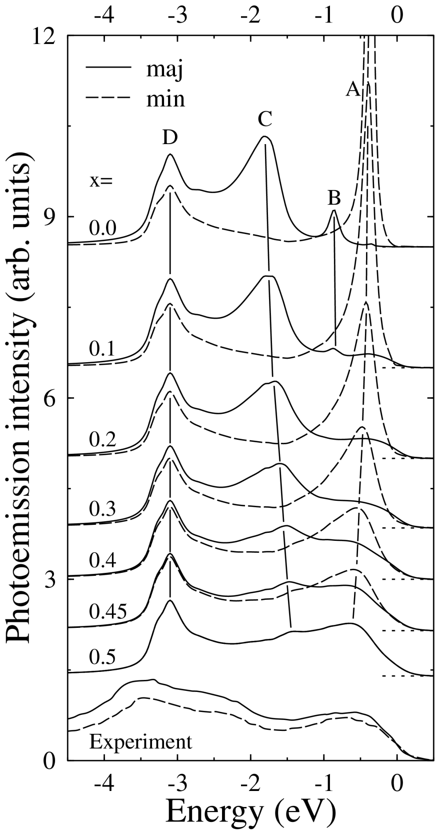

**Abbildung 4.12.** Spinaufgelöste normale Photoemission von 2 ML Co/Cu(001). Die theoretischen Spektren für Majoritäts- (durchgezogen) und Minoritätsorientierung (gestrichelt) sind für verschiedene Konzentrationen $x$ (links angegeben) im DLM-Bild berechnet worden. Im Text diskutierte Strukturen sind mit A bis D gekennzeichnet. Ein bei Raumtemperatur aufgenommenes experimentelles Spektrum ist unten gezeigt (Ref. [118] entnommen; s-polarisiertes Licht, 21.22 eV Photonenenergie).

magnetische Nahordnung, also die Korrelation benachbarter lokaler magnetischer Momente, ist demnach von geringer Bedeutung. Das Temperaturverhalten sowohl der Intensitäten als auch der Spinpolarisation erlaubt Rückschlüsse auf den Ursprung der Strukturen in den Spektren: die Bindungsenergie der Anfangszustände, die im Co-Film lokalisiert sind, wird verändert, während Substratzustände nicht betroffen sind.

## 4.7. Photoemission korrelierter Elektronenpaare

Korrelationen innerhalb des Elektronensystems werden in *Ab–initio*-Rechnungen meist im Rahmen der *Local density approximation* (LDA) oder einer ihrer Erweiterungen wie Gradientenkorrekturen [*Generalized gradient approximation* (GGA)] behandelt. Die Photoemission hingegen bietet darüber hinausgehend die Möglichkeit, die Elektron–Elektron-Wechselwirkung genauer zu stu-

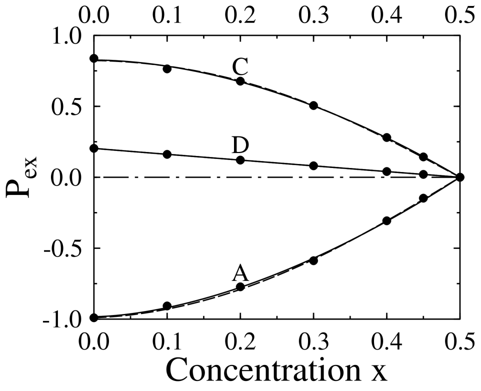

**Abbildung 4.13.** Spinpolarisation der Photoelektronen in normaler Photoemission von 2 ML Co/Cu(001). Die theoretische Spinpolarisationen der prominenten Strukturen A, C und D aus Abb. 4.12 sind über der Konzentration $x$ des DLM-Bildes aufgetragen (sämtliche Parameter wie in Abb. 4.12).

dieren. Dazu werden nicht einzelne Elektronen, sondern korrelierte Elektronenpaare koinzident detektiert. Da der Dipoloperator nur auf einzelne Elektronen wirkt, kann die koinzidente Messung nur die Elektron–Elektron-Wechselwirkung als Ursache haben. Die Diskrimination zwischen der Anregung eines korrelierten Elektronenpaares und der Anregung zweier unkorrelierter Elektronen erfolgt im Photoemissionsexperiment mittels Koinzidenz, d. h. durch gleichzeitigen Nachweis nach Anregung durch einzelne Photonen. Die Zählraten sind daher im Vergleich zur konventionellen Photoemission um mehrere Größenordnungen geringer.

Die folgende theoretische Beschreibung der Photoemission korrelierter Elektronenpaare macht Unterschiede zur gewöhnlichen Photoemission deutlich. Die erforderlichen Zweiteilchenzustände und Zweiteilchen-Green-Funktionen werden aus Einteilchengrößen konstruiert, und die Elektron–Elektron-Wechselwirkung wird explizit berücksichtigt.

Ausgangspunkt sind zwei Teilchen, die zu identischen Hilbert-Räumen $A$ und $B$ gehören. Die Hamilton-Operatoren $H_A$ in $A$ und $H_B$ in $B$ seien ebenfalls gleich (Replika). Um Zustände in $A$ und $B$ unterscheiden zu können, werden alle Einteilchengrößen mit den Hilbert-Räumen indiziert. Insbesondere gelten dann $\sum_i |i_k\rangle \langle i_{k'}| = \delta_{kk'}$, $\langle i_k | j_{k'} \rangle = \delta_{ij}\delta_{kk'}$ und $H_k |i_{k'}\rangle = \delta_{kk'}\epsilon_i |i_{k'}\rangle$, mit $k, k' = A, B$. Die Einteilchen-Green-Funktionen werden durch

$$G_{kk'}(z) = \sum_i \frac{|i_k\rangle \langle i_{k'}|}{z - \epsilon_i}, \quad k, k' = A, B, \tag{4.20}$$

definiert. $G_{kk}$ ist die bekannte Einteilchen-Green-Funktionen, $G_{kk}(1, 1'; z) = \left\langle 1 \middle| (z - H_k)^{-1} \middle| 1' \right\rangle$. Die gemischtindizierte Green-Funktion $G_{kk'}$ „bewegt“ ein Teilchen von $k'$ nach $k$: $G_{kk'}(z) \sum_j \varphi_j |j_{k'}\rangle = \sum_j \varphi_j |j_k\rangle / (z - \epsilon_j)$ ($\varphi_j$ beliebige Entwicklungskoeffizienten).

Mit den antisymmetrisierten Zweiteilchenzuständen

$$|ij\rangle = \frac{1}{\sqrt{2}} \left( |i_A\rangle |j_B\rangle - |j_A\rangle |i_B\rangle \right), \tag{4.21}$$

die $\langle ij | kl \rangle = \delta_{ik}\delta_{jl} - \delta_{il}\delta_{jk}$ erfüllen, wird die Zweiteilchen-Green-Funktion

$$G^{+}(12, 1'2'; E) = \sum_{ij} \frac{\langle 12 | ij \rangle \langle ij | 1'2' \rangle}{E - \epsilon_{ij}} \tag{4.22}$$

auf Einteilchen-Green-Funktionen zurückgeführt,

$$\begin{aligned} G^{+}(12, 1'2'; E) = \frac{1}{2\pi \mathrm{i}} \int \mathrm{d}E' \, \big[ & G^{+}_{AA}(11'; E') G^{+}_{BB}(22'; E - E') \\ & - G^{+}_{AB}(12'; E') G^{+}_{BA}(21'; E - E') \big] . \end{aligned} \tag{4.23}$$

Aus dem entsprechenden Ausdruck für die Zweiteilchendichtematrix $\gamma(12, 1'2'; \epsilon) = -\mathrm{Im}\, G^{+}(12, 1'2'; \epsilon)/\pi$ ist ersichtlich, dass die Zweiteilchenzustandsdichte $n_2(E) = \int \mathrm{d}E' n(E') \, n(E - E')$ die Faltung der Einteilchenzustandsdichten $n(E)$ ist.

In Analogie zur konventionellen Photoemission kann man den Zweiteilchenphotostrom durch $I \sim -\left\langle \Psi \middle| \Delta \mathrm{Im}\, G^{+} \Delta^{\dagger} \middle| \Psi \right\rangle$ ausdrücken. Für den Endzustand reicht es aus, ein Produkt von Einteilchenzuständen anzusetzen, $|\Psi\rangle = |\Psi_A\rangle |\Phi_B\rangle$. Da der Zweiteilchendipoloperator eine Summe von Einteilchendipoloperatoren ist, $\Delta = \Delta_A + \Delta_B$, zerfällt der Photostrom in einen direkten Beitrag ($I_{\mathrm{dir}}$) und in einen Austauschbeitrag ($I_{\mathrm{ex}}$): $I = I_{\mathrm{dir}} - I_{\mathrm{ex}}$. Ersterer entsteht durch $G_{AA}G_{BB}$, letzterer durch $G_{AB}G_{BA}$. Zusammengefasst lautet der direkte Beitrag

$$\begin{aligned} I_{\mathrm{dir}} \sim - \int \mathrm{d}E' \, \Big[ & \left\langle \Psi_A \middle| \Delta_A \mathrm{Im}\, G^{+}_{AA}(E') \Delta_A^{\dagger} \middle| \Psi_A \right\rangle \left\langle \Phi_B \middle| \mathrm{Im}\, G^{+}_{BB}(E - E') \middle| \Phi_B \right\rangle \\ & + \left\langle \Psi_A \middle| \Delta_A \mathrm{Im}\, G^{+}_{AA}(E') \middle| \Psi_A \right\rangle \left\langle \Phi_B \middle| \mathrm{Im}\, G^{+}_{BB}(E - E') \Delta_B^{\dagger} \middle| \Phi_B \right\rangle \\ & + \left\langle \Psi_A \middle| \mathrm{Im}\, G^{+}_{AA}(E') \Delta_A^{\dagger} \middle| \Psi_A \right\rangle \left\langle \Phi_B \middle| \Delta_B \mathrm{Im}\, G^{+}_{BB}(E - E') \middle| \Phi_B \right\rangle \\ & + \left\langle \Psi_A \middle| \mathrm{Im}\, G^{+}_{AA}(E') \middle| \Psi_A \right\rangle \left\langle \Phi_B \middle| \Delta_B \mathrm{Im}\, G^{+}_{BB}(E - E') \Delta_B^{\dagger} \middle| \Phi_B \right\rangle \Big] . \end{aligned} \tag{4.24}$$

Dieser entspricht vier Feynman-Diagrammen, oder genauer: einem Paar von zwei Diagrammen (obere Reihe in Abb. 4.14). Der Austauschbeitrag ist durch

$$\begin{aligned} I_{\mathrm{ex}} \sim \int \mathrm{d}E' \Big[ & \Big\langle \Psi_A \Big| \Delta_A \mathrm{Im}\, G^{+}_{AB}(E') \Delta^{\dagger}_{B} \Big| \Phi_B \Big\rangle \left\langle \Phi_B \middle| \mathrm{Im}\, G^{+}_{BA}(E-E') \middle| \Psi_A \right\rangle \\ & + \left\langle \Psi_A \middle| \Delta_A \mathrm{Im}\, G^{+}_{AB}(E') \middle| \Phi_B \right\rangle \Big\langle \Phi_B \Big| \mathrm{Im}\, G^{+}_{BA}(E-E') \Delta^{\dagger}_{A} \Big| \Psi_A \Big\rangle \\ & + \Big\langle \Psi_A \Big| \mathrm{Im}\, G^{+}_{AB}(E') \Delta^{\dagger}_{B} \Big| \Phi_B \Big\rangle \left\langle \Phi_B \middle| \Delta_B \mathrm{Im}\, G^{+}_{BA}(E-E') \middle| \Psi_A \right\rangle \\ & + \left\langle \Psi_A \middle| \mathrm{Im}\, G^{+}_{AB}(E') \middle| \Phi_B \right\rangle \Big\langle \Phi_B \Big| \Delta_B \mathrm{Im}\, G^{+}_{BA}(E-E') \Delta^{\dagger}_{A} \Big| \Psi_A \Big\rangle \Big] \end{aligned} \tag{4.25}$$

gegeben. Dessen Diagramme entsprechen denen des direkten Anteils, jedoch für gekreuzte Anfangszustandspropagatoren (untere Reihe in Abb. 4.14).

Um einzusehen, dass der Zweiteilchenphotostrom verschwindet, wenn die Elektronen unkorreliert sind, betrachtet man zum Beispiel ein Überlappmatrixelement von Typ $\left\langle \Psi_A \middle| \mathrm{Im}\, G^{+}_{AA} \middle| \Psi_A \right\rangle$. Dieses ist Null, wenn der Endzustand orthogonal zu den Einteilchenanfangszuständen ist. Durch die Elektron–Elektron-Wechselwirkung innerhalb des Elektronenpaares wird diese Orthogonalität aufgehoben und der Übergang in den Endzustand ermöglicht.

Im nächsten Schritt wird die Elektron–Elektron-Wechselwirkung dergestalt modelliert, dass sie in bestehende Computerprogramme für die Einteilchenphotoemission implementiert werden kann. Dazu wird die abgeschirmte Coulomb-Wechselwirkung eines freien Elektronengases in zwei Beiträge zerlegt,

$$U(\boldsymbol{r}_1, \boldsymbol{r}_2) = \frac{1}{|\boldsymbol{r}_2 - \boldsymbol{r}_2|} \exp(-\lambda |\boldsymbol{r}_2 - \boldsymbol{r}_2|) = \frac{\exp(-2a_1 r_1/\lambda)}{a_1 r_1} + \frac{\exp(-2a_2 r_2/\lambda)}{a_2 r_2}, \tag{4.26}$$

mit $a_j = |\boldsymbol{r}_2 - \boldsymbol{r}_2|/(2r_j)$, $j = 1, 2$. Die Abschirmlänge $\lambda$ hängt mittels $\lambda = 1/\sqrt{4\pi N(E_{\mathrm{F}})}$ mit der Zustandsdichte $N(E_{\mathrm{F}})$ zusammen (für Cu beträgt $\lambda$ ungefähr $2.66$ Å). Die obige Formulierung legt eine Interpretation im Sinne eines modifizierten Einteilchenpotentials nahe:

$$U(\boldsymbol{r}_1, \boldsymbol{r}_2) = \frac{Z_1(\boldsymbol{r}_1, \boldsymbol{r}_2)}{r_1} + \frac{Z_2(\boldsymbol{r}_1, \boldsymbol{r}_2)}{r_2}, \tag{4.27}$$

$Z_j(\boldsymbol{r}_1, \boldsymbol{r}_2) = a_j^{-1} \exp(-2a_j r_j/\lambda)$, $j = 1, 2$. Dazu müssten allerdings die „Ladungen“ $Z_j$ unabhängig von den Elektronenkoordinaten sein. Nun zeigt die nichtlokale Wechselwirkung folgende Merkmale: sie ist abstoßend, wenn die beiden Elektronen in die gleiche Richtung emittiert

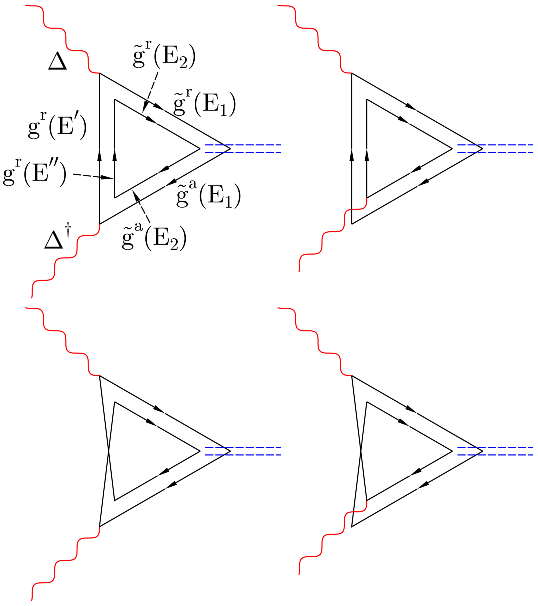

**Abbildung 4.14.** Feynman-Diagramme für den direkten (obere Reihe) und den Austauschbeitrag (untere Reihe) zum Zweiteilchenphotostrom. Jede Linie stellt hier Einteilchenzustände dar.

werden (Korrelationsloch). Und sind die Elektronen weit voneinander entfernt, ist die Abschirmung vernachlässigbar gering. Eine Näherung, die diesen Eigenschaften Rechnung trägt, besteht darin, $Z_j$ durch $\overline{Z}_j(\boldsymbol{r}_j) = \overline{a}_j^{-1} \exp(-2a_j r_j/\lambda)$ und $\overline{a}_j = |\boldsymbol{k}_2 - \boldsymbol{k}_1|/k_j$ zu ersetzen. Diese lokale Form der Elektron–Elektron-Wechselwirkung modifiziert die Potentiale der einzelnen Gitterplätze, $V_i \to V_i + \overline{Z}/r$. Die mit diesen Potentialen berechneten Einteilchen-Green-Funktionen enthalten daher die Elektron–Elektron-Wechselwirkung explizit, über die LDA hinausgehend. Die obige Transformation der nichtlokalen Wechselwirkung in eine lokale wurde erfolgreich in der Zweielektronenstreuung (e,2e) angewendet [119]. Beispiele für die Photoemission korrelierter Elektronenpaare enthält die Publikation 10 (S. P107ff); siehe auch [121]).

Um Unterschiede zwischen der gewöhnlichen Einfachphotoemission [($\gamma$,e); *Single photoemission* (SPE)] und der Doppelphotoemission [($\gamma$,2e); *Double photoemission* (DPE)] zu visualisieren, bietet es sich an, die Winkelverteilung des Photostroms zu untersuchen. Liegen die Anfangszustände energetisch auf dem Fermi-Niveau, erhält man in diesem Falle eine Abbildung der Fermi-Fläche (*Fermi-surface mapping*). Diese besitzt die Symmetrie der Kristalloberfläche, wenn der Winkel zwischen Detektor und Lichteinfallsrichtung festgehalten wird und nur die Probe bewegt wird. Die Beschränkung auf die Fermi-Energie hat den Vorteil, dass die Energieintegration in der DPE entfällt. Die Unterschiede zwischen den SPE- und den DPE-Spektren sind somit eine direkte Manifestation der Elektronenkorrelation in der DPE.

Um SPE und DPE miteinander vergleichen zu können, sollten beide möglichst im Rahmen der gleichen Methode und mit den gleichen Approximationen berechnet werden. Dieses wurde dadurch gewährleistet, dass den Spektren dieselben DFT-Rechnungen zugrunde liegen. Ferner wurde der gleiche Computercode mit identischen freien Parametern verwendet, einerseits im SPE-, andererseits im DPE-Modus. Die Qualität der theoretischen SPE wurde anhand der Winkelverteilung des Photostroms von der Cu(001)-Oberfläche durch Vergleich mit dem Experiment überprüft (obere Reihe in Abb. 4.15). Die Punktgruppe $4mm$ der Oberfläche wird insbesondere an den Bereichen hoher Intensität deutlich.

Die Symmetrie der Oberfläche bleibt in DPE erhalten, wenn eines der Elektronen in normaler Emission detektiert wird. Die Detektorposition ist durch den weißen Punkt in den Spektren der unteren Reihe in Abb. 4.15 gekennzeichnet. Für den anderen Detektor wird der Winkelbereich wie in der SPE durchfahren. Die Photonenenergie wurde gegenüber derjenigen in der SPE verdoppelt, sodass beide Elektronen des korrelierten Photoelektronenpaars die gleiche kinetische Energie besitzen. Somit werden Effekte durch unterschiedliche Dipolübergangsmatrixelemente ausgeschlossen.

In der Tat zeigt sich eine auf den ersten Blick ähnliche Intensitätsverteilung wie in der SPE (b und c). In der DPE erscheint die Intensität auf einen Ring konzentriert zu sein. Die Ursache dafür liegt zum einen in der spektralen Dichte, die sich in den SPE-Spektren manifestiert: nur für Wellenvektoren $\boldsymbol{k}_{\parallel}$, für die elektronische Zustände existieren, ist ein Photostrom messbar. Zum anderen ist die beobachtete Konzentration der Intensität durch die Korrelation zu erklären. Werden die beiden Elektronen unter gleichen Winkeln emittiert ($\boldsymbol{k}_1 \approx \boldsymbol{k}_2$), so wird der Wirkungsquerschnitt für diesen Fall gering sein, weil die Elektron–Elektron-Wechselwirkung abstoßend ist. Es wird daher das Korrelationsloch direkt in der DPE als „Intensitätswüste“ um die fixierte Austrittsrichtung sichtbar. Unterscheiden sich allerdings die Austrittsrichtungen stark voneinander ($|\boldsymbol{k}_1 - \boldsymbol{k}_2|$ groß), so ist die Korrelation zwischen den Elektronen klein, und die DPE-Intensität ist gering. Daraus folgt, dass die Elektronenkorrelation nur in einem Ring um die fixierte Austrittsrichtung zu einem signifikanten Photostrom führt. Ferner folgt der „Intensitätsring“ der fixierten Austrittsrichtung (Abb. 4.15d): wird die Position des fixierten Detektors aus der Oberflächennormalen gedreht (zum Beispiel entlang der $k_x$-Achse), so reduziert sich die Symmetrie der Winkelverteilung auf die Punktgruppe $m$ (Spiegelung an der $xz$-Ebene).

Weiter auffällig ist die im Vergleich zur SPE-Intensität sehr geringe DPE-Intensität (etwa sechs Größenordnungen in Abb. 4.15). Der Ausdruck für den DPE-Photostrom enthält neben den Dipolmatrixelementen auch Überlappintegrale [Gl. (4.24) und Gl. (4.25)]. Für Wellenfunktionen unkorrelierter Elektronen verschwinden letztere, da die Zustände orthogonal sind. Durch die Modifikation des Einteilchenpotentials aufgrund der Korrelation verschwinden die Überlappinte-

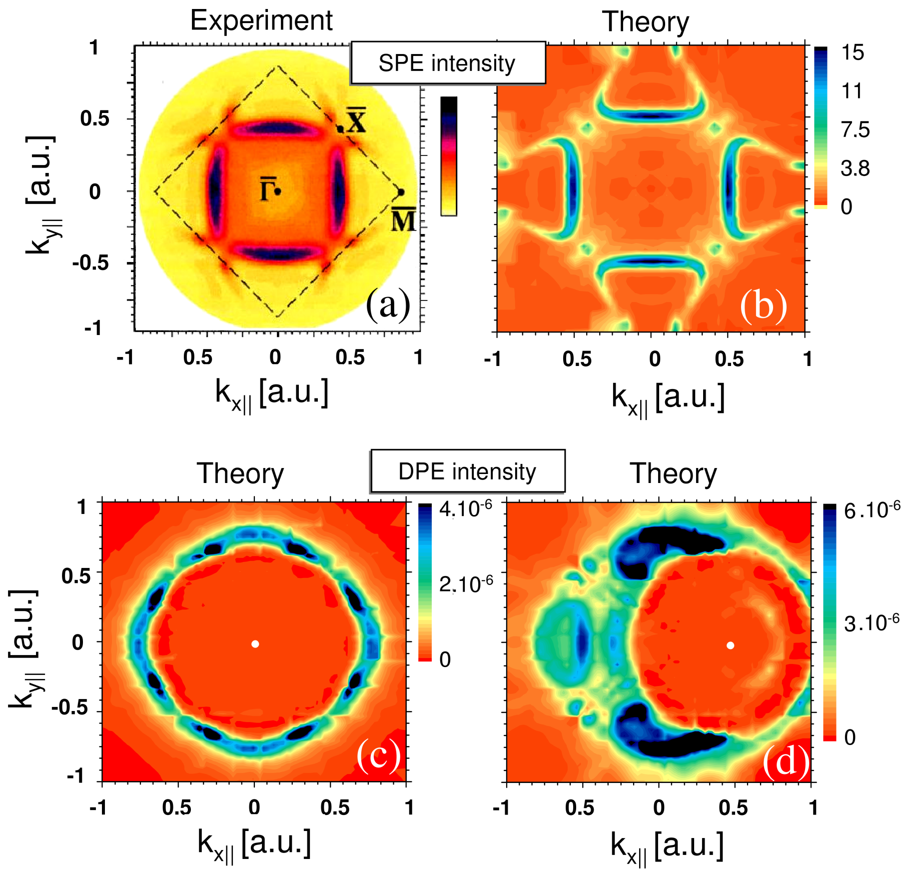

**Abbildung 4.15.** Einfach- und Doppelphotoemission von Cu(001). Obere Reihe: Experimentelle (a, links) und theoretische (b, rechts) Abbildung der Fermi-Fläche mittels Einfachphotoemission (SPE). Die experimentelle Winkelverteilung wurde Ref. [122] entnommen. Untere Reihe: Theoretische Doppelphotoemission von der Fermi-Energie. Der weiße Punkt markiert die Position des fixierten Detektors.

grale nicht mehr, bleiben jedoch klein gegenüber den Dipolmatrixelementen und führen daher zu einem geringen Photostrom. Die physikalische Begründung verweist auf die Messmethode der Koinzidenz, denn nur wenn gleichzeitig Elektronen detektiert wurden, wurde ein korreliertes Elektronenpaar nachgewiesen. Technisch müssen daher geringe Photonenflüsse verwendet werden, um den Untergrund aufgrund des nichtkorrelierten Photostroms gering zu halten und somit den Einzelnachweis von Elektronenpaaren zu ermöglichen.

Ein anderer signifikanter Unterschied von SPE und DPE ist die Oberflächensensitivität. Die mittlere freie Weglänge $\lambda_{\mathrm{MFP}}$ [*Mean free path* (MFP)] der Photoelektronen liegt für kinetische Energien der VUV-Photoemission im Bereich weniger Atomschichten [123]. Näherungsweise lässt sich der Beitrag der $n$-ten oberflächennahen Schicht zum SPE-Photostrom durch $I_n^{\mathrm{SPE}} = I_1^{\mathrm{SPE}} \exp[-(n-1)d/\lambda_{\mathrm{mfp}}]$ ausdrücken ($d$ Zwischenlagenabstand, $I_1^{\mathrm{SPE}}$ Beitrag der ersten Schicht). In der DPE muss nun ein Photoelektronenpaar koinzident nachgewiesen werden, so dass der Beitrag der Schicht $n$ durch $I_n^{\mathrm{DPE}} = I_1^{\mathrm{DPE}} \exp[-2(n-1)d/\lambda_{\mathrm{mfp}}]$ gegeben ist, wenn beide Elektronen aus derselben Schicht stammen. Effektiv wird also die mittlere freie Weglänge halbiert und liegt somit im Bereich von ein bis zwei Schichtabständen.

Mit einem Photoemissionscomputerprogramm lässt sich nun der Unterschied in der Oberflächensensitivität illustrieren. Dazu wird die Summation über die Beiträge der einzelnen Schichten zum Photostrom eingeschränkt. Dieses Vorgehen verändert *nicht* die zugrundeliegende elektronische Struktur des Systems. In Abbildung 4.16 wurde die SPE von Cu(001) auf Beiträge der ersten zwei [links oben, (a)] und fünf [links unten, (a')] Schichten beschränkt. Typischerweise müssen ca. 20 bis 30 Schichten in Betracht gezogen werden, um konvergierte Resultate zu bekommen. Daher ist es verständlich, dass sich die hier gezeigten Intensitätsverteilungen stark unterscheiden. Im Falle der DPE hingegen finden sich kaum signifikante Unterschiede in den entsprechenden Spektren

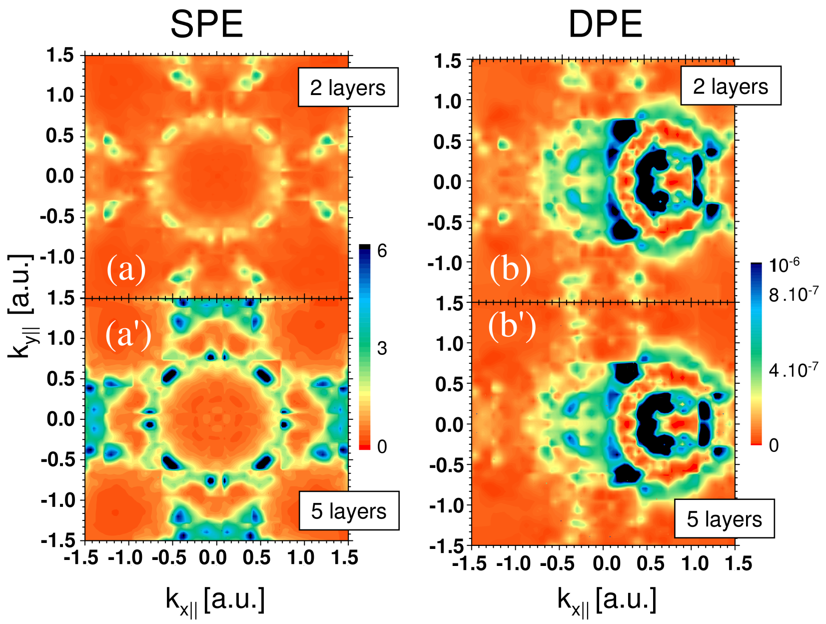

**Abbildung 4.16.** Oberflächensensitivität der Einfach- [SPE, links; (a) und (a')] und Doppelphotoemission [DPE, rechts; (b) und (b')] von Cu(001). Die Beiträge der oberflächennahen Atomlagen des halbunendlichen Kristalls zum Photostrom wurden dabei auf zwei (obere Reihe) und fünf (untere Reihe) Schichten beschränkt.

(rechte Spalte in Abb. 4.16), was die größere Oberflächensensitivität der DPE im Vergleich zur SPE belegt.

Zusammenfassend lässt sich feststellen, dass die DPE eine Methode ist, die Elektronenkorrelation *direkt* darzustellen. In der SPE manifestiert sich diese ebenfalls, jedoch eher *indirekt* als Abweichung vom erwarteten Einteilchenverhalten.

## Resümee

In diesem Kapitel wurde exemplarisch gezeigt, wie die Spin–Bahn-Kopplung zur Spinpolarisation in der winkelaufgelösten Photoemission von nichtmagnetischen System führt. Das Zusammenwirken von Magnetismus und SBK resultiert im mit diesem Effekt eng verknüpften Magnetischen Dichroismus. Die Photoemissionsintensität von dünnen Filmen zeigt für Quantentrogzustände Modulationen, die zur Charakterisierung dieser herangezogen werden können. Die Temperaturabhängigkeit der magnetischen Eigenschaften sehr dünner magnetischer Filme manifestiert sich ebenfalls in den Spektren und kann im Fall von Co/Cu(001) im Bild ungeordneter magnetischer Momente beschrieben werden (*Disordered local moment*). Die Elektronenkorrelation lässt sich mit Hilfe der koinzidenten Emission von Elektronenpaaren visualiseren. Deren Beschreibung basiert auf antisymmetrisierten Einteilchenzuständen und einer lokalen Näherung für die abgeschirmte Coulomb-Wechselwirkung.

# 5. Spinabhängiger ballistischer Transport

In diesem Kapitel werden Aspekte des spinabhängigen ballistischen Transport durch planare Tunnelkontakte behandelt. Die Grundlage für die numerische Behandlung liefert die Landauer–Büttiker-Theorie [Landauer-Büttiker (LB)], die den elektrischen Leitwert als Transmission durch die Probe beschreibt. Nach der Skizzierung der Theorie (Abschn. 5.1) wird eine neue Methode zur Integration über die zweidimensionale Brillouin-Zone (2BZ) anhand resonanten Tunnelns diskutiert (Abschn. 5.2). Dienen Co(0001)-Kontakten zur Untersuchung der *Zero bias anomaly* (ZBA) beim Vakuumtunneln (Abschn. 5.3), so wird der Einfluss der mikroskopischen Struktur von Grenzflächen am Beispiel von Fe(001)/MgO/Fe(001) behandelt (Abschn. 5.4). In beiden Fällen erfolgt der Transport bei Energien nahe der Fermi-Energie der Elektroden. Für die Untersuchung der *Spin motion*, d. i. die Kopplung von Elektronenbewegung und Elektronenspin, bei wesentlich höheren Energien wird die spinaufgelöste Photoelektronenspektroskopie als neuer Ansatz diskutiert (Abschn. 5.5).

## 5.1. Theorie des spinabhängigen Transports in planaren Tunnelkontakten

Im Drude–Sommerfeld-Modell der diffusen elektrischen Leitung in Metallen nimmt die Leitfähigkeit die Form $\sigma = g\, e^2\, k_\mathrm{F}^2\, l_\mathrm{MFP}/(3\pi h)$ an. Hier ist die mittlere freie Weglänge $l_\mathrm{MFP}$ [*Mean free path* (MFP)] mit der Relaxationszeit $\tau$ verknüpft. Die Fermi-Wellenzahl der Elektronen ist durch $k_\mathrm{F}$ gegeben, und der Entartungsgrad $g$ beträgt $2$ aufgrund der Spinentartung.

Um Quanteneffekte in den Transporteigenschaften zu verstehen, unterscheidet man zwischen elastischen und inelastischen Streuprozessen. In den Ersteren bleibt der Betrag des Wellenvektors $\boldsymbol{k}$, und somit die Information über die Phase der Wellenfunktion, erhalten. Bei Letzteren wird Energie mit Quasiteilchen (z. B. Phononen, Magnonen) ausgetauscht, sodass die Phaseninformation verlorengeht. Bei niedrigen Temperaturen gilt für die mit diesen Prozessen verbundenen Relaxationszeiten $\tau_\mathrm{inel} \gg \tau_\mathrm{el}$, während im Drude–Sommerfeld-Modell $\tau_\mathrm{inel} < \tau_\mathrm{el}$ gilt (Abb. 5.1a und b). Beim ballistischen Transport bleibt die Phaseninformation sogar von der Injektion des Elektrons ins System bis zu dessen Austritt erhalten (kohärenter Transport, Abb. 5.1c).

Verbunden mit diesen drei Typen der elektrischen Leitung sind verschiedene Längenskalen: die räumliche Ausdehnung des Systems (beschrieben durch die Länge $l$), die Wellenlänge $\lambda_\mathrm{F}$ der

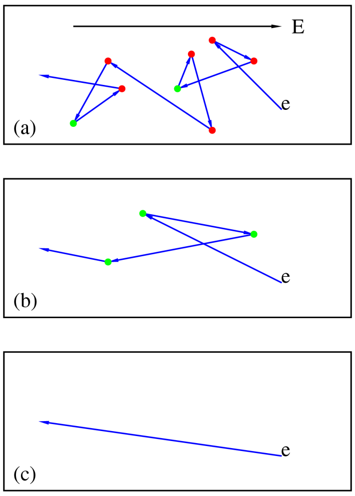

**Abbildung 5.1.** Elektrische Leitfähigkeit. (a) Konventionelle Drude–Sommerfeld-Leitung in einem Metall bei mittleren Temperaturen. Das Elektron $e$ wird häufiger inelastisch (rote Punkte) als elastisch (grüne Punkte) gestreut ($\tau_\mathrm{inel} < \tau_\mathrm{el}$). (b) Bei niedrigeren Temperaturen können Quanteneffekte auftreten ($\tau_\mathrm{inel} \gg \tau_\mathrm{el}$). (c) Ballistischer Transport. $E$ bezeichnet das angelegte elektrische Feld.

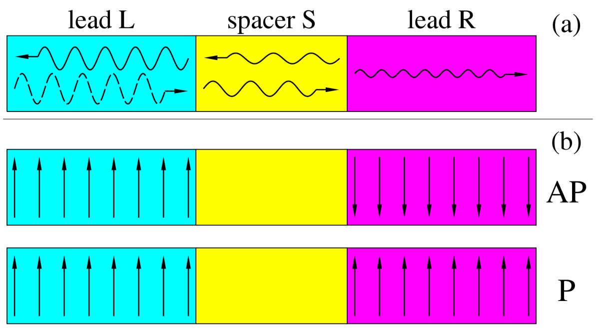

**Abbildung 5.2.** Planarer Tunnelkontakt, bestehend aus den Elektroden $\mathcal{L}$ (cyan) und $\mathcal{R}$ (magenta), die durch die Barriere $\mathcal{S}$ (gelb) voneinander getrennt sind. (a) Ein in $\mathcal{L}$ einlaufender Streukanal (gestrichelt) wird an den beiden Grenzflächen gestreut und erzeugt einen reflektierten (auslaufend in $\mathcal{L}$) und einen transmittierten (auslaufend in $\mathcal{R}$) Streukanal (durchgezogen). (b) Magnetische Konfigurationen für den Tunnelmagnetwiderstand. In der P-Konfiguration sind die Magnetisierungen (Pfeile) in den Elektroden parallel zueinander ausgerichtet, in der AP-Konfiguration antiparallel.

Elektronen auf der Fermi-Fläche, die elastische Streulänge $l_{\mathrm{el}}$ und die Phasenkohärenzlänge $l_{\phi}$. In den drei skizzierten Regimen besitzen diese Längen spezifische Relationen zueinander. Im Drude–Sommerfeld-Modell zum Beispiel gilt $l \gg l_{\mathrm{MFP}} \gg \lambda_{\mathrm{F}}$ (diffuser Transport). Beim ballistischen Transport hingegen hat man $l_{\phi} \gg l$ und $l_{\mathrm{MFP}} \gg l$, womit eine Beschreibung des elektrischen Transport im Rahmen der Landauer–Büttiker-Theorie möglich wird. Insbesondere findet (elastische) Streuung an Defekten nicht statt, z. B. in defektarmen Proben geringer räumlicher Ausdehnung.

Ein magnetischer Tunnelkontakt besteht aus zwei ferromagnetischen Elektroden $\mathcal{L}$ und $\mathcal{R}$, die durch eine Tunnelbarriere $\mathcal{S}$ voneinander getrennt sind (Abb. 5.2). Letztere besteht aus einem Isolator, etwa aus einem Oxid (MgO, $\mathrm{Al_2O_3}$) oder aus Vakuum (Rastertunnelmikroskop). Als charakteristische Größen des spinabhängigen Transports werden i. A. die Strom–Spannungs-Kennlinie oder der Tunnelmagnetwiderstand [*Tunnel magneto-resistance* (TMR)] gemessen. Mit TMR wird die Änderung des durch den Tunnelkontakt fließenden Stroms bei Umkehr der Magnetisierungsrichtung in einer der Elektroden bezeichnet. Man misst oder berechnet dazu den Strom für die parallele (P) und die antiparallele (AP) Anordnung der Magnetisierungen.

**Das Jullière–Maekawa–Gafvert-Modell.** Das wohl einfachste Modell für ballistischen Transport wurde von Jullière vorgeschlagen [124] und kennzeichnet sich dadurch aus, dass es die Eigenschaften der Tunnelbarriere ebensowenig berücksichtigt wie die detaillierte elektronische Struktur der Elektroden. Der Leitwert wird durch die spinaufgelösten Anzahlen der Elektronen der Zuleitungen oder, nach Maekawa und Gafvert [125], durch die Zustandsdichten an der Fermi-Energie bestimmt.

Der Leitwert $G$ ist proportional zur Zustandsdichte der Elektrode, *aus* der getunnelt wird (Quelle), und proportional zu derjenigen der Elektrode, *in* die getunnelt wird (Senke). Für kleine Biasspannungen ist die Tunnelenergie die gemeinsame Fermi-Energie $E_{\mathrm{F}}$ der Elektroden. Bleibt der Spin beim Tunneln erhalten (keine Spin–Bahn-Kopplung), ergibt sich somit für die P-Konfiguration $G(\mathrm{P}) \propto L_{\uparrow}R_{\uparrow} + L_{\downarrow}R_{\downarrow}$, wobei $L$ und $R$ die Zustandsdichten in der linken und rechten Elektrode bezeichnen. In der AP-Konfiguration wechselt in einer Elektrode, zum Beispiel in der rechten, die Orientierung der magnetischen Momente. Da nun die $\uparrow$-Elektronen die Minoritätselektronen sind, während die $\downarrow$-Elektronen zur Majorität werden, ist $G(\mathrm{AP}) \propto L_{\uparrow}R_{\downarrow} + L_{\downarrow}R_{\uparrow}$. Für Übergangsmetalle ist die Majoritätszustandsdichte bei $E_{\mathrm{F}}$ kleiner als die Minoritätszustandsdichte, was $G(\mathrm{P}) > G(\mathrm{AP})$ impliziert (Abb. 5.3).

Der Tunnelmagnetwiderstand $\delta$ ist in dieser Arbeit als Asymmetrie der Leitwerte definiert,[1]

$$\delta = \frac{G(\mathrm{P}) - G(\mathrm{AP})}{G(\mathrm{P}) + G(\mathrm{AP})}, \tag{5.1}$$

---

[1] Andere populäre Definitionen sind der „optimistische“ und der „pessimistische“ TMR, in denen der Nenner in Gl. (5.1) durch $G(\mathrm{AP})$ bzw. $G(\mathrm{P})$ ersetzt wird. Eine Wertangabe des TMR erfordert daher immer die Angabe der verwendeten Definition.

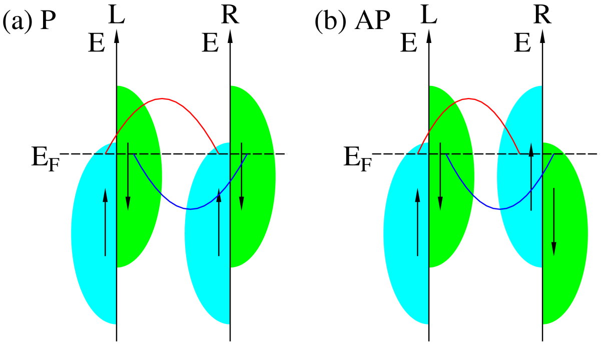

**Abbildung 5.3.** Jullière-Modell für den Tunnelmagnetwiderstand. (a) In der P-Konfiguration tunneln Elektronen unter Erhaltung des Spins von der linken Elektrode $\mathcal{L}$ zur rechten $\mathcal{R}$. Der Leitwert ist proportional zum Produkt der spinaufgelösten Zustandsdichten (cyan und grün) an der Fermi-Energie $E_F$. Die Spinorientierung ist durch die senkrechten Pfeile gegeben. (b) In der AP-Konfiguration vertauschen Majoritäts- und Minoritätsorientierung die Rollen in der rechten Elektrode.

und lässt sich prägnant als $\delta = P_\mathcal{L} P_\mathcal{R}$ zusammenfassen. Hier sind $P_\mathcal{L}$ und $P_\mathcal{R}$ die Spinpolarisationen der Elektroden, $P_\mathcal{N} = (N_\uparrow - N_\downarrow)/(N_\uparrow + N_\downarrow)$, $N = L, R$, wobei $\mathcal{N}$ die jeweilige Elektrode bezeichnet. Das Resultat für den TMR impliziert, dass der Leitwert allein durch die Spinpolarisationen der Elektroden gegeben und unabhängig von der Tunnelbarriere ist, ein Befund der nicht mit Experimenten in Einklang steht. Allerdings ist der TMR energieabhängig. Somit könnte die *Zero bias anomaly* als Zustandsdichteeffekt erklärt werden (Abschn. 5.3).

**Tunneln freier Elektronen – das Slonczewski-Modell.** Der Tunnelstrom sollte im wesentlichen durch delokalisierte Elektronen vermittelt werden, während lokalisierte Elektronen nicht wesentlich zum Tunnelstrom beitragen. Daher erscheint es naheliegend, ein Modell für freie Elektronen zu entwickeln. Beschränkt man sich weiterhin auf den Fall kleiner Biasspannung, so kann die Tunnelbarriere als rechteckige Stufe angenommen werden. Dieses Modell wurde von Slonczewski vorgeschlagen [126] und wird hier für den eindimensionalen Fall vorgestellt.

Die Tunnelenergie $E$ sei kleiner als die Barrierenhöhe $W$ $(0 < E < W)$. Die elektronischen Zustände werden so gewählt, dass sie die Randbedingungen eines Streuproblems erfüllen. In der linken Elektrode besteht die $\uparrow$-Wellenfunktion demnach aus einer einlaufenden ebenen Welle mit Amplitude $1/\sqrt{k_{\mathcal{L}\uparrow}}$ und einer reflektierten Welle mit Amplitude $R_\uparrow$, $\Psi_{\mathcal{L}\uparrow}(x) = \exp(\mathrm{i}k_{\mathcal{L}\uparrow}x)/\sqrt{k_{\mathcal{L}\uparrow}} + R_\uparrow \exp(-\mathrm{i}k_{\mathcal{L}\uparrow}x)$. Die einfallende Welle ist auf den Strom normiert. In der Barriere sind exponentiell anwachsende und abklingende ebene Wellen überlagert, $\Psi_{\mathcal{S}\uparrow}(x) = A_\uparrow \exp(\kappa_\uparrow x) + B_\uparrow \exp(-\kappa_\uparrow x)$, während in der rechten Elektrode nur eine auslaufende Welle auftritt, $\Psi_{\mathcal{R}\uparrow}(x) = T_\uparrow \exp(\mathrm{i}k_{\mathcal{R}\uparrow}x)$. Ein analoger Ansatz wird für die $\downarrow$-Wellenfunktion vorgenommen. Die Wellenzahlen sind hier durch $k_\uparrow = \sqrt{2E}$, $k_\downarrow = \sqrt{2(E - V_0)}$ und $\kappa = \sqrt{2(W - E)}$ gegeben, wobei $V_0 > 0$ die Austauschaufspaltung in den Elektroden repräsentiert (Abb. 5.4). Die acht Koeffizienten ($R$, $A$, $B$ und $T$, jeweils für beide Spinorientierungen) ergeben sich aus den Stetigkeitsforderungen an die Gesamtwellenfunktion an den beiden Grenzflächen (linke Elektrode-Stufe und Stufe-rechte Elektrode).

Der Tunnelmagnetwiderstand $\delta = P_\mathcal{L} P_\mathcal{R} \Delta$ entspricht im wesentlichen dem Jullière'schen Ergeb-

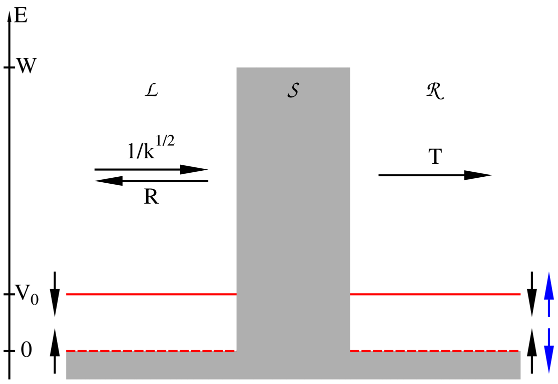

**Abbildung 5.4.** Slonczewski-Modell für den Tunnelmagnetwiderstand. Ein in der linken Elektrode einlaufendes Elektron ($1/k^{1/2}$) wird an der Stufenbarriere reflektiert ($R$) und in die rechte Elektrode transmittiert ($T$). Die konstanten Potentiale in den Elektroden sind spinabhängig (schwarze Pfeile in $\mathcal{R}$ für die P-Konfiguration, blaue für die AP-Konfiguration).

nis, d. i. das Produkt der Spinpolarisationen $P_{\mathcal{N}} = (k_{\mathcal{N}\uparrow} - k_{\mathcal{N}\downarrow})/(k_{\mathcal{N}\uparrow} + k_{\mathcal{N}\downarrow})$, $\mathcal{N} = \mathcal{L}, \mathcal{R}$, der Elektroden, welches jedoch durch den Transmissionsfaktor

$$\Delta = \frac{\kappa^2 - k_{\mathcal{L}\uparrow} k_{\mathcal{L}\downarrow}}{\kappa^2 + k_{\mathcal{L}\uparrow} k_{\mathcal{L}\downarrow}} \frac{\kappa^2 - k_{\mathcal{R}\uparrow} k_{\mathcal{R}\downarrow}}{\kappa^2 + k_{\mathcal{R}\uparrow} k_{\mathcal{R}\downarrow}} \tag{5.2}$$

modifiziert ist. Dieser beinhaltet die elektronische Struktur der Elektroden und der Barriere vermöge der Wellenzahlen. Die funktionale Form des TMR bleibt unverändert, wenn das Modell auf drei Dimensionen erweitert wird. Nach Integration über alle planaren Wellenvektoren besitzt der resultierende TMR-Ausdruck diese Gestalt allerdings nicht mehr. Das Slonczewski-Modell beschreibt Leitung als „Transmission“, wie die LB-Theorie, die im folgenden Abschnittt diskutiert wird. Letztere ist jedoch allgemeiner und historisch früher formuliert worden.

**Ballistischer Transport als Transmission – die Landauer–Büttiker-Theorie.** Der Leitwert $G = I/\Delta V$ kann als globale Größe angesehen werden, da er das Verhältnis des Gesamtstroms $I$ durch die Probe und den Spannungsabfall $\Delta V$ zwischen Eingang der Ladungsträger in das System und ihrem Austritt aus dem System beschreibt. Im Gegensatz dazu kann die Leitfähigkeit $\sigma$ als lokale Materialgröße betrachtet werden, da mit ihr das Konzept eines Ladungsflusses (Stromdichte), vermittelt durch ein lokales elektrisches Feld, verbunden ist. Kurz: der Leitwert beschreibt ein System (bestehend aus Reservoirs, Elektroden und Tunnelkontakt), die Leitfähigkeit hingegen ein Material. Selbstverständlich bestimmen Materialeigenschaften den Leitwert mit.

Die LB-Theorie kann als „Leitung durch Transmission“ charakterisiert werden [127]. Die Transmissionsmoden werden durch interne Freiheitsgrade (z. B. Wellenvektor $\boldsymbol{k}$) und externe Größen (angelegte Spannung, Dimension der Probe) charakterisiert und als Streukanäle bezeichnet. Das Resultat für die Leitfähigkeit $G$ hängt von den Annahmen ab, die man über die Kopplung der Elektroden an die Reservoire macht (Abb. 5.5). In der Landauer–Büttiker-Formulierung wird Folgendes vorausgesetzt [128]. *(i)* Die Reservoire $\mathcal{L}_{\mathrm{res}}$ und $\mathcal{R}_{\mathrm{res}}$ speisen nur Elektronen mit Energien unterhalb der chemischen Potentiale $\mu_{\mathcal{L}_{\mathrm{res}}}$ und $\mu_{\mathcal{R}_{\mathrm{res}}}$ in die idealen Elektroden ein. *(ii)* Die in Richtung der Barriere einlaufenden Streukanäle werden inkohärent emittiert, sodass Interferenzeffekte zwischen verschiedenen Kanälen vernachlässigt werden. *(iii)* Von der Barriere auslaufende Elektronen werden von den Reservoirs vollständig absorbiert und thermalisiert.

Ein vom linken Reservoir $\mathcal{L}_{\mathrm{res}}$ einlaufender Streukanal $i_{\mathcal{L}}$ besitzt die Wahrscheinlichkeit $T_{ji}^{++}$ in einen auslaufenden Kanal $j_{\mathcal{R}}$ der rechten Elektrode $\mathcal{R}$ gestreut zu werden. Die Reflexionswahrscheinlichkeit lautet analog $R_{ji}^{-+}$, wobei $j$ einen Zustand in $\mathcal{L}$ indiziert. Die Superskripte bezeichnen hier die Propagationsrichtung der Elektronen nach und vor der Streuung. Entsprechend ergeben sich die Streuwahrscheinlichkeiten für von rechts einlaufende Kanäle. Zur Verein-

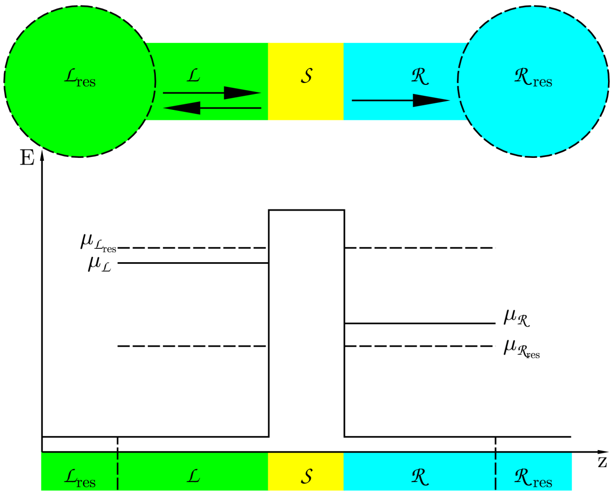

**Abbildung 5.5.** Schematische Darstellung eines Tunnelkontakts. Oben: Die Streuzone $\mathcal{S}$ (gelb) ist mit idealen Elektroden $\mathcal{L}$ (links, grün) und $\mathcal{R}$ (rechts, cyan) verbunden. Diese werden durch die Reservoirs $\mathcal{L}_{\mathrm{res}}$ und $\mathcal{R}_{\mathrm{res}}$ (Kreise) mit Elektronen versorgt. Die Pfeile repräsentieren einen von $\mathcal{L}_{\mathrm{res}}$ einlaufenden Streukanal, der einerseits an $\mathcal{S}$ reflektiert und im $\mathcal{L}_{\mathrm{res}}$ absorbiert wird und andererseits in einen Streukanal in $\mathcal{R}$ transmittiert und in $\mathcal{R}_{\mathrm{res}}$ absorbiert wird. Unten: Chemische Potentiale im Tunnelkontakt. $\mathcal{L}_{\mathrm{res}}$ emittiert Elektronen mit Energien bis zur Quasi-Fermi-Energie $\mu_{\mathcal{L}_{\mathrm{res}}}$, während $\mathcal{R}_{\mathrm{res}}$ bis $\mu_{\mathcal{R}_{\mathrm{res}}}$ emittiert. Die chemischen Potentiale von $\mathcal{L}$ und $\mathcal{R}$ sind mit $\mu_{\mathcal{L}}$ und $\mu_{\mathcal{R}}$ bezeichnet. Die $z$-Achse definiert die positive Propagationsrichtung der Elektronen.

fachung werden die totalen Transmissions- und Reflexionswahrscheinlichkeiten $R_j^{-+} = \sum_i R_{ji}^{-+}$ und $T_j^{++} = \sum_i T_{ji}^{++}$ *in* den auslaufenden Streukanal $j$ in $\mathcal{L}$ bzw. in $\mathcal{R}$ eingeführt.

Wie im Vorangegangenen beschränkt man sich auf den Fall kleiner Biasspannungen (lineare Antwort). Der Strom der Streukanals $j_{\mathcal{L}}$, der vom Reservoir $\mathcal{L}_{\mathrm{res}}$ in das System injiziert wird, ist durch $ev_{j_{\mathcal{L}}}(\partial n_{j_{\mathcal{L}}}/\partial E)(\mu_{\mathcal{L}} - \mu_{\mathcal{R}})$ gegeben. Die Zustandsdichte dieses Zustands mit positiver Gruppengeschwindigkeit $v_{j_{\mathcal{L}}}$ lautet $\partial n_{j_{\mathcal{L}}}/\partial E = v_{j_{\mathcal{L}}}/h$, wodurch der Strom im Kanal $j_{\mathcal{L}}$ unabhängig von der Geschwindigkeit ist: $I_{j_{\mathcal{L}}} = e(\mu_{\mathcal{L}} - \mu_{\mathcal{R}})/h$. Das linke Reservoir führt demnach allen Kanälen den gleichen Strom zu.

Der Kanal $i_{\mathcal{R}}$ auf der rechten Seite wird von allen einlaufenden Kanälen $j_{\mathcal{L}}$ gespeist. Somit ist der von ihm getragene Strom durch $\sum_j T_{ij}^{++} I_{j_{\mathcal{L}}}$ gegeben. Den gesamten Strom erhält man durch Summation über alle auslaufenden Kanäle $i_{\mathcal{R}}$,

$$I_{\mathrm{tot}} = \frac{e}{h}(\mu_{\mathcal{L}} - \mu_{\mathcal{R}}) \sum_i T_i^{++} = \frac{e}{h}(\mu_{\mathcal{L}} - \mu_{\mathcal{R}}) \sum_i (1 - R_i^{-+}), \tag{5.3}$$

wobei $\sum_i T_i^{++} = \sum_i (1 - R_i^{-+})$ durch die Stromerhaltung erzwungen wird. Dividiert man den Gesamtstrom durch die Biasspannung $V$ $(eV = \mu_{\mathcal{L}} - \mu_{\mathcal{R}})$, so erhält man den Leitwert

$$G = \frac{e^2}{h} \sum_i T_i^{++} = \frac{e^2}{h} \sum_{ij} T_{ij}^{++} \tag{5.4}$$

als Summe über alle Transmissionswahrscheinlichkeiten. Das Quantum der Leitfähigkeit beträgt $G_0 = e^2/h$. Dieser Herleitung liegt die Annahme zugrunde, dass in den Elektroden eindeutig bestimmte chemische Potentiale existieren. Dazu muss der Spannungsabfall über der Barriere auf letztere lokalisiert sein, was im Allgemeinen durch die elektronische Abschirmung in den metallischen Elektroden gewährleistet ist.

Das Ergebnis für $G$ mag auf den ersten Blick verwundern, da sich für ideale Transmission, d. h. für $T_{ij}^{++} = 1$, ein endlicher Leitwert ergibt. Der maximale Leitwert ist jedoch durch die Anzahl der zur Verfügung stehenden Kanäle nach oben beschränkt[2] und divergiert nicht, wie erwartet werden könnte. Das „Problem" des endlichen Leitwerts bei idealer Transmission wird durch den Vierpunktleitwert gelöst. Dazu wird das System durch zwei Kontakte an den idealen Zuleitungen erweitert, was $\mu_{\mathcal{L}_{\mathrm{res}}} \neq \mu_{\mathcal{L}}$ und $\mu_{\mathcal{R}_{\mathrm{res}}} \neq \mu_{\mathcal{R}}$ impliziert (Abb. 5.5). Daraus ergibt sich der Leitwert zu

$$G = \frac{e^2}{h} \frac{\sum_i T_i^{++}}{1 + \frac{1}{g_{\mathcal{L}}} \sum_{i=1}^{N_{\mathcal{L}}} (R_i^{-+}/v_{i\mathcal{L}}) - \frac{1}{g_{\mathcal{R}}} \sum_{i=1}^{N_{\mathcal{R}}} (T_i^{++}/v_{i\mathcal{R}})}, \tag{5.5}$$

mit $g_{\mathcal{N}} = \sum_i v_{i\mathcal{N}}$, $\mathcal{N} = \mathcal{L}, \mathcal{R}$. Im Falle sehr kleiner Transmissionen $T_i^{++}$ reduziert sich der Vierpunktleitwert zum Zweipunktresultat. Die Gruppengeschwindigkeiten sind nur bei sehr dünnen oder leitenden Barrieren $\mathcal{S}$ relevant. Eine rigorose Rechtfertigung des Landauer-Resultats im Rahmen des Lineare–Antwort-Formalismus von Kubo resultiert ebenfalls im Vierpunktleitwert.

Bisher wurde der Leitwert in der Linearen–Antwort-Theorie berechnet. Um endliche Biasspannungen behandeln zu können, muss die Theorie erweitert werden. Eine naheliegende Methode besteht darin, den Leitwert in Linearer–Antwort-Theorie für die jeweilige Tunnelenergie zu berechnen und anschließend über den gesamten Energiebereich der angelegten Spannung zu integrieren [„Tunnelfenster"; Publikation 12 (S. P118) und [130]].

**Anwendung auf den Tunnelmagnetwiderstand planarer Kontakte.** Nach der allgemeinen Formulierung wird nun die Spezialisierung auf den ballistischen Transport durch planare magnetische Tunnelkontakte vorgenommen (Abb. 5.2).

---

[2] Der Leitwert der Elektroden selbst (Sharvin-*Conductance* [129]) ist endlich, da für diesen speziellen „Tunnelkontakt" $T_{ji}^{++} = \delta_{j_{\mathcal{R}} i_{\mathcal{L}}}$ ist. Die Transmission ist in diesem Fall identisch mit der Anzahl der Streukanäle.

Die Streukanäle sind identisch mit den ein- und auslaufenden Eigenzuständen weit entfernt vom Tunnelkontakt, d. h. mit den Bloch-Zuständen $n_{\mathcal{L}}$ und $m_{\mathcal{R}}$ der Elektroden, die neben dem Bandindex und dem Wellenvektor $\boldsymbol{k}_{\|}$ nach ihrer Propagationsrichtung $\pm z$ klassifiziert werden. Die Tunnelwahrscheinlichkeiten

$$P_{n_{\mathcal{L}} m_{\mathcal{R}}}(E_{\mathrm{t}}, \boldsymbol{k}_{\|}) = |S^{++}_{n_{\mathcal{L}} m_{\mathcal{R}}}(E_{\mathrm{t}}, \boldsymbol{k}_{\|})|^2 \tag{5.6}$$

der Bloch-Zustände durch den Tunnelkontakt werden aus der Streumatrix $S$ der Barriere berechnet (S. 9ff). Die Transmission

$$T(E_{\mathrm{t}}, \boldsymbol{k}_{\|}) = \sum_{n_{\mathcal{L}} m_{\mathcal{R}}} P_{n_{\mathcal{L}} m_{\mathcal{R}}}(E_{\mathrm{t}}, \boldsymbol{k}_{\|}). \tag{5.7}$$

erhält man dann durch Summation der Wahrscheinlichkeiten für alle in $\mathcal{L}$ ein- und in $\mathcal{R}$ auslaufenden Bloch-Zustände. Der Leitwert

$$G(E_{\mathrm{t}}) = G_0 \int_{2\mathrm{BZ}} T(E_{\mathrm{t}}, \boldsymbol{k}_{\|}) \, \mathrm{d}k^2. \tag{5.8}$$

ist durch die über die zweidimensionale Brillouin-Zone (2BZ) integrierte Transmission gegeben. Für nicht verschwindende Biasspannung $V_{\mathrm{b}}$ können Elektronen in besetzten Zuständen der einen Elektrode (Quelle) in unbesetzte der anderen Elektrode (Senke) tunneln. Der Energiebereich, in dem Tunneln stattfinden kann („Tunnelfenster"), ist demnach durch $[\min(E_{\mathrm{F}\mathcal{L}}, E_{\mathrm{F}\mathcal{R}}), \max(E_{\mathrm{F}\mathcal{L}}, E_{\mathrm{F}\mathcal{R}})]$ gegeben. Für den Strom folgt

$$I = \int_{\min(E_{\mathrm{F}\mathcal{L}}, E_{\mathrm{F}\mathcal{R}})}^{\max(E_{\mathrm{F}\mathcal{L}}, E_{\mathrm{F}\mathcal{R}})} G(E_{\mathrm{t}}) \, \mathrm{d}E_{\mathrm{t}}, \tag{5.9}$$

und der gemittelte Leitwert $G_{\mathrm{av}}$ kann durch

$$G_{\mathrm{av}} = \frac{1}{|E_{\mathrm{F}\mathcal{L}} - E_{\mathrm{F}\mathcal{R}}|} \int_{\min(E_{\mathrm{F}\mathcal{L}}, E_{\mathrm{F}\mathcal{R}})}^{\max(E_{\mathrm{F}\mathcal{L}}, E_{\mathrm{F}\mathcal{R}})} G(E_{\mathrm{t}}) \, \mathrm{d}E_{\mathrm{t}} \tag{5.10}$$

definiert werden. Der Tunnelmagnetwiderstand

$$\delta = \frac{G_{\mathrm{av}}(\mathrm{P}) - G_{\mathrm{av}}(\mathrm{AP})}{G_{\mathrm{av}}(\mathrm{P}) + G_{\mathrm{av}}(\mathrm{AP})}, \tag{5.11}$$

ist die Asymmetrie der gemittelten Leitwerte, die für die parallele (P) und die antiparallele (AP) Konfiguration der Elektrodenmagnetisierungen berechnet wurden (Abb. 5.2b). Die hier skizzierte Theorie lässt sich innerhalb der *Layer*-KKR implementieren [131]. Die im Folgenden vorgestellten Resultate wurden mit einem vom MacLaren *et al.* vorgeschlagenen Verfahren berechnet, das auf den in Abschn. 2.2 beschriebenen Algorithmen basiert.

Zuletzt ist ein Kommentar zu einem alternativen Ansatz im Rahmen der VST angebracht. Die Äquivalenz von LB-Theorie und Linearer–Antwort-Theorie wurde von Mavropoulos und Mitarbeitern gezeigt [132] (siehe auch [133, 134]). Ausgehend von der Kubo–Greenwood-Formel für den symmetrischen Anteil des Leitfähigkeitstensors $\sigma$,

$$\sigma_{\mu\nu} = \frac{\pi}{N\Omega} \sum_{mn} J^{\mu}_{mn} J^{\nu}_{nm} \delta(E_{\mathrm{F}} - E_m) \, \delta(E_{\mathrm{F}} - E_n), \quad \mu, \nu = x, y, z, \tag{5.12}$$

($N$ und $\Omega$ bezeichnen die Anzahl der Atome bzw. deren Volumen), die die Matrixelemente $J^{\mu}_{mn}$ des Stromdichteoperators der Eigenzustände des Systems enthält ($H|m\rangle = E_m|m\rangle$), lässt sich der Leitwert des Tunnelkontakts als $G = \int_{\partial_{\mathcal{L}}} \int_{\partial_{\mathcal{R}}} \sigma_{zz}(\boldsymbol{r}, \boldsymbol{r}') \mathrm{d}r^2 \mathrm{d}r'^2$ schreiben. Die Flächenintegrale sind innerhalb der Elektroden auszuwerten, wobei zu beachten ist, dass $\partial_{\mathcal{L}}$ und $\partial_{\mathcal{R}}$ die idealen Elektroden von der Wechselwirkungszone, also von der Tunnelbarriere, trennen. Die Elemente

$$\sigma_{\mu\nu}(\boldsymbol{r}, \boldsymbol{r}') = \frac{1}{\pi N\Omega} \mathrm{tr} \left[ j_{\mu} \mathrm{Im} G^{+}(E_{\mathrm{F}}; \boldsymbol{r}, \boldsymbol{r}') j_{\nu} \mathrm{Im} G^{+}(E_{\mathrm{F}}; \boldsymbol{r}', \boldsymbol{r}) \right] \tag{5.13}$$

des Leitfähigkeitstensors werden schließlich durch die Green-Funktion ausgedrückt, wobei die Spur über die internen Freiheitsgrade zu nehmen ist.

Die Implementierung dieses Verfahrens ist nicht ohne Probleme. So erfordert, um nur ein Beispiel zu geben, die Berechnung der Matrixelemente des Stromdichteoperators $\boldsymbol{j}$ eine größere Anzahl von Drehimpulsen als für die korrekte Beschreibung der elektronischen Struktur notwendig ist. Ferner ist die Berechnung der Flächenintegrale nicht leicht zu implementieren. Deren Umwandlung in Volumenintegrale über MT-Kugeln ist jedenfalls nur approximativ. Da die Bloch-Zustände nicht explizit berechnet werden, muss die Integration in Bereichen des Konfigurationsraums erfolgen, in denen keine Modifikation der elektronischen Volumenstruktur durch Grenzflächenzustände oder -resonanzen vorliegt, d. h. weit im Inneren der Elektroden. Ein Vorteil des Mavropoulos-Verfahrens im Vergleich zum MacLaren-Verfahren [131] kann darin gesehen werden, dass nur in der Drehimpulsentwicklung gearbeitet werden darf, was durch die Verwendung relativ kleiner Matrizen numerisch effizient ist.

## 5.2. *Hot spots* und Integration mittels adaptiver Netze

Elektronische Zustände, die an den Grenzflächen eines Tunnelkontakts lokalisiert sind, tragen nicht zur Transmission $T(E_{\mathrm{t}}, \boldsymbol{k}_{\parallel})$ bei, da sie energetisch in Bandlücken der Elektrodenbandstruktur liegen und orthogonal zu den Bloch-Zuständen sind. Grenzflächenresonanzen hingegen koppeln an die Bloch-Zustände und zeigen eine signifikante Erhöhung der schichtaufgelösten spektralen Dichte nahe der Grenzfläche. Sie können somit die Tunnelwahrscheinlichkeit stark erhöhen: in der Transmission treten extrem scharfe Maxima auf, sogenannte *Hot spots* (Abb. 5.6). Für resonantes Tunneln ist ein Zustand ausreichend, der an einer der Grenzflächen des Tunnelkontakts lokalisiert ist; ein Paar von Resonanzen, jeweils an beiden Grenzflächen präsent, würde die Tunnelwahrscheinlichkeit zusätzlich erhöhen. Der letzte Fall sollte für reale Tunnelkontakte, die verschiedene Elektrodenmaterialien verwenden, untypisch sein, da die Resonanzen in verschiedenen Punkten der 2BZ auftreten. Ferner zerstört strukturelle Unordnung an den Grenzflächen die *Hot spots*, da in diesem Fall $\boldsymbol{k}_{\parallel}$ keine „gute Quantenzahl“ ist [135, 136].

Wie in Abbildung 5.6 für Vakuumtunneln mit Ni(001)-Elektroden deutlich wird, zeigt die Transmission eine ausgeprägte Struktur mit scharfen Maxima. Letztere tragen signifikant zum Leitwert bei, obwohl sie in nur kleinen Bereichen der 2BZ auftreten. Um diese Beiträge in der Integration über die 2BZ erfassen zu können [Gl. (5.8)], ist einerseits ein sehr dichtes Stützstellennetz erforderlich. Andererseits ändert sich die Transmission in großen Bereichen der 2BZ nur gering, sodass dort eine grobes Netz ausreichen würde. Offensichtlich sind Integrationsmethoden, die ein festes, äquidistantes Stützstellennetz verwenden (z. B. sogenannte *Special points* [50]), dem Problem nicht angemessen. Einen Ausweg bieten adaptive Netze, die die Stützstellendichte genau

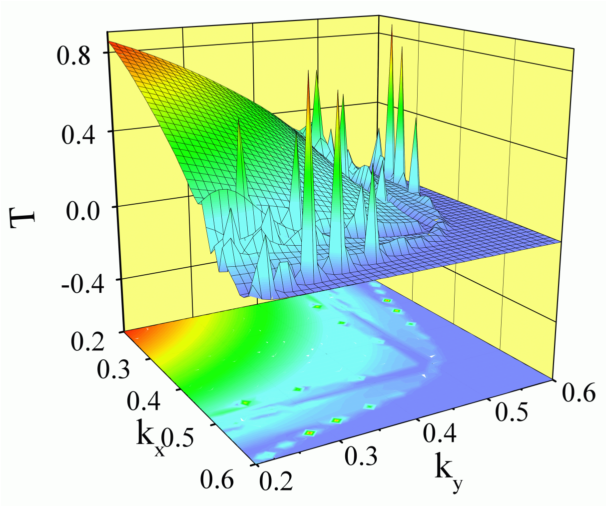

**Abbildung 5.6.** Transmission $T(E_{\mathrm{F}}, \boldsymbol{k}_{\parallel})$ [Gl. (5.7)] eines Ni(001)/Vakuum/Ni(001)-Tunnelkontakts in AP-Konfiguration. *Hot spots* sind als scharfe Maxima zu erkennen. Die Wellenvektoren $\boldsymbol{k}_{\parallel} = (k_x, k_y)$ sind in Einheiten von 1/Bohr angegeben. Es ist nur einen Bruchteil der 2BZ dargestellt.

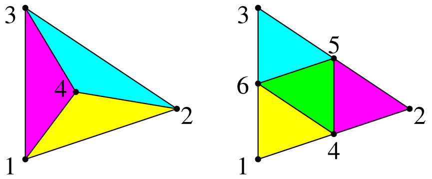

**Abbildung 5.7.** Adaptive Netze für die Integration über die 2BZ. Ausgehend vom Dreieck <123> wird entweder ein neuer Punkt im Inneren des Simplex (4; links) oder es werden neue Punkte auf den Kanten (4, 5, 6; rechts) plaziert.

dort erhöhen, wo es aufgrund des Integranden notwendig ist. Ein zugrundeliegender Algorithmus müsste Bereiche mit starken Änderungen des Integranden detektieren und dort neue Stützstellen setzen. Ist die Änderung der zu integrierenden Funktion hingegen gering, so bliebe das Netz grobmaschig. Die Effizienz eines solchen Ansatzes in Bezug auf spinabhängiges Tunneln wurde in der Publikation 11 (S. P112ff) untersucht und wird hier skizziert.

Dem rekursiven Algorithmus der adaptiven Verfeinerung von Netzen (*Adaptive mesh refinement*) liegt der Vergleich eines Integrals, das für eine Masche eines groben Netzes berechnet wurde, mit einem auf einem verfeinerten Netz berechneten, zugrunde. In zwei Dimensionen liegen die Netzpunkte auf den Ecken eines Dreiecks (Simplex). In Abbildung 5.7 bilden die Punkte 1, 2 und 3 das Dreieck <123>, die Integration darüber liefert das Integral $I_{<123>}$. Verfeinerte Netze ergeben sich, in dem man entweder einen neuen Punkt ins Innere des Simplex' legt (Punkt $4$ in Abb. 5.7, links) oder neue Punkte auf den Simplexkanten plaziert (Punkte $4$, $5$ und $6$ in Abb. 5.7, rechts). Damit ergeben sich im ersten Fall auf dem verfeinerten Netz drei Integale ($I_{<124>}$, $I_{<234>}$ und $I_{<314>}$), im zweiten vier Integrale ($I_{<146>}$, $I_{<425>}$, $I_{<365>}$ und $I_{<456>}$). Deren Summe liefert eine verbesserte Approximation des wahren Integrals als $I_{<123>}$. Ist nun die Differenz zwischen der groben und der feinen Approximationen kleiner als eine vorgegebene Schranke $\epsilon$, so wird die genauere Approximation ($I_{<124>} + I_{<234>} + I_{<314>}$ bzw. $I_{<146>} + I_{<425>} + I_{<365>} + I_{<456>}$) akzeptiert. Anderenfalls wird eine erneute Verfeinerung auf den Teildreiecken von <123> vorgenommen. Insgesamt wird dergestalt eine lokale Verfeinerung des Stützstellennetzes realisiert.

Wie dieser Algorithmus zu einer lokalen Verfeinerung des Stützstellennetzes in Abhängigkeit der Fehlerschranke $\epsilon$ führt, ist in Abb. 5.8 für die Transmission im Falle des Vakuumtunnels zwischen Ni(001)-Elektroden gezeigt (vgl. Abb. 5.6). Im Falle einer großen Schranke wird das ursprünglich ausgelegte Netz nicht verfeinert (Abb. 5.8; oben). Die Verringerung von $\epsilon$ (von oben nach unten in Abb. 5.8) führt zum Hinzufügen neuer Stützstellen, jedoch nur dort, wo sich der Integrand stark verändert (große Krümmung). Anderenfalls bleibt das Netz grobmaschig. Die Vorteile der adaptiven Netzverfeinerung treten bei der Integration der Transmissionen planarer Tunnelkontakte deutlich zutage, da hier in vielen Fällen nur kleine Bereiche der Brillouin-Zone signifikant zum Leitwert beitragen [131].

## 5.3. *Zero bias anomaly*

Planare Tunnelkontakte mit oxidischen Tunnelbarrieren zeigen ein ausgeprägtes Maximum im TMR bei verschwindender Biasspannung, die sogenannte ZBA (ZBA) (Abb. 5.9). Für den Ursprung der ZBA werden verschiedene Gründe diskutiert. Durch die Variation der Biasspannung verschieben sich die spinaufgelösten Zustandsdichten der Elektroden gegeneinander, was im Jullière-Modell in einer energieabhängigen Variation des TMR vermöge der Spinpolarisationen resultiert. Dieser Zustandsdichteeffekt wäre damit unabhängig von der verwendeten Barriere, was allerdings experimentellen Befunden widerspricht. Andere Möglichkeiten zur Erklärung der ZBA bemühen die spinabhängige inelastische Streuung an Defekten, an Magnonen und an Phononen [137, 138].

Ein Hinweis auf eine alternative Ursache ergibt sich, wenn die ZBA mit der zeitlichen Entwicklung der Probenpräparation verfolgt wird. Genügten zunächst geringe Biasspannungen $E_{\mathrm{b}}$, um den TMR auf die Hälfte des Maximalwerts bei $E_{\mathrm{b}} = 0$ zu reduzieren, so mussten mit der Verbesse-

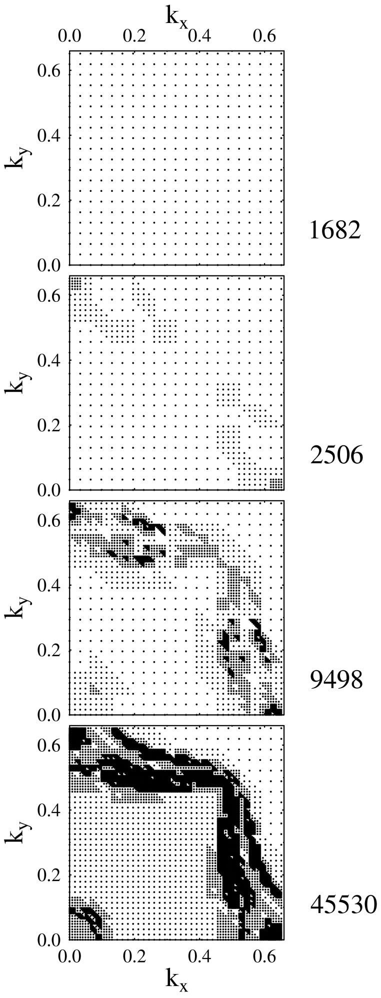

**Abbildung 5.8.** Adaptierte Netze für die Integration der Transmission über die 2BZ am Beispiel des Vakuumtunnels zwischen Ni(001)-Elektroden. Die Komponenten $k_x$ und $k_y$ des Wellenvektors sind in Einheiten von inversen Bohr-Radien angegeben. Die Zahlen rechts spezifizieren die Anzahl der Stützstellen (Punkte). Die vorgegebene Fehlertoleranz $\epsilon$ sinkt in den vier Beispielen von oben nach unten.

rung der Probenpräparation zunehmend höhere Biasspannungen an die Tunnelkontakte angelegt werden. Da die Qualität der Probenherstellung im wesentlichen die Grenzflächen zwischen den Elektroden und der Oxidbarriere betrifft, liegt es nahe, den Urspung der ZBA in Defekten in diesen Grenzflächen oder im Oxid selbst zu vermuten. Um diese Annahme zu untermauern, müsste an einer defektfreien Tunnelbarriere keine ZBA gemessen werden.

Realisiert wurde die Überprüfung der soeben beschriebenen Annahme mit Hilfe des spinauflösenden Rastertunnelmikroskops (RTM) [140]. Bei diesem Messaufbau wird die Oxidbarriere durch Vakuum ersetzt, ist also *per se* defektfrei, während die mit den Elektroden verbundenen Zustandsdichte- und Streueffekte präsent bleiben. Die Resultate von Ding und Mitarbeitern für

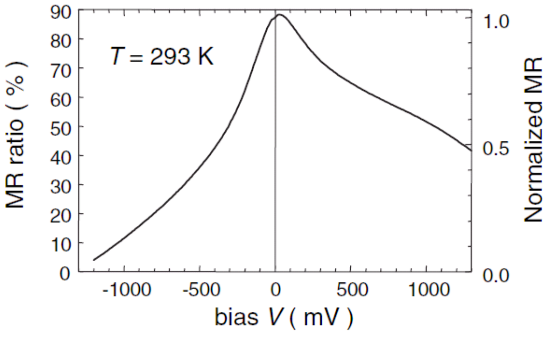

**Abbildung 5.9.** Experimenteller Tunnelmagnetwiderstand von Fe/MgO/Fe-Tunnelkontakten in Abhängigkeit der Biasspannung $V$ bei Raumtemperatur. Die Spannungen, bei denen der TMR die Hälfte des Maximums (bei $V = 0$) annimmt, betragen $-390\,\mathrm{mV}$ und $+1250\,\mathrm{mV}$. Entnommen Ref. [139].

**Abbildung 5.10.** Experimenteller Tunnelmagnetwiderstand des Vakuumtunnels von Co(0001). (a) Tunnelstrom *vs.* Biasspannung für 7 Å Abstand zwischen Probenoberfläche und Spitze des RTM. (b) Wie (a), jedoch für 5 Å Abstand. (c) und (d) Tunnelmagnetwiderstände *vs.* Biasspannung für die Proben-Spitzenabstände wie in (a) bzw. (b). Experiment: H.-F. Ding *et al.* [140].

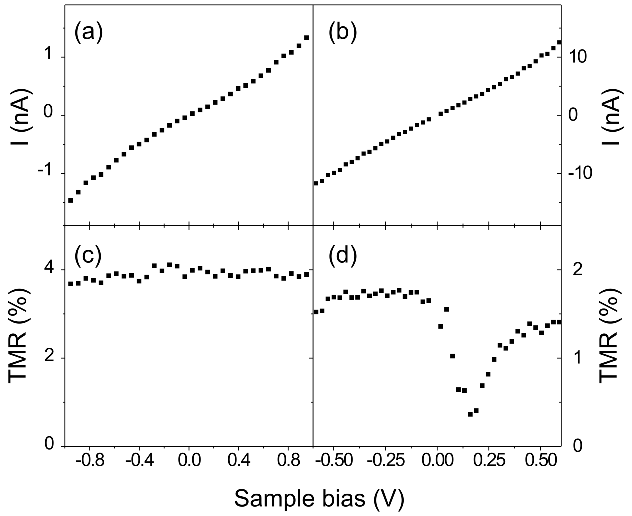

Co(0001)/Vakuum/Co(0001) zeigen in der Tat keine ZBA, sondern einen von der Biasspannung nahezu unabhängigen TMR (Abb. 5.10).

Um diese Ergebnisse mit Transportrechnungen unterstützen oder widerlegen zu können, wurde ein pragmatischer Ansatz gewählt. Durch die Biasspannung befindet sich der Tunnelkontakt im Nichtgleichgewicht und erfordert somit eine Beschreibung im Rahmen der Keldysh-Theorie. Diese mit DFT-Rechnungen zu verbinden, ist sehr aufwendig. Allerdings sollte sich das Potential durch die angelegte Spannung nur im Bereich der Barriere gegenüber dem Gleichgewichtsfall ($E_\mathrm{b} = 0$) ändern, da die Abschirmung in den Elektroden für ein konstantes externes Potential sorgt. Als Aufgabe bleibt daher die Bestimmung des elektrostatischen Potentials im Bereich der Vakuumbarriere, wie sie für ein Elektronengas als Elektrodenmaterial von Lang durchgeführt wurde [141]. Dessen Arbeit und die Erfahrungen mit Oberflächenbarrieren, die typisch in Rechnungen zu Elektronenspektroskopien verwendet werden (S. 8), führten zu einem heuristischen Potentialverlauf innerhalb der Vakuumbarriere. Dieser hat folgende Forderungen zu erfüllen. *(i)* Für unendlich weit voneinander entfernte Elektroden soll sich die Potentialbarriere der freistehenden Oberfläche mit ihrer Bildladungsasymptotik ergeben. *(ii)* Das elektrostatische Potential soll einen linearen Abfall bei nicht verschwindender Biasspannung zeigen, wie in der klassischen Elektrostatik und wie von Lang gefunden wurde. *(iii)* Die Parameter, die in die Beschreibung der elektrostatischen Barriere eingehen, sollen für den Gleichgewichtsfall aus Rechnungen erster Prinzipien bestimmt werden können. Hier bieten sich DFT-Rechnungen für das halbunendliche System (freistehende Oberfläche) an. Das Potential der Tunnelbarriere ist dann vollständig durch den Abstand der Elektroden voneinander und durch die Biasspannung bestimmt. Zusammenfassend kann man sagen, dass das Nichtgleichgewichtsproblem durch ein stationäres ersetzt wurde, wobei letzteres heuristisch gelöst wurde. Eine selbstkonsistente Lösung des stationären Problems im Rahmen der DFT ist möglich, wenn man annimmt, dass die Biasspannung ein konstantes externes Potential in den Elektroden erzeugt [142].

Im Folgenden werden Resultate für Co/Vakuum/Co-Tunnelkontakte mit fester Breite der Vakuumbarriere ($7.5\,\text{Å}$), jedoch variabler Biasspannung $E_\mathrm{b}$ präsentiert (Abb. 5.11; Publikation 12 auf S. P118ff; vgl. auch [130]). Die Leitwerte sind symmetrisch zu $E_\mathrm{b} = 0$, weil die linke mit der rechten Elektrode identisch ist. Im Experiment dagegen (Abb. 5.10) besteht die eine Elektrode aus der Co(0001)-Oberfläche, die andere aus der CoFeSiB-Spitze des RTM. Deswegen sind asymmetrische Strom–Spannungs-Kennlinien und TMR-Spektren möglich. Die Leitwerte für die beiden magnetischen Konfigurationen P und AP hängen nur gering von $E_\mathrm{b}$ ab. Dieses Verhalten lässt sich anhand der $\boldsymbol{k}_\parallel$-aufgelösten Transmissionen verstehen. Diese sind im Wesentlichen auf einem Ring in der 2BZ von Null verschieden, wobei der Ringdurchmesser von der Tunnelenergie abhängt. Der Leitwert für eine bestimmte Tunnelenergie $E_\mathrm{t}$ ist nun proportional zur Fläche des

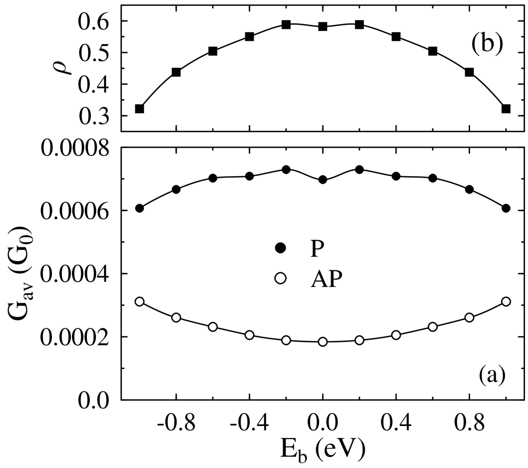

**Abbildung 5.11.** Theoretischer Tunnelmagnetwiderstand für einen planaren Co/Vakuum/Co-Tunnelkontakt in Abhängigkeit von der Biasspannung. Der Elektrodenabstand beträgt $7.5$ Å. (a) Gemittelte Leitwerte $G_{\rm av}$ für die P- und die AP-Konfiguration. $G_0$ bezeichnet das Quantum der Leitfähigkeit, $e^2/h$. (b) Tunnelmagnetwiderstände $\rho$, die aus den Leitwerten in (a) bestimmt wurden.

Rings. Die Variation des Ringdurchmessers und die Breite des Energiefensters, in dem Tunneln erlaubt ist [Gl. (5.10)], kompensieren einander und resultieren letztlich in dem gezeigten Verhalten der gemittelten Leitwerte $G_{\rm av}$. Der Tunnelmagnetwiderstand $\rho$ ist daher ebenfalls nahezu unabhängig von der Biasspannung, seine Variation ist klein im Vergleich mit der ZBA für Oxidbarrieren (Abb. 5.9). In diesen reduziert sich $\rho$ typischerweise um $80\%$ gegenüber dem Maximalwert für $E_{\rm b} = \pm 0.5$ eV.

Der experimentelle Tunnelmagnetwiderstand zeigt für kleine Elektrodenabstände ein signifikantes Minimum bei $E_{\rm b} = +0.2$ eV (Abb. 5.10, rechts), welches in der Theorie nicht beobachtet wird. Die Transmission im Co/Vakuum/Co-System findet vorwiegend mittels Minoritätszuständen statt, wie die spinaufgelöste Bandstruktur für $\boldsymbol{k}_{\|} = 0$ nahelegt. Eine Reduktion des TMR würde daher, gemäß des Jullière-Modells, einen Majoritätszustand erfordern. Dieser könnte durch den Oberflächenzustand bei $+0.2$ eV und $\boldsymbol{k}_{\|} = 0$ geliefert werden (Abb. 5.12c). An der Barriere lokalisierte Zustände tragen jedoch in der Landauer–Büttiker-Theorie nicht zur Transmission bei, da sie orthogonal zu den Eigenzuständen der Elektroden sind. Die Kopplung der Bloch-Zustände der Elektroden an den Oberflächenzustand erfordert daher Prozesse, die $\boldsymbol{k}_{\|}$ nicht erhalten. Letztere könnten durch die Spitze des RTM hervorgerufen werden, da diese die Translationsinvarianz parallel zur Probenoberfläche bricht, im Gegensatz zum planaren Tunnelkontakt.

## 5.4. Einfluss der Grenzflächengeometrie

Wie stark die geometrische Struktur der Grenzflächen zwischen Elektroden und Tunnelbarriere die Transporteigenschaften beeinflusst, lässt sich eindrucksvoll am Beispiel Fe(001)/MgO/Fe(001) studieren. Dieses System wurde ausgiebig theoretisch behandelt, meist jedoch in der idealen Geometrie [143]. Letztere ist dadurch gekennzeichnet, dass die MgO-Schichten an der Fe–MgO-Grenzfläche ihre Volumenstruktur beibehalten, eine Annahme, die durch die gute Gitteranpassung von Fe und MgO nahegelegt wird. Tatsächlich kann sich jedoch eine partiell besetzte FeO-Schicht ausbilden (Abb. 5.13), wie Meyerheim mittels Röntgendiffraktion gezeigt hat [144]. Desweiteren verstärkt sich die Lokalisierung der Zustände in der FeO-Schicht, was einerseits zu einer Änderung der magnetischen Struktur hinsichtlich der idealen Struktur führt, und daher die spinabhängige Streuung direkt betrifft, andererseits die Grenzen der Beschreibung des Systems im Rahmen der LSDA aufzeigt (S. 5). Beide Aspekte werden im Folgenden diskutiert.

Um den Einfluss der geometrischen Struktur zu untersuchen, werden drei Systeme miteinander verglichen: die ideale Struktur (links in Abb. 5.13), die FeO-Struktur (rechts) und die sog. FeE-Struktur. Letztere unterscheidet sich von der FeO-Struktur dadurch, dass die O-Atome in der FeO-Schicht durch leere MT-Kugeln (E) ersetzt wurden.

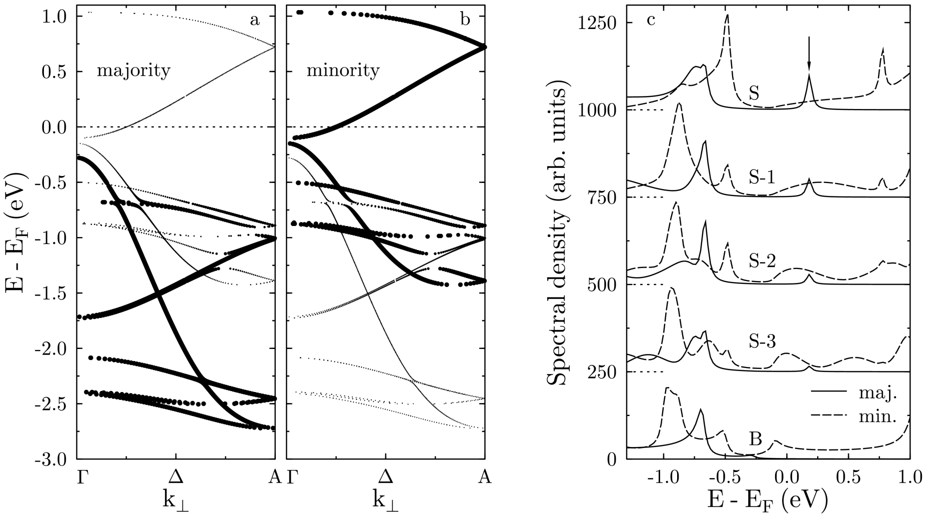

**Abbildung 5.12.** Elektronische Struktur von Co(0001). (a) und (b) Spinaufgelöste Bandstruktur für die Richtung Γ–Δ–A der Volumen-Brillouin-Zone (links: Majorität, rechts: Minorität). Die Größe der gefüllten Kreise ist proportional zur Spinpolarisation der zugehörigen elektronischen Zustände. (c) Spin- und lagenaufgelöste Spektraldichte der Co(0001)-Oberfläche (durchgezogen: Majorität; gestrichelt: Minorität). Die Oberflächenschichten sind mit S, S-1, S-2 und S-3 gekennzeichnet, beginnend mit der äußersten Lage. Eine Volumenschicht trägt die Bezeichnung B. Der Pfeil in der Schicht S deutet auf einen Majoritätsoberflächenzustand.

Die lagenaufgelösten magnetischen Momente (Magnetisierungsprofile) der idealen und der FeO-Struktur unterscheiden sich deutlich voneinander (Abb. 5.14). Im ersten Fall sind die Grenzflächenmomente, wie ebenfalls die an der reinen Fe-Oberfläche, gegenüber dem Volumenmoment von $2.26\ \mu_\mathrm{B}$ deutlich erhöht und streben monoton gegen den Volumenwert. Die FeO-Geometrie resultiert ebenfalls in einer Erhöhung, insbesondere an der FeO-Schicht selbst aufgrund der Lokalisierung elektronischer Zustände, jedoch weist das magnetische Profil Oszillationen auf. So ist das Moment der angrenzenden Fe-Schicht gegenüber dem Volumenwert reduziert. Die FeE-Profil ist dem der FeO-Struktur sehr ähnlich. In allen drei Strukturen sind die im MgO induzierten Momente klein.

Die magnetischen Profilen lassen vermuten, dass die Transporteigenschaften ebenfalls stark differieren. Zur Überprüfung werden die Transmissionen $T(E_\mathrm{F}, \boldsymbol{k}_\parallel)$ für Tunnelkontakte mit 6 MgO-Schichten herangezogen (Abb. 5.15). In P-Konfiguration zeigen die Transmission der idealen und der FeE-Struktur ein breites Maximum im Zentrum der 2BZ. Dieses ist in der FeO-Struktur voll-

**Abbildung 5.13.** Geometrische Struktur von Fe–MgO-Grenzflächen. In der idealen Struktur (links) sitzen O-Atome (blaue Kugeln) der ersten MgO-Schicht direkt oberhalb der Fe-Atome (rot) der letzten Fe-Schicht, während Mg-Atome (grün) oberhalb der Fe-Atome der zweitletzten Schicht liegen. Die Struktur der Grenzfläche mit FeO-Schicht (rechts) ist ähnlich der idealen, jedoch sind O-Atome innerhalb der letzten Fe-Schicht plaziert. Zur Verdeutlichung der bcc-Struktur des Eisens sind einige Gitterplätze miteinander verbunden. (grau).

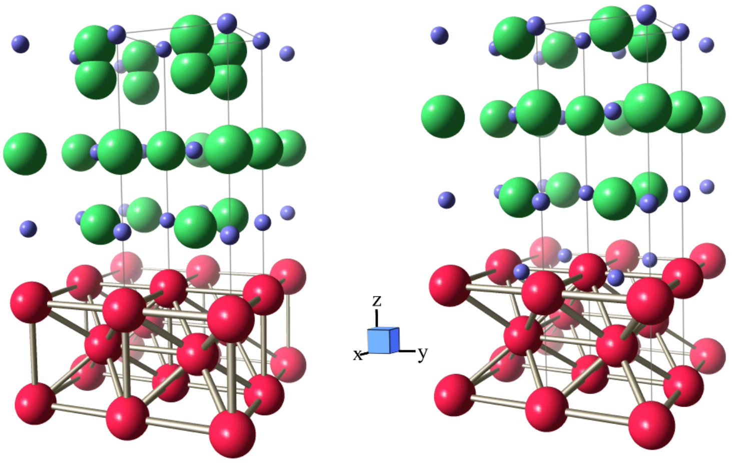

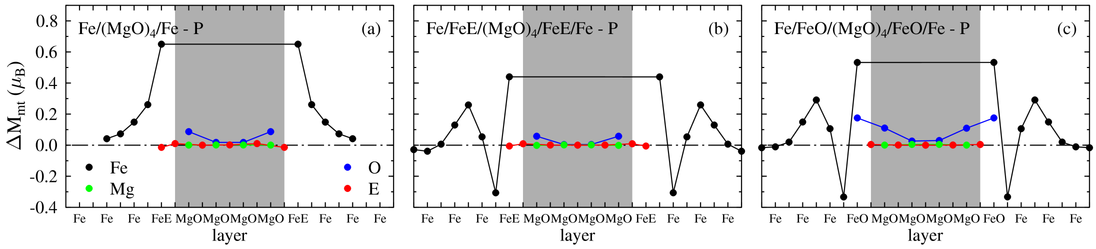

**Abbildung 5.14.** Magnetisierungsprofile von Fe/MgO/Fe-Tunnelkontakten mit 4 MgO-Schichten als Barriere in P-Konfiguration: für die ideale Struktur (a), die FeE-Struktur (b) und die FeO-Struktur (c). Die lagen- und atomaufgelösten magnetischen Momente $\Delta M_{\mathrm{mt}}$ sind als Abweichungen vom jeweiligen Volumenwert dargestellt. Anstelle des Schichtindex ist die atomare Konstitution der Lagen angegeben („Fe“, „FeE“, etc.).

ständig unterdrückt; stattdessen tritt ein Ring scharfer Maxima auf. Letzterer lässt den Schluss zu, dass die Streuung an den Grenzflächen in der FeO-Struktur wesentlich stärker als in den erstgenannten Geometrien ist. Der Einfluss der Magnetisierungsprofile auf die Transmission erscheint demnach von geringer Bedeutung zu sein, denn die FeE- und FeO-Profile sind ähnlich, ihre Transmissionen hingegen nicht. Die Transmissionen in der AP-Konfiguration unterstützen die für die P-Konfiguration gewonnenen Resultate (rechte Spalte in Abb. 5.15).

Die in den Transmissionen gefundenen Merkmale äußern sich in den Leitwerten $G(E_{\mathrm{F}})$, deren Abhängigkeit von der Anzahl der MgO-Schichten in Abb. 5.16 gezeigt ist. Zunächst nehmen alle Leitwerte mit wachsender MgO-Dicke exponentiell ab (Abb. 5.16 unten), was durch die fundamentale Bandlücke von MgO erklärt wird [135, 145]: die Streukanäle koppeln an die exponentiell abklingenden Zustände in der komplexen MgO-Bandstruktur, in Analogie zum Slonczewski-Modell (S. 49). Zwischen den Leitwerten der verschiedenen Grenzflächengeometrien bestehen allerdings deutliche Unterschiede. So sind diejenigen der FeO-Struktur beträchtlich geringer als die der anderen Geometrien, was auf die stärkere Streuung an der FeO-Schicht zurückgeführt

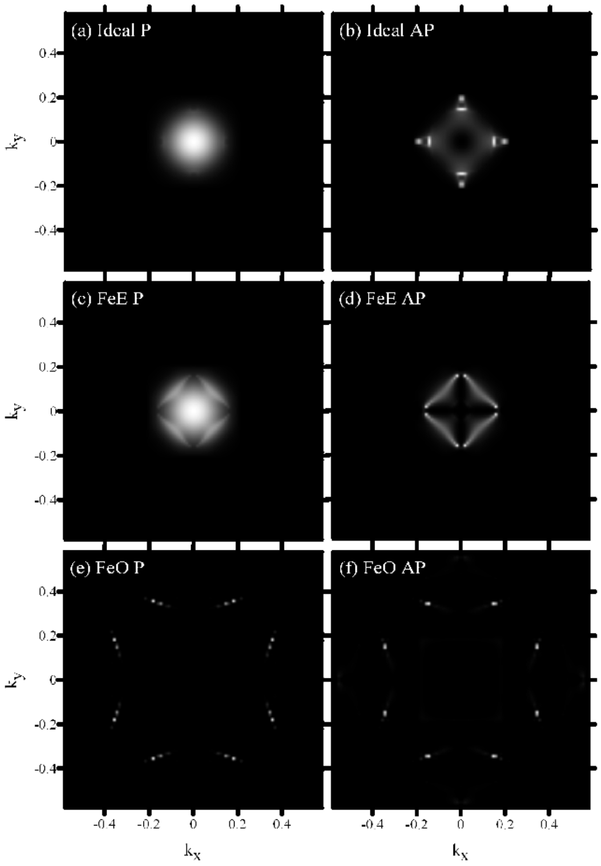

**Abbildung 5.15.** Transmission $T(E_{\mathrm{F}}, \boldsymbol{k}_{\|})$ von Fe/MgO/Fe-Tunnelkontakten mit 6 MgO-Schichten in P- (linke Spalte) und AP-Konfiguration (rechte Spalte). Gezeigt ist $T(E_{\mathrm{F}}, \boldsymbol{k}_{\|})$ in der 2BZ für die ideale Struktur (obere Reihe, „Ideal“), die FeE-Struktur (Mitte, „FeE“) und die FeO-Struktur (unten, „FeO“). Die Graustufenskala ist nicht einheitlich, sodass Absolutwerte nicht miteinander verglichen werden können (schwarz geringe, weiß hohe Transmission; $k_x$ und $k_y$ in 1/Bohr).

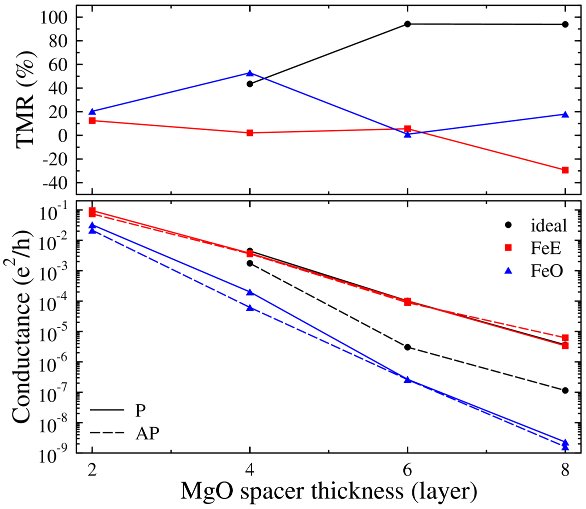

**Abbildung 5.16.** Leitwerte (unten) und TMR (oben) von Fe/MgO/Fe-Tunnelkontakten *vs.* Anzahl von MgO-Schichten für die ideale (schwarze Kreise), die FeE- (rote Quadrate) und die FeO-Geometrie (blaue Dreiecke). Die Leitwerte sind für die P- (durchgezogen) und die AP-Konfiguration (gestrichelt) gezeigt. Es wurden 40 000 $\boldsymbol{k}_{\parallel}$-Punkte in der 2BZ-Integration verwendet.

werden kann (vgl. die Ringstruktur der Transmissionen in Abb. 5.15e und f). Auch dass $G(\mathrm{P})$ der idealen und der FeE-Geometrie einen fast identischen Verlauf zeigen, folgt aus den Transmissionen (Abb. 5.15a und c).

Typisch für die ideale Geometrie ist, dass der TMR mit zunehmender MgO-Dicke ansteigt (Abb. 5.16 oben; [131]). Im Gegensatz zum monotonen Verhalten ist der TMR der FeE-Struktur deutlich geringer und nahezu konstant, während derjenige der FeO-Geometrie beträchtliche Oszillationen und sogar einen Vorzeichenwechsel zeigt [146].

Zusammenfassend lässt sich feststellen, dass die Grenzflächeneigenschaften den spinabhängigen ballistischen Transport in Tunnelkontakten erheblich beinflussen können. Diese Beobachtung wird durch Experimente an Fe/MgO/Fe-Tunnelkontakten, die arm an Störstellen an den Grenzflächen sind, unterstützt [139].

Die bisher vorgestellten Resultate wurden im Rahmen der LSDA gewonnen. Die Formierung einer Oxidschicht an der Fe/MgO-Grenzfläche legt nahe, dass Elektronen in der FeO-Schicht lokalisiert werden. Deren Beschreibung mittels LSDA erscheint daher fragwürdig, wie *Ab–initio*-Rechnungen für Oxide (z. B. NiO, MgO, ZnO) schließen lassen. Es ist somit wünschenswert, über die LSDA hinauszugehen. Hier bietet sich, neben der $GW$-Näherung, die SIC an, die im Folgenden kurz dargestellt wird.

Die *Self-interaction correction* (SIC) ist eine Korrektur, die ein wesentliches Defizit der LDA beheben soll. Dieses wirkt sich insbesondere bei lokalisierten Zuständen aus, weniger bei räumlich ausgedehnten Bloch-Zuständen. Für die wahre Grundzustandsdichte $n(\boldsymbol{r})$ heben sich das Austausch-Korrelationsfunktional $E_{\mathrm{xc}}$ und die Elektron–Elektron-Wechselwirkung $U$ auf, $0 = U[n] + E_{\mathrm{xc}}[m]$. Für das im Rahmen der LDA genäherte Austausch-Korrelationspotential und dessen Grundzustandsdichte gilt diese Aufhebung nicht mehr: die LSDA enthält die Wechselwirkung des Elektrons mit sich selbst. Ein Zustand $\alpha$ besitzt daher die Selbstwechselwirkung $\delta_{\alpha} = U[n_{\alpha}] + E_{\mathrm{xc}}^{\mathrm{LSDA}}[m_{\alpha}]$. Das SIC-Funktional $E^{\mathrm{SIC}} = T[m] + U[n_{\alpha}] + V_{\mathrm{ext}}[n] + E_{\mathrm{xc}}^{\mathrm{LSDA}}[m] - \sum_{\alpha} \delta_{\alpha}$ entspricht dem LSDA-Funktional, von dem die Selbstwechselwirkungen $\delta_{\alpha}$ subtrahiert wurden. Dieses führt zum zustandsabhängigen Potential

$$V_{\alpha}^{\mathrm{SIC}}(\boldsymbol{r}) = -2 \int \frac{n_{\alpha}(\boldsymbol{r}')}{|\boldsymbol{r} - \boldsymbol{r}'|} \mathrm{d}r'^{3} - V_{\mathrm{xc}}^{\mathrm{LSDA}}(m_{\alpha}(\boldsymbol{r})). \tag{5.14}$$

Für delokalisierte Zustände verschwindet dieses Potential und man erhält das LSDA-Resultat. Lokalisierte Zustände hingegen werden noch stärker lokalisiert. Die Zustandsabhängigkeit des Potentials lässt einem die Freiheit, die SIC nur für bestimmte Zustände zu berücksichtigen. Dem Gedanken der DFT folgend, wird die Gesamtenergie durch die Grundzustandskonfiguration, d. i. die Auswahl an Zuständen $\alpha$, auf die die SIC angewendet wird, minimiert.

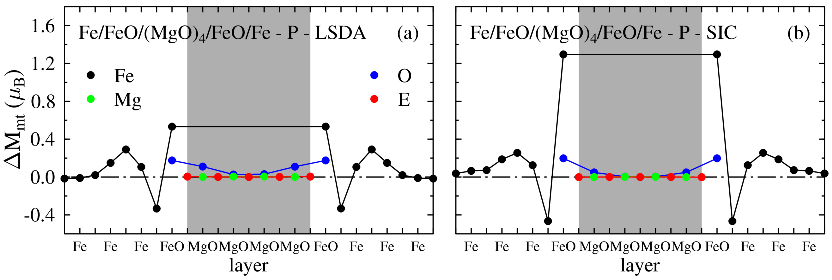

**Abbildung 5.17.** Magnetisierungsprofile von Fe/MgO/Fe-Tunnelkontakten mit FeO-Grenzschichten und 4 MgO-Schichten in P-Konfiguration: (a) für die LSDA, (b) für die SIC. Analog zu Abb. 5.14.

Um den Einfluss der SIC zu demonstrieren, sind in Abb. 5.17 die Magnetisierungsprofile von Tunnelkontakten mit FeO-Schicht verglichen, die im Rahmen der LSDA und der SIC berechnet wurden. Während die magnetischen Momente an den O-, Mg- und E-Gitterplätzen kaum von der verwendeten Näherung abhängen, sind die Fe-Momente der SIC im Vergleich zum LSDA-Fall in der FeO-Schicht drastisch erhöht. Betrachtet man die zunehmende Lokalisierung der Fe-$d$-Zustände als Übergang vom Festkörper (magnetisches Moment $2.26\,\mu_{\mathrm{Bohr}}$) zum Atom ($4\,\mu_{\mathrm{Bohr}}$), so wird das SIC-Resultat plausibel.

## 5.5. *Spin motion*

Werden spinpolarisierte Elektronen durch eine ferromagnetische Schicht $\mathcal{F}$ transmittiert, so zeigt die transmittierte Spinpolarisation $\boldsymbol{P}^{\mathrm{tr}}$ *Spin motion*, wenn die Spinpolarisation $\boldsymbol{P}^{\mathrm{in}}$ der einfallenden Elektronen schräg zur Magnetisierung $\boldsymbol{M}$ des Ferromagneten liegt. Unter *Spin motion* versteht man dabei die Präzession von $\boldsymbol{P}^{\mathrm{tr}}$ um $\boldsymbol{M}$ und deren Relaxation gegen $\boldsymbol{M}$ (Abb. 5.18).

Die Präzession entsteht durch elastische Prozesse innerhalb der magnetischen Schicht $\mathcal{F}$. Für freie Elektronen ist in $\mathcal{F}$ die Wellenzahl $k_{\perp}$ durch die Austauschaufspaltung spinabhängig, sodass sich für die Wellenfunktion der Ansatz

$$\Psi \propto \exp(\mathrm{i}\boldsymbol{k}_{\|}\cdot\boldsymbol{\rho})\left[\alpha^{\uparrow}\exp(\mathrm{i}k_{\perp}^{\uparrow}z)\chi^{\uparrow}+\alpha^{\downarrow}\exp(\mathrm{i}k_{\perp}^{\downarrow}z)\chi^{\downarrow}\right],\qquad \boldsymbol{\rho}=(x,y), \tag{5.15}$$

ergibt (mit Pauli-Spinoren $\chi^{\uparrow}$ und $\chi^{\downarrow}$). Die Spinquantisierungsachse fällt mit der Magnetisierungsrichtung zusammen. Die Präzession von $\boldsymbol{P}^{\mathrm{tr}}$ entsteht durch die Phasendifferenz der Partialwellen der Majoritäts- und Minoritätselektronen am Ort $(\boldsymbol{\rho}, z)$. Die Wellenlänge der Präzession ist $2\pi/(k_{\perp}^{\uparrow} - k_{\perp}^{\downarrow})$ und beträgt in Fe für typische VLEED-Energien ca. 200 ML. Durch die Reflexion der Partialwellen an den beiden Grenzflächen von $\mathcal{F}$ wird die Präzession moduliert, wobei die Wellenlänge $2\pi/(k_{\perp}^{\uparrow} + k_{\perp}^{\downarrow})$ dieses Quantisierungseffekts im Bereich weniger ML liegt.

Die Relaxation entsteht durch spinabhängige inelastische Prozesse, die sich in der unterschiedlichen mittleren freien Weglänge ($\lambda^{\uparrow}$ und $\lambda^{\downarrow}$) für Majoritäts- und Minoritätselektronen äußert. Da $\lambda^{\uparrow}$ größer als $\lambda^{\downarrow}$ ist, steigt der relative Anteil der Majoritätselektronen mit wachsendem $z$, und $\boldsymbol{P}^{\mathrm{tr}}$ wird entlang der Magnetisierung $\boldsymbol{M}$ ausgerichtet. Für VLEED-Energien liegen die mittleren freien Weglängen in der Größenordnung weniger Atomlagen [123].

Zur Erklärung der *Spin motion* ist zu bemerken, dass die Spinpolarisation $\boldsymbol{P}$ immer durch Pauli-Spinoren beschrieben werden kann, die für die Magnetisierungsrichtung quantisiert sind [103]. Liegt $\boldsymbol{P}$ schräg zur Quantisierungsachse, erzeugt die Hemmung eines Spinkanals eine Rotation von $\boldsymbol{P}$, während im Falle einer entlang $\boldsymbol{M}$ ausgerichteten Spinpolarisation Relaxation auftritt (Spinfilter).

Experimente zur *Spin motion* messen die Spinpolarisation $\boldsymbol{P}^{\mathrm{tr}}$ der durch $\mathcal{F}$ transmittierten Elektronen in Abhängigkeit der Dicke der ferromagnetischen Schicht. Eine Standardmethode verwendet freitragende dünne Filme, die typischer Weise mit Gold bedeckt sind [147, 148]. Als Quelle

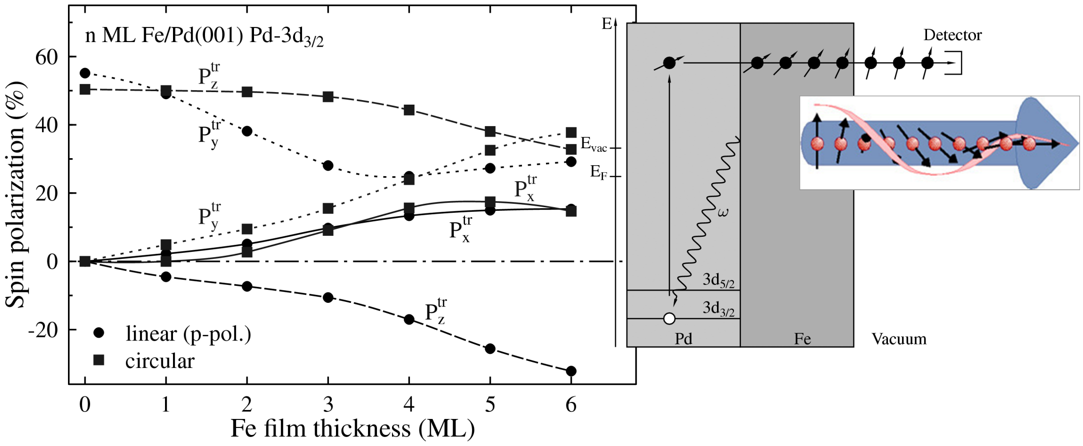

**Abbildung 5.18.** *Spin motion* von Photoelektronen des Systems Fe/Pd(001). Links: Spinpolarisation der Photoelektronen bei Anregung mit zirkular polarisertem (Quadrate) und p-polarisiertem (Dreiecke) Licht in Abhängigkeit von der Fe-Filmdicke (0 bis 6 ML). Die kinetische Energie der Photoelektronen beträgt 17.5 eV. Mitte: schematische Darstellung des Messaufbaus. Rechts: Präzession und Relaxation. Die Spinpolarisation der Elektronen (schwarze Pfeile) präzessiert um und relaxiert gegen die Magnetisierungsrichtung des Ferromagneten (blauer Pfeil in Bewegungsrichtung der Elektronen).

für die spinpolariserten Elektronen dient dabei GaAs, das mit zirkular polarisiertem Licht beleuchtet wird („optische Orientierung“ in der Photoemission). Für gedehntes GaAs ergeben sich Polarisationsgrade für $\boldsymbol{P}_{\text{in}}$ von ca. 70%. Die transmittierte Spinpolarisation kann mittels eines Mott- oder eines SPLEED-Detektors bestimmt werden. Der Vorteil dieses Verfahrens liegt darin, dass die *Spin motion* für Energien nahe des Fermi-Niveaus untersucht werden kann, also gerade für Magnetoelektronik-Anwendungen relevante Energien. Aufgrund der großen mittleren freien Weglängen lassen sich auch dicke Filme untersuchen. Von Nachteil könnte die relativ schwierige Präparation der Proben sein, die Streuung an den Deckschichten sollte hingegen von geringer Bedeutung sein. Der Nachteil freitragender Schichten ließe sich durch Integration der Elektronenquelle in die Probe wett machen. Diese Idee wurde schon von Berger aufgenommen [149], der für planare Tunnelkontakte ferromagnetische Schichten zur Erzeugung und zur Detektion der spinpolarisierten Elektronen vorschlug [150, 151].

Ein neuer Ansatz verlegt die Quelle der spinpolarisierten Elektronen ebenfalls in die Probe, die nun aus einem dünnen magnetischen Film auf einem Substrat besteht. Als Quelle dient hierbei die Anregung mittel Photoemission aus Rumpfniveaus des Substrats, wodurch nebenbei sichergestellt wird, dass die einfallenden Elektronen nicht aus dem Film selbst stammen. Die einfallende Spinpolarisation $\boldsymbol{P}^{\text{in}}$ entsteht durch die Spin–Bahn-Kopplung in den Rumpfniveaus (Abschn. 4.3). Durch weiche Röntgenstrahlung lassen sich die probeninternen Photoelektronen auf Energien oberhalb des Vakuumniveaus anregen und nach der Transmission durch den magnetischen Film spinaufgelöst detektieren. Die *Spin motion* wird, wie gewöhnlich, als Dickenabhängigkeit von $\boldsymbol{P}^{\text{tr}}$ analysiert. Vorteile dieses Verfahrens liegen darin, dass die Präparation freitragender Filme unnötig wird und dass die einfallende Spinpolarisation leicht durch Veränderung von Einfallsrichtung und Polarisation der Röntgenstrahlung eingestellt werden kann. Durch geeignete Wahl der Rumpfniveaus lassen sich Polarisationsgrade erhalten, die vergleichbar mit denen von GaAs-Quellen sind. Die geringen freien Weglängen implizieren, dass nur Proben untersucht werden können, die wenige Atomlagen dick sind. Ferner ist die Mindestenergie der Transmission durch das Vakuumniveau bestimmt.

Zur Demonstration dieses Ansatzes, der der experimentellen Bestätigung harrt, wurde das System Fe/Pd(001) ausgewählt, weil aufgrund der starken Spin–Bahn-Kopplung im Pd-Substrat und der großen Austauschaufspaltung im Fe-Film eine beträchtliche *Spin motion* erwartet werden darf (Abb. 5.18). Als Anfangszustand dienen die Pd-$3d_{3/2}$-Rumpfniveaus, deren Photoemission gut im Einteilchenbild beschrieben werden kann. Im Folgenden bezeichnen die $z$-Achse die Oberflächennormale und die $x$-Achse die Richtung der Magnetisierung. Für zirkular polarisiertes Licht, welches normal auf die Probe einfällt, erzeugt „optische Orientierung“ Elektronen im Pd-Substrat,

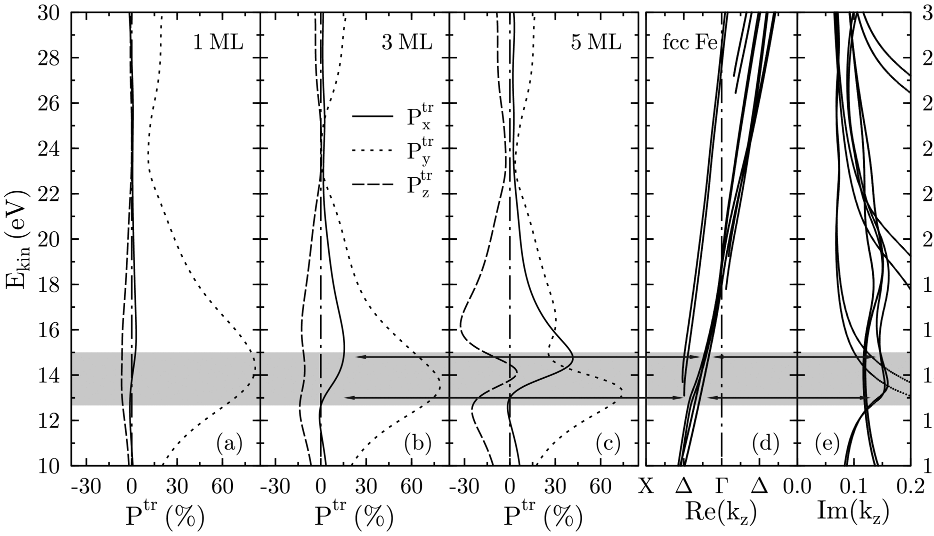

**Abbildung 5.19.** *Spin motion* von Photoelektronen des Systems Fe/Pd(001) für Anregung mit p-polarisiertem Licht in Abhängigkeit von der kinetischen Energie der Photoelektronen. (a)–(c) Spinpolarisation für Fe-Filmdicken von 1, 3 und 5 ML. (d) Unbesetzte komplexe Bandstruktur von fcc-Fe. Die im Text diskutierte Bandlücke ist grau unterlegt, Pfeile weisen auf markante Extrema in der Spinpolarisation hin.

deren Spinpolarisation entlang der Oberflächennormale ausgerichtet ist. Für schräg auf die Probe einfallendes p-polarisertes Licht erhält man ähnlich große Effekte (Abb. 5.18, links), jedoch ist die Spinpolarisation im Substrat entlang der $y$-Achse ausgerichtet.

Analytische Rechnungen für fast freie Elektronen in einem magnetischen Quantentrog, in die die Parameter für die Pd- und die Fe-Bandstruktur eingehen, geben eine Wellenlänge für die Präzession von ca. 200 ML. Somit ist eine volle Rotation um die Magnetisierung mit diesem Photoemissionsansatz nicht zugänglich, da die mittlere freie Weglänge der Photoelektronen nur wenige Monolagen beträgt. Die Wellenlänge der Modulation aufgrund der Grenzflächenreflexionen beträgt 4 bis 5 ML, die deshalb in der *Spin motion* deutlich zu beobachten ist (Abb. 5.18 links).

Signifikante Effekte in der *Spin motion* sollten sich für Bandlücken in der Fe-Bandstruktur manifestieren. Variiert man die Photonenenergie bei festgehaltener Anfangsenergie (CIS-Modus), so durchfährt die kinetische Energie der Photoelektronen eine spinaufgespaltene Bandlücke und somit energetische Bereiche, in denen die Transmission einer Spinorientierung gegenüber der anderen bevorzugt ist. Dieser Effekt ist in Abb. 5.19 demonstriert: mit wachsender Dicke des Fe-Films zeigt $\boldsymbol{P}^{\mathrm{tr}}$ zunehmende Variation im grau unterlegten Energiebereich. Gerade dort weist die unbesetzte Fe-Bandstruktur eine Bandlücke auf, die jedoch in der komplexen Bandstruktur für einen nicht verschwindenden Imaginärteil des optischen Potentials nur schwer auszumachen ist.

Modellrechnungen für fast freie Elektronen bestätigen die hier gezeigten *Ab–initio*-Photoemissionsresultate. Um die *Spin motion* klar hervorzuheben, wurde der Imaginärteil des optischen Potentials Null gesetzt. Die starke Variation von $\boldsymbol{P}^{\mathrm{tr}}$ entsteht durch die spinabhängige Transmission im Bereich der Bandlücke. Liegt die Energie, bei der die Photoelektronen durch den Fe-Film transmittiert werden, unterhalb der Bandlücke (Bereich I in Abb. 5.20), so werden beide Spinkanäle transmittiert. Im Bereich II werden ↑-Elektronen aufgrund des anwachsenden Imaginärteils des Wellenvektors im Film zunehmend geringer transmittiert [*Evanescent states*, $\mathrm{Im}(k_{\perp\uparrow}) \neq 0$], während die ↓-Elektronen weiterhin ungedämpft durch den Film propagieren [$\mathrm{Im}(k_{\perp\downarrow}) \neq 0$]. Im Bereich III werden dann auch diese Elektronen gedämpft. Für größere Energien kehrt sich diese spinabhängige Hemmung um: in Bereich IV dürfen die ↑-Elektronen wieder frei propagieren, in Bereich V dann beide Spinorientierungen.

Dieser auf der spin- und winkelaufgelösten Photoelektronenspektroskopie basierende Ansatz zur Untersuchung der *Spin motion* erlaubt es, die unbesetzte elektronische Struktur dünner magnetischer Filme im Detail zu untersuchen. Eventuell lassen sich sogar Aussagen über die magnetische

**Abbildung 5.20.** Einfluss von Bandlücken in der austausch-aufgespaltenen Bandstruktur auf die *Spin motion* von durch einen magnetischen Film transmittierten Elektronen. (a) Nach Komponenten aufgelöste Spinpolarisation $\boldsymbol{P}^{\mathrm{tr}}$ in Abhängigkeit von der kinetischen Energie $E_{\mathrm{kin}}$ der transmittierten Elektronen. (b), (c) Komplexe Bandstruktur $k_z(E_{\mathrm{kin}})$ des Films, aufgelöst nach Spinkomponenten entlang der Magnetisierung (*up*, *dn*; $\boldsymbol{M} \parallel \boldsymbol{x}$) und des Substrats (einfallend, *in*). Die auf den Film einfallenden und entlang $\boldsymbol{z}$ propagierenden Elektronen sind entlang $\boldsymbol{y}$ spinpolarisiert ($P_y^{\mathrm{in}} = 50\%$). Die rechts spezifizierten Energiebereiche I–V sind im Text diskutiert.

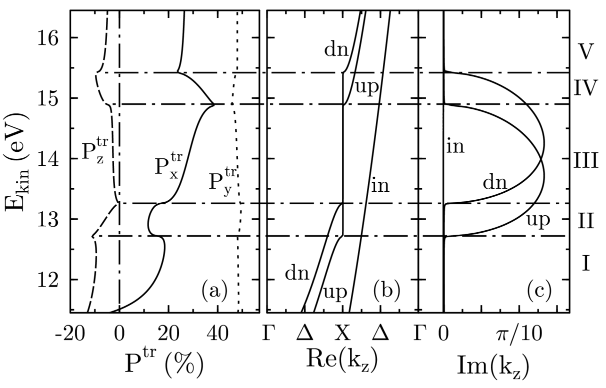

Struktur treffen, die sogar nichtkollinear sein darf. Hier sollten Experiment und Theorie Hand in Hand arbeiten, da die Interpretation der gemessenen Spektren ohne begleitende theoretische Unterstützung schwierig sein kann.

## Resümee

In diesem Kapitel wurde gezeigt, wie eine *Ab–initio*-Theorie einzelne Aspekte des spinabhängigen ballistischen Transports durch planare Tunnelkontakte beleuchten kann. Neben technischen Problemen wie der Integration über die zweidimensionale Brillouin-Zone und ihren Lösungen dienen als Beispiele an den Grenzflächen lokalisierte elektronische Zustände, die den Leitwert beträchtlich erhöhen können. Rechnungen für das Vakuumtunneln in Co(0001) legen nahe, dass der Ursprung der *Zero bias anomaly*, die in Proben mit Oxidbarrieren beobachtet wird, in Defekten an Grenzflächen oder im Oxid zu sehen ist. Dass die Grenzflächen signifikanten Einfluss auf die Transporteigenschaften haben, wurde am Beispiel von Fe/MgO/Fe-Tunnelkontakten belegt. Die Ausbildung einer FeO-Schicht an den Fe–MgO-Grenzflächen verändert neben der elektronischen und magnetischen Struktur die Streuung and der Grenzfläche und damit letztendlich den Leitwert. Abschließend wurde ein auf der spin- und winkelaufgelösten Photoelektronenspektroskopie basierender Zugang zur *Spin motion* in der Transmission durch dünne magnetische Filme vorgeschlagen und anhand von *Ab–initio*- und Modellrechnungen diskutiert.

# 6. Zusammenfassung und Ausblick

Die vorliegende Arbeit gibt einen Überblick der Theorie von Elektronenspektroskopien von Festkörpern aus ersten Prinzipien. Als Basis dient die relativistische Vielfachstreutheorie für spinpolarisierte Systeme (Kap. 2), sodass Effekte, die auf der Spin–Bahn-Kopplung und auf dem Magnetismus der Proben beruhen, gleichermaßen beschrieben werden können. Deren Manifestationen werden anhand ausgewählter Beispiele erläutert: einerseits für den Grundzustand, andererseits in der Photoelektronenspektroskopie und im spinabhängigen ballistischen Transport.

Im elektronischen Grundzustand manifestiert sich die Spin–Bahn-Kopplung (SBK) in der energetischen Aufspaltung der Zustände, in deren Spinpolarisation und in der magnetokristallinen Anisotropie (Kap. 3). Die Photoemission liefert einen vergleichsweise direkten Zugang zu den elektronischen Eigenschaften der Festkörper (Kap. 4). Hier führt die SBK zur Spinpolarisation der Photoelektronen in der Emission von nichtmagnetischen Oberflächen und zum damit eng verwandten Magnetischen Dichroismus. Die Quantisierung elektronischer Zustände in dünnen Filmen resultiert in einer charakteristischen Modulation der Spektren. Die Temperaturabhängigkeit der magnetischen Eigenschaften lässt sich erfolgreich als Unordnungsphänomen im Rahmen der *Coherent potential approximation* (CPA) beschreiben. Und die Elektronenkorrelation kann mit Hilfe der Zweielektronenphotoemission direkt untersucht werden. Der spinabhängige Transport liefert detaillierte Informationen über die geometrische, elektronische und magnetische Struktur von Tunnelkontakten, insbesondere von denen der Grenzflächen im System (Kap. 5).

Die ausgewählten Beispiele machen deutlich, wie die *Ab–initio*-Theorie nicht nur Grundzustandseigenschaften von Systemen erfolgreich beschreiben kann, sondern mittels Berechnung von Messgrößen zu weiteren Erkenntnissen führt. Der letzte Aspekt erfordert ein enges Zusammenwirken mit dem Experiment.

Abschließend werden einige weiterführende Projekte genannt, die auf den Resultaten der vorliegen Arbeit beruhen. Das Zusammenspiel der räumlichen Lokalisierung von Oberflächenzuständen und der SBK lässt sich z. B. auf vizinalen Au(111)-Oberflächen untersuchen (Abschn. 3.2). Die *Ab–initio*-Beschreibung der Photoemission sollte Vielteilcheneffekte besser berücksichtigen, was im Rahmen der $GW$-Näherung für die Selbstenergie geschehen könnte. Obwohl Experimente der Photoemission korrelierter Elektronenpaare gut mit der lokalen Näherung für die Elektron–Elektron-Wechselwirkung beschrieben werden (Abschn. 4.7), erscheint es ratsam, die nichtlokale Wechselwirkung explizit zu behandeln. Beim spinabhängigen Transport sollte die geometrische Unordnung in den Proben berücksichtigt werden, vorzugsweise im Rahmen der CPA. Eine andere Fragestellung betrifft die *Ab–initio*-Beschreibung des Transport im Nichtgleichgewicht, d. h. bei einer endlichen angelegten Spannung. Aktuelle Probleme des Transports durch Nanokontakte und im Rastertunnelmikroskop betreffen die Elektronenkorrelation und den Einfluss der Geometrie.

# Literaturverzeichnis

[1] Encyclopædia Britannica Deluxe Edition. CD-ROM (2003).

[2] U. von Barth, L. Hedin. J. Phys. C: Sol. State Phys. **5** (1972) 1629.

[3] M. M. Pant, A. K. Rajagopal. Sol. State Commun. **10** (1972) 1157.

[4] G. Vignale, M. Rasolt. Phys. Rev. Lett. **59** (1987) 2360.

[5] G. Vignale. In Gross und Dreizler [6], S. 485.

[6] E. K. U. Gross, R. M. Dreizler (Hrsg.). *Density Functional Theory*, Bd. 337 der *NATO ASI Series B Physics* (Plenum Press, New York, 1995).

[7] S. H. Vosko, L. Wilk, M. Nusair. Can. J. Phys. **58** (1980) 1200.

[8] J. P. Perdew, Y. Wang. Phys. Rev. B **45** (1992) 13 244.

[9] D. J. W. Geldart. In Gross und Dreizler [6], S. 33.

[10] J. Korringa. Physica **13** (1947) 392.

[11] W. Kohn, N. Rostoker. Phys. Rev. **94** (1954) 1111.

[12] J. Korringa. Phys. Rep. **238** (1994) 341.

[13] J. M. MacLaren, S. Crampin, D. D. Vvedensky, J. B. Pendry. Phys. Rev. B **40** (1989) 12 164.

[14] I. Mertig, E. Mrosan, P. Ziesche. *Multiple Scattering Theory of Point Defects in Metals: Electronic Properties* (B. G. Teubner, Leipzig, 1987).

[15] P. Weinberger. *Electron Scattering Theory of Ordered and Disordered Matter* (Clarendon Press, Oxford, 1990).

[16] A. Gonis. *Green Functions for Ordered and Disordered Systems*, Bd. 4 der *Studies in Mathematical Physics* (North-Holland, Amsterdam, 1992).

[17] J. Henk. In H. S. Nalwa (Hrsg.), *Handbook of Thin Film Materials*, Bd. 2, Kap. 10, S. 479 (Academic Press, San Diego, 2001).

[18] S. Bei der Kellen, A. J. Freeman. Phys. Rev. B **54** (1996) 11 187.

[19] A. Gonis, P. Turchi, J. Kudrnovský, V. Drchal, I. Turek. J. Phys.: Condens. Matt. **8** (1996) 7869.

[20] E. M. Rose. *Relativistic Electron Theory* (Wiley & Sons, New York, 1961).

[21] B. Ackermann. *Relativistische Theorie der Photoemission und Streuung langsamer Elektronen von ferromagnetischen Oberflächen*. Dissertation, Universität Duisburg (1985).

[22] E. Tamura. Phys. Rev. B **45** (1992) 3271.

[23] D. D. Koelling, B. N. Harmon. J. Phys. C: Sol. State Phys. **10** (1977) 3107.

[24] H. Gollisch, L. Fritsche. phys. stat. sol. (b) **86** (1978) 156.

[25] T. Takeda. J. Phys. F: Met. Phys. **9** (1979) 815.

[26] H. Ebert, H. Freyer, A. Vernes, G. Y. Guo. Phys. Rev. B **53** (1996) 7721.

[27] H. Ebert, H. Freyer, M. Deng. Phys. Rev. B **56** (1997) 9454.

[28] E. Tamura (1996). Private Mitteilung.

[29] K. Kambe. Z. Naturf. **22a** (1967) 322.

[30] L. A. Mac Coll. Phys. Rev. **56** (1939) 699.

[31] R. O. Jones, P. J. Jennings, O. Jepsen. Phys. Rev. B **29** (1984) 6474.

[32] C. S. Lent, D. J. Kirkner. J. Appl. Phys. **67** (1990) 6353.

[33] Y. Joly. Phys. Rev. Lett. **68** (1992) 950.

[34] J. Henk, W. Schattke, H. Carstensen, R. Manzke, M. Skibowski. Phys. Rev. B **47** (1993) 2251.

[35] S. Lorenz, C. Solterbeck, W. Schattke, J. Burmeister, W. Hackbusch. Phys. Rev. B **55** (1997) R13 432.

[36] P. M. Morse, H. Feshbach. *Methods of Theoretical Physics*, Bd. I (McGraw Hill, New York, 1953).

[37] J. S. Faulkner, G. M. Stocks. Phys. Rev. B **21** (1980) 3222.

[38] L. Szunyogh, B. Újfalussy, P. Weinberger. Phys. Rev. B **51** (1995) 9552.

[39] K. Wildberger, R. Zeller, P. H. Dederichs. Phys. Rev. B **55** (1997) 10 074.

[40] J. Henk, A. M. N. Niklasson, B. Johansson. Phys. Rev. B **59** (1999) 13 986.

[41] M. Weinelt, P. Trischberger, W. Widdra, K. Eberle, P. Zebisch, S. Gokhale, D. Menzel, J. Henk, R. Feder, H. Dröge, H.-P. Steinrück. Phys. Rev. B **52** (1995) R17 048.

[42] P. Trischberger, H. Dröge, S. Gokhale, J. Henk, H.-P. Steinrück, W. Widdra, D. Menzel. Surf. Sci. **377–379** (1996) 155.

[43] W. Widdra, P. Trischberger, J. Henk. Phys. Rev. B **60** (1999) R5161.

[44] Y. A. Bychkov, E. I. Rashba. J. Phys.: Condens. Matt. **17** (1984) 6039.

[45] G. Dresselhaus. Phys. Rev. **100** (1955) 580.

[46] A. Mugarza, A. Mascaraque, V. Repain, S. Rousset, K. N. Altmann, F. J. Himpsel, Y. M. Koroteev, E. V. Chulkov, F. J. García de Abajo, J. E. Ortega. Phys. Rev. B **66** (2002) 245419.

[47] J. Henk, A. Ernst, P. Bruno. Phys. Rev. B **68** (2003) 165416.

[48] S. LaShell, B. A. McDougall, E. Jensen. Phys. Rev. Lett. **77** (1996) 3419.

[49] G. Nicolay, F. Reinert, S. Hüfner, P. Blaha. Phys. Rev. B **65** (2001) 033407.

[50] R. Evarestov, V. Smirnow. phys. stat. sol. (b) **119** (1983) 9.

[51] K. Baberschke. In Baberschke *et al.* [52], S. 27.

[52] K. Baberschke, W. Nolting, M. Donath (Hrsg.). *Band-Ferromagnetism: Ground-State and Finite-Temperature Phenomena*, Bd. 580 der *Lecture Notes in Physics* (Springer, Berlin, 2001).

[53] P. Bruno. Phys. Rev. B **39** (1989) 865.

[54] P. Gambardella, S. Rusponi, M. Veronese, S. S. Dhesi, C. Grazioli, A. Dallmeyer, I. Cabria, R. Zeller, P. H. Dederichs, K. Kern, C. Carbone, H. Brune. Sci. **300** (2003) 1130.

[55] G. Schütz, W. Wagner, W. Wilhelm, P. Kienle, R. Zeller, R. Frahm, G. Materlik. Phys. Rev. Lett. **58** (1987) 737.

[56] G. van der Laan. J. Electron Spectrosc. Relat. Phenom. **101–103** (1999) 859.

[57] G. H. O. Daalderop, P. J. Kelly, M. F. H. Schuurmans. Phys. Rev. B **41** (1990) 11 919.

[58] X. Wang, D.-S. Wang, R. Wu, A. J. Freeman. J. Magn. Magn. Mater. **159** (1996) 337.

[59] H. J. F. Hansen. Phys. Rev. B **59** (1999) 4699.

[60] J. Henk, A. M. N. Niklasson, B. Johansson. Phys. Rev. B **59** (1999) 9332.

[61] O. Hjortstam, K. Baberschke, J. M. Wills, B. Johansson, O. Eriksson. Phys. Rev. B **55** (1997) 15 026.

[62] C. Uiberacker, J. Zabloudil, P. Weinberger, L. Szunyogh, C. Sommers. Phys. Rev. Lett. **82** (1999) 1289.

[63] H. Bonzel, C. Kleint. Prog. Surf. Sci. **49** (1995) 107.

[64] A. Einstein. Ann. Phys. **17** (1905) 132.

[65] K. Siegbahn, C. Nordling, A. Fahlman, R. Nordberg, K. Hamrin, J. Hedman, G. Johanson, T. Bergmark, S.-E. Karlsson, I. Lindgren, B. Lindberg. *ESCA – Atomic, Molecular and Solid State Structure Studied by Means of Electron Spectroscopy* (Almqvist och Wiksells, Uppsala, 1967).

[66] E. O. Kane. Phys. Rev. Lett. **12** (1964) 97.

[67] M. Campagna, R. Rosei (Hrsg.). *Photoemission and Absorption Spectroscopy of Solids and Interfaces with Synchrotron Radiation* (North-Holland, Amsterdam, 1990).

[68] R. Z. Bachrach (Hrsg.). *Synchrotron Radiation Research. Advances in Surface and Interface Science*, Bd. 1. Techniques (Plenum Press, New York, 1992).

[69] R. Z. Bachrach (Hrsg.). *Synchrotron Radiation Research. Advances in Surface and Interface Science*, Bd. 2. Issues and Technology (Plenum Press, New York, 1992).

[70] C. Berglund, W. Spicer. Phys. Rev. **136** (1964) A1030.

[71] M. Cardona, L. Ley (Hrsg.). *Photoemission in Solids I.* Number 26 in Topics in Applied Physics (Springer, Berlin, 1978).

[72] A. Liebsch. In B. Feuerbacher, B. Fitton, R. F. Willis (Hrsg.), *Photoemission and the electronic properties of surfaces*, S. 167 (Wiley, Chichester, 1978).

[73] S. V. Kevan (Hrsg.). *Angle-resolved Photoemission: Theory and Current Applications* (Elsevier, Amsterdam, 1992).

[74] J. B. Pendry. J. Phys. C: Sol. State Phys. **8** (1975) 2431.

[75] J. B. Pendry. Surf. Sci. **57** (1976) 679.

[76] J. F. L. Hopkinson, J. B. Pendry, D. J. Titterington. Comp. Phys. Commun. **19** (1980) 69.

[77] J. Braun. Rep. Prog. Phys. **59** (1996) 1267.

[78] G. Thörner, G. Borstel. phys. stat. sol. (b) **126** (1984) 617.

[79] J. Braun, G. Thörner, G. Borstel. phys. stat. sol. (b) **130** (1985) 643.

[80] J. Braun, G. Thörner, G. Borstel. phys. stat. sol. (b) **144** (1987) 609.

[81] M. Wöhlecke, G. Borstel. In F. Meier, B.P. Zakharchenya (Hrsg.), *Optical Orientation* (North-Holland, Amsterdam, 1984).

[82] I. Žutić, J. Fabian, S. Das Sarma. Rev. Mod. Phys. **76** (2004) 323.

[83] E. Tamura, W. Piepke, R. Feder. Phys. Rev. Lett. **59** (1987) 934.

[84] E. Tamura, R. Feder. Europhys. Lett. **16** (1991) 695.

[85] J. Henk, R. Feder. Europhys. Lett. **28** (1994) 609.

[86] B. Schmiedeskamp, B. Vogt, U. Heinzmann. Phys. Rev. Lett. **60** (1988) 651.

[87] B. Schmiedeskamp, N. Irmer, R. David, U. Heinzmann. Appl. Phys. A **A53** (1991) 418.

[88] N. Irmer, F. Frentzen, S.-W. Yu, B. Schmiedeskamp, U. Heinzmann. J. Electron Spectrosc. Relat. Phenom. **78** (1996) 321.

[89] R. Feder, J. Henk. In H. Ebert, G. Schütz (Hrsg.), *Spin-Orbit Influenced Spectroscopies of Magnetic Solids*, number 466 in Lecture Notes in Physics, S. 85 (Springer, Berlin, 1996).

[90] W. Kuch, A. Dittschar, K. Meinel, M. Zharnikov, C. Schneider, J. Kirschner, J. Henk, R. Feder. Phys. Rev. B **53** (1996) 11 621.

[91] A. Fanelsa, E. Kisker, J. Henk, R. Feder. Phys. Rev. B **54** (1996) 2922.

[92] A. Rampe, G. Güntherodt, D. Hartmann, J. Henk, T. Scheunemann, R. Feder. Phys. Rev. B **57** (1998) 14 370.

[93] J. Henk. J. Phys.: Condens. Matt. **13** (2001) 833.

[94] P. J. Feibelman, D. E. Eastman. Phys. Rev. B **10** (1974) 4932.

[95] C. Caroli, D. Lederer-Rozenblatt, B. Roulet, D. Saint-James. Phys. Rev. B **8** (1973) 4552.

[96] W. Schattke. Prog. Surf. Sci. **54** (1997) 211.

[97] L. Hedin, J. Michiels, J. Inglesfield. Phys. Rev. B **58** (1998) 15 565.

[98] L. Hedin. J. Phys.: Condens. Matt. **11** (1999) R489.

[99] T. Fujikawa, L. Hedin. Phys. Rev. B **40** (1989) 11 507.

[100] J. Hermanson. Sol. State Commun. **22** (1977) 9.

[101] J. Henk, T. Scheunemann, S. V. Halilov, R. Feder. J. Phys.: Condens. Matt. **8** (1996) 47.

[102] R. Feder (Hrsg.). *Polarized Electrons in Surface Physics*. Advanced Series in Surface Science (World Scientific, Singapore, 1985).

[103] J. Kessler. *Polarized Electrons*, Bd. 1 der *Springer Series on Atoms and Plasmas* (Springer, Berlin, 1985), 2nd edition.

[104] B. Ginatempo, P. J. Durham, B. L. Gyorffy, W. M. Temmerman. Phys. Rev. Lett. **54** (1985) 1581.

[105] J. Henk, B. Johansson. J. Electron Spectrosc. Relat. Phenom. **94** (1998) 259.

[106] E. Merzbacher. *Quantum Mechanics* (John Wiley & Sons, New York, 1970), 2 edition.

[107] G. Bastard. Phys. Rev. B **24** (1981) 5693.

[108] G. Bastard. Phys. Rev. B **25** (1982) 7584.

[109] P. D. Loly, J. B. Pendry. J. Phys. C: Sol. State Phys. **16** (1983) 423.

[110] A. Ernst, J. Henk, M. Lüders, Z. Szotek, W. M. Temmerman. Phys. Rev. B **66** (2002) 165435.

[111] E. M. Haines, V. Heine, A. Ziegler. J. Phys. F: Met. Phys. **15** (1985) 661.

[112] E. M. Haines. J. Comp. Phys. **60** (1985) 353.

[113] E. M. Haines, V. Heine, A. Ziegler. J. Phys. F: Met. Phys. **16** (1986) 1343.

[114] D. Reiser, J. Henk, H. Gollisch, R. Feder. Sol. State Commun. **93** (1995) 231.

[115] P. J. Durham. J. Phys. F: Met. Phys. **11** (1981) 2475.

[116] P. J. Durham, J. Staunton, B. L. Gyorffy. J. Magn. Magn. Mater. **45** (1984) 38.

[117] P. J. Durham, B. L. Gyorffy, A. J. Pindor. J. Phys. F: Met. Phys. **10** (1980) 661.

[118] W. Clemens, T. Kachel, O. Rader, E. Vescovo, S. Blügel, C. Carbone, W. Eberhardt. Sol. State Commun. **81** (1992) 739.

[119] R. Feder, H. Gollisch, T. Scheunemann, J. Berakdar, J. Henk. In Berakdar und Kirschner [120], S. 435.

[120] J. Berakdar, J. Kirschner (Hrsg.). *Many-Particle Spectroscopy of Atoms, Molecules, Clusters, and Surfaces* (Plenum Press, London, 2001).

[121] N. Fominykh, J. Henk, J. Berakdar, P. Bruno, H. Gollisch, R. Feder. Sol. State Commun. **113** (2000) 665.

[122] T. Straub, R. Claessen, P. Steiner, S. Hüfner, V. Eyert, K. Friemelt, E. Bucher. Phys. Rev. B **55** (1997) 13 473.

[123] M. P. Seah, W. A. Dench. Surf. Interf. Anal. **1** (1979) 2.

[124] M. Jullière. Phys. Lett. A **54** (1975) 225.

[125] S. Maekawa, U. Gafvert. IEEE Transact. Magn. **MAG-18** (1982) 707.

[126] J. C. Slonczewski. Phys. Rev. B **39** (1989) 6995.

[127] R. Landauer. IBM J. Res. Devel. **1** (1957) 223.

[128] M. Büttiker, Y. Imri, R. Landauer, S. Pinhas. Phys. Rev. B **31** (1985) 6207.

[129] Y. Y. Sharvin. Sov. Phys. JETP **21** (1965) 655.

[130] J. Henk, P. Bruno. Phys. Rev. B **68** (2003) 174430.

[131] J. M. MacLaren, X.-G. Zhang, W. H. Butler, X. Wang. Phys. Rev. B **59** (1999) 5470.

[132] P. Mavropoulos, N. Papanikolaou, P. H. Dederichs. Phys. Rev. B **69** (2004) 125104.

[133] K. Palotás, B. Lazarovits, L. Szunyogh, P. Weinberger. Phys. Rev. B **67** (2003) 174404.

[134] H. U. Baranger, A. D. Stone. Phys. Rev. B **40** (1989) 8169.

[135] P. H. Dederichs, P. Mavropoulos, O. Wunnicke, N. Papanikolaou, V. Bellini, R. Zeller, V. Drchal, J. Kudrnovský. J. Magn. Magn. Mater. **240** (2002) 108.

[136] O. Wunnicke, N. Papanikolaou, R. Zeller, P. H. Dederichs, V. Drchal, J. Kudrnovský. Phys. Rev. B **65** (2002) 064425.

[137] M. P. Gokhale, D. L. Mills. Phys. Rev. Lett. **66** (1991) 2251.

[138] L. Sheng, D. Y. Xing, D. N. Sheng. Phys. Rev. B **70** (2004) 094416.

[139] S. Yuasa, A. Fukushima, T. Nagahama, K. Ando, Y. Suzuki. Jap. J. Appl. Phys. **43** (2004) L588.

[140] H. F. Ding, W. Wulfhekel, J. Henk, P. Bruno, J. Kirschner. Phys. Rev. Lett. **90** (2003) 116603.

[141] N. D. Lang. Phys. Rev. Lett. **55** (1985) 230. Erratum p. 2925.

[142] C. Zhang, X.-G. Zhang, P. S. Krstić, H.-P. Cheng, W. H. Butler, J. M. MacLaren. Phys. Rev. B **69** (2004) 134406.

[143] W. H. Butler, X.-G. Zhang, T. C. Schulthess, J. M. MacLaren. Phys. Rev. B **63** (2001) 054416.

[144] H. L. Meyerheim, R. Popescu, J. Kirschner, N. Jedrecy, M. Sauvage-Simkin, B. Heinrich, R. Pinchaux. Phys. Rev. Lett. **87** (2001) 076102.

[145] X.-G. Zhang, W. H. Butler. J. Phys.: Condens. Matt. **15** (2003) R1603.

[146] X.-G. Zhang, W. H. Butler, A. Bandyopadhyay. Phys. Rev. B **68** (2003) 092402.

[147] W. Weber, S. Riesen, H. C. Siegmann. In Baberschke *et al.* [52], S. 320.

[148] W. Weber, S. Riesen, H. C. Siegmann. Sci. **291** (2001) 1015.

[149] L. Berger. IEEE Transact. Magn. **31** (1995) 3871.

[150] T. Valet, A. Fert. Phys. Rev. B **48** (1993) 7099.

[151] M. Johnson, R. H. Silsbee. Phys. Rev. Lett. **55** (1985) 1790.

# Abkürzungen

**2BZ** zweidimensionale Brillouin-Zone
**2DEG** zweidimensionales Elektronengas
**ATA** *Averaged $t$-matrix approximation*
**bcc** *Body-centered cubic*
**BZ** Brillouin-Zone
**CDAD** *Circular dichroism in angular distribution*
**CFS** *Constant final-state*
**CIS** *Constant initial-state*
**CPA** *Coherent potential approximation*
**DFT** Dichtefunktionaltheorie
**DLM** *Disordered local moment*
**DPE** *Double photoemission*
**EFG** elektrischer Feldgradient
**fcc** *Face-centered cubic*
**fct** *Face-centered tetragonal*
**GF** Green-Funktion
**GGA** *Generalized gradient approximation*
**hcp** *Hexagonally closed packed*
**JJJ** Jones–Jennings–Jepsen
**KKR** Korringa–Kohn–Rostoker
**LB** Landauer-Büttiker
**LDA** *Local density approximation*
**LEED** *Low-energy electron diffraction*
**LKKR** *Layer*-KKR
**LSDA** *Local spin-density approximation*
**MAE** magnetokristalline Anisotropieenergie
**MCA** *Magneto-crystalline anisotropy*
**MCD** *Magnetic ciruclar dichroism*
**MD** Magnetischer Dichroismus
**MFP** *Mean free path*
**ML** Monolage
**MLD** *Magnetic linear dichroism*
**MT** *Muffin tin*
**LMM** lokales magnetisches Moment
**VST** Vielfachstreutheorie
**QWS** *Quantum–well state*
**RTM** Rastertunnelmikroskop
**SPLEED** *Spin-polarized low-energy electron diffraction*
**SBK** Spin–Bahn-Kopplung
**SIC** *Self-interaction correction*
**SPE** *Single photoemission*
**SPO** Streupfadoperator
**SRT** *Spin-reorientation transition*
**TB** *Tight-binding*
**TMR** *Tunnel magneto-resistance*
**VCA** *Virtual crystal approximation*
**VLEED** *Very low-energy electron diffraction*
**VUV** *Vacuum ultraviolet*
**ZBA** *Zero bias anomaly*

# Dank

Die Untersuchungen, die sich in dieser Arbeit dokumentiert finden, sind ohne Hilfe, Unterstützung, Kritik, Ansporn, Diskussionen und — naturgemäß — Zusammenarbeit undenkbar gewesen. So gilt mein Dank einer Vielzahl von Kollegen: Jamal Berakdar, Klaus Baberschke, Peter Bose, Patrick Bruno, Arthur Ernst, Andreas Fanelsa, Roland Feder, Natasha Fominykh, Focke Frentzen, Herbert Gollisch, Gernot Güntherodt, Samed Halilov, Detlef Hartmann, Ulli Hillebrecht, U. Heinzmann, Moritz Hoesch, Norbert Irmer, Börje Johansson, Jürgen Kirschner, Eberhard Kisker, Wolfgang Kuch, Minn-Tsong Lin, Dirk Meinert, Ingrid Mertig, Thomas Michael, Yonko T. Millev, Anders Niklasson, Jürg Osterwalder, Andreas Rampe, Dirk Reiser, Silke Roether, Thomas Scheunemann, Claus M. Schneider, Kai Starke, Hans-Peter Steinrück, Eiichi Tamura, Walter M. Temmerman, Peter Trischberger, Wolf Widdra, Wulf Wulfhekel, Peter Zahn.

Einen wesentlichen Beitrag zum Gelingen des Projekts „Habilitation“ haben die Kollegen und Freunde vom Max-Planck-Institut für Mikrostrukturphysik geleistet.

Mein besonders herzlicher Dank gilt „meiner“ Frau Annette und „meinen“ Söhnen Jan-Malte und Kai-Hendrik. Nur ihre Liebe und ihr Vertrauen mag sie die Verquickung von privatem Leben und wissenschaftlicher Arbeit erdulden lassen.

# Eidesstattliche Erklärung

Hiermit erkläre ich, dass ich die Habilitationsschrift selbstständig und ohne fremde Hilfe verfasst und andere als die angegebenen Quellen und Hilfsmittel nicht benutzt und die den benutzten Werken wörtlich oder inhaltlich entnommenen Stellen als solche kenntlich gemacht habe.

Halle (Saale), den 17. Dezember 2004

Dr. Jürgen Henk

# Lebenslauf

## Anschrift

| | **Privat** | **Beruflich** |
|---|---|---|
| Adresse: | Sonnenblumenweg 8<br>D-06198 Salzmünde | MPI für Mikrostrukturphysik<br>Weinberg 2<br>D-06120 Halle (Saale) |
| Email: | JuergenHenk@web.de | henk@mpi-halle.de |
| Telefon: | +49 (0)34609 2 20 82<br>+49 (0)173 3 95 61 74 | +49 (0)345 5582–970 |
| Fax: | | +49 (0)345 5582–765 |
| WWW: | | http://www.mpi-halle.mpg.de/∼henk |

## Persönliche Details

| | |
|---|---|
| Geburtsdatum: | 23. September 1960 |
| Geburtsort: | Plön |
| Geschlecht: | männlich |
| Staatsangehörigkeit: | Deutscher |
| Ehestand: | verheiratet mit Annette Alsen-Henk |
| Kinder: | Kai-Hendrik und Jan-Malte |

## Wissenschaftliche Ausbildung

**1980–1986** Studium der Physik, Universität Kiel

Schwerpunkte: Theoretische Physik, Festkörperphysik und Mathematik

**1986** Diplom in Physik

Institut für Theoretische Physik, Universität Kiel
Anleitung: Prof. Dr. Wolfgang Schattke
Diplomarbeit: *Berechnung der Bandstruktur von GaAs für den Kristall mit Oberfläche*

**1991** Promotion in Physik

Institut für Theoretische Physik, Universität Kiel
Anleitung: Prof. Dr. Wolfgang Schattke
Doktorarbeit: *Theoretische Analyse von Photoemissionsspektren am Beispiel von GaAs(110)*

## Wissenschaftlicher Werdegang

**1987–1992** Wissenschaftlicher Mitarbeiter
Institut für Theoretische Physik, Universität
Prof. Dr. Wolfgang Schattke

**1992** Institut für Festkörperforschung (IFF), Forschungszentrum Jülich
2 Monate als Gast von Dr. Eichii Tamura

**1992–1997** Wissenschaftlicher Mitarbeiter
Institut für Theoretische Festkörperphysik, Universität Duisburg
Prof. Dr. Roland Feder

**1997–1999** Post-Doc
*Condensed Matter Theory Group*, Universität Uppsala, Schweden
Prof. Dr. Börje Johansson

**Seit 1999** Wissenschaftler
Max-Planck-Institut für Mikrostruktur Physik, Halle (Saale)
Prof. Dr. Patrick Bruno (Abteilung Theorie)

Halle (Saale), den 17. Dezember 2004

Dr. Jürgen Henk

# P. Publikationen

## P.1. Übersicht der beigefügten Publikationen

Die beigefügten Publikationen dokumentieren die Arbeiten, die in der vorliegenden Schrift diskutiert wurden. Sie werden gemäß deren thematischer Gliederung präsentiert.

Da die vorliegende Arbeit recht unterschiedliche Themen behandelt, erscheint es m. E. nützlich, die Beifügungen zu klassifizieren: nach Systemen, Geometrien, Spektroskopien und dem Ursprung der in ihnen behandelten Effekte (Tab. P.1).

**Tabelle P.1.** Klassifizierung der beigefügten Publikationen. Die Abkürzungen bedeuten nichtmagnetisch (nm), magnetisch (m), Oberfläche (of), Adsorbat (a), ultradünner Film (uf), Tunnelkontakt (tk), Photoemission (spe), Zweielektronenphotoemission (dpe), Transport (t), Spin–Bahn-Kopplung (sbk), Spinpolarisation (sp), Magnetischer Dichroismus (md), *Quantum–size*-Effekt (qse), *Spin motion* (sm), Magnetwiderstand (mr) und Magnetische Anisotropie (ma).

| Publ. | Systeme | | Geometrie | | | | Spektroskopie | | | Effekte | | | | | | |
|---|---|---|---|---|---|---|---|---|---|---|---|---|---|---|---|---|
| Nr. | nm | m | of | a | uf | tk | spe | dpe | t | sbk | sp | md | qse | sm | mr | ma |
| 1 | x | | | x | | | x | | | x | | | | | | |
| 2 | x | | x | | | | x | | | x | x | | | | | |
| 3 | | x | | | x | | | | | x | | | | | | x |
| 4 | x | x | x | | | | x | | | x | x | x | | | | |
| 5 | x | | x | | | | x | | | x | x | | | | | |
| 6 | | x | | | x | | x | | | x | | x | | | | |
| 7 | | x | x | | | | x | | | x | | x | | | | |
| 8 | | x | | | x | | x | | | x | x | x | | | | |
| 9 | x | | | | x | | x | | | | | | x | | | |
| 10 | x | | x | | | | | x | | | | | | | | |
| 11 | | x | | | | x | | | x | | | | | | x | |
| 12 | | x | | | | x | | | x | | | | | | x | |
| 13 | | x | | | x | | x | | | | x | | | x | | |

## P.2. Spin–Bahn-Kopplung und elektronische Struktur

**1 (S. P2ff)** W. Widdra, P. Trischberger, J. Henk.
*Band formation and quadrupole interaction of one-dimensional adsorbate chains: Xenon adsorbed on hydrogen-modified Pt(110).*
Physical Review B **60** (1999) R5161.

**2 (S. P6ff)** J. Henk, M. Hoesch, J. Osterwalder, A. Ernst, P. Bruno.
*Spin polarization in the L-gap surface states on Au(111): Spin-resolved photoemission experiments and first-principles calculations.*
Journal of Physics: Condensed Matter **16** (2004) 7581.

**3 (S. P23ff)** J. Henk, A. M. N. Niklasson, B. Johansson.
*Magnetism and anisotropy of ultra-thin Ni films on Cu(001).*
Physical Review B **59** (1999) 9332.

## Publikation 1

# Band formation and quadrupole interaction of one-dimensional adsorbate structures: Xenon chains on hydrogen-modified Pt(110)

W. Widdra* and P. Trischberger†
*Physik-Department E20, Technische Universität München, D-85747 Garching, Germany*

J. Henk
*Kondenserade Materiens Teori, Fysiska Institutionen, University Uppsala, S-751 21 Uppsala, Sweden*

(Received 16 June 1999)

Using angle-resolved photoemission, we investigated the electronic valence-band structure of one-dimensional (1D) Xe chains adsorbed on a hydrogen-modified Pt(110)-$(1\times2)$ surface. By varying the Xe coverage, the Xe-Xe next-neighbor distance within the chains can be modified, which results in similar band structures but with different widths of up to 800 meV. For these 1D systems, the Xe-5$p_{3/2}$ states show a reversed energetic ordering with respect to two-dimensional Xe adlayers. Numerical band-structure calculations and analytical considerations show that the Pt substrate affects the Xe valence bands negligibly. The energetic ordering of the Xe states can be explained in terms of the electric quadrupole interaction along the chains. [S0163-1829(99)51832-8]

The influence of dimensionality on various physical properties of solids has attracted attention experimentally as well as theoretically. It is well established that at surfaces, as one example for a two-dimensional (2D) system, the behavior of a physical quantity, e.g., the electronic structure, may differ from that in the three-dimensional (3D) bulk. Further geometrical structuring can lead to one-dimensional (1D) structures (e.g., ''quantum wires''). Often these structures exhibit different orientations or size distributions or even exist only locally, thus requiring a local spectroscopy, e.g., scanning tunneling microscopy, and simultaneously complicating an analysis with nonlocal (integral) but momentum-resolving techniques, e.g., with photoelectron spectroscopy. This might explain why there are only a few reports on electronic properties of low-dimensional structures on surfaces; e.g., on metal-oxygen rows on O-$(2\times1)$ reconstructed (110) surfaces of Cu, Ag, and Ni;[1–3] on surface states of a system ordered in one dimension only,[4] and on 1D delocalized Bloch waves within adsorbate layers on Si(100)-$(2\times1)$.[5]

Rare-gas atoms adsorbed on surfaces form zero-dimensional (well-separated adatoms), 1D (chains), 2D (adlayers), and three-dimensional (thin films) systems. Because the interaction of the rare gas with the substrate is small, the electronic structures of the various systems reflect the dimension of the system. This allows a comparison of equivalent systems (built by identical constituents but with different dimensionality), which is not the case for the systems mentioned above. In this paper, we report an experimental and theoretical study of electronic band-structure formation of 1D adsorbate chains with a tunable lattice constant. Xe adsorbed on a hydrogen-modified Pt(110)-$(1\times2)$ surface forms well-defined 1D structures (chains) with a coverage-dependent next-neighbor distance. This makes a variation of the valence-band width possible, which was mapped in the whole Brillouin zone using photoelectron spectroscopy. The reduced dimensionality leads to an important difference with respect to the 2D and 3D cases: the energetic ordering of the spin orbit-split valence states is partially reversed. We will show that this can be understood as a consequence of the changed electric-field gradient and a rotation of the spin-orbit quantization axis. The discussion of the electronic properties of 1D and zero-dimensional structures given below can contribute to the understanding of such weakly interacting systems.

As shown recently, rare-gas adsorption on the bare Pt(110)-$(1\times2)$ surface takes place in the troughs between, as well as on top of, the densely packed Pt rows, thus leading to two different adsorbate species. For Xe, both species are present for coverages down to 0.05 monolayers (ML) (with ratio 2:1)[6]. The lateral interaction stabilizes the weaker bonded species and a quasi-1D electronic behavior at low coverages is found.[7] But both analysis and interpretation of the photoemission results are complicated due to the occurrence of the two Xe species, despite their slightly different binding energies. In this work, we used hydrogen coadsorption to selectively destabilize one Xe species. In the $\beta_2$ phase (hydrogen coverage of 1/3 ML), hydrogen is most likely located below the close-packed Pt rows.[8] Xe adsorbed on this hydrogen-modified surface shows also two species (desorption energies of 310 meV and 190 meV), but by thermal desorption, one species can be removed selectively (for details of preparation and experimental setup see Ref. 6). The remaining species form well-defined chains in the troughs of the $(1\times2)$ surface. In the following, we report on the electronic structure of these Xe chains.

In Fig. 1, typical angle-resolved photoemission spectra for detection with surface-parallel wave vector, parallel ($\vec{k}_\parallel \| [1\bar{1}0]$) and perpendicular ($\vec{k}_\parallel \| [001]$) to the Xe chains, are shown for a Xe coverage of $\Theta_{\mathrm{Xe}}=0.45$ ML. In the [001] direction [Fig. 1(b)], three dispersionless maxima that are related to the Xe valence bands show up. In the $[1\bar{1}0]$ direction [Fig. 1(a)], however, all three bands exhibit strong dispersion. Spectra taken at various photon energies show that the Xe-related maxima disperse with the parallel component of the wave vector. Both findings prove the 1D char-

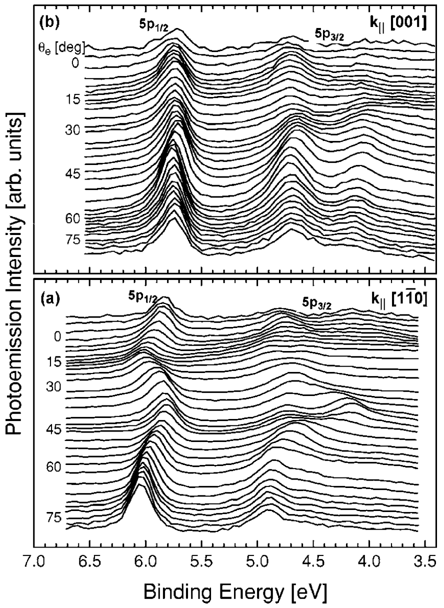

FIG. 1. Angle-resolved UV photoelectron spectra for 1D Xe chains adsorbed on a hydrogen-modified Pt(110)-(1×2) surface. The spectra are shown with increasing photoelectron momentum $k_{\|}$ (increasing polar emission angle) from top to bottom along the $[1\bar{1}0]$ and the [001] direction in panels (a) and (b), respectively. Synchrotron light with a photon energy of 30 eV was used with a 45° angle of incidence.

acter of the electronic structure, which is expected due to the separation of the troughs—and therefore of the Xe chains—by 7.84 Å.

In Fig. 2, the photoemission results are condensed into a band structure. The Xe valence bands show binding energies of 4.1 eV, 4.8 eV, and 5.8 eV at $\bar{\Gamma}$, i.e., the $5p_{3/2}$ states are split in energy. A similar splitting has been observed for 2D Xe layers[9] that was initially attributed to crystal fields[10] and final-state screening dependent on the individual $5p$ states,[11,12] until finally it was attributed to lateral interactions.[9,13–16] In order to further analyze the splitting for the 1D Xe chains, we performed photoemission experiments using light with an electric-field vector along $[1\bar{1}0]$ and photoelectron detection with $\vec{k}_{\|}\|[001]$. Spectra showed emission strong at 4.1 eV, weaker at 5.8 eV, but negligible at 4.8 eV binding energy (note that only the $p$ orbital aligned along the chains can be excited in this geometry). The periodicity along $[1\bar{1}0]$ of the three bands with widths of 800 meV, 240 meV, and 220 meV corresponds to a Xe distance of 4.5 Å, which agrees nicely with that more accurately determined by low-energy electron diffraction [LEED: (4.37±0.03) Å].[6]

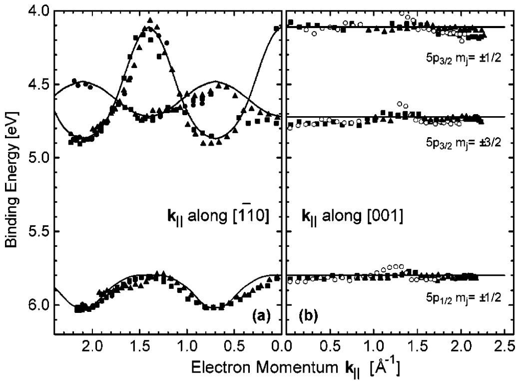

FIG. 2. Experimental band structure for Xe adsorbed on a hydrogen-modified Pt(110)-(1×2) surface along (a) and perpendicular (b) to the Xe chains. Symbols correspond to data sets with different photon energies (26 eV and 30 eV) and different directions of light incidence (normal incidence and 45° off-normal). The theoretical band structure is represented by solid lines.

In order to illuminate the origin of the above band structure, we performed fully relativistic Korringa-Kohn-Rostoker (KKR) calculations for freestanding Xe chains using the Xe-Xe distance determined by LEED. The results are displayed in Fig. 2 and show good agreement with the experimentally determined band structure. Obviously, the valence-band structure is dominantly determined by the Xe-Xe interactions along the chains. The substrate acts only as a template.

We further applied the empirical tight-binding method in order to study the influence of symmetry breaking. As basis functions we used Cartesian $p$ orbitals $p_i$, $i=x,y,z$, which are related to the spin-orbit wave functions $|j,m_j\rangle$ by

$$|3/2,\pm 3/2\rangle=(\pm p_x+\mathrm{i}p_y)\chi^{\pm}/\sqrt{2}, \tag{1a}$$

$$|3/2,\pm 1/2\rangle=[(\pm p_x+\mathrm{i}p_y)\chi^{\mp}+2p_z\chi^{\pm}]/\sqrt{6}, \tag{1b}$$

$$|1/2,\pm 1/2\rangle=[(\pm p_x+\mathrm{i}p_y)\chi^{\mp}\mp p_z\chi^{\pm}]/\sqrt{3}, \tag{1c}$$

where $\chi^{\pm}$ denotes the spin state (Pauli spinor). Note that the $z$ axis has to be chosen along the chain axis (see below). Consequently, the $\sigma$-type overlap between $p_z$ orbitals along the chains is by far larger than the $\pi$-type overlap between $p_{x,y}$ orbitals. In this way, the experimental Xe bands can be described as well as with the KKR method. The tight-binding parameters were fitted to the experimental data and are close to those found for 2D Xe layers.[13] Using slightly different Coulomb integrals for laterally and perpendicularly oriented $5p$ orbitals, the effect of the substrate can be modeled. As a major consequence, crossings in the band structure are avoided.

The wave functions [Eq. (1)] allow us to explain the experimental findings for $\bar{\Gamma}$. The band at 4.8 eV can be assigned to the $|3/2,\pm 3/2\rangle$ state because it has no $p_z$ part and thus no emission for ''$s$-polarized'' light. The energetic ordering—$|3/2,\pm 1/2\rangle$, $|3/2,\pm 3/2\rangle$, and $|1/2,\pm 1/2\rangle$—is straightforward. Additionally, the dispersions of the individual bands can also be explained by their orbital composition. The $p_z$ part of the $|j,\pm 1/2\rangle$ states leads via the dominant $\sigma$-type overlap to dispersion with an antibonding situation at $\bar{\Gamma}$. At $\bar{X}$, the Bloch phase changes sign at each Xe site which results in a bonding situation. The $|3/2,\pm 1/2\rangle$ band shows stronger dispersion than the $|1/2,\pm 1/2\rangle$ band due to the larger $p_z$ part. The $|3/2,\pm 3/2\rangle$ states have no $p_z$ admixture and show therefore only the weak $\pi$-type overlap that leads to the observed bonding and antibonding situations at $\overline{\Gamma}$ and $\overline{X}$, respectively.

The observed energetic sequence of the $5p_{3/2}$ states is reversed with respect to that of hexagonally close-packed Xe layers. We regard this as a consequence of the reduced dimensionality, which can be related to the electric-field gradient (EFG) $V_{xy}=d^2V/dxdy$ due to the charge distribution of neighboring atoms.[15,16] Note that in any spherical environment the choice of the $z$ axis is arbitrary and all $5p_{3/2}$ states are degenerate. However, with a quadrupolar splitting of the $5p_{3/2}$ state into the $|3/2,\pm 3/2\rangle$ and the $|3/2,\pm 1/2\rangle$ states the $z$ axis is *dictated* by the quadrupole interaction. The $5p_{3/2}$ states are eigenstates of the Hamiltonian only if the $z$ axis is chosen along the greatest principle axis of the EFG tensor (called $V_{zz}$) and if the asymmetry $\eta=(V_{xx}-V_{yy})/V_{zz}$ vanishes.[17,18] In this case, which applies here and also for 2D layers at $\overline{\Gamma}$, the $5p_{3/2}$ levels split into $|3/2,\pm 3/2\rangle$ and $|3/2,\pm 1/2\rangle$ levels with a quadrupole splitting of $6h\nu_q$.[18] The quadrupole energy is $h\nu_q=eQV_{zz}/2$ with $Q$ being the quadrupole moment of the $5p_{3/2}$ charge distribution. The EFG $V_{zz}$ can be calculated from the charge distribution $\rho(\vec{r})$ at a Xe site[18] via

$$V_{zz}=\frac{1}{4\pi\epsilon_0}\int\frac{3\cos^2\vartheta-1}{r^3}\rho(\vec{r})d^3r. \qquad (2)$$

For 2D Xe layers, the EFG is aligned along the surface normal while the charge distribution due to the next-neighbor Xe atoms is located mainly in the adlayer plane. Thus, the main contribution to the EFG comes from $\vartheta=90°$, which leads to a negative $V_{zz}$. For the freestanding Xe chain, however, the principal axis of the EFG tensor is oriented along the chain. Consequently, the $z$ axis has to be chosen along the adsorbate chains. Since the charge is located near the $z$ axis ($\vartheta=0°$), the $V_{zz}$ is positive. Due to the different signs of $V_{zz}$, the ordering of the $|3/2,\pm 3/2\rangle$ and $|3/2,\pm 1/2\rangle$ states is *reversed* for 2D and 1D laterally interacting systems.

In the experimental situation, with the Xe chains adsorbed on Pt(110), the Xe charge density may be altered upon interaction with the metal surface, and the rotational symmetry of a freestanding chain would be broken, at least in principle. Therefore, the EFG asymmetry $\eta$ is nonzero and an $\eta$-proportional term is added to the Hamiltonian, which causes mixing between states with $\Delta m_j=\pm 2$. It is most significant at such $\vec{k}_\parallel$ where band crossings occur [for example, $k_\parallel=0.35$/Å in Fig. 2(a)]. At these, it produces a gap of $2\sqrt{3}h\nu_q\eta$ between bands derived from the $|3/2,\pm 3/2\rangle$ and $|3/2,\mp 1/2\rangle$ states. In other words, all crossings in Fig. 2 would be lifted.

The experimental data cannot rule out the existence of such a small gap. But they give an upper limit of 100 meV, which corresponds to an upper limit for the EFG asymmetry, $|\eta|<0.2$. The absence of a considerable gap indicates that the rotational symmetry is not significantly disturbed by the substrate and corroborates that the dominant quadrupolar component of the electric field of adsorbed Xe is due to the interaction with neighboring Xe atoms. These findings question the significant chemical contribution of the $5p$ orbitals to the bonding on metal surfaces that has—by definition—to alter the valence-charge distribution.

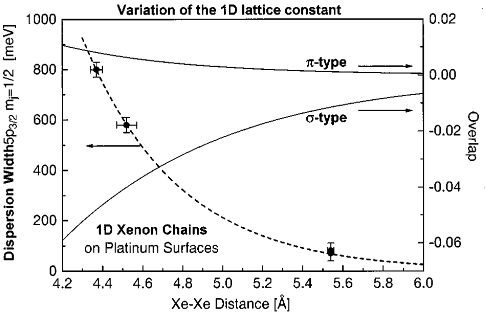

FIG. 3. Dependence of the experimentally obtained $|3/2,\pm 1/2\rangle$ bandwidth on the Xe-Xe next-neighbor separation. The dashed line is an exponential with decay constant of 0.47 Å. The solid lines (right scale) show the calculated distance dependence of the $\sigma$- and $\pi$-type overlaps along and perpendicular to the chains based on the tight-binding wave functions.

Annealing of the saturated Xe chains to 110 K reduces the Xe coverage to $\Theta_{\mathrm{Xe}}=0.23$ ML. The Xe-Xe distance is increased to $(4.52\pm 0.05)$ Å, as determined by LEED. The band structure is similar to that shown in Fig. 2, but shows reduced bandwidths of 150 meV, 150 meV, and 600 meV for the $|1/2,\pm 1/2\rangle$, $|3/2,\pm 3/2\rangle$, and $|3/2,\pm 1/2\rangle$ bands, respectively. At $\overline{\Gamma}$, the $m_j$ splitting of the $5p_{3/2}$ states is decreased from 650 meV to 470 meV.

As a third system, we briefly mention Xe adsorption at step edges of a vicinal Pt(997) surface.[6,19] Step decoration leads to a Xe-Xe distance of 5.54 Å (by LEED). Here, we found a $|3/2,\pm 1/2\rangle$ bandwidth less than 80 meV, which clearly indicates zero-dimensional behavior. The quadrupole splitting—and therefore the EFG—vanishes for this system, which again questions chemical contributions of the $5p$ orbitals to Xe adsorption and points towards a $6s$-to-metal chemical interaction at most.

In Fig. 3, the $|3/2,\pm 1/2\rangle$ bandwidths are compiled for all three systems. Tight-binding theory evidences that the bandwidth scales approximately with the wave-function overlap.[20] The right axis shows the $5p$ overlaps perpendicular and along the chains. The latter is the relevant one for the $|3/2,\pm 1/2\rangle$ band because of the dominance of the $p_z$ contribution. Fitting an exponential function to the experimental bandwidths yields a decay constant of 0.47 Å (dashed line in Fig. 3) that corresponds reasonably well to that from the simple tight-binding theory.

In conclusion, we presented photoemission data and band-structure calculations for 1D adsorbate chains with tunable lattice constant: Xe adsorption on a hydrogen-modified Pt(110)-$(1\times 2)$ exhibits a valence-band dispersion of up to 800 meV along the adsorbate rows but is negligible perpendicular. The observed band structure and band splitting can be well explained by electric quadrupole interaction along the Xe chains. Due to its reduced dimensionality compared to corresponding 2D adsorbate systems, we find a partially reversed energetic ordering of the valence states that is related to a rotation of the spin-orbit quantization axis. Increasing Xe-Xe distances reduces the valence-band widths and finally leads to electronically localized states as for Xe/Pt(997).

This work has been supported by the German BMBF (Grants Nos. 05625WOA and 05SF8WOA) and by the TMR network. The continuous stimulating support by D. Menzel as well as the fruitful and valuable discussions with H.-P. Steinrück and D. Menzel are gratefully acknowledged.

---

[*] Author to whom correspondence should be addressed. FAX: 49-89-2891-2338. Electronic address: widdra@physik.tu-muenchen.de

[†] Present address: IXTRA Software GmbH, D-85630 Grasbrunn, Germany.

[1] R.A. DiDio, D. Zehner, and E. Plummer, J. Vac. Sci. Technol. A **2**, 852 (1984).

[2] R. Courths, S. Hüfner, P. Kemkes, and G. Wiesen, Surf. Sci. **376**, 43 (1997).

[3] R. Matzdorf and A. Goldmann, Surf. Sci. **412-413**, 61 (1998).

[4] U. Bischler and E. Bertel, Phys. Rev. Lett. **71**, 2296 (1993).

[5] W. Widdra, A. Fink, S. Gokhale, P. Trischberger, D. Menzel, U. Birkenheuer, U. Gutdeutsch, and N. Rösch, Phys. Rev. Lett. **80**, 4269 (1998).

[6] P. Trischberger, H. Dröge, S. Gokhale, J. Henk, H.-P. Steinrück, W. Widdra, and D. Menzel, Surf. Sci. **377-379**, 155 (1996).

[7] M. Weinelt, P. Trischberger, W. Widdra, K. Eberle, P. Zebisch, D. Menzel, J. Henk, R. Feder, H. Dröge, and H.-P. Steinrück, Phys. Rev. B **52**, R17 048 (1995).

[8] E. Kirsten, G. Parschau, W. Stocker, and K.H. Rieder, Surf. Sci. Lett. **231**, 183 (1990).

[9] K. Horn, M. Scheffler, and A.M. Bradshaw, Phys. Rev. Lett. **41**, 822 (1978).

[10] B.J. Waclawski and J.F. Herbst, Phys. Rev. Lett. **35**, 1594 (1975).

[11] J.A.D. Matthew and M.G. Devey, Solid State Phys. **9**, L413 (1976).

[12] P.R. Antoniewicz, Phys. Rev. Lett. **38**, 374 (1977).

[13] K. Kambe, Surf. Sci. **105**, 95 (1981).

[14] M. Scheffler, K. Horn, A.M. Bradshaw, and K. Kambe, Surf. Sci. **80**, 69 (1979).

[15] K. Hermann, J. Noffke, and K. Horn, Phys. Rev. B **22**, 1022 (1980).

[16] J. Henk and R. Feder, J. Phys.: Condens. Matter **6**, 1913 (1994).

[17] The EFG can always be represented by a tensor of rank 2 and diagonal form with vanishing trace (in order to exclude a monopole term) by choosing an appropriate coordinate system.

[18] A. Abragam, *The Principles of Nuclear Magnetism* (Oxford, London, 1961).

[19] W. Widdra, P. Trischberger, W. Frieß , D. Menzel, S.H. Payne, and H.J. Kreuzer, Phys. Rev. B **57**, 4111 (1998).

[20] P. Vogl, H. Hjalmarson, and J. Dow, J. Phys. Chem. Solids **44**, 365 (1983).

**Publikation 2**

# Spin–orbit coupling in the L-gap surface states of Au(111): spin-resolved photoemission experiments and first-principles calculations

**J Henk[1], M Hoesch[2,3], J Osterwalder[2], A Ernst[1] and P Bruno[1]**

[1] Max-Planck-Institut für Mikrostrukturphysik, Weinberg 2, D-06120 Halle, Saale, Germany
[2] Physik-Institut, Universität Zürich, Winterthurerstrasse 190, CH-8057 Zürich, Switzerland
[3] Swiss Light Source, Paul-Scherrer-Institut, CH-5232 Villigen PSI, Switzerland

E-mail: henk@mpi-halle.de

Received 9 August 2004, in final form 14 September 2004
Published 15 October 2004
Online at stacks.iop.org/JPhysCM/16/7581
doi:10.1088/0953-8984/16/43/002

## Abstract

The spin–orbit-split L-gap surface states on Au(111) are investigated by means of spin- and angle-resolved photoelectron spectroscopy and relativistic first-principles calculations, the latter including both electronic structure and photoemission. The dispersion, momentum distribution and spin polarization of the surface states are consistent with those of a two-dimensional electron gas with Rashba–Bychkov spin–orbit coupling (SOC). The surface symmetry manifests itself in the spin-integrated photoemission intensities, thereby providing details of the orbital composition of the surface states. For the spin polarization, modulations which show up in theory are below the experimental detection limit of 5%. The dependence of both dispersion and spin polarization on the SOC strength are addressed theoretically. The combination of experiment and theory establishes a consistent picture of the L-gap surface states.

(Some figures in this article are in colour only in the electronic version)

## 1. Introduction

Spin–orbit-split electronic states are commonly realized by a two-dimensional electron gas (2DEG) in a semiconductor heterojunction. The structural asymmetry at the interface between the two semiconductors gives rise to the Rashba–Bychkov interaction [1, 2] which leads to both splitting and spin polarization of these free-electron-like states. Detailed investigations of the electronic structure were performed mainly by means of de Haas–van Alphen oscillations and by optical methods which are—compared to spin- and angle-resolved photoelectron spectroscopy—rather indirect spectroscopies.

Recently, it turned out that the Shockley surface states on the (111) surfaces of noble metals are paradigmatic realizations of spin–orbit-split electronic states, too [3, 4]. Located at a metal surface, these can be easily accessed by angle-resolved photoelectron spectroscopy, providing information on the dispersion and on the strength of the spin–orbit interaction [5, 6]. In particular for Au(111), spin–orbit coupling is strong enough for detecting the splitting even in spin-integrated photoelectron spectroscopy. The spin polarization of the L-gap surface states was first predicted by theory [6, 7] and later investigated experimentally [8, 9]. These studies focused mainly on the basic properties, such as the experimental demonstration of spin-polarized emission and the observation of the spin structure in reciprocal space. The purpose of the present paper is to explore details of the surface states by means of a joint experimental and theoretical investigation. We combine spin- and angle-resolved photoemission experiments, relativistic first-principles calculations and—based on the latter—photoemission calculations that form a direct link between the experimental spectra and the *ab initio* results.

The L-gap surface states can be simply described as free electrons, providing a connection to a two-dimensional electron gas. Looking more closely, however, deviations from the behaviour of an isotropic 2DEG show up [10], which are related to the symmetry of the Au(111) surface. The threefold rotational symmetry manifests itself in an azimuthal modulation of the spin polarization and of the photoemission intensity. A second effect is brought about by the corrugation of the surface potential which results in a small but non-zero spin-polarization component normal to the surface. The question arises of whether these effects which showed up in recent theoretical calculations [11] appear also in the present experiment, in particular in spin-resolved Fermi surface mapping [12].

Spin-integrated photoemission spectra in off-normal emission show a distinct intensity relation upon reversal of the detection azimuth. This ‘linear dichroism’ can be explained analytically on the basis of the orbital composition of the surface states which results from the surface symmetry and from spin–orbit coupling, supported by first-principles calculations.

To reach a conclusion from the experimental spin polarization of the photoelectron on that of the L-gap surface states could—in principle—be difficult because the photoemission process itself produces spin-polarized electrons even from non-spin-polarized initial states, an effect of the spin–orbit interaction [13]. Therefore, one needs to link the photoemission experiments (i.e., the excited states) with *ab initio* calculations for the initial states. This connection is provided by photoemission calculations within the relativistic one-step model. The theoretical spectra depend sensitively on some of the free parameters which could be fixed by comparison of a few theoretical spectra with their experimental counterparts. The overall agreement of experimental and theoretical spectra establishes thus a consistent picture of the anatomy of the L-gap surface states.

The paper is organized as follows. Spin–orbit coupling at a metal surface is sketched in section 2, with mathematical details being provided in the appendix. Experimental and theoretical aspects are discussed in sections 3 and 4. Section 5 comprises the discussion of selected results. First, it focuses on spin-integrated data, namely on the dispersion and momentum distribution (section 5.1) and on ‘linear dichroism’ (section 5.2). The spin polarization is addressed for normal emission (section 5.3) and for angular scans in constant-initial-energy mode (section 5.4). Finally, the effect of spin–orbit coupling on the surface states is discussed theoretically (section 5.5).

## 2. Spin–orbit coupling at a metal surface

Spin–orbit coupling (SOC) at a metal surface with free-electron-like surface states shows a close analogy to that in a two-dimensional electron gas, as was established recently for the

(111) surfaces of noble metals [7, 14]. The main ideas and results will be briefly repeated in the following.

Spin–orbit coupling is strong where the crystal potential changes rapidly. This is in particular the case for heavy atoms—such as Au—close to the atomic nucleus. A second contribution is attributed to the presence of the surface. The latter breaks the symmetry of the bulk system, for example the inversion symmetry or the mirror symmetry with respect to the surface-parallel layers. Hence, the surface potential barrier can be regarded as a structural asymmetry which results in additional SOC, in analogy to the Rashba–Bychkov effect in 2DEGs [2] and the Dresselhaus effect in bulk systems without inversion symmetry [15]. To be more specific: a 2DEG is confined to the interface between two different semiconductors (say, GaAs and GaAlAs). A free-electron-like surface state at the (111) surface of a noble metal is asymmetrically confined to the surface region: towards the interior of the solid by the bulk band gap, towards the vacuum by the surface barrier. The strength of the 'atomic' SOC exceeds that of the surface contribution, as was argued by Mugarza *et al* [16].

The free-electron nature of the surface states lends support to a description in terms of plane waves (see the appendix), with the advantage that the atomic contribution to the SOC need not be considered explicitly. In a 2DEG with Rashba–Bychkov SOC, Kramers' degeneracy is lifted and the eigenstates are split in energy,

$$E_{\pm}(\boldsymbol{k}_{\|}) = \tfrac{1}{2}\boldsymbol{k}_{\|}^{2} \pm \gamma|\boldsymbol{k}_{\|}|, \tag{1}$$

with $\boldsymbol{k}_{\|} = (k_x, k_y)$. The momentum distribution consists of two concentric circles separated by $\approx 2\gamma$. The quantity $\gamma$ reflects the strength of the structural asymmetry which for Au(111) is 3–5 times larger than in typical semiconductor 2DEGs [14]. Its sign determines which state is the 'inner' one ('+' for $\gamma > 0$, '$-$' for $\gamma < 0$) and which is the 'outer' one ('$-$' for $\gamma > 0$, '+' for $\gamma < 0$).

Associated with the above splitting is a complete spin polarization $\boldsymbol{P}_{\pm}$ of the electronic states which is within the $xy$-plane and perpendicular to the in-plane wavevector $\boldsymbol{k}_{\|} = |\boldsymbol{k}_{\|}|(\cos\varphi_{\mathrm{e}}, \sin\varphi_{\mathrm{e}})$,

$$P_{\pm}^{x}(\boldsymbol{k}_{\|}) = \alpha_{\pm}\sin\varphi_{\mathrm{e}}, \qquad P_{\pm}^{y}(\boldsymbol{k}_{\|}) = -\alpha_{\pm}\cos\varphi_{\mathrm{e}}, \qquad P_{\pm}^{z}(\boldsymbol{k}_{\|}) = 0, \tag{2}$$

with $\alpha_{\pm} = \mp 1$ (compare (A.7)). For the discussion, it is advantageous to decompose $\boldsymbol{P}_{\pm}$ into radial and tangential components,

$$P_{\pm}^{\mathrm{rad}} = P_{\pm}^{x}\cos\varphi_{\mathrm{e}} + P_{\pm}^{y}\sin\varphi_{\mathrm{e}}, \qquad P_{\pm}^{\mathrm{tan}} = P_{\pm}^{x}\sin\varphi_{\mathrm{e}} - P_{\pm}^{y}\cos\varphi_{\mathrm{e}}. \tag{3}$$

The spin polarization of the + ($-$) surface state rotates anticlockwise (clockwise) about the $z$-axis, that is, $P_{\pm}^{\mathrm{rad}} = 0$ and $P_{\pm}^{\mathrm{tan}} = \mp 1$. By measuring $P_{\pm}^{\mathrm{tan}}$ for the two surface states, the inner surface state can be associated either with the + or with the $-$ state and analogously for the outer surface state. By this means, one can reach a conclusion as regards the sign of $\gamma$ which is *a priori* not known.

For Au(111), the $x$- and $y$-axes of the coordinate system were chosen along the crystallographic $[1\bar{1}0]$ and $[\bar{1}\bar{1}2]$ directions, respectively, with the $z$-axis pointing along the surface normal (towards the vacuum). Hence, the $yz$-plane is a mirror plane of the crystal (figure 1). In reciprocal space, the $k_x$-axis is along the $\overline{\mathrm{K}}$–$\overline{\Gamma}$–$\overline{\mathrm{K}}$ direction of the two-dimensional Brillouin zone (2BZ), whereas the $k_y$-axis is along $\overline{\mathrm{M}}$–$\overline{\Gamma}$–$\overline{\mathrm{M}}$.

The Au(111) surface shows a threefold rotational symmetry which allows in principle for a non-zero $P_{\pm}^{z}$ as well as for a deviation from the circular momentum distribution. It turned out that the latter is negligible, suggesting expanding $\boldsymbol{P}_{\pm}$ in terms of $\varphi_{\mathrm{e}}$. The leading terms of $P_{\pm}^{x}$ and $P_{\pm}^{y}$ remain as in (2), but $P_{\pm}^{z}$ turns into

$$P_{\pm}^{z}(\boldsymbol{k}_{\|}) = \beta_{\pm}\cos 3\varphi_{\mathrm{e}}. \tag{4}$$

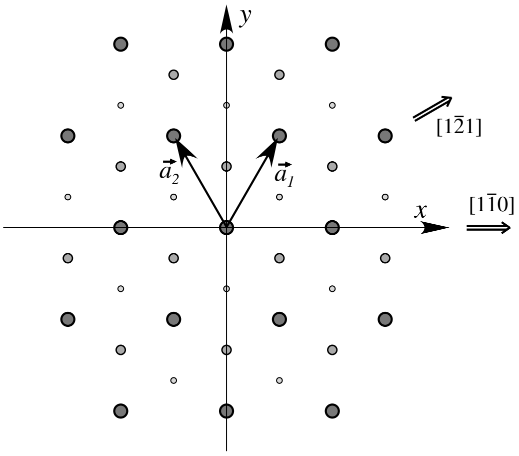

**Figure 1.** The atomic arrangement of the Au(111) surface, represented by the three outermost layers (large dots: first layer; medium-sized: second layer; small: third layer). The basis vectors $\boldsymbol{a}_1$ and $\boldsymbol{a}_2$ span the hexagonal layer lattice. The $[1\bar{2}1]$ ($\bar{\Gamma}$–$\bar{\mathrm{M}}$ in reciprocal space) and $[1\bar{1}0]$ ($\bar{\Gamma}$–$\bar{\mathrm{K}}$) crystallographic directions are indicated.

The presence of a non-zero $P^z_\pm$ requires non-vanishing in-plane components of the potential gradient (compare (A.1)). Thus, $P^z_\pm$ is brought about by the surface corrugation, i.e., the in-plane asymmetry of the surface potential and, hence, is expected to be small ($|\beta_\pm| \ll 1$). A non-zero $P^z_\pm$ is accompanied by a non-complete in-plane spin polarization ($|\alpha_\pm| < 1$).

The mirror $yz$-plane of the system forces the spin polarization $\boldsymbol{P}_\pm$ of the L-gap surface states along $x$ for $\varphi_\mathrm{e} = 90°$ ((2) and (4)). Note that the system remains non-magnetic since time-reversal symmetry dictates $\boldsymbol{P}_\pm(\boldsymbol{k}_\|) = -\boldsymbol{P}_\pm(-\boldsymbol{k}_\|)$.

## 3. Experimental aspects

Spin-integrated and spin-resolved photoelectron spectroscopy measurements were performed using the photoemission instrument `COPHEE` [12] at the surface and interface spectroscopy beamline (SIS) at the Swiss synchrotron light source. `COPHEE`, the `CO`mplete `PH`oto`E`mission Experiment is equipped with a three-dimensional polarimeter. The sample is mounted on a two-axis goniometer, in order to allow performance of angle-scanned experiments. For all results presented in this paper, the light source was set to a photon energy of $h\nu = 21.1$ eV with linear p polarization. The angle between the photon incidence and the emission directions was kept fixed at $\alpha = 45°$ (figure 2).

The sample was cleaned by many repeated cycles of Ar-ion bombardment and annealing. During the experiments it was cooled to approximately 150 K. The sample quality remained unchanged over at least half a day, as judged from the photoemission linewidth of the surface states at normal emission. An account of the experimental spectra is given in [8] and the measured spin structure is discussed in [9].

To be more specific, the schematic set-up of the experiment is shown in figure 2. The sample can be rotated about the polar rotation axis in the surface plane and the azimuthal axis normal to the surface. Two Mott detectors (MDs) are mounted in such a way that both of them can measure the longitudinal polarization component $P^z_\mathrm{MD}$ along the photoemission direction. The other sensitive axes $P^x_\mathrm{MD}$ and $P^y_\mathrm{MD}$ of each MD are inclined at ±45° with respect to the polar rotation axis. To measure the surface-state electrons, the sample was rotated by small

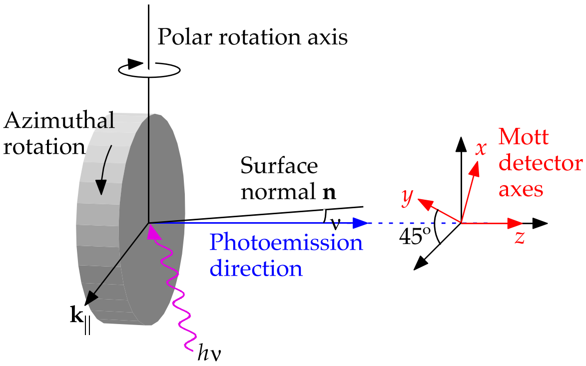

**Figure 2.** The set-up of the photoemission experiment. The sample (grey) can be rotated about two axes. The surface normal $\boldsymbol{n}$ lies within the scattering plane, the latter spanned by the light incidence direction and the detection direction (indicated in addition by $\boldsymbol{k}_\parallel$). The local coordinate system of the Mott detector (MD (red)) comprises the $z$-axis along the detection direction and the $x$- and $y$-axes which are at 45° with respect to the polar rotation axis.

polar angles of up to $\theta = 7°$ and, thus, $P^z_{\mathrm{MD}}$ corresponds well to the out-of-plane polarization component (along the surface normal), while $P^{\mathrm{tan}}$ and $P^{\mathrm{rad}}$ are measured as 45° projections onto the $P^x_{\mathrm{MD}}$- and $P^y_{\mathrm{MD}}$-axes. All spin-resolved data were acquired using just one of the Mott detectors and the direction of the spin-polarization vector was cross-checked for a sufficiently large number of scans with the other detector. The 45° projection was taken into account for the analysis of the in-plane polarization component ($P^{\mathrm{tan}} = \sqrt{2}\, P^y_{\mathrm{MD}}$).

Conventional spin-integrated photoemission spectra and Fermi surface maps were taken using the channeltron detector mounted in a standard geometry in the hemispherical electron analyser. The resolution of the spectrometer was better than 20 meV in energy and 0.5° FWHM in angle for these data sets. Spin-resolved data were acquired both as energy distribution and as angular distribution scans, the latter translating into curves for $\boldsymbol{k}_\parallel$ momentum distribution. In both cases, the energy and angular resolutions of the spectrometer were relaxed to 120 meV and 1.8° FWHM, respectively.

The measurement of spin-resolved spectra from a non-magnetic sample imposes two specific requirements on the data analysis.

(i) The lack of a macroscopically defined magnetization direction—as is present in a magnetic sample—implies that a natural and unique spin-quantization axis for *all* measurement geometries is missing. Instead, the spin-quantization axis depends on the azimuth of electron motion, as given by $\boldsymbol{k}_\parallel$ (section 2). In the rotating-sample geometry of the `COPHEE` experiment, the tangential ($P^{\mathrm{tan}}$) and the normal ($P^z$) spin-polarization components are naturally projected onto the sensitive axes of the MDs.

(ii) In a conventional experiment on a magnetic sample, a systematic offset of the spin-resolved intensities—due to the residual intrinsic detection asymmetry of the MDs—can be cancelled out by reversing the magnetization direction. This procedure, however, cannot be carried out in the case of a non-magnetic sample because there is no net magnetization to reverse. It is thus necessary to deduce the instrumental detection asymmetry from the data themselves, relying on very fundamental assumptions (e.g., time-reversal symmetry). For Au(111), an angular scan across the normal-emission direction which covers both positive and negative polar angles $\vartheta_e$ is equivalent to reversing the spin of the initial states (if the theoretical model in section 2 is correct). To get rid of the asymmetry, the sensitivity of one of the detector channels in each detector pair in the polarimeter is adjusted until a well-balanced result was obtained for a complete data set, including angular scans across the surface normal [8]. This procedure is *a posteriori* corroborated by comparison with the theoretical photoemission intensities.

The error margin of the spin-polarization measurements is dominated by the statistical error of counting the electrons in the detectors. An additional systematic uncertainty is imposed by the procedure for removing the instrumental detector asymmetry. The total detection limit for the spin polarization at intensity maxima is approximately $\Delta P = \pm 5\%$ (degree of polarization).

The in-plane wavevector $\boldsymbol{k}_{\|}$ is determined by the kinetic energy $E_{\mathrm{kin}}$ of the photoelectrons and the detection angles $\vartheta_{\mathrm{e}}$ and $\varphi_{\mathrm{e}}$, the latter taken with respect to the $z$-axis (surface normal) and the $x$-axis (figure 1),

$$\boldsymbol{k}_{\|} = \sqrt{2E_{\mathrm{kin}}} \begin{pmatrix} \cos\varphi_{\mathrm{e}} \\ \sin\varphi_{\mathrm{e}} \end{pmatrix} \sin\vartheta_{\mathrm{e}}. \tag{5}$$

## 4. Theoretical aspects

### *4.1. Ab initio calculations*

The electronic structure of Au(111) was computed within the local spin-density approximation (LSDA) to density-functional theory (DFT), using the Perdew–Wang exchange–correlation potential [17]. The electronic structure of the $1 \times 1$ surface was calculated self-consistently by the Korringa–Kohn–Rostoker (KKR) method, with the muffin-tin potentials of the six outermost surface layers and of the three adjacent vacuum layers (with so-called empty muffin-tin spheres) allowed to differ from the bulk potential. A comparison of the potential of the sixth surface layer with that of the bulk showed no significant difference, implying that the surface region is sufficiently large for a correct description of the surface states.

The potential in the vacuum region required particular attention. Using the fcc parent lattice of the bulk also in the vacuum layers resulted in too low a binding energy of the L-gap surface states, indicating too steep a surface barrier. While there is no reason which forces one to use the parent lattice in vacuum (because of the missing ionic core potentials), the interlayer distance for the vacuum layers in the self-consistent calculations was deliberately increased. An increase by 4% with respect to the bulk interlayer distance resulted in good agreement with the experimentally obtained surface-state binding energies (0.51 eV compared to 0.49 eV [6] at $\overline{\Gamma}$). This relaxation is further corroborated by the work function, which is too high for the fcc case (5.97 eV) but agrees nicely for the relaxed case (5.23 eV) with experimental data (5.31 eV [18]).

The Au(111) surface shows a $22 \times \sqrt{3}$ reconstruction (the so-called herringbone reconstruction [19, 20]), which mainly leads to surface *umklapp* processes and, hence, affects slightly the photoemission intensities [21]. Since Fourier transform scanning tunnelling spectroscopy showed no effect of the reconstruction and reveals the L-gap surface states of the $1 \times 1$ unit cell, the latter was exclusively considered in theory.

The effect of SOC on the electronic structure was addressed by interpolating between the relativistic (Dirac equation) and the scalar-relativistic case [22, 23]. This allowed us to manipulate SOC while keeping the other relativistic effects, a method which is superior to the usual scaling of the speed of light $c$. Even a 'super-relativistic' case could be investigated, by artificially enhancing the SOC (section 5.5).

The electron density at the surface is significantly changed with respect to that in the bulk. In particular, its gradient can be become considerable. Therefore, the LSDA might be not sufficient and gradient corrections—such as the generalized gradient approximation (GGA)—might be in order. However, it turned out that the GGA is not without problems [24]. Although the GGA gives in general good total energies, it leads to an unphysical charge accumulation close to a classical turning point of the potential. The surface barrier imposes such a classical turning point and, thus, a LSDA exchange–correlation potential [17] was used in the present investigation.

### *4.2. Photoemission calculations*

Besides the electronic structure, spin- and angle-resolved photoemission intensities were calculated within the relativistic one-step model, formulated in a layer KKR manner [25, 26]. The possibility of directly comparing experimental and theoretical results is of particular importance for systems with strong SOC. Since SOC can lead to spin-polarized photocurrents even from non-spin-polarized initial states [13], one should be aware that the spin polarization of photoelectrons excited from a spin-polarized L-gap surface state could differ from that of the respective initial state. In this context, it appears worth noting that the photoemission calculations rely on the same *ab initio* potentials as the electronic structure calculations for the ground-state properties (section 4.1) and take into account SOC via the Dirac equation.

The *ab initio* calculations provide the ground-state properties of the system, whereas photoemission deals with an excited system. The associated many-body effects could be accounted for by the self-energy $\Sigma$. The latter can in principle be obtained from first principles, e.g., within the $GW$ approximation [27], but these computations are very demanding—especially for surfaces—and are beyond the scope of the present paper. Instead, one typically approximates $\Sigma$ by an energy-dependent but homogeneous optical potential $V_{\mathrm{opt}}(E)$ which is added to the energy $E$. The real part of $V_{\mathrm{opt}}$ shifts the energies of the electronic states; its imaginary part accounts for the finite lifetimes of the quasi-particles, i.e., for both the photohole ($E < E_{\mathrm{F}}$) and the photoelectron ($E > E_{\mathrm{F}}$). In contrast to the case in a previous publication [14], the actual values of $V_{\mathrm{opt}}$ could now be determined by comparing theoretical with experimental spectra. Here, the focus lay in particular on the intensity relations of the 'inner' and the 'outer' surface state for opposite detection azimuths $\varphi_{\mathrm{e}}$. This allowed a unique determination of $V_{\mathrm{opt}}$ for the photoelectrons. It turned out that just in the experimental kinetic energy range (around 16 eV for 21.1 eV photon energy), several comparably flat bands exist in the unoccupied band structure, beside a free-electron-like band. These are shifted in energy by $\mathrm{Re}(V_{\mathrm{opt}})$ and affect the final state of photoemission (i.e., the time-reversed LEED state), therefore explaining the strong dependence of the theoretical intensities on the optical potential. For 21.1 eV photon energy, $V_{\mathrm{opt}} = (0 - 0.06\mathrm{i})$ eV and $V_{\mathrm{opt}} = (-1.5 - 2.4\mathrm{i})$ eV were taken for the initial states (photoholes) and for the final states (photoelectrons), respectively.

Other free parameters in the photoemission calculations were fixed by convergence tests (see [26] for details on layer KKR and photoemission approaches). For example, 30 atomic layers contributed to the photocurrent, the maximum angular momentum in the expansion of the scattering solutions was $l_{\mathrm{max}} = 4$ and the number of plane waves in the interlayer scattering was about 60.

The electric field $\boldsymbol{A}$ of the incident light was treated within the framework of Fresnel's theory. Thus, taking $\boldsymbol{A}$ constant inside the solid, in particular at the surface, gradient corrections to the photoemission matrix elements are neglected [25]. To support this procedure we note that Fresnel's theory proved to be successful in describing experimental photoemission from Fe(110) [28]. Second, going beyond Fresnel's theory did not significantly improve theoretical spectra for metal surfaces [29].

### 4.3. *Definitions of spin polarization*

In the discussion of various aspects of spin polarization, attention has to be directed briefly to its definition [30, 31]. The spin polarization $P_N$ of the initial states is defined in terms of the spin-resolved spectral density $N(E, \boldsymbol{k}_\parallel)$, namely

$$P_N(E, \boldsymbol{k}_\parallel) = \frac{N_\uparrow(E, \boldsymbol{k}_\parallel) - N_\downarrow(E, \boldsymbol{k}_\parallel)}{N_\uparrow(E, \boldsymbol{k}_\parallel) + N_\downarrow(E, \boldsymbol{k}_\parallel)}, \tag{6}$$

where the spin orientations ↑ and ↓ refer to a chosen spin-quantization axis (compare section 2). This is an intrinsic spin polarization which is independent of any measurement and can be calculated from first principles. The spin polarization $P_I$ of the photoelectrons, however, relies on the particular set-up which is used in the experiment (e.g., detection direction, light incidence direction and polarization, photon energy). It is defined by the spin-resolved photocurrent $I(E_{\text{kin}}, \boldsymbol{k}_\parallel)$ obtained for this specific set-up,

$$P_I(E_{\text{kin}}, \boldsymbol{k}_\parallel) = \frac{I_\uparrow(E_{\text{kin}}, \boldsymbol{k}_\parallel) - I_\downarrow(E_{\text{kin}}, \boldsymbol{k}_\parallel)}{I_\uparrow(E_{\text{kin}}, \boldsymbol{k}_\parallel) + I_\downarrow(E_{\text{kin}}, \boldsymbol{k}_\parallel)}. \tag{7}$$

It is *prima vista* not obvious how closely $P_N$ and $P_I$ are connected. Their relation is provided by photoemission theory, in particular by numerical photoemission calculations. Sometimes we do not explicitly distinguish between $P_N$ and $P_I$ because it should be clear from the context what definition is meant.

## 5. Discussion and results

In the following, our experimental and theoretical results are presented. After the discussion of the dispersion of the L-gap surface states (section 5.1), their intensity variation with polar angle of detection is addressed (section 5.2). Subsequently, the focus lies on the spin polarization, in particular for normal emission (section 5.3) and for off-normal emission (section 5.4). The effects of SOC strength and of the surface potential corrugation are addressed theoretically in section 5.5.

### 5.1. *Dispersion and momentum distribution*

A first check of whether the free-electron model and the first-principles calculations describe the experiment appropriately is provided by the comparison of the dispersion relations $E_\pm(\boldsymbol{k})$ and of the momentum distributions. Inspection of figure 3 shows that the L-gap surface states do indeed behave almost like free electrons with Rashba–Bychkov spin–orbit interaction. In both the experimental dispersion and the momentum distribution (figures 3(c) and (d)) obtained from the spin-integrated measurements, the splitting in energy and in $\boldsymbol{k}_\parallel$ is clearly seen.

Parabolic fits to the peak positions in the experimental energy distribution curves and in the theoretical spectral densities gave binding energies of 0.47 eV (experiment) and 0.51 eV (theory) at $\boldsymbol{k}_\parallel = 0$. An effective mass of $m^\star = 0.25\ m_{\text{e}}$ in experiment indicates that the dispersion is too strong in theory, the latter showing $m^\star = 0.20\ m_{\text{e}}$. This is also evident from the Fermi wavenumbers $k_{\text{F}}$ which read 0.160 and 0.186 $\text{Å}^{-1}$ in experiment (figures 3(c) and (d)) and 0.149 and 0.172 $\text{Å}^{-1}$ in theory (figures 3(a) and (b)).

The SOC strength $\gamma$ shows up as a splitting $\Delta k_\parallel$ (compare (1)). The experimental $\Delta k_\parallel$ of 0.026 $\text{Å}^{-1}$ agrees well with 0.023 $\text{Å}^{-1}$ from theory. The former corresponds to $\gamma = 396$ meV Å, which is about 3–5 times larger than for 2DEGs in semiconductor heterojunctions [14].

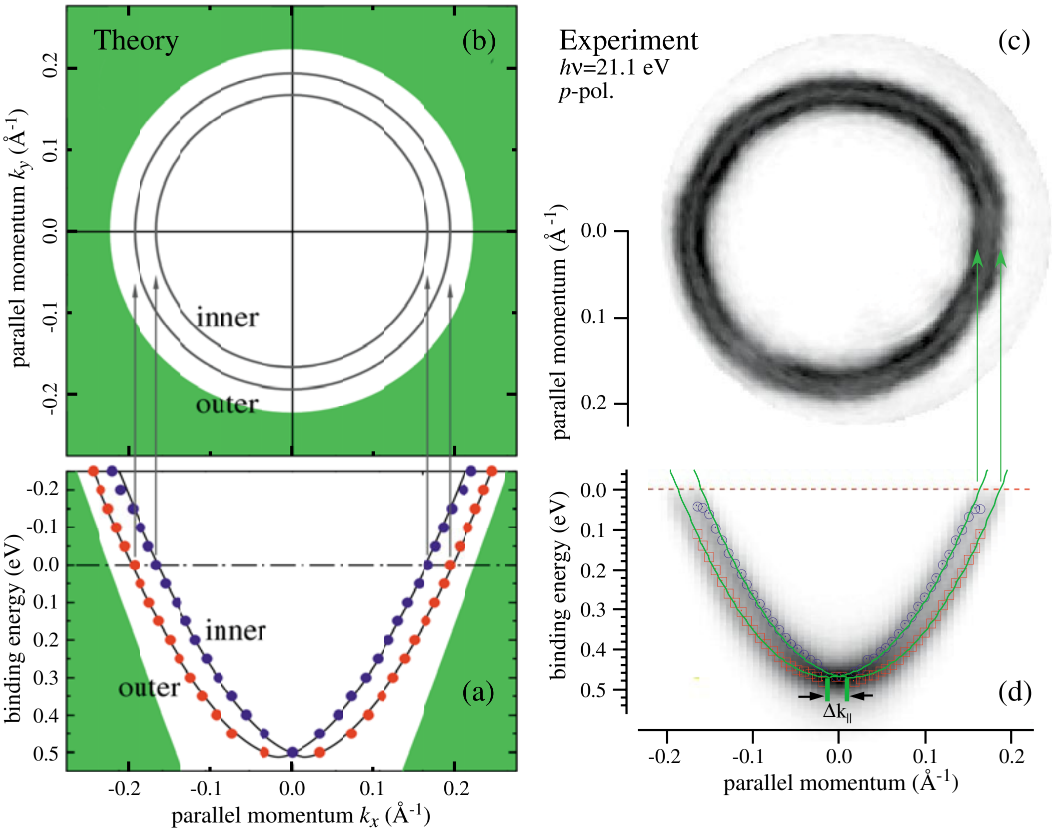

**Figure 3.** Spin–orbit splitting of the L-gap surfaces states on Au(111). (a) The dispersion along $k_x$ of the inner (black (blue) circles) and the outer (grey (red) circles) surface state, as obtained from the first-principles calculations. The region of bulk bands is shaded in grey (green). (b) The theoretical momentum distribution of the surface states at the Fermi energy $E_F$. (c) The experimental Fermi surface map, as obtained from the spin-integrated photoemission intensities. (d) The experimental dispersion map in an arbitrary azimuth. The peak positions as determined from peak fitting to the energy distribution curves are indicated by circles (red and blue) and parabolic fits to these positions are shown by solid lines (green). In both experimental panels, the measured intensity is shown on a linear scale, with black corresponding to the largest intensity.

### *5.2. Variation of the photoemission intensity with the polar angle of emission*

Considering solely the dispersion does not provide detailed information on the surface-state wavefunctions. The latter can be probed by analysing the angular dependence of the photoemission intensities, an approach which already proved to be successful in determining the orbital composition of the dangling-bond surface state on GaAs(110) [32].

The angular dependence of the spin-integrated intensities is exemplified for three polar angles of emission: $\vartheta = 0°$ (normal emission, $\boldsymbol{k}_\parallel = 0$) and $\pm 3.6°$ (off-normal emission at $|\boldsymbol{k}_\parallel| = \pm 0.135$ Å$^{-1}$). For $\vartheta = 0°$, the measured surface states are degenerate ($E_{\mathrm{outer}}(0) = E_{\mathrm{inner}}(0)$) and produce the sharp maximum at 0.47 eV binding energy (solid in figure 4(b)). For off-normal emission, this peak is split into two maxima with significantly less intensity: the outer surface state shows a binding energy of about 0.22 eV, the inner, one of about 0.12 eV ($E_{\mathrm{outer}}(\boldsymbol{k}_\parallel) < E_{\mathrm{inner}}(\boldsymbol{k}_\parallel)$). The most striking fact, however, is the intensity variation at the peak positions upon reversal of $\vartheta$. The intensity $I_{\mathrm{outer}}$ of the outer surface state increases when turning $\vartheta = -3.6°$ (dashed (purple) in figure 4(b)) to +3.6° (solid (green)),

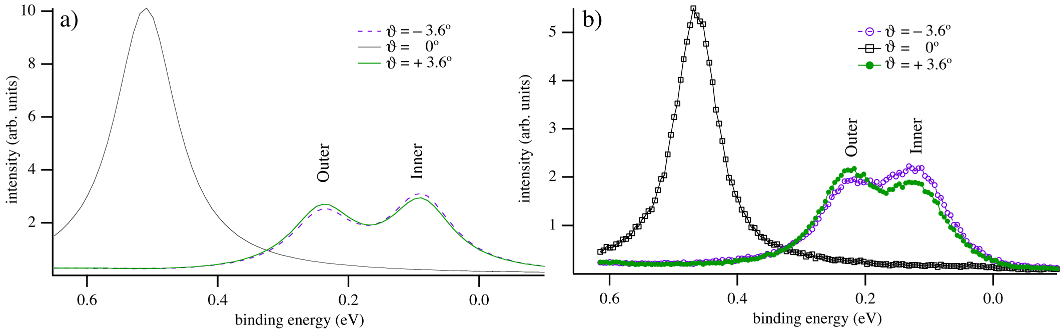

**Figure 4.** Spin-integrated intensities for different polar angles of detection (as indicated) in the $\varphi = 75°$ azimuth (compare figure 1). (a) Theoretical energy distribution curves. (b) Measured spectra from the data set shown in figure 3.

whereas the intensity $I_{\text{inner}}$ of the inner one shows the opposite behaviour. Note further that the intensity differences are of about the same amount, $\Delta I$. With the definitions $\boldsymbol{k} = (+\boldsymbol{k}_{\parallel}, k_{\perp})$ and $\tilde{\boldsymbol{k}} = (-\boldsymbol{k}_{\parallel}, k_{\perp})$, the experimental intensity relations can be simply cast as $I_{\text{outer}}(\boldsymbol{k}) = I_{\text{inner}}(\tilde{\boldsymbol{k}}) = \overline{I} + \Delta I$ and $I_{\text{outer}}(\tilde{\boldsymbol{k}}) = I_{\text{inner}}(\boldsymbol{k}) = \overline{I} - \Delta I$ (we note in passing that these relations hold also for other $\boldsymbol{k}_{\parallel}$). The theoretical photoemission intensities (figure 4(a)) agree reasonably well with the experimental ones, with differences being attributed to the surface-state dispersion and the SOC strength $\gamma$. The question arises of how these similarities and differences in behaviour can be explained.

At $\boldsymbol{k}_{\parallel} = 0$, the surface states belong to the $\Lambda_6$ representation of the double group $C_{3v}$ (in Schoenflies notation [33]), with the spatial part of the wavefunction belonging to the $\Lambda^1$ single-group representation. Thus, the surface states consist mainly of s, $p_z$ and $d_{z^2}$ orbitals, with relative spectral weights of 8.2%, 76.0% and 8.9%, respectively (as obtained from the first-principles calculations). Note that these orbitals are even under mirror operations of the surface. At $\boldsymbol{k}_{\parallel} \neq 0$ in an azimuth which lies not within a mirror plane of the surface (here: $\varphi_e = 75°$; compare figure 1), the wavefunctions achieve additional contributions from p orbitals oriented within the surface plane. For the polar angles in figure 4 these have relative spectral weights of up to about 23%.

Expressing the surface-state wavefunctions as $|e\rangle \pm |o\rangle$ (with energy $E_i$) and taking a single plane wave $|\boldsymbol{k}\rangle$ (with energy $E_f$) as the final state, the photoemission intensity $I(\boldsymbol{k})$ is given by Fermi's golden rule,

$$I_{\pm}(\boldsymbol{k}) \propto |\langle \boldsymbol{k}|\boldsymbol{A}\cdot\boldsymbol{\nabla}|e\rangle \pm \langle \boldsymbol{k}|\boldsymbol{A}\cdot\boldsymbol{\nabla}|o\rangle|^2\,\delta(h\nu - E_f - E_i). \tag{8}$$

Here, $\boldsymbol{A}$ is the electric field vector of the incident light. Simple manipulation yields $I_{\pm}(\boldsymbol{k}) = \overline{I}(\boldsymbol{k}) \pm \Delta I(\boldsymbol{k})$, with

$$\overline{I}(\boldsymbol{k}) \propto |\boldsymbol{A}\cdot\boldsymbol{k}|^2 \left(|\langle \boldsymbol{k}|e\rangle|^2 + |\langle \boldsymbol{k}|o\rangle|^2\right)\delta(h\nu - E_f - E_i), \tag{9$a$}$$

$$\Delta I(\boldsymbol{k}) \propto 2|\boldsymbol{A}\cdot\boldsymbol{k}|^2\,\mathrm{Re}(\langle \boldsymbol{k}|e\rangle\langle o|\boldsymbol{k}\rangle)\delta(h\nu - E_f - E_i). \tag{9$b$}$$

The even part $|e\rangle$ of the surface-state wavefunction comprises mainly s and $p_z$ orbitals and, hence, obeys $\langle \boldsymbol{k}|e\rangle = \langle \tilde{\boldsymbol{k}}|e\rangle$. The odd part $|o\rangle$, however, contains mainly p orbitals oriented along $\boldsymbol{k}_{\parallel}$ and shows $\langle \boldsymbol{k}|o\rangle = -\langle \tilde{\boldsymbol{k}}|o\rangle$. This establishes $\overline{I}(\tilde{\boldsymbol{k}}) = \overline{I}(\boldsymbol{k})$ and $\Delta I(\tilde{\boldsymbol{k}}) = -\Delta I(\boldsymbol{k})$, which yield immediately $I_{\pm}(\tilde{\boldsymbol{k}}) = I_{\mp}(\boldsymbol{k})$ (note that $\boldsymbol{A}\cdot\boldsymbol{k}$ is constant in the present experimental set-up (figure 2)).

Associating the inner and the outer surface-state wavefunctions with $|e\rangle \pm |o\rangle$, respectively, the intensity variation observed in figure 4 can be related to the interference term $\Delta I(\boldsymbol{k})$.

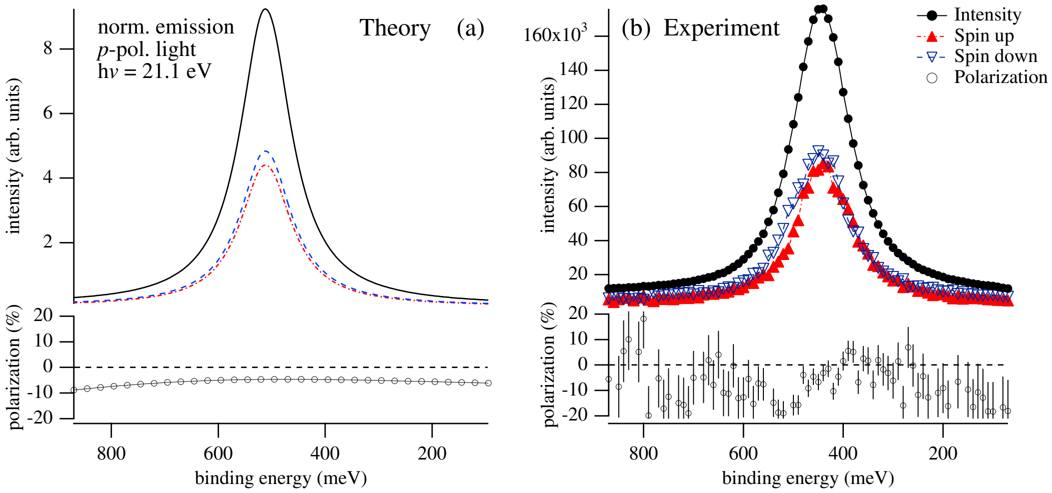

**Figure 5.** Spin-resolved normal photoemission from the L-gap surface states. (a) Theoretical intensities are obtained for p-polarized light incident within the $yz$-plane ($\overline{\Gamma}$–$\overline{\mathrm{M}}$ azimuth) and 21.1 eV photon energy. The total intensity (solid, black) is decomposed into spin up (dashed, blue) and spin down (dashed-dotted, red), with the spin-quantization axis along $x$. (b) The experimental spectrum at normal emission. The spin polarization is calculated from the $P^{\mathrm{rad}}$ component of the Mott detector.

Without this term, the two surface states would have the same intensity $\overline{I}(\boldsymbol{k})$ at a given $\boldsymbol{k}_{\parallel}$, as is the case to a good approximation (figure 4).

Summarizing, a comparison of the intensities of the inner and the outer surface state for $\boldsymbol{k}_{\parallel}$ and $-\boldsymbol{k}_{\parallel}$ mainly provides information on the orbital composition of their wavefunctions. The structure of the intensity, $I = \overline{I} \pm \Delta I$, is similar to those used to describe magnetic linear dichroism [34]. Therefore, one could term the above effect 'linear dichroism in angular distribution'. We note in passing that this dichroism cannot be explained within the free-electron model (see the appendix) and, therefore, can be attributed to the surface symmetry.

### *5.3. Spin-resolved normal photoemission*

As stated in section 4.3, the spin polarization of an initial state and of the related photoelectron may differ, depending on the chosen set-up (i.e., in-plane wavevector $\boldsymbol{k}_{\parallel}$ and energy $E$). One example where $\boldsymbol{P}_N$ and $\boldsymbol{P}_I$ deviate from each other is that of normal emission ($\boldsymbol{k}_{\parallel} = 0$). Here, the two surface states are degenerate (figure 3) and the net spin polarization $\boldsymbol{P}_N$ vanishes. By excitation with off-normally incident p-polarized light, the photoelectrons excited from the surface states can, however, be spin polarized, with $\boldsymbol{P}_I$ normal to the scattering plane (spanned by the surface normal and the incidence direction of the light) [35, 36]. For light incident within the mirror $yz$-plane, $P_I^x$ can be the only non-zero $\boldsymbol{P}_I$ component, which in systems with strong SOC can be as large as several tens per cent (e.g., for Pt). A considerable $P_I^x$ could therefore be expected for the Au surface states as well.

It turned out, however, that in the present experiments $P_I^x$ was rather small, i.e., close to the detection limit of about 5% (figure 5(b)). The photoemission calculations could only reproduce these findings when taking into account the real part of the optical potential $V_{\mathrm{opt}}$ that was fixed by reproducing the experimental intensity relations (sections 4.2 and 5.2). The theoretical normal-emission spectrum still shows a significant spin polarization (figure 5(a)), but $P_I^x$ is as small as 4.5% (in absolute value) at the peak position. Thus, experiment and theory are consistent with respect to both intensity and photoelectron spin polarization.

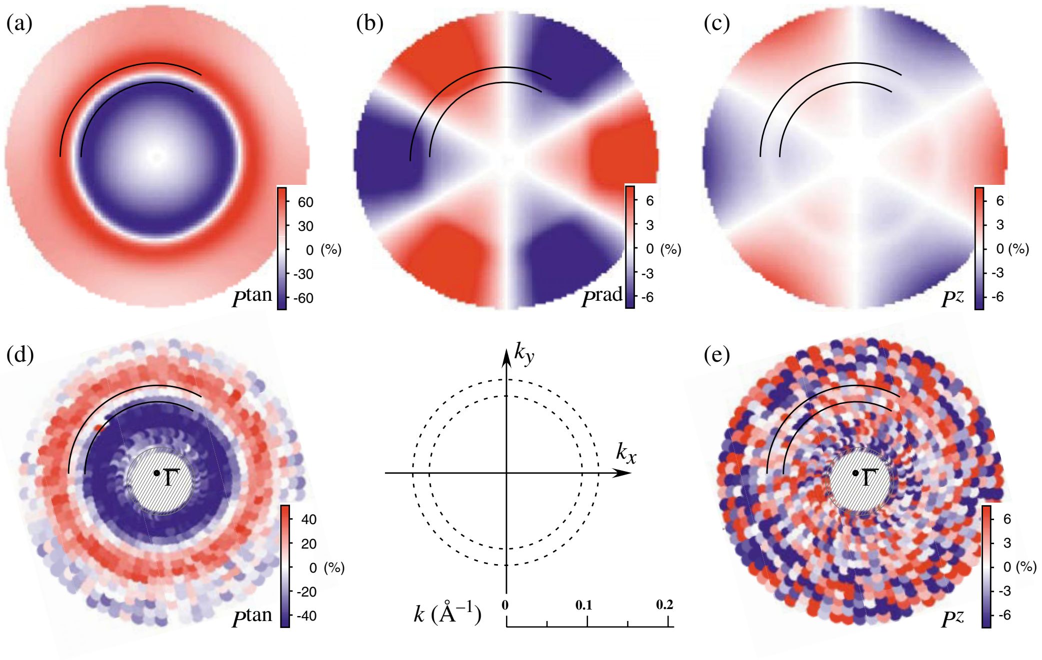

**Figure 6.** The spin polarization of the photocurrent in the angular distribution at 0.17 eV binding energy. Top row: the calculated polarization maps are decomposed into the tangential component $P^{\mathrm{tan}}$ (a), radial component $P^{\mathrm{rad}}$ (b) and normal component $P^{z}$ (c). The peak positions of the inner and outer surface states are indicated by black arcs in a part of the plots. Bottom row: the measured maps for $P^{\mathrm{tan}}$ as derived from $P^{x}_{\mathrm{MD}}$ (d) and $P^{z}$ (e) are shown for comparison. The $P^{\mathrm{rad}}$ map was not measured. Note the different colour scales for the various data sets.

### *5.4. Spin-resolved off-normal photoemission*

In order to investigate the spin polarization of the surface states, angle-scanned photoemission calculations and experiments were performed at a fixed binding energy (0.17 eV). The angular distributions of the three components $P_I^{\mathrm{tan}}$, $P_I^{\mathrm{rad}}$ and $P_I^{z}$ of the photoelectron spin polarization $\boldsymbol{P}_I$ are shown in figure 6.

The description of the L-gap surface states in terms of a 2DEG with Rashba–Bychkov SOC suggests reaching a conclusion from the tangential spin polarization $P_I^{\mathrm{tan}}$—measured for both the inner and the outer surface state—as regards the sign of the SOC strength $\gamma$ (section 2). In both experiment and theory, $P_I^{\mathrm{tan}}$ shows a circularly symmetric distribution, with the maximum spin polarization (in absolute value) showing up at the positions of the surface states (indicated by black arcs). Its central part is negative and its outer part is positive (colour coded as blue and red in figures 6(a) and (d)), hence implying that $\gamma > 0$. Since $\gamma$ is proportional to the $z$ derivative of the crystal potential ($\gamma \propto \partial_z V(z)$; see the appendix) and the maximum spectral weight of the surface states is in the outermost Au layer, the spin–orbit-induced splitting can be attributed to the surface barrier, the potential of which increases from the bulk towards the vacuum.

As was discussed for normal emission (section 5.3), the effect of spin–orbit coupling in the photoemission process itself is rather small in the chosen set-ups. Therefore, $\boldsymbol{P}_N$ and $\boldsymbol{P}_I$ did not differ significantly at $\boldsymbol{k}_{\parallel} = 0$. For off-normal emission, the theoretical $P_I^{\mathrm{tan}}$ is about $\pm 75\%$ at the surface states, which compares rather well with $P_N^{\mathrm{tan}}$ for the inner and the outer surface state ($-97\%$ and $93\%$ for $\alpha$). This agreement shows up also in $P^{z}$, for which the tiny $P_I^z$ is consistent with $\beta$ values of 1.4% and $-1.3\%$ for the inner and the outer surface state (compare (4)). The experimental counterparts for $P^{\tan}$ and $P^z$ are shown in figures 6(d) and (e). For the tangential component one finds a nice agreement with theory considering the ring structure of the spin polarization. The maximum values of $P^{\tan}$ are about 2/3 of those in theory due to the strong overlap of the peaks that appear broadened by the relaxed resolution and due to the contribution of an unpolarized background in the spectra (these effects are not included in the theoretical calculations). The observed degrees of polarization are consistent with the instrumental resolution. Summarizing, for off-normal emission one can also reach a conclusion—at least semi-quantitatively—from the spin polarization of the photoelectrons on that of the surface states.

Both the analytical theory (section 2) and the first-principles calculations allow for a modulation of the spin polarization $\boldsymbol{P}_N$ with azimuth $\varphi_e$ due to the threefold symmetry of the Au(111) surface, which should lead to a modulation in $\boldsymbol{P}_I$. Symmetry dictates that for emission within a mirror plane of the surface the radial component $P^{\text{rad}}$ vanishes (only $P^{\tan} \neq 0$ is permitted). This is clearly visible in the $\overline{\Gamma}$–$\overline{\text{K}}$ azimuth ($k_x = 0$) and its two equivalents, the latter being rotated about ±60°. The mirror symmetry implies further that $P^{\text{rad}}(90° - \varphi_e) = -P^{\text{rad}}(90° + \varphi_e)$, which turns positive into negative polarization and vice versa, under reflection at the $k_y$-axis (centre of figure 6(b)). Note that the magnitude of $P_I^{\text{rad}}$ becomes almost zero at the radii of the surface states, indicating a very small threefold modulation with the azimuth (point group $C_3$). For the normal component $P_I^z$ (figure 6(c)) the same symmetry considerations as for $P^{\text{rad}}$ hold. Compared to the $P_I^{\text{rad}}$ case, two rings of almost zero spin polarization at the radii of the surface states can be clearly observed. There is apparently no significant threefold modulation in $P_I^{\tan}$ for both experiment and theory.

Former photoemission calculations showed a threefold modulation of the spin polarization [14] which was considerably larger than that presented here. The improved agreement between theory and experiment results from fine-tuning the free parameters in photoemission theory, in particular the real part of the optical potential. The latter could be calculated from first principles within the $GW$ approximation [37]. Therefore, the Au(111) surface lends support to so demanding an investigation.

Focusing on the experimental $P^z$ (figure 6(e)), one finds no significant structure in the angular distribution within the noise. Taking into account the detection limit of about 5%, this finding is consistent with the theoretical results (figure 6(c)) because in the latter the spin polarization is less than this limit (in absolute value).

In summary, for the chosen set-up (p-polarized light with 21.1 eV photon energy) the photoelectron spin polarization $\boldsymbol{P}_I$ is tangentially aligned and no significant threefold modulation shows up (within the detection limit). Hence, it is fully consistent with the spin polarization $\boldsymbol{P}_N$ of the initial surface states, except as regards its degree. The latter is about ±96%, as obtained from first-principles calculations, considerably larger than that in the photoemission (about ±45% in experiment and ±75% in theory).

### *5.5. Effects of spin–orbit coupling and surface corrugation*

The effect of spin–orbit coupling on the spin polarization of the surface states is addressed theoretically. The different behaviours of inner and outer surface states can be elucidated by scaling the SOC strength $x$ in the Dirac Hamiltonian of the *ab initio* calculations (compare section 4.1). In the scalar-relativistic case ($x = 0$ in figure 7(a)), the splitting of the L-gap surface states vanishes, leading to $P_N^{\tan} = 0$ (figure 7(b)). The splitting increases with $x$, leaving the position (along the $k_y$-axis) of the inner state almost unaffected, while the outer is shifted to larger $k_y$. For $x = 0.5$, both states almost maintain their pure spin up and spin

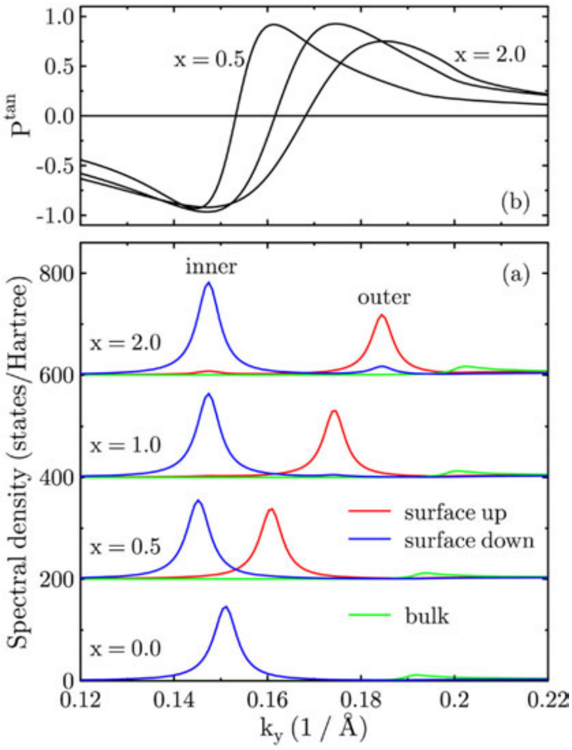

**Figure 7.** The effect of spin–orbit coupling on the L-gap surface states. (a) Spin-resolved spectral densities of the surface states (solid and dashed (blue and red)) at the outermost Au layer and of a bulk layer (dotted (green)) for SOC scaled from $x = 0$ (scalar-relativistic) via $x = 1$ (fully relativistic) to $x = 2.0$ ('super-relativistic'), as indicated on the left. The wavevector is along $\overline{\Gamma}$–$\overline{\text{M}}$ (along the $k_y$-axis); the energy is $E_\text{F}$. The offset between adjacent spectra is 200 states Hartree$^{-1}$. 'Surface up' and 'surface down' refer to $P_N^{\text{tan}} > 0$ and $P_N^{\text{tan}} < 0$, respectively. (b) The tangential spin polarization $P_N^{\text{tan}}$ of the L-gap surface states obtained from the data presented in (a).

down character, while for $x = 1$ (fully relativistic case) contributions to the spectral density of the other spin orientation become mixed in. This is particularly evident for the outer surface state where a significant spin down maximum (dashed (blue) in figure 7(a)) shows up. For the inner surface state, the admixture is considerably less. In the 'super-relativistic' case ($x = 2.0$) these opposite-spin contributions become even more pronounced, further reducing the spin polarization (in absolute value) as compared to the case $x = 1$ (figure 7(b)).

A reason for this difference between the inner and the outer surface state can be seen in spin-dependent scattering at bulk states (green in figure 7(a)). Because the outer surface state is closer in reciprocal space to the bulk states than the inner one, it might be more affected by spin–orbit-induced spin-flip scattering, as is corroborated from $P_N^{\text{tan}}$ (figure 7(b)). Note in this context that the two surface states are not strongly localized at the surface but show considerable spectral weight in the first ten surface layers [6, 14]. Further, the $k_y$ distance between the outer surface state and the bulk states decreases with increasing $x$. Accompanied with the reduction of the spin polarization of the outer surface state, compared to that of the inner, is an increased modulation of $\boldsymbol{P}$ with $\varphi_\text{e}$, as is evident from figures 6(a)–(c). This finding is consistent with the smaller degree of modulation in the experimental momentum distribution: the experimental $\boldsymbol{k}$ distance between the outer surface state and the bulk states of 0.044 Å$^{-1}$ (compare figure 2 in [6]) is larger than in theory (0.026 Å$^{-1}$ for $x = 1$). To summarize, the different locations of the surface states in reciprocal space manifest themselves in deviations from the 2DEG behaviour. The inner surface state behaves more like a free-electron state; the outer is slightly more influenced by bulk states. In order to test the proposed explanation, one could investigate the spin polarization of the surface states on different vicinal Au(111) surfaces, thereby changing the $\boldsymbol{k}$ distance to the bulk states.

In order to test the effect of corrugation on the spin polarization of the L-gap surface states, the surface barrier built with the muffin-tin potentials was replaced by a smooth *uncorrugated* barrier shape [32]. The parameters of the latter were obtained by fitting the dispersions of the L-gap surface states to those for the *corrugated* muffin-tin barrier. Since dispersions and binding energies agreed very well for the two surface barriers, one could switch the surface corrugation on and off without affecting relevant parts of the electronic structure. The corrugation manifests itself particularly in a non-zero $P_N^z$ (section 2). At the Fermi energy for $\boldsymbol{k}_\parallel$ along $\overline{\Gamma}$–$\overline{\mathrm{K}}$, one obtains from the spectral density for the corrugated surface +1.45% for the inner and −1.32% for the outer surface state. For the uncorrugated surface, $P_N^z$ is slightly reduced (in absolute value) to +0.99% and −0.88%, respectively. This humble change in $P_N^z$ is explained by the considerable extension of the surface-state wavefunction within the ten outermost surface layers. Hence, only a small part of it is affected by the surface barrier potential, which, however, is sufficiently large to produce an observable spin–orbit splitting.

## 6. Concluding remarks

The present joint investigation on the L-gap surface states on Au(111) provides details of their anatomy. The spin- and angle-resolved photoemission experiments agree qualitatively and semi-quantitatively with first-principles calculations, being directly linked by numerical photoemission calculations.

One could think of several extensions of the present work. First, one could deal with a modification of the electronic structure at vicinal Au(111) surfaces. The surface states would propagate freely along the terraces but could be confined to directions perpendicular to the steps. Thus, the two-dimensional surface states become one-dimensional [38, 39]. The step-induced umklapp processes would lower the binding energy and would also lead to smaller lifetimes due to increased scattering at bulk states. As was evidenced in section 5.5, this could have a pronounced effect on both degree and direction of the surface-state spin polarization. Second, one could investigate the modification of the surface states upon adding magnetic atoms onto Au(111). Here, the electronic structure of the 2DEG is subject to spin-dependent scattering at the magnetic impurities. And lastly, one could compute the self-energy within the $GW$ approximation, in order to compare it with the optical potential deduced here from the comparison of experimental with theoretical photoemission spectra (section 4.2).

## Acknowledgments

This work was performed at the Swiss Light Source, Paul-Scherrer-Institut, Villigen, Switzerland. It was supported by the Swiss National Science Foundation. We wish to thank V N Petrov, M Hengsberger, M Muntwiler, T Greber, L Patthey, M Shi and M Falub for assistance with the experiments.

## Appendix. Two-dimensional electron gas with Rashba–Bychkov spin–orbit interaction

The non-relativistic Hamilton operator for electrons with spin–orbit interaction is given by [40, 41]

$$H = \frac{1}{2}\boldsymbol{p}^2 + V(\boldsymbol{r}) + \frac{1}{2c^2}\boldsymbol{\sigma} \cdot [\boldsymbol{\nabla} V(\boldsymbol{r}) \times \boldsymbol{p}], \tag{A.1}$$

with $\boldsymbol{\sigma}$ the vector of Pauli matrices and $\boldsymbol{p} = -\mathrm{i}\boldsymbol{\nabla}$ the momentum operator (in Hartree atomic units, $e = m = \hbar = 1, c \approx 137$). In order to form a two-dimensional electron gas (2DEG), the potential $V$ has to confine the electrons to a plane (say $z = 0$) and allow for free motion within that plane (i.e., $V = V(z)$). Assuming without loss of generality $V(0) = 0$, the Hamiltonian for the 2DEG then reads

$$H = -\frac{1}{2}(\partial_x^2 + \partial_y^2) + \mathrm{i}\frac{\partial_z V(z)|_{z=0}}{2c^2}\left(\sigma_x \partial_y - \sigma_y \partial_x\right). \tag{A.2}$$

The ansatz $\psi_{\boldsymbol{k}}$ for the eigenfunctions consists of a plane-wave spinor,

$$\psi_{\boldsymbol{k}}(\boldsymbol{r}) = (\mu_{\boldsymbol{k}}\chi^+ + \nu_{\boldsymbol{k}}\chi^-)\mathrm{e}^{\mathrm{i}(k_x x + k_y y)}, \tag{A.3}$$

with $\boldsymbol{k} = (k_x, k_y)$ and $\boldsymbol{r} = (x, y)$. The Pauli spinors $\chi^\pm$ are quantized with respect to the $z$-axis ($\sigma_z\chi^\pm = \pm\chi^\pm$). With $\sigma_x\chi^\pm = \chi^\mp$ and $\sigma_y\chi^\pm = \pm\mathrm{i}\chi^\mp$, the Schrödinger equation $H\psi_{\boldsymbol{k}} = E(\boldsymbol{k})\psi_{\boldsymbol{k}}$ yields the condition

$$(k_y + \mathrm{i}k_x)\nu_{\boldsymbol{k}}^2 = (k_y - \mathrm{i}k_x)\mu_{\boldsymbol{k}}^2 \tag{A.4}$$

for the coefficients $\mu_{\boldsymbol{k}}$ and $\nu_{\boldsymbol{k}}$. Normalization of $\psi_{\boldsymbol{k}}$ results in two sets of coefficients (indexed by $\pm$),

$$\mu_{\boldsymbol{k}\pm} = \frac{1}{\sqrt{2}}, \qquad \nu_{\boldsymbol{k}\pm} = \mp\frac{1}{\sqrt{2}}\sqrt{\frac{k_y - \mathrm{i}k_x}{k_y + \mathrm{i}k_x}} \qquad \text{for } \boldsymbol{k} \neq 0. \tag{A.5}$$

The eigenvalues of $\psi_{\boldsymbol{k}\pm}$ are given by

$$E_\pm(\boldsymbol{k}) = \tfrac{1}{2}k^2 \pm \gamma|\boldsymbol{k}|, \tag{A.6}$$

with $\gamma = \partial_z V(z)|_{z=0}/(2c^2)$. Hence, the strength of the spin–orbit-induced splitting, $E_+(\boldsymbol{k}) - E_-(\boldsymbol{k}) = 2\gamma$, is proportional to the structural asymmetry given by $\partial_z V$. The spin polarization $\boldsymbol{P}_\pm(\boldsymbol{k}) = \psi_{\boldsymbol{k}\pm}^\dagger\boldsymbol{\sigma}\psi_{\boldsymbol{k}\pm}$ is complete and perpendicular to $\boldsymbol{k}$,

$$P_\pm^x(\boldsymbol{k}) = \mp\frac{k_y}{|\boldsymbol{k}|}, \qquad P_\pm^y(\boldsymbol{k}) = \pm\frac{k_x}{|\boldsymbol{k}|}, \qquad P_\pm^z(\boldsymbol{k}) = 0. \tag{A.7}$$

Hence, $\boldsymbol{P}_+$ ($\boldsymbol{P}_-$) rotates anticlockwise (clockwise) around the $z$-axis.

Note that the sign of $\gamma$ determines the order of the spin–orbit-split states in reciprocal space, that is, which one is the inner and which one is the outer in the momentum distribution. But since it does not affect the spin polarization, the latter—for instance obtained from experiment—is a measure for the sign of $\gamma$.

## References

[1] Rashba E I 1960 *Sov. Phys.—Solid State* **2** 1109

[2] Bychkov Y A and Rashba E I 1984 *Sov. Phys.—JETP Lett.* **39** 78

[3] LaShell S, McDougall B A and Jensen E 1996 *Phys. Rev. Lett.* **77** 3419

[4] Reinert F 2003 *J. Phys.: Condens. Matter* **15** S693

[5] Reinert F, Nicolay G, Schmidt S, Ehm D and Hüfner S 2001 *Phys. Rev.* B **63** 115415

[6] Nicolay G, Reinert F, Hüfner S and Blaha P 2001 *Phys. Rev.* B **65** 033407

[7] Petersen L and Hedegård P 2000 *Surf. Sci.* **459** 49

[8] Muntwiler M, Hoesch M, Petrov V N, Hengsberger M, Patthey L, Shi M, Falub M, Greber T and Osterwalder J 2004 *J. Electron Spectrosc. Relat. Phenom.* **137** 119

[9] Hoesch M, Muntwiler M, Petrov V N, Hengsberger M, Patthey L, Shi M, Falub M, Greber T and Osterwalder J 2004 *Phys. Rev.* B **69** 241401

[10] Bürgi L, Petersen L, Brune H and Kern K 2000 *Surf. Sci.* **447** L157

[11] Henk J, Ernst A and Bruno P 2003 Spin polarization of the L-gap surface states on Au(111) *Preprint* cond-mat/0305530

[12] Hoesch M, Greber T, Petrov V N, Muntwiler M, Hengsberger M, Auwärter W and Osterwalder J 2002 *J. Electron Spectrosc. Relat. Phenom.* **124** 263

[13] Feder R and Henk J 1996 *Spin–Orbit Influenced Spectroscopies of Magnetic Solids* (*Springer Lecture Notes in Physics* vol 466) ed H Ebert and G Schütz (Berlin: Springer) p 85

[14] Henk J, Ernst A and Bruno P 2003 *Phys. Rev.* B **68** 165416

[15] Dresselhaus G 1955 *Phys. Rev.* **100** 580

[16] Mugarza A, Mascaraque A, Repain V, Rousset S, Altmann K N, Himpsel F J, Koroteev Y M, Chulkov E V, García de Abajo F J and Ortega J E 2002 *Phys. Rev.* B **66** 245419

[17] Perdew J P and Wang Y 1992 *Phys. Rev.* B **45** 13244

[18] Hüfner S 2003 *Photoelectron Spectroscopy* 3rd edn (Berlin: Springer)

[19] Fujita D, Amemya K, Yakabe T, Nejoh H, Sato T and Iwatsuki M 1999 *Surf. Sci.* **423** 160

[20] Crljen Ž, Lasić P, Šokčević D and Brako R 2003 *Phys. Rev.* B **68** 195411

[21] Reinert F and Nicolay G 2004 *Appl. Phys.* A **78** 817

[22] Tamura E 1996 private communication

[23] Ebert H, Freyer H and Deng M 1997 *Phys. Rev.* B **56** 9454

[24] Taut M, Ernst A and Eschrig H 1998 *J. Phys. B: At. Mol. Opt. Phys.* **31** 2689

[25] Braun J 1996 *Rep. Prog. Phys.* **59** 1267

[26] Henk J 2001 *Handbook of Thin Film Materials* vol 2, ed H S Nalwa (San Diego, CA: Academic) chapter 10, p 479

[27] Hedin L 1999 *J. Phys.: Condens. Matter* **11** R489

[28] Rampe A, Güntherodt G, Hartmann D, Henk J, Scheunemann T and Feder R 1998 *Phys. Rev.* B **57** 14370

[29] Scheunemann T 1993 Zur Theorie der Photoemission: Elektromagnetisches Feld an Metalloberflächen im hydrodynamischen Modell *Diploma Thesis* Universität Duisburg Theoretische Festkörperphysik

[30] Mazin I I 1999 *Phys. Rev. Lett.* **83** 1427

[31] Jonker B T, Hanbicki A T, Pierce D T and Stiles M D 2004 *J. Magn. Magn. Mater.* **277** 24

[32] Henk J, Schattke W, Carstensen H, Manzke R and Skibowski M 1993 *Phys. Rev.* B **47** 2251

[33] Inui T, Tanabe Y and Onodera Y 1990 *Group Theory and its Applications in Physics* (*Springer Series in Solid State Sciences* vol 78) (Berlin: Springer)

[34] Henk J, Scheunemann T, Halilov S V and Feder R 1996 *J. Phys.: Condens. Matter* **8** 47

[35] Tamura E, Piepke W and Feder R 1987 *Phys. Rev. Lett.* **59** 934

[36] Tamura E and Feder R 1991 *Europhys. Lett.* **16** 695

[37] Aryasetiawan F and Gunnarson O 1998 *Rep. Prog. Phys.* **61** 237

[38] Mugarza A, Mascaraque A, Pérez-Dieste V, Repain V, Rousset S, García de Abajo F J and Ortega J E 2001 *Phys. Rev. Lett.* **87** 107601

[39] Ortega J E, Mugarza A, Repain V, Rousset S, Pérez-Deiste V and Mascaraque A 2002 *Phys. Rev.* B **65** 165413

[40] Rose E M 1961 *Relativistic Electron Theory* (New York: Wiley)

[41] Kessler J 1985 *Polarized Electrons* (*Springer Series on Atoms and Plasmas* vol 1) 2nd edn (Berlin: Springer)

## Publikation 3

# Magnetism and anisotropy of ultrathin Ni films on Cu(001)

J. Henk, A. M. N. Niklasson, and B. Johansson
*Condensed Matter Theory Group, Physics Department, University Uppsala, S-751 21 Uppsala, Sweden*

(Received 3 September 1998; revised manuscript received 10 November 1998)

Both magnetic structure and magnetic-anisotropy energies are calculated for cubic and tetragonal Ni films on Cu(001) for thicknesses from 1 to 10 monolayers. The magnetic reorientation transition from in-plane to perpendicular anisotropy can be attributed to the volume contribution in tetragonal films which is discussed in terms of layer-resolved band energies. The transition takes place at six to seven monolayers, in agreement with experiments. The layer-dependent magnetic properties are brought into relation to those at a Ni(001) surface and a Ni(001)/Cu(001) interface, thus allowing the identification of contributions which are due to quantum-size effects. For films of a few monolayer thickness, the effect of quantized electronic states on the anisotropy appears to be significant. [S0163-1829(99)05613-1]

## I. INTRODUCTION

Ultrathin Ni films grown on Cu(001) show a peculiar behavior regarding the magnetic anisotropy: at film thicknesses between 5 monolayers (ML) and 7 ML—depending on film preparation and temperature—a sharp spin reorientation transition (SRT) from in-plane to perpendicular magnetization is observed experimentally. At much higher thickness, in the range from about 35 ML to 70 ML, the magnetic moments reorientate gradually and become again parallel to the surface.[1–4] This remarkable finding is contrary to those for Fe or Co films grown on Cu(001): the first show a SRT from perpendicular to in-plane anisotropy at about 5 ML; the latter show in-plane anisotropy for all thicknesses and thus no SRT [this has attracted a lot of attention and among a vast literature we refer to Refs. 5–9 for Fe/Cu(001) and Refs. 10–13 for Co/Cu(001)].

Ni films grow epitaxially on Cu(001), but due to the lattice mismatch between Ni(001) and Cu(001), the films become tetragonally distorted on Cu(001). The first SRT can be understood by the magnetoelastic anisotropy due to this tetragonal distortion of the Ni films—as has been shown experimentally by Farle *et al.*[14] and theoretically by Hjortstam *et al.*[15] for hypothetical fct-bulk Ni, thus focusing on the volume contribution to the magnetic-anisotropy energy (MAE). However, from calculations for bulk materials with different $c/a$ ratios it is hardly possible to conclude at which particular film thickness a SRT will occur. For example, bulk calculations cannot address the quantization of electronic states within the Ni film which may affect the MAE considerably, in particular for very thin films. Further, the anisotropy at both the surface and the Ni/Cu interface may affect the MAE—and thus the transition thickness—substantially. Therefore, calculations for ultrathin Ni films which take into account the correct boundary conditions as well as the film relaxation are absolutely necessary in order to explain the first SRT.

The second (gradual) SRT can be understood by the formation of films with misfit dislocations which occur due to strain relaxation, as has been observed experimentally.[3,4] The latter lowers the MAE and thus causes the magnetization to switch back from perpendicular to in-plane anisotropy. Further, island growth has been reported[16] which makes it difficult—if not impossible—to conclude from theory on the second SRT.

Ni films with thickness of a few or more ML can be regarded as composed by a Ni(001)/Cu(001) interface and a Ni(001) surface. These two contributions to the magnetic moments and the MAE should be easy to identify. However, the quantization of electronic states within the film should also influence these quantities, in particular for very thin films where the above decomposition into surface and interface should become at least questionable. Sophisticated calculations of the magnetization profiles (layer-dependent magnetic moments) or the MAE are very time consuming. Therefore, it appears desirable—for both theoreticians and experimentalists—to be able to derive reliable quantitative results from a knowledge of only the magnetization profiles or anisotropy energies of the interface and the surface, constructing from these the profile for the entire film. In this procedure, one neglects, however, the quantum-well contribution.

In this paper, we report on calculations of both the magnetic structure and the MAE of cubic as well as tetragonally distorted Ni films on Cu(001) for thicknesses from 1 ML up to 10 ML. In Sec. II we provide the reader with definitions, address our theoretical approach, and discuss the ingredients used in the numerical calculations. In Sec. III we consider the superposition of magnetization and band-energy profiles in order to understand better our results. The latter will be discussed in Sec. IV, in particular the magnetization profiles (Sec. IV A) and the magnetic anisotropy (Sec. IV B). Conclusions are given in Sec. V.

## II. THEORETICAL AND COMPUTATIONAL ASPECTS

Our procedure to calculate the MAE is based on two steps. First, the scalar-relativistic linear muffin-tin orbital (LMTO) method is applied for the generation of self-consistent spin-dependent potentials of the semi-infinite system consisting of substrate layers, ferromagnetic film layers, and vacuum, thus ignoring at this step spin-orbit coupling (SOC). Second, fully relativistic layer Korringa-Kohn-Rostoker (LKKR) calculations yield the layer-resolved Bloch spectral functions, from which the MAE is calculated. Here, magnetic exchange and the SOC are treated on equal footing. This scheme is not self-consistent and therefore relies on a good approximation of the potentials. On the other hand, the SOC is not treated as a perturbation.

The Green function (GF) technique of the LMTO method[17,18] was developed by Skriver and Rosengaard[19] and is used in the calculation of the self-consistent potentials in the tight-binding,[20] frozen-core, and atomic-sphere approximations in conjunction with the local spin-density approximation as parametrized by Vosko, Wilk, and Nusair.[21] It does not rely on a slab or supercell geometry. Thus, a correct description of the loss of translational symmetry perpendicular to the surface—as is present in semi-infinite systems—is ensured. Furthermore, the principle-layer technique[22] leads to minimal computational effort which scales linearly with the number of layers taken into account. The results of this first step are spin- and layer-dependent muffin-tin potentials (the Wigner-Seitz radius is 2.669 a.u.) which are used as input for the LKKR calculations.

The method used in the calculation of the LKKR Green function should also be sketched.[23] The layer-diagonal part $G_{ll}$ is obtained by first calculating the GF of an empty layer, i.e., a layer with zero potential, embedded in the host system and taking into account the correct boundary conditions (reflection at the surface side and at the bulk side of the empty layer). Then the Dyson equation for this empty layer is solved, giving the $\vec{k}_\parallel$- and energy-resolved scattering-path operator.[24] Because only matrices related to single layers are involved in this computational scheme, the computing time scales linearly with the number of layers, without using any screened representation (''tight binding''). The layer-nondiagonal parts $G_{ll'}$ (not used in this paper, though) can by obtained from $G_{ll}$ and the multiple-scattering transfer matrices from layer $l$ to layer $l'$. Details of this method will be published elsewhere.

The LKKR calculations were performed for two collinear magnetic configurations: $\vec{M}^{(\parallel)}$ with all local magnetic moments aligned parallel to the layers and $\vec{M}^{(\perp)}$ with all local magnetic moments aligned perpendicular to the layers (parallel to the surface normal). We applied the so-called force theorem; i.e., both calculations used the same potentials. The layer-dependent electronic structure for a magnetic configuration $\vec{M}$ is conveniently discussed in terms of the Bloch spectral function $D^{(l)}$,

$$D^{(l)}(\vec{k}_\parallel,E;\vec{M}) = \frac{1}{\pi}\lim_{\eta\to 0_+} \mathrm{Im}\,\mathrm{Tr}\, G_{ll}(\vec{k}_\parallel,E-\mathrm{i}\eta;\vec{M}), \qquad (1)$$

which for layer $l$, energy $E$, and surface-parallel wave vector $\vec{k}_\parallel$ is calculated from the layer-diagonal part of the GF, $G_{ll}(\vec{k}_\parallel,E-\mathrm{i}\eta;\vec{M}),\ \eta>0$. The layer-density of states (LDOS) is obtained from $D^{(l)}$ by integration over the surface Brillouin zone (SBZ),

$$N^{(l)}(E;\vec{M}) = \int_{\mathrm{SBZ}} D^{(l)}(\vec{k}_\parallel,E;\vec{M})\, d\vec{k}_\parallel . \qquad (2)$$

For the above integration we generated special-point sets by the Monkhorst-Pack method for two-dimensional lattices.[25,26] Although in the case of perpendicular magnetization the point group is $C_4$ (in Schönflies notation), we used the $\vec{k}_\parallel$ mesh for the point group $C_s$—which is the relevant one in the case of in-plane magnetization—in order to avoid any inconsistencies. Convergence was checked for sets from 120 points with up to 1830 points. For films thicker than about 5 ML we found convergence for point sets with 600–800$\vec{k}_\parallel$. Thin films, in particular 1 ML and 2 ML, showed rather slow convergence. The results of the calculations presented here were obtained with a 1275 point set. Note that the number of $k$-points is rather small compared to that used in calculations of the bulk MAE.[27,28] But due to the calculation of the layer-resolved GF of a semi-infinite system, the integration over $k_\perp$ is in principle included (although it is not performed explicitly due to the computational scheme for the GF), and we thus use—roughly speaking—a sampling over symmetry-adapted $\vec{k}$ directions.

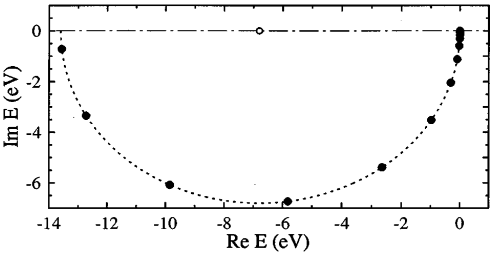

FIG. 1. Contour and mesh used in the complex energy integration. Solid circles represent points on a logarithmic angular mesh; cf. Eq. (6). The open circle is the center of the semicircle contour with radius 0.5 Ry; the Fermi energy is at 0 eV.

The band energy $E^{(l)}_{\mathrm{bnd}}$ of layer $l$ is given by

$$E^{(l)}_{\mathrm{bnd}}(\vec{M}) = \int_{-\infty}^{E_\mathrm{F}} (E-E_\mathrm{F}) N^{(l)}(E;\vec{M})\, dE, \qquad (3)$$

with $E_\mathrm{F}$ denoting the Fermi energy. The total band energy of a system with $n$ ferromagnetic layers on a nonmagnetic substrate, in brief Ni$_n$/Cu(001), is then simply a sum over all magnetic layers,

$$E_{\mathrm{bnd}}(\vec{M}) = \sum_{l=1}^{n} E^{(l)}_{\mathrm{bnd}}(\vec{M}). \qquad (4)$$

Note that in principle the magnetic film (Ni) induces magnetic moments in the substrate layers (Cu) at the interface. This can be accounted for by extending the above sum, Eq. (4), over all energetically perturbed layers. For the energy integration in Eq. (3) we exploit the analytical properties of the GF and replace the integral along the real energy axis by a contour integration. Because $E_{\mathrm{bnd}}$ of the core levels are expected not to depend significantly on the magnetization direction, we take into account only the valence-band regime (frozen-core approximation). As contour we chose a semicircle with radius $R$ and center $E_\mathrm{F}-R$ (see Fig. 1). The applied Gaussian quadrature with 16 sampling points on an angular logarithmic mesh appeared to be very accurate and robust, and has the advantage that sampling on the real axis is avoided. The sampling points $z_j$ are given by

$$z_j = E_\mathrm{F} + R[\exp(i\vartheta_j)-1], \quad j=1,\dots,16, \qquad (5)$$

with angles $\vartheta_j$ on a logarithmic mesh in $[-\pi,0]$,

$$\vartheta_j = -\pi \frac{\exp(\beta)-\exp(\beta x_j)}{\exp(\beta)-\exp(-\beta)}, \quad j=1,\dots,16, \tag{6}$$

and $x_j \in ]-1,1[, j=1,\dots,16$, are the zeros of the respective Legendre polynomial used in the Gaussian quadrature.[29] The density of the sampling points near the Fermi energy is controlled by $\beta > 0$. The radius $R$ is chosen in such a way that the whole valence-band regime is covered. In the calculations presented below we chose $\beta = -3.222\,32$ and $R = 0.5$ Ry.

The magnetic-anisotropy energy $E_{\mathrm{MA}}$ is finally given by the differences of the band energies and the dipole-dipole interaction energies $E_{\mathrm{dd}}(\vec{M})$ for in-plane ($\vec{M}^{(\parallel)}$) and perpendicular magnetization ($\vec{M}^{(\perp)}$),

$$E_{\mathrm{MA}} = E_{\mathrm{bnd}}(\vec{M}^{(\parallel)}) + E_{\mathrm{dd}}(\vec{M}^{(\parallel)}) - E_{\mathrm{bnd}}(\vec{M}^{(\perp)}) - E_{\mathrm{dd}}(\vec{M}^{(\perp)}). \tag{7}$$

We used the Ewald summation technique as outlined in Ref. 30 for the calculation of $E_{\mathrm{dd}}(\vec{M})$.

In order to check the numerical accuracy, the band energies were calculated for $\vec{M} \parallel [001]$ and $\vec{M} \parallel [010]$ for semi-infinite Ni(001) (in the Cu lattice). We found an energy difference less than 0.4 $\mu$eV for bulklike layers ($l = 10$). Note that in the bulk the above difference should be zero. As will be seen below, the above value is about two to three orders of magnitude smaller than the MAE in thin films.

The Ni layers are assumed to continue epitaxially the Cu fcc lattice in the [001] direction. We distinguish three cases of relaxations in the Ni films. (i) In the ‘‘fcc case,’’ the interlayer distance is that of bulk Cu, (ii) In the ‘‘fct case,’’ the interlayer distance is reduced by 6.9% in order to retain the volume of the bulk-Ni unit cell. (iii) Using low-energy electron diffraction (LEED), Müller *et al.*, obtained experimentally the interlayer distances for 3-ML, 5-ML, and 11-ML films[31] which we refer to as the ‘‘fct LEED’’ case. In all three cases, we use the in-plane lattice constant of bulk Cu, i.e., a next-nearest neighbor distance of 2.55 Å. A theoretical LEED analysis on Cu(001), however, found best agreement with experimental data with a slightly reduced in-plane lattice constant (0.8%), indicating strain even at uncovered Cu(001) surfaces.[32] For convenience, we denote the surface layer by *S*, the second layer by $S-1$, etc.

## III. SUPERPOSITION OF MAGNETIZATION AND BAND-ENERGY PROFILES

In the following, we show that magnetization and band-energy profiles of Ni/Cu films can essentially be regarded as superimposed by profiles which originate from two independent perturbations at the two boundaries of the film, i.e., the Ni/Cu interface and the Ni surface.[33]

We describe unperturbed bulk Ni by a spin-dependent nonrelativistic Green function $G_B^\sigma$, $\sigma = \pm$ being the spin index. We construct a Ni film on a Cu substrate by replacing an infinite Ni crystal [bulk ($B$)] by Cu ($R$) on the right-hand side and by vacuum ($L$) on the left-hand side of the Ni layers which constitute the film (cf. Fig. 2). The film layers are then influenced by spin-dependent perturbations $V_L^\sigma$ and $V_R^\sigma$, at the two boundaries. The film GF $G^\sigma$ thus has to fulfill the Dyson equation $G^\sigma = G_B^\sigma + G_B^\sigma (V_L^\sigma + V_R^\sigma) G^\sigma$. Its series expansion can be written as

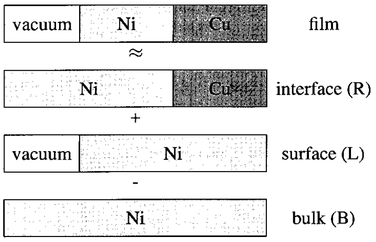

FIG. 2. Schematic construction of a Ni film on Cu (top). Starting from Ni bulk (bottom, light grey), two semi-infinite solids are replaced by vacuum (white) and by Cu (dark grey), yielding the surface ($L$) and the interface ($R$) system, respectively. For letters $B$, $L$, and $R$ see Sec. III. The mathematical signs ($\approx$, $+$, $-$) refer to Eqs. (9) and (14).

$$G^\sigma = \sum_{j=0}^{\infty} G_B^\sigma [(V_L^\sigma + V_R^\sigma) G_B^\sigma]^j \tag{8a}$$

$$= G_B^\sigma + \delta G_L^\sigma + \delta G_R^\sigma + \delta G_{QW}^\sigma, \quad \sigma = \pm. \tag{8b}$$

The second and third terms $\delta G_L^\sigma$ and $\delta G_R^\sigma$ describe perturbations due to scattering solely on the left or right boundary, respectively, and thus comprise only expressions with $V_L^\sigma$ or $V_R^\sigma$, respectively. The last term $\delta G_{QW}^\sigma$ collects all expressions with both $V_L^\sigma$ and $V_R^\sigma$ and thus results from multiple scattering between both interfaces, i.e., due to scattering in the quantum well (QW) formed by the two interfaces. The latter may give rise to spin-polarized QW states in the Ni film.[34,35]

If $\delta G_{QW}^\sigma$ is neglected, the properties of the film can be regarded as a superposition of perturbations originating from the two independent interfaces. In particular, the magnetization profile of the film $M(l)$—$l$ being the layer index—can be regarded as a superposition of the magnetization profiles originating from the Ni/Cu interface, $M_R(l)$, and from the Ni surface, $M_L(l)$,

$$M(l) \approx M_L(l) + M_R(l) - M_B, \tag{9}$$

where $M_B$ is the magnetic moment of bulk Ni. Since the contribution from the QW term usually gives rise only to small constant shifts of the magnetization profile,[33] the superposition provides a good estimate of the magnetization profiles in films. By definition, quantum-size effects show up as the difference between the superimposed and the true magnetization profile of the film.

The above approximative decomposition is not limited to magnetization profiles. Indeed, the response to additional perturbations can be estimated by a superposition of independent interface perturbations as well. This way we are, for example, able to analyze different contributions to the MAE in films, as will be discussed in the following.

Regarding spin-orbit coupling as a perturbation of the Hamiltonian, the Green function will depend on the magnetization direction, for example perpendicular ($\vec{M}^{(\perp)}$) or parallel ($\vec{M}^{(\parallel)}$) to the interfaces. Further, the spin $\sigma$ is no longer a good quantum number. In matrix representation, the resulting Green functions can be written as $2\times 2$ block matrices where each block has the size of the unperturbed GF matrix. We denote the corresponding SOC perturbation operator as $\Theta(\vec{M})$, emphasizing its dependence on the direction of the magnetic moments. The GF of the perturbed Ni film, $G(\vec{M})$, is implicitly given by

$$G(\vec{M}) = G + G\Theta(\vec{M})G(\vec{M}) = G + \delta G(\vec{M}). \tag{10}$$

The Green function $G$ is diagonal in spin space (no spin-orbit coupling) and constructed from $G^{+}$ and $G^{-}$ of the film with $G^{\pm}_{QW}$ being neglected; cf. Eq. (8b). Here $\delta G(\vec{M})$ is given by the Dyson series

$$\delta G(\vec{M}) = G\Theta(\vec{M})G + G\Theta(\vec{M})G\Theta(\vec{M})G + \cdots \tag{11}$$

$$\begin{aligned} &= G_B\Theta(\vec{M})G_B + G_B\Theta(\vec{M})G_B\Theta(\vec{M})G_B + \cdots \\ &\quad + \delta G_L\Theta(\vec{M})\delta G_L + \delta G_L\Theta(\vec{M}) \\ &\quad \times \delta G_L\Theta(\vec{M})\delta G_L + \cdots + \delta G_R\Theta(\vec{M})\delta G_R \\ &\quad + \delta G_R\Theta(\vec{M})\delta G_R\Theta(\vec{M}) \\ &\quad \times \delta G_R + \cdots + \delta G_{QW}(\vec{M}). \end{aligned} \tag{12}$$

Eventually, we obtain the grouping of terms

$$\delta G(\vec{M}) = \delta G_B(\vec{M}) + \delta G_L(\vec{M}) + \delta G_R(\vec{M}) + \delta G_{QW}(\vec{M}), \tag{13}$$

where $\delta G_L(\vec{M})$ and $\delta G_R(\vec{M})$ include contributions solely from scattering at the left-hand and right-hand side perturbations, respectively. The term $\delta G_B(\vec{M})$ represents the spin-orbit perturbation of bulk Ni, and $\delta G_{QW}(\vec{M})$ includes multiple scattering at both interfaces. If we neglect the latter, the band energy can be expressed as

$$E_{\mathrm{bnd}}(\vec{M}) \approx E_{\mathrm{bnd},L}(\vec{M}) + E_{\mathrm{bnd},R}(\vec{M}) - E_{\mathrm{bnd},B}(\vec{M}), \tag{14}$$

with

$$E_{\mathrm{bnd},B}(\vec{M}) = -\frac{1}{\pi}\int_{-\infty}^{E_{\mathrm{F}}} \mathrm{Im}\,\mathrm{Tr}\,E\,\delta G_B(\vec{M})\,dE \tag{15}$$

and

$$E_{\mathrm{bnd},D}(\vec{M}) = -\frac{1}{\pi}\int_{-\infty}^{E_{\mathrm{F}}} \mathrm{Im}\,\mathrm{Tr}\,E[\delta G_B(\vec{M}) + \delta G_D(\vec{M})]\,dE, \tag{16}$$

where $D = L,R$. According to Eq. (14), this is simply a superposition of three band-energy profiles which result from two independent interfaces on the left- and right-hand sides—$E_{\mathrm{bnd},L}(l)$ and $E_{\mathrm{bnd},R}(l)$—in conjunction with the subtraction of the bulk contribution $E_{\mathrm{bnd},B}$. It provides a picture derived from individual contributions from different kinds of interfaces and surfaces. Again, finite-size effects can be obtained from the difference between the superimposed and the true band energy for the thin film. Considering the band-energy differences $\Delta E_{\mathrm{bnd},D} = E_{\mathrm{bnd},D}(\vec{M}^{(\parallel)}) - E_{\mathrm{bnd},D}(\vec{M}^{(\perp)}), D = B,L,R$, only a small number of constituents has to be regarded in order to understand the magnetic anisotropy of layered structures. In analogy with earlier analysis,[36,37] we may thus regard the MAE of thin films as the sum of a surface, an interface part and a bulk contribution if multiple-scattering effects are neglected. However, all three contributions will be of importance and may give rise to a broad spectrum of possible effects on the MAE of thin films.

## IV. RESULTS AND DISCUSSION

In this section we discuss the layer-resolved spin moments and the magnetic anisotropy. For the latter we address in particular the effect of lattice relaxations on the band-energy contribution to the MAE and higher-order contributions.

### A. Layer-resolved magnetic structure

As is well known, an increase in volume—as well as a reduction of the coordination number—usually favors an increase of the magnetic moment. Thus, the bulk spin magnetic moment of Ni ($0.67\mu_{\mathrm{B}}$) in the fcc case (with Cu lattice constant) is slightly enhanced with respect to that of bulk Ni ($0.62\mu_{\mathrm{B}}$, with Ni lattice constant).[38]

In Fig. 3 the spin magnetization profiles of fcc Ni films on Cu(001) are depicted for coverages from 1 ML up to 10 ML. At 1 ML coverage the magnetic moment is only 44% ($0.296\mu_{\mathrm{B}}$) of the Ni bulk value. For 2 ML the magnetic moments are increased to $0.741\mu_{\mathrm{B}}$ and $0.499\mu_{\mathrm{B}}$ for layers $S$ and $S-1$, respectively. This increase is continued for the 3-ML film. The surface layer of the latter has the largest moment of all systems considered here ($0.762\mu_{\mathrm{B}}$). At 4 ML coverage the building up of a plateau region starts: the interior Ni layers start to show nearly the moments of bulk Ni, while that of the surface layer is enhanced and those at the interface are reduced by about 30% for the first interface Ni layer (adjacent to the first Cu substrate layer, $S-n+1$) and 3% for the second interface Ni layer ($S-n+2$). This ''evolution'' of the magnetization profile is completed at about 7 ML coverage.

The surface magnetic structure of films with $n \geqslant 7$ shows a nearly complete agreement with that of semi-infinite Ni(001) ($n=\infty$ in Fig. 3). The magnetic moment of the outermost Ni layer ($S$, $0.746\mu_{\mathrm{B}}$ for $n=\infty$) compared to those of the interior Ni layers of the film and that of bulk Ni with Cu lattice constant ($0.667\mu_{\mathrm{B}}$) is enhanced by about 12%. This enhancement of moments is typical for surface layers[35] and is due to the reduction in coordination number.

The reduced Ni magnetic moment at the interface can be understood from the behavior of binary bulk alloys $\mathrm{Ni}_x\mathrm{Cu}_{1-x}$ when the concentration $x$ is adjusted to correspond to the Ni-Ni coordination number at the fcc(001) interface.[39] The magnetic properties of binary $3d$ transition-metal alloys are often essentially determined by the nearest-neighbor correlation, i.e., the local environment of a particular atom. The Ni atoms at the Ni/Cu interface can be regarded as constituents of a ''perfectly ordered alloy'' where only 8 of 12 nearest neighbors surrounding an interface Ni site are of the same kind. This corresponds to a local Ni concentration of $x = 2/3$. According to the Slater-Pauling curve,[40,41] there is a

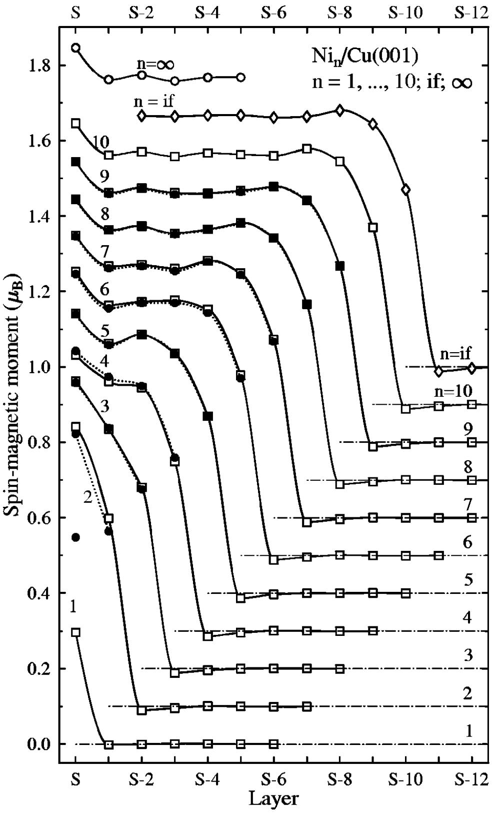

FIG. 3. Layer-resolved spin magnetic moments of fcc Ni films on Cu(001) (squares, solid lines) with thicknesses $n=1,\ldots,10$ as obtained by LMTO calculations. The moments of a Ni(001)/Cu(001) interface [$n=$if, diamonds; interface at layers $S-10$ (Ni) and $S-11$ (Cu)] and semi-infinite Ni(001) ($n=\infty$, open circles)—both with Cu lattice constant—are shown in addition. Magnetic moments obtained by superposition of the surface and the interface profile—cf. Eq. (9)—are indicated by solid circles and dotted lines. For clarity, the data sets are shifted by $0.1(n-1)\mu_B$ ($1.0\mu_B$ for $n=$if, $1.1\mu_B$ for $n=\infty$); their respective zeros are represented by dash-dotted lines. Layers are labeled $S, S-1, S-2, \ldots,$ starting with the surface layer $S$. Solid and dotted lines serve as guide to the eye.

substantial reduction of the nickel magnetic moment to approximately $0.3\mu_B$ in the Ni$_x$Cu$_{1-x}$ alloy.

The Cu layers next to the interface show induced magnetic moments of about $0.015\mu_B$ with an antiferromagnetic coupling to Ni. For example, this common antiparallel spin behavior has been observed for Fe films on Au(001) by Szunyogh *et al.*[30]

The small oscillations of the size of the magnetic moments in the interior of thicker Ni films ($n>6$) can be regarded as 'magnetic' Friedel oscillations due to the spin-dependent perturbations from the surface and the Ni/Cu interface [they were also found for Co films on Cu(001) (Ref. 37)]. In Fig. 3, both the surface ($n=\infty$) and the interface ($n=if$) system show oscillations which decay rapidly.

We now turn to the picture of the magnetization as a superposition of magnetic profiles [Sec. III, in particular Eq. (9)]. In Fig. 3, the superimposed profiles are compared with their exactly calculated counterparts. Except for the 1-ML film—where the superposition is apparently questionable—we find excellent agreement which means that QW contributions to the spin magnetic moment are generally very small. The largest deviations are found for 2 ML and 4 ML but are smaller than $0.03\mu_B$. As mentioned above, the 3-ML film shows the largest surface magnetic moment. This can easily be explained within the superposition picture: The moment of the surface layer $S$ is obtained from the surface layer $S$ of the surface system and the third Ni layer of the interface system (layer $S-8$ in Fig. 3). Both show the largest moments of their systems and, therefore, give rise to the enhanced surface moment of the 3-ML film. In conclusion, one can construct layer-dependent spin magnetic profiles of films from the surface and the interface profiles with high accuracy, the only exception being the 1-ML case.

Finally, the magnetization profiles shown in Fig. 3 exhibit no spectacular features but rather the expected behavior: enhancement at the surface, reduction at the interface, oscillations in between. Relevant for the discussion of the anisotropy, in particular the band energy, may be the building up of a plateau, i.e., the appearance of bulklike layers, which starts at 6–7 ML.

### B. Magnetic anisotropy

The magnetic-anisotropy energy is composed of two parts, the dipole-dipole interaction energy $\Delta E_{\mathrm{dd}}=E_{\mathrm{dd}}(\vec{M}^{(\parallel)})-E_{\mathrm{dd}}(\vec{M}^{(\perp)})$ and the band-energy contribution $\Delta E_{\mathrm{bnd}}=E_{\mathrm{bnd}}(\vec{M}^{(\parallel)})-E_{\mathrm{bnd}}(\vec{M}^{(\perp)})$, Eq. (7). The former is negative for all thicknesses, thus favoring in-plane anisotropy, and depends almost linearly on film thickness. Therefore, the first spin reorientation transition can exclusively be attributed to the band-energy part which is discussed in the following by means of the layer-resolved band-energy difference $\Delta E^{(l)}_{\mathrm{bnd}}=E^{(l)}_{\mathrm{bnd}}(\vec{M}^{(\parallel)})-E^{(l)}_{\mathrm{bnd}}(\vec{M}^{(\perp)})$, with $l$ denoting the layer.

We first address films with fcc structure (fcc case, solid lines in Fig. 4). An interface between Ni(001) and Cu(001) favors an in-plane orientation of the magnetic moments ($\Delta E_{\mathrm{bnd}}=-65$ $\mu$eV$<0$), as is evident from the "$n=$if" curve in Fig. 4. Here, the last Ni layer is $S-9$, and the first Cu layer is $S-10$. Further, there are oscillations within the Ni half-space with a wavelength of approximately five layers. The surface of semi-infinite Ni(001) ("$n=\infty$" curve in Fig. 4) also favors in-plane anisotropy ($\Delta E_{\mathrm{bnd}}=-43$ $\mu$eV). Remarkably, the second and third outermost layers $S-1$ and $S-2$ appear to have a rather large positive band-energy difference which, however, is overridden by the subsequent layers. Regarding only the first three outermost layers, $\Delta E_{\mathrm{bnd}}=22$ $\mu$eV. The most significant layers, i.e., those layers which show the largest absolute value of band-energy difference, are the first outermost four layers in the case of semi-infinite Ni(001) and the nearest and second-nearest Ni layers to the Ni/Cu interface.

The layer-resolved band-energy difference of the 10-ML film can be regarded as composed by the interface and the surface profiles. This is evident by comparing its profile ob-

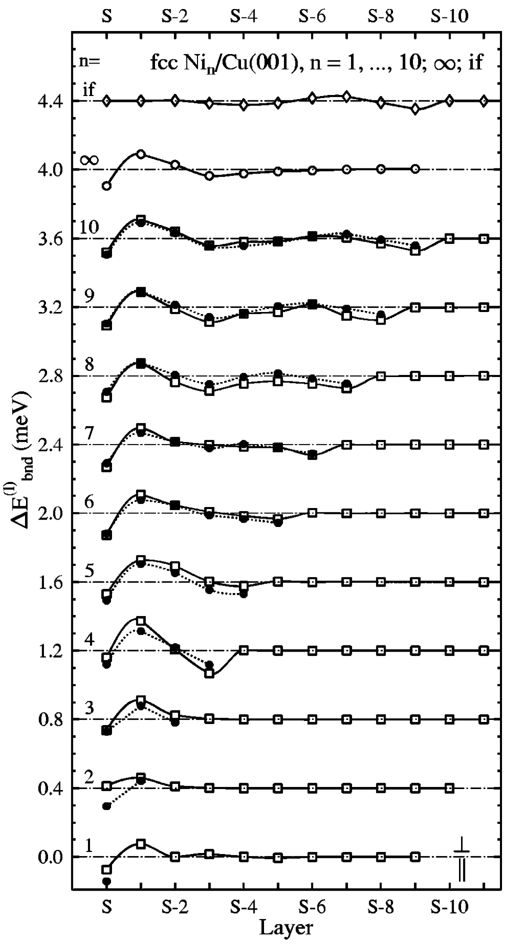

FIG. 4. Layer-resolved band-energy contribution to the magnetic-anisotropy energy of fcc Ni films (fcc case) on Cu(001) with thicknesses $n=1,\ldots,10$ (squares), $\infty$ (open circles), and a Ni/Cu interface at layer $S-9$ (diamonds, "if"). Solid circles connected by dotted lines refer to band-energy differences obtain by superposition of the surface ($n=\infty$) and the interface ($n=$if) contribution [cf. Eq. (14)]. For clarity, the data sets are shifted by $0.4(n-1)$ meV (4.0 meV for $n=\infty$, 4.4 meV for "if"); their respective zeros are represented by dash-dotted lines. Layers are labeled $S$, $S-1$, $S-2,\ldots$, starting with the surface layer $S$. Solid and dotted lines serve as guide to the eye.

tained from the LKKR calculations with that obtained from a superposition of the latter profiles using Eq. (14). We find this agreement also for film thicknesses of 6 ML, 7 ML, and 9 ML. The composed profile of the 8-ML film shows slightly too high values; the shape of the profile, however, is nicely reproduced. In conclusion, the superposition of profiles works well at higher film thicknesses, meaning that the QW part of the band-energy difference is small. Further, this corresponds nicely with the onset of bulklike magnetization profiles (Sec. IV A) which we observed in the interior of thick films ($n \geqslant 6$).

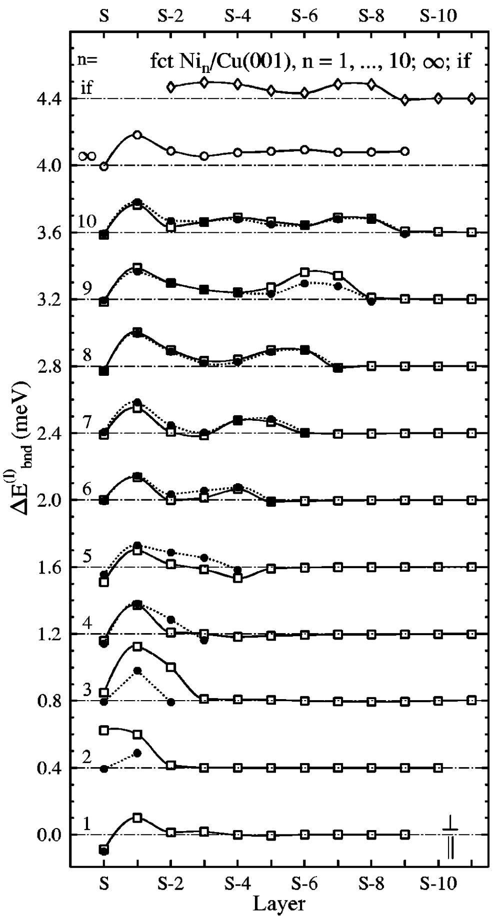

FIG. 5. Same as Fig. 4, but for tetragonally distorted Ni films (fct case).

For small film thicknesses, 1–5 ML, the above-mentioned significant ranges of layers of semi-infinite Ni and the Ni/Cu interface overlap in the superposition picture. From 3 ML to 5 ML, the superposition yields the correct shapes of the profiles and also correct signs of the values, but mostly gives too small absolute values compared to those of the full calculation. For 1 ML and 2 ML, the value for the layer $S$ is overestimated in absolute value. Further, the sign is wrong in the case of 2 ML. We regard these deviations as manifestations of the QW part of the band-energy difference.

In the whole range of film thicknesses, except for 1 ML, we find no significant contribution to $\Delta E_{\mathrm{bnd}}$ from the Cu layers. For the 1-ML film, however, the Cu layer $S-1$ shows a considerable positive band-energy difference, although the layer shows only a very small magnetic moment (compared to that of the Ni layer $S$). This finding emphasizes that there is no simple relation between magnetic moment and band-energy difference. Note that the latter is the first energy moment of the former [cf. Eq. (3)].

We now focus on films with fct structure (fct case), the tetragonal distortion of which leads to an uniaxial system.

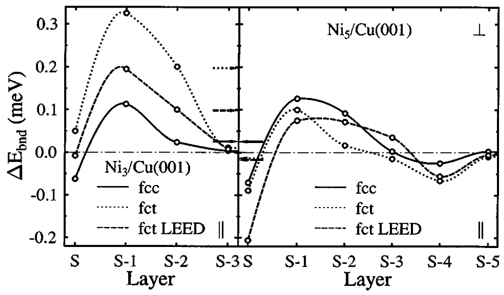

FIG. 6. Layer-resolved band-energy contribution to the magnetic-anisotropy energy of Ni films on Cu(001) with thicknesses $n=3$ (left) and $n=5$ (right) for cubic (solid lines, fcc), homogeneously tetragonal distorted (dotted lines, fct), and inhomogeneously tetragonal distorted (dashed lines, fct LEED) systems. Arrows mark averages over the Ni layers. The layers are labelled $S, S-1, S-2, \ldots$, starting with the surface layer $S$. Lines serve as guide to the eye.

For bulklike layers we find a volume contribution ($K_v$) of 0.081 meV/atom which corresponds nicely with theoretical and experimental results.[15] At first glance, the band-energy difference profile of the Ni/Cu interface (cf. "$n=$if" in Fig. 5) appears to be just shifted to positive values but also the wavelength of the oscillations has decreased to approximately four layers. Also the profile of semi-infinite Ni(001) can be regarded as shifted by the volume contribution; its shape remains nearly unchanged. Evidently, both the surface and the interface system clearly favor perpendicular anisotropy ($\Delta E_{\mathrm{bnd}}>0$) due to the tetragonal distortion. If the superposition of profiles works as well as in the fcc case, we expect that films with larger film thickness will also show perpendicular anisotropy.

The overall enhancement of $\Delta E_{\mathrm{bnd}}^{(l)}$ is clearly visible for films with $n \geqslant 6$ (cf. Fig. 5). For example, both the surface layers $S$ and the interface layer $S-n+1$ show values around zero, in the fcc case negative values, though. The profiles are again well reproduced by the superposition, an exception being layers $S-6$ and $S-7$ for $n=9$. For thinner films, the shape of the profiles is not as well reproduced by the superposition as for the thicker films, (cf. in particular $n=2$ and $n=3$), which means that QW contributions are important. Thus, a shift in $\Delta E_{\mathrm{bnd}}^{(l)}$ due to the tetragonal distortion is hard to detect because it might be covered by the QW contribution. So the origin of the significant shift for 2 ML and 3 ML, compared to the fcc case, cannot be unambiguously determined.

For the 3-ML and 5-ML films we now discuss the effect of the tetragonal distortion on the band-energy difference in more detail. In Fig. 6 the layer-resolved band energies for the fcc, fct, and fct LEED cases are shown. As the fct LEED case can be regarded as an intermediate case between the fcc and fct cases, one would expect that its band-energy profile lies between those of the latter. For the 3-ML film this is apparently true (left panel in Fig. 6). The interlayer distances in the fct LEED case[31] are reduced by about 2.6% with respect to that of bulk Cu. So one would be led to the conclusion that—despite possible QW contributions—the result of Fig. 6 is consistent with a volume contribution to the MAE.

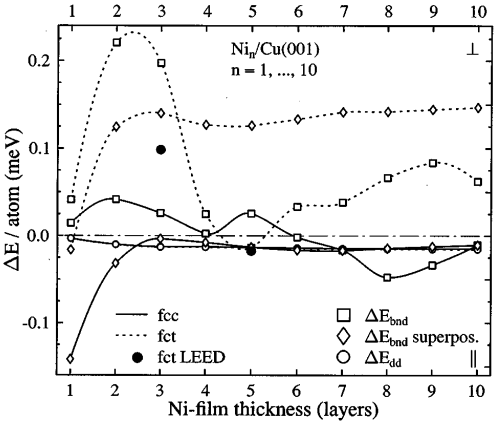

FIG. 7. Magnetic-anisotropy energies per atom of Ni films on Cu(001). Their band-energy contributions $\Delta E_{\mathrm{bnd}}$ are represented by squares, their dipole-dipole interaction energy $\Delta E_{\mathrm{dd}}$ by open circles. Diamonds denote band-energy contributions obtained by superposition of the surface and the interface profiles; cf. Eq. (14). Solid lines refer to cubic Ni films (fcc case), dotted lines to homogeneously tetragonal distorted Ni films (fct case). Solid circles show band-energy data obtained for in-homogeneously tetragonal distorted Ni films of 3 ML and 5 ML thickness (fct LEED case). Lines serve as guide to the eye.

For the 5-ML film, however, we observe a completely different dependence on the relaxation (right panel in Fig. 6). Here, the average contraction is 3.8%, but with an outward relaxation of the surface layer by 1.7%. This outward relaxation could explain that the band-energy difference for this layer is the lowest of all three cases. Further, the fcc profile is larger than the fct case for all layers, but the fct LEED profile shows the smallest (layer $S$) as well as the largest values (layers $S-3$). Considering the averaged band-energy differences ($\Delta E_{\mathrm{bnd}}$, arrows in Fig. 6), both fct cases show negative values, i.e., favor in-plane anisotropy. In conclusion, we find no simple relation between relaxation and band-energy contribution to the magnetic anisotropy for thin films.

We now turn to the magnetic-anisotropy energy. The total band-energy difference per Ni atom, Eq. (4), together with the dipole-dipole interaction energy per Ni atom is shown in Fig. 7. For the latter (open circles in Fig. 7), the tetragonal distortion leads to a slightly stronger interaction of the local magnetic moments and thus to an insignificant lower $\Delta E_{\mathrm{dd}}$/atom. As mentioned earlier, $\Delta E_{\mathrm{dd}}$ shows negative values throughout the whole thickness range and depends almost linearly on film thickness. Therefore, $\Delta E_{\mathrm{dd}}$/atom is nearly independent on the film thickness for films thicker than three layers. Thus, as was mentioned before, the band-energy contribution to the MAE must be considered as responsible for the first spin reorientation transition.

In the fcc case, $\Delta E_{\mathrm{bnd}}$/atom (squares connected by solid lines in Fig. 7) is positive for films with $n \leqslant 5$ and negative otherwise. Summing up both contributions yields perpendicular anisotropy for film thicknesses $n=1$, 2, 3, and 5.

Thus, it completely fails to reproduce the experimental finding of in-plane anisotropy for thin films ($n \leqslant 5$) and perpendicular anisotropy for thicker films ($n \geqslant 6$). However, in the fct case (squares connected by dotted lines in Fig. 7) we observe a volume contribution to the band energy for thicker films. This gives rise to an almost linear increase of $\Delta E_{\mathrm{bnd}}$ with film thickness for $n \geqslant 6$. It overrides $\Delta E_{\mathrm{dd}}$ and therefore yields perpendicular anisotropy. For thin films, in particular the 2-ML and 3-ML films, we observe also a strong positive band-energy contribution which results in perpendicular anisotropy. We recall that the fct case by far overestimates the tetragonal distortion. So the fct LEED case is more appropriate (solid circles in Fig. 7) but leads also to perpendicular anisotropy for the 3-ML film. (To our knowledge, LEED investigations for all relevant film thicknesses have not been published up to date.) We would like to note that other calculations[42,43] also show perpendicular anisotropy for 2 ML and 3 ML films with band-energy differences of comparable size. This corroborates that—at least—the thinner films are idealizations of the experimental ones. In experiment, in-plane anisotropy is observed for thin films, but one should keep in mind that experimental samples are not as ''ideal'' as those in a zero-temperature theory due to, e.g., interface roughness, vacancies, and impurities, all of which lower the MAE.[15] Recent experiments[44] show that the quality of Ni films on Cu(001) indeed increases with film thickness. We have therefore performed simple test calculations within the virtual crystal approximation and the averaged *t*-matrix approximation in order to investigate the effect of interface roughness. For thicker films, the effect on the MAE is very small, but for thin films we observe a strong decrease of the MAE or even in-plane anisotropy. These calculations fully confirm the expectations, but we are aware that they can only reveal trends. More sophisticated calculations are therefore needed and are currently in progress.

The band-energy difference $\Delta E_{\mathrm{bnd}}$/atom obtained by superposition [diamonds in Fig. 7, Eq. (14)] show identical general shapes in both the fcc and fct cases: at very thin films (one and two layers) there is a strong increase whereas for thicker films ($n \geqslant 3$) the energies are nearly independent on the film thickness. Due to the volume contribution to the MAE, the latter curve is shifted to higher energies. This results in perpendicular anisotropy for film thicknesses $n \geqslant 2$ in the fct case, but in-plane anisotropy for all thicknesses in the fcc case. Thus, the latter fails completely to reproduce the experimental observed spin reorientation transition. The former, however, is able to reproduce the experimentally observed trends correctly but fails to reproduce the SRT film thickness. Quantum-size effects show up in the deviation of band-energy contributions obtained by the full calculation and the superposition of the surface and the interface profile (squares and diamonds in Fig. 7, respectively). In both the fcc and fct cases, quantum-well contributions to the band-energy contribution are strong and influence the anisotropy considerably.

In conclusion, we observe a strong perpendicular anisotropy from 6 ML and beyond which corresponds well with the experimental findings of the first SRT. The interior part of the film—roughly speaking the volume contribution to the MAE—can be regarded as responsible for the first SRT. However, quantum-well contributions to the MAE are strong and effect the film thickness at which the first SRT will occur. In particular, very thin fct films (e.g., 2 ML and 3 ML) show perpendicular anisotropy—in contrast to experiment—which indicates differences between the experimental films and the idealized films in theory. Our calculations show that the correct geometry (as, for example, obtained by LEED) as well as film imperfections have to be included in future work in order to explain this disagreement. To conclude on the second SRT (transition from perpendicular to in-plane magnetic moments which occurs around 35–70 ML) is difficult due to strain relaxation in thick films and island growth in experiment.[3,4,16]

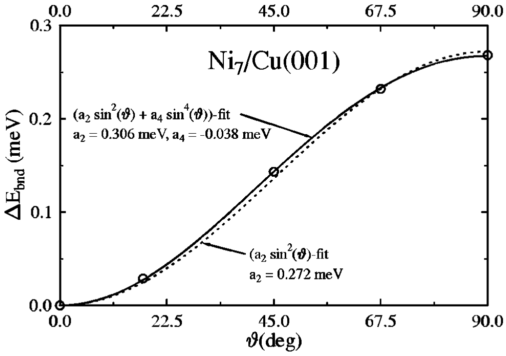

FIG. 8. Higher-order contribution to the band-energy difference $\Delta E_{\mathrm{bnd}}$ of 7 ML fct Ni on Cu(001). $\vartheta$ is the polar tilt angle of the magnetic moments [cf. Eq. (17)]. Circles represent results of the numerical calculations. The dotted line is a fit taking into account only the first-order contribution ($a_2$); the solid line is a fit for both first- and second-order contributions ($a_2$ and $a_4$).

At last, we address higher-order contributions to the MAE. For the film thickness of 7 ML in the fct case, the band-energy difference $\Delta E_{\mathrm{bnd}}$ was calculated for magnetic moments tilted at an polar angle $\vartheta$: $\vec{M}(\vartheta)=\vec{M}^{(\perp)}\cos\vartheta+\vec{M}^{(\parallel)}\sin\vartheta$. The dipole-dipole interaction energy is proportional to $\sin^2\vartheta$.[37] For the band energy we make the ansatz

$$E_{\mathrm{bnd}}(\vartheta)=a_2\sin^2\vartheta+a_4\sin^4\vartheta \tag{17}$$

and determined the coefficients $a_2$ and $a_4$ by least-squares fitting to the numerical results; cf. Fig. 8. The dotted line in Fig. 8 is the best fit when setting $a_4=0$, i.e., taking into account only the first-order contribution ($a_2=0.272$ meV). Apparently, it deviates visibly from the numerically obtained data. Taking into account the second-order contribution we find a perfect fit ($a_2=0.306$ meV, $a_4=-0.038$ meV). As in experiment, the first-order contribution is positive while the second-order contribution is negative.[14] To compare the theoretical anisotropy constants (obtained in a zero-temperature model) with experimental ones is difficult because they depend significantly on temperature (cf. Fig. 6 in Ref. 45). Thus, experimental values should be extrapolated to zero temperature which is—at present—hardly possible. At a reduced temperature $T/T_{\mathrm{C}}=0.2$ Baberschke and Farle[45] found for 7–8-ML films $a_2\approx 0.101$ meV and $a_4\approx -0.019$ meV. Thus, theory gives values approximately a factor of 2–3 too high which—besides the finite temperature—can be attributed to sample imperfections in experiment (which lower the MAE) or an overestimation of the lattice relaxation in theory (which increases the MAE).

Having focused on the film-averaged anisotropy constants, we now address briefly the layer-resolved values of $a_2$ and $a_4$. A closer analysis reveals that $a_2$ follows the band-energy difference profile very closely (cf. Fig. 5); in other words the first-order contribution is dominant for all layers. $a_4$ is negative for all Ni layers except for layer $S-1$ where it is positive but very small $(<0.0005\ \mathrm{meV})$. Multiplied by a factor, it agrees surprisingly nicely with the band-energy difference profile but appears to be shifted down in energy. The largest deviations are at layers $S,\ S-5$, and $S-6$, i.e., at the surface and at the interface. Further, $a_2$ and $a_4$ show the same sign for layers $S,\ S-1$, and $S-3$. As a rule of thumb, the layer-dependent first-order contribution $a_2$ can in good approximation be taken from the band-energy difference profiles, the second-order contribution $a_4$ as layer-independent and negative for all layers.

## V. CONCLUDING REMARKS

Film geometry, i.e., tetragonal distortion, and magnetic properties, in particular the anisotropy, of ultrathin Ni layers on Cu(001), are closely related. We have calculated both magnetization profiles and magnetic anisotropy of cubic and tetragonally distorted films for thicknesses from 1 ML up to 10 ML.

Thick fct films (with thicknesses larger than five monolayers) show an increase of the volume contribution to the magnetic-anisotropy energy which overrides the dipole-dipole interaction contribution. Thus, the experimentally observed spin reorientation transition from in-plane to perpendicular anisotropy at around six monolayers Ni can be attributed to this volume contribution. The surface anisotropy, i.e., perpendicular anisotropy at the outermost two to three layers, is too small compared to the volume contribution and thus cannot account for the observed transition. Further, the interface contribution favors an in-plane anisotropy which partially cancels the surface anisotropy.

In thin fct films (with thicknesses less than 6 ML) effects due to the quantization of electronic states within the Ni film are found to be significant. For these, we observe also perpendicular anisotropy, in particular for 2 ML and 3 ML thickness. This is in contrast to experiments but in agreement with other calculations[42,43] and, thus, gives evidence that idealized theoretical systems do not fully describe the experimental situation. Especially, mechanisms which lower the band-energy contribution to the MAE—such as surface and interface roughness[44]—are yet not taken into account. Simple test calculations for the effect of interface roughness yield a decrease of the MAE—as expected—but should be followed by more advanced work.

## ACKNOWLEDGMENTS

We very much appreciate fruitful discussions with K. Baberschke (Berlin) and H. L. Skriver (Lyngby). This work has been performed within the Training and Mobility of Researchers (TMR) Network ‘‘Interface Magnetism.’’ We also thank the Swedish Natural Science Research Council (NFR) and the Swedish Materials Consortium No. 9 financed by NUTEK and NFR for valuable support.

---

[1] B. Schulz and K. Baberschke, Phys. Rev. B **50**, 13 467 (1994).

[2] B. Schulz, R. Schwarzwald, and K. Baberschke, Surf. Sci. **307-309**, 1102 (1994).

[3] W. L. O'Brien and B. P. Tonner, J. Appl. Phys. **79**, 5623 (1996).

[4] W. L. O'Brien, T. Droubay, and B. P. Tonner, Phys. Rev. B **54**, 9297 (1996).

[5] J. Hunter Dunn, D. Arvinitis, and N. Mårtensson, Phys. Rev. B **54**, R11 157 (1996).

[6] R. Lorenz and J. Hafner, Phys. Rev. B **54**, 15 937 (1996).

[7] B. Újfalussy, L. Szunyogh, and P. Weinberger, Phys. Rev. B **54**, 9883 (1996).

[8] M. Zharnikov, A. Dittschar, W. Kuch, C. M. Schneider, and J. Kirschner, J. Magn. Magn. Mater. **174**, 40 (1997).

[9] A. Berger, B. Feldmann, H. Zillgen, and M. Wuttig, J. Magn. Magn. Mater. **183**, 35 (1998).

[10] C. M. Schneider, Ph.D. thesis, Freie Universität Berlin, 1990.

[11] W. Weber, A. Bischof, R. Allenspach, C. Back, J. Fassbender, U. May, B. Schirmer, R. Jungblut, G. Güntherodt, and B. Hillebrands, Phys. Rev. B **54**, 4075 (1996).

[12] Q. Y. Jin, H. Regensburger, R. Vollmer, and J. Kirschner, Phys. Rev. Lett. **80**, 4056 (1998).

[13] A. B. Shick, D. L. Novikov, and A. J. Freeman, J. Magn. Magn. Mater. **177-181**, 1223 (1998).

[14] M. Farle, B. Mirwald-Schulz, A. N. Anisimov, W. Platow, and K. Baberschke, Phys. Rev. B **55**, 3708 (1997).

[15] O. Hjortstam, K. Baberschke, J. M. Wills, B. Johansson, and O. Eriksson, Phys. Rev. B **55**, 15 026 (1997).

[16] J. Shen, J. Giergiel, and J. Kirschner, Phys. Rev. B **52**, 8454 (1995).

[17] O. K. Andersen, Phys. Rev. B **12**, 3060 (1975).

[18] H. Skriver, *The LMTO-Method* (Springer, Berlin, 1984).

[19] H. L. Skriver and N. M. Rosengaard, Phys. Rev. B **43**, 9538 (1991).

[20] O. K. Andersen and O. Jepsen, Phys. Rev. Lett. **53**, 2571 (1984).

[21] S. H. Vosko, L. Wilk, and M. Nusair, Can. J. Phys. **58**, 1200 (1980).

[22] B. Wenzien, J. Kudrnovský, V. Drchal, and M. Šob, J. Phys.: Condens. Matter **1**, 9893 (1989).

[23] E. Tamura, in *Applications of Multiple Scattering Theory to Materials Science*, edited by W. H. Butler, P. H. Dederichs, A. Gonis, and R. L. Weaver, MRS Symposia Proceedings No. 253 (Materials Research Society, Pittsburgh, 1992), p. 347.

[24] *Electron Scattering Theory of Ordered and Disordered Matter*, edited by P. Weinberger (Clarendon Press, Oxford, 1990).

[25] H. J. Monkhorst and J. D. Pack, Phys. Rev. B **13**, 5188 (1976).

[26] R. Evarestov and V. Smirnow, Phys. Status Solidi B **119**, 9 (1983).

[27] S. S. A. Razee, J. B. Staunton, and F. J. Pinski, Phys. Rev. B **56**, 8082 (1997).

[28] S. V. Halilov, A. Y. Perlov, P. M. Openeer, A. N. Yaresko, and

V. N. Antonov, Phys. Rev. B **57**, 9557 (1998).

[29] *Handbook of Mathematical Functions*, edited by M. Abramowitz and I. Stegun (Dover, New York, 1970).

[30] L. Szunyogh, B. Újfalussy, and P. Weinberger, Phys. Rev. B **51**, 9552 (1995).

[31] S. Müller, B. Schulz, G. Kostka, M. Farle, K. Heinz, and K. Baberschke, Surf. Sci. **364**, 235 (1996).

[32] S. Müller, A. Kinne, M. Kottke, R. Metzler, P. Bayer, L. Hammer, and K. Heinz, Phys. Rev. Lett. **75**, 2859 (1995).

[33] A. M. N. Niklasson, S. Mirbt, H. L. Skriver, and B. Johansson, Phys. Rev. B **53**, 8509 (1996).

[34] J. E. Ortega, F. J. Himpsel, G. J. Mankey, and R. F. Willis, Phys. Rev. B **47**, 1540 (1993).

[35] F. J. Himpsel, J. E. Ortega, G. J. Mankey, and R. F. Willis, Adv. Phys. **47**, 511 (1998).

[36] B. Heinrich and J. F. Cochran, Adv. Phys. **42**, 523 (1993).

[37] L. Szunyogh, B. Újfalussy, C. Blaas, U. Pustogowa, C. Sommers, and P. Weinberger, Phys. Rev. B **56**, 14 036 (1997).

[38] K. Baberschke, Appl. Phys. A: Mater. Sci. Process. **62**, 427 (1996).

[39] A. M. N. Niklasson, B. Johansson, and H. L. Skriver, Phys. Rev. B **59**, 6373 (1999).

[40] K. Adachi, D. Bonnenberg, K. A. Hempel, and H. P. J. Wijn, in *Magnetic Properties of Metals*, edited by H. P. J. Wijn, Landolt-Börnstein, New Series, Group 3, Vol. 19, Pt. a (Springer, Berlin, 1986), Chap. 1.2, p 142.

[41] P. James, O. Eriksson, B. Johansson, and I. A. Abrikosov, Phys. Rev. B **59**, 419 (1999).

[42] C. Uiberacker, J. Zabloudil, P. Weinberger, L. Szunyogh, and C. Sommers, Phys. Rev. Lett. **82**, 1289 (1999).

[43] D. Spišák and J. Hafner (unpublished).

[44] W. Platow, A. N. Anisimov, G. L. Dunifer, M. Farle, and K. Baberschke, Phys. Rev. B **58**, 5611 (1998).

[45] K. Baberschke and M. Farle, J. Appl. Phys. **81**, 5038 (1997).

## P.3. Photoelektronenspektroskopie

**4 (S. P34ff)** J. Henk, T. Scheunemann, S. V. Halilov, R. Feder.
*Magnetic dichroism and electron spin polarization in photoemission: Analytical results.*
Journal of Physics: Condensed Matter **8** (1996) 47.

**5 (S. P53ff)** J. Henk, R. Feder.
*Spin polarization in normal photoemission by linearly polarized light from non-magnetic (110) surfaces.*
Europhysics Letters **28** (1994) 609.

**6 (S. P59ff)** W. Kuch, A. Dittschar, K. Meinel, M. Zharnikow, C. M. Schneider, J. Kirschner, J. Henk, R. Feder.
*Magnetic-circular-dichroism study of the valence states of perpendicularly magnetized Ni(001) films.*
Physical Review B **53** (1996) 11 621.

**7 (S. P69ff)** A. Rampe, G. Güntherodt, D. Hartmann, J. Henk, T. Scheunemann, R. Feder.
*Magnetic linear dichroism in valence-band photoemission: Experimental and theoretical study of Fe(110).*
Physical Review B **57** (1998) 14 370.

**8 (S. P80ff)** J. Henk.
*Temperature-dependent electronic structure, spin-resolved photoemission, and magnetic dichroism from ultra-thin ferromagnetic films: Co/Cu(001).*
Journal of Physics: Condensed Matter **13** (2001) 833.

**9 (S. P97ff)** J. Henk, B. Johansson.
*Quantum–size effects in photoemission from ultra-thin films: Theory and application to Cu-films on fcc-Co(001).*
Journal of Electron Spectroscopy & Related Phenomena **105** (1999) 187.

**10 (S. P107ff)** N. Fominykh, J. Berakdar, J. Henk, P. Bruno.
*Spectroscopy of the electron-electron interaction in solids.*
Physical Review Letters **89** (2002) 086402.

**Publikation 4**

# Magnetic dichroism and electron spin polarization in photoemission: analytical results

J Henk, T Scheunemann, S V Halilov and R Feder
Theoretische Festkörperphysik, Universität Duisburg, D-47048 Duisburg, Germany

Received 21 June 1995, in final form 26 October 1995

**Abstract.** For cubic (001), (110) and (111) surface systems with in-plane or perpendicular magnetization, valence-band photoemission along the surface normal is studied analytically by evaluating electric dipole transition matrix elements between half-space initial and final states of the appropriate double-group symmetry. Explicit expressions are obtained for the spin-polarization vector of the photoelectrons, and the spin-averaged intensity and its change upon reversal of the magnetization direction, i.e. magnetic dichroism, for circularly and linearly polarized incident light. These results firstly elucidate the origin of spin polarization and dichroism in terms of an interplay between spin–orbit coupling and exchange, and secondly provide a systematic overview of possible effects. In particular, we predict new types of magnetic linear dichroism for s-polarized light in the case of magnetization perpendicular to surfaces with a twofold rotation axis and in the case of in-plane magnetization of fcc (111) or hcp (0001) surfaces.

## 1. Introduction

Spin-resolved photoemission is well established as a powerful tool for studying magnetic properties of surfaces and ultrathin films (see, e.g., monographs by Feder (1985) and Kevan (1992), recent original articles by Hartmann *et al* (1993a, b), Carbone *et al* (1993), Rader *et al* (1994), Smith *et al* (1994), Wu *et al* (1994), and references therein). The traditional analysis of the photoelectron spin-polarization component along the magnetization direction has recently been complemented by asymmetries in the spin-averaged photocurrent produced by circularly or linearly polarized radiation upon reversal of the magnetization. This so-called magnetic circular dichroism (MCD) and linear dichroism (MLD) in photoemission was first experimentally observed from core levels (Baumgarten *et al* 1990, Roth *et al* 1993a, b). Its potential relevance for magnetic storage technology was recently highlighted by the successful element-specific imaging of magnetic domains (Schneider *et al* 1994). There is also experimental evidence of MCD and MLD in valence-band photoemission (Schneider *et al* 1991a, b, Bansmann *et al* 1992, Rose *et al* 1994). A systematic overview and classification of the rather wide variety of magnetic dichroism effects have been provided by Venus (1993, 1994) (see also Venus *et al* 1993). On the theoretical side, there have been a series of many-body-type studies (see Thole and van der Laan (1994) and references therein), which are however in practice restricted to an atomic approximation not quantitatively valid for crystalline systems. Quantitative explanations of MCD and MLD in photoemission from core levels have been obtained by means of relativistic multiple-scattering formalisms, treating the final state as bulk-like (Ebert *et al* 1991) and as a time-reversed LEED state

(Tamura *et al* 1994). As regards valence-band photoemission, a relativistic multiple-scattering formalism (Halilov *et al* 1993) has recently been applied to Ni(001), yielding prototype numerical results on MCD for magnetization normal to the surface (Scheunemann *et al* 1994) and on two types of MLD due to s-polarized and p-polarized light in the case of in-plane magnetization (Henk *et al* 1994). While this type of numerical calculation is indispensable for a detailed quantitative analysis of experimental results, more information on general features and insight into the underlying physical mechanisms might be gained by analytical calculations.

In this paper, we therefore present an analytical study of spin-polarization and magnetic dichroic effects in valence-band photoemission. For the sake of transparency, we focus on highly symmetric set-ups: normal emission, i.e. with $\boldsymbol{k}_\parallel = 0$, from low-index surfaces with a perpendicular fourfold, threefold or twofold rotational axis. In line with experimental reality, the magnetization is assumed normal to the surface or parallel to it along a high-symmetry direction. Within a relativistic single-particle framework, we calculate the photoelectron spin-density matrix by evaluating electric dipole transition matrix elements produced by s-, p- and circularly polarized radiation between initial and final half-space states, which are constructed from symmetry-adapted basis functions. From this density matrix, we obtain explicit expressions for the photoelectron spin-polarization vector, the spin-averaged intensity and its asymmetry upon magnetization reversal, i.e. magnetic dichroism. Firstly, we thus derive general relations, which are valid both in valence-band and in core-level photoemission. Apart from their fundamental interest, they might be useful in checking the reliability of experimental and of numerically calculated spectra. Secondly, the origin of the components of the electron spin-polarization (ESP) vector is elucidated by explicitly expressing them in terms of spin–orbit- and exchange-derived contributions. The occurrence of the two contributions in a component is generally associated with magnetic dichroism. Comparison of our results for ferromagnetic surface systems with their nonmagnetic limit reveals an intimate connection between MLD and spin-polarization effects, which are produced by linearly polarized light from nonmagnetic surfaces due to SOC. If such a ‘linear spin-polarization effect’ (LSPE) involves an ESP component parallel to the magnetization, MLD is found. The situation is analogous in the case of MCD, where the purely spin–orbit-induced ESP component is due to optical orientation (Fano effect) by circularly polarized light. We thus reach a unified understanding of both MCD and MLD.

This paper is organized as follows. In section 2 we give some basic properties of relativistic electronic states in connection with photoemission. In section 3 we present analytical results for normal photoemission from systems with magnetization normal to the surface, before turning to the case of in-plane magnetization in section 4. In section 5 we discuss the connection between magnetic dichroism and spin-polarization effects. Some concluding remarks are made in section 6.

## 2. Symmetry-adapted electronic states and photoemission

The general framework of a fully relativistic one-step theory of photoemission from semi-infinite crystalline systems, which incorporates both spin–orbit coupling and a ferromagnetic ground state, and simpler spin-dependent approximations have been presented in chapter 4.5 in a monograph by Feder (1985). It may therefore suffice here to briefly specify the approach used in the present work. Whilst a relativistic Green function formulation, like the one worked out in detail by Halilov *et al* (1993), should be employed in numerical calculations aiming at a quantitative comparison with experimental spectra, analytical expressions are more transparent and instructive if one firstly replaces the initial-state Green function by its spectral representation in terms of states $|i\rangle$ (solutions of the Dirac equation without an imaginary potential part), and secondly approximates the initial- and final-state four-component spinors with two-component spinors $|i_s\rangle$ and $|f_s\rangle$, with $s = \pm$, which are eigenfunctions of a Pauli-like Hamiltonian retaining of course spin–orbit coupling (see, e.g., Feder (1985), p 131). One thus obtains a golden rule form for the spin-density matrix of the photocurrent with elements

$$\varrho_{ss'}(E_f) = \sum_{i,s''} \langle f_s|H'|i_{s''}\rangle\langle i_{s''}|H'|f_{s'}\rangle\ \delta(E_f - \hbar\omega - E_{i_{s''}}). \tag{1}$$

The final states $|f_+\rangle$ and $|f_-\rangle$ both have the energy $E_f$, and only initial states with energy $E_f - \hbar\omega$ contribute. As a consequence of lattice periodicity parallel to the surface, all states have the same surface-parallel wave vector $\boldsymbol{k}_\parallel$. The photon–electron interaction $H'$ is $\boldsymbol{E}\cdot\boldsymbol{r}$ with a spatially constant electric field vector $\boldsymbol{E}$ of the incident light, i.e. we adopt the electric dipole approximation, which is adequate for valence-band photoemission by radiation in the vacuum–ultraviolet regime. With a view to explicitly evaluating equation (1) for highly symmetrical set-ups, we now introduce symmetry-adapted forms of the initial and final states.

Consider two sets of basis functions, $\{|g_n^+\rangle\}$ and $\{|g_n^-\rangle\}$—consisting of an angular part and a Pauli spinor (Rose 1961)—of an extra irreducible representation of the double group associated with some point group, which transform under time reversal $\widetilde{T}$ as $\widetilde{T}|g_n^+\rangle = |g_n^-\rangle$ and $\widetilde{T}|g_n^-\rangle = -|g_n^+\rangle$. The basis function sets are not unique, but the results presented below do not depend on the particular choice. Electronic eigenstates of the Pauli Hamiltonian of a *nonmagnetic* semi-infinite system can be expressed as $|\Psi_s\rangle = \sum_n \alpha_n|R_n\rangle|g_n^s\rangle$, $s = \pm$, where $|R_n\rangle$ are normalized radial functions and $\alpha_n$ are real coefficients. These states obviously transform under time reversal like their respective basis sets. Both have the same $\alpha_n$ and $|R_n\rangle$ as well as the same energy, i.e. Kramers' degeneracy. For *magnetic* systems, Kramers' degeneracy is lifted and we have

$$|\Psi_s\rangle = \sum_n \alpha_n^{(s)}|R_n^s\rangle|g_n^s\rangle \qquad s = \pm \tag{2}$$

with $\alpha_n^{(+)} \neq \alpha_n^{(-)}$ and $|R_n^+\rangle \neq |R_n^-\rangle$ and exchange-split energy eigenvalues. As a consequence of spin–orbit coupling, the spin-polarization expectation value $\boldsymbol{P}$ of $|\Psi_s\rangle$ generally has an absolute value less than unity and may change sign with energy. But it is still meaningful to refer to 'majority' and 'minority' states according to the direction of their $\boldsymbol{P}$.

We now use the above for further evaluating the photocurrent-density matrix $\varrho$. The final states $|f_s\rangle$ at energy $E_f$ are the time-reversed LEED spinors with electron spin $s$ (relative to some fixed direction) at the detector. They are expressed in the form of equation (2) with complex coefficients $\beta_m^{(s)}$:

$$|f_s\rangle = \sum_m \beta_m^{(s)}|\tilde{R}_m^s\rangle|g_m^s\rangle \qquad s = \pm. \tag{3}$$

As is evident from group theory, the set of conceivable initial states (with energy $E_f - \hbar\omega$) decomposes into pairs of initial states $|i_+^r\rangle$ and $|i_-^r\rangle$, where $r$ denotes the relevant representations (cf. Falicov and Ruvalds 1968). The total photocurrent is thence the sum of the photocurrents obtained for each pair. We note that in many practical cases only one pair or even only one of its partners actually contributes, and therefore focus on these partial photocurrents, drop the symmetry index $l$ and express the initial states $|i_s\rangle$ as in equation (2). The dipole transition matrix elements

$$W_{ss'} = \langle f_s|\boldsymbol{E}\cdot\boldsymbol{r}|i_{s'}\rangle \qquad s, s' = \pm \tag{4}$$

then become linear combinations of matrix elements between the basis functions. The (spatially uniform) electric field vector $\boldsymbol{E}$ of the incident light is decomposed into $E_{\parallel}$ and $E_{\perp}$ parallel and normal to the plane of incidence. Defining

$$H_{\perp}(\varphi) = \frac{\mathrm{i}}{\sqrt{2}}\left(\exp(\mathrm{i}\varphi)Y_1^{-1} + \exp(-\mathrm{i}\varphi)Y_1^{1}\right) \tag{5$a$}$$

$$H_{\parallel}(\varphi) = \frac{1}{\sqrt{2}}\left(\exp(\mathrm{i}\varphi)Y_1^{-1} - \exp(-\mathrm{i}\varphi)Y_1^{1}\right) \tag{5$b$}$$

$$H_z = Y_1^0 \tag{5$c$}$$

where $Y_l^m$ are the usual spherical harmonics, we obtain for the electric dipole operator

$$\boldsymbol{E}\cdot\boldsymbol{r} = \sqrt{\frac{4\pi}{3}}\, r\left(E_{\parallel}(-\sin\vartheta\ H_z + \cos\vartheta\ H_{\parallel}(\varphi)) + E_{\perp}H_{\perp}(\varphi)\right). \tag{6}$$

The polar and azimuthal angles $\vartheta$ and $\varphi$ refer to the direction of light incidence. For s- and p-polarized light we have $(E_{\parallel}, E_{\perp}) = (0, E)$ and $(E, 0)$, and for left- (right-) handed circularly polarized light $(E_{\parallel}, E_{\perp}) = E(\pm\mathrm{i}, 1)/\sqrt{2}$. Equation (6) and the state expansion equations (2) and (3) are then used to evaluate the matrix elements $W_{ss'}$. The resulting expressions are employed in the photoelectron spin-density matrix

$$\varrho = \begin{pmatrix} |W_{++}|^2 + |W_{+-}|^2 & W_{++}W_{-+}^{\star} + W_{+-}W_{--}^{\star} \\ W_{++}^{\star}W_{-+} + W_{+-}^{\star}W_{--} & |W_{-+}|^2 + |W_{--}|^2 \end{pmatrix}. \tag{7}$$

The (not spin-resolved) intensity $I(\varphi, \vartheta)$ and the electron spin-polarization (ESP) vector $\boldsymbol{P}(\varphi, \vartheta)$ of the energy- and angle-resolved symmetry-specific photocurrent are then easily obtained as $I(\varphi, \vartheta) = \mathrm{tr}(\varrho)$ and $\boldsymbol{P}(\varphi, \vartheta) = \mathrm{tr}(\boldsymbol{\sigma}\varrho)/I(\varphi, \vartheta)$. Magnetic dichroism can be characterized by the (not normalized) asymmetry $A(\varphi, \vartheta) = I(\varphi, \vartheta, \boldsymbol{M}) - I(\varphi, \vartheta, -\boldsymbol{M})$, i.e. the intensity change upon magnetization reversal.

## 3. Results for magnetization normal to the surface

We now evaluate the above expressions for normal emission from surface systems with two-, three-, and fourfold rotational axes and with magnetization $\boldsymbol{M}$ normal to the surface. The underlying nonmagnetic point groups are $2mm$, $3m$, and $4mm$, i.e. $C_{2v}$, $C_{3v}$, and $C_{4v}$ in the Schönflies notation. Taking into account $\boldsymbol{M}$, the surface normal remains an $n$-fold rotation axis, but the mirror operations $m$ are no longer symmetry operations, since they reverse $\boldsymbol{M}$. We thus have a *reduction of symmetry* with respect to the nonmagnetic case. Instead of applying magnetic double-group theory (Falicov and Ruvalds 1968, Ruvalds and Falicov 1968), we adopt a more transparent approach, which facilitates contact with the nonmagnetic case and reveals easily the roles played by the spin–orbit and by the exchange interaction in producing the photoelectron spin-polarization vector and magnetic dichroism. The essential idea is to express initial and final states in terms of the basis functions of the irreducible representations of the *nonmagnetic double groups*, but with Kramers' degeneracy lifted. We then use these forms to evaluate the dipole transition matrix elements $W_{ss'}$ (cf. equation (4)). Details of this approach are given in the case of twofold rotation symmetry, to which we now turn.

### 3.1. The twofold rotational axis

Spin–orbit coupling mixes the four one-dimensional representations $\Sigma^1, \ldots, \Sigma^4$ of the single group $2mm$ into one representation $\Sigma_5$ of the corresponding double group (see, for example, Inui *et al* 1990). Initial and final states can then be written in the form

$$|\Psi_s\rangle = c_1^{(s)}|\Sigma_5^{1s}\rangle|s\rangle + c_2^{(s)}|\Sigma_5^{2s}\rangle|s\rangle + c_3^{(s)}|\Sigma_5^{3s}\rangle|-s\rangle + c_4^{(s)}|\Sigma_5^{4s}\rangle|-s\rangle. \tag{8}$$

The $|s\rangle$ are the Pauli spinors (aligned with respect to $\boldsymbol{M}$) and the $|\Sigma_5^{is}\rangle$ (with $i = 1, \dots, 4$) are normalized spatial parts of the single-group symmetry $\Sigma^i$; the weight coefficients $c_n^{(s)}$ directly reflect the spin–orbit coupling. The upper index $s = \pm$ is needed because of the absence of Kramers' degeneracy due to the exchange interaction. Without magnetization, $|\Sigma_5^{n+}\rangle = |\Sigma_5^{n-}\rangle$. Dipole matrix elements between states of the form of equation (8) are easily evaluated, since the dipole operator does not affect the Pauli spinors and couples the spatial parts according to the usual nonrelativistic dipole selection rules. As the final states have pure $\Sigma_5^1$ spatial symmetry outside the crystal and still predominantly so inside, we approximate them in the following as $|f_s\rangle = |\Sigma_5^{1s}\rangle|s\rangle$, i.e. we neglect SOC in the final state. The nonvanishing partial matrix elements involving final-state spatial parts $\Sigma_5^{1s}$ and initial-state parts $\Sigma_5^{is'}$ are denoted by $M^{iss'}$. The dipole matrix elements then become

$$W_{++} = -\sin\vartheta\ E_\parallel M_\perp^{(1++)} \tag{9$a$}$$

$$\begin{aligned} W_{+-} = E_\perp &\left\{-\sin\varphi\ M_\parallel^{(3+-)} + \mathrm{i}\cos\varphi\ M_\parallel^{(4+-)}\right\} \\ &+E_\parallel \cos\vartheta \left\{\cos\varphi\ M_\parallel^{(3+-)} + \mathrm{i}\sin\varphi\ M_\parallel^{(4+-)}\right\} \end{aligned} \tag{9$b$}$$

$$\begin{aligned} W_{-+} = E_\perp &\left\{\sin\varphi\ M_\parallel^{(3-+)} + \mathrm{i}\cos\varphi\ M_\parallel^{(4-+)}\right\} \\ &+E_\parallel \cos\vartheta \left\{-\cos\varphi\ M_\parallel^{(3-+)} + \mathrm{i}\sin\varphi\ M_\parallel^{(4-+)}\right\} \end{aligned} \tag{9$c$}$$

$$W_{--} = -\sin\vartheta\ E_\parallel M_\perp^{(1--)}. \tag{9$d$}$$

The corresponding results for a nonmagnetic system are easily recovered from the above by noting that for vanishing exchange splitting $M^{i+-} = M^{i-+} = M^i$.

For *s-polarized light*, i.e. $E_\perp = E$ and $E_\parallel = 0$, we obtain upon substitution of equation (8) into equation (7)

$$\begin{aligned} I(\varphi) = \sin^2\varphi &\left(|M_\parallel^{(3+-)}|^2 + |M_\parallel^{(3-+)}|^2\right) + \cos^2\varphi \left(|M_\parallel^{(4+-)}|^2 + |M_\parallel^{(4-+)}|^2\right) \\ &+ \sin 2\varphi \left(\mathrm{Im}(M_\parallel^{(3-+)} M_\parallel^{(4-+)\star}) - \mathrm{Im}(M_\parallel^{(3+-)} M_\parallel^{(4+-)\star})\right) \end{aligned} \tag{10}$$

and

$$\begin{aligned} P_z(\varphi) = &\left\{\sin^2\varphi \left(|M_\parallel^{(3+-)}|^2 - |M_\parallel^{(3-+)}|^2\right) + \cos^2\varphi \left(|M_\parallel^{(4+-)}|^2 - |M_\parallel^{(4-+)}|^2\right)\right. \\ &\left. - \sin 2\varphi \left(\mathrm{Im}(M_\parallel^{(3-+)} M_\parallel^{(4-+)\star}) + \mathrm{Im}(M_\parallel^{(3+-)} M_\parallel^{(4+-)\star})\right)\right\} \Big/ I(\varphi). \end{aligned} \tag{11}$$

The surface-parallel spin-polarization components $P_x$ and $P_y$ are zero. Since reversal of the magnetization interchanges $M_\parallel^{(i+-)}$ with $M_\parallel^{(i-+)}$, the asymmetry, which constitutes the MLD, is obtained from equation (10) as

$$A(\varphi) = 2\sin 2\varphi \left(\mathrm{Im}(M_\parallel^{(3-+)} M_\parallel^{(4-+)\star}) - \mathrm{Im}(M_\parallel^{(3+-)} M_\parallel^{(4+-)\star})\right). \tag{12}$$

This expression directly reveals spin–orbit coupling as the physical origin of this type of MLD: the products $M_\parallel^{(3-+)} M_\parallel^{(4-+)\star}$ arise from the simultaneous presence of symmetry types $\Sigma_5^3$ and $\Sigma_5^4$ in the initial state, equation (8), which is brought about by SOC. In the nonmagnetic limit, $A(\varphi)$ is seen to be identically zero, as it should be. Also, there is no

MLD if the electric field vector lies in a mirror plane ($\varphi = 0$ or $\pi/2$). The spin–orbit-induced product terms also occur in the above expression for $P_z$ in addition to the first two terms, which are due to exchange interaction. If $\boldsymbol{M}$ equals zero, this expression becomes

$$P_z(\varphi) = 2\sin 2\varphi\ \mathrm{Im}(M_\parallel^{(3)} M_\parallel^{(4)\star}) \Big/ I(\varphi) \tag{13}$$

i.e. the 'linear spin-polarization effect' predicted by Henk and Feder (1994) for $2mm$-symmetry nonmagnetic surfaces.

Our above analytical expressions are in line with what follows from general symmetry arguments. The reflection operations $m_1$ and $m_2$ at the $(x, z)$- and $(y, z)$-plane do not leave the total set-up invariant, but their combination $m_1 m_2$ does. The latter dictates that $P_x$ and $P_y$ are zero, since it reverses their signs, but does not impose any restriction on $P_z$. Reflection $m_1$ implies the relations $I(\varphi, \boldsymbol{M}) = I(-\varphi, -\boldsymbol{M})$ and $P_z(\varphi, \boldsymbol{M}) = -P_z(-\varphi, -\boldsymbol{M})$, which can also be seen directly from our above formulae.

For off-normally incident *p-polarized light*, we obtain for the intensity

$$\begin{aligned} I(\vartheta, \varphi) = {} & \sin^2\vartheta \left(|M_\perp^{(1++)}|^2 + |M_\perp^{(1--)}|^2\right) + \cos^2\vartheta\cos^2\varphi \left(|M_\parallel^{(3+-)}|^2 + |M_\parallel^{(3-+)}|^2\right) \\ & + \cos^2\vartheta\sin^2\varphi \left(|M_\parallel^{(4+-)}|^2 + |M_\parallel^{(4-+)}|^2\right) \\ & + \cos^2\vartheta\sin 2\varphi \left(\mathrm{Im}(M_\parallel^{(3+-)} M_\parallel^{(4+-)\star}) - \mathrm{Im}(M_\parallel^{(3-+)} M_\parallel^{(4-+)\star})\right) \end{aligned} \tag{14}$$

and three nonzero ESP components

$$\begin{aligned} P_z(\vartheta, \varphi) = {} & \frac{1}{I(\vartheta, \varphi)} \Big[\sin^2\vartheta \left(|M_\perp^{(1++)}|^2 - |M_\perp^{(1--)}|^2\right) \\ & + \cos^2\vartheta\cos^2\varphi \left(|M_\parallel^{(3+-)}|^2 - |M_\parallel^{(3-+)}|^2\right) \\ & + \cos^2\vartheta\sin^2\varphi \left(|M_\parallel^{(4+-)}|^2 - |M_\parallel^{(4-+)}|^2\right) \\ & + \cos^2\vartheta\sin 2\varphi \left(\mathrm{Im}(M_\parallel^{(3+-)} M_\parallel^{(4+-)\star}) + \mathrm{Im}(M_\parallel^{(3-+)} M_\parallel^{(4-+)\star})\right)\Big] \end{aligned} \tag{15$a$}$$

$$\begin{aligned} P_x(\vartheta, \varphi) = {} & \frac{\sin 2\vartheta}{I(\vartheta, \varphi)} \Big[\cos\varphi \left(\mathrm{Re}(M_\perp^{(1++)} M_\parallel^{(3-+)\star}) - \mathrm{Re}(M_\perp^{(1--)} M_\parallel^{(3+-)\star})\right) \\ & - \sin\varphi \left(\mathrm{Im}(M_\perp^{(1++)} M_\parallel^{(4-+)\star}) + \mathrm{Im}(M_\perp^{(1--)} M_\parallel^{(4+-)\star})\right)\Big] \end{aligned} \tag{15$b$}$$

$$\begin{aligned} P_y(\vartheta, \varphi) = {} & -\frac{\sin 2\vartheta}{I(\vartheta, \varphi)} \Big[\cos\varphi \left(\mathrm{Im}(M_\perp^{(1++)} M_\parallel^{(3-+)\star}) + \mathrm{Im}(M_\perp^{(1--)} M_\parallel^{(3+-)\star})\right) \\ & - \sin\varphi \left(\mathrm{Re}(M_\perp^{(1++)} M_\parallel^{(4-+)\star}) - \mathrm{Re}(M_\perp^{(1--)} M_\parallel^{(4+-)\star})\right)\Big]. \end{aligned} \tag{15$c$}$$

The asymmetry $A(\vartheta, \varphi)$ is the same as for s-polarized light (equation (12)) but multiplied by $\cos^2\vartheta$, i.e. there is again MLD, which is due to SOC between $\Sigma_5^3$ and $\Sigma_5^4$ symmetry initial-state parts.

$P_z$ again consists of an exchange-induced part (the first three terms in equation (15$a$)) and a spin–orbit-induced part (the last term in equation (15$a$)), which in the nonmagnetic limit again becomes the recently predicted LSPE (Henk and Feder 1994). $P_x$ and $P_y$ also do not vanish in the nonmagnetic case, but reproduce the LSPE due to p-polarized light, with $\boldsymbol{P}$ normal to the reaction plane, which was predicted by Tamura and Feder (1991a, b) and experimentally verified by Heinzmann's group (Schmiedeskamp *et al* 1991, Irmer *et al* 1992).

The intensity and ESP fulfil the symmetry relation

$$(I, P_x, P_y, P_z) \overset{\varphi\to-\varphi, \boldsymbol{M}\to-\boldsymbol{M}}{\longrightarrow} (I, -P_x, P_y, -P_z). \tag{16}$$

The relations for $P_x$ and $P_y$ follow immediately from the symmetry operation $2 \circ m_1 \circ m_2$. Furthermore,

$$(I, P_x, P_y, P_z) \overset{\vartheta\to-\vartheta}{\longrightarrow} (I, -P_x, -P_y, P_z) \tag{17}$$

as is obvious from the twofold rotational symmetry. Note that the transformation $\vartheta \to -\vartheta$ is identical to $\varphi \to \varphi + \pi$. The results for s-polarized light can be easily obtained from equations (14) and (15*c*) by setting $\vartheta = 0$ and $\varphi \to \varphi + \pi/2$.

For *circularly polarized light*, we confine ourselves (in this paper) to the case of normal incidence, i.e. $\vartheta = 0$. The intensity and ESP are given by

$$\begin{aligned} I(\sigma_\pm) = \frac{1}{2} \Big( &|M_\parallel^{(3+-)}|^2 + |M_\parallel^{(3-+)}|^2 + |M_\parallel^{(4+-)}|^2 + |M_\parallel^{(4-+)}|^2 \\ &\mp \Big( \mathrm{Re}(M_\parallel^{(3+-)} M_\parallel^{(4+-)\star}) - \mathrm{Re}(M_\parallel^{(3-+)} M_\parallel^{(4-+)\star}) \Big) \Big) \end{aligned} \tag{18}$$

and

$$\begin{aligned} P_z(\sigma_\pm) = \frac{1}{2I(\sigma_\pm)} \Big( &|M_\parallel^{(3+-)}|^2 - |M_\parallel^{(3-+)}|^2 + |M_\parallel^{(4+-)}|^2 - |M_\parallel^{(4-+)}|^2 \\ &\mp \Big( \mathrm{Re}(M_\parallel^{(3+-)} M_\parallel^{(4+-)\star}) + \mathrm{Re}(M_\parallel^{(3-+)} M_\parallel^{(4-+)\star}) \Big) \Big) \end{aligned} \tag{19}$$

where the two signs correspond to the two helicities of the light $(\sigma_\pm)$. The asymmetry, i.e. the MCD, is immediately obtained as

$$A(\sigma_\pm) = \mp 2 \Big( \mathrm{Re}(M_\parallel^{(3+-)} M_\parallel^{(4+-)\star}) - \mathrm{Re}(M_\parallel^{(3-+)} M_\parallel^{(4-+)\star}) \Big). \tag{20}$$

Obviously, it requires for its existence SOC between initial-state parts of $\Sigma_5^3$ and $\Sigma_5^4$ symmetry as well as exchange splitting. It is interesting to note that MCD (equation (20)) involves the real part of the matrix element product, whereas MLD (cf. equation (12)) is described by its imaginary part. By measuring, in addition to the intensity, the asymmetries for circularly and linearly polarized light, one can therefore obtain information not only about the modulus of the transition matrix elements, but also about their real and imaginary parts, i.e. their phase.

The intensity and ESP obey the relations $I(\sigma_\pm, \boldsymbol{M}) = I(\sigma_\mp, -\boldsymbol{M})$, and $P_z(\sigma_\pm, \boldsymbol{M}) = -P_z(\sigma_\mp, -\boldsymbol{M})$. Furthermore, the intensity is closely related to that for s-polarized light,

$$I(s, \varphi = 0) + I(s, \varphi = \pi/2) = I(\sigma_+) + I(\sigma_-). \tag{21}$$

### 3.2. *The fourfold rotational axis*

Electronic states of surface systems with 4*mm* symmetry, i.e. $C_{4v}$ in Schönflies notation, can be classified according to two irreducible representations, $\Delta_6$ and $\Delta_7$, of the (nonmagnetic) double group. For magnetization normal to the surface, this classification still holds except for the lifting of Kramers' degeneracy. We recall that in the case of $\Delta_6$ SOC mixes spatial parts of $\Delta_6^1$ and $\Delta_6^5$ spatial symmetry. The final states have $\Delta_6$ symmetry, and we restrict ourselves again to the dominant part, $\Delta_6^1$.

Let us first consider photoemission from $\Delta_6$ initial states. Proceeding analogously to the above method for twofold rotational symmetry, we obtain for s-polarized light the intensity

$$I = |M_\parallel^{(5+-)}|^2 + |M_\parallel^{(5-+)}|^2 \tag{22}$$

and for the ESP, which only has a component normal to the surface,

$$P_z = \left(|M_{\|}^{(5+-)}|^2 - |M_{\|}^{(5-+)}|^2\right) \Big/ I. \tag{23}$$

In contrast to our above findings for surfaces with twofold rotational axes, both the intensity and the ESP are independent of the azimuth $\varphi$, and there is no MLD. This is easily understood from our previous results: going from $2mm$ to $4mm$ symmetry we get $M_{\|}^{(3+-)} = M_{\|}^{(4+-)}$ and $M_{\|}^{(3-+)} = M_{\|}^{(4-+)}$. Further we obtain, in accordance with symmetry arguments, the following (rather trivial) relations: $I(\boldsymbol{M}) = I(-\boldsymbol{M})$ and $P_z(\boldsymbol{M}) = -P_z(-\boldsymbol{M})$.

We now turn to p-polarized light. In this case, the intensity is obtained as

$$I(\vartheta) = \sin^2\vartheta \left(|M_{\perp}^{(1++)}|^2 + |M_{\perp}^{(1--)}|^2\right) + \cos^2\vartheta \left(|M_{\|}^{(5+-)}|^2 + |M_{\|}^{(5-+)}|^2\right). \tag{24}$$

All three components of the ESP are nonzero:

$$P_z(\vartheta) = \left\{\sin^2\vartheta \left(|M_{\perp}^{(1++)}|^2 - |M_{\perp}^{(1--)}|^2\right) + \cos^2\vartheta \left(|M_{\|}^{(5+-)}|^2 - |M_{\|}^{(5-+)}|^2\right)\right\} \Big/ I(\vartheta) \tag{25$a$}$$

$$\begin{aligned} P_x(\vartheta,\varphi) = -\sin 2\vartheta & \left\{\cos\varphi \left(\mathrm{Re}(M_{\perp}^{(1++)} M_{\|}^{(5-+)\star}) - \mathrm{Re}(M_{\perp}^{(1--)} M_{\|}^{(5+-)\star})\right)\right. \\ & \left. - \sin\varphi \left(\mathrm{Im}(M_{\perp}^{(1++)} M_{\|}^{(5-+)\star}) + \mathrm{Im}(M_{\perp}^{(1--)} M_{\|}^{(5+-)\star})\right)\right\} \Big/ I(\vartheta) \end{aligned} \tag{25$b$}$$

$$\begin{aligned} P_y(\vartheta,\varphi) = \sin 2\vartheta & \left\{\cos\varphi \left(\mathrm{Im}(M_{\perp}^{(1++)} M_{\|}^{(5-+)\star}) + \mathrm{Im}(M_{\perp}^{(1--)} M_{\|}^{(5+-)\star})\right)\right. \\ & \left. - \sin\varphi \left(\mathrm{Re}(M_{\perp}^{(1++)} M_{\|}^{(5-+)\star}) - \mathrm{Re}(M_{\perp}^{(1--)} M_{\|}^{(5+-)\star})\right)\right\} \Big/ I(\vartheta). \end{aligned} \tag{25$c$}$$

There is no MLD. Reflection at the $(x, z)$-plane implies

$$(I, P_x, P_y, P_z) \overset{\varphi\to-\varphi, M\to-M}{\longrightarrow} (I, -P_x, P_y, -P_z). \tag{26}$$

Furthermore, we have

$$P_x(\vartheta,\varphi) = \cos\varphi \; P_x(\vartheta, 0) - \sin\varphi \; P_y(\vartheta, 0) \tag{27$a$}$$

$$P_y(\vartheta,\varphi) = \sin\varphi \; P_x(\vartheta, 0) + \cos\varphi \; P_y(\vartheta, 0). \tag{27$b$}$$

For right-handed ($\sigma_+$) and left-handed ($\sigma_-$) circular light, we obtain

$$I(\sigma_+) = 2|M_{\|}^{(5+-)}|^2 \qquad \text{and} \qquad I(\sigma_-) = 2|M_{\|}^{(5-+)}|^2. \tag{28}$$

In the first case ($\sigma_+$), only transitions from initial states of symmetry $\Delta_6^5$ of the function class $|f_n^-\rangle$ into the final state of the function class $|f_m^+\rangle$ can take place. In the latter case, the two function classes are interchanged. In general, this may lead to a pronounced MCD (Scheunemann *et al* 1994). The photoelectrons are completely polarized, $P_z(\sigma_\pm) = \pm 1$. But note that the ESP given here is in fact a partial polarization, in the sense that the complete intensity (due to both $\Delta_6$ and $\Delta_7$ initial states) is replaced by that arising only from $\Delta_6$ initial states. The intensity asymmetry (MCD) can be obtained by reversing the magnetization or by reversing the photon helicity, $I(\sigma_\pm, \boldsymbol{M}) = I(\sigma_\mp, -\boldsymbol{M})$ and $P_z(\sigma_\pm, \boldsymbol{M}) = -P_z(\sigma_\mp, \boldsymbol{M})$. Furthermore, the intensity is closely related to that for s-polarized light, $I(s) = (I(\sigma_+) + I(\sigma_-))/2$.

Now we consider emission from initial states with $\Delta_7$ symmetry. Because $W_{11}$ and $W_{22}$ are equal to zero, only $P_z$ is nonzero. For s-polarized light, we obtain the same result as for $\Delta_6$ initial states (see equation (22) and subsequent equations).

In contrast to $\Delta_6$ initial states (where $\Delta_6^1$ couples to the electric field vector component normal to surface), $\Delta_7$ initial states couple only to the electric field vector component parallel to the surface. Therefore, the intensity and ESP for p-polarized light are very closely related to those for s-polarized light, carrying an additional (geometrical) factor:

$$I(p) = \cos^2\vartheta\,\left(|M_{\|}^{(5+-)}|^2 + |M_{\|}^{(5-+)}|^2\right) = \cos^2\vartheta\, I(s) \tag{29}$$

and $P_z(p) = P_z(s)$.

For circularly polarized light, the intensity and ESP are given by

$$I(\sigma_+) = 2|M_{\|}^{(5-+)}|^2 \qquad \text{and} \qquad I(\sigma_-) = 2|M_{\|}^{(5+-)}|^2 \tag{30}$$

and $P_z(\sigma_\pm) = \mp 1$. Note that the ESP is reversed with respect to that for $\Delta_6$ initial states (compare, e.g., equation (28)) (Wöhlecke and Borstel 1984) and both the intensity and the ESP obey the same symmetry relations as for $\Delta_6$ initial states.

### 3.3. *The threefold rotational axis*

Electronic states at surfaces with $3m$ symmetry, i.e. $C_{3v}$ in Schönflies notation, may be classified according to two irreducible representations of the respective double group, $\Lambda_6$ and $\Lambda_{4,5}$. The final state has $\Lambda_6^1$ symmetry.

First, consider transitions from $\Lambda_6$ initial states. Comparing the transition matrix elements with those obtained for $\Delta_6$ initial states ($4mm$ symmetry), we note that $M_{\|}^{(3+-)}$ corresponds to $M_{\|}^{(5+-)}$ and $M_{\|}^{(3-+)}$ to $M_{\|}^{(5-+)}$. Therefore, we get the same results as given in equations (22)–(28), but with $M_{\|}^{(5ss')}$ replaced by $M_{\|}^{(3ss')}$. In particular, there is also no MLD.

We now turn to photoemission from $\Lambda_{4,5}$ initial states. For s-polarized light we obtain the intensity

$$I = \frac{1}{2}\left(|M_{\|}^{(3++)}|^2 + |M_{\|}^{(3+-)}|^2 + |M_{\|}^{(3-+)}|^2 + |M_{\|}^{(3--)}|^2\right). \tag{31}$$

The $z$-component of the ESP is exclusively due to exchange splitting and is given by

$$P_z = \frac{1}{2I}\left(|M_{\|}^{(3++)}|^2 + |M_{\|}^{(3+-)}|^2 - |M_{\|}^{(3-+)}|^2 - |M_{\|}^{(3--)}|^2\right). \tag{32}$$

The components parallel to the surface are due to both exchange and SOC, i.e.

$$\begin{aligned} P_x(\varphi) = \frac{1}{I}\Big[ &-\sin 2\varphi\left(\mathrm{Re}(M_{\|}^{(3++)}M_{\|}^{(3-+)\star}) - \mathrm{Re}(M_{\|}^{(3--)}M_{\|}^{(3+-)\star})\right) \\ &-\cos 2\varphi\left(\mathrm{Im}(M_{\|}^{(3++)}M_{\|}^{(3-+)\star}) + \mathrm{Im}(M_{\|}^{(3--)}M_{\|}^{(3+-)\star})\right)\Big] \end{aligned} \tag{33$a$}$$

$$\begin{aligned} P_y(\varphi) = \frac{-1}{I}\Big[ &-\cos 2\varphi\left(\mathrm{Re}(M_{\|}^{(3++)}M_{\|}^{(3-+)\star}) - \mathrm{Re}(M_{\|}^{(3--)}M_{\|}^{(3+-)\star})\right) \\ &-\sin 2\varphi\left(\mathrm{Im}(M_{\|}^{(3++)}M_{\|}^{(3-+)\star}) + \mathrm{Im}(M_{\|}^{(3--)}M_{\|}^{(3+-)\star})\right)\Big]. \end{aligned} \tag{33$b$}$$

Without exchange splitting, we have $M_{\|}^{(3++)} = M_{\|}^{(3--)}$ and $M_{\|}^{(3+-)} = M_{\|}^{(3-+)}$. This leads to the intensity

$$I = \left(|M_{\|}^{(3++)}|^2 + |M_{\|}^{(3+-)}|^2\right) \tag{34}$$

and to

$$P_z = 0 \tag{35$a$}$$

$$P_x(\varphi) = \frac{-2}{I}\cos 2\varphi\ \mathrm{Im}(M_{\|}^{(3++)}M_{\|}^{(3-+)\star}) \tag{35$b$}$$

$$P_y(\varphi) = \frac{2}{I}\sin 2\varphi\ \mathrm{Im}(M_{\|}^{(3++)}M_{\|}^{(3-+)\star}) \tag{35$c$}$$

which may be expressed as

$$P_x(\varphi) = \cos 2\varphi \ P_x(0) \qquad \text{and} \qquad P_y(\varphi) = -\sin 2\varphi \ P_x(0). \tag{36}$$

We thus retrieve the result for the LSPE of $3m$ surfaces (Tamura *et al* 1987), where s-polarized light produces an in-plane spin polarization.

We obtain the (typical) symmetry relations for the intensity and the normal component of the ESP,

$$(I, P_x, P_y, P_z) \overset{\varphi\to-\varphi, M\to -M}{\longrightarrow} (I, P_x, -P_y, -P_z) \tag{37}$$

and

$$P_x(\varphi) = \cos 2\varphi \ P_x(0) - \sin 2\varphi \ P_y(0) \tag{38$a$}$$

$$P_y(\varphi) = -\sin 2\varphi \ P_x(0) + \cos 2\varphi \ P_y(0). \tag{38$b$}$$

Analogously to the case for $4mm$ symmetry, $\Lambda_{4,5}$ initial states couple only to the components of the electric field vector parallel to the surface. Therefore, results for p-polarized light are like those for s-polarized light except for the geometrical factor $\cos^2\vartheta$ (cf. equation (29)).

For circularly polarized light we find

$$I(\sigma_+) = |M_\|^{(3-+)}|^2 + |M_\|^{(3--)}|^2 \qquad \text{and} \qquad I(\sigma_-) = |M_\|^{(3+-)}|^2 + |M_\|^{(3++)}|^2 \tag{39}$$

and $P_z(\sigma_\pm) = \mp 1$. The (partial) polarization is complete and reversed with respect to that of $\Lambda_6$ initial states.

**Table 1.** Magnetic dichroic effects and photoelectron spin-polarization components for magnetization $M$ normal to surfaces (parallel to the $z$-axis) with twofold, threefold, or fourfold rotational axes, i.e. with spatial symmetry groups $2mm$, $3m$, and $4mm$ in the nonmagnetic limit. s, p, and circ. stand for s-, p-, and normally incident circularly polarized light. The signs in brackets indicate whether the respective ESP component occurs (+ sign) or does not occur (− sign) if only SOC (first sign), only exchange (second sign), or both (third sign) are present. MLD and MCD occur if a spin-polarization component parallel to $M$ is produced by SOC in the nonmagnetic case.

| $2mm$<br>light | $P_x$ | $P_y$ | $P_z$ | $I$ |
|---|---|---|---|---|
| s | (−, −, −) | (−, −, −) | (+, +, +) | MLD |
| p | (+, −, +) | (+, −, +) | (+, +, +) | MLD |
| circ. | (−, −, −) | (−, −, −) | (+, +, +) | MCD |
| $4mm$<br>light | $P_x$ | $P_y$ | $P_z$ | $I$ |
| s | (−, −, −) | (−, −, −) | (−, +, +) | |
| p | (+, −, +) | (+, −, +) | (−, +, +) | |
| circ. | (−, −, −) | (−, −, −) | (+, +, +) | MCD |
| $3m$<br>light | $P_x$ | $P_y$ | $P_z$ | $I$ |
| s | (+, −, +) | (+, −, +) | (−, +, +) | |
| p | (+, −, +) | (+, −, +) | (−, +, +) | |
| circ. | (−, −, −) | (−, −, −) | (+, +, +) | MCD |

In table 1 we summarize our findings for photoemission from systems with magnetization normal to the surface. For systems with twofold rotational axes, we observe both MLD and MCD, whereas for surfaces with three- or fourfold rotational symmetry we find only MCD but no MLD.

## 4. Results for magnetization parallel to the surface

We now address surface systems with in-plane magnetization $\boldsymbol{M}$. Irrespective of whether the corresponding nonmagnetic system has $2mm$, $3m$ or $4mm$ symmetry, the magnetic system in this case has no rotational symmetry axis and at most one mirror plane. Nevertheless, the photoemission intensity and ESP expressions and in particular the occurrence of magnetic dichroism depend on the specific mirror symmetries of the corresponding nonmagnetic system and on the orientation of $\boldsymbol{M}$ relative to these mirror planes. We can distinguish three practically important cases. (i) The nonmagnetic system has two mirror planes (perpendicular to each other and to the surface plane) and $\boldsymbol{M}$ is parallel to one of them, for example the $(yz)$-plane. This is a typical for cubic (001) and (110) surfaces, where $\boldsymbol{M}$ points from an atom to one of its nearest neighbours. The other two cases involve only one mirror plane (chosen as the $(xz)$-plane), like (111) surfaces of cubic crystals and (0001) surfaces of hcp crystals. (ii) $\boldsymbol{M}$ is perpendicular to the mirror plane (pointing to a nearest-neighbour atom) or (iii) $\boldsymbol{M}$ is not perpendicular to the mirror plane. In the first two cases, the system is characterized by the spatial symmetry group $m$ (i.e. $C_s$ in the Schönflies notation). In the third case there is no nontrivial symmetry operation.

**Table 2.** Symmetry-adapted basis functions for systems with two mirror planes—$(x, z)$ and $(y, z)$—(in the nonmagnetic limit) and $\boldsymbol{M}$ parallel to the $x$-axis, i.e. parallel to the surface and to the $(y, z)$ mirror plane. The angular-momentum-quantization axis is normal to the surface; the spin-quantization axis is parallel to the magnetization (Pauli spinors $|\alpha\rangle$ and $|\beta\rangle$). $l$ and $m$ denote the quantum numbers of the angular momentum and its projection onto the $z$-axis.

| | $\lvert g_n^+\rangle$ | $\lvert g_n^-\rangle$ | |
|---|---|---|---|
| $S_1$ | $Y_l^0\lvert\alpha\rangle$ | $Y_l^0\lvert\beta\rangle$ | $l \geqslant 0$ |
| | $(1/\sqrt{2})\left(Y_l^m + Y_l^{-m}\right)\lvert\alpha\rangle$ | $[(-1)^m/\sqrt{2}]\left(Y_l^m + Y_l^{-m}\right)\lvert\beta\rangle$ | $l \geqslant 1, -l \leqslant m \leqslant l$ |
| $S_2$ | $(1\sqrt{2})\left(Y_l^m - Y_l^{-m}\right)\lvert\beta\rangle$ | $[-(-1)^m/\sqrt{2}]\left(Y_l^m - Y_l^{-m}\right)\lvert\alpha\rangle$ | $l \geqslant 1, -l \leqslant m \leqslant l$ |

**Table 3.** The connection of single-group representations of the symmetry-adapted basis functions given in table 2 and those for $2mm$ and $4mm$ symmetry.

| | $S_1$ | $S_2$ |
|---|---|---|
| $2mm$ | $\Sigma_1, \Sigma_4$ | $\Sigma_2, \Sigma_3$ |
| $4mm$ | $\Delta_1, \Delta_2, \Delta_5$ | $\Delta_1', \Delta_2', \Delta_5$ |

### 4.1. Cubic (001) and (110) surfaces

We are now dealing with case (i), with $\boldsymbol{M}$ chosen along the $x$-axis. It is convenient to introduce symmetry-adapted basis functions (see table 2), the angular-momentum-quantization axis of which is normal to the surface, whereas the spin-quantization axis is parallel to the magnetization. These are closely related to those for $2mm$ symmetry (Inui *et al* 1990). In table 3 we give the connection between spatial parts of basis functions for $2mm$ and $4mm$ symmetry and the symmetry-adapted basis functions. Because the quantization axes for angular momentum and spin differ, a unitary transformation has to be applied to the spin-density matrix (Kessler 1985). Initial and final states then have the form

$$|\Psi_s\rangle = c_1^{(s)}|S^{1s}\rangle|s\rangle + c_2^{(s)}|S^{2s}\rangle|-s\rangle \qquad s = \pm \tag{40}$$

where the notation is analogous to what we used in equation (8) and again explicitly displays SOC. The evaluation of the photoelectron spin-density matrix proceeds in the same way as described in subsection 3.1. It should be noted, however, that now there are two types of matrix element involving initial-state parts of $S^1$ spatial symmetry: $M_\parallel^{(1ss)}$ is due to the dipole operator part $H_\parallel$ and $M_\perp^{(1ss)}$ to $H_z$ (cf. equations (5*c*) and (6)).

For *p-polarized light* we obtain

$$\begin{aligned} I(\vartheta,\varphi) = {} & \sin^2\vartheta\,\Big(|M_\perp^{(1++)}|^2 + |M_\perp^{(1--)}|^2\Big) + \cos^2\vartheta\,\sin^2\varphi\,\Big(|M_\parallel^{(1++)}|^2 + |M_\parallel^{(1--)}|^2\Big) \\ & + \cos^2\vartheta\,\cos^2\varphi\,\Big(|M_\parallel^{(2+-)}|^2 + |M_\parallel^{(2-+)}|^2\Big) \\ & + \sin 2\vartheta\,\sin\varphi\,\Big(\mathrm{Im}(M_\perp^{(1++)\star}M_\parallel^{(1++)}) - \mathrm{Im}(M_\perp^{(1--)\star}M_\parallel^{(1--)})\Big) \end{aligned} \tag{41}$$

and

$$\begin{aligned} P_x(\vartheta,\varphi) = {} & \Big\{\sin^2\vartheta\,\Big(|M_\perp^{(1++)}|^2 - |M_\perp^{(1--)}|^2\Big) + \cos^2\vartheta\,\sin^2\varphi\,\Big(|M_\parallel^{(1++)}|^2 - |M_\parallel^{(1--)}|^2\Big) \\ & + \cos^2\vartheta\,\cos^2\varphi\,\Big(|M_\parallel^{(2+-)}|^2 - |M_\parallel^{(2-+)}|^2\Big) \\ & + \sin 2\vartheta\,\sin\varphi\,\Big(\mathrm{Im}(M_\perp^{(1++)\star}M_\parallel^{(1++)}) + \mathrm{Im}(M_\perp^{(1--)\star}M_\parallel^{(1--)})\Big)\Big\}\Big/ I \end{aligned} \tag{42$a$}$$

$$\begin{aligned} P_z(\vartheta,\varphi) = {} & -\Big\{\sin 2\vartheta\,\cos\varphi\,\Big(\mathrm{Re}(M_\perp^{(1++)}M_\parallel^{(2-+)\star}) - \mathrm{Re}(M_\perp^{(1--)}M_\parallel^{(2+-)\star})\Big) \\ & + \cos^2\vartheta\,\sin 2\varphi\,\Big(\mathrm{Im}(M_\parallel^{(1++)}M_\parallel^{(2-+)\star}) + \mathrm{Im}(M_\parallel^{(1--)}M_\parallel^{(2+-)\star})\Big)\Big\} \end{aligned} \tag{42$b$}$$

$$\begin{aligned} P_y(\vartheta,\varphi) = {} & -\Big\{\sin 2\vartheta\,\cos\varphi\,\Big(\mathrm{Im}(M_\perp^{(1++)}M_\parallel^{(2-+)\star}) + \mathrm{Im}(M_\perp^{(1--)}M_\parallel^{(2+-)\star})\Big) \\ & - \cos^2\vartheta\,\sin 2\varphi\,\Big(\mathrm{Re}(M_\parallel^{(1++)}M_\parallel^{(2-+)\star}) - \mathrm{Re}(M_\parallel^{(1--)}M_\parallel^{(2+-)\star})\Big)\Big\}\,. \end{aligned} \tag{42$c$}$$

Since the last term in the above intensity expression reverses sign upon reversal of $\boldsymbol{M}$, there is an MLD, which is maximal for the azimuthal angle of photon incidence $\varphi = \pi/2$ and vanishes for $\varphi = 0$. In the first case, the reaction plane is the $(y, z)$-plane, i.e. perpendicular to $\boldsymbol{M}$ (aligned along the $x$-axis). From the above expressions, the ESP components $P_y$ and $P_z$ are seen to vanish, and the nonzero $P_x$ is composed of two exchange-induced terms, which change sign upon reversal of $\boldsymbol{M}$, and a third spin–orbit-induced term, which does not change sign and survives in the nonmagnetic limit, retrieving the 'linear spin-polarization effect' predicted by Tamura and Feder (1991a, b). We thus find again, as above in the case of twofold symmetry with magnetization normal to the surface, that the occurrence of both an exchange- and a spin–orbit-induced additive contribution in one of the ESP components is associated with MLD. This connection is explicit in our above formulae: the last term in $I$, which is responsible for MLD, and the last term in $P_x$, the spin–orbit contribution, involve the same matrix element combinations $\mathrm{Im}(M_\perp^{(1ss)\star}M_\parallel^{(1ss)})$ (with $s = \pm$).

In the case where $\varphi = 0$, in which $\boldsymbol{M}$ is parallel to the reaction plane, equation (41) shows that there is no MLD, but all three ESP components are nonzero. $P_x$ is seen to be due to exchange only, reversing its sign upon reversal of $\boldsymbol{M}$, and $P_y$ due to SOC only, whereas $P_z$ involves both interactions in such a way that it would vanish if one or the other were absent. This interplay between exchange interaction and SOC is clearly different from the additive one in forming $P_x$ in the previously discussed case where $\varphi = \pi/2$.

For general $\varphi$, our formulae yield the relation

$$(I, P_x, P_y, P_z) \overset{\varphi\to-\varphi,\boldsymbol{M}\to-\boldsymbol{M}}{\longrightarrow} (I, -P_x, P_y, -P_z). \tag{43}$$

This also follows directly by considering reflection of the total set-up at the $(x, z)$-plane (which is, however, not a symmetry operation).

The results for *s-polarized light* incident at azimuth $\varphi$ can very easily be obtained from the above ones for p-polarized light by setting $\vartheta = 0$ (i.e. normal incidence) and replacing $\varphi$ by $\varphi + \pi/2$. Intensity and ESP components are then seen to obey the relations

$$(I, P_x, P_y, P_z) \overset{M \to -M}{\longrightarrow} (I, -P_x, -P_y, P_z) \tag{44a}$$

$$(I, P_x, P_y, P_z) \overset{\varphi \to -\varphi, M \to -M}{\longrightarrow} (I, P_x, -P_y, -P_z). \tag{44b}$$

In particular, there is no MLD in the sense of an intensity asymmetry upon reversal of $\boldsymbol{M}$. There is, however, a difference between the intensities for $\varphi = 0$ and $\varphi = \pi/2$, i.e. for normally incident s- and p-polarized light. If one defines dichroism as an intensity asymmetry occurring for two orthogonal states of photon polarization, one can therefore identify a MLD.

For off-normally incident *circularly polarized light* of helicity $\sigma_+$ or $\sigma_-$, the intensity is

$$\begin{aligned} I(\vartheta, \varphi, \sigma_\pm) = \frac{1}{2} \Big\{ & \sin^2\vartheta \; \left(|M_\perp^{(1++)}|^2 + |M_\perp^{(1--)}|^2\right) \\ & \pm 2\sin\vartheta \;\cos\varphi \; \left(\mathrm{Re}(M_\perp^{(1++)} M_\parallel^{(1++)\star}) - \mathrm{Re}(M_\perp^{(1--)} M_\parallel^{(1--)\star})\right) \\ & - \sin 2\vartheta \;\sin\varphi \; \left(\mathrm{Im}(M_\perp^{(1++)} M_\parallel^{(1++)\star}) - \mathrm{Im}(M_\perp^{(1--)} M_\parallel^{(1--)\star})\right) \\ & + (1 - \sin^2\vartheta \;\sin^2\varphi) \left(|M_\parallel^{(1++)}|^2 + |M_\parallel^{(1--)}|^2\right) \\ & + (1 - \sin^2\vartheta \;\cos^2\varphi) \left(|M_\parallel^{(2+-)}|^2 + |M_\parallel^{(2-+)}|^2\right) \Big\} . \end{aligned} \tag{45}$$

The two terms involving real and imaginary parts of $M$-products imply two different types of MCD. The second one is associated with the MLD for p-polarized light—cf. the last term in equation (41)—which vanishes for $\varphi = 0$, i.e. for $\boldsymbol{M}$ in the plane of incidence. This MCD is independent of the helicity of the incident radiation. The first MCD arises if $\boldsymbol{M}$ is not perpendicular to the plane of incidence. It further shows the symmetry relation $I(\sigma_+, +\boldsymbol{M}) = I(\sigma_-, -\boldsymbol{M})$. Since the ESP expressions are rather lengthy, it may suffice to say that all three components are generally nonzero.

For normally incident *circularly polarized light* ($\vartheta = 0$ and arbitrary $\varphi$) the above intensity formula reduces to

$$I(\sigma_\pm) = \left(|M_\parallel^{(1++)}|^2 + |M_\parallel^{(1--)}|^2 + |M_\parallel^{(2+-)}|^2 + |M_\parallel^{(2-+)}|^2\right) \Big/ 2 \tag{46}$$

and the ESP is given by

$$P_x(\sigma_\pm) = \frac{1}{2I} \left(|M_\parallel^{(1++)}|^2 - |M_\parallel^{(1--)}|^2 + |M_\parallel^{(2+-)}|^2 - |M_\parallel^{(2-+)}|^2\right) \tag{47a}$$

$$P_y(\sigma_\pm) = \pm \left(\mathrm{Im}(M_\parallel^{(1++)} M_\parallel^{(2-+)\star}) - \mathrm{Im}(M_\parallel^{(1--)} M_\parallel^{(2+-)\star})\right) \Big/ I \tag{47b}$$

$$P_z(\sigma_\pm) = \mp \left(\mathrm{Re}(M_\parallel^{(1++)} M_\parallel^{(2-+)\star}) + \mathrm{Re}(M_\parallel^{(1--)} M_\parallel^{(2+-)\star})\right) \Big/ I. \tag{47c}$$

Evidently, there is no MCD and all three components of the ESP are generally nonzero, in contrast to the case '$\boldsymbol{M}$ normal to the surface' treated above. $P_x$ (along the direction of $\boldsymbol{M}$) is seen to be exchange induced, reversing its sign upon reversal of $\boldsymbol{M}$, whereas $P_z$ can be produced by SOC alone, reducing to the usual optical orientation (Fano) effect in the nonmagnetic limit. $P_y$ requires the simultaneous presence of magnetic exchange and SOC. This situation is analogous to the above-discussed case of p-polarized light for $\varphi = 0$.

On the grounds of our results it may appear surprising that in a recent photoemission experiment using normally incident circularly polarized light (Schneider *et al* 1991b), no ESP component $P_z$ normal to the surface was detected. This finding was interpreted as follows. First, the spin-quantization axis is predominantly defined by $\boldsymbol{M}$, which should lead to vanishing ESP components normal to the magnetization. Second, because of the exchange splitting and the reduced symmetry (with respect to the nonmagnetic solid) the electronic wave functions change symmetry and the dipole selection rules leading to optical orientation do not hold. We therefore wish to point out that our above analytical results are supported by numerical calculations for Ni(001) (Henk *et al* 1994), which yield not only a strong ESP in the direction of $\boldsymbol{M}$ but also two ESP components normal to $\boldsymbol{M}$. The latter are, however, much smaller with values within the statistical error of the above experiment.

Reversing the photon helicity or $\boldsymbol{M}$, we obtain the relations

$$(I, P_x, P_y, P_z) \overset{\sigma_\pm \to \sigma_\mp}{\longrightarrow} (I, P_x, -P_y, -P_z) \tag{48a}$$

$$(I, P_x, P_y, P_z) \overset{M \to -M}{\longrightarrow} (I, -P_x, -P_y, P_z). \tag{48b}$$

Dichroic effects and spin polarizations for magnetization parallel to the surface are summarized in table 5. Prototype numerical results for Ni(001) with a single photon energy (Henk *et al* 1994) fully confirm the present qualitative predictions.

### *4.2. The fcc (111) and hcp (0001) surfaces*

We now turn to the above-defined cases (ii) and (iii) relating to magnetic surfaces with in-plane magnetization, which in the nonmagnetic limit have threefold rotational symmetry and three mirror planes (symmetry $3m$), e.g. (111) surfaces of fcc or (0001) surfaces of hcp systems. We recall that for $3m$ symmetry the irreducible representations of the double group consist of the two-dimensional one, $\Lambda_6$, and two one-dimensional ones degenerate by time-reversal symmetry, $\Lambda_4$ and $\Lambda_5$.

**Table 4.** Symmetry-adapted basis functions for systems with one mirror plane—$(x, z)$—and $\boldsymbol{M}$ along the $y$-axis, i.e. parallel to the surface and perpendicular to the mirror plane. The spin- and angular-momentum-quantization axes are chosen normal to the surface (Pauli spinors $\chi^+$ and $\chi^-$). $l$ and $m$ denote the quantum numbers of the angular momentum and its projection onto the $z$-axis.

| | $\lvert g_n^+\rangle$ | $\lvert g_n^-\rangle$ | |
|---|---|---|---|
| $\gamma_1$ | $Y_l^{-m}\chi^- + \mathrm{i}Y_l^m\chi^+$ | $Y_l^m\chi^+ + \mathrm{i}Y_l^{-m}\chi^-$ | $m$ odd |
| $\gamma_2$ | $-Y_l^{-m}\chi^- + \mathrm{i}Y_l^m\chi^+$ | $Y_l^m\chi^+ - \mathrm{i}Y_l^{-m}\chi^-$ | $m$ even |

Let us now specialize to case (ii), i.e. where $\boldsymbol{M}$ is perpendicular to a mirror plane, for example the $(xz)$-plane, with $\boldsymbol{M}$ pointing in nearest-neighbour directions. There remains one nontrivial symmetry operation, the reflection at this plane, i.e. we are concerned with the double group $m$. In the magnetic case there are only two one-dimensional representations, $\gamma_1$ and $\gamma_2$, which are connected to the former by $\Lambda_4 \to \gamma_1$, $\Lambda_5 \to \gamma_2$, and $\Lambda_6 \to \gamma_1 + \gamma_2$ (Falicov and Ruvalds 1968). Furthermore, $\gamma_1$ and $\gamma_2$ are degenerate by time-reversal symmetry. Their spin-angular basis functions are given in table 4.

For s-polarized light with the azimuthal angle $\varphi$ of the electric field vector $\boldsymbol{E}$, we obtain the following expression for the photoemission intensity:

$$I(\varphi) = 2\sin^2\varphi \, \left(|M_1^{(++)}|^2 + |M_2^{(--)}|^2\right) + 2\cos^2\varphi \, \left(|M_1^{(-+)}|^2 + |M_2^{(+-)}|^2\right) \tag{49}$$

and for the ESP

$$P_x = -\frac{2}{I}\sin 2\varphi\left(\mathrm{Re}(M_1^{(++)}M_1^{(-+)\star}) - \mathrm{Re}(M_2^{(--)}M_2^{(+-)\star})\right) \tag{50$a$}$$

$$P_y = \frac{2}{I}\left\{\sin^2\varphi\left(|M_1^{(++)}|^2 - |M_2^{(--)}|^2\right) - \cos^2\varphi\,\left(|M_1^{(-+)}|^2 - |M_2^{(+-)}|^2\right)\right\} \tag{50$b$}$$

$$P_z = -\frac{2}{I}\sin 2\varphi\left(\mathrm{Im}(M_1^{(++)}M_1^{(-+)\star}) + \mathrm{Im}(M_2^{(--)}M_2^{(+-)\star})\right) \tag{50$c$}$$

where $M_1^{(s+)}$ ($M_2^{(s-)}$) denotes a transition matrix element from initial state $|i_+\rangle$ ($|i_-\rangle$) with complex expansion coefficients $\alpha_n^+$ ($\alpha_n^-$), cf. equation (2), into final state $|f_s\rangle$. It is important to note that in the present case the expansion coefficients cannot be chosen as real because the basis functions behave differently under time reversal and mirror operations. Thus, in $M_2$ the complex conjugate expansion coefficients of the respective initial state appear, in contrast to the case for $M_1$.

The above expressions evidently obey the symmetry relation

$$(I, P_x, P_y, P_z) \overset{\varphi\to-\varphi}{\longrightarrow} (I, -P_x, P_y, -P_z). \tag{51}$$

Since the matrix elements $M_1$ and $M_2$ differ from each other, the intensity $I(\varphi)$ changes upon reversal of the magnetization, i.e. there is MLD. This MLD is closely related to the ‘linear spin-polarization effect’, which occurs in photoemission by s-polarized light from nonmagnetic surfaces with $3m$ symmetry (Tamura *et al* 1987). In the nonmagnetic limit we have $M_1^{(++)} = M_1^{(-+)}$ and $M_2^{(--)} = M_2^{(+-)}$. Equations (49) and (50$c$) thus become

$$I(\varphi) = 2\left(|M_1|^2 + |M_2|^2\right) \tag{52$a$}$$

$$P_x = -\frac{2}{I}\sin 2\varphi\left(|M_1|^2 - |M_2|^2\right) \tag{52$b$}$$

$$P_y = -\frac{2}{I}\cos 2\varphi\left(|M_1|^2 - |M_2|^2\right) \tag{52$c$}$$

$$P_z = 0 \tag{52$d$}$$

where $M_1$ and $M_2$ denote matrix elements of transitions from a linear combination of initial states with $\Lambda_4$ and $\Lambda_5$ double-group symmetry into $\Lambda_6^1$ final states. In the rather complicated derivation of the last equations from those for the magnetic case one has to employ the fact that the final state is of $\Lambda_6^1$ spatial symmetry. The photoemission intensity and the modulus of the ESP vector are independent of the azimuth $\varphi$. For $\varphi = \pi/4$ no ESP component parallel to the $y$-axis, i.e. parallel to the magnetization, is brought about by SOC and there is no MLD in this case.

If $\boldsymbol{M}$ is not perpendicular to a mirror plane of the nonmagnetic system, i.e. our case (iii), there is no spatial symmetry operation except the trivial one. Our analytical results (not shown here) indicate that for general $\boldsymbol{M}$ and general azimuthal angles $\varphi$ of the surface-parallel electric field vector $\boldsymbol{E}$ there is always MLD. It is absent, however, in the special cases where $\boldsymbol{M}$ is in the mirror plane and $\boldsymbol{E}$ is either parallel or perpendicular to $\boldsymbol{M}$. From the ‘nonmagnetic’ expressions (52) we see that in these special cases $P_x$, the (SOC-induced) ESP component parallel to $\boldsymbol{M}$, vanishes.

The above MLDs for *s-polarized* light and the ESP symmetry relations are confirmed by numerical relativistic layer KKR photoemission calculations, which we have carried out for ferromagnetic Ni(111). At photon energies around 28 eV these new types of MLD are so strong that they should be easily detectable in experiments.

For *circularly polarized* light at *normal* incidence, which is a coherent superposition of s-polarized light with $\varphi$ and $\varphi + \pi/2$, the above impressions imply that there is no intensity asymmetry, i.e. no MCD, and all three ESP components are generally nonzero.

For *p-polarized* light the analytical expressions get rather lengthy. Suffice it to say that one generally obtains three nonzero ESP components and a MLD, which is a superposition of the MLD found for s-polarized light with a new one, which is akin to the one found in section 4.2. For *circularly polarized* light at *off-normal* incidence, we obtain MCD, if $\boldsymbol{M}$ is parallel to the plane of incidence.

## 5. The connection between magnetic dichroism and nonmagnetic spin-polarization effects

From the various specific cases which we have analysed above, a general picture emerges of the interplay of exchange interaction and spin–orbit coupling (SOC) producing photoelectron spin polarization and magnetic dichroism.

Since the spin-polarization effects, which occur in *nonmagnetic* systems as a consequence of SOC, are an essential ingredient for understanding the results from magnetic systems, we first briefly summarize these effects. *Circularly polarized light* produces an electron spin-polarization (ESP) vector $\boldsymbol{P}$ aligned with the helicity of the light, which is well known as the Fano effect or optical orientation (cf., e.g., Wöhlecke and Borstel 1984, and references therein). In the case of normal incidence, there is thus $\boldsymbol{P}$ normal to the surface. Contrary to a long-held common belief, ESP also occurs for *linearly polarized light* in three different ways. The first such ‘linear spin-polarization effect’ (LSPE) was theoretically predicted by Tamura *et al* (1987) and experimentally confirmed by Heinzmann’s group (Schmiedeskamp *et al* 1988) for surfaces with threefold rotational symmetry: s-polarized light produces an in-plane $\boldsymbol{P}$ because of a peculiarity of the double-group symmetry $\Lambda_{4,5}$. A second LSPE was found theoretically (Tamura and Feder 1991a, b) and experimentally (Schmiedeskamp *et al* 1991, Irmer *et al* 1992) for off-normally incident p-polarized light for surfaces with two-, three- and fourfold rotational symmetry. It consists in an ESP component perpendicular to the reaction plane. Thirdly, for surfaces with twofold rotational symmetry, s-polarized light was recently predicted to produce an ESP component normal to the surface (Henk and Feder 1994). This effect is due to spin–orbit coupling between states with $\Sigma^3$ and $\Sigma^4$ spatial symmetry. It was recently verified by experiment (Irmer *et al* 1995).

Now consider light of arbitrary polarization incident on a *magnetic* semi-infinite system with magnetization $\boldsymbol{M}$. If there was no spin–orbit coupling, the exchange interaction would produce only a photoelectron spin-polarization vector $\boldsymbol{P}_{\mathrm{ex}}$ aligned parallel to $\boldsymbol{M}$. Upon reversal of $\boldsymbol{M}$, $\boldsymbol{P}_{\mathrm{ex}}$ is reversed and the intensity does not change. Taking into account spin–orbit coupling and going to the limit of vanishing exchange splitting, one retrieves the above-described ESP exclusively due to SOC, which we may call $\boldsymbol{P}_{\mathrm{so}}$. Naturally it does not change sign with $\boldsymbol{M}$. The phenomena observed for magnetic systems depend on the relative orientation of $\boldsymbol{P}_{\mathrm{so}}$ and $\boldsymbol{M}$. If $\boldsymbol{P}_{\mathrm{so}}$ is perpendicular to $\boldsymbol{M}$, the $\boldsymbol{P}$ of the photoelectrons has three components: an exchange-induced one along $\boldsymbol{M}$, a SOC-induced one along $\boldsymbol{P}_{\mathrm{so}}$, and a third one which requires the simultaneous presence of exchange and SOC. In this case, the intensity does not depend on the direction of $\boldsymbol{M}$, i.e. there is no magnetic (circular or linear) dichroism. If $\boldsymbol{P}_{\mathrm{so}}$ is parallel to $\boldsymbol{M}$, $\boldsymbol{P}$ consists of two additive terms, an exchange-induced one, which changes sign with $\boldsymbol{M}$, and a SOC-induced one, which does not. The matrix element combinations, which occur in the latter, also provide an additive contribution to the total intensity, which changes sign with $\boldsymbol{M}$. Consequently, the intensity changes upon reversal of $\boldsymbol{M}$, i.e. there is *magnetic dichroism*. We would like to emphasize that these findings are quite general and hold for both MCD and for the various types of MLD associated with the above spin–orbit-induced ‘linear spin-polarization effects’.

**Table 5.** Magnetic dichroic effects and photoelectron spin-polarization components for magnetization $\boldsymbol{M}$ parallel to the surface ($x$-axis) and linearly polarized (s, p) as well as circularly polarized light. The signs in brackets indicate whether the respective ESP component occurs ($+$ sign) or does not occur ($-$ sign) if only SOC (first sign), only exchange (second sign), or both (third sign) are present. MLD and MCD arise if a spin-polarization component $P_x$ parallel to $\boldsymbol{M}$ is produced by SOC in the nonmagnetic limit. For circularly polarized light, $\vartheta$ denotes the polar angle of incidence, and the azimuthal angle $\varphi$ is taken as arbitrary.

| Light | Group | $P_x$ | $P_y$ | $P_z$ | $I$ |
|---|---|---|---|---|---|
| | | | | | Linear |
| s | $2mm$ | $(-,+,+)$ | $(-,-,+)$ | $(+,-,+)$ | |
| | $4mm$ | $(-,+,+)$ | $(-,-,+)$ | $(-,-,+)$ | |
| | $3m$ | $(+,+,+)$ | $(+,-,+)$ | $(-,-,+)$ | MLD |
| p | $2mm$ | $(+,+,+)$ | $(+,-,+)$ | $(+,-,+)$ | MLD |
| | $4mm$ | $(+,+,+)$ | $(+,-,+)$ | $(-,-,+)$ | MLD |
| | $3m$ | $(+,+,+)$ | $(+,-,+)$ | $(-,-,+)$ | MLD |
| | | | | | Circular |
| $\vartheta = 0$ | | $(-,+,+)$ | $(-,-,+)$ | $(+,-,+)$ | |
| $\vartheta \neq 0$ | | $(+,+,+)$ | $(+,-,+)$ | $(+,-,+)$ | MCD |

Our main results are summarized in tables 1 and 5. In the case of ‘magnetization $\boldsymbol{M}$ normal to the surface’, $2mm$ surfaces exhibit both MLD and MCD, whereas for $3m$ and $4mm$ no MLD occurs, because the nonmagnetic LSPEs produce no ESP component normal to the surface, i.e. in the direction of $\boldsymbol{M}$. In all three cases, MCD occurs. If $\boldsymbol{M}$ is parallel to the surface (see table 5), p-polarized light produces MLD for all surfaces, and s-polarized light produces MLD for $3m$ surfaces. Circularly polarized light generally produces MCD except in the special case of normal incidence.

## 6. Concluding remarks

Our analytical results explicitly confirm findings from general symmetry arguments. Moreover, however, they reveal in detail the physical origin of the various magnetic dichroisms and spin-polarization effects in terms of an interplay between spin–orbit coupling and exchange. In the limit of vanishing magnetization we retrieve purely spin–orbit-induced spin-polarization effects, which occur for circularly and for linearly polarized light on nonmagnetic surfaces. This connection provides a deeper understanding of MCD and several types of MLD. As our dichroism and spin-polarization expressions contain terms involving single-group initial states mixed by spin–orbit coupling, they can be employed to infer from experimental data the types of initial states and their hybridization underlying individual spectral features.

Experimentally, in addition to MCD for various cases, MLD has so far been observed for *p-polarized* light and magnetization parallel to the surface, which is in line with our analytical results. Beyond this we predict, for surfaces with a twofold normal rotation axis and magnetization normal to the surface, a new type of *s-polarized-light* MLD associated with a photoelectron spin polarization normal to the surface. Since clean surfaces usually have an in-plane magnetization, we would like to emphasize that our results are also valid for ultrathin magnetic films (i.e. in the monolayer regime). Further, we predict another MLD for surfaces with a threefold rotational axis (in the nonmagnetic limit) and magnetization parallel to the surface. This MLD is associated with the spin–orbit effect for *s-polarized* light, which for nonmagnetic surfaces is known to produce an in-plane component of the photoelectron spin polarization.

Since our analytical expressions rely on an effective one-electron picture, which provides a good approximation for valence-band photoemission, their applicability to core-state photoemission, where many-body effects like multiplet and satellite structure are important (cf., e.g., Thole and van der Laan (1994) and references therein), is restricted to special cases for which a modified one-electron picture may still lead to reasonable results (cf., e.g., Tamura *et al* 1994).

The formulae derived in this paper could be computationally implemented and applied to specific crystalline surface systems. This would, however, have two drawbacks: firstly, stationary initial states of a semi-infinite system imply the neglect of hole lifetime effects, which are well known to be important; secondly, the present two-component approximation is presumably not sufficiently accurate. Quantitatively realistic calculations should therefore rather be based on our relativistic Green function formalism (Halilov *et al* 1993). The results of such calculations for Ni(001) with $M$ normal and parallel to the surface (see, Scheunemann *et al* (1994) and Henk *et al* (1994), respectively) and for ultrathin Co films on Cu(001) (Henk *et al* 1995) are fully in line with the present analytical findings.

## Acknowledgment

This work was funded by the German Ministry for Research and Technology under Contracts 055PGABB7 and 05621PGA.

## References

Bansmann J, Westphal C, Getzlaff M, Fegel F and Schönhense G 1992 *J. Magn. Magn. Mater.* **104** 1691
Baumgarten L, Schneider C M, Petersen H, Schäfers F and Kirschner J 1990 *Phys. Rev. Lett.* **65** 492
Carbone C, Vescovo E, Rader O, Gudat W and Eberhardt W 1993 *Phys. Rev. Lett.* **71** 280
Ebert H, Baumgarten L, Schneider C M and Kirschner J 1991 *Phys. Rev.* B **44** 4406
Falicov L M and Ruvalds J 1968 *Phys. Rev.* **172** 498
Feder R 1985 (ed) *Polarized Electrons in Surface Physics* (Singapore: World Scientific)
Halilov S V, Tamura E, Gollisch H, Meinert D and Feder R 1993 *J. Phys.: Condens. Matter* **5** 3859
Hartmann D, Weber W, Wesner D A, Popovic S and Güntherodt G 1993a *J. Magn. Magn. Mater.* **121** 160
——1993b *Phys. Rev.* B **48** 16837
Henk J and Feder R 1994 *Europhys. Lett.* **28** 609
Henk J, Halilov S V, Scheunemann T and Feder R 1994 *Phys. Rev.* B **50** 8130
Henk J, Scheunemann T, Halilov S V and Feder R 1995 *Phys. Status Solidi* b **192**
Inui T, Tanabe Y and Onodera Y 1990 *Group Theory and Its Applications in Physics (Springer Series in Solid State Sciences 78)* (Berlin: Springer)
Irmer N, David R, Schmiedeskamp B and Heinzmann U 1992 *Phys. Rev.* B **45** 3849
Irmer N, Frentzen F, Yu S W, Schmiedeskamp B and Heinzmann U 1995 *Verh. Deutsch. Phys. Ges.* **7** 1573
Kessler J 1985 *Polarized Electrons (Springer Series on Atoms and Plasmas 1)* 2nd edn (Berlin: Springer)
Kevan S V (ed) 1992 *Angle-resolved Photoemission: Theory and Current Applications* (Amsterdam: Elsevier)
Rader O, Vescovo E, Redinger J, Blügel S, Carbone C, Eberhardt W and Gudat W 1994 *Phys. Rev. Lett.* **72** 2247
Rose M E 1961 *Relativistic Electron Theory* (New York: Wiley)
Rose H B, Roth C, Hillebrecht F U and Kisker E 1994 *Solid State Commun.* **91** 129
Roth C, Hillebrecht F U, Rose H B and Kisker E 1993a *Phys. Rev. Lett.* **70** 3479
Roth C, Rose H B, Hillebrecht F U and Kisker E 1993b *Solid State Commun.* **86** 147
Ruvalds J and Falicov L M 1968 *Phys. Rev.* **172** 508
Scheunemann T, Halilov S V, Henk J and Feder R 1994 *Solid State Commun.* **91** 487
Schmiedeskamp B, Irmer N, David R and Heinzmann U 1991 *Appl. Phys.* A **53** 418
Schmiedeskamp B, Vogt B and Heinzmann U 1988 *Phys. Rev. Lett.* **60** 651
Schneider C M, Celinski Z, Neuber M, Wilde C, Grunze M, Meinel K and Kirschner J 1994 *J. Phys.: Condens. Matter* **6** 1177

Schneider C M, Hammond M S, Schuster P, Cebollada A, Miranda R and Kirschner J 1991a *Phys. Rev.* B **44** 12 066

Schneider C M, Schuster P, Hammond M S and Kirschner J 1991b *Europhys. Lett.* **16** 689

Smith N V, Brookes N B, Chang Y and Johnson P D 1994 *Phys. Rev.* B **49** 332

Tamura E and Feder R 1991a *Solid State Commun.* **79** 989

Tamura E, Piepke W and Feder R 1987 *Phys. Rev. Lett.* **59** 934

——1991b *Europhys. Lett.* **16** 695

Tamura E, Waddill G D, Tobin J G and Sterne P A 1994 *Phys. Rev. Lett.* **73** 1533

Thole B T and van der Laan G 1994 *Phys. Rev.* B **50** 11 474

Venus D 1993 *Phys. Rev.* B **48** 6144

——1994 *Phys. Rev.* B **49** 8821

Venus D, Baumgarten L, Schneider C M, Boeglin C and Kirschner J 1993 *J. Phys.: Condens. Matter* **5** 1239

Wöhlecke M and Borstel G 1984 *Optical Orientation* ed F Meier and B P Zakharchenya (Amsterdam: North-Holland)

Wu S C, Garrison K, Begley A M, Jona F and Johnson P D 1994 *Phys. Rev.* B **49** 14 081

**Publikation 5**

# Spin Polarization in Normal Photoemission by Linearly Polarized Light from Non-Magnetic (110) Surfaces.

J. Henk and R. Feder

*Theoretische Festkörperphysik, Universität Duisburg - D-47048 Duisburg, Germany*

(received 8 June 1994; accepted in final form 25 October 1994)

PACS. 79.60 – Photoemission and photoelectron spectra.
PACS. 71.70E – Spin-orbit coupling, Zeeman, Stark and strain splitting.

**Abstract.** – For linearly polarized radiation with a non-zero surface projection of the electric-field vector, photoelectrons emitted normal to non-magnetic surfaces with an at most twofold rotation axis generally have a spin polarization component perpendicular to the surface. This is firstly substantiated by symmetry arguments. For cubic (110) surfaces, an analytical calculation reveals that this effect is due to the spin-orbit–induced hybridization of basis functions of different spatial-symmetry types. Numerical relativistic one-step-model multiple-scattering calculations for Pt(110) yield polarization values up to 60%, which depend sensitively on the surface reconstruction.

The power of photoemission (see, *e.g.*,[1] and references therein) as a source of information on the electronic structure of solids, surfaces and thin films is substantially enhanced if in addition to the photocurrent the electron spin polarization vector is measured. This is immediately plausible for ferromagnets but, due to spin-orbit coupling, also valid for non-magnetic systems (see reviews [2, 3], some recent original articles [4-8] and references therein). For the latter, the traditional use of circularly polarized incident radiation was recently complemented by two spin polarization effects, which occur for linearly polarized radiation in photoemission normal to the surface. The first of these effects was predicted by theory [9] and confirmed by experiment [10] to exist for *s*-polarized radiation impinging on (111) surfaces. The second type of effect was theoretically predicted [11] and experimentally confirmed [12, 13] for *p*-polarized and even unpolarized radiation incident off-normally on cubic (001) and (111) surfaces. In both cases, the photoelectron spin polarization is parallel to the surface and carries information on details of the electronic initial state. Since both effects owe their existence, in addition to spin-orbit coupling, to the existence of a surface, they are sensitive to the electronic and geometrical structure of the surface region.

In this paper, we theoretically predict a third «linear light» effect, which manifests itself in normal photoemission by linearly polarized radiation as a spin polarization component normal to surfaces, which have at most a twofold rotation axis. Our investigation—and consequently its presentation in this paper—consists of three parts. Firstly, we obtain some general features by means of symmetry arguments. Secondly, an analytical evaluation of the dipole transition matrix elements and of the photoelectron density matrix for (110) surfaces provides qualitative information and in particular reveals the physical origin of the effect: a spin-orbit–produced mixing (hybridization) of initial-state basis functions of (single-group) spatial-symmetry types $\Sigma^3$ and $\Sigma^4$. Thirdly, we present numerical results for the large-$Z$ surface Pt(110) calculated by means of a relativistic one-step-model photoemission formalism.

General properties of the photoelectron spin polarization $\boldsymbol{P}$ can be obtained by symmetry considerations. If a spatial transformation $S$ is applied to the entire system (semi-infinite crystal, incident light, and electron detection direction), the axial vector $\boldsymbol{P}$ is transformed accordingly. In many cases $\boldsymbol{P}$ undergoes a sign change in one or more of its components. If $S$ is a symmetry operation, which leaves the entire system unchanged, $\boldsymbol{P}$ must also remain unchanged.

We now apply these ideas to normal photoemission by linearly polarized light from (110) surfaces of cubic crystals, *i.e.* surfaces with $2mm$ symmetry ($C_{2v}$ in the Schoenflies notation). Let the $x$- and the $y$-axis be parallel to the [001]- and [$\bar{1}$10]-direction, respectively. First consider *s-polarized* radiation. The electric field $\boldsymbol{E}$ is then $(E_x, E_y, 0)$. The mirror operation $m_1$ at the $(x, z)$-plane changes the signs of $P_z$ and of $P_x$, and the mirror operation $m_2$ at the $(y, z)$-plane those of $P_z$ and of $P_y$. If $\boldsymbol{E}$ is parallel to the $x$- or $y$-axis, both $m_1$ and $m_2$ are symmetry operations of the entire system. Consequently, $\boldsymbol{P} = -\boldsymbol{P} = 0$. If $\boldsymbol{E}$ has an arbitrary direction parallel to the surface, $m_1$ and $m_2$ are no longer symmetry operations of the system (which includes $\boldsymbol{E}$), but their combination $m_1 \cdot m_2$ still is. The latter symmetry dictates $P_x = 0$ and $P_y = 0$, but imposes no restriction on $P_z$. Since there is also no other symmetry operation which would do this, $P_z$ will in general be non-zero with values which depend on details of the surface and on the energies of the initial electron state and of the photon. Now consider (off-normally incident) *p-polarized* radiation. For the special cases of azimuthal angle 0 or $\pi/2$ $m_1$ or $m_2$ are symmetry operations. This implies $P_z = 0$ together with $P_x = 0$ and $P_y \neq 0$ or $P_x \neq 0$ and $P_y = 0$, as was found earlier [11-14] for (111) and (001) surfaces. For a general azimuthal angle, however, there is no more symmetry operation and all three components of $\boldsymbol{P}$ will consequently be non-zero.

Our symmetry results are confirmed explicitly by an analytical calculation of the photoelectron spin density matrix $\rho$. In addition, this calculation reveals the physical origin of $P_z$. The essential quantities are the dipole matrix elements $\langle f_s | \boldsymbol{E} \cdot \boldsymbol{r} | i_{s'} \rangle$ between «final state» and «initial state» half-space solutions of the Dirac equation. In the absence of spin-orbit coupling, these solutions belong to the irreducible representations $\Sigma^1, \ldots, \Sigma^4$ of the single group $2mm$. Spin-orbit coupling mixes these representations into one double-group representation $\Sigma_5$. The two Kramers-degenerate solutions $\psi_s$ at a given energy can then be expressed in the form

$$|\psi_s\rangle = c_1\,|\Sigma_5^1\rangle|s\rangle + c_2\,|\Sigma_5^2\rangle|s\rangle + c_3\,|\Sigma_5^3\rangle|-s\rangle + c_4\,|\Sigma_5^4\rangle|-s\rangle, \tag{1}$$

where the $|\Sigma_5^i\rangle$—with $i = 1, \ldots, 4$—are spatial parts of single-group symmetry $\Sigma^i$ and $|s\rangle$ are the Pauli spinors. The coefficients $c_i$ directly reflect the spin-orbit coupling. While all states have the above form inside the crystalline half-space, final states $|f_s\rangle$, which can be detected outside the crystal (including the surface potential barrier), become plane waves with spin $s = \pm 1/2$, *i.e.* $|\Sigma_5^1\rangle|s\rangle$. For the matrix elements, obviously all final-state parts inside the crystal are relevant in principle, but usually $|\Sigma_5^1\rangle|s\rangle$ dominates. From eq. (1) and the non-relativistic dipole selection rules one then obtains that matrix elements for the components $E_x$, $E_y$ and $E_z$ of $\boldsymbol{E}$ require initial states with spatial parts $\Sigma_5^3$, $\Sigma_5^4$ and $\Sigma_5^1$, respectively. We denote these three types of matrix element by $M_\parallel^{(3)}$, $M_\parallel^{(4)}$ and $M_\perp^{(1)}$.

Now consider *p-polarized light* incident at polar angle $\theta$ and azimuth $\varphi$ relative to the $x$-axis. An elementary but somewhat lengthy calculation explicitly yields the (2×2) spin density matrix $\rho$ in terms of the incidence angles and the matrix elements. The intensity of the photocurrent $I = \mathrm{tr}(\rho)$ and the components of the electron spin polarization vector $\boldsymbol{P} = (\mathrm{tr}\, \boldsymbol{\sigma}\rho)/I$ are then obtained as

$$I = 2\sin^2(\theta)|M_\perp^{(1)}|^2 + 2\cos^2(\theta)(\cos^2(\varphi)|M_\parallel^{(3)}|^2 + \sin^2(\varphi)|M_\parallel^{(4)}|^2)\,, \tag{2a}$$

$$P_x = -2\sin(2\theta)\sin(\varphi)\,\mathrm{Im}\,(M_\perp^{(1)}M_\parallel^{(4)*})/I\,, \tag{2b}$$

$$P_y = -2\sin(2\theta)\cos(\varphi)\,\mathrm{Im}\,(M_\perp^{(1)}M_\parallel^{(3)*})/I\,, \tag{2c}$$

$$P_z = 2\cos^2(\theta)\sin(2\varphi)\,\mathrm{Im}\,(M_\parallel^{(3)}M_\parallel^{(4)*})/I\,. \tag{2d}$$

The corresponding expressions for *s-polarized light* simply arise from the above by replacing $\varphi$ by $\varphi + \pi/2$ and putting $\theta = 0$.

The most important implication of our analytical expressions concerns the spin polarization component $P_z$ normal to the surface. While it vanishes for $\varphi = 0$ and $\varphi = \pi/2$, *i.e.* when $\boldsymbol{E}$ is parallel to a mirror plane, it is generally non-zero for arbitrary angles $\varphi$. Equation (2*d*) further reveals the underlying physical mechanism: according to eq. (1), the transition matrix elements $M_\parallel^{(3)}$ and $M_\parallel^{(4)}$ are proportional to the spin-orbit coupling coefficients $c_3$ and $c_4$; $P_z$ of photoelectrons from a pair of Kramers-degenerate initial states therefore contains a factor $c_3 \cdot c_4^*$. This demonstrates that $P_z$ has its origin in spin-orbit coupling. In contrast to $I$, $P_z$ is seen from eq. (2*d*) to depend not only on the modulus of the transition matrix elements but also on the phase relation between them, thus providing additional information. In the special case of $4mm$ symmetry ($C_{4v}$) $P_z$ becomes identically zero, since $M_\parallel^{(3)} = M_\parallel^{(4)}$. For unpolarized light—an incoherent superposition of $p$- and $s$-polarized light—one obtains $P_z = 0$ firstly if $\theta = 0$ and secondly if $\theta \neq 0$ and $\varphi = 0$ or $\pi/2$. At general values of $\theta$ and $\varphi$, however, the difference in the intensities of $s$- and $s$-polarized light implies $P_z \neq 0$ for unpolarized light. The surface-parallel spin components $P_x$ and $P_y$ in eqs. (2*b*), (2*c*) are seen to arise from spin-orbit coupling between a $\Sigma_5^1$ part and a $\Sigma_5^4$ and $\Sigma_5^3$ part, respectively. They are thus of the same nature as the spin polarization effect found for (001) and (111) surfaces [11-13]. In contrast to the latter surfaces, however, $I$, $P_x$ and $P_y$ for (110) surfaces depend on the azimuthal angle as a consequence of the reduced rotation symmetry.

Quantitative numerical calculations of spin-resolved photoemission spectra, the corresponding bulk band structure and the layer-resolved density of states were performed for Pt(110), the large atomic number ($Z = 78$) of which entails strong spin-orbit coupling, by means of a computer code, in which we have implemented our fully relativistic Green's function theory for semi-infinite crystals [14]. The effective quasi-particle potential is taken in the muffin-tin approximation, with its spherical part obtained by a self-consistent LMTO calculation using the Barth-Hedin exchange-correlation approximation. The real part of the inner potential is chosen as 14.75 eV for the lower states and 14.75 eV $-\,0.12(E - E_\mathrm{F})$ for the upper states, where $E_\mathrm{F}$ is the Fermi energy, $E$ the state energy, and all energies are given in eV. For the imaginary part we adopt energy-dependent forms increasing (in absolute value) away from $E_\mathrm{F}$ as $0.025(E - E_\mathrm{F})$ for the lower and as $0.04(E - E_\mathrm{F})^{1.25}$ for the upper states. The surface potential barrier is simply taken as a refracting step, which is assumed as reflecting for the lower states (for which there is actually total internal reflection, since their energy is below the vacuum level) and—drawing upon LEED experience—as non-reflecting for the upper states. For the surface geometry we firstly use a simple bulk truncation, labelled $(1\times1)$, and secondly a more realistic $(1\times2)$ reconstruction determined by a LEED

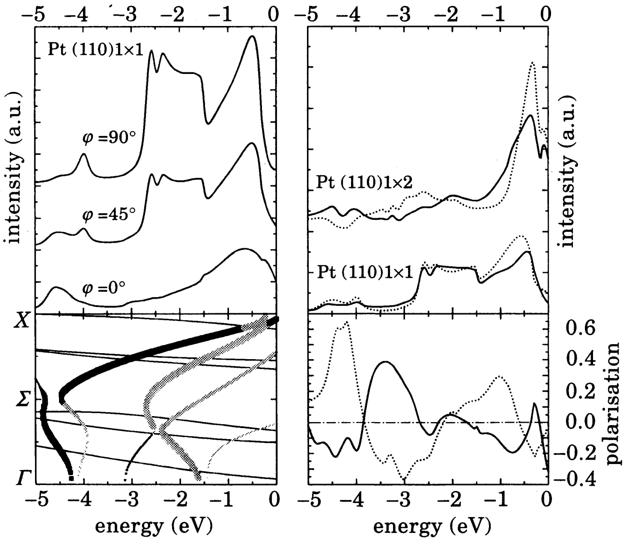

Fig. 1. – Normal photoemission from Pt(110) by *s*-polarized light with photon energy 21.22 eV. Left-hand part: upper panel: spin-averaged intensity spectra from unreconstructed (1 × 1) surface for azimuthal angles $\varphi$ of the electric-field vector (relative to the [001]-direction) as indicated. Lower panel: relativistic bulk band structure along [110] ($\Gamma(\Sigma)K$); for the initial-state bands the thickness corresponds to the joint weight of the $\Sigma^3$ and $\Sigma^4$ symmetry parts, and dark (light) shading indicates the dominance of $\Sigma^3$ ($\Sigma^4$); the upper bands of dominant spatial symmetry $\Sigma^1$ (as calculated for complex inner potential and shifted downward by the photon energy 21.22 eV) are given by thin solid lines. Right-hand part: spin-resolved spectra with —— $I_+$ ····· $I_-$, (upper panel) and spin polarization component $P_z$ (lower panel) at $\varphi = 45°$ for unreconstructed (——) and (1 × 2)-reconstructed (·····) surface.

analysis [15]: missing [$\bar{1}$10] rows with a reduction of the topmost interlayer spacing by 20% relative to the bulk value.

We now present some typical numerical results as obtained in normal emission from Pt(110) by *s*-polarized light of photon energy 21.22 eV. As can be seen in the left-hand part of fig. 1, the spin-averaged intensity spectra from the unreconstructed surface can be understood in terms of direct transitions between the relativistic bulk bands. For $\boldsymbol{E} \| [001]$ ($\varphi = 0$), selection rules require initial states with spatial symmetry $\Sigma^3$, and in fact spectral peaks occur at the crossing points between dominant $\Sigma_5^3$ initial- and $\Sigma_5^1$ final-state bands at $-4.5$ eV, $-0.7$ eV and $-0.2$ eV. For $\boldsymbol{E} \| [\bar{1}10]$ ($\varphi = 90°$), crossing points with $\Sigma^4$ initial states are seen under all spectral peaks. In particular, this holds for the three additional peaks between $-3.0$ eV and $-1.5$ eV. At $\varphi = 45°$, both $\Sigma_5^3$ and $\Sigma_5^4$ contribute, and the spectrum is the average of the $\varphi = 0°$ and the $\varphi = 90°$ spectra.

As expected above from symmetry and analytical evaluation, the calculated spin polarization vector $\boldsymbol{P}$ is zero for $\varphi = 0$ and $\varphi = 90°$. For $\varphi = 45°$, the component $P_z$ normal to the surface is found to assume values up to 40% and to exhibit a pronounced variation with energy (see bottom panel of the right-hand part of fig. 1). Comparing, for the (1 × 1) surface, with the corresponding spin-resolved intensity spectra (lower part of the top panel), the peaks between $-5$ eV and $-4$ eV and those above $-1.5$ eV are associated with rather large spin polarization, in contrast to the peaks between $-3.0$ eV and $-1.5$ eV. This is easily understood from our above analytical finding that the present new spin polarization effect originates from a hybridization between $\Sigma_5^3$ and $\Sigma_5^4$ initial-state parts. As is seen from the band structure in fig. 1, both symmetry types are sizeable at the energies of the former set of peaks, whereas the latter set (between $-3$ eV and $-1.5$ eV) arises from initial states of almost exclusively $\Sigma_5^4$ symmetry.

For the $(1\times 2)$-reconstructed Pt(110) surface, the spin-resolved intensity spectra (in the right-hand top panel of fig. 1) differ appreciably from their $(1\times 1)$ counterparts. In particular, they exhibit additional peaks between $-3.0$ eV and $-1.5$ eV and at $-0.1$ eV. These can be understood as a consequence of «surface umklapp» by a reciprocal lattice vector of the $(1\times 2)$ surface layer. The difference between $(1\times 2)$ and $(1\times 1)$ is much stronger in the spin polarization $P_z$ spectra (right-hand bottom panel of fig. 1), especially in the region of the peaks between $-5.0$ eV and $-3.5$ eV, where $P_z$ reverses sign and reaches values up to 60%, and between $-2$ eV and $E_F$. This strong sensitivity of $P_z$ to details of the surface is due to the fact that back-scattering by the surface is crucial for the existence of the present spin polarization effect, which is absent in a three-step model of photoemission involving bulk interband transitions.

Calculations for $p$-polarized light also confirm our analytical results. In particular, we obtain for $\varphi = 45°$ the simultaneous presence of a sizeable $P_z$ and the surface-parallel $\boldsymbol{P}_\parallel$ found earlier [11-13] for (001) and (111) surfaces. In contrast to the latter cases, $\boldsymbol{P}_\parallel$ is, however, not perpendicular to the reaction plane (defined by the direction of photon incidence and the surface normal) any more.

Recently, an experimental spin-resolved photoemission study on Pt(110) [16] was performed with unpolarized radiation incident off-normally at azimuthal angles $\varphi = 0$ and $\pi/2$. In line with our above equations (2*b*), (2*c*) and (2*d*), the surface-parallel spin polarization *vs.* energy profiles for these two angles were found to differ appreciably from each other, and the $P_z$ effect is absent in this geometry.

The high sensitivity of $P_z$ to details of the electronic and geometrical structure of the surface recommends its joint experimental and theoretical determination as a tool for obtaining additional and more precise information, in particular on reconstructed clean surfaces and on adsorbate systems. Since $P_z$ is produced by the surface-parallel component of $\boldsymbol{E}$ alone, it has—compared to the $\boldsymbol{P}_\parallel$ effect, which also requires $E_z$—the advantage that its calculation is not plagued by the still poorly known surface optical response.

* * *

This work was funded by the German Ministry for Research and Technology under Contract No. 055PGABB7. The numerical calculations were performed on the supercomputer SNI S-600/20 of the Land NRW (project number P047).

## REFERENCES

[1] Kevan S. V. (Editor), *Angle-Resolved Photoemission: Theory and Current Applications* (Elsevier, Amsterdam) 1992.

[2] Feder R. (Editor), *Polarized Electrons in Surface Physics* (World Scientific, Singapore) 1985.

[3] Heinzmann U., in *Photoemission and Absorption Spectroscopy of Solids and Interfaces with Synchrotron Radiation*, edited by M. Campagna and R. Rosei (North Holland, Amsterdam) 1990.

[4] Ginatempo B., Guo G. Y., Temmerman W. M., Staunton J. B. and Durham P. J., *Phys. Rev. B*, **42** (1990) 2761.

[5] Schmiedeskamp B., Irmer N., Stoppmanns P., Vogt B. and Heinzmann U., *Europhys. Lett.*, **20** (1992) 657.

[6] Halilov S. V., Gollisch H., Tamura E. and Feder R., *J. Phys. Condens. Matter*, **5** (1993) 4711.
[7] Henk J. and Feder R., *J. Phys. Condens. Matter*, **6** (1994) 1913.
[8] Braun J. and Borstel G., *Phys. Rev. B*, 48 (1993) 14373.
[9] Tamura E., Piepke W. and Feder R., *Phys. Rev. Lett.*, **59** (1987) 934.
[10] Schmiedeskamp B., Vogt B. and Heinzmann U., *Phys. Rev. Lett.*, **60** (1988) 651.
[11] Tamura E. and Feder R., *Europhys. Lett.*, **16** (1991) 695; *Solid State Commun.*, **79** (1991) 989.
[12] Irmer N., David R., Schmiedeskamp B. and Heinzmann U., *Phys. Rev. B*, **45** (1992) 3849.
[13] Schmiedeskamp B., Irmer N., David R. and Heinzmann U., *Appl. Phys. A*, **53** (1991) 418.
[14] Halilov S. V., Tamura E., Gollisch H., Meinert D. and Feder R., *J. Phys. Condens. Matter*, **5** (1993) 3859.
[15] Fery P., Moritz W. and Wolf D., *Phys. Rev. B*, 38 (1988) 7275.
[16] Irmer N., Frentzen F., Schmiedeskamp B. and Heinzmann U., *Surface Sci.*, **307-309** (1994) 1114.

## Publikation 6

# Magnetic-circular-dichroism study of the valence states of perpendicularly magnetized Ni(001) films

W. Kuch, A. Dittschar, K. Meinel, M. Zharnikov, C. M. Schneider, and J. Kirschner
*Max-Planck-Institut für Mikrostrukturphysik, Am Weinberg 2, D-06120 Halle, Germany*

J. Henk and R. Feder
*Theoretische Festkörperphysik, Universität Duisburg, D-47048 Duisburg, Germany*

(Received 20 October 1995)

Magnetic circular dichroism in valence-band photoemission from perpendicularly magnetized Ni thin films on Cu(001) has been studied both experimentally and theoretically. Over the photon energy range of 11–27 eV for normal emission and normal incidence, intensity asymmetries up to 20% upon light helicity or magnetization direction reversal were found. Fully relativistically calculated photoemission spectra agree well with experiment and reveal the interplay between spin-orbit coupling and exchange splitting, which is at the origin of magnetic dichroism. From comparison of theory and experiment the band dispersion is determined and points of hybridization along the $\Delta$ axis are identified.

## I. INTRODUCTION

As is well known, the electronic structure of metals is influenced significantly by spin-orbit coupling.[1–4] A variety of effects including spin polarization of photoelectrons in paramagnets[5–7] and the polar Kerr effect, owe their existence to the presence of spin-orbit coupling. Great effort has been put, especially in the last few years, in the investigation of spin-orbit-induced effects[8–10] and it has turned out that even in the valence-band structure of low $Z$ materials, as for example Cu, spin-orbit coupling is significant.[11,12]

Magnetic dichroism in photoemission or absorption, which is the modification of intensity-distribution curves by reversal of the magnetization direction, is exclusively due to the interplay of spin-orbit and exchange coupling (see for example Refs. 13–16). Magnetic dichroism in x-ray absorption as well as in core-level photoemission probes the interaction of spin-orbit split core levels with spin polarized valence electrons. It is hence considered as a tool for element-specific investigations of magnetic properties. For the determination of the electronic band structure, angle-resolved photoemission spectroscopy (ARPES) of valence electrons is one of the most commonly used and powerful methods.[8,17,18] Magnetic circular dichroism in the angular distribution (MCDAD) of valence-band photoemission is caused by the interplay between exchange-splitting and spin-orbit coupling in the valence states. ARPES with the extension of measuring the accompanying MCDAD therefore is a most appropriate tool for the direct investigation of the electronic structure of ferromagnets, including both exchange and spin-orbit coupling.

For MCDAD from core levels, calculations for single atoms reproduce qualitatively the experimentally observed findings (see, for example, Refs. 14, 19, and 20). Recent experiments, however, show effects on the MCDAD asymmetry due to the crystallinity of the sample; in other words, they reveal the limits of atomic calculations.[21,22]

The interpretation of magnetic dichroism in valence-band photoemission is more complicated than that in core-level photoemission. The knowledge of both the detailed valence- and conduction-band structures of the semi-infinite crystal is necessary to interpret adequately the experimental findings. Using an experimental arrangement of high symmetry facilitates the interpretation by means of dipole selection rules. For normally incident circularly polarized light and normal emission of photoelectrons from an (001) surface of a cubic crystal, selection rules allow only transitions from valence states with $\Delta^5$ single-group symmetry spatial parts into final states with $\Delta^1$ symmetry.[23] Furthermore, the photoelectron spin polarization is complete[23,24] and is aligned with the direction of light incidence.[11,12,25–27] The presence of a magnetization generally reduces the symmetry of the semi-infinite solid, however, when it is perpendicular to the crystal surface, the surface normal remains a rotation axis, and the electronic states can still be classified according to irreducible double-group representations of the nonmagnetic case.[15,28] Such a totally symmetric geometry thus opens the possibility to discuss the MCDAD in terms of a simple interband transition model, including both spin-orbit coupling and exchange interaction.

The purpose of the present paper is to relate the valence-band magnetic circular dichroism in Ni to the underlying band structure. Starting with a simple picture of band symmetries and selection rules, a thorough comparison with fully relativistic band-structure calculations provides a deeper insight into the details of the band structure. Points of hybridization between bands of different spin occupancy and different orbital symmetry, where the expectation value of the spin polarization is low and the illustrative picture ceases to work, may be identified this way. Whereas the main MCDAD features can be qualitatively explained by the symmetry of the involved initial states, extended statements on the origin of all of the observed dichroic features and their relation to exchange and spin-orbit coupling are only possible with access to fully relativistic photoemission calculations. The procedure is to check as a first step the input parameters for the calculations by comparison of the experimental spectra to one-step photoemission calculations. The next step is to correlate specific dichroic features to the calculated relativistic band structure. This serves to finally end up with an experimental determination of the exchange- and spin-orbit split band structure, which may in details of dispersion and hybridization quite possibly differ from the calculated one.

The chosen system to do this is that of an epitaxial Ni film deposited on a Cu(001) substrate. The interplay between exchange and spin-orbit interaction can be preferably observed in nickel as a prototype system, where both interactions are of the same order of magnitude ($\approx 0.3/0.1$ eV). The relatively small exchange splitting in nickel compared to that of iron or cobalt has the advantage that there are extended regions in the Brillouin zone in which both corresponding majority and minority bands are occupied. The dispersion of such bands may thus be followed experimentally over a distinct range of $\mathbf{k}$ by photoemission spectroscopy. The observed dichroism also exhibits more spectral features when both majority and minority states contribute to the photoemission signal, which is advantageous for the unambiguous correlation to certain electronic states of the band structure.

Furthermore, for Ni(001) as a prototype case one-step photoemission calculations have already been performed to demonstrate the origin of specific features in MCDAD spectra.[15] Calculated photoemission spectra for normal electron emission from perpendicularly magnetized Ni(001) were presented for both helicities of the incoming circularly polarized UV radiation. The calculated spectral features of the magnetic circular dichroism could be correlated to relativistic band-structure calculations and were discussed by means of direct transitions.

The choice of the Ni/Cu thin-film system was also governed by other considerations. For the reasons mentioned above it is advantageous to have a magnetization perpendicular to the sample surface. For bulk Ni the easy axis of the magnetization is the [111] direction, thus prohibiting the totally symmetric configuration with the vectors of photon and electron momentum, light helicity, and magnetization all collinear with the [001] surface normal. In ultrathin magnetic films, however, other contributions to the magnetic anisotropy due to the shape and the influence of surface and interface of the thin-film system as well as magneto-elastic contributions to the magnetocrystalline anisotropy can lead to different orientations of the magnetization direction. In most of the cases the predominant influence of the magnetic dipole interaction, the shape anisotropy, results in an easy direction parallel to the film plane. In a number of special cases and for limited thickness ranges, there is the possibility that the shape anisotropy can be overcome by other contributions to the magnetic anisotropy related directly to the thin-film nature of the system.[29–31] In such a case the total anisotropy may manifest itself in a resulting magnetization direction perpendicular to the film surface. It is therefore important to select an appropriate substrate to induce the required anisotropic properties in the epitaxially deposited ferromagnetic film. It is reported in the literature that thin films of Ni deposited on a Cu(001) substrate exhibit a perpendicular orientation of the easy axis of magnetization over an extended thickness range.[32–34] The published values of the film thicknesses for perpendicular magnetization vary between 7 and 10 ML for the lower limit and between 56 and 75 ML for the upper limit.[33,34] This is at present the highest film thickness where a simple magnetic overlayer shows a perpendicular magnetization. It is attributed to the magneto-elastic volume anisotropy caused by substrate-induced strain in the epitaxial Ni film.[34–36] The Ni/Cu(001) system thus offers the unique possibility to study the magnetic circular dichroism for a perpendicular magnetization at relatively high film thicknesses, where the electronic structure can be thought of as bulklike. Because of the strain in the film the electronic structure will of course not be fully identical to that of bulk Ni. However, there are no indications for a nonhomogeneous crystalline structure over the whole film thickness,[34,37] so that the magnetic circular dichroism can be studied in the advantageous fully symmetric configuration as provoked by the bulklike electronic structure of the homogeneously strained Ni film.

The origin of the perpendicular anisotropy of Ni/Cu(100) itself is also of great interest. Perpendicularly magnetized films of some ten monolayers are much more favorable for technological applications than those of just one monolayer. The contributions to the magnetic anisotropy overcompensating the in-plane magnetic dipole energy are directly related to the spin-orbit coupled electronic structure of the system. To explore the relativistic band-structure may therefore help to identify the nature of this anisotropy together with supplementary work on structure and morphology of the films.

The organization of this paper is as follows: In the next section details of the experiment are described. In Sec. III the computational method is presented, and the origin of MCDAD in the present geometry is discussed analytically. Both experimental and theoretical results are presented in Sec. IV. In Sec. V they are correlated to the relativistic band structure, and specific information about the electronic structure of the system is drawn from the comparison of experiment and theory.

## II. EXPERIMENTAL ASPECTS

The experiments were carried out in a UHV chamber (base pressure $1\times10^{-8}$ Pa) equipped with facilities for low-energy electron diffraction (LEED), Auger electron spectroscopy (AES), magneto-optical Kerr effect (MOKE), medium energy electron diffraction (MEED), and thin-film growth. Details of the setup can be found in Ref. 38.

Nickel was evaporated from a high-purity nickel rod by electron bombardment. Typical deposition rates were 0.5 ML/min, while the overall pressure in the chamber did not exceed $2\times10^{-8}$ Pa. No surface contamination above the AES detection limit ($\approx 1\%$) could be detected after nickel deposition. The sample temperature during deposition was 300 K. All experiments presented in this publication refer to film thicknesses of 15 ML. This is well in the range of perpendicular magnetization, the presence of which was checked before and after acquisition of photoelectron spectra by means of polar MOKE measurements. All films produced rectangular hysteresis loops at room temperature. During the collection of the photoemission spectra presented here the sample temperature was maintained at 300 K.

MEED measurements during Ni evaporation exhibit distinct oscillations in the specular beam intensity for the first five monolayers, indicating layer-by-layer growth. This is followed by a three-dimensional film growth at higher thicknesses manifesting itself in a monotonously decreasing MEED specular beam intensity. This growth behavior was also observed by scanning tunneling microscopy measurements.[37] The films showed a $(1\times1)$ LEED pattern identical to that of the clean Cu substrate, from which a pseudomorphic fcc structure with the lateral lattice constant of Cu(100) is concluded. In order to determine a tetragonal distortion often observed in pseudomorphic fcc films with a certain lattice mismatch to the substrate, LEED-$I(V)$ measurements of the (00) beam were performed. From the shift of energetic positions of the sequence of single-scattering Bragg maxima $6.0\%\pm0.3\%$ compression of the vertical layer spacing with respect to the copper substrate is obtained. This is slightly less that one would expect assuming constant atomic volumes of the nickel atoms, which leads to a value of 6.9%.

To minimize the film roughness, the sample is heated to 450 K for 10 min immediately after completion of the deposition. This procedure is reported to result in flat pseudomorphic films of good quality without copper segregation.[37,39] After the annealing procedure, no change of structure or magnetization could be detected, and the AES Ni to Cu intensity ratio remained identical.

Photoemission spectra were taken at the 6.5 m normal-incidence monochromator beamline of the Berlin synchrotron radiation facility (BESSY), with circular polarization of about 90%.[40] As already discussed in Sec. I, the spectra presented in this paper were taken in the totally symmetric configuration, i.e., normal incidence of the incoming radiation and normal emission of the outgoing photoelectrons.

The electron spectrometer is described in detail elsewhere.[11] It was operated at a fixed pass energy of 8 eV, resulting in an overall energy resolution of approximately 200 meV (including the monochromator resolution). The angular acceptance can be estimated to be less than $\pm2°$. To rule out apparatus-induced asymmetries, spectra for both helicities of the incoming light were taken for both magnetization directions of the sample. The magnetization was reversed after approximately 1 h measuring time, whereas the light helicity was changed after each scan of about 5 min.

All spectra in this paper are shown normalized to the photon flux. This is done by considering the energy dependence of the monochromator photon flux for both gratings from Ref. 40 and normalizing to the ring current. Due to variations of the beam position and size with the ring current, the relation between photon flux at the sample and the ring current is nonlinear. Normalizing linearly with the ring current would result in too small (large) intensities at high (low) ring currents. To account for this effect, the relation between photon flux and ring current was extracted from measurements at constant photon energy for different ring currents and used for the normalization procedure. The remaining uncertainty in comparing experimental intensities at different photon energies is in the range of about 10%.

## III. THEORETICAL ASPECTS

### A. Computational details

Theoretical photoemission spectra and the corresponding bulk band structure were obtained by fully relativistic calculations of the layer Korringa-Kohn-Rostoker type using a Green's-function formalism.[41] In this method, spin-orbit coupling and exchange interaction are included on an equal footing. Photoelectron spectra are calculated within the one-step model involving relativistic dipole-transition-matrix elements to time-reversed LEED states of the semi-infinite solid. Hole lifetime is incorporated from the start. Our method is strictly valid at $T=0$ K and in good approximation at temperatures well below the Curie temperature.

The effective quasiparticle potential is taken in the muffin-tin shape approximation, which is adequate for closely packed metallic systems. Its spin-dependent real part inside the muffin-tin spheres is adopted from a bulk potential, which we calculated self-consistently by the linear muffin-tin orbital method. Since for Ni this leads to exchange splittings of about 0.6 eV as opposed to an average value of 0.3 eV observed in photoemission experiments, we modified it by an *ad hoc* spin-dependent self-energy correction reducing the splitting between the majority- and the minority-spin potentials by a factor of 0.5. The real part of the inner potential is chosen as 14.67 eV for initial and as $14.67-0.15(E-E_F)$ for the final states. For the imaginary part we adopt energy-dependent forms increasing (in absolute value) away from the Fermi energy $E_F$ as $0.025(E-E_F)$ for the lower and as $0.03(E-E_F)^{1.25}$ for the upper states. The surface potential barrier is simply approximated by a reflecting (nonreflecting) step for the lower (upper) states.

For the geometrical structure of the Ni film we assume a tetragonally-distorted fcc lattice (fct) with the in-plane lattice constant of bulk Cu, namely 2.55 Å (compared to 2.49 Å for bulk Ni). The vertical layer spacing is suggested as 1.69 Å by the results of our LEED-$I(V)$ measurements, which indicate a 6% tetragonally compressed fcc structure (bulk value of Ni: 1.76 Å). All layer spacings of the atomic layers were taken to be equal, thus neglecting possible relaxations in the vicinity of the surface. Because we found experimentally no emission from the Cu substrate, we calculated the photoemission spectra and the bulk band structure for a semi-infinite Ni crystal (with the above fct structure) instead of a 15 layer Ni slab on top of the Cu substrate.

The tetragonal distortion of the Ni lattice, i.e., the decrease of the interlayer spacing compared to the fcc case with Cu lattice constant, increases the dispersion of the bulk bands, as is expected. The band structure for the present fct structure is rather similar to that of bulk-fcc Ni. Differences are obtained in the position of the spin-orbit-induced band gaps. In photoemission, spectra obtained for the three different Ni lattices, namely the tetragonally distorted lattice, the bulk Ni lattice, and the undistorted fcc lattice with the Cu lattice constant, show the same general shape. Minor peaks and shoulders, which are brought about by spin-orbit coupling, differ slightly in intensity and energy position.

### B. Analytical considerations

Before turning to the experimental results and their interpretation, it is useful to present briefly some analytical results on MCDAD. The presence of perpendicular magnetization reduces the symmetry of the (001) surface from $C_{4\mathrm{v}}$ to $C_4$, because each mirror operation reverses the magnetization and, thus, is no symmetry operation of the entire system. The electronic states can be classified according to four one-dimensional irreducible representations of the double group. Instead of the nomenclature of Falicov and Ruvalds[42] we prefer to use the one of the nonmagnetic system,[15] since the reader is likely to be more familiar with the latter. Because magnetic exchange breaks the time-reversal symmetry, i.e., Kramer's degeneracy is lifted, each of the two-dimensional irreducible double-group representations $\Delta_6$ and $\Delta_7$ of the nonmagnetic case decomposes into a pair of one-dimensional representations, i.e., $\Delta_6+$, $\Delta_6-$, $\Delta_7+$, and $\Delta_7-$. The basis functions of these obey the relations $\hat{T}|\Delta_i+\rangle = |\Delta_i-\rangle$ and $\hat{T}|\Delta_i-\rangle = -|\Delta_i+\rangle$, $\hat{T}$ denoting the time-reversal operator and $i=6,7$. It is important to note that the $+$ $(-)$ sign does not refer to "majority" ("minority") spin because the latter is not a "good quantum number" in the presence of spin-orbit coupling. All the above irreducible representations comprise basis functions with spin-up and basis functions with spin-down Pauli spinors. For example, the double-group representation $\Delta_6+$ has basis functions $\Delta_6^1+$, with $\Delta^1$ spatial symmetry and spin-up, and $\Delta_6^5+$, with $\Delta^5$ spatial symmetry and spin-down. The actual states of the semi-infinite crystal are linear combinations of these two types of basis functions.

After calculating the spin-density matrix for photoemission with circularly polarized light, we obtain analytical expressions for the intensity $I(\sigma_\pm)$ and the electron-spin polarization $P_z(\sigma_\pm)$, where $\sigma_\pm$ indicates the helicity of the incident light. $P_z$ can only assume the values $+1$ and $-1$, and the in-plane polarization components are identically zero. For each dipole transition, the photoelectrons are thus completely spin polarized parallel to the surface normal.

The intensity for right-handed circular light reads

$$I(\sigma_+) = 2(|M_6^{+-}|^2 + |M_7^{-+}|^2), \qquad (1)$$

where $M_i^{ss'}$ denotes the transition-matrix element from a $\Delta_i s'$ initial state with single-group symmetry $\Delta^5$ into a $\Delta_6 s$ final state with single-group symmetry $\Delta^1$. For left-handed circular light we obtain

$$I(\sigma_-) = 2(|M_6^{-+}|^2 + |M_7^{+-}|^2). \qquad (2)$$

Equations (1) and (2) reflect the symmetry relation $I(\sigma_\pm, +\vec{M}) = I(\sigma_\mp, -\vec{M})$, which is obvious from the mirror operations of the point group $C_{4v}$. Consequently, the intensity asymmetry, which constitutes MCDAD, can be obtained by reversing either the magnetization $\vec{M}$ or the light helicity. In the following we denote $I(\sigma_+, +\vec{M})$ and $I(\sigma_-, -\vec{M})$ as $I(\uparrow\uparrow)$, and $I(\sigma_+, -\vec{M})$ and $I(\sigma_-, +\vec{M})$ as $I(\uparrow\downarrow)$. According to Eqs. (1) and (2), $I(\uparrow\uparrow)$ consists of contributions from initial states of $\Delta_6^5-$ and $\Delta_7^5+$ symmetry, and $I(\uparrow\downarrow)$ of those of $\Delta_6^5+$ and $\Delta_7^5-$ symmetry. In the nonmagnetic limit, Kramer's degeneracy implies $M_i^{+-} = M_i^{-+} =: M_i$, with $i=6,7$, and the MCDAD vanishes, as it should.

### C. Illustration of magnetic dichroism

More detailed insight into the physical origin of magnetic circular dichroism is provided in Fig. 1 by a typical set of numerical results for normal emission from perpendicularly magnetized Ni(001). In panel (a) the fully relativistic band structure is shown, calculated with the parameters mentioned above. The bands are distinguished according to their spin expectation value: thick (thin) solid lines indicate majority (minority) character, corresponding to a positive (negative) spin expectation value. The effect of the magnetization, i.e.,

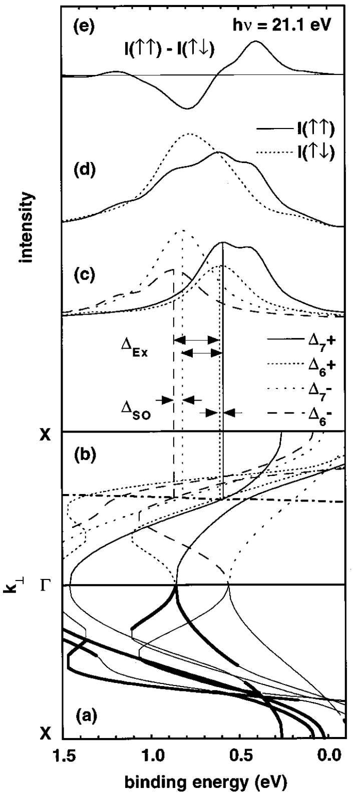

FIG. 1. Illustration of the origin of observed MCDAD. (a) Fully relativistic bulk band structure of Ni along the $\Delta$ axis with magnetization along the same axis, calculated with a real effective potential. Bands with majority- (minority-) spin expectation value are shown as thick (thin) solid lines. (b) As in (a), but with bands distinguished according to their double group symmetry as labeled in the figure. A final state band with mainly $\Delta^1$ spatial symmetry, shifted downwards by 21.1 eV, is shown as dash-dotted line. The vertical lines mark crossing points of the final state band with four initial bands of predominating $\Delta^5$ spatial symmetry (see text). The influence of spin-orbit ($\Delta_{SO}$) and exchange interaction ($\Delta_{Ex}$) is indicated by arrows. (c) Spin-resolved photoemission spectra for 21.1 eV photon energy, calculated with the above potential augmented by a uniform imaginary part describing the finite hole lifetime. Majority (minority) spin spectra are labeled as $\Delta_7-$ and $\Delta_6-$ ($\Delta_7+$ and $\Delta_6+$) in correspondence with the underlying initial-state bands, spectra for parallel (antiparallel) alignment of $\boldsymbol{\sigma}$ and $\mathbf{M}$ as $\Delta_7+$ and $\Delta_6-$ ($\Delta_6+$ and $\Delta_7-$) bands (see text). (d) Calculated photoemission intensity spectra for parallel (solid line) and antiparallel alignment (dotted line) of photon spin $\boldsymbol{\sigma}$ and magnetization vector $\mathbf{M}$. (e) Difference of the two curves of (d).

the exchange splitting of 0.3 eV, is easily recognized. It is also obvious that the spin is no longer a ‘‘good quantum number’’ due to spin-orbit coupling, because some bands change from minority to majority character.

In panel (b) the same bands are distinguished according to their double-group symmetry $\Delta_7+$, $\Delta_6+$, $\Delta_7-$, and $\Delta_6-$. The final state band which is reached by photoexcitation is also shown as dash-dotted line, shifted downwards by 21.1 eV. In the direct transition model, which is useful for interpretation purposes, the initial state binding energy is given by the crossing points of this line with the initial state bands. As already mentioned, only bands with $\Delta^5$ spatial symmetry contribute to the photoelectron spectra in the present totally symmetric geometry. Without spin-orbit and exchange coupling, there is only one band with this symmetry. This band is split by spin-orbit and exchange interaction into four energetically separated bands. The vertical lines in Fig. 1 originate at the crossing points of these four bands with the shifted final state band. Because of their prevailing spatial symmetry they can be labeled $\Delta_7^5+$, $\Delta_6^5+$, $\Delta_7^5-$, and $\Delta_6^5-$. The influence of spin-orbit ($\Delta_{\mathrm{SO}}$) and exchange interaction ($\Delta_{\mathrm{Ex}}$) is indicated by arrows between the vertical lines.

Figure 1 (c) shows calculated spin-resolved photoemission spectra for 21.1 eV photon energy. As discussed in the previous section, for parallel (antiparallel) alignment of photon spin and magnetization direction, only $\Delta_7^5+$ and $\Delta_6^5-$ ($\Delta_6^5+$ and $\Delta_7^5-$) states contribute to the spectrum. The spin polarization of the respective photoelectrons is complete in the sense that $\Delta_7^5+$ and $\Delta_6^5+$ bands contribute to the minority-spin spectra, whereas $\Delta_7^5-$ and $\Delta_6^5-$ appear in the majority-spin spectra. The four resulting spectra are depicted in Fig. 1 (c), using the line types corresponding to the initial state double-group symmetry: Minority peaks are given by solid and dashed lines, corresponding to the nomenclature used for $\Delta_7+$ and $\Delta_6+$ symmetry, majority peaks by dotted and broken lines, corresponding to $\Delta_7-$ and $\Delta_6-$ symmetry. Sizeable peaks in the photoemission spectra in panel (c) are seen to be associated with the four discussed crossing points in panel (b). As can be seen, there are also significant contributions to the spectra at other than the marked crossing points. This is due to the fact that hybridization between bands of the same double-group symmetry but different spatial symmetry can occur, leading to a larger number of initial states containing $\Delta^5$ spatial symmetry parts. At the photon energy of 21.1 eV, such hybridization is mainly observed in bands of $\Delta_7+$ and $\Delta_6-$ double-group symmetry, leading to peaks at 0.45 and 1.2 eV binding energy, respectively.

Without spin resolution in the photoemission experiment, the spectra cannot be distinguished according to the electron-spin polarization as in Fig. 1 (c). As the calculated spin-integrated photoemission intensities in Fig. 1 (d) show, there is however a strong MCDAD, which still contains much information on the relativistic band structure. The solid (dotted) lines correspond to parallel (antiparallel) alignment of photon spin and magnetization direction [$I(\uparrow\uparrow)$ and $I(\uparrow\downarrow)$, respectively]. Each spectrum is the sum of the two corresponding spectra of panel (c): $\Delta_7+$ and $\Delta_6-$ give $I(\uparrow\uparrow)$, $\Delta_6+$ and $\Delta_7-$ give $I(\uparrow\downarrow)$.

The topmost panel of Fig. 1 represents MCDAD as the difference between the two curves of panel (d). It shows a pronounced minus feature at 0.8 eV binding energy, which is due to emission from $\Delta_7-$ and, to a lesser extent, from $\Delta_6+$ states. The other large feature, a positive peak around 0.4 eV binding energy, is mainly due to emission from the higher $\Delta_7+$ band, which crosses the shifted final-state band at this energy.

The above example clearly illustrates how spin-orbit and exchange interaction in conjunction with relativistic dipole selection rules lead to MCDAD. Comparison of the results of one-step photoemission calculations with the relativistic band structure shows that all of the observed spectral features can—via direct transitions—be correlated with the respective details of the electronic bulk band structure. Magnetic dichroism, which does not require the experimentally more cumbersome spin resolution of the photocurrent, hence is a powerful tool for analyzing the spin character of the initial states. While in the above example only bulklike states are relevant, we note that this also holds for photoemission from surface states and thin-film states, in which cases a similar interpretation, based on layer-resolved densities of states rather than the bulk band structure, can be given (see, e.g., Ref. 43).

## IV. RESULTS

The left-hand side of Fig. 2 shows a series of experimental intensity spectra of 15 ML Ni on Cu(001) for different photon energies from 11.1 up to 27.4 eV. Spectra for parallel (antiparallel) alignment of the light helicity and the magnetization direction are represented by solid (dotted) lines, following the nomenclature already used in Fig. 1 (d). The vertical lines mark special peak positions which will be discussed later.

On the right-hand side, calculated photoemission spectra for the same photon energies are depicted. Again, spectra for parallel (antiparallel) alignment of the light helicity and the magnetization direction are depicted by solid (dotted) lines.

Good qualitative agreement between experimental and theoretical data can be stated already at first sight. The spectra for 11.1 eV photon energy display relatively sharp peaks just below the Fermi energy. With increasing photon energy a dispersion towards higher binding energies and a broadening of the peaks are observed. The higher intensity in the peak maximum of the dotted curves in the spectra from $h\nu = 11.1$ up to 21.1 eV is reproduced well in the theory. From 19.1 to 27.4 eV photon energy, intensity for antiparallel alignment of photon spin and magnetization dominates the peak on the higher binding energy side in both the experimental and theoretical curves. Sharp structures are better resolved in the theoretical curves. A distinct MCDAD, that is the difference between dotted and continuous lines, is seen from both experimental and theoretical spectra. Although the MCDAD is significantly larger in theory, the qualitative agreement to the experimental one is quite good. The lower experimental MCDAD must be attributed to the limited energetic and angular resolution, to possible imperfections in film morphology, and to the background of inelastically scattered electrons not considered in the calculations. Further-

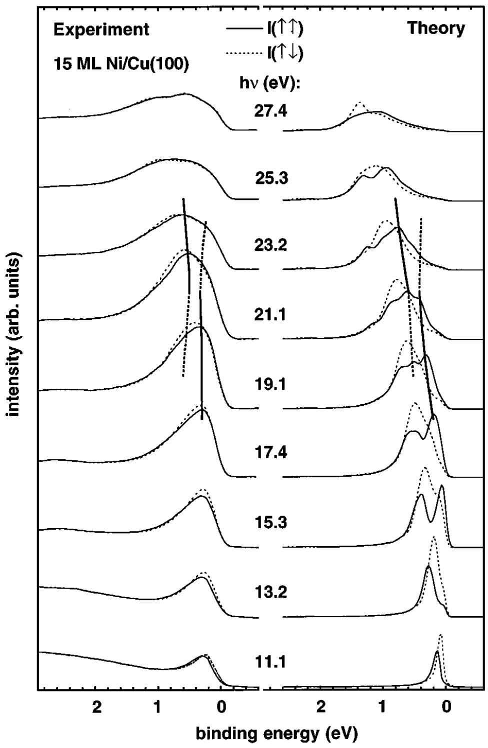

FIG. 2. Series of partial intensity spectra for different photon energies $h\nu$. Shown are spectra for parallel (solid lines) and antiparallel alignment (dotted lines) of photon spin and magnetization direction. Left: Experimental spectra, right: Theoretical spectra. The vertical lines indicate the occurrence of a hybridization region as explained in the text.

more, the theoretical spectra were calculated for $T=0$ K and 100% circular polarization.

To visualize the dichroism more clearly, in Fig. 3 the normalized asymmetry of the spectra of Fig. 2 is shown. The normalized asymmetry $A$ is defined as $A=[I(\uparrow\uparrow)-I(\uparrow\downarrow)]/[I(\uparrow\uparrow)+I(\uparrow\downarrow)]$. Again, experimental results are depicted on the left-hand side, theoretical on the right-hand side. We firstly note that the experimental spectrum at $h\nu=11.1$ eV shows an asymmetry of $-20\%$ near the Fermi edge, which is an unusually large dichroism for valence-band photoemission, and to our knowledge among the largest ever reported. To facilitate comparison with the experimental data, the theoretical asymmetry curves have been scaled down by a factor of 0.2. The original theoretical asymmetry values substantially exceed their experimental counterparts for the following reasons. Firstly, the experimental energy and angular resolution and the inelastic background, which have not been taken into account in our calculations, tend to reduce $A$. Secondly, the calculated $A$ depends on the choice of the imaginary parts $V_i$ of the optical potential for lower and upper states (with $A$ decreasing for increasing $V_i$), and we have deliberately chosen a very small $V_i$ for the lower states (below $E_F$) in order to make the connection of MCDAD with the band structure clearer (cf. Fig. 1). Apart from the thus-explained different scale, the agreement between experiment and theory in Fig. 3 is rather good. Several characteristics of the photon energy series can be seen in both the experimental and theoretical asymmetries. With increasing photon energy the asymmetry is reduced. We ascribe this mainly to the decrease of the lifetime of the initial states moving away from $E_F$ and to a lesser extent to the decrease of the photoelectron lifetime with increasing kinetic energy. At all photon energies there is one pronounced minus feature, which disperses towards higher binding energies with increasing photon energy. The dotted vertical lines in Fig. 3 indicate the dispersion of this minus indentation. The experimentally observed dispersion is slightly smaller than the calculated one: At 11.1 eV photon energy the minus peak is located just below the Fermi edge in both experiment and theory, whereas at 27.4 eV it exhibits binding energies of 1.25 and 1.4 eV in experiment and theory, respectively. Its

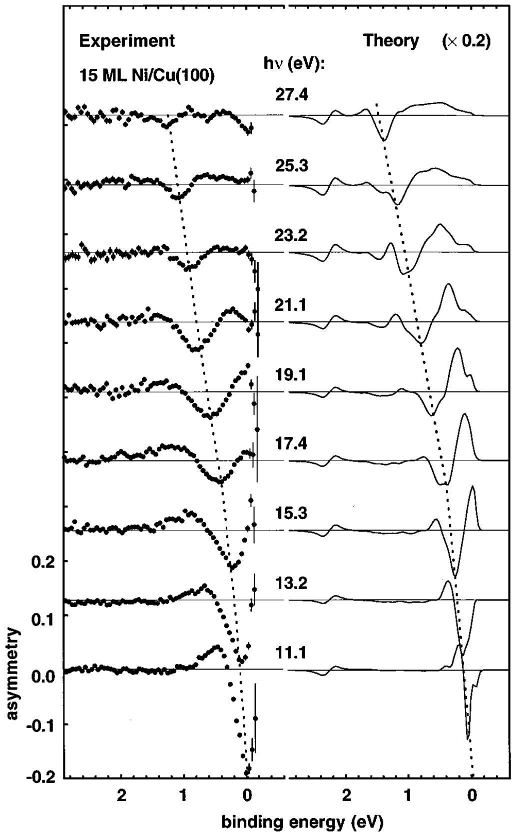

FIG. 3. Series of asymmetry spectra for different photon energies $h\nu$, calculated from the corresponding spectra of Fig. 2 as $[I(\uparrow\uparrow)-I(\uparrow\downarrow)]/[I(\uparrow\uparrow)+I(\uparrow\downarrow)]$. Left: Experimental asymmetries, right: Theoretical asymmetries (note the different scales). The vertical dotted lines mark the dispersion of the prominent minus peak.

absolute size shrinks with increasing photon energy. At 27.4 eV it amounts only to $-2\%$ in experiment and $-20\%$ in theory. For $h\nu \geqslant 15.3$ eV this minus peak is accompanied by plus peaks at both sides, the relative size of which differs between experiment and theory. They are seen most clearly at $h\nu = 19.1$ and 21.1 eV, and disperse together with the minus peak towards higher binding energies. From Fig. 3 it appears that the pronounced minus feature is too small (large) in the theoretical spectra (after reducing them by the factor 0.2) at low (high) photon energies. This discrepancy is, like the factor 0.2 itself, associated with the imaginary potential part $V_i$ for the initial states, and indicates that the simple linear form, which we assumed in the absence of realistic first-principles knowledge, underestimates the increase of $V_i$ with increasing binding energy.

In the theoretical spectra an additional plus/minus sequence around 2.3 eV binding energy is observed, which shows no dispersion. This asymmetry stems from emission from a surface resonance. It is not resolved in the experiment, which might be due to the relatively intense background of inelastic electrons compared to the low intensity of this resonance (cf. Fig. 2).

The dispersion of the asymmetry peaks and the observed plus/minus/plus feature can be understood from the illustrative picture of band symmetries and relativistic dipole selection rules mentioned in Sec. III C. In the case with no hybridization of the bands with $\Delta^5$ spatial symmetry present, the situation is like the one shown in Fig. 1, but more symmetric. Only the four bands of $\Delta^5$ spatial symmetry contribute in that case to the photoemission signal. When different lifetime broadening of states with different binding energies is ignored, the maximum of the minus peak in the dichroic asymmetry then gives the energetic position of the center of the bands with $\Delta^5$ spatial symmetry, always disregarding possible hybridizations. The dispersion of this peak, indicated by dotted lines in Fig. 3, thus reflects the dispersion of the four bands with $\Delta^5$ spatial symmetry. Its experimental observation allows an estimation of the band dispersion, which would be very difficult from intensity spectra alone (Fig. 2).

This example demonstrates that exploiting the magnetic dichroism already in the simple qualitative interpretation without access to relativistic photoemission calculations offers a significant plus of information with respect to conventional photoemission. Details of the band structure, however, or quantitative statements on the size of spin-orbit and exchange interaction can only be made with the help of relativistic calculations.

## V. DISCUSSION

Before it is possible to deduce information about the spin-orbit and exchange split valence-band structure, the relation between the calculated photoemission spectra, obtained in a one-step formalism, and the fully relativistic band structure, calculated with the same parameters, has to be provided. As has been seen already from Fig. 1, the model of direct transitions serves to correlate specific details of the photoemission spectra to details of the relativistic band structure.

In Fig. 4 the theoretical band structure along the $\Delta$ axis from Fig. 1 is depicted on a larger scale. The bands are, like in Fig. 1 (b), again reproduced with differently dashed and dotted lines according to their double-group symmetry, as labeled in the figure. No classifications according to spin-occupancy or single-group symmetry are made. However, the four bands originating from the $\Delta^5$ band in the nonrelativistic case, which lead to the dispersion of the minus peak in the asymmetry spectra, are marked by arrows on both sides of the panel: Starting at the $\Gamma$ point, they have binding energies between 1.5 and 1.9 eV. When going along the $\Delta$ axis towards the $X$ point, they disperse together upwards, interrupted by hybridization with other bands, to reach the $X$ point at energies between 0.15 eV below and 0.3 eV above the Fermi energy. As the content of $\Delta^5$ spatial symmetry of a band is necessary for the observation by photoemission in the present geometry, these bands and bands involved in hybridization with them are the origin of all of the observed spectra, as outlined before.

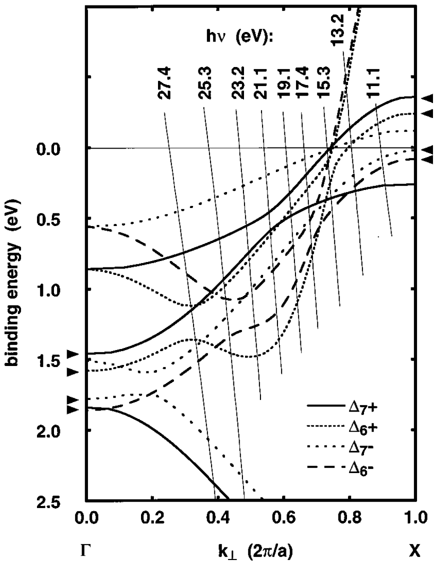

FIG. 4. Symmetry-resolved real valence band structure of Ni along the $\Delta$ axis, calculated with the same parameters as the photoemission spectra. Bands with $\Delta_7+$, $\Delta_6+$, $\Delta_7-$, and $\Delta_6-$ double group symmetry are distinguished as labeled in the figure. The arrows indicate bands of $\Delta^5$ orbital symmetry at $X$ and $\Gamma$. The thin solid lines are sections of the final-state band, shifted down by the photon energy indicated at the respective line.

To facilitate the correlation with the photoemission spectra, nine sections of the calculated final-state band of $\Delta_6^1$ symmetry, shifted down by the nine photon energies used in the experiment, are depicted in Fig. 4 by weak solid lines. As demonstrated in Fig. 1 for 21.1 eV photon energy, the crossings between these lines and the bands mark the energetic positions at which in the spectrum of the respective photon energy the transitions should be observed.

We will now first turn to the description of the band structure, which is essential in the qualitative interpretation of photoemission results. Because in Ni both exchange energy and spin-orbit coupling possess approximately the same magnitude ($\approx 0.1$–$0.3$ eV), the valence-band structure shows a lot of small band gaps, i.e., regions where bands of different single-group symmetry but identical double-group symmetry hybridize. Double-group theory implies that bands with the same double-group symmetry but different spatial symmetry couple due to spin-orbit interaction (e.g., $\Delta_7^2+$, $\Delta_7^{2\prime}+$, and $\Delta_7^5+$). Here, we will focus on electronic initial states with prominent $\Delta^5$ spatial symmetry, because that is what we observe in the present experimental geometry.

In the energy range from $-2$ eV up to the Fermi level (0 eV), $\Delta_6+$ initial states show spin-orbit induced band gaps at $k_\perp = 0.30(2\pi/a)$ and at $k_\perp = 0.75(2\pi/a)$, whereas $\Delta_6-$ initial states show such gaps at $k_\perp = 0.45(2\pi/a)$ and $k_\perp = 0.70(2\pi/a)$. For occupied bands with $\Delta_7+$ ($\Delta_7-$) symmetry there is only one gap around $k_\perp = 0.55(2\pi/a)$ ($k_\perp = 0.20 \cdot 2\pi/a$).

Let us first consider the hybridization of bands with $\Delta_7+$ symmetry. The hybridization gap is the result of an avoided crossing of bands with $\Delta^2$ and $\Delta^5$ spatial symmetry. The steeper $\Delta_7^5+$ band of minority-spin character changes symmetry (and spin occupancy) with the flatter $\Delta_7^2+$ majority band. This hybridization should occur in the photoemission spectra of 19.1 and 21.1 eV photon energy, as seen from Fig. 4. In Fig. 1 it was already demonstrated how both of the $\Delta_7+$ bands in the hybridization region contribute to the photoelectron spectra. The vertical lines in Fig. 2 indicate the hybridization region. They mark the corresponding peaks in the photoemission intensity spectra for $\boldsymbol{\sigma}$ and $\mathbf{M}$ parallel [$I(\uparrow\uparrow)$, solid lines in Fig. 2]. The continuous lines show the positions of bands containing $\Delta_7^5+$ symmetry, and fade out into dotted lines where the $\Delta_7^2+$ symmetry character in these bands predominates. In the calculated spectra (right-hand side of Fig. 2), both of the hybridizing bands can be distinguished as separate peaks in the solid line spectra. It is clearly seen how the hybridization leads to an energetic displacement towards higher binding energies of the respective peak in the $I(\uparrow\uparrow)$ spectrum when the photon energy is increased from 17.4 to 23.2 eV. In the experimental spectra (left-hand side of Fig. 2), the hybridization occurs as energetic shift of the intensity weight of the peak in $I(\uparrow\uparrow)$ between 19.1 and 21.1 eV. Whereas at 19.1 eV the peak is asymmetrically shaped with higher weight at the low binding energy side, at 21.1 eV the weight is shifted to the side with higher binding energy. This leads also to an energetic shift of the first plus peak in the corresponding experimental asymmetry curves (left-hand side of Fig. 3) from 0.1 eV binding energy at $h\nu = 19.1$ to 0.3 eV at $h\nu = 21.1$ eV.

The next hybridization region we will discuss in more detail is the hybridization of $\Delta_6-$ bands. One of the hybridizing bands with $\Delta_6^-$ symmetry is the *sp*-like minority band with $\Delta^1$ spatial symmetry which starts at the $\Gamma$ point at $E_B \approx 0.6$ eV and reaches a minimum in binding energy at $k_\perp \approx 0.5(2\pi/a)$. It hybridizes with a band of $\Delta_6^5-$ symmetry, producing the two hybridization gaps at $k_\perp = 0.45(2\pi/a)$ and $k_\perp = 0.70(2\pi/a)$. Between these gaps both bands are separated by less than 0.35 eV. In this region, the bands have a low expectation value of the spin polarization, and exhibit a considerable mixing of spatial symmetry. Both bands contain thus a significant portion of $\Delta_6^5-$ symmetry, and should hence both appear in the photoemission spectra for parallel alignment of photon spin and magnetization direction, according to the double-group symmetry $\Delta_6-$.

In the calculated photoemission spectra (right-hand side of Fig. 2), this hybridization can be followed in the $I(\uparrow\uparrow)$ spectra from 19.1 eV up to 25.3 eV photon energy. At lower photon energies, there is only one peak at the higher binding energy side of the solid curves. This peak is due to transitions from $\Delta_6-$ initial states. At $h\nu = 19.1$ eV, and most clearly at $h\nu = 21.1$ eV and $h\nu = 23.2$ eV, this peak is split into two peaks, one of them producing a shoulder around 1.2 eV binding energy. This is the consequence of the hybridization, which leads to two bands of $\Delta_6-$ double-group symmetry having partially $\Delta^5$ spatial symmetry. The shoulder at $E_B = 1.2$ eV is due to emission from the lower of the two bands. The maximum separation of both bands should be observed at photon energies of 21.1 and 23.2 eV (cf. Fig. 4), which leads to the clear separation of the observed shoulders. At higher photon energies the hybridization is weaker, and the higher band consists of mainly $\Delta_6^1-$ symmetry. At $h\nu = 25.3$ eV therefore only one peak as contribution from the $\Delta_6-$ bands is observed at 1.3 eV binding energy.

The hybridization induced shoulder is also seen in the experimental spectra of Fig. 2. It is most clearly identified at $h\nu = 21.1$ eV at 1.2 eV binding energy, but shows up already at $h\nu = 19.1$ eV. The separation of the different peaks is better in the calculated spectra, which may be a consequence of the experimental resolution. By comparison of experiment with theory, however, this shoulder in the experimental spectra is unequivocally identified as emission from the hybridizing $\Delta_6-$ bands.

The other hybridization regions of initial bands containing $\Delta^5$ character which have not yet been discussed concern bands of $\Delta_7-$ and $\Delta_6+$ double-group symmetry. The hybridization gap of the $\Delta_7-$ bands at $k_\perp = 0.20(2\pi/a)$ should not be visible in the photon energy range used in the experiment (cf. Fig. 4). Transitions from $\Delta_6+$ bands appear in the spectra for antiparallel alignment of photon spin and magnetization direction [$I(\uparrow\downarrow)$]. As the energetic sequence of the four $\Delta^5$ containing bands is $\Delta_7^5+$, $\Delta_6^5+$, $\Delta_7^5-$, $\Delta_6^5-$ (cf. Fig. 4), the emission from $\Delta_6^5+$ and $\Delta_7^5-$ bands overlaps in the spectra to give one broad peak in the dotted curves of Fig. 2. It is therefore much more difficult to observe the hybridization of these bands. The hybridization of the $\Delta_6^5+$ band with the *sp*-like $\Delta_6^1+$ band which has a strong dispersion and an energetic minimum at $k_\perp \approx 0.5(2\pi/a)$ is in fact hardly observable in the photoemission spectra.

The comparison of experimental data with the calculated spectra enables us to draw specific information about the relativistic band structure from the experiment. Keeping in mind that certain experimental circumstances as, for example, the temperature and the experimental energetic as well as angular resolution are not considered in the calculations, the good qualitative agreement proves that the correlation of the experimentally observed features to the details of the band structure, as delineated in the previous section, is correct. Deviations between experiment and calculation can then be judged as experimental evidence for a distinct behavior of the system.

Such a deviation regards the dispersion of the observed dichroic structures (dotted lines in Fig. 3). The experimentally observed dispersion is about 0.15 eV smaller than the theoretical one. This can, however, either be explained by a different behavior of the lower or of the upper bands. Although the comparison of theory and experiment can also be used to judge the authenticity of the values taken for the real part of the inner potential, this is not accurate enough to decide between the two possibilities. The good agreement of the experimental and theoretical photon energies at which the $\Delta_7+$ hybridization is observed (cf. Fig. 2), shows that the real part of the inner potential is basically well chosen. The small deviation of 0.15 eV in the dispersion of the initial bands may nevertheless still be assigned to both a slightly different behavior of the upper bands as well as a different dispersion of the valence bands.

The different dispersion in theory explains the disagreement in the height and the width of the first plus peak near the Fermi edge observed in the asymmetry spectra of Fig. 3. Especially at 15.3 and 17.4 eV photon energies this peak is much more pronounced in theory. This can be explained by the slightly stronger dispersion of the calculated photoemission peaks. In theory, the $\Delta_7^5+$ band responsible for this plus structure is already significantly below the Fermi edge at these photon energies, whereas in the experiment full emission from that band is observed only at higher photon energies. Furthermore, the broader peaks due to experimental energetic resolution lead to a higher intensity of also the $I(\uparrow\downarrow)$ spectra at the Fermi edge and thus to a lower asymmetry.

Another property of the system which can be extracted from the present data concerns the hybridization between bands of the same double-group symmetry. The experimentally observed hybridization gaps agree very well with theory, so that the calculated band structure of Fig. 4 (or Fig. 1) is fully confirmed in this respect. The content of $\Delta^5$ spatial symmetry in the hybridization regions, which is necessary for the experimental observation in the totally symmetric geometry, is also confirmed by the comparison of experiment with theory. It is for the sake of clarity not shown in the figures but principally also available.

Taking advantage of special points in the Brillouin zone, it is also possible to determine information about important parameters of the relativistic band structure. At 11.1 eV photon energy, for example, only two minority bands of $\Delta_7-$ and $\Delta_6-$ symmetry contribute to the spectra (cf. Fig. 4). They are energetically separated by the spin-orbit interaction, and appear each for a different alignment of photon spin and magnetization direction. The separation of the corresponding peaks in the experimental spectra for parallel and antiparallel alignment of $\boldsymbol{\sigma}$ and $\mathbf{M}$ (Fig. 2) is then an experimental measure of the strength of spin-orbit coupling in the valence bands. At that particular point of the Brillouin zone $(50\pm5)$ meV are obtained compared to 60 meV from the calculations. This is the same order of magnitude but nevertheless significantly smaller than the 100 meV obtained formerly for copper.[11,12]

It is more difficult to estimate an experimental value for the exchange splitting from the present spin-integrating measurements. The comparison with the calculations concerning the appearance of the bands below the Fermi edge and the positions of the hybridization gaps indicates that the value of 0.3 eV taken for the calculations is correct.

We have used Ni/Cu(001) as a prototype system to demonstrate the capability of valence-band MCDAD measurements supported by relativistic calculations. The perpendicular magnetization of this system allows us the direct correlation of the dichroism to the band structure. However, in systems with a lower symmetry, the content of information of MCDAD is similar. The comparison with relativistic calculations should also provide a detailed understanding of the electronic properties of the spin-orbit and exchange split system, even when a correlation with interband transitions is not possible.

## VI. CONCLUSIONS

It has been shown, using Ni/Cu(001) as a prototype system, how from the comparison of experimental MCDAD data to fully relativistic calculations even fine details of the band structure can be resolved. Whereas the experiment alone is already capable to deliver qualitative information about the electronic structure, the access to fully relativistic calculations provides the possibility to extract specific information about the valence states. The dispersion of the $\Delta^5$-type valence bands, the position and type of spin-orbit-induced hybridization gaps, and values for the strength of spin-orbit and exchange interaction and for the inner potential could be determined from the experiment that way. It was demonstrated how MCDAD in a totally symmetric arrangement is directly related to the relativistic band structure. The capability of magnetic circular dichroism in valence-band photoemission for the investigation of the exchange and spin-orbit split relativistic band structure of ferromagnets is thus proven.

## ACKNOWLEDGMENTS

This work was supported by the German minister of education, science, research, and technology (BMBF) under Contracts No. 05 621EFA and No. 05 5PGABB7. We like to thank B. Zada for her technical assistance, and are indebted to the Freie Universität Berlin for its hospitality.

---

[1] C. S. Wang and J. Callaway, Phys. Rev. B **9**, 4897 (1974).

[2] B. Ackermann, R. Feder, and E. Tamura, J. Phys. F **14**, L178 (1984).

[3] L. Fritsche, J. Noffke, and H. Eckardt, J. Phys. F **17**, 943 (1987).

[4] P. Strange, H. Ebert, J. B. Staunton, and B. L. Gyorffy, J. Phys. Cond. Matter **1**, 2959 (1989).

[5] E. Tamura, W. Piepke, and R. Feder, Phys. Rev. Lett. **59**, 934 (1987).

[6] E. Tamura and R. Feder, Solid State Commun. **79**, 989 (1991); Europhys. Lett. **16**, 695 (1991).

[7] J. Henk and R. Feder, Europhys. Lett. **28**, 609 (1994).

[8] *Polarized Electrons in Surface Physics*, edited by R. Feder

(World Scientific, Singapore, 1985).

[9] N. Irmer, R. David, B. Schmiedeskamp, and U. Heinzmann, Phys. Rev. B **45**, 3849 (1992).

[10] D. Venus and H. L. Johnston, Phys. Rev. B **50**, 15 787 (1994).

[11] C. M. Schneider, J. J. de Miguel, P. Bressler, P. Schuster, R. Miranda, and J. Kirschner, J. Electron Spectrosc. Relat. Phenom. **51**, 263 (1990).

[12] W. Kuch, M.-T. Lin, K. Meinel, C. M. Schneider, J. Noffke, and J. Kirschner, Phys. Rev. B **51**, 12 627 (1995).

[13] L. Baumgarten, C. M. Schneider, H. Petersen, F. Schäfers, and J. Kirschner, Phys. Rev. Lett. **65**, 492 (1990).

[14] B. T. Thole and G. van der Laan, Phys. Rev. B **44**, 12 424 (1991).

[15] T. Scheunemann, S. V. Halilov, J. Henk, and R. Feder, Solid State Commun. **91**, 487 (1994).

[16] J. Henk, S. V. Halilov, T. Scheunemann, and R. Feder, Phys. Rev. B **50**, 8130 (1994).

[17] *Photoemission and the Electronic Properties of Surfaces*, edited by B. Feuerbacher, B. Fitton, and R. F. Willis (Wiley, New York, 1978).

[18] *Angle-Resolved Photoemission: Theory and Current Applications*, edited by S. V. Kevan (Elsevier, Amsterdam, 1992).

[19] G. van der Laan and B. T. Thole, Phys. Rev. B **48**, 210 (1993).

[20] N. A. Cherepkov, Phys. Rev. B **50**, 13 813 (1994).

[21] D. Venus, L. Baumgarten, C. M. Schneider, C. Boeglin, and J. Kirschner, J. Phys. Condens. Matter **5**, 1239 (1993).

[22] H. B. Rose, F. U. Hillebrecht, E. Kisker, R. Dennecke, and L. Ley, J. Magn. Magn. Mater. **148**, 62 (1995).

[23] M. Wöhlecke and G. Borstel, Phys. Rev. B **23**, 980 (1981).

[24] F. Meier, *Polarized Electrons in Surface Physics* (Ref. 8), p. 423.

[25] A. Eyers, F. Schäfers, G. Schönhense, U. Heinzmann, H. P. Oepen, K. Hünlich, J. Kirschner, and G. Borstel, Phys. Rev. Lett. **52**, 1559 (1984).

[26] C. M. Schneider, J. Garbe, K. Bethke, and J. Kirschner, Phys. Rev. B **39**, 1031 (1989).

[27] C. M. Schneider and J. Kirschner, Crit. Rev. Solid State Mater. Sci. **20**, 179 (1995).

[28] J. Henk, T. Scheunemann, S. V. Halilov, and R. Feder, J. Phys. Condens. Matter. **8**, 47 (1996).

[29] L. Néel, J. Phys. Rad. **15**, 376 (1954).

[30] U. Gradmann, J. Magn. Magn. Mater. **54–57**, 733 (1986); **100**, 481 (1991).

[31] P. Bruno and J. Renard, App. Phys. A **49**, 499 (1989).

[32] F. Huang, M. T. Kief, G. J. Mankey, and R. F. Willis, Phys. Rev. B **49**, 3962 (1994).

[33] W. L. O'Brien and B. P. Tonner, Phys. Rev. B **49**, 15 370 (1994).

[34] B. Schulz and K. Baberschke, Phys. Rev. B **50**, 13 467 (1994).

[35] B. Schulz, R. Schwarzwald, and K. Baberschke, Surf. Sci. **307–309**, 1102 (1994).

[36] G. Bochi, C. A. Ballentine, H. E. Inglefield, C. V. Thompson, R. C. O'Handley, H. J. Hug, B. Stiefel, A. Moser, and H.-J. Güntherodt, Phys. Rev. B **52**, 7311 (1995).

[37] J. Shen, J. Giergiel, and J. Kirschner, Phys. Rev. B **52**, 8454 (1995).

[38] F. Baudelet, M.-T. Lin, W. Kuch, K. Meinel, B. Choi, C. M. Schneider, and J. Kirschner, Phys. Rev. B **51**, 12 563 (1995).

[39] J. Shen, M.-T. Lin, J. Giergiel, C. Schmidthals, M. Zharnikov, C. M. Schneider, and J. Kirschner, J. Magn. Magn. Mater. (to be published).

[40] F. Schäfers, W. Peatman, A. Eyers, C. Heckenkamp, G. Schönhense, and U. Heinzmann, Rev. Sci. Instrum. **57**, 1032 (1986).

[41] S. V. Halilov, E. Tamura, H. Gollisch, D. Meinert, and R. Feder, J. Phys. Condens. Matter **5**, 3859 (1993).

[42] L. M. Falicov and J. Ruvalds, Phys. Rev. **172**, 498 (1968).

[43] J. Henk, T. Scheunemann, S. V. Halilov, and R. Feder, Phys. Status Solidi B **192**, 325 (1995); S. V. Halilov, J. Henk, T. Scheunemann, and R. Feder, Phys. Rev. B **52**, 14 235 (1995).

## Publikation 7

# Magnetic linear dichroism in valence-band photoemission: Experimental and theoretical study of Fe(110)

A. Rampe and G. Güntherodt
*2. Physikalisches Institut, Rheinisch-Westfälische Technische Hochschule Aachen, D-52056 Aachen, Germany*

D. Hartmann
*Siemens AG, Hofmannstr. 51, D-81359 München, Germany*

J. Henk
*Condensed Matter Theory Group, Physics Department, Uppsala University, S-751 21 Uppsala, Sweden*

T. Scheunemann and R. Feder
*Theoretische Festkörperphysik, Universität Duisburg, D-47048 Duisburg, Germany*

(Received 10 September 1997; revised manuscript received 14 January 1998)

Magnetic linear dichroism (MLD) in angle-resolved valence-band photoemission of Fe(110) has been investigated by means of symmetry considerations, analytical theory, numerical calculations, and photoemission measurements. The dichroic photoemission spectra and their dependence on photon energy clearly show that the microscopic origin of MLD is an interference effect induced by hybridization of initial states of different spatial symmetry at band gaps arising from spin-orbit coupling. The dependence of MLD on the light incidence angle evidences that it is substantially influenced by the optical response of the metal, the approximation of which according to classical Fresnel theory is adequate to reproduce our experimental data.

[S0163-1829(98)04618-9]

## I. INTRODUCTION

Spin-orbit coupling (SOC) in the valence bands is the microscopic origin of magnetic phenomena such as the magneto-optical Kerr effect and the magnetocrystalline anisotropy. However, up to the present it has not been clarified in detail how SOC influences these effects. For example, the question arises which electronic states are responsible for a large Kerr rotation or determine the direction of the easy axis of the magnetization. In principle, the mechanism is well understood: starting from the spin-polarized band structure of a ferromagnet, SOC further reduces the symmetry of the system. Hybridization between spin-up and spin-down bands occurs and degeneracies between them are removed. Consequently, the energy levels depend on the magnetization direction and total-energy calculations yield the easy axis. Therefore, it is of general interest to have a wide basis of experimental and theoretical data in order to answer in detail the question of how SOC influences the electronic structure.

In the last few years it has experimentally[1–6] and theoretically[7–15] been shown that SOC is a necessary ingredient for the various types of magnetic dichroism. Under the term magnetic dichroism those phenomena are collected where an observable, e.g., the x-ray absorption coefficient or the photoemission intensity, depends on the magnetization direction (for reviews on SOC-influenced spectroscopies we refer to Ref. 16). One of these dichroism effects is magnetic linear dichroism (MLD) in the angular distribution of photoelectrons. It commonly denotes the dependence of the angle-resolved photoemission intensity under excitation by linearly polarized light on magnetization reversal. Due to the close connection of SOC-induced spin polarization to dichroism, the relativistic electronic structure has been successfully investigated by magnetic circular dichroism for Ni(100).[17] How MLD can be used to study in detail relativistic band structures will be shown in this paper.

In this joint experimental and theoretical study we focus on MLD in the valence-band photoemission from Fe(110). Our investigations rely on an analytical theory,[12] the application of which to Fe(110) is presented in Sec. III A. It allows us to show, in Sec. IV C, that the microscopic origin of the actually observed MLD is a SOC-induced hybridization between wave functions with spatial $\Sigma^1$ and $\Sigma^3$ symmetry. To make more quantitative contact with the experimental data, we performed numerical calculations using a spin-polarized relativistic layer Korringa-Kohn-Rostoker (KKR) formalism. The comparison of experiment, numerical calculations, and analytical theory in Sec. IV provides a consistent picture and in particular evidences the adequacy of our theoretical methods. Additionally, it reveals how the MLD for $p$-polarized light is modified by the optical response of the solid.

MLD by itself is an interference effect, so it is very sensitive, for example, to SOC (Ref. 19) and to the magnetization. Founded upon this result, we discuss in which way MLD can be used to obtain detailed information on the relativistic valence-band structure or other magnetic properties, e.g., the arrangement of magnetic moments.[20]

## II. EXPERIMENTAL ASPECTS

Experimental spectra were recorded at the monochromator beam line TGM3 of the synchrotron radiation facility BESSY, Berlin. It provides photons in the energy range from

14 to 30 eV and from 30 to 70 eV with two different gratings. The degree of linear polarization of the light decreases monotonously over the whole photon energy range from 90% at 15 eV down to 70% at 70 eV. The kinetic-energy analysis of the photoelectrons was performed by an 180° hemispherical analyzer with 50 mm diameter and an angular resolution of $\pm 2°$. The combined energy resolution of photons and electrons was 200 meV. Additionally, the photon flux has continuously been recorded during the measurements in order to normalize the spectra. The geometrical setup is described in Sec. III A.

Ferromagnetic Fe layers were grown *in situ* on a W(110) single crystal in an UHV chamber with base pressure of $5\times10^{-11}$ mbar, which increases during electron-beam evaporation to $1\times10^{-10}$ mbar. The bulklike, 15 atomic layer (AL) thick Fe layers were evaporated at a rate of 0.5 AL/min and at a substrate temperature of 450 K. The layer thickness was measured during the evaporation with a calibrated quartz microbalance with an accuracy of $\pm 5\%$.

These preparation conditions result in sharp low-energy electron-diffraction (LEED) spots with a low background evidencing the epitaxial growth of the Fe layers on the bcc W(110) substrate. Three growth phases can be distinguished. During all phases the symmetry of the LEED pattern is $2mm(C_{2v})$. The first two monolayers grow pseudomorphically, i.e., the LEED pattern of the Fe and the clean W substrate are identical. For thicknesses between 2 AL and 10 AL one observes a superstructure in the LEED patterns caused by periodic lattice distortions compensating the lattice misfit of 9.4% between Fe and W. Above 10 AL Fe the distortion-induced superstructure is no longer visible in LEED and one observes the LEED pattern of a clean bcc(110) surface. The distance between the spots and intensity vs energy curves evidence that the film grows now with the lattice constant of bulk bcc Fe. In addition, growth and cleanliness have been checked with Auger electron spectroscopy. Distinct kinks for each completed monolayer in the intensity of the 47 eV Auger line as a function of Fe thickness evidence layer-by-layer growth up to 3 AL. Further details of the preparation have been published elsewhere.[21]

## III. THEORETICAL ASPECTS

### A. Analytical results

In this section we discuss briefly the microscopic origin of MLD by means of symmetry considerations and analytical calculations, both applied to our specific setup (cf. Fig. 1). For the MLD the Fe(110) film is remanently magnetized along the two in-plane easy axes, i.e., in the [$\bar{1}10$] and [$1\bar{1}0$] direction ($\pm y$ axis) and the magnetization reads $\vec{M}_\pm=(0,\pm M,0)$. $P$-polarized light impinges under a polar angle $\vartheta$ on the surface. We distinguish two light polarizations $p_\pm$ with electric-field vectors $\vec{E}(p_\pm)=E_0(\pm\cos\vartheta,0,\sin\vartheta)$. The electrons are detected along the surface normal ([110], $z$ axis).

As mentioned above, the point group of a cubic (110) surface of a nonmagnetic solid, $2mm(C_{2v})$, has four symmetry operations: the identity $E$, the twofold rotation about the surface normal $C_2$, the reflection at the $(x,z)$ plane $m_y$, and the reflection at the $(y,z)$ plane $m_x$. Its single group has four one-dimensional irreducible representations, $\Sigma^s, s=1,\ldots,4$, its double group a single two-dimensional irreducible representation, $\Sigma_5$. The presence of the magnetization $\vec{M}$ reduces the symmetry to point group $m$, with symmetry operations $E$ and $m_y$. Its double group has two one-dimensional irreducible representations, $\gamma_+$ and $\gamma_-$, which are degenerate by time reversal.[22,23] Already at this point, symmetry considerations show that MLD should exist (cf. Table I). The operations of $2mm$ leave $(p_+,\vec{M}_+)$ either invariant or turn it into $(p_-,\vec{M}_-)$. In other words, there is no operation that reverses $\vec{M}$ and simultaneously leaves the light polarization invariant: there is MLD. The operation $m_y$ gives for the components of the photoelectron spin polarization $P_x=P_z=0$ and $P_y\neq0$. The latter component is already present in the nonmagnetic case due to the linear spin-polarization effect (LSPE) by Tamura and Feder[24,25] (discussed below). For normal incidence $[\vartheta=0°,\ \vec{E}(p_+)=-\vec{E}(p_-)]$ or grazing incidence $[\vartheta=90°,\ \vec{E}(p_+)=\vec{E}(p_-)]$, there is no MLD (cf. operation $m_x$).

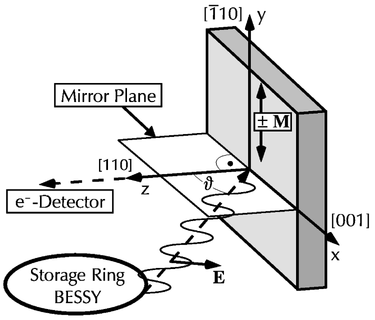

FIG. 1. Standard setup for magnetic linear dichroism in photoemission from cubic (110) surfaces. The crystal is remanently magnetized along the [$\bar{1}10$] ($\vec{M}_+$) or the [$1\bar{1}0$] ($\vec{M}_-$) direction. $P$-polarized light impinges at a polar angle $\vartheta$ onto the surface. Its electric field vector $\vec{E}$ lies within the mirror plane that is perpendicular to $\vec{M}$ and contains the surface normal. Photoelectrons are detected in normal emission.

To elucidate the origin of the MLD in detail, we decompose the electronic states of the semi-infinite system into wave functions $|R^s_\pm\Sigma^s\tau^s\rangle$. The spin $\tau^s$ is described by Pauli spinors $|\alpha\rangle$ and $|\beta\rangle$ quantized along the magnetization direction. The angular parts belonging to $\Sigma^s$, with $s=1,\ldots,4$ consist of symmetry-adapted combinations of spherical harmonics. Collecting the various parts, each electronic state $\Psi_\pm$ belonging to $\gamma_\pm$ can be written as

TABLE I. Effect of symmetry operations of the point group $2mm$ on light polarization $p_+$, magnetization $\vec{M}_+$, and photoelectron spin polarization $\vec{P}=(P_x,P_y,P_z)$.

| | | | | | |
|---|---|---|---|---|---|
| $E$: | $p_+$ | $\vec{M}_+$ | $+P_x$ | $+P_y$ | $+P_z$ |
| $C_2$: | $p_-$ | $\vec{M}_-$ | $-P_x$ | $-P_y$ | $+P_z$ |
| $m_x$: | $p_-$ | $\vec{M}_-$ | $+P_x$ | $-P_y$ | $-P_z$ |
| $m_y$: | $p_+$ | $\vec{M}_+$ | $-P_x$ | $+P_y$ | $-P_z$ |

$$|\Psi_+\rangle = |R_+^1\Sigma^1\alpha\rangle + |R_+^3\Sigma^3\alpha\rangle + |R_+^2\Sigma^2\beta\rangle + |R_+^4\Sigma^4\beta\rangle, \tag{1a}$$

$$|\Psi_-\rangle = |R_-^1\Sigma^1\beta\rangle + |R_-^3\Sigma^3\beta\rangle + |R_-^2\Sigma^2\alpha\rangle + |R_-^4\Sigma^4\alpha\rangle. \tag{1b}$$

The superscript $s$ on the radial parts $R_\pm^s$ refers to the single-group representation $\Sigma^s$. Their subscripts are not to be confused with a spin index: each state contains both Pauli spinors due to SOC. In the nonmagnetic case, Kramers' degeneracy requires $R_+^s = R_-^s, s=1,\dots,4$. Since in the magnetic case Kramers' degeneracy is lifted, one member of a pair of exchange-split electronic states belongs to $\gamma_+$, the other to $\gamma_-$, and we have $R_+^s \neq R_-^s$.

We now sketch the analytical calculation of the photoemission intensity $I$ (for details, see Ref. 12). Initial states are given by Eq. (1). Final states are mainly of $\Sigma^1$ spatial symmetry[26] due to the absence of exchange and SOC in the vacuum. In fact, SOC leads to scattering into wave-function parts with other spatial symmetries. However, the dominant component is of $\Sigma^1$ spatial symmetry. We therefore approximate the final-state wave function by regarding only the latter component. The transition-matrix elements $M^{(sfi)}$ are indicated by the single-group representation ($\Sigma^s, s=1,\dots,4$) of the respective radial-angular part of the initial state, the double-group representation $\gamma_i$ ($i=\pm$) of the initial state, and $\gamma_f(f=\pm)$ of the final state. The radiation field inside the solid is approximated macroscopically according to classical electrodynamics[27] (Snell's law and Fresnel's formula) that leads to significant effects on the photoelectron spin polarization and on magnetic dichroism (for details see Refs. 18 and 28). We denote internal quantities (field vector $E_0'$ and propagation angle $\vartheta'$) of the light by a prime. In dipole approximation, selection rules yield: (i) $E_{0x}'$ induces transitions from $\Sigma^3$ components of the initial states, the corresponding matrix elements being $E_0'\cos\vartheta' M^{(3fi)}$. (ii) $E_{0z}'$ connects initial- and final-state functions both with $\Sigma^1$ spatial symmetry and matrix elements $E_0'\sin\vartheta' M^{(1fi)}$. (iii) In our setup, $\Sigma^2$ and $\Sigma^4$ components of the initial states cannot be observed. (iv) Spin conservation within the excitation process requests $f=i$ for the matrix elements $M^{(1fi)}$ and $M^{(3fi)}$.

These selection rules in conjunction with the formation of SOC-induced hybrids have two important consequences. (i) Each initial state with an admixture of $\Sigma^1$ or $\Sigma^3$ functions can be observed; i.e., also a band with nonrelativistic $\Sigma^2$ or $\Sigma^4$ symmetry can contribute to the photoemission intensity. (ii) Initial states with simultaneously nonzero $\Sigma^1$ and $\Sigma^3$ parts have the same final state in the excitation process. Hence, there is interference between the $\Sigma^1$- and $\Sigma^3$-related transitions.

From the photoemission intensities $I(M_\pm)$ for the two magnetization directions,[12] we define the difference $D^{\mathrm{MLD}} = [I(\vec{M}_+) - I(\vec{M}_-)]/2$ and the sum $S^{\mathrm{MLD}} = [I(\vec{M}_+) + I(\vec{M}_-)]/2$. The resulting expressions are

$$D^{\mathrm{MLD}}(\vartheta') = 2|E_0'|^2 \mathrm{Im}[\sin\vartheta' \cos\vartheta'^{*}(M^{(1++)*}M^{(3++)} - M^{(1--)\star}M^{(3--)})], \tag{2a}$$

$$S^{\mathrm{MLD}}(\vartheta') = |\sin\vartheta' E_0'|^2(|M^{(1++)}|^2 + |M^{(1--)}|^2) + |\cos\vartheta' E_0'|^2(|M^{(3++)}|^2 + |M^{(3--)}|^2), \tag{2b}$$

with initial states $|\Psi_+\rangle$ and $|\Psi_-\rangle$ at the same initial-state energy $E_{\mathrm{i}}$. [The energy- and $\vec{k}_\|$-conserving terms $\delta(E_{\mathrm{f}} - E_{\mathrm{i}} - h\nu)\times\delta(\vec{k}_\|)$ have been omitted for clarity. The asterisk denotes the complex conjugation.] Reversal of the magnetization turns $M^{(sfi)}$ into $M^{(s,-f,-i)}$, which changes the sign of $D^{\mathrm{MLD}}$, whereas $S^{\mathrm{MLD}}$ is invariant. Without SOC there would be no products of matrix elements with different spatial index $i$ that leads to a vanishing $D^{\mathrm{MLD}}$. In the nonmagnetic limit, the matrix elements $M^{(sfi)}$ and $M^{(s,-f,-i)}$ become equal and there is obviously no MLD. At last, the MLD vanishes also, in accordance with symmetry arguments, for normal incidence ($\vartheta = 0°$) and grazing incidence ($\vartheta = 90°$) because in these cases only one hybrid component is excited.

The origin of MLD in standard geometry can be attributed to the LSPE for $p$-polarized light.[24,25,29] In the nonmagnetic limit, the ''surviving'' term in the expression for $P_y$ (not shown here) is an interference term that in this case is exclusively due to SOC, i.e., it is due to the LSPE. Furthermore, this LSPE can be regarded as the origin of MLD, because the corresponding transition-matrix elements are involved in the interference terms in both the intensity and spin-polarization expressions.[30]

Collecting Snell's law, Fresnel's formula, and Eq. (2), a rather complicated dependence of $S^{\mathrm{MLD}}$ and $D^{\mathrm{MLD}}$ on the incidence angle $\vartheta$ is obtained. Approximating the internal field by the external one, $D^{\mathrm{MLD}}$ shows a $\sin 2\vartheta$ dependence and $S^{\mathrm{MLD}}$ can be written as $A\sin^2\vartheta + B\cos^2\vartheta$, with $A(B)$ comprising the terms with the $M^{(1fi)}(M^{(3fi)})$ matrix elements. Note, within this approximation, $S^{\mathrm{MLD}}$ is extremal at normal or grazing incidence, whereas $D^{\mathrm{MLD}}$ is extremal at 45°.

In summary, our model of MLD is based on four ingredients: (i) SOC induces the formation of hybrids consisting of wave functions with different spatial-spin symmetry. (ii) The simultaneous excitation of partial waves from the different hybrid components results in an interference term in the photoemission intensity. (iii) This additional contribution to the photocurrent is spin polarized and changes sign, if the magnetization is reversed, i.e., MLD is observed. (iv) The optical response of the solid has been incorporated by taking the macroscopic classical electrodynamics into account.

### B. Computational method

Numerical calculations of band structures, of layer-resolved densities of states (DOS), and of photoemission intensities have been performed within the framework of the spin-polarized relativistic layer KKR method.[31,32] Instead of the bcc Fe film of 15 AL finite thickness used in the experiment, we take semi-infinite bcc Fe(110) with bulk lattice constant $a=2.87$ Å. This approximation is justified since first, due to the small escape depth of the photoelectrons, emission from the actual W substrate is negligible, and second, quantum-well states are not resolved in the present experiment. The surface geometry is not relaxed, as one expects for a closed packed surface and as has been determined by LEED for Fe(110).[33]

The effective spin-dependent muffin-tin potential has been obtained by a self-consistent bulk linear muffin-tin orbital (LMTO) calculation, but modified in some respects. First, the real part of the inner potential (10.5 eV with reference to $E_\mathrm{F}$) has, for the occupied states, been augmented by a self-energy correction term $0.1(E-E_\mathrm{F})$ in order to reproduce the measured quasiparticle exchange splitting. Second, the spin-dependent potential in the topmost layer has been linearly rescaled[34] such as to achieve a magnetic moment enhanced by 20% relative to that in the bulk.[33–35]

The surface-potential barrier has been approximated by a reflecting step function $0.48a$ above the outermost internuclear plane. This simple model is adequate for the present purpose, since it yields a layer-resolved DOS almost identical with the one from a self-consistent surface LMTO calculation.

In our photoemission calculations, lifetime effects are incorporated by an energy-dependent imaginary part of the inner potential $V_i$. For the lower states (holes) we use $V_i=-0.2(E_\mathrm{F}-E+0.25$ eV) and for the upper states $V_i=-0.05(E-E_\mathrm{F})$. $V_i$ leads to broadening and shifts of peaks to lower binding energy with respect to the real-potential band structure. The radiation field inside the metal has been taken into account according to classical optics (Snell's and Fresnel's formulas).[18,28]

## IV. RESULTS AND DISCUSSION

Since our photoemission spectra and their MLD can be interpreted in terms of direct bulk interband transitions, we first focus on the relativistic band structure. Subsequently, measured and calculated photoemission spectra are presented, and the microscopic origin of the MLD is discussed. Finally, the dependence of the MLD on the incidence angle of the photons is shown.

### A. Band structure

Figure 2 shows the relativistic band structure of ferromagnetic Fe along the $\Gamma$–$\Sigma$–$N$ direction, the relevant one in normal emission geometry from the bcc(110) surface. For its calculation we used the bulk part of the potential as specified in Sec. III B, except that the imaginary part of the optical potential for the lower states has been set to zero, which yields so-called real bands. The bands are classified according to their double-group representation, $\gamma_+$ and $\gamma_-$. In addition, the dominant spatial-spin representation is indicated. This usual nonrelativistic characterization is a good approximation over large parts of the bands, but of course breaks down at SOC-induced band gaps due to the high degree of hybridization.

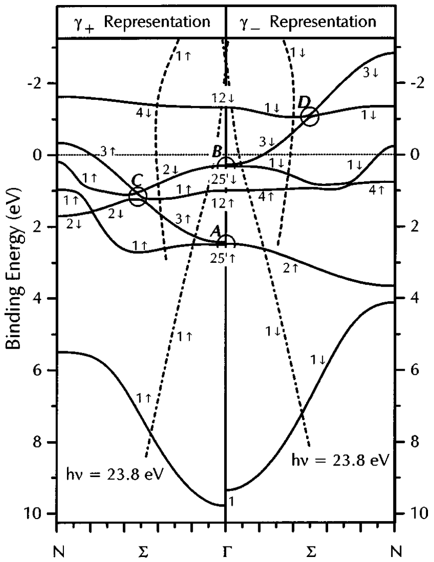

FIG. 2. Relativistic valence band structure of Fe(110) separated into representations $\gamma_+$ (left panel) and $\gamma_-$ (right panel) of double group $m$. Labels indicate the spatial-spin symmetry of the dominating component of the respective initial state. Circles denote SOC-induced band gaps between $\Sigma^1$ and $\Sigma^3$ bands. Additionally, the two possible final-state bands with dominant $\Sigma^1$-spatial symmetry (shifted down by 23.8 eV photon energy) are represented by the dash-dotted line for low damping and the dashed line for high damping within the solid.

Four of these particularly interesting regions, in which $\Sigma^1$ and $\Sigma^3$ states are strongly hybridized, are marked in Fig. 2 by circles $A$ to $D$. Circles $A$ and $B$ belong to the band gaps at the "nonrelativistic" points $\Gamma^{25'}\uparrow$ and $\Gamma^{25'}\downarrow$, respectively. At $C$ (left panel) the situation is more complicated; three band gaps occur in this region, the largest one between the $\Sigma^1\uparrow$ and the $\Sigma^3\uparrow$ band. The anticrossing point $D$ between $\Sigma^1\downarrow$ and $\Sigma^3\downarrow$ belongs to the unoccupied states.

Table II summarizes energy levels and splittings from Fig. 2 at high symmetry points of the Brillouin zone in comparison with other calculations and with experiment. The nonrelativistic band structure of Ref. 36 (last column) is very close to our original LMTO results (not shown), with minor differences attributable to the use of relativistic theory (Dirac equation) in our work. The exchange splitting is increased by about 0.2 eV to 2.17 eV (cf. first column) due to our energy-dependent real self-energy correction. Inclusion of the imaginary part, which accounts for the finite hole lifetime, slightly reduces it to 2.11 eV (cf. second column).

In view of interpreting our dichroic photoemission spectra, we added to Fig. 2 final-state bands with dominant $\Sigma^1$ symmetry (steep-dashed and dash-dotted lines), which were calculated with the complex optical potential. These bands have been shifted downward by 23.8 eV photon energy (because at this photon energy the maximum MLD is observed, see below) so that crossings with the occupied bands correspond to possible direct photoemission transitions from bulk initial states. For each relativistic representation there are two final-state bands. Our calculation shows that the corresponding states differ in their decay length along the [110]

TABLE II. Binding energies, exchange splittings, and spin-orbit splittings at $\Gamma$ (in eV relative to $E_F$). Theoretical values from band structures (calculated with real potential) and from densities of states (calculated with potential including the imaginary part specified in Sec. III) are indicated by ''bands'' and ''DOS,'' respectively. The former are compared to results from Ref. 36. Energy levels are labeled by their single-group representations; $\langle\ \rangle$ denotes the mean value.

| | This work | | | Ref. 36 |
|---|---|---|---|---|
| | bands | DOS | Expt. | bands |
| Energy levels: | | | | |
| $\Gamma^1 = \langle \Gamma^1\uparrow\ \Gamma^1\downarrow \rangle$ | 9.56 | | | 8.24 |
| $\Gamma^{25'}\uparrow$ | 2.47 | 2.40 | 2.4 | 2.26 |
| $\Gamma^{12'}\uparrow$ | 0.99 | 0.95 | 0.9 | 0.94 |
| $\Gamma^{25'}\downarrow$ | 0.30 | 0.29 | 0.3 | 0.34 |
| $\Gamma^{12'}\downarrow$ | −1.31 | | | |
| $\Delta_{\mathrm{EXC}}$: | | | | |
| $\Gamma^{25'}\downarrow - \Gamma^{25'}\uparrow$ | 2.17 | 2.11 | 2.1 | 1.92 |
| $\Delta_{\mathrm{SOC}}$: | | | | |
| $\Gamma^{25'}\uparrow$ | 0.07 | | | |
| $\Gamma^{25'}\downarrow$ | 0.057 | | | |

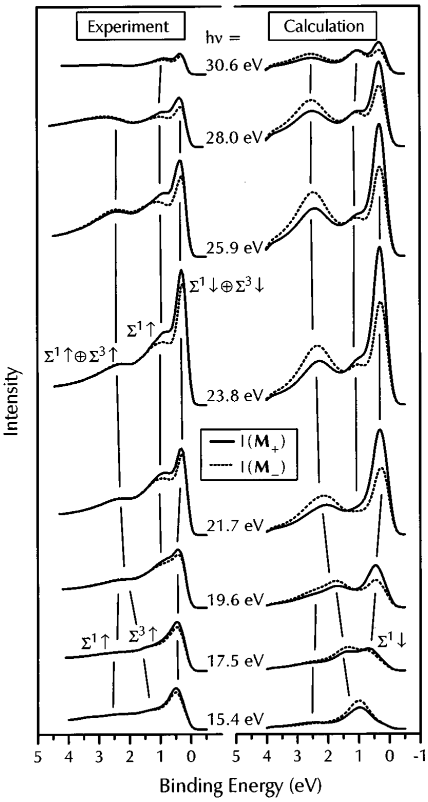

FIG. 3. Experimental (left panel) and calculated (right panel) photoemission intensities $I(\vec{M}_+)$ (solid line) and $I(\vec{M}_-)$ (dotted line) of Fe(110) for various photon energies $h\nu$. Vertical lines sketch the dispersion of the corresponding initial state. The labels give the spatial-spin symmetry of the dominating component of the respective initial state. The $\oplus$ denotes an incoherent superposition of the two initial states.

direction, i.e., in their penetration depth into the solid. The $1/e$ penetration depth of the final states of the dash-dotted band is larger than $10\ a_\perp/\pi$, whereas the one for the dashed band is smaller than $2\ a_\perp/\pi$.

### B. Photoemission spectra

Results of our photoemission experiments and our corresponding calculations—obtained as specified in Secs. II and III B—are shown in Fig. 3 for a sequence of photon energies (as indicated) and both magnetization directions (solid and dotted curves). The experimental data are normalized to equal photon flux, i.e., plotted on the same intensity scale. The theoretical spectra have been multiplied by the Fermi function, folded by a Gaussian function corresponding to the experimental energy resolution and scaled such as to match the experimental $S^{\mathrm{MLD}}$ leading peak at 23.8 eV photon energy. Therefore, experimental and calculated spectra can directly be compared, bearing in mind the following differences. In the calculations, we used completely linearly polarized light and ''perfect'' angle resolution. Furthermore, the theoretical spectra are for zero temperature and do not contain an inelastic background.

We first establish that the peaks in the theoretical spectra, which were obtained within a one-step-model approach to photoemission, can be interpreted in terms of direct interband transitions from the initial-state bands shown in Fig. 2, if one takes into account the slight shift of the photoemission peaks to lower binding energies due to the imaginary potential describing the finite hole lifetime. For 23.8 eV photon energy, such transitions can be expected at energies where the final-state bands in Fig. 2 cross with initial-state bands of spatial symmetry character $\Sigma^1$ and $\Sigma^3$.

Since the final states belonging to the dash-dotted bands have an averaged six-times larger penetration depth into the solid than those belonging to the dashed bands, they should dominate the interpretation. This leaves us with five crossing points: (i) with the $\Sigma^1\uparrow$ band at 2.5 eV, (ii) with the $\Sigma^3\uparrow$ band at 2.3 eV, (iii) with the $\Sigma^1\uparrow$ band at 1 eV, (iv) with the $\Sigma^1\downarrow$ band at 0.3 eV, and (v) with the $\Sigma^3\downarrow$ band at 0.25 eV.

Since the spacing of points (i) and (ii) is less than the imaginary potential part (and of the order of the experimental energy resolution taken into account in the calculated spectra), the two transitions cannot be resolved, and in fact manifest themselves as a broad peak near 2.4 eV (for each magnetization direction) in the spectra in Fig. 3. With respect to nonrelativistic spatial-spin symmetry of the initial states this peak is labeled by $\Sigma^1\uparrow\oplus\Sigma^3\uparrow$. (The $\oplus$ denotes the incoherent superposition of the two transitions that cannot be resolved due to the limited energy resolution.) Crossing point (iii) corresponds to the photoemission peak $\Sigma^1\uparrow$ at 0.9 eV in Fig. 3. Transitions pertaining to (iv) and (v) are merged due to the experimental energy resolution and show up as the dominant peak $\Sigma^1\downarrow\oplus\Sigma^3\downarrow$ at 0.3 eV. The above discussion extends analogously to the other photon energies. The changes of peak energies with photon energy, which reflect the dispersions of these bands, are sketched by the solid vertical lines in Fig. 3.

We now proceed to a more detailed discussion. The structure $\Sigma^1\uparrow\oplus\Sigma^3\uparrow$ shows no significant dispersion above 22 eV photon energy. Below 22 eV it splits into the two peaks $\Sigma^3\uparrow$ and $\Sigma^1\uparrow$ following the upwards dispersion of the $\Sigma^3$ and the nearly constant binding energy of the $\Sigma^1$ band. The transition at $\Gamma^{25'}\uparrow$ is reached at 29 eV photon energy (obtained by further downshifting the final-state dispersion). Dispersion and peak form are well described by the calculation, but it overrates the intensities of the $\Sigma^1\uparrow\oplus\Sigma^3\uparrow$ structure. The intensity is determined by the transition-matrix elements as well as self-energy corrections that are nonlocal and depend on the binding energy. In our calculations we assume a spatially constant self-energy and a linear dependence on the energy (cf. Sec. III B). Thus this deviation can be explained by the breakdown of the linear approximation at these binding energies.

The corresponding exchange-split $\gamma_-$ states give rise to the big $\Sigma^1\downarrow\oplus\Sigma^3\downarrow$ feature close to the Fermi level. For photon energies below 21 eV, the $\Sigma^3\downarrow$ disperses above $E_{\mathrm{F}}$. Both in the experimental and the theoretical spectra, one observes with decreasing photon energy only the dispersion of $\Sigma^1\downarrow$ to higher binding energies, a decrease of the intensity and a broadening of the peak form. With increasing photon energy, the $\Gamma^{25'}\downarrow$ point is reached at 26.8 eV.

Emission from the $\Sigma^2\uparrow$ and the $\Sigma^2\downarrow$ band, which near $\Gamma$ might add to the $\Sigma^1\uparrow\oplus\Sigma^3\uparrow$ and the $\Sigma^1\downarrow\oplus\Sigma^3\downarrow$ peak, respectively, is negligible, because first, spatial symmetry $\Sigma^2$ parts cannot contribute to the transition-matrix elements in normal emission, and second, the $\Sigma^1$ and $\Sigma^3$ admixtures, which can contribute, are very small.

Around 0.9 eV binding energy, the $\Sigma^1\uparrow$ peak appears, for which the transition at $\Gamma^{12}\uparrow$ takes place at 27.25 eV photon energy. While experiment and theory agree in the binding energy of this peak, its intensity is much larger in the experimental than in the calculated spectra. In search for an explanation, we turn to the $\gamma_-$ band with dominant $\Sigma^4\uparrow$ symmetry. For purely $p$-polarized light incident in the [001] azimuth, this band yields hardly any emission, since matrix element parts with $\Sigma^4$ states vanish and $\Sigma^1$ and $\Sigma^3$ admixtures are very small. For $s$-polarized light, however, $\Sigma^4$-derived emission is quite sizable. Since the light used in our experiment is not completely $p$ polarized, i.e., contains an $s$-polarized component, the measured peak near 0.9 eV may have an additional $\Sigma^4$-derived contribution, which is absent in its theoretical counterpart.

For the critical points of the quasiparticle band structure, experimental binding energies have been obtained by fitting the measured $S^{\mathrm{MLD}}$ by Gaussians after subtraction of a Shirley-like background for the corresponding photon energy for which the transitions take place at $\Gamma$. These values and the exchange splitting are seen, in Table II, to agree excellently with their calculated quasiparticle counterparts (in the column ''DOS''). The deviations from the results of the ground-state band structure of Ref. 36, which are very close to our own LMTO ground-state band structure, clearly demonstrate that a real and an imaginary self-energy correction as specified in Sec. III is significant. The comparison of earlier experimental binding energies for Fe(110) with various ground-state calculation results, which has been shown in Table II of Ref. 37, further supports this finding. For a more detailed discussion on self-energy corrections in photoemission from Fe—as obtained for Fe(001)—we refer to Refs. 38 and 39.

### C. Magnetic linear dichroism

We now turn to the MLD. Figure 3 reveals that for various photon energies the two spectra $I(\vec{M}_+)$ and $I(\vec{M}_-)$ measured for the two different orientations of the magnetization along [110] are different. Hence, a magnetic dichroism is observed and $D^{\mathrm{MLD}}$ is unequal zero.

In detail, the $\Sigma^1\uparrow\oplus\Sigma^3\uparrow$ transition possesses a negative difference $D^{\mathrm{MLD}}$, i.e., the $I(\vec{M}_-)$ intensity exceeds the $I(\vec{M}_+)$ one. Its calculated MLD exists in the whole investigated photon-energy range with a pronounced maximum at around 23 eV, whereas the experimental MLD is significantly nonzero only from approximately 24 eV up to 29 eV with its maximum at 26 eV. For the $\Sigma^1\downarrow\oplus\Sigma^3\downarrow$ structure a positive MLD is observed in both the experimental and theoretical spectra in the whole photon-energy range. For excitations below 21 eV, the photoemission calculations with a very small imaginary part of the self-energy (not shown here) reveal that both $\Sigma$ states contribute to the MLD with the same sign.

We now address the question of whether the analytical theory sketched in Sec. III A is capable of explaining the observed MLD. As a first step, one has to identify those initial states within the Brillouin zone from which MLD is expected. Referring to the theory, these are states significantly hybridized by SOC, i.e., states near SOC-induced band gaps where hybridization is strongest. In our geometry the relevant anticrossing points are between nonrelativistic $\Sigma^1$ and $\Sigma^3$ bands with the same spin, i.e., the points $A$ and $B$ at the $\Gamma$ point and the points $C$ and $D$ in the middle of the Brillouin zone (cf. Fig. 2).

As a second step, one has to show that MLD is observed if the corresponding direct transitions are near such anticrossing points. This statement will be discussed for the example of the prominent $\Sigma^1\downarrow\oplus\Sigma^3\downarrow$ structure for which the dependence of $S^{\mathrm{MLD}}$ and $D^{\mathrm{MLD}}$ on the photon energy is given in Fig. 4. A comparison of experiment with theory is facilitated for this structure by the low background of secondary electrons for transitions directly below $E_{\mathrm{F}}$. $D^{\mathrm{MLD}}$ and $S^{\mathrm{MLD}}$ have been obtained from the intensities $I(\vec{M}_+)$ and $I(\vec{M}_-)$ at the respective peak position. Some remarks on the errors in Fig. 4 should be made. The statistical error in the intensity and the systematical one in the photon energy is within the symbol size. Due to the strong dependence of $S^{\mathrm{MLD}}$, and especially of $D^{\mathrm{MLD}}$ on the binding energy, the systematical error in $S^{\mathrm{MLD}}$ and $D^{\mathrm{MLD}}$ is larger and can be approximated by the scattering of the points. The scaling between calculation and experiment is the same as in Fig. 3; experimental and calculated $S^{\mathrm{MLD}}$ at 23.8 eV photon energy have the same height. Therefore $S^{\mathrm{MLD}}$ and $D^{\mathrm{MLD}}$ can directly be compared to the experimental data. Note that the difference $D^{\mathrm{MLD}}$ has been plotted on a five-times larger scale

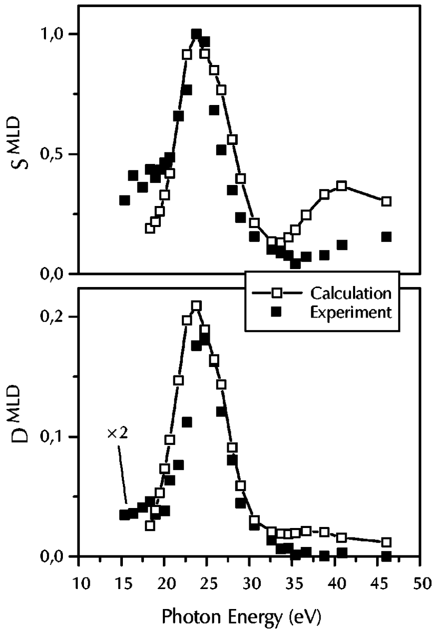

FIG. 4. Photon-energy dependence of sum $S^{\mathrm{MLD}}$ (upper panel) and difference $D^{\mathrm{MLD}}$ (lower panel) of the $\Sigma^1\!\downarrow\oplus\ \Sigma^3\!\downarrow$ structure. Experimental and calculated $S^{\mathrm{MLD}}$ are scaled to have the same height at 23.8 eV, $D^{\mathrm{MLD}}$ is plotted on a fivefold larger scale. Within this scale the experimental $D^{\mathrm{MLD}}$ has been multiplied by a factor of 2.

in comparison to $S^{\mathrm{MLD}}$. Within this scale the measured $D^{\mathrm{MLD}}$ has been multiplied by a factor of 2 to fit approximately the calculated one.

We find a good qualitative agreement between experiment and calculation of $S^{\mathrm{MLD}}$ and $D^{\mathrm{MLD}}$ regarding the photon-energy dependence below 31 eV. Both quantities exhibit a pronounced maximum at around 24 eV. For photon energies above 33 eV the calculated $S^{\mathrm{MLD}}$ differs from the measured one by a second weaker maximum at around 40 eV. For $D^{\mathrm{MLD}}$ the agreement above 33 eV is much better; in both experiment and calculation a decreasing MLD difference is observed.

In order to explain the dependence of $S^{\mathrm{MLD}}$ and $D^{\mathrm{MLD}}$ on the photon energy, we have additionally projected out the parts of $\Sigma^1\!\downarrow$ and $\Sigma^3\!\downarrow$ functions of each of the two relevant initial-state bands. The result is shown in the middle and lower panels of Fig. 5 as a function of $k_\perp$. In addition, the final-state energy is given in the upper horizontal scale of Fig. 5. This scale is based on the corresponding direct transition into that final state with practically no damping (dash-dotted line in Fig. 2). Above $-27$ eV binding energy, both final states contribute approximately equally to the photoemission spectra due to their comparable damping. The upper panel of Fig. 5 repeats the relevant part of the band structure. The two initial states are represented by bold lines and labeled as bands *I* and *II*. The inset shows the detailed band structure near the Γ point.

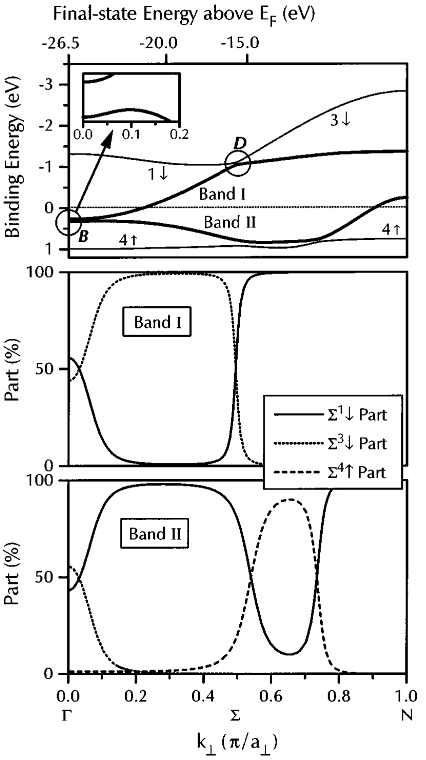

FIG. 5. Detailed dispersion of the initial states of the $\Sigma^1\!\downarrow\oplus\Sigma^3\!\downarrow$ structure labeled by bands *I* and *II* represented in the upper panel and in the inset by thick lines. Dependence of the $\Sigma^1\!\downarrow$ and $\Sigma^3\!\downarrow$ parts of band *I* (middle panel) and of the $\Sigma^1\!\downarrow$, $\Sigma^3\!\downarrow$, and $\Sigma^1\!\downarrow$ parts of band *II* (lower panel) on $k_\perp$ and the final-state energy above $E_{\mathrm{F}}$.

Figure 5 reveals that the bands change their character due to hybridization; both bands at band gap *B* and additionally band *I* at point *D* and band *II* at the two anticrossing points with the flat $\Sigma^4\!\uparrow$ band at about 1 eV binding energy. Note that due to the complicated dispersion at *B* (cf. the inset in Fig. 5) the maximum degree of hybridization between $\Sigma^1\!\downarrow$ and $\Sigma^3\!\downarrow$ for the two bands are at $k_\perp = 0.03\pi/a_\perp$ and not directly at $\Gamma(k_\perp = 0)$.

We now return to the discussion and show how the photon-energy dependence of the $\Sigma^1\!\downarrow\oplus\Sigma^3\!\downarrow$ MLD can be explained by the band structure and hybridization at point *B*. At around 15 eV photon energy, the transitions take place nearly in the middle of the Brillouin zone. Up to 21 eV, only transitions from the initial-state band *II* are observed with a broad peak below $E_{\mathrm{F}}$ in the photoemission spectra. At the corresponding $\vec{k}$ points the initial state consists of a hybrid of $\Sigma^1\!\downarrow$ and $\Sigma^4\!\uparrow$ functions (cf. Fig. 5, lower panel) so that, if the model is correct, no MLD should be observed. In fact a small and nearly constant experimental $D^{\mathrm{MLD}}$ is observed, caused by the breakdown of the direct-transition picture into one final state.

Above 21 eV, band-*I*-derived transitions are possible. In the photoemission spectra the prominent structure $\Sigma^1\!\downarrow$

$\oplus\Sigma^3\downarrow$ occurs and therefore $S^{\mathrm{MLD}}$ increases with a maximum at 23.8 eV. Additionally, the increase of $D^{\mathrm{MLD}}$ is observed. Within our model this can easily be explained by the increasing hybridization of the initial states near band gap $B$. The maximum of $D^{\mathrm{MLD}}$ is reached at 24.8 eV or $k_\perp = 0.05\pi/a_\perp$, which is nearly exact at the maximum degree of hybridization of the two bands at $k_\perp = 0.03\pi/a_\perp$. Above 25 eV, $S^{\mathrm{MLD}}$ decreases, i.e., the transition-matrix elements become smaller. Therefore, $D^{\mathrm{MLD}}$, which depends linearly on the matrix elements, decreases. Note that the above interpretation assumes that the transition-matrix elements vary slowly with photon energy.

The above comparison between the photon-energy dependence of $D^{\mathrm{MLD}}$ with the initial-state dispersion shows that the $\Sigma^1\downarrow\oplus\Sigma^3\downarrow$ MLD can be explained by the dispersion and the hybridization of the corresponding initial states of bands $I$ and $II$. We want to emphasize at this point that the MLD is not caused by incoherent superposition of the transitions from the two individual initial states that would lead to a vanishing $D^{\mathrm{MLD}}$. In fact, MLD is an interference effect caused by the coherent excitation of a $\Sigma^1\downarrow$- and a $\Sigma^3\downarrow$-related part from each of the two initial states.

In the same way the MLD of the exchange-split $\Sigma^1\uparrow\oplus\Sigma^3\uparrow$ structure can be explained by the hybridization at the SOC-induced band gap $A$. Additionally, within the analytical framework, it is easy to explain the opposite signs of the $\Sigma^1\uparrow\oplus\Sigma^3\uparrow$ and $\Sigma^1\downarrow\oplus\Sigma^3\downarrow$ structures. Basing on nearly the same dispersion near $\Gamma$ of the $\Sigma^1\uparrow$ and $\Sigma^3\uparrow$ initial states on the one side and the $\Sigma^1\downarrow$ and $\Sigma^3\downarrow$ initial states on the other side, it is a good assumption that the corresponding transition-matrix elements are comparable. But, as can be seen in Eq. (2), the interference terms of the exchange-split states $\gamma_+$ and $\gamma_-$ possess opposite signs in $D^{\mathrm{MLD}}$. Hence, if now the matrix elements are independent of the photon energy, especially the phase difference between the two partial waves, the sign reversal is observed.

In the experimental spectra the $\Sigma^1\uparrow$ transition at 0.9 eV also seems to have a MLD for photon energies larger than 19.6 eV. But in our interpretation its MLD can be explained by an artifact caused by the rather small energy separation of about 0.7 eV from the $\Sigma^1\downarrow\oplus\Sigma^3\downarrow$ structure and its dominating positive MLD. This interpretation is proven first by the fact that in the experimental 25.9 eV spectra the MLD reverses sign at the $\Sigma^1\uparrow$ peak position and, second, by fitting the individual peaks of the experimental spectra for both magnetization directions (after subtracting a Shirley-like background). In addition, in the calculated spectra this peak shows no MLD.

This observation is expected within the direct-transition picture combined with hybridization analysis. Transitions near $C$ are possible at photon energies around 16 eV. But for these photon energies the $\Sigma^1\uparrow$ emission near 0.9 eV decreases as can be seen in Fig. 3, i.e., corresponding matrix elements and hence the interference terms become small. For higher photon energies the emission from the $\Sigma^1\uparrow$ band increases but possible $\Sigma^3\uparrow$ admixtures are negligible due to the large energy separation in comparison to the exchange splitting from the downwards dispersing $\Sigma^3\uparrow$ band (cf. Fig. 2). Hence, no MLD is observed.

Point $D$ belongs to the unoccupied band structure and cannot be observed in the experimental photoemission spectra. But calculated (inverse photoemission) spectra that include transitions from initial states above $E_{\mathrm{F}}$ also show MLD at this point.

In summary, the MLD of photoemission calculations and of measurements can qualitatively be explained by the analytical theory in combination with the band structure accompanied by hybridization analysis. Differences between analytical theory and measurements as well as calculations can be attributed to simplifications in the above discussion, for example, the neglect of the dependence of $E'$, $\vartheta'$, and the phase difference between the two partial waves on photon energy and the restriction to one direct transition.

In the following we now want to discuss the discrepancies between photoemission calculations and measurements: (i) For photon energies above 31 eV the calculated intensity $S^{\mathrm{MLD}}$ increases, whereas the experimental one is almost independent of the photon energy. As mentioned above, the photoemission intensity is additionally determined by self-energy corrections. Thus the different dependence of $S^{\mathrm{MLD}}$ on the photon energy can be attributed to the self-energy corrections in the upper state regime that cannot be described by our linear approximation (cf. Sec. III B).

(ii) The calculations overrate the MLD approximately by a factor of 2 in the whole investigated photon-energy range under the assumption that experimental and calculated $S^{\mathrm{MLD}}$ at 23.8 eV have the same value. The overrating of the MLD has two possible reasons; first, the calculations have been done under ‘‘perfect conditions,’’ i.e., with fully linearly polarized light and the magnetization at zero temperature. Therefore, the calculated MLD should exceed the experimental one. Additionally, effects of spin-dependent and inelastic scattering as well as a spin-dependent lifetime have not been incorporated in the calculations. This could lead to a decrease of the dichroism. For the same reason it is possible that the experimental $D^{\mathrm{MLD}}$ of the $\Sigma^1\uparrow\oplus\Sigma^3\uparrow$ structure is smaller in comparison to the $\Sigma^1\downarrow\oplus\Sigma^3\downarrow$ MLD. Second, as an interference effect the MLD should be very sensitive to experimental conditions as well as numerical modeling. From the experimental point of view these are the preparation conditions and possible contamination at the surface that can influence the MLD. (An effect of contamination in our experiment can be neglected, since it was checked by repeated measurements of the MLD after several hours.)

Based on these results, we can offer a few comments on the question of how MLD in the valence-band photoemission can be used to obtain further information on the magnetic ground state of the system, such as spin and orbital magnetic moments. Because MLD depends strongly on the detailed electronic structure, this seems to be hardly possible. For example, if the phase difference between the two partial waves $\Delta\mu$ satisfies $\mathrm{Im}[\sin\vartheta'\cos\vartheta'^{\star}\exp(\Delta\mu)]=0$, no MLD is observed. Furthermore, MLD depends on the absolute value of the involved matrix elements. So that, if the transition is forbidden due to the selection rule $\Delta l = \pm 1$, again no MLD is observed. This may be the reason why different MLDs are observed for the same initial state. In our case, for example, the transitions of $\Sigma^1\downarrow\oplus\Sigma^3\downarrow$ at 24 and 29 eV photon energy into the same final state start at the same initial states of band $I$ and $II$. But both exhibit different $D^{\mathrm{MLD}}$,

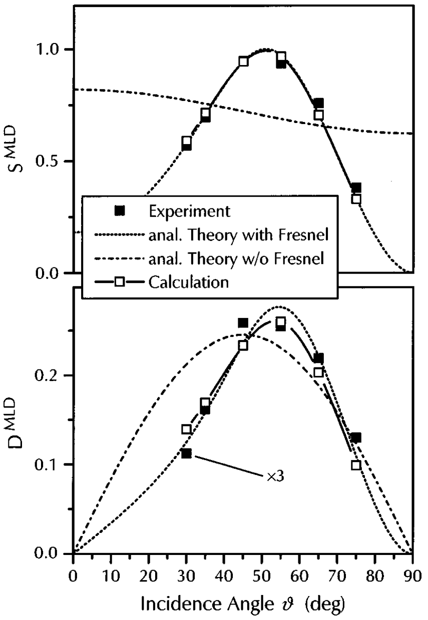

FIG. 6. Dependence on the angle of the impinging light for $S^{\mathrm{MLD}}$ (upper panel) and $D^{\mathrm{MLD}}$ (lower panel) of the $\Sigma^1\!\downarrow\oplus\Sigma^3\!\downarrow$ structure at 25.9 eV photon energy. Additionally, two fits are given based on the analytical theory with (dotted line) and without (dash-dotted line) optical response. Experimental and calculated $S^{\mathrm{MLD}}$ are scaled to have the same height, $D^{\mathrm{MLD}}$ is plotted on a fourfold larger scale. Within this scale the experimental $D^{\mathrm{MLD}}$ has been multiplied by a factor of 3.

which can easily be explained by the different absolute values of matrix elements. This may be called a *final-state effect* because the initial-state wave functions are the same at both photon energies.

The detailed analysis above shows a delicate behavior of MLD on both exchange splitting and SOC. Thus, a simple rule of thumb, for example, that magnetic dichroism depends linearly on the magnetization and therefore can be regarded as a measure for the latter, can hardly be true, in particular in valence-band photoemission. Such information can possibly be derived by comparing the measurements with fully relativistic photoemission and band-structure calculations.

### D. Dependence on light incidence angle

Correctness and relevance of both the analytical and numerical calculations can directly be proven by comparing the experimental and the theoretical dependence of $S^{\mathrm{MLD}}$ and $D^{\mathrm{MLD}}$ on the polar angle of incidence $\vartheta$ of the light. To verify the theoretical predictions, $S^{\mathrm{MLD}}$ and $D^{\mathrm{MLD}}$ of the $\Sigma^1\!\downarrow\oplus\Sigma^3\!\downarrow$ structure at 25.9 eV photon energy (0.4 eV binding energy) have been recorded experimentally for various polar angles $\vartheta$. The result is represented by the solid squares in Fig. 6. For the errors the same argumentation holds as in Fig. 4.

The numerical data (open squares with solid lines) have been obtained from photoemission calculations. These have been scaled by a common factor in order to best fit the experimental $S^{\mathrm{MLD}}$. At this photon energy the numerical $D^{\mathrm{MLD}}$ overrates the experimental one by a factor of 3, which has been incorporated in the lower panel of Fig. 6.

Within the external field approximation, i.e., without Snell's law and Fresnel's formula (dash-dotted lines in Fig. 6), the analytical formula predicts a $\sin 2\vartheta$ dependence of $D^{\mathrm{MLD}}$ and a superposition of $\sin^2\vartheta$ and $\cos^2\vartheta$ dependences of $S^{\mathrm{MLD}}$. The result of a fit to $D^{\mathrm{MLD}}$ based on this approximation is additionally shown. The discrepancy between both experimental and calculated $S^{\mathrm{MLD}}$ and $D^{\mathrm{MLD}}$ completely rules out the external field approximation. Thus, the refraction of the light has to be incorporated.

The analytical results with optical response of the metal (dotted lines in Fig. 6) were obtained from Eq. (2) by fitting simultaneously $S^{\mathrm{MLD}}$ and $D^{\mathrm{MLD}}$ and using Snell's law and Fresnels' formula, regarding the transition-matrix elements as parameters. For the complex index of refraction we took $\epsilon=0.54+0.31i$ (as in the photoemission calculations) from Ref. 40. We assumed two initial states, i.e., the bands with nonrelativistic $\Sigma^1\!\downarrow$ and $\Sigma^3\!\downarrow$ symmetry, both with three independent parameters; the absolute values $|M^{(1fi)}|$ and $|M^{(3fi)}|$ of the transition-matrix elements and the phase difference between them.

The experimental as well as the numerical data are well reproduced by the analytical fit. This proves clearly that MLD is described correctly by our analytical theory, especially by Eq. (2). The good agreement for $D^{\mathrm{MLD}}$ is only achieved if one assumes two initial states. Thus, one can conclude about the number of initial states for the $\Sigma^1\!\downarrow\oplus\Sigma^1\!\downarrow$ structure by measuring the incidence-angle dependence of $D^{\mathrm{MLD}}$.

Additionally, one concludes that the angular dependence of the MLD observed in the valence-band structure of Fe(110) is properly described by classical Fresnel theory. At first glance, it seems surprising that the optical response in the topmost surface layers can be neglected in the interpretation of photoemission spectra from Fe(110) in the VUV energy range, contrary to findings for layered semiconductors.[41] The next step beyond the Fresnel approximation, the so-called hydrodynamical model,[42] leads to longitudinal electromagnetic partial waves, which in spin-polarized photoemission from Pt(001) can be completely neglected due to the very low effective plasmon energy with respect to the photon energy.[28] The latter result may be regarded as valid also for Fe(110).

In principle, referring to the incidence angle dependence of the MLD, it is possible to calculate the *absolute* values of the photoemission transitions and the phase difference between them. Unfortunately, in our case this is not possible because the corresponding peak is a superposition of two maxima and, therefore, the fit is not unambiguous. However, in the bare calculated spectra (without folding with the experimental resolution) the initial states can be separated.

## V. CONCLUSION

We have presented an investigation of MLD in valence-band photoemission from Fe(110) in a fourfold way: by symmetry considerations, analytical theory, numerical calculations, and measurements. We have shown that by comparing experimental and theoretical results the microscopic origin of MLD is mainly the SOC-induced hybridization of the initial states. If the various components of such a hybrid are simultaneously excited, one observes an interference between the partial waves. The sign of the interference term depends on the magnetization direction and thus MLD is observed. The agreement of the experimental results with both the predictions of the analytical formula and the quantitative results of the numerical calculations proves that our theoretical description of MLD is adequate. Other models, if properly enhanced, for example, by relativistic group theory and relativistic photoemission theory, should also lead to the same conclusions.[13–15] In summary, one can use MLD to identify SOC-induced band gaps or hybridization zones in the band structure by measuring the photon-energy dependence of $D^{\mathrm{MLD}}$.

For the case of Fe(110) on W(110), we have further shown that the observed MLD is derived from the SOC-induced gaps at $\Gamma^{25'}\uparrow$ and $\Gamma^{25'}\downarrow$ and that the MLD signals of the exchange-split states possess opposite sign. The photon-energy dependence of the $\Gamma^{25'}\downarrow$-related MLD can be explained by means of the initial-state band structure of bulk Fe(110) within the direct-transition picture. Furthermore, theory reveals a substantial influence of the refraction of the incident radiation on the MLD, and comparison with experiment shows that a description of the radiation field inside the metal in terms of classical Fresnel optics is adequate for photon energies in the VUV regime.

## ACKNOWLEDGMENTS

We thank M. Mast and W. Braun for their help during the measurements at BESSY, Berlin. The experiments have been supported by the Bundesministerium für Bildung, Wissenschaft, Forschung und Technologie (BMBF) under Contract No. 05 5PCFXB 2 and by the Deutsche Forschungsgemeinschaft through SFB 341. The theoretical work has been financially supported by the BMBF under Contract No. 05 621PGA.

---

[1] G. Schütz, W. Wagner, W. Wilhelm, P. Kienle, R. Zeller, R. Frahm, and G. Materlik, Phys. Rev. Lett. **58**, 737 (1987).

[2] L. Baumgarten, C. M. Schneider, H. Petersen, F. Schäfers, and J. Kirschner, Phys. Rev. Lett. **65**, 492 (1990).

[3] C. M. Schneider, M. S. Hammond, P. Schuster, A. Cebollada, R. Miranda, and J. Kirschner, Phys. Rev. B **44**, 12 066 (1991).

[4] H. B. Rose, C. Roth, F. U. Hillebrecht, and E. Kisker, Solid State Commun. **91**, 129 (1994).

[5] C. Roth, F. U. Hillebrecht, H. B. Rose, and E. Kisker, Phys. Rev. Lett. **70**, 3479 (1993).

[6] M. Getzlaff, C. Ostertag, G. H. Fecher, N. A. Cherepkov, and G. Schönhense, Phys. Rev. Lett. **73**, 3030 (1994).

[7] B. T. Thole and G. van der Laan, Phys. Rev. B **44**, 12 424 (1991).

[8] G. van der Laan, Phys. Rev. B **51**, 240 (1995).

[9] D. Venus, Phys. Rev. B **48**, 6144 (1993).

[10] T. Scheunemann, S. Halilov, J. Henk, and R. Feder, Solid State Commun. **91**, 487 (1994).

[11] J. Henk, S. Halilov, T. Scheunemann, and R. Feder, Phys. Rev. B **50**, 8130 (1994).

[12] J. Henk, T. Scheunemann, S. Halilov, and R. Feder, J. Phys.: Condens. Matter **8**, 47 (1996).

[13] D. Venus, Phys. Rev. B **49**, 8821 (1994).

[14] D. Venus, J. Magn. Magn. Mater. **170**, 29 (1997).

[15] D. Venus, Phys. Rev. B **56**, 2661 (1997).

[16] *Spin-Orbit Influenced Spectroscopies of Magnetic Solids*, Vol. 466 of Lecture Notes in Physics, edited by H. Ebert and G. Schütz (Springer, Berlin, 1996).

[17] W. Kuch, A. Dittschar, K. Meinel, M. Zharnikov, C. Schneider, J. Kirschner, J. Henk, and R. Feder, Phys. Rev. B **53**, 11 621 (1996).

[18] J. Henk and R. Feder, Phys. Rev. B **55**, 11 476 (1997).

[19] A. Fanelsa, E. Kisker, J. Henk, and R. Feder, Phys. Rev. B **54**, 2922 (1996).

[20] W. Kuch, A. Dittschar, M.-T. Lin, M. Salvietti, M. Zharnikov, C. M. Schneider, J. Kirschner, J. Camamero, and J. J. de Miguel, J. Magn. Magn. Mater. **170**, L13 (1997).

[21] U. Gradmann and G. Waller, Surf. Sci. **116**, 539 (1982); H. J. Elmers and U. Gradmann, Appl. Phys. A: Solids Surf. **51**, 255 (1990); H. Bethge, D. Heuer, C. Jensen, K. Reshöft, and U. Köhler, Surf. Sci. **331-333**, 878 (1995).

[22] T. Inui, Y. Tanabe, and Y. Onodera, in *Group Theory and Its Applications in Physics*, Vol. 78 of *Springer Series in Solid State Sciences*, edited by M. Cardona (Springer, Berlin, 1990).

[23] L. Falicov and J. Ruvalds, Phys. Rev. **172**, 498 (1968).

[24] E. Tamura and R. Feder, Solid State Commun. **79**, 989 (1991).

[25] E. Tamura and R. Feder, Europhys. Lett. **16**, 695 (1991).

[26] J. Hermanson, Solid State Commun. **22**, 9 (1977).

[27] J. D. Jackson, *Classical Electrodynamics* (Wiley, New York, 1975).

[28] J. Henk, T. Scheunemann, and R. Feder, J. Phys.: Condens. Matter **9**, 2963 (1997).

[29] B. Schmiedeskamp, N. Irmer, R. David, and U. Heinzmann, Appl. Phys. A: Solids Surf. **53**, 418 (1991).

[30] R. Feder and J. Henk, in Ref. 16.

[31] *Polarized Electrons in Surface Physics*, edited by R. Feder, Advanced Series in Surface Science (World Scientific, Singapore, 1985).

[32] *Electron Scattering Theory of Ordered and Disordered Matter*, edited by P. Weinberger (Clarendon, Oxford, 1990).

[33] E. Tamura, R. Feder, G. Waller, and U. Gradmann, Phys. Lett. B **157**, 627 (1990).

[34] J. W. Krewer and R. Feder, Phys. Lett. B **172**, 135 (1991).

[35] R. Wu and A. Freeman, Phys. Rev. Lett. **69**, 2867 (1992).

[36] K. Hathaway, H. Jansen, and A. Freeman, Phys. Rev. B **31**, 7603 (1985).

[37] A. M. Turner, A. W. Donoho, and J. L. Erskine, Phys. Rev. B **29**, 2986 (1984).

[38] R. Feder, A. Rodriguez, U. Baier, and E. Kisker, Solid State Commun. **52**, 57 (1984).

[39] R. Clauberg and R. Feder, in *Polarized Electrons in Surface*

*Physics*, (Ref. 31), Chap. 14, p. 565.

[40] H. Hagemann, W. Gudat, and C. Kunz, Technical Report No. SR-74/7, Deutsches Elektronen-Synchrotron Hamburg (unpublished).

[41] D. Samuelsen, A. Yang, and W. Schattke, Surf. Sci. **287**, 676 (1993).

[42] F. Forstmann and R. Gerhardts, *Metal Optics Near the Plasma Frequency* (Springer, Berlin, 1986).

## Publikation 8

# Temperature-dependent electronic structure, spin-resolved photoemission, and magnetic dichroism of ultrathin ferromagnetic films: Co/Cu(001)

**J Henk**

Max-Planck-Institut für Mikrostrukturphysik, Weinberg 2, D-06120 Halle (Saale), Germany

E-mail: henk@mpi-halle.mpg.de

Received 4 October 2000, in final form 8 December 2000

### Abstract

The temperature dependences of the electronic structure, spin-resolved photoemission, and magnetic linear dichroism of the prototypical system 2 ML Co on Cu(001) (ML stands for monolayer(s)) are presented in a detailed theoretical study. Relativistic *ab initio* electronic structure calculations were carried out within the framework of multiple-scattering theory; the spin-resolved photoemission was calculated within the one-step model. The temperature dependence was taken into account within the disordered local moment picture.

The spectral features show a distinct dispersion and broadening with temperature, in particular those derived from quantum-well states in the Co film. These findings can be traced back to the layer- and spin-resolved Bloch spectral function. Further, Co-derived maxima in the photoemission intensities behave significantly differently with temperature to Cu-derived ones. The spin-resolved photoemission intensities compare well with experimental data and with theoretical data obtained within the fluctuating local moment picture. Magnetic linear dichroism in spin-resolved photoemission is discussed in terms of asymmetries which are related to the spin polarizations.

## 1. Introduction

Joint experimental and theoretical investigations of solids, in particular those of 3d ferromagnets, by photoelectron spectroscopy have proved to be very successful and allowed detailed statements to be made as regards the spin- and symmetry-resolved electronic structure (see for example [1]). Theoretical photoemission calculations are—like the underlying *ab initio* band-structure calculations—usually performed for zero temperature. The corresponding experiments, however, are carried out at elevated temperatures, e.g. at room temperature. Theoretical and experimental photoemission spectra agree well in general for ferromagnetic systems with the Curie temperatures $T_C$ which are high compared to the actual temperature at which the experiments were performed. However, the agreement is rather poor for systems with low Curie temperatures, for example ultrathin films. For two monolayers (ML) of Co on

Cu(001), $T_{\mathrm{C}}$ was estimated at only 320 K [2], as compared to a bulk $T_{\mathrm{C}}$ of 1388 K [3] (Huang *et al* found a value of about 500 K by means of the surface magneto-optic Kerr effect [4]). In order to overcome this temperature 'mismatch' between theory and experiment, one can either cool the samples in experiment down to temperatures close enough to zero or extend the theory to non-zero temperatures—obviously a far better approach. The latter allows detailed studies of the temperature dependence of significant electron-spectroscopic quantities: for example magnetic moments, spin polarization, and magnetic dichroism (MD) in photoemission.

Temperature effects can be divided into vibrational and electronic effects. The former, i.e. phonons, are treated in multiple-scattering theories of electron spectroscopies (e.g. low-energy electron diffraction (LEED) and photoemission) via temperature-dependent scattering phase shifts (see for example [5, 6]). The electronic temperature effects can be taken into account by an energy-, spin-, and temperature-dependent self-energy $\Sigma$ which can be approached in different ways. In a first approach, one can combine density-functional theory and many-body treatments. For example, a Hubbard-type multiband model allows the computation of spin-resolved photoemission spectra within a generalized one-step model [7–9]. For low-index surfaces of Ni the comparison of spectra calculated within this framework showed good agreement with experimental data. No indication of a stationary exchange splitting independent of temperature could be found. Instead, majority and minority spin states merged in energy upon approaching $T_{\mathrm{C}}$. Another treatment is based on a periodic cluster approach with exact diagonalization of the many-particle Hamiltonian for ultrathin transition-metal films [10].

A further approach is based on the coherent potential approximation (CPA) [11] as formulated in the Korringa–Kohn–Rostoker (KKR) method [12–14]. The disorder in the solid gives rise to the electron self-energy operator $\Sigma$ [15]. Therefore, the electronic structure has to be described by means of the Bloch spectral function (BSF) $A_{\mathrm{B}}(E, \boldsymbol{k})$ (i.e. the energy- and wavevector-resolved density of states) instead of by means of the more familiar band structure $E(\boldsymbol{k})$. The real part of $\Sigma$ shifts the energy levels (e.g. defined as maxima in $A_{\mathrm{B}}(E, \boldsymbol{k})$); its imaginary part gives rise to broadening, i.e. to a finite lifetime of the quasi-particles. The CPA can be used for binary substitutional alloys $\mathrm{A}_x\mathrm{B}_{1-x}$ to formulate a first-principles theory of phase transitions in ferromagnets [16, 17]: in the disordered local moment (DLM) picture, one identifies the atomic species A and B as atoms of the same kind but with opposite orientations of the local magnetic moment $\boldsymbol{M}$: $\boldsymbol{M}_{\mathrm{A}} = -\boldsymbol{M}_{\mathrm{B}}$. For given concentration $x$ and energy $E$, an effective medium is computed, which is determined by the condition that inserting a defect of type A weighted with its concentration $x$ and inserting a defect of type B weighted with its concentration $1 - x$ into the effective medium imposes no additional scattering (for details see references [14, 15]). For example, for concentration $x = 0$ all local magnetic moments are aligned parallel and one has the ferromagnetic case for $T = 0$, since all sites are occupied by atoms of species B. For $x = 0.5$ the net magnetization vanishes due to there being equal numbers of sites occupied by species A and B; hence one is concerned with the paramagnetic case for $T = T_{\mathrm{C}}$. A theory of photoemission from binary substitutional alloys has been formulated by Durham [18] and successfully applied within the DLM picture to Fe at elevated temperatures [19].

If the CPA calculations are performed within the single-site approximation, magnetic short-range order (SRO), i.e. correlation between the local magnetic moments, is neglected (note that within the embedded-cluster method, SRO can of course be treated [20]). In order to take into account the spin–spin correlations, Haines *et al* [21, 22] proposed the fluctuating local moment (FLM) picture which uses clusters with a magnetic moment located at each site. The configurations of local magnetic moments have to be compatible with a given average magnetic moment $\langle m(T)\rangle$ and a spin–spin correlation length $\Lambda(T)$ [23]. Physical quantities are then obtained by averaging over the configurations. Gollisch and Feder applied this approach successfully to photoemission from Ni(111) and $Fe_3Pt$ [24–26]. The joint effect of lattice vibrations and magnetic fluctuations in Ni has been investigated by Delgadillo *et al* [27].

As mentioned above, ultrathin films show a low $T_C$ with respect to the bulk system. Thus, significant temperature effects on spin-resolved photoemission intensities can be expected even at room temperature. Reiser *et al* [28] investigated theoretically 2 ML Co on Cu(001) within the FLM theory and found good agreement with experiment at $T = 0.65\,T_C$ [29] for a certain pair of average magnetic moment and correlation length ($\langle m(T)\rangle = 0.2\,m(0)$ and $\Lambda(T)$ less than the intersite distance). However, they applied an empirical tight-binding description of the electronic structure and did not take into account spin–orbit coupling (SOC), an essential ingredient for the description of magnetic dichroism (MD) in photoemission, i.e. the change of the photocurrent upon reversal of the magnetization orientation [30]. Hence, there appears to be a need for a theoretical investigation of the temperature dependences of the electronic structure, spin-resolved photoemission, and MD from ultrathin films. Its basis should be an *ab initio* electronic structure calculation which treats exchange and spin–orbit interactions on an equal footing. In this paper we present results of such an investigation by means of the fully relativistic layer-KKR method but within the DLM picture instead of the FLM picture. As a prototypical system we chose 2 ML Co/Cu(001) and address further the temperature dependence of the magnetic linear dichroism (MLD) in valence band photoemission. Since we are dealing with spin-resolved MLD, we introduce asymmetries which turn out to be related to the exchange- and the spin–orbit-induced photoelectron spin polarizations (ESPs). In recent works the temperature dependence of the MD has been exclusively (at least to our knowledge) investigated in an element-specific way, exploiting core levels [31, 32]. Further, Alders *et al* presented a joint experimental and theoretical study of the spin–spin correlation function and magnetic long-range order in x-ray absorption in NiO [33].

This paper is organized as follows. In section 2 we sketch the theoretical methods, in particular the numerical details (section 2.1) and the asymmetries (section 2.2). Results are presented and discussed in section 3, in particular for the electronic structure (section 3.1), photoemission (section 3.2), and magnetic linear dichroism (section 3.3). Concluding remarks are made in section 4.

## 2. Theoretical aspects

### 2.1. Numerical details

As a prototypical system we chose 2 ML Co on Cu(001) in order to allow comparison of our results with experiment [29] and previous theoretical results [28]. Cobalt grows in a layer-by-layer mode on Cu(001) and continues the fcc Cu lattice but with a slight tetragonal distortion (for growth of Co on Cu(001), see for example [34–36]). In our calculations we did not take into account any tetragonal distortion at the surface, but assumed the fcc parent Cu lattice to extend throughout the whole semi-infinite system. Nor do we consider Cu–Co intermixing at the interface. The layers are denoted as S, S − 1, S − 2, ..., starting from the outermost surface layer. Bulk layers are denoted by B.

As the first step of the calculations, spin-dependent muffin-tin potentials $V_\pm(r)$ were self-consistently determined by the spin-polarized scalar-relativistic layer-KKR method (within the local spin-density approximation of density-functional theory). We used the exchange–correlation potential of Perdew and Wang [37]. At this step, spin–orbit coupling (SOC) was not taken into account. For maximum angular momentum $l_{\max} = 3$, the magnetic moments of the Co sites are $m(\mathrm{S}) = 1.79\ \mu_\mathrm{B}$ and $m(\mathrm{S}-1) = 1.62\ \mu_\mathrm{B}$. These values correspond to changes of +7.8% and $-2.4\%$ of the bulk moment ($m(\mathrm{B}) = 1.66\ \mu_\mathrm{B}$) and compare well with those obtained by other self-consistent methods (Clemens *et al* give $m(\mathrm{S}) = 1.84\ \mu_\mathrm{B}$ and $m(\mathrm{S}-1) = 1.60\ \mu_\mathrm{B}$ [29]; Niklasson gives $m(\mathrm{S}) = 1.81\ \mu_\mathrm{B}$, $m(\mathrm{S}-1) = 1.61\ \mu_\mathrm{B}$, and $m(\mathrm{B}) = 1.68\ \mu_\mathrm{B}$ [38]). The induced spin moment in the adjacent Cu layer is $m(\mathrm{S}-2) = 0.02\ \mu_\mathrm{B}$. We found no significant charge transfer from Co to Cu. The spin-dependent potentials $V_\pm$ serve as input for the fully relativistic layer-KKR calculations.

The description of magnetic dichroism in photoemission—one of the aims in this investigation—has to deal with both SOC and exchange splitting, which are best treated on an equal footing. Therefore, we applied in the second step the spin-polarized relativistic layer-KKR method [39] in order to determine the layer-resolved Green function, the most important quantity in electronic structure and photoemission calculations, from which all observables can be calculated. Following the ideas of the DLM picture, the electronic temperature effects are treated within the inhomogeneous CPA for binary substitutional alloys [16, 17]. As input for atomic species A we took the spin-dependent potentials from the first step, for species B the same but with opposite spin orientation (i.e. $V_\pm^\mathrm{A} = V_\mp^\mathrm{B}$; thus $M_\mathrm{A} = -M_\mathrm{B}$). For concentration $x = 0$ the layer- and spin-resolved Bloch spectral functions (BSFs) obtained from the fully relativistic and the scalar-relativistic calculations agreed almost perfectly. The slight deviations can unambiguously be attributed to the inclusion of SOC in the former, as can easily be checked by scaling the SOC while keeping the other relativistic effects unchanged [40, 41].

For selected concentrations $x$ ranging from 0 ($T = 0$) to 0.5 ($T = T_\mathrm{C}$), we calculated from the Green function the layer- and spin-resolved BSF $A_\mathrm{B}(E, \boldsymbol{k}_\parallel)$ and the spin-resolved photoemission intensities within the one-step model following the work of Durham *et al* [19]. Instead of treating the photoelectron state, i.e. the time-reversed spin-polarized LEED state, within the averaged $t$-matrix approximation (ATA), we treated it like the hole state within the CPA because of the rather small number of CPA self-consistency iterations required. Additionally, the CPA results were compared with those obtained within the virtual-crystal approximation (VCA) and the ATA. The ATA yielded the same general trends as the CPA but the results at certain energies differed significantly. As expected, the VCA results did not agree well with those obtained within the CPA or with those obtained within the ATA.

Finally, we present some technical details. From the layer-dependent ‘impurity matrices’ $D^\mathrm{A}$ and $D^\mathrm{B}$ (see for example [13]), the configurationally averaged $D^\mathrm{C}$ was obtained from $D^\mathrm{C} = xD^\mathrm{A} + (1-x)D^\mathrm{B}$, from which the effective single-site $t$-matrices of the coherent system were calculated. Starting from the ATA $t$-matrices we did not encounter any convergence problems in the CPA self-consistency loop. Further, the averaging over reciprocal space was carefully checked, applying both special-point sets as well as self-adapting grid methods (see for example [42]). Note that the Fermi energy $E_\mathrm{F}$ is independent of the concentration $x$ because it is fixed by the non-magnetic Cu substrate.

Many-particle effects play an important role for transition metals, one prominent example being the 6 eV satellite for Ni. These effects are expected to be larger in systems with reduced dimensionality, e.g. ultrathin films, than in bulk systems. In a series of publications (see for example references [43–45]), Chen investigated in detail many-particle effects in ultrathin Co films within a non-perturbative many-body approach [46]. One of the main results was the importance of hybridization between the Co d states of the film and the Cu s states of the substrate [10]. The photoemission intensity of a strong satellite peak in the theoretical spectra was considerably reduced if the Co d/Cu s hybridization was taken into account, thus improving the agreement between experiment [29] and theory. Further, many-body effects showed up as a transfer of spectral weight to lower energies than predicted by a single-particle approach (in particular at energies $E < -5.2$ eV).

Such sophisticated many-body calculations are beyond the scope of our investigation. Instead, in our single-particle calculations we model many-particle effects via an energy-dependent optical potential. In the calculations of the BSF a constant imaginary part of the energy of 0.025 eV was used. In the photoemission calculations the hole lifetimes were simulated via an energy-dependent imaginary part of the energy of $\mathrm{Im}\, E = 0.1(E - E_\mathrm{F})$ for Co layers and $\mathrm{Im}\, E = 0.025(E - E_\mathrm{F})$ for Cu layers. For the photoelectron states a constant value of 3.5 eV was taken (note that due to the larger imaginary parts in the photoemission calculations, a slight shift of the electronic states to higher energies with respect to the BSF calculations occurs). Further, the photoemission intensities were collected from the first 20 outermost layers, the maximum angular momentum was $l_\mathrm{max} = 4$, and the number of reciprocal-lattice vectors was about 50. Fresnel's equations and Snell's law were not taken into account.

We wish to stress that our aim was to investigate the basic temperature effects on photoemission and magnetic dichroism. Therefore, we did not optimize the above parameters in order to achieve perfect agreement with experiment. However, in future work we shall incorporate the self-energy $\Sigma$ within the $GW$ approximation [47–49]. This would account for changes in both the layer- and energy-dependent exchange splitting and in the quasi-particle lifetimes via $\mathrm{Re}\, \Sigma$ and $\mathrm{Im}\, \Sigma$, respectively.

Finally, we briefly compare the approach of Nolting *et al* [9] with the DLM approach. In the former, one first computes the electronic band structure of the paramagnetic bulk system. This is used in a second step as input for a Hubbard-type many-particle model with Coulomb and exchange parameters $U$ and $J$, respectively. The latter are chosen to reproduce the ground-state magnetization at $T = 0$ K. The resulting set of equations is solved self-consistently and yields the energy-, spin-, and temperature-dependent self-energy for the occupied states. In a third step, the spin-resolved photocurrent is calculated in a generalized one-step model of photoemission, in which the many-particle effects are taken into account only for the occupied states. This approach has the advantage (like that of Chen [10]) that correlations are accounted for in a sophisticated manner. In the DLM approach, however, these are considered in a rather rudimentary form (see above). In favour of the DLM approach one can say that it can easily be applied to ultrathin films (since it does not rely on bulk properties), that the temperature dependence is considered for both occupied states and the photoelectron state, and that additional parameters do not enter.

### *2.2. Asymmetries for magnetic dichroism in spin-resolved photoemission*

In the following we introduce the asymmetries used in the discussion of magnetic linear dichroism (MLD) in spin-resolved photoemission (see section 3.3 below). In an experiment or a calculation for magnetic dichroism, one records the photocurrent $I$ as a function of the magnetization orientation, $I(\pm \boldsymbol{M})$. If the photocurrent is further spin-analysed ($\pm\sigma$) with respect to the direction of $+\boldsymbol{M}$, one is concerned with a set of four spectra, $I(\pm\sigma, \pm\boldsymbol{M})$, or for short, $I_{\pm\pm}$.

The electron spin polarization (ESP) can be decomposed into an even part and an odd part in terms of $\boldsymbol{M}$: $P(\boldsymbol{M}) = P_\mathrm{ex}(\boldsymbol{M}) + P_\mathrm{so}(\boldsymbol{M})$, with $P_\mathrm{ex}(\boldsymbol{M}) = -P_\mathrm{ex}(-\boldsymbol{M})$ and $P_\mathrm{so}(\boldsymbol{M}) = P_\mathrm{so}(-\boldsymbol{M})$. In terms of the intensities, these ESPs are given by

$$\begin{aligned} P_\mathrm{so} &= \frac{I_{++} - I_{-+}}{2I_+} + \frac{I_{+-} - I_{--}}{2I_-} \\ P_\mathrm{ex} &= \frac{I_{++} - I_{-+}}{2I_+} - \frac{I_{+-} - I_{--}}{2I_-} \end{aligned} \tag{1}$$

with the spin-averaged intensities $I_\mu = \sum_\sigma I_{\sigma\mu}$. Vice versa, the intensities can be written as

$$I_{\sigma\mu} = \frac{1}{2}\left[1 + \sigma(P_{\mathrm{so}} + \mu P_{\mathrm{ex}})\right] I_\mu \qquad \sigma, \mu = \pm. \tag{2}$$

The origins of the ESP contributions become evident on considering the following limiting cases for $I_+ = I_-$. If there is no magnetization ($M = 0$) the ESP is exclusively due to SOC ($P_{\mathrm{so}} \neq 0$ and $P_{\mathrm{ex}} = 0$). If on the other hand there is no SOC, the polarization changes sign upon reversal of $M$ ($P_{\mathrm{ex}} \neq 0$ and $P_{\mathrm{so}} = 0$). In short, $P_{\mathrm{ex}}$ can be attributed to exchange splitting, $P_{\mathrm{so}}$ to SOC.

The four intensities $I_{\pm\pm}$ allow the definition of three asymmetries:

$$\begin{aligned} A_{\mathrm{un}} &= \frac{1}{I_0}(I_{++} + I_{-+} - I_{+-} - I_{--}) \\ A_{\mathrm{so}} &= \frac{1}{I_0}(I_{++} - I_{-+} + I_{+-} - I_{--}) \\ A_{\mathrm{ex}} &= \frac{1}{I_0}(I_{++} - I_{-+} - I_{+-} + I_{--}) \end{aligned} \tag{3}$$

with the total current $I_0 = \sum_{\sigma\mu} I_{\sigma\mu}$, which in terms of the ESPs can be compactly written as

$$\begin{aligned} A_{\mathrm{un}} &= \frac{1}{I_0}(I_+ - I_-) \\ A_{\mathrm{so}} &= P_{\mathrm{so}} + P_{\mathrm{ex}} A_{\mathrm{un}} \\ A_{\mathrm{ex}} &= P_{\mathrm{ex}} + P_{\mathrm{so}} A_{\mathrm{un}}. \end{aligned} \tag{4}$$

There is no dichroism ($A_{\mathrm{un}} = 0$) if there is either no exchange splitting or no SOC. In the first case, $I_{\pm\pm} = I_{\pm\mp}$ leads to $P_{\mathrm{ex}} = 0$ and, thus, $A_{\mathrm{ex}} = 0$ but $A_{\mathrm{so}} = P_{\mathrm{so}}$. In the second case, $I_{\pm\pm} = I_{\mp\mp}$ leads to $P_{\mathrm{so}} = 0$ and $A_{\mathrm{so}} = 0$ but $A_{\mathrm{ex}} = P_{\mathrm{ex}}$. Now consider 'perfect' dichroism, i.e. $A_{\mathrm{un}} = \pm 1$. For $A_{\mathrm{un}} = 1$ one has $I_+ \neq 0$, $I_- = 0$, and $A_{\mathrm{so}} = A_{\mathrm{ex}} = P_{\mathrm{so}} + P_{\mathrm{ex}}$; for $A_{\mathrm{un}} = -1$, $I_+ = 0$, $I_- \neq 0$, and $A_{\mathrm{so}} = -A_{\mathrm{ex}} = P_{\mathrm{so}} - P_{\mathrm{ex}}$. In conclusion, $A_{\mathrm{un}}$ is the commonly used spin-averaged asymmetry, whereas $A_{\mathrm{so}}$ and $A_{\mathrm{ex}}$ probe asymmetries which can be attributed to SOC and exchange splitting, respectively, if the dichroism is rather small. The asymmetries defined above can thus be regarded as generalizations of spin polarizations to the case of magnetic dichroism.

Sometimes it is stated that MD can be used as a substitute for spin-resolved measurements (for a discussion see [50]), possibly with the ulterior motive of achieving information on the spin polarization $P_{\mathrm{ex}}$ from the spin-averaged asymmetry $A_{\mathrm{un}}$ (the apparent advantage of MD measurements is the much higher count rate with respect to that in spin-resolved experiments). Considering (4), this is impossible, because the three asymmetries are linearly independent. Further, the expression for $A_{\mathrm{un}}$ contains neither $P_{\mathrm{ex}}$ nor $P_{\mathrm{so}}$. Therefore, in order to obtain the ESP one has to measure $A_{\mathrm{ex}}$ or $A_{\mathrm{so}}$, which requires spin resolution. Nevertheless, we shall briefly analyse our results for spin-resolved MLD with regard to the relations of the asymmetries to the ESPs (see section 3.3 below).

## 3. Results and discussion

In the following we present and discuss results for 2 ML fcc Co on Cu(001) which have been obtained by the spin-polarized relativistic layer-KKR method sketched in section 2.1. First, we turn to the electronic valence band structure which is essential for understanding the photoemission results (sections 3.2 and 3.3).

### *3.1. Electronic structure of 2 ML Co on Cu(001)*

In figure 1 the spin- and layer-resolved Bloch spectral function $A_{\mathrm{B}}(E, \boldsymbol{k}_{\parallel})$ is shown for $\boldsymbol{k}_{\parallel} = 0$ and concentration $x$ varied from 0 ($T = 0$) to 0.5 ($T = T_{\mathrm{C}}$). Due to SOC, spin is not a good quantum number and, hence, the spin polarization of individual states is not equal to $\pm 1$. Despite this, we use the terms 'majority' and 'minority' because in general the spin polarization is rather close to +1 (majority) or $-1$ (minority). Exceptions are for example states near spin–orbit-induced band gaps (see e.g. [51]).

We first address the case $x = 0$; cf. the uppermost curves in figure 1.

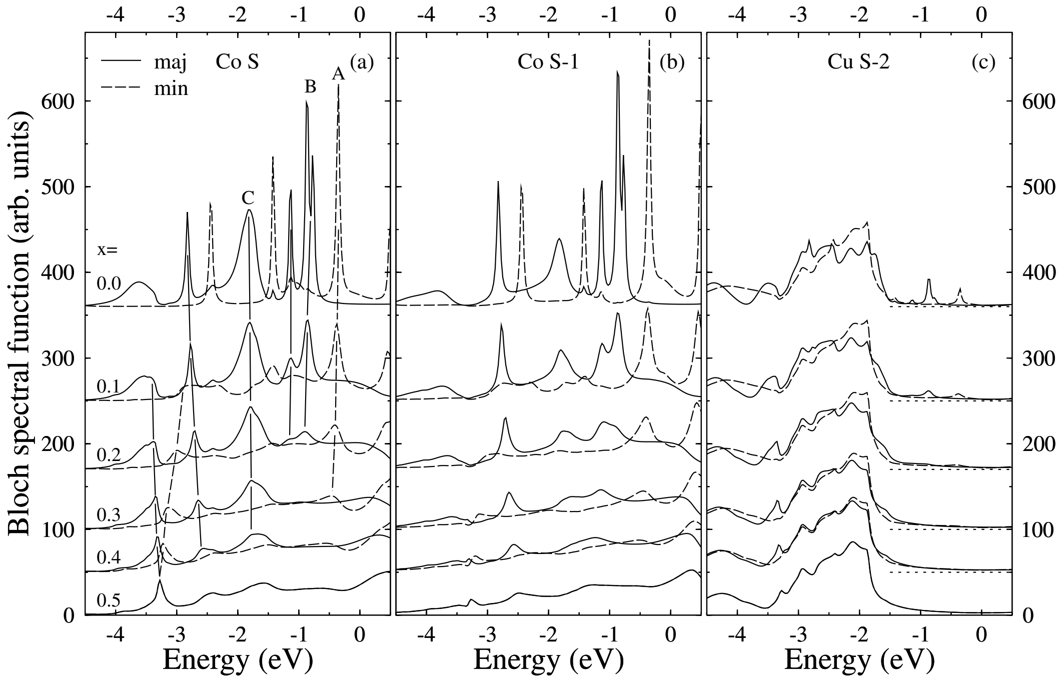

**Figure 1.** The spin- and layer-resolved Bloch spectral function of 2 ML Co on Cu(001) for $\boldsymbol{k}_{\parallel} = 0$ and concentrations $x = 0.0, \ldots, 0.5$, as indicated in (a). Majority-spin ('maj', ——) and minority-spin ('min', - - - -) projections are shown for the three outermost layers: Co S (a), Co S − 1 (b), and Cu S − 2 (c). In (a) maxima discussed in the text are connected by lines to guide the eye, three of them labelled A, B, and C. The respective zero abscissae are marked by dotted (· · · · · ·) lines in (c). The Fermi energy is 0 eV. For $x = 0.5$, the majority and minority curves coincide.

Due to the reflection at the Co/Cu interface and at the surface barrier, electrons become confined to the Co film and thus show up as spin-split quantum-well states (QWSs) and quantum-well resonances in the Co layers S and S − 1 (cf. panels (a) and (b)). Within the sp-band range of Cu, i.e. at energies larger than $\approx -1.8$ eV, there is a strong minority state at $-0.35$ eV (labelled A in panel (a)). A majority double maximum is found at $-0.78$ eV and $-0.84$ eV (labelled B). Distinct traces of these QWSs are visible in the adjacent Cu layer S − 2 (panel (c)). Another important majority-spin state is indicated by the rather broad maximum at $-1.83$ eV which is resonant with the d bands of Cu (labelled C). The spin polarization of the individual states in the Co film can easily be derived from the bulk band structure of fcc Co [52].

With increasing concentration $x$ the sharp maxima become smeared out, which can be explained by the CPA. Within this approximation, the BSF is given by a sum of concentration-weighted terms which either depend explicitly on the actual $\boldsymbol{k}_{\parallel}$ or which include averaging over reciprocal space [14, 15]. For $x = 0$ the $\boldsymbol{k}_\parallel$-averaged terms cancel and one is left with the sharp maxima at $\boldsymbol{k}_\parallel = 0$. Upon increasing $x$ the $\boldsymbol{k}_\parallel$-averaged terms become mixed in and thus lead to broadening of the peaks.

The Co states within the Cu sp-band range become rather continuously smeared out with increasing $x$. However, there are states whose BSF depends strongly on the concentration. For example the minority state at $-2.45$ eV (panel (a)) shows a high density of states for $x = 0$ but has practically disappeared for $x = 0.1$. Its majority partner at $-2.83$ eV, however, can be traced even up to $x = 0.4$ (cf. the guiding lines in panel (a)). On the other hand, one can find states which show sharp maxima for $x = 0.5$ but broad ones at $x = 0.0$, for example in layer S the peak at $-3.28$ eV.

For $x = 0.5$ the spin polarization of all layers vanishes because the net magnetic moment is zero ($T = T_C$, paramagnetic case). In a Stoner-type model one would expect majority and minority maxima to merge with decreasing exchange splitting. The maxima in the BSF do indeed show a slight dispersion with $x$ (cf. the lines to guide the eye in panel (a)). Majority maxima disperse to higher energies, minority ones to lower energies, as expected. A very clear example of peak merging is found in layer S at $-3.28$ eV for $x = 0.5$: with decreasing $x$ this maximum splits into two with opposite spin orientations. Note that the dispersion is non-symmetric, i.e. the majority peak shows less dispersion than its minority partner ($\approx$0.12 eV versus $\approx$0.38 eV). This behaviour can be attributed to the Cu band structure. The latter affects the reflection properties at the Co/Cu interface—in particular the phase shift—in a spin- and energy-dependent manner [53]. These reflection properties determine the energy positions of the QWSs: viewing the Co film as an interferometer [54], a QWS occurs at an energy at which the round-trip criterion is fulfilled, i.e. the phase accumulated in a round-trip is an even multiple of $\pi$. There are no further sharp maxima in layers S and $\mathrm{S} - 1$ for $x = 0.5$. The individual peaks at $x = 0$ cannot be traced well to $x = 0.5$ because of the broadening and decay of the spectral weight upon increasing $x$. However, from figure 1 it is evident that there is dispersion with $x$, but it is difficult to strictly evidence merging of maxima.

Summing up, our results for the spin- and layer-resolved BSF at various concentrations $x$ reveal splitting, broadening, and in some cases merging of individual electronic states in the Co film. The individual maxima show a rather different behaviour as regards the spectral weight: some depend rather strongly on $x$, while others do not. In the following we turn to the temperature dependence of the photoemission and discuss whether the findings for the BSF can also be observed in the spin-resolved intensities.

### *3.2. Spin-resolved photoemission from 2 ML Co on Cu(001)*

Spin-resolved experimental data for 2.5 ML Co/Cu(001) were recorded for s-polarized light at 45 eV photon energy and normal emission ($\boldsymbol{k}_\parallel = 0$) by Clemens *et al* [29] (cf. the bottom spectra in figure 2). The spectra were taken at room temperature, which corresponds to $T \approx 0.65\ T_C$ with $T_C(2.5\ \mathrm{ML}) \approx 465$ K according to [2]. Note that in this set-up there is no magnetic dichroism because $P_{\mathrm{so}}$ vanishes [55]. The main question that arises is that of whether our theoretical approach which neglects magnetic SRO is able to reproduce the experimental data or whether magnetic SRO has to be taken into account.

In the current set-up the electric field vector of the s-polarized light is parallel to the surface plane and lies within a mirror plane of the solid. Therefore, only transitions from initial states of the representations $\Delta_5^\pm$ to the $\Delta_1^\pm$ final states are allowed [55] (here we prefer the more familiar but strictly speaking incorrect notation of single-group representations combined with a spin index instead of that of magnetic double groups).

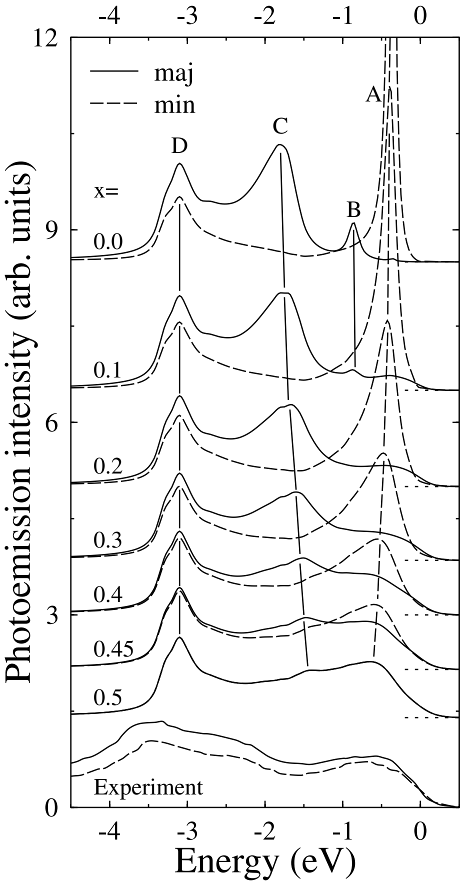

**Figure 2.** Spin-resolved photoemission intensities for 2 ML Co on Cu(001) for normal emission ($\boldsymbol{k}_{\|} = 0$) and concentrations $x = 0.0, \ldots, 0.5$. The photon energy of the s-polarized light is 45 eV. Majority ('maj') and minority ('min') spin projections are indicated by full (——) and dashed (- - - -) lines, respectively, whereas the zero abscissae are marked by dotted (· · · · · ·) lines. Maxima discussed in the text are denoted as A–D; almost vertical lines serve to guide the eye. The experimental spectra for 2.5 ML Co on Cu(001) were taken at room temperature (reproduced from [29]). Note that there is no magnetic dichroism in this set-up. The Fermi energy is 0 eV.

Before discussing the ESP in more detail we have to sketch its origins. As mentioned above, the spin–orbit-induced part $P_{\mathrm{so}}$ of the ESP vanishes in the current set-up and we are therefore concerned only with its exchange-induced part $P_{\mathrm{ex}}$. The valence electrons in the Co film are spin polarized and this polarization is transferred in the excitation process to that of the outgoing photoelectrons (note that the ESP of the photoelectrons is *not* identical to those of the valence electrons, due to matrix-element effects). The valence electrons in the Cu substrate, however, are not spin polarized, and, hence, neither are the photoelectrons in the substrate. These photoelectrons have to pass the magnetic Co film on their path to the detector, and the spin-dependent transmission of the latter induces a spin polarization of the outgoing electrons. In turn, if one produces spin-polarized photoelectrons in the non-magnetic substrate, e.g. by optical orientation, the magnetic film can be exploited as a spin detector [56]. Summing up, the spatial origin of the photoelectrons—either the Co film or the Cu substrate—is reflected by two different mechanisms for producing ESP. And further, the latter should differ considerably in their temperature dependence since in the first case both initial and final states are affected by $T$ whereas in the other only the final states are affected.

The top curves in figure 2 are theoretical spin-resolved spectra for concentration $x = 0$. At $-0.35$ eV the minority QWS A (cf. panel (a) in figure 1) gives rise to a very strong intensity maximum, whereas the majority QWS B at $-0.84$ eV shows up as a comparably small peak (the 'matrix-element effect'). The rather broad majority maximum $C$ at $-1.85$ eV is related to that in the BSF. In contrast to these spectral features which show strong ESP, the maximum D at $-3.10$ eV contains considerable contributions from both spin orientations. Since the BSF at this energy is very small in the Co layers but comparably large in the Cu layers, it seems likely that D is due to emission from the Cu substrate. Its spin polarization can thus be attributed to the Co-induced magnetic moments in the Cu layers at the Co/Cu interface or to the spin-dependent transmission of the photoelectron through the Co film ('spin filter'). But since the magnetic moment induced in Cu layer S $-$ 2 is too small (0.02 $\mu_\mathrm{B}$) to be regarded as responsible for the D ESP of about 20%, the ESP can be attributed unambiguously to the spin-dependent transmission through the Co film.

The origin of peak D becomes even more evident when considering the temperature dependence of the intensity: with increasing concentration $x$ there is no shift in energy of this particular maximum because the electronic structure in the substrate does not depend on $x$ (of course, the electronic structure of the Cu layers near the Co/Cu interface slightly depends on $x$ due to the Co film; see panel (c) in figure 1). The most prominent effect is a reduction of the spin polarization which vanishes for $x = 0.5$. As in the BSF (figure 1), QWSs A and C show no significant intensity maximum for $x = 0.5$. Their intensity drops rapidly upon increasing $x$, in contrast to that of the Cu-related state D. Further, A and C disperse with $x$: those maxima with majority spin orientation (C) to higher energies, those with minority spin orientation (A) to lower energies (cf. the guiding lines in figure 2). For example, C disperses by approximately 0.3 eV, A by $-0.2$ eV. These dispersions are considerably larger than those obtained from the BSF (from figure 1 one can extract for A and C $-0.09$ eV and 0.04 eV, respectively) which nicely confirms that there is no strict one-to-one correspondence between maxima in the BSF and those in the photoemission spectra. This 'dispersion feature' can be attributed to the broadening of maxima A and C: we recall that the intensity of the photoemission from a QWS shows a maximum right at its binding energy, even if the $k_\perp$-selection is weak for ultrathin films [52]. With increasing $x$, QWSs become 'less well defined' in energy due to the mixing in of $\boldsymbol{k}_\parallel$-averaged contributions and, thus, a shift in the photoemission maximum via the $k_\perp$-selection may occur.

In order to compare our theoretical results with the experimental ones, we first recall that the experiment has been carried out for a 2.5 ML film. Thus, the positions and intensities of the Co-related peaks might differ from those for a 2.0 ML film due to the excess of 0.5 ML Co. The Cu-related peak D is about 0.5 eV too high in energy compared to experiment which can be explained by shortcomings of the local density approximation used in the *ab initio* calculations. An extension to a non-local density approximation shifts the Cu d bands by about 0.5 eV to lower energies and gives almost perfect agreement with experimental data for Cu(111) [57]. Despite this shortcoming, the theoretical spectrum for $x = 0.45$ corresponds rather well to the experimental one as regards the number of maxima, the intensity relations of the individual maxima, and the spectral shape near $E_\mathrm{F}$. In particular, the relative heights of the intensity peaks from QWS A and that of the Cu d-band peak D agree well and illustrate clearly the failure of describing the experiment by the zero-temperature theory. The most striking difference is that in experiment the majority spectrum exceeds the minority spectrum over the whole energy range. A definitive explanation of this feature is still lacking (for a brief discussion see [28]).

Comparing the results for $x = 0$ with those obtained by Reiser *et al* we find good agreement (cf. figure 2 in [28]). The small differences in the intensity relations between the individual maxima can be traced back to differences in the parameters—for example, electron and hole lifetimes—and approximations in the transition-matrix elements in the work of Reiser *et al.* Even our spectra for $x \approx 0.45$ obtained within the DLM picture compare well with those of Reiser *et al* for $\langle m(T)\rangle = 0.2\,m(0)$ and moderate correlation length $\Lambda(T)$ obtained within the FLM picture. In summary, the different methods used—the *ab initio* layer-KKR method combined with CPA versus the empirical tight-binding method combined with a real-space cluster approach—give essentially the same results if the spin–spin correlation length $\Lambda(T)$ is small, i.e. if magnetic SRO can be neglected.

Another aspect seems worth mentioning. Our results and those of Reiser *et al* agree with experiment if the net magnetization is rather low: $\langle m(T)\rangle \approx 0.2\,m(0)$ or $x \approx 0.45$, i.e. if $T$ is very close to $T_C$. The experimental data were recorded at a temperature $T \approx 0.65\,T_C$ which is not too close to $T_C$. This apparent discrepancy might be explained by imperfections of the film (e.g. defects and interdiffusion) which lower the actual Curie temperature in experiment. As noted in [2], the magnetism of ultrathin films—and therefore their $T_C$—is rather sensitive to the preparation conditions (see also [58] for Gd/W(110)).

The electron spin polarization obtained from the spectra of figure 2 is shown in figure 3. As mentioned above, the ESP is due solely to exchange splitting. Its global shape can be described as of moderate majority character at the Cu-related emissions (around D), of strong majority character around the Co quantum-well resonance C, and of strong minority character at the Co QWS A. The fact that maximum B shows identifiable intensity only for $x = 0.0$ and 0.1 is also reflected in the ESP. A strong maximum appears for $x = 0.0$ which for $x = 0.1$ shows up as a shoulder and has disappeared for larger $x$. The ESP of the other states, A, C, and D, can be traced clearly over the whole range of concentration, allowing a discussion of the concentration dependence.

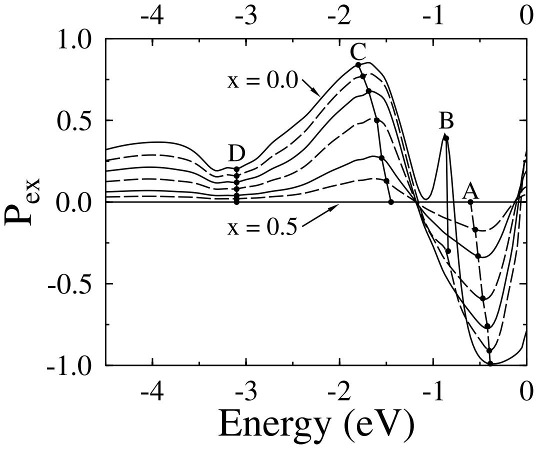

**Figure 3.** Spin polarization of the photocurrent from 2 ML Co on Cu(001) for normal emission, as obtained from the theoretical spectra of figure 2. For concentrations $x = 0.0, \ldots, 0.5$ the line styles alternate between full (——) and dashed (- - - -). For a better orientation, the polarizations of maxima A–D from figure 2 are indicated by lines to guide the eye and dots. The Fermi energy is 0 eV.

As argued above, the different origins of the states A, C, and D should also be reflected in differences in the temperature dependences of the photo-ESP (cf. the dots in figure 3 and figure 4). In order to achieve quantitative results we fitted the ESP of maxima A, C, and D obtained for the set of concentrations $x$ to a phenomenological power law

$$P_{ex}(x) = P_{ex}(0)[1 - (2x)^b]$$

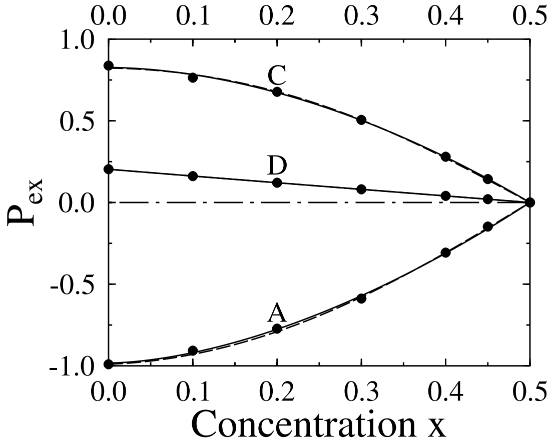

**Figure 4.** The dependence of the spin polarization $P_{\mathrm{ex}}$ for maxima A, C, and D as obtained from figure 3 on the concentration $x$ (dots). The lines show fits of $P_{\mathrm{ex}}(x)$ (——) and of $\widetilde{P}_{\mathrm{ex}}(x)$ (- - - -)—see the text—to the numerical data with the parameters $P_{\mathrm{ex}}(0)$, $b$, $\widetilde{P}_{\mathrm{ex}}(0)$, and $\tilde{b}$ taken from table 1.

and to

$$\widetilde{P}_{\mathrm{ex}}(x) = \widetilde{P}_{\mathrm{ex}}(0)[(1-x)^{\tilde{b}} - x^{\tilde{b}}]/[(1-x)^{\tilde{b}} + x^{\tilde{b}}]$$

for $x \in [0, \ldots, 0.5]$ (cf. the lines in figure 4). As can be seen from figure 4, the fits are almost perfect, with $\widetilde{P}$ yielding a slightly better fit. The results for $P_{\mathrm{ex}}(0)$, $b$, $\widetilde{P}_{\mathrm{ex}}(0)$, and $\tilde{b}$ are given in table 1. For A and C we obtain exponents $b$ and $\tilde{b}$ which differ considerably from those for D, i.e. the latter indicate an almost perfect linear dependence over the whole range of concentrations. Critical exponents $\beta$ for the ESP can be obtained by considering $\lim_{x\to 0.5} \alpha(1-2x)^{\beta}$. Expansion of both $P_{\mathrm{ex}}(x)$ and $\widetilde{P}_{\mathrm{ex}}(x)$ in Taylor series around $x = 0.5$ gives $\beta$-values very close to 1 for all three peaks.

**Table 1.** Parameters describing the dependence of the electron spin polarization for peaks A, C, and D on the concentration $x$. The values of $P_{\mathrm{ex}}(0)$, $b$, $\widetilde{P}_{\mathrm{ex}}(0)$, and $\tilde{b}$ have been obtained by fitting the numerical data to $P_{\mathrm{ex}}(x)$ and to $\widetilde{P}_{\mathrm{ex}}(x)$ (see the text) for $x \in [0, \ldots, 0.5]$.

| Peak | $P_{\mathrm{ex}}(0)$ | $b$ | $\widetilde{P}_{\mathrm{ex}}(0)$ | $\tilde{b}$ |
|---|---|---|---|---|
| A | −0.98 | 1.70 | −0.98 | 1.58 |
| C | 0.83 | 1.84 | 0.82 | 1.69 |
| D | 0.20 | 0.98 | 0.20 | 0.99 |

Summing up, the behaviours of the maxima in the BSF, e.g. the dispersion, broadening, and merging, show up also in the spin-resolved photoemission intensities. The spatial origin of individual peaks, Co film or Cu substrate, can be discriminated by considering their ESPs. Also, the theoretical spectra compare reasonably well with their experimental counterparts.

### *3.3. Magnetic linear dichroism for 2 ML Co on Cu(001)*

Magnetic dichroism in angle-resolved photoemission is the change of the photocurrent upon magnetization reversal. In the case of magnetic linear dichroism (MLD) in angular distribution, the incoming light is linearly polarized, in contrast to magnetic circular dichroism, for which the light is circularly polarized. In the standard set-up of MLD, p-polarized light impinges off-normally onto the sample, and the photoelectrons are detected in normal emission. The surface-parallel magnetization direction $\boldsymbol{M}$ is normal to the reaction plane which is spanned by the directions of the light incidence and the electron emission. For magnetization orientations $\pm\boldsymbol{M}$ one records the photocurrents $I(\pm\boldsymbol{M})$. Or, equivalently, one fixes the magnetization and changes the azimuth of light incidence by 180°, the associated electric field vectors being denoted as $\boldsymbol{p}_+$ and $\boldsymbol{p}_-$. The spin-averaged asymmetry then reads

$$A_{\mathrm{un}} = [I(\boldsymbol{p}_+) - I(\boldsymbol{p}_-)]/[I(\boldsymbol{p}_+) + I(\boldsymbol{p}_-)]$$

where $I(\boldsymbol{p}_\pm)$ are the photocurrents recorded for $\boldsymbol{p}_\pm$ light incidence (cf. also (3)). Note that $I(\pm\boldsymbol{M}, \boldsymbol{p}_\pm) = I(\mp\boldsymbol{M}, \boldsymbol{p}_\mp)$. Since the surface-parallel component of the electric field vector mediates excitations from the $\Delta_5^\pm$ initial states, its surface-normal component allows for excitations of the $\Delta_1^\pm$ initial states. Thus, we expect additional maxima in the MLD spectra with respect to those presented in figure 2.

In contrast to the case of s-polarized light, there is now an ESP component perpendicular to the reaction plane (i.e. parallel to the magnetization) which is due to SOC (see [30] and references therein) and therefore is present even at $x = 0.5$. The 'general rule' of MD states that if in the non-magnetic case ($x = 0.5$) there is a non-zero ESP component and if in the ferromagnetic case ($x < 0.5$) there is a magnetization component parallel to this ESP component, then there will be MD in the ferromagnetic case.

In order to investigate the temperature dependence of the standard MLD for ultrathin films, we performed the same calculations as in section 3.2 but with the light chosen in accordance with the set-up described above. The photoemission spectra $I(\boldsymbol{p}_\pm)$ for $x = 0$ are shown at the top of figure 5. Besides changes in the intensities and the occurrence of the additional maximum E which is due to a $\Delta_1$ initial state, the most important difference from the spectra in figure 2 is the dichroism. The maxima show the same general trends with increasing concentration $x$

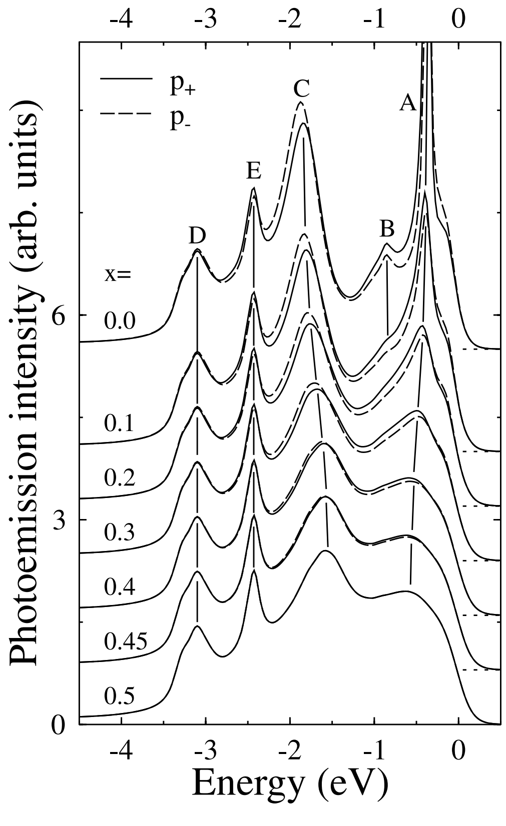

**Figure 5.** Magnetic linear dichroism (MLD) for 2 ML Co on Cu(001) for normal emission ($\boldsymbol{k}_\parallel = 0$). In the standard set-up for MLD, p-polarized light with photon energy 45 eV impinges at a 45° polar angle onto the surface. For concentrations $x = 0.0, \ldots, 0.5$, the photoemission intensities for incidence directions $\boldsymbol{p}_+$ (——) and $\boldsymbol{p}_-$ (- - - -) are shown, with zero abscissae marked by dotted (······) lines. The maxima discussed in the text are denoted as A–E; almost vertical lines serve as guides to the eye. The Fermi energy is 0 eV.

as in figure 2, in particular broadening and dispersion. Exceptions are features D and E which remain sharp and show no dispersion, both hints of their Cu origin.

In figure 6, the contributions $P_{\mathrm{so}}$ and $P_{\mathrm{ex}}$ to the ESP are shown. The exchange-induced part $P_{\mathrm{ex}}$ shows essentially the same global shape as in figure 3, and the spin–orbit-induced part $P_{\mathrm{so}}$ does not vanish for $x = 0.5$. Since for 3d transition metals the spin–orbit interaction is small compared to the exchange interaction, $P_{\mathrm{ex}}$ is much larger in absolute value than $P_{\mathrm{so}}$. At energies less than $-2.2$ eV, $P_{\mathrm{so}}$ is virtually independent of $x$ which can be attributed to the fact that emissions in that energy range stem almost exclusively from the Cu substrate.

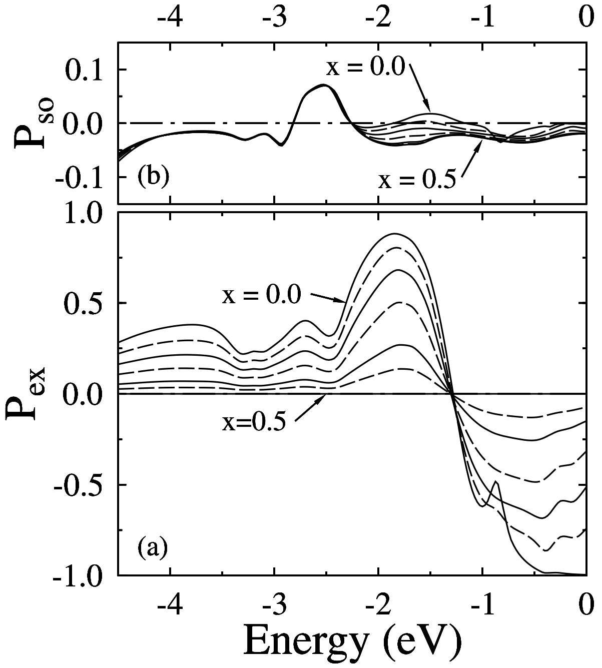

**Figure 6.** Spin polarizations of the photocurrent from 2 ML Co on Cu(001) for normal emission, as obtained from the theoretical spectra of figure 5. The exchange-related ($P_{\mathrm{ex}}$, (a)) and the spin–orbit-related ($P_{\mathrm{so}}$, (b)) spin polarizations are calculated according to (1) for concentrations $x = 0.0, \ldots, 0.5$, as indicated. Note the different ordinate scales. The Fermi energy is 0 eV.

We now discuss the $x$-dependence of the asymmetries which have been introduced in section 2.2. In figure 7 the spin-averaged ($A_{\mathrm{un}}$), the spin–orbit-related ($A_{\mathrm{so}}$), and the exchange-related ($A_{\mathrm{ex}}$) spin asymmetries are shown. Because the dichroism and $P_{\mathrm{so}}$ are comparably small (both $A_{\mathrm{un}}$ and $P_{\mathrm{so}}$ are less than 10% in absolute value), $A_{\mathrm{ex}} = P_{\mathrm{ex}} + P_{\mathrm{so}}A_{\mathrm{un}}$ coincides almost perfectly with $P_{\mathrm{ex}}$ (cf. panel (a) in figure 6). As mentioned above, for $x = 0.5$ we have $P_{\mathrm{ex}} = A_{\mathrm{ex}} = 0$ and thus $A_{\mathrm{so}} = P_{\mathrm{so}}$. Upon decreasing $x$, $P_{\mathrm{ex}}$ becomes mixed into $A_{\mathrm{so}} = P_{\mathrm{so}} + P_{\mathrm{ex}}A_{\mathrm{un}}$. Therefore, one observes a rather strong effect on $A_{\mathrm{so}}$ at energies at which $A_{\mathrm{un}}$ is changed considerably, for example at energies higher than $\approx -2.5$ eV and in particular at $-0.5$ eV (note that this is the energy range of Co-related emissions). At lower energies, $A_{\mathrm{so}}$ is virtually independent of $x$ because in this energy range $A_{\mathrm{un}}$ is also very small.

We now briefly analyse our spin-resolved results with regard to relations between the spin asymmetries and the ESPs. For example, at those energies where $A_{\mathrm{un}} = 0$, both $A_{\mathrm{so}}$ and $A_{\mathrm{ex}}$ are in general non-zero and show negative as well as positive values. Further, one could hope that $A_{\mathrm{ex}}$ would govern the behaviour of the other asymmetries. But $A_{\mathrm{ex}}$ shows a general +/− shape which is reflected neither in $A_{\mathrm{so}}$ nor in $A_{\mathrm{un}}$. Summarizing briefly, we would like to emphasize

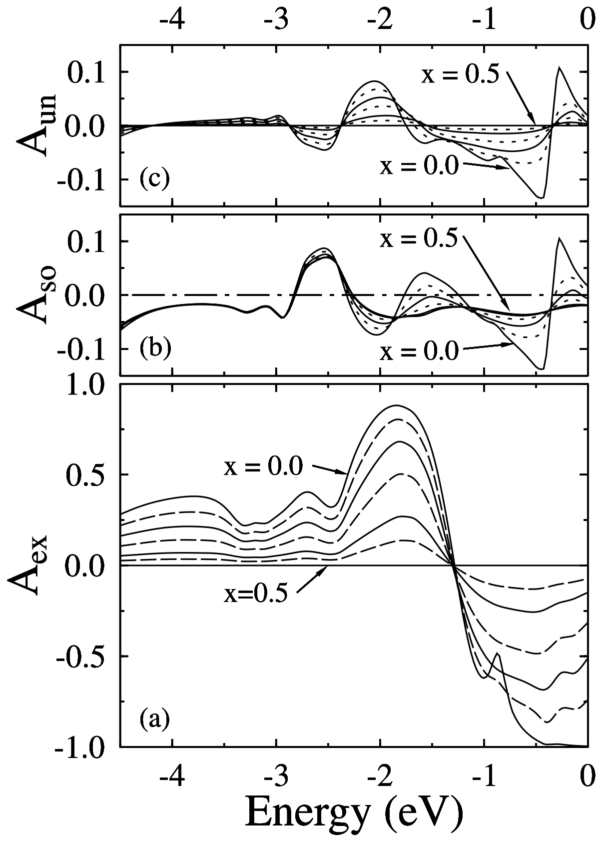

**Figure 7.** Asymmetries of the photocurrent from 2 ML Co on Cu(001) for normal emission, as obtained from the theoretical spectra of figure 5. The exchange-related ($A_{ex}$, (a)), the spin–orbit-related ($A_{so}$, (b)), and the spin-averaged ($A_{un}$, (c)) asymmetries are calculated according to (3) for concentrations $x = 0.0, \ldots, 0.5$, as indicated. Note the different ordinate scales. The Fermi energy is 0 eV.

that MD and spin-resolved photoemission complement each other [50]. Therefore, it appears desirable from our point of view to perform a more complete experiment or calculation, e.g. one based on spin-resolved instead of spin-averaged MD.

Finally, the 'critical exponents' of the spin asymmetries are discussed very briefly. As for $P_{ex}$ in the case of s-polarized light, we find a perfect linear dependence on $x$ of $A_{un}$ for maxima D and E which again evidences the bulk origin of the respective initial states. For states A and C the $x$-dependence is monotonic but cannot be fitted well with a power law.

## 4. Conclusions

For the prototypical system 2 ML Co on Cu(001) we carried out relativistic *ab initio* layer-KKR calculations in order to investigate the temperature dependences of the electronic structure and spin-resolved (dichroic) photoemission within the disordered local moment picture.

In particular, for quantum-well states in the Co film, our results show distinct dispersion, broadening, and in some cases merging with temperature in the Bloch spectral function and in the photocurrent. In contrast, Cu-derived maxima show no dispersion and significantly different dependences of both the electron spin polarization and the magnetic linear dichroism.

We would like to stress that this can be used in experiments to discriminate between Cu- and Co-derived states. Further, the spin-resolved photoemission intensities compare well with experimental data and other theoretical ones, the latter obtained within the fluctuating local moment picture.

As an extension of the present study one might think of treating the spin–spin correlation within the FLM picture, i.e. taking into account magnetic short-range order. This can be done for example within the real-space KKR approach. We hope that the present study will prompt experimental investigations of the temperature dependence of magnetic dichroism in valence band photoemission.

## Acknowledgments

Fruitful discussions with Yonko T Millev are gratefully acknowledged. We are also grateful to Arthur Ernst for help with the self-consistent computations.

## References

[1] Campagna M and Rosei R (ed) 1990 *Photoemission and Absorption Spectroscopy of Solids and Interfaces with Synchrotron Radiation* (Amsterdam: North-Holland)
[2] Schneider C M, Bressler P, Schuster P, Kirschner J, de Miguel J J and Miranda R 1990 *Phys. Rev. Lett.* **64** 1059
[3] Crangle J 1955 *Phil. Mag.* **46** 499
[4] Huang F, Kief M T, Mankey G J and Willis R F 1994 *Phys. Rev.* B **49** 3962
[5] Duke C B and Laramore G E 1970 *Phys. Rev.* B **2** 4765
[6] Laramore G E and Duke C B 1970 *Phys. Rev.* B **2** 4783
[7] Nolting W, Braun J, Borstel G and Borgiel W 1990 *Phys. Scr.* **41** 601
[8] Braun J, Nolting W and Borstel G 1991 *Surf. Sci.* **251/252** 22
[9] Braun J, Borstel G and Nolting W 1992 *Phys. Rev.* B **46** 3510
[10] Chen C 1993 *Phys. Rev.* B **48** 1318
[11] Soven P 1967 *Phys. Rev.* **156** 809
[12] Faulkner J S and Stocks G M 1980 *Phys. Rev.* B **21** 3222
[13] Durham P J, Gyorffy B L and Pindor A J 1980 *J. Phys. F: Met. Phys.* **10** 661
[14] Gonis A 1992 *Green Functions for Ordered and Disordered Systems (Studies in Mathematical Physics vol 4)* (Amsterdam: North-Holland)
[15] Weinberger P 1990 *Electron Scattering Theory of Ordered and Disordered Matter* (Oxford: Clarendon)
[16] Gyorffy B L, Pindor A J, Staunton J, Stocks G M and Winter H 1985 *J. Phys. F: Met. Phys.* **15** 1337
[17] Staunton J, Gyorffy B L, Pindor A J, Stocks G M and Winter H 1985 *J. Phys. F: Met. Phys.* **15** 1387
[18] Durham P J 1981 *J. Phys. F: Met. Phys.* **11** 2475
[19] Durham P J, Staunton J and Gyorffy B L 1984 *J. Magn. Magn. Mater.* **45** 38
[20] Weinberger P, Dirl R, Boring A M, Gonis A and Freeman A J 1988 *Phys. Rev.* B **37** 1383
[21] Haines E M, Heine V and Ziegler A 1985 *J. Phys. F: Met. Phys.* **15** 661
[22] Haines E M, Heine V and Ziegler A 1986 *J. Phys. F: Met. Phys.* **16** 1343
[23] Haines E M 1985 *J. Comput. Phys.* **60** 353
[24] Gollisch H and Feder R 1989 *Physica* B **161** 169
[25] Gollisch H and Feder R 1989 *Solid State Commun.* **69** 579
[26] Gollisch H and Feder R 1990 *Solid State Commun.* **76** 237
[27] Delgadillo I, Gollisch H and Feder R 1994 *Phys. Rev.* B **50** 15 808
[28] Reiser D, Henk J, Gollisch H and Feder R 1995 *Solid State Commun.* **93** 231
[29] Clemens W, Kachel T, Rader O, Vescovo E, Blügel S, Carbone C and Eberhardt W 1992 *Solid State Commun.* **81** 739
[30] Feder R and Henk J 1996 *Spin–Orbit Influenced Spectroscopies of Magnetic Solids (Springer Lecture Notes in Physics vol 466)* ed H Ebert and G Schütz (Berlin: Springer) p 85
[31] Sirotti F, Panaccione G and Rossi G 1995 *Phys. Rev.* B **52** R17 063
[32] Schmitz D, Rader O, Carbone C and Eberhardt W 1996 *Phys. Rev.* B **54** 15 352
[33] Alders D, Vogel J, Levelut C, Peacor S D, Hibma T, Sacchi M, Tjeng L H, Chen C T, van der Laan G, Thole B T and Sawatzky G A 1995 *Europhys. Lett.* **32** 259

[34] Weber W, Bischof A, Allenspach R, Back C, Fassbender J, May U, Schirmer B, Jungblut R, Güntherodt G and Hillebrands B 1996 *Phys. Rev.* B **54** 4075

[35] Ramsperger U, Vaterlaus A, Pfäffli P, Maier U and Pescia D 1996 *Phys. Rev.* B **53** 8001

[36] Fassbender J, Allenspach R and Dürig U 1997 *Surf. Sci.* **383** L742

[37] Perdew J P and Wang Y 1992 *Phys. Rev.* B **45** 13 244

[38] Niklasson A M N 1999 private communication

[39] Henk J, Scheunemann T, Halilov S V, Tamura E and Feder R 2000 *omni2k—Fully Relativistic Electron Spectroscopy Calculations*

The computer code is available from the authors. Electronic address: henk@mpi-halle.mpg.de.

[40] Ebert H, Freyer H and Deng M 1997 *Phys. Rev.* B **56** 9454

[41] Tamura E 1996 private communication

[42] Bruno E and Ginatempo B 1997 *Phys. Rev.* B **55** 12 946

[43] Chen C 1990 *Phys. Rev. Lett.* **64** 2176

[44] Chen C 1991 *Int. J. Mod. Phys.* B **5** 1147

[45] Chen C 1994 *Phys. Rev. Lett.* **73** 1982

[46] Chen C 1990 *Phys. Rev.* B **41** 5031

[47] Aryasetiawan F and Gunnarson O 1998 *Rep. Prog. Phys.* **61** 237

[48] Hedin L 1999 *J. Phys.: Condens. Matter* **11** R489

[49] Ernst A and Bruno P 2001 $GW$ approximation: KKR implementation, to be published

[50] Venus D, Kuch W, Lin M T, Schneider C M, Ebert H and Kirschner J 1997 *Phys. Rev.* B **55** 2594

[51] Rampe A, Güntherodt G, Hartmann D, Henk J, Scheunemann T and Feder R 1998 *Phys. Rev.* B **57** 14 370

[52] Henk J and Johansson B 1999 *J. Electron Spectrosc. Relat. Phenom.* **105** 187

[53] Dederichs P H, Wildberger K and Zeller R 1997 *Physica* B **237+238** 239

[54] Paggel J J, Miller T and Chiang T C 1999 *Science* **283** 1709

[55] Henk J, Scheunemann T, Halilov S and Feder R 1996 *J. Phys.: Condens. Matter* **8** 47

[56] Kuch W, Lin M T, Meinel K, Schneider C M, Noffke J and Kirschner J 1995 *Phys. Rev.* B **51** 12 627

[57] Courths R, Lau M, Scheunemann T, Gollisch H and Feder R 2000 From the Shockley surface state on Cu(111) to sp-like surface resonances on $\mathrm{Cu_3Au}(111)$ *Phys. Rev.* B submitted

[58] Farle M, Baberschke K, Stetter U, Aspelmeier A and Gerhardter F 1993 *Phys. Rev.* B **47** 11 571

## Publikation 9

# Quantum-size effects in photoemission from ultra-thin films: Theory and application to Cu-films on fcc-Co(001)

Jürgen Henk*, Börje Johansson

*Condensed Matter Theory Group, Physics Department, University of Uppsala, S-751 21 Uppsala, Sweden*

Received 22 February 1999; received in revised form 3 May 1999; accepted 4 May 1999

### Abstract

We report on detailed calculations of quantum-size effects on the electronic structure of the valence-band regime and their manifestation in photoemission. Model calculations reveal the basic features of photoemission from quantum-well states (QWS). First, emission from QWS shows intensity variations with photon energy which is similar to that of semi-infinite systems, despite the discrete binding energies of the QWS. Second, conservation of the wave-vector component normal to the surface is directly related to the film thickness. Numerical calculations within the relativistic one-step model of photoemission show that these effects should be observable in 'real' systems. This is demonstrated to be the case for Cu films on fcc-Co(001). © 1999 Elsevier Science B.V. All rights reserved.

*Keywords:* Angle-resolved photoemission; Ultra-thin films; Quantum-well states

## 1. Introduction

The availability of light sources with tunable photon energy, in particular synchrotron-radiation facilities, has had and still continues to have a great impact on electronic structure investigations of solids [1]. One of the most successful methods for the analysis of electronic states in the valence regime is angle-resolved photoemission using VUV light (For reviews on photoemission, see Refs. [2–5]). For fixed photo-electron detection angles, the experimentally obtained intensity maxima disperse in binding energy with photon energy. The interpretation of this behaviour is usually based on the very popular and successful direct-transition approximation which relates the energy position of the intensity maxima to the bulk-band structure $E(\boldsymbol{k})$. This relies on the assumption that the wave-vector $\boldsymbol{k}$ is conserved in the excitation process.

In the last years, ultra-thin films and multi-layers have become very popular because of their interesting and novel physical properties. In recent experimental works on films with a few layer thickness, the intensity maxima show dispersion – as in the bulk case – and can, surprisingly, be well described within the direct-transition model using bulk-band structures. This leads to the conclusion that even ultra-thin films 'show a (bulk) band structure' [6,7].

Regarding the dispersion, the experimental ob-

---

*Corresponding author. Present address: Max-Planck-Institut für Mikrostrukturphysik, Weinberg 2, D-06120 Halle (Saale), Germany.

servations become even more puzzling when films with identical number of layers but different crystallographic orientation on the same substrate material were observed to show different behaviour. Hansen and co-workers [8] found for 14 layers Cu on fcc-Co(111) a bulk-like dispersion in the Cu-*sp* states, but three quantized states with fixed energy for fcc-Co(100) and fcc-Co(110) substrates. This finding was explained by the Co-band structure: only in the latter two cases do the effective band gaps lead to a confinement of the valence electrons to the Cu films and thus to so-called quantum-well states [9]. Further, it was observed that for the (100)- and (110)-films the photoemission intensity from the quantum-well states shows a behaviour similar to that of semi-infinite Cu(100) or Cu(110), respectively. A closer inspection at the intensity variation may give hints, however, that the maxima show more structure in their dependence on both the binding energy and the photon energy (see Fig. 1 in Ref. [8]).

From a strict theoretical point of view, our statement above, namely that ‘ultra-thin films show a band structure’, appears to be questionable. A surface or an interface break the translational invariance normal to the layers which implies that the normal component $k_\perp$ of the wave-vector is not a good quantum number. Further, due to the confinement of the valence electrons to the film, the binding energies of the valence electrons become quantized: instead of a band structure one finds a series of quantum-well states, i.e. maxima in the Bloch spectral function, at discrete energies $E_i$. Thus, there should be no dispersion of the photoemission maxima. This means in turn that the direct-transition model cannot be applied – at least not in principle. This leaves the questions, (i) why there is an intensity variation like the one for semi-infinite solids and, (ii) whether this variation shows more structure, in particular additional maxima. So it appears necessary to solve the above discrepancy: the successful interpretation of experimental data using bulk-band structures versus its theoretical denial.

In the present paper, valence-band photoemission from ultra-thin films is analyzed using model calculations in order to reveal basic effects. Further, sophisticated calculations within the one-step model of photoemission based on multiple-scattering theory were performed in order to mimic the experiments as accurate as possible. As a system we choose Cu films on fcc-Co(001). Experimental [10–14] and theoretical [15] papers dealing with this system have focused mainly on the properties of the quantum-well states (e.g. binding energy and spin polarization) as a function of the film thickness. Usually such analyses were performed at a fixed photon energy. Here, we focus on a few film thicknesses, but extend the analysis to variable photon energy in order to work out the manifestation of quantum-size effects in photoemission.

This paper is organized as follows. In Section 2 we focus on a simple model for photoemission from ultra-thin films, in particular on basic features of quantum-well states and their appearance in photoemission. In Section 3 we turn to more sophisticated calculations for Cu films on fcc-Co(001). Concluding remarks are given in Section 4.

## 2. Simple theory of photoemission from ultra-thin films

There are two limits in which valence electrons in a film can be described (For recent work on quantized electronic states see for example Refs. [9,13,16–18]): (i) In a plane-wave representation, free electrons can be confined to a quantum well. Or (ii) in a tight-binding description, electrons are only allowed to hop within a finite number of layers. The prototypical realization of the latter model are rare-gas layers on a (metal) substrate [19]. In this paper, we apply a simple tight-binding model, the details of which are given below.

The film is represented by a linear chain oriented along the $z$ axis (perpendicular to the surface) with $n$ equidistant sites $i$, $i = 1, \dots, n$, with one orbital $\Phi(\boldsymbol{r} - ia\boldsymbol{e}_z)$ per site, $a$ denoting the inter-site distance [20–22]. The substrate is completely neglected. Thus, the elements of the Hamiltonian matrix $H^{(n)}$ read

$$H^{(n)}_{ij} = \epsilon\delta_{ij} + t\delta_{|i-j|,1}, \quad i,j = 1, \dots, n, \tag{1}$$

with on-site energies $\epsilon = \langle\Phi(\boldsymbol{r} - ia\boldsymbol{e}_z)|H^{(n)}|\Phi(\boldsymbol{r} - ia\boldsymbol{e}_z)\rangle$ and hopping energies $t = \langle\Phi(\boldsymbol{r} - ia\boldsymbol{e}_z)|H^{(n)}|\Phi(\boldsymbol{r} - (i+1)a\boldsymbol{e}_z)\rangle$. The overlap between orbitals located on different sites is assumed as zero. The eigenvalues of $H^{(n)}$ can be written as

$$\lambda_i^{(n)} = \epsilon + 2t\cos\left(k_i^{(n)}a\right), \quad i = 1, \ldots, n, \tag{2}$$

with $k_i^{(n)} = \pi i/[a(n+1)]$. For $n = 1$, we have the case of a single site with $\lambda_1^{(1)} = \epsilon$. In the limit $n \to \infty$, $k_i^{(n)}a$ is dense in $[0,\pi]$ and, thus, the eigenvalues $\lambda_i^{(n)}$ represent the bulk-band structure $E(k) = \epsilon + 2t\cos(ka)$, cf. Fig. 1. An eigenfunction $\Psi_i^{(n)}$ of $H^{(n)}$ with energy $\lambda_i^{(n)}$ can be written as

$$\Psi_i^{(n)}(\boldsymbol{r}) = \sum_{j=1}^{n} c_{ij}^{(n)} \Phi(\boldsymbol{r} - ja\boldsymbol{e}_z), \quad i = 1, \ldots, n, \tag{3}$$

the coefficients $c_{ij}^{(n)}$ of which can be calculated recursively by

$$c_{ij}^{(n)} = 2\cos\left(k_i^{(n)}a\right)c_{i,j-1}^{(n)} - c_{i,j-2}^{(n)}, \quad j = 2, \ldots, n, \tag{4}$$

with $c_{i0}^{(n)} = 0$ and $c_{i1}^{(n)} = 1$. The additional equation

$$2\cos\left(k_i^{(n)}a\right)c_{i,n}^{(n)} = c_{i,n-1}^{(n)} \tag{5}$$

ensures that $k_i^{(n)}$ has to be chosen properly. Strictly speaking, $k_i^{(n)}$ is not a wave number as it is in the case of Bloch functions because there is no translational symmetry and therefore no periodicity. Due to the inversion symmetry, the eigenstates $\Psi_i^{(n)}$ show the expected even–odd alternation and the number of nodes increases with $|k_i^{(n)}|$. There are no surface states due to the choice of the tight-binding parameters at the surfaces [20].

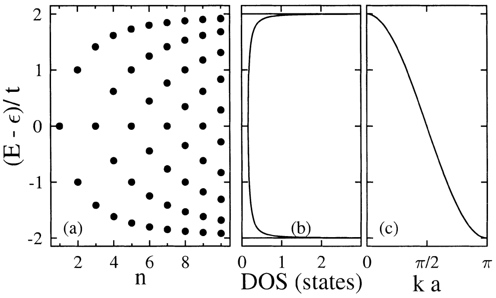

Fig. 1. Tight-binding electronic structure of linear chains. The tight-binding parameters are $\epsilon$ and $t$, cf. Eq. (1). (a) Eigenenergies $\lambda_i^{(n)}$ (dots; cf. Eq. (2)) of chains with $n = 1, \ldots, 10$ sites (left). (b) Density of states (DOS) of the infinite chain (middle). (c) Band-structure $E(k) = \epsilon + 2t\cos(ka)$ (right) of the infinite chain.

The photo-electron state $\Psi_\mathrm{f}$ can crudely be approximated by a single plane wave, $\Psi_\mathrm{f}(\boldsymbol{r}) = \exp(\mathrm{i}\boldsymbol{k}_\mathrm{f}\cdot\boldsymbol{r})$, as is often done in the interpretation of experimental data. This way, quantum-size effects in the upper band structure are ignored [23]. The wave vector $\boldsymbol{k}_\mathrm{f}$ is determined by both the position of the detector and the energy of the photo-electron, $E_\mathrm{f} \sim k_\mathrm{f}^2$. The photocurrent $I_i^{(n)}$ at photon energy $\mathrm{h}\nu$ from the initial-state $\Psi_i^{(n)}$ is given by the 'golden rule'

$$I_i^{(n)} \propto \left|\langle\Psi_i^{(n)}|\boldsymbol{E}\cdot\boldsymbol{r}|\Psi_\mathrm{f}\rangle\right|^2 \delta\left(E_\mathrm{f} - \mathrm{h}\nu - \lambda_i^{(n)}\right). \tag{6}$$

Inserting the above expressions for the wave functions and defining the Fourier-transformed atomic wave function $F(\boldsymbol{k})$ by $F(\boldsymbol{k}) = \int \Phi^\star(\boldsymbol{r}) \exp(\mathrm{i}\boldsymbol{k}\cdot\boldsymbol{r})\,\mathrm{d}^3r$, we obtain eventually

$$I_i^{(n)} \propto |\boldsymbol{E}\cdot\boldsymbol{k}_\mathrm{f}|^2 |F(\boldsymbol{k}_\mathrm{f})|^2 |\Delta_i^{(n)}(k_{\mathrm{f}z})|^2 \delta(E_\mathrm{f} - \mathrm{h}\nu - \lambda_i^{(n)}). \tag{7}$$

The function $\Delta_i^{(n)}(k)$, defined by

$$\Delta_i^{(n)}(k) = \sum_{j=1}^{n} c_{ij}^{(n)} \exp(\mathrm{i}kja), \tag{8}$$

determines considerably the dependence of the photocurrent on the photon energy and, thus, should be discussed in more detail. Obviously, $\Delta_i^{(n)}$ is periodic, i.e. $\Delta_i^{(n)}(k) = \Delta_i^{(n)}(k + 2\pi m/a)$, $m$ integer. In the case of a single site, $n = 1$, we have $|\Delta^{(1)}(k)| = 1$ and the photon-energy dependence of the photocurrent is determined by $F(\boldsymbol{k}_\mathrm{f})$ alone. In the bulk case, $n = \infty$, we obtain the well-known strict wave-vector conservation, $\Delta^{(\infty)}(k_{\mathrm{f}z}) = \delta(k_{\mathrm{f}z} - k)$, i.e. the direct-transition model.

Setting all $c_{ij}^{(n)} = 1$, leads to a geometrical series for $\Delta^{(n)}$ which can be easily summed up,

$$\Delta^{(n)}(k) = \begin{cases} n & \text{for } k = 0 \\ (q^n - 1)/(q - 1) & \text{otherwise'} \end{cases} \tag{9}$$

with $q = \exp(\mathrm{i}ka)$. Obviously, $\Delta^{(n)}$ shows $n - 1$ zeroes in $[0,2\pi]$ at $k = 2\pi i/n$ with $i = 1, \ldots, n-1$. Its absolute value increases with $n$ in the vicinity of $k = 0$ while it decreases in the interior of the interval $[0,2\pi]$. In short, $\Delta^{(n)}$ is an approximation to Dirac's $\delta$-functional (Fig. 2). The main intensity comes from the region around $k = 0$ (i.e. $k_{\mathrm{f}z} = k_i^{(n)}$), but addition-

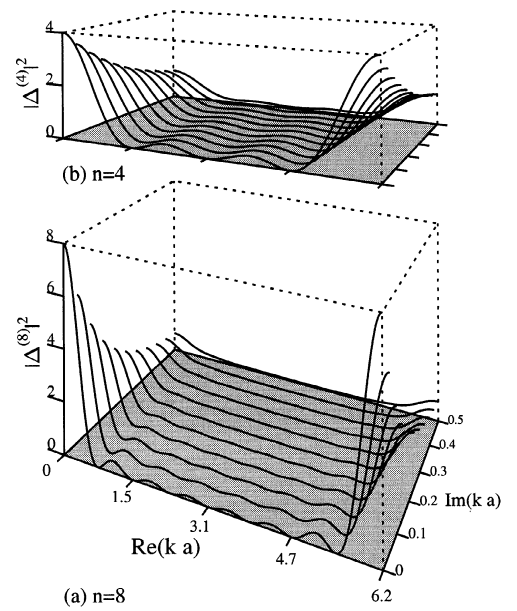

Fig. 2. The '$k$-conservation' function $|\Delta^{(n)}|^2$, as defined in Eq. (9), in dependence of complex wave number $k$ for linear chains with $n = 8$ (a, bottom) and $n = 4$ (b, top) sites.

al intensity maxima, which are due to oscillatory behaviour of $\Delta^{(n)}$, should occur.

So far, we have considered only the case of infinite life-time of the photo-electron. Introducing a finite life-time leads to a complex wave-number [24] which results in an additional weakening of $k$-conservation, as is also shown in Fig. 2. $\Delta^{(n)}$ decreases rapidly around $k = 0$ with increasing Im($k$) (as is evident from the geometrical series), but the oscillatory behaviour is still visible, except for very strong damping, e.g. Im($ka$) $= 0.5$ in Fig. 2b.

In Fig. 3, we compare photoemission from chains with length of five and ten sites. The intensities were obtained from Eq. (7) with $|\boldsymbol{E} \cdot \boldsymbol{k}_\mathrm{f}|^2 |F(\boldsymbol{k}_\mathrm{f})|^2$ set to 1, but $\Delta_i^{(n)}$ calculated with the coefficients $c_{ij}^{(n)}$ obtained from Eq. (4). At the bottom of each box, the initial-state band structure $E(k_\mathrm{fz})$ is shown (Note that $k_\mathrm{fz}$ is related to the photon energy h$\nu$ by $\boldsymbol{k}_\mathrm{f}^2 \sim \lambda_i^{(n)} + \mathrm{h}\nu$). The individual photoemission intensities show main maxima at wave numbers $k_i^{(n)}$, i.e. $E(k_\mathrm{fz}) = \lambda_i^{(n)}$. In other words, we obtain approximate $k$-conservation. However, the intensities show oscillatory behaviour (cf. Fig. 2). Further, the main maxima for $n = 5$ (Fig. 3b) are much broader than those for $n = 10$ (Fig. 3a) due to the weakening of the $k$-conservation for shorter chains.

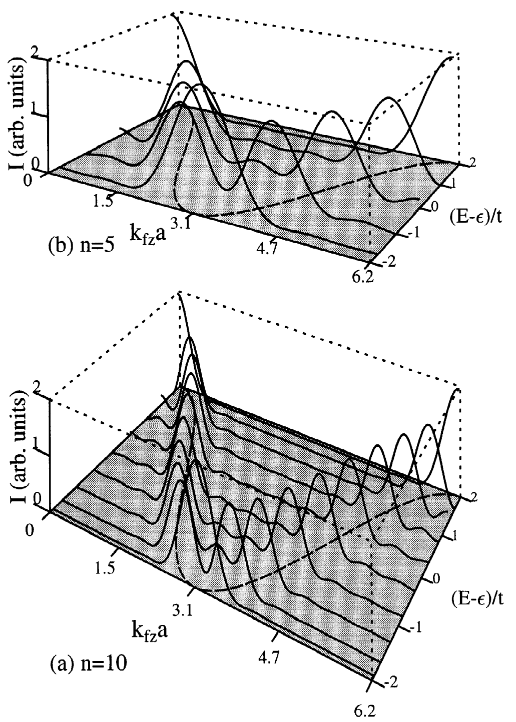

Fig. 3. Photoemission from linear chains with lengths ten (a, bottom) and five sites (b, top), respectively. The intensity $I$ is shown for each initial state at energy $\lambda_i^{(n)}$ (cf. Eq. (2) for final-state wave numbers $k_\mathrm{fz}$ ranging from 0 to $2\pi/a$ and Im($k_\mathrm{fz}a$) $= 0$. The initial-state band structure $E(k) = \epsilon + 2t\cos(ka)$ (dashed) is shown at the bottom of each box. Intensities are scaled to the same maximum in each box.

The finite photo-electron life-time can be modeled using complex energies [24] which leads to complex final-state wave numbers $k_\mathrm{fz}$. Its effect is addressed for a ten-site chain in Fig. 4. For a rather large life-time (Im($k_\mathrm{fz}a$) $= 0.2$, Fig. 4b) there are still oscillations with $k_\mathrm{fz}$ in the photoemission intensities from the individual initial states. These become smeared out for decreasing life time (e.g. Im($k_\mathrm{fz}a$) $=$ 0.5 in Fig. 4a). However, the intensities follow the bulk-band structure in both cases. For a fixed photon energy – or a fixed Re($k_\mathrm{fz}$), for example Re($k_\mathrm{fz}$) $= 0$

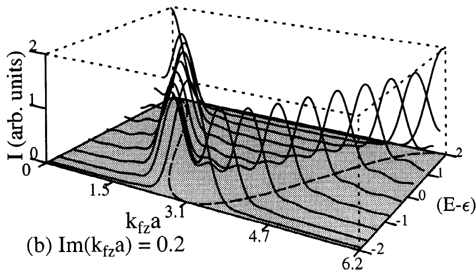

(b) Im($k_{fz}a$) = 0.2

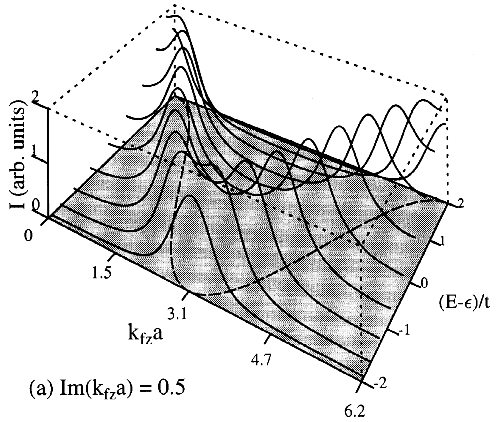

(a) Im($k_{fz}a$) = 0.5

Fig. 4. Same as Fig. 3, but for photoemission from chains with ten sites for Im($k_{fz}a$) = 0.5 (a, bottom) and Im($k_{fz}a$) = 0.2 (b, top), respectively.

– the energy distribution becomes broader with increasing Im($k_{fz}$), which is due to the smearing out of the individual maxima and not to the uncertainty in $k_{fz}$.

In summary, we found the following properties of photoemission from ultra-short chains. (i) The confinement of the valence electrons to the chain leads to a weakening of the wave-number conservation: the shorter the chain, the broader the photoemission maxima in $k_{fz}$. (ii) Besides the periodicity with $2\pi/a$, individual photoemission intensities show oscillations with $k_{fz}$, the number of which is proportional to the chain length. These oscillations become smaller in intensity with decreasing photo-electron life-time (increasing Im($k_{fz}$)). (iii) Even for very small lengths, the main maxima in the photoemission intensity follow the initial-state bulk-band structure, despite the fact that the initial-state energies are discrete.

## 3. Application to (001)-films of Cu on fcc-Co(001)

In this Section, we investigate if the properties of photoemission from ultra-thin films – which have been obtained within a simple tight-binding model – can be found in more sophisticated calculations, the results of which can directly be compared to experimental results. The numerical photoemission results presented in the following have been obtained within the relativistic one-step model of photoemission [25,26] as formulated within the layer–KKR scheme. Details of the computational procedures can be found elsewhere [27].

As a prototypical example we chose normal emission from Cu(001) films on fcc-Co(001) [8] and p-polarized light which impinges with 45° polar angle onto the surface. Surface emission which is due to the strong variation of the electromagnetic field at the surface [28,29] leads to asymmetric shapes of the *sp*-band derived spectral features [30]. In our theory, this effect is neglected and we therefore obtain rather symmetric maxima. However, Fresnel's equations and Snell's law are taken into account. Dielectric constants were taken from Ref. [31].

We used the Cu lattice constant for both film and substrate and neglected any possible tetragonal distortion (fcc parent lattice). In experiment, the Cu/Co(001) system is typically realized as a trilayer (Cu-film/Co-film/Cu(001)-substrate). Thus, the fct distortion is mainly found in the Co layers. The band structure of fct-Co differs slightly from that of fcc-Co [32]; in particular the effective band gaps which are responsible for the quantum-well states in the Cu film. The general properties of photoemission from ultra-thin films on which we focus in the present paper remain unchanged.

In order to distinguish between surface states, interface states and quantum-well states, we calculated the layer-resolved density of states (LDOS) for $\boldsymbol{k}_{\|} = 0$ in the whole Cu film and the subsequent Co layers. Surface and interface states, the energies of which may also lie in a band gap of the substrate, are localized at the respective boundary (vacuum/Cu and Cu/Co). This means that the corresponding maxima in the LDOS decrease with distance from the boundary. Quantum-well states however show maxima in the whole Cu film but decreasing maxima in the Co substrate (due to the band gap in the Co-band structure). Further, the energetic position of surface and interface state is expected not to depend significantly on the number of Cu layers, whereas quantum-well states should show the typical dispersion with film thickness [9].

Before turning to the photoemission results we analyze briefly the electronic structure of Cu films on fcc-Co(001) at $\Gamma$ which is relevant for normal emission ($\boldsymbol{k}_{\parallel} = 0$, $\Gamma - \Delta - X$ in the bulk Brillouin zone). The Cu-*sp* band belongs to the double-group representation $\Delta_6$, the related wave functions show a prominent $\Delta^1$ single-group (spatial) contribution. In order to confine these electrons completely within the Cu film, the Co-substrate has to have a gap in the $\Delta^1$ bands. This is the case for minority electrons below $-0.65$ eV (light gray area in Fig. 5), for majority electrons below $-2.09$ eV (dark gray area in Fig. 5). The Bloch spectral density for a 14 ML Cu film indeed shows two sharp maxima (cf. quantum-well states *A* and *B* in Fig. 5b) of minority spin character [10,11] with energies $-1.52$ and $-0.80$ eV, respectively. The latter agree reasonably well with those obtained experimentally by Hansen and co-workers [8] ($-1.5$ and $-0.9$ eV). Above $-0.65$ eV, the Bloch spectral functions show weak maxima which may also be associated with quantum-well states but lack the complete confinement due to the weak reflection at the Cu/Co interface at these energies [33]. There is no even–odd alternation of the quantum-well states, as found in the tight-binding model (Section 2), due to the lack of inversion symmetry in the Cu film.

We have, in addition, calculated the electronic structure of 9 ML Cu on Co(001) and find good agreement with the results of van Gelderen et al. [15] The Cu-band structure obtained from the central-layer potential agrees very well with that of bulk Cu. Further, the quantum-well dispersion with layer thickness agrees well with experimental and other theoretical results (see for example Ref. [12]).

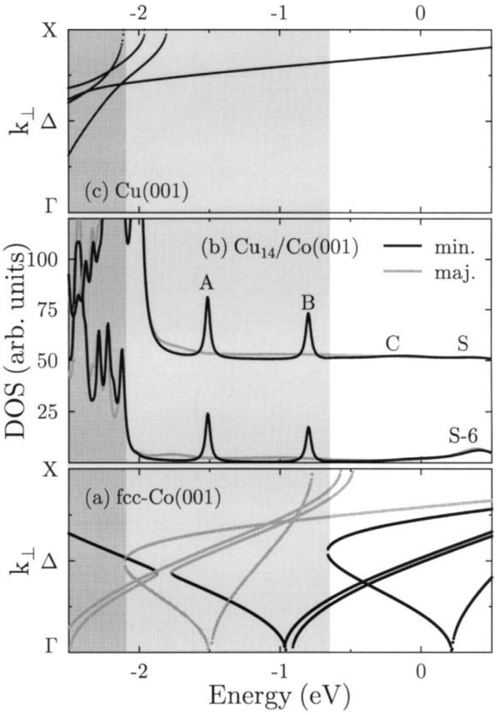

Fig. 5. Spin-resolved relativistic electronic structure of 14 ML Cu on fcc-Co(001) for $\Gamma$ ($\boldsymbol{k}_{\parallel} = 0$, $\Gamma - \Delta - X$ in the bulk Brillouin zone). (a) Band structure of fcc-Co(001) along $\Gamma - \Delta - X$. The sliding gray scale of the bands indicates dominant majority (minority) spin orientation with black (light gray). (b) Density of states of 14 ML Cu on fcc-Co(001) for the outermost ($S$) and a central ($S-6$) layer with black (light gray) lines indicating minority (majority) spin orientation. (c) As bottom panel a, but for Cu(001). Gray areas indicate gaps in the Co-band structure: dark gray for both majority and minority electrons, light gray for minority electrons with prominent $\Delta^1$ spatial symmetry. The latter leads to confinement of minority electrons in the Cu film, see maxima *A* and *B* in panel b. For *C*, see text. The Fermi energy is at 0 eV.

In Fig. 6, photoemission from semi-infinite Cu(001) is compared to that of 14 ML Cu on fcc-Co(001). For the former (Fig. 6a), the intensity at energies below $-2$ eV stems from the *d*-band regime. The maximum which disperses from the Fermi energy at 10 eV photon energy down to $-2$ eV at 17 eV photon energy is due to emission from the Cu-*sp* band (cf. Fig. 5c). The direct transition model can be used to explain the width of these maxima: the *sp*-band and the final-state band are almost parallel in the band structure and, thus, there is a certain energy range where the difference of the respective $k_\perp$ is rather small [34]. The slightly weakened $k_\perp$ selection results therefore in a broad maximum. For the 14 ML Cu film on fcc-Co(001)

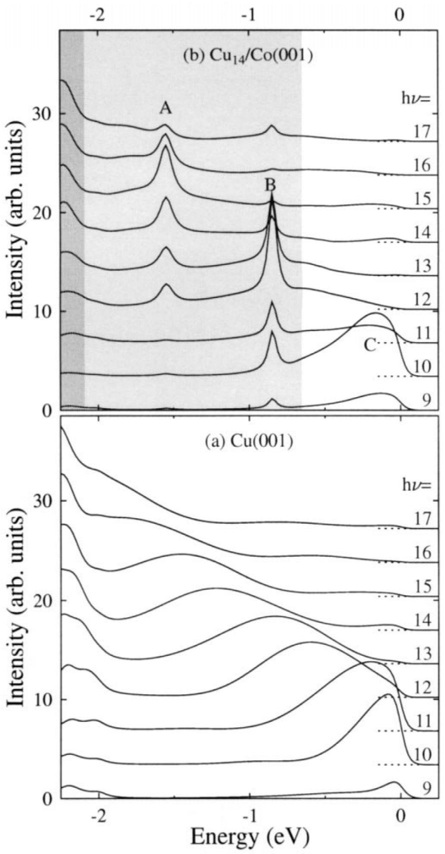

Fig. 6. Photoemission for $\boldsymbol{k}_\parallel = 0$ with p-polarized light incident at 45° off-normal from Cu(001) (panel a, bottom) and 14 ML Cu on fcc-Co(001) (panel b, top). The photon energy h$\nu$ ranges from 9 eV (bottom spectra) to 17 eV (top spectra), as indicated on the right. Gray areas in panel b indicate gaps in the Co-band structure as in Fig. 5. *A*, *B*, and *C* refer to quantum-well states (see text and Fig. 5). The Fermi energy is at 0 eV.

(Fig. 6b), the energies of the quantum-well states are obviously discrete and lead to narrow maxima [35]. The two sharp peaks, *A* and *B*, correspond to those found in the density of states (Fig. 5b). The intensity distribution of structure *C*, however, agrees with that found for Cu(001) which can be also explained by the density of states: near the Fermi energy, there are no strictly confined electronic states in the Cu film because the reflection at the Cu/Co interface is too small. This qualitative difference between on one hand *A* and *B* and on the other *C* is further established in the photo-electron spin polarization. *A* and *B* show strong minority polarization ($P \approx -0.75$), whereas *C* is weakly spin-polarized ($P \approx -0.05$), as expected from the LDOS.

The intensity variation with photon energy of maxima *A* and *B* is similar to that found for semi-infinite Cu(001) at the respective binding energies, a finding which confirms nicely both the simple theory of Section 2 and experiment [8]. At this point, quantum-size effects seem to occur only in the width of the intensity maxima which are associated with quantum-well states [35]. This feature should be observable with high-resolution photoemission techniques [36] (However, hints about this behaviour may be seen, for example, in the work by Hansen and co-workers [8]).

We now address the more pronounced manifestation of quantum-size effects in the photoemission intensities, i.e. the intensity oscillations with photon energy due to electron confinement. These can be observed in constant initial-state (CIS) photoemission: the initial-state energy is chosen as that of a quantum-well state and the photon energy is varied while keeping $\boldsymbol{k}_\parallel$ fixed [37]. The results for semi-infinite Cu(001) and 14 ML on fcc-Co(001) are shown in Fig. 7 where the initial-state energies were chosen as those of features *A*, *B*, and *C*.

For semi-infinite Cu(001) (Fig. 7a), we observe for each initial-state energy a dominating maximum and a few smaller maxima and shoulders. The former directly reflects the $k_\perp$-selection, the latter can easily be explained by the final-state band structure. Further, because the wave function of the initial state does not change rapidly with energy – as is evident from the band structure – the three CIS spectra show almost the same shape which appears only shifted in photon energy (see inset in Fig. 7a). In other words, the CIS-spectral shapes are governed by the final-states. The fine-structure for the energy of state *C* is slightly more pronounced when compared to that for *A* and *B* because of the larger photo-electron lifetime which increases with kinetic energy. But the most important observation is the absence of significant oscillations with photon energy.

For the 14 ML film (Fig. 7b), we find a similar behaviour regarding the overall CIS-intensity distribution. In particular, the relative heights of the

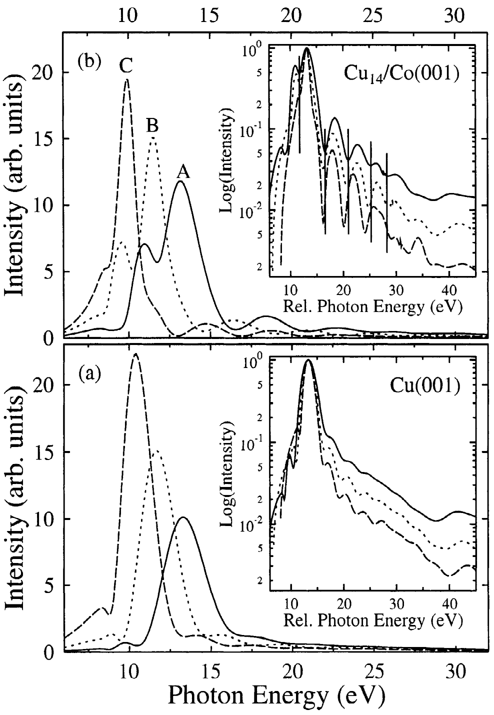

Fig. 7. Constant initial-state photoemission for $\boldsymbol{k}_{\parallel} = 0$ with p-polarized light incident at 45° off-normal from Cu(001) (panel a, bottom) and 14 ML Cu on fcc-Co(001) (panel b, top). The initial-state energies are chosen as those of quantum-well states *A* (solid lines), *B* (dotted lines), and *C* (dashed lines); see text as well as Figs. 5 and 6. Insets show the logarithm of the intensities which are normalized to 1 and shifted in energy such that the maximum intensity is at 13 eV (*relative photon energy*). Vertical lines in the inset of panel b indicate intensity minima of state *A*.

main maxima for *A*, *B*, and *C* are close to their counterparts of Cu(001). The main differences are distinct intensity oscillations which become clearly visible in the insets showing the logarithm of the intensities. In particular, *A* and *B* show almost the same oscillation period which is indicated by vertical lines in the inset of Fig. 7b. The period for *C*, however, differs significantly from that of *A* and *B*. Further, the spectral shapes of *A* and *B* are nearly identical and differ from that of *C*, in particular the double-peak structure near the maximum intensity occurs for both *A* and *B* but is missing for *C*. As we will show below, this double-peak structure is clearly due to the quantum-size induced oscillations of the CIS intensity. We regard these findings as direct evidence of the different confinements of the corresponding initial states: strict confinement for *A* and *B*, less confinement for *C*. It is worth mentioning that feature *C* shows a dominating maximum in intensity at about 10 eV. The next maximum is at about 15 eV, a finding which corresponds well with the experimental observations (see Fig. 1 in Ref. [8]).

At last, we address the dependence of the oscillatory behaviour on film thickness. Following the simple photoemission theory of Section 2, the period should decrease with increasing film thickness. For quantum-well state *A* of the 14 ML film and the corresponding states for films with thicknesses of 9 ML, 19 ML, 24 ML, and 29 ML, the energy positions are almost identical (energy differences for both *A* and *B* less than 0.1 eV). This means that hole and photo-electron life-times are also almost identical, and the main differences in the CIS spectra can unambiguously be attributed to the difference in film thickness. Note that all these quantum-well states are strictly confined to the Cu film. The CIS spectra for the various film thicknesses are shown in Fig. 8. Both, the width of the main maximum and the oscillation period decrease with film thickness, which is visualized by guide lines in Fig. 8. Further, the intensity at higher photon energies decreases with film thickness which is also evident from the analytical considerations of Section 2, particularly from Fig. 2. The double-peak structure which was mentioned above can clearly be attributed to the quantum-size induced oscillations: for the Cu film, the main intensity maximum is broadened with respect to the semi-infinite case due to the weakening of the wave-vector conservation, as is evident from Fig. 8. This maximum is ‘divided’ into two due to the intensity oscillations (cf. the dash-dotted guide line in Fig. 8). With increasing film thickness, the double-peak structure disappears.

To conclude, we like to mention results for a 4-ML film. The variation with photon energy of photoemission intensities which stem from the quantum-well states follow the general trends, as for example presented in Fig. 8; in other words, ‘they show a band structure’. Due to the small number of Cu layers, the spectra also exhibit Co-related structures in the energy range of the Cu-*sp*-band.

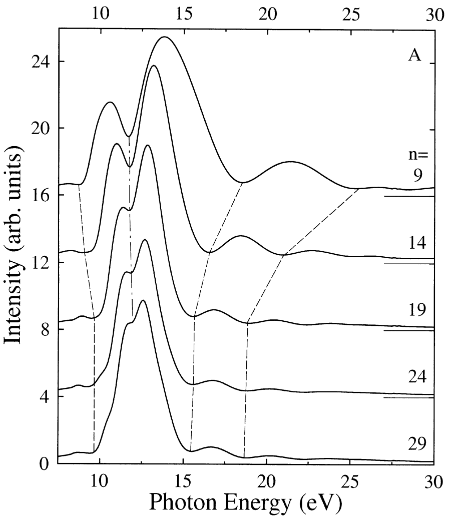

Fig. 8. Constant initial-state photoemission for $\boldsymbol{k}_{\parallel} = 0$ with p-polarized light incident at 45° off-normal from Cu films on fcc-Co(001). The initial-state energies are chosen as those of quantum-well state *A* for selected film thicknesses *n* from 9 ML (top spectrum) to 29 ML (botton spectrum), as indicated on the right. Dashed and dashed-dotted lines visualize the behaviour of oscillations. Short horizontal lines represent zero intensity for each respective spectrum.

## 4. Concluding remarks

The presented investigation of quantum-size effects in photoemission from ultra-thin films has shown the following basic features. (i) Strict confinement of valence electrons to the film leads to a weakening of the wave-vector conservation: the thinner the film, the broader the photoemission maxima. (ii) Photoemission intensities from individual quantum-well states show oscillations with photon energy, the period of which decreases with film thickness. (iii) Even for films of only a few layer thickness, the main maxima in the photoemission intensity follow the initial-state bulk-band structure, despite the fact that the initial-state energies are discrete. These theoretical findings confirm earlier experimental observations.

Further, constant-initial state (CIS) spectroscopy can be successfully used to analyze the confinement of electronic states without prior knowledge of a theoretical bulk-band structure of the substrate. For the prototypical example of 14 ML Cu on Co(001), our investigations show that the electronic state with the lowest binding energy, *C*, is not strictly confined to the Cu film although it shows no (or very small) dispersion [8]. The next states, *A* and *B*, are completely confined to the films. This work implies further that the intensity oscillations with photon energy in the CIS spectra might be used to conclude on the film thickness, particularly in the range of a few ML where the changes are most significant (cf. Fig. 8). Because photoemission samples a considerable area of the surface, these oscillations may help to conclude on film quality, e.g. distribution of thickness or steps [35]. We hope that this work will stimulate new experiments.

## Acknowledgements

We are grateful to A.M.N. Niklasson (Uppsala) for supplying us with the potentials used in the Cu(001)/Co(001) calculations. We acknowledge very fruitful discussions with I.T. Steinberger (Jerusalem) and M. Grüne (Bonn) on models of quantum wells. This work has been performed within the Training and Mobility of Researchers (TMR) Network 'Interface Magnetism'.

## References

[1] R.Z. Bachrach (Ed.), Synchrotron radiation research. Advances in surface and interface science, Techniques, Vol. 1, Plenum Press, New York, 1992.

[2] M. Cardona, L. Ley (Eds.), Photoemission in Solids I, no. 26 in Topics in Applied Physics, Springer, Berlin, 1978.

[3] A. Liebsch, in: B. Feuerbacher, B. Fitton, R.F. Willis (Eds.), Photoemission and the Electronic Properties of Surfaces, Wiley, Chichester, 1978, p. 167.

[4] S.V. Kevan (Ed.), Angle-resolved Photoemission: Theory and Current Applications, Elsevier, Amsterdam, 1992.

[5] H. Bonzel, C. Kleint, Prog. Surf. Sci. 49 (1995) 107.

[6] C. Schneider, J. de Miguel, P. Bressler, P. Schuster, R. Miranda, J. Kirschner, J. Electron Spectrosc. Relat. Phenom. 51 (1990) 263.

[7] W. Kuch, A. Dittschar, M. Salvietti, M.-T. Lin, M. Zharnikov, C.M. Schneider, J. Camarero, J.J. de Miguel, R. Miranda, J. Kirschner, Phys. Rev. B 57 (1998) 5340.

[8] E.D. Hansen, T. Miller, T.-C. Chiang, J. Phys.: Condens. Matt. 9 (1997) L435.

[9] J.E. Ortega, F.J. Himpsel, G.J. Mankey, R.F. Willis, Phys. Rev. B 47 (1993) 1540.
[10] K. Garrison, Y. Chang, P. Johnson, Phys. Rev. Lett. 71 (1993) 2801.
[11] C. Carbone, E. Vescovo, O. Rader, W. Gudat, W. Eberhardt, Phys. Rev. Lett. 71 (1993) 2805.
[12] C. Carbone, E. Vescovo, R. Kläsges, D. Sarma, W. Eberhardt, Solid State Commun. 100 (1996) 749.
[13] P. Segovia, E.G. Michel, J.E. Ortega, Phys. Rev. Lett. 77 (1996) 3455.
[14] R. Kläsges, D. Schmitz, C. Carbone, W. Eberhardt, P. Lang, R. Zeller, P.H. Dederichs, Phys. Rev. B 57 (1998) R696.
[15] P. Gelderen, S. Crampin, J. Inglesfield, Phys. Rev. B 53 (1996) 9115.
[16] R. Paniago, R. Matzdorf, G. Meister, A. Goldmann, Surf. Sci. 325 (1995) 336.
[17] R. Schmitz-Hübsch, K. Oster, J. Radnik, K. Wandelt, Phys. Rev. Lett. 74 (1995) 2995.
[18] F.G. Curti, A. Danese, R.A. Bartynski, Phys. Rev. Lett. 80 (1998) 2213.
[19] M. Grüne, T. Pelzer, K. Wandelt, I.T. Steinberger, J. Electron Spectrosc. Relat. Phenom. 98–99 (1999) 121.
[20] H. Hoekstra, Surf. Sci. 205 (1988) 523.
[21] J. Henk, W. Schattke, Comp. Phys. Commun. 77 (1993) 69.
[22] S. Halilov, J. Henk, T. Scheunemann, R. Feder, Surf. Sci. 343 (1995) 148.
[23] T. Scheunemann, R. Feder, J. Henk, E. Bauer, T. Duden, H. Pinkvos, H. Poppa, K. Wurm, Solid State Commun. 104 (1997) 787.
[24] J.C. Slater, Phys. Rev. 51 (1937) 840.
[25] Polarized electrons in surface physics, in: R. Feder (Ed.), Advanced Series in Surface Science, World Scientific, Singapore, 1985.
[26] J. Braun, Rep. Prog. Phys. 59 (1996) 1267.
[27] J. Henk, T. Scheunemann, R. Feder, J. Phys.: Condens. Matt. 9 (1997) 2963.
[28] P. Feibelman, Phys. Rev. B 12 (1975) 1319.
[29] D. Samuelsen, W. Schattke, Surf. Sci. 327 (1995) 379.
[30] E.D. Hansen, T. Miller, T.-C. Chiang, Phys. Rev. Lett. 78 (1997) 2807.
[31] H.J. Hagemann, W. Gudat, C. Kunz, J. Opt. Soc. Am. 65 (1975) 742.
[32] A. Fanelsa, E. Kisker, J. Henk, R. Feder, Phys. Rev. B 54 (1996) 2922.
[33] P.H. Dederichs, K. Wildberger, R. Zeller, Phys. B 237–238 (1997) 239.
[34] R. Matzdorf, Surf. Sci. Rep. 30 (1998) 154.
[35] J.J. Paggel, T. Miller, T.-C. Chiang, Phys. Rev. Lett. 81 (1998) 5632.
[36] R. Matzdorf, A. Gerlach, R. Hennig, G. Lauff, A. Goldmann, J. Electron Spectrosc. Relat. Phenom. 94 (1998) 279.
[37] Strictly speaking, this method is constant initial-state energy spectroscopy, except for $\boldsymbol{k}_{\parallel} = 0$, which is chosen in this work.

## Publikation 10

# Spectroscopy of the Electron-Electron Interaction in Solids

N. Fominykh, J. Berakdar,* J. Henk, and P. Bruno
*Max-Planck Institut für Mikrostrukturphysik, Weinberg 2, 06120 Halle, Germany*

(Received 26 March 2002; published 2 August 2002)

The spectrum of a photoexcited electron pair carries detailed information on the electron-electron interaction in metals. This is deduced from the results of a theoretical model presented here for the treatment of the double-photoelectron emission from surfaces. Main features in the two-particle spectra are assigned to (a) the exchange-correlation interaction, (b) the electronic band structure, (c) the photoelectron diffraction, and (d) the specific experimental setup. Comparison with experiments is made and common features and differences to the atomic case are pointed out.

DOI: 10.1103/PhysRevLett.89.086402 PACS numbers: 71.20.–b, 32.80.Rm, 33.55.Ad, 79.20.Kz

In recent years, angular and spin-resolved ultraviolet (UV) single-photoelectron spectroscopy [1] has witnessed an impressive refinement in resolution, allowing for a yet more detailed study of material properties. Currently this technique is intensively applied to unravel features governed by many-body effects, such as superconductivity [2,3], correlated excitations in low-dimensional systems [4–6], and the influence of electronic correlation on the spectrum [7,8]. Single-particle techniques have, however, a principle limitation in exposing the details of electronic correlation: An external perturbation introduced to probe the sample may excite simultaneously many degrees of freedom of the specimen; e.g., interacting electrons share the energy of a UV photon and the compound as a whole is then excited. Resolving the excited state of *one* of the electrons, as in single-photoelectron emission (SPE), yields integral information on the influence of the coupling to the surrounding medium. Obviously, more details are revealed on how and whether the particles are interacting if the states of *two* photoexcited particles are measured. For example, the *double*-photoelectron emission (DPE) is forbidden in the absence of correlation [9]; in case the DPE reaction may take place, the measured two-particle spectra provide direct insight into the energy and the angular dependence of the pair-correlation functions (cf. below).

In atomic and molecular physics, this kind of correlation spectroscopy has recently been realized and is currently under intensive experimental and theoretical research (cf. [10–12] for earlier references). While electronic correlation has some striking manifestations in solids [13], it is only recently that fully resolved DPE measurements from surfaces have been conducted [14]. The main experimental obstacle in this case are the low-counting coincidence rates of two *correlated* electrons as compared to the large amount of (background) uncorrelated secondary electrons. With the development of a new generation of detectors [15], it is, however, conceivable that the DPE technique for solids will undergo major advances in the near future.

On the theoretical side, an adequate treatment of electronic correlation, in particular, of the interaction between the photoexcited electron pair, is a prerequisite for the description of DPE [9,16,17]. An important step in this direction is the recent development of a version of the density-functional theory (DFT) that describes the ground state in terms of correlated many-particle densities [18,19]. For the calculation of DPE spectra, one needs, however, in addition to the correlated ground state, an expression for the correlated two-particle state.

This Letter provides the first theory for DPE from solids with a realistic *ab initio* calculation of the (single-particle) electronic structure of the sample. Correlated two-particle states are generated upon the coupling of two single-particle states via a model potential of the screened Coulomb type. The goals of this work are (i) the calculation of both SPE and DPE spectra within the same approach to contrast conclusively the information obtained from both techniques and to assess the reliability of the single-particle part of the DPE theory, (ii) the analysis of how the electron-electron interaction manifests itself in the DPE spectra, (iii) the study of the DPE surface sensitivity (compared to SPE) and of the dependence of DPE on the photoelectron energies and emission angles, (iv) the comparison of theory with available experiments, and (v) the analysis of differences and similarities to DPE from single atoms.

*Theory.*—Within the one-step model of SPE, the current $J^{(1)}$ [20] of photoelectrons emitted with a surface-parallel wave vector $\boldsymbol{k}_{\parallel}$ and an energy $\epsilon$, upon the absorption of a UV photon with energy $\omega$, is given by

$$J^{(1)} \propto -\mathrm{Im}\langle\Psi^{(1)}|\Delta g^{r}(\epsilon-\omega)\Delta^{\dagger}|\Psi^{(1)}\rangle. \quad (1)$$

The final state $|\Psi^{(1)}\rangle = g^{a}|\boldsymbol{k}_{\parallel}, \epsilon\rangle$ is obtained by propagating (back) the detector state $|\boldsymbol{k}_{\parallel}, \epsilon\rangle$ using the advanced Green function $g^{a}$. The photohole state is described by the retarded Green function $g^{r}$, and $\Delta$ is the dipole operator of the incident radiation. In the one-step DPE process, one photon ejects *two* electrons with wave vectors $\boldsymbol{k}_{1\parallel}$ and $\boldsymbol{k}_{2\parallel}$ and energies $E_1$ and $E_2$ from the occupied states of a metal surface. The double-photoelectron current $J^{(2)}$ can be approximated by [16]

$$J^{(2)} \propto \int_{E_{\min}}^{E_{\mathrm{F}}} \langle\Psi^{(2)}|\Delta \mathrm{Im} g^{r}(\epsilon)\mathrm{Im} g^{r}(E-\omega-\epsilon)\Delta^{\dagger}|\Psi^{(2)}\rangle d\epsilon, \quad (2)$$

where $E_F$ is the Fermi energy, $E = E_1 + E_2$, and $E_{\min} = E - \omega - E_F$. The correlated two-particle final state $|\Psi^{(2)}\rangle = G^a|\boldsymbol{k}_{1\|}, E_1; \boldsymbol{k}_{2\|}, E_2\rangle$ is obtained from the uncorrelated detector states $|\boldsymbol{k}_{1\|}, E_1; \boldsymbol{k}_{2\|}, E_2\rangle = |\boldsymbol{k}_{1\|}, E_1\rangle \otimes |\boldsymbol{k}_{2\|}, E_2\rangle$ via the two-particle Green function $G^a$. The occupied nonlocal density related to electron $j$ is determined by $\mathrm{Im} g^r(\boldsymbol{k}_{j\|}, \epsilon_j)$, $j = 1, 2$.

To elucidate the features of DPE as compared to SPE, we employ a calculational scheme for the currents $J^{(1)}$ and $J^{(2)}$ in which the single-particle states are evaluated simultaneously. The ground-state single-particle electronic structure is obtained from an *ab initio* linear muffin-tin orbital method based on the local density approximation of DFT. For the photoemission calculations, we utilize the layer Korringa-Kohn-Rostoker (LKKR) method [21].

The explicit incorporation of the mutual interaction $U$ between the two excited photoelectrons is indispensable for an adequate description of DPE [9]. Here, this is achieved as follows: For a nearly free electron metal, $U$ is screened with a screening length $\lambda$ dependent on the density of states $N(E_F)$ [$\lambda = 1/\sqrt{4\pi N(E_F)}$; for Cu, $\lambda \approx 2.66$ Bohr]. In the long-wavelength limit, $U$ depends only on the coordinate difference $\boldsymbol{r}_1 - \boldsymbol{r}_2$, namely, $U(\boldsymbol{r}_1, \boldsymbol{r}_2) = e^{(-|\boldsymbol{r}_1 - \boldsymbol{r}_2|/\lambda)}/|\boldsymbol{r}_1 - \boldsymbol{r}_2|$. To determine the two-particle state $|\Psi^{(2)}\rangle$, we first employ the LKKR method and obtain the single-particle states $|\psi_j(\boldsymbol{k}_j)\rangle = g^r|\boldsymbol{k}_{j\|}, \epsilon_j\rangle$, $j = 1, 2$. Using the procedure developed in [22], $|\psi_1(\boldsymbol{k}_1)\rangle$ and $|\psi_2(\boldsymbol{k}_2)\rangle$ are then coupled to each other via $U$ to determine the state $|\Psi^{(2)}\rangle$ [and subsequently the current $J^{(2)}$, Eq. (2)]. In this way, single-particle and two-particle photocurrents are calculated within the same scheme allowing a sensible comparison. From the functional form of $U$, it is clear that $J^{(2)}$ depends not only on the energies and emission directions of the photoelectrons, as in the SPE case, but also on the mutual angle between the photoelectrons: If the electrons are close to each other, $U$ provides a strong coupling, whereas $U$ (and, hence, the DPE signal [9]) is strongly suppressed when the photoelectrons are separated at distances larger than $\lambda$. This general statement is quantified below by numerical results.

*Reliability of the SPE part.*—Figure 1(a) shows a measured angular distribution of the SPE intensity from Cu(001) [23]. Our calculations for $J^{(1)}$ [Fig. 1(b)] agrees with the experiments which indicates an adequate treatment of the single-particle part of the problem.

*Symmetry of the angular distribution.*—The SPE angular distributions reflect the $4mm$ symmetry of the Cu(001) surface [Figs. 1(a) and 1(b)]. In contrast, the presence of a second photoelectron in DPE dictates a different symmetry of the angular distribution. In Figs. 1(c) and 1(d), the DPE current is depicted as a function of $\boldsymbol{k}_\|$ of one electron, while $\boldsymbol{k}_\|$ of the other electron is fixed. If this "fixed" electron is detected in off-normal emission, the symmetry is reduced [to $m$ in Fig. 1(d)]. However, if the fixed electron is detected with $\boldsymbol{k}_\| = 0$, the distributions of DPE and SPE show the same symmetry [$4mm$ in Fig. 1(c)].

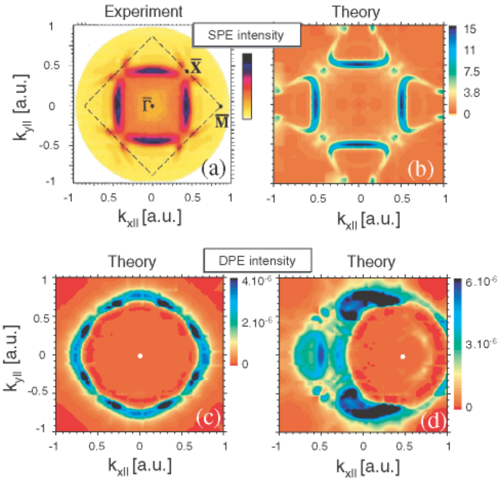

FIG. 1 (color online). Angular distribution of photoemission from the Fermi level of Cu(001). (a) Experimental single-photoelectron emission (SPE) intensity vs surface-parallel wave vector $\boldsymbol{k}_\| = (k_{x\|}, k_{y\|})$. The photon energy of the unpolarized light is $\omega = 21.2$ eV. (b) Theoretical results corresponding to case (a) with light incident normally to the surface. (c) and (d) Double-photoemission (DPE) intensities for photoelectrons having equal energies of 16 eV and $\omega = 42.4$ eV. One electron is detected at a fixed direction marked by the white dot [at 0° (c) and 30° (d) polar angle]. The DPE intensity is then scanned as a function of $\boldsymbol{k}_\|$ of the other photoelectron.

*Exchange-correlation hole.*—The most notable structure in the DPE angular distributions is the intensity minimum centered at $\boldsymbol{k}_\|$ of the fixed electron [Figs. 1(c) and 1(d)]. This "hole" is a direct manifestation of exchange and correlation between the two photoelectrons. The former is accounted for by the antisymmetry of the two-particle state, whereas the latter is mediated by the potential $U$. The high intensity surrounding the hole can be explained by the competition of two factors: (i) the electron-electron repulsion and the exchange interaction prevent the two electrons from escaping with comparable wave vectors within a proximity determined by the screening length. Therefore, the extent of the hole is a qualitative measure of the strength of the electron-electron interaction [for specified $(\boldsymbol{k}_{1\|}, E_1; \boldsymbol{k}_{2\|}, E_2)$]. (ii) If the two electrons are well separated from each other, the electron-electron interaction $U$ becomes negligible and the DPE signal diminishes, for the DPE process is forbidden in the absence of $U$ [9]. Combining these two effects, the distribution of the intensity around the direction of the fixed electron becomes comprehensible.

Both the shape and the extent of the correlation hole depend on the photoelectron energies: At low energies, it is large and dominates the distribution, whereas at higher ones, it is limited to a small region [cf. Figs. 1(d) and 2(d)]. This behavior can be understood from the properties of $U$ as reflected in the transition-matrix elements [Eq. (2)].

In those regions where the two electrons are far away from each other ($U$ is then weak), one observes a remote reminiscence of the DPE spectra to the corresponding SPE distributions; e.g., the influence of the single-electron diffraction is observable, slightly distorted due to the presence of the second (fixed) electron (Fig. 2).

*Surface sensitivity.*—Since *two* electrons have to escape the surface, DPE is expected to be more surface sensitive than SPE. In a crude model, the escape probability $p$ for a single electron decays exponentially with the distance from the surface, $p \sim \exp(-z/\ell)$, where $\ell$ is the escape depth. The escape probability for two electrons is then $\exp(-2z/\ell)$; i.e., the escape depth is effectively halved. Hence, in SPE theory one has to sum up contributions from deep layers (typically from the first 15 surface layers) to obtain $J^{(1)}$, as is evident from Figs. 2(a) and 2(c). In DPE, both the shape and the magnitude of the photocurrent are determined by including contributions from the first two to four surface layers [Figs. 2(b) and 2(d)].

*Photoelectron diffraction.*—DPE experiments from crystal surfaces reported in Refs. [14] show pronounced features in the distributions of the electron-pair total energy ($E = E_1 + E_2$) between the two electrons [Fig. 3(a)]. To uncover the origin of structures occurring in the corresponding theoretical spectra [Fig. 3(b)], it is constructive to contrast with the results of the present theory for the double photoionization of the ground state [He($^1S^e$)] of the helium atom [Fig. 3(c)]. For the "single-site" DPE from atomic He, the cross section vanishes if $\boldsymbol{k}_1 + \boldsymbol{k}_2$ is perpendicular to the polarization vector of the incoming photon [12], which occurs in Fig. 3(c) at $E_1 = E_2$. This propensity rule holds for solids, too, but in the absence of photoelectron diffraction [9]. Indeed, we argue here that the photoelectron diffraction is the reason for the finite photocurrent $J^{(2)}$ at $E_1 = E_2$ found for Ni(001) in Figs. 3(a) and 3(b): For a periodic surface, the electronic states are eigenstates of the lattice translations; i.e., they can be expanded into plane waves. Hence, the effect of the lattice can be investigated by varying the number $n$ of plane waves included in the expansion of the photoelectron states. The inset of Fig. 3(b) shows the DPE current for $E_1 = E_2$ and $\theta_1 = \theta_2$ vs $n$. Indeed, $J^{(2)}$ decreases rapidly with decreasing $n$ and saturates at about $n \approx 20$. This behavior corroborates both the propensity rule and the explanation of the finite DPE photocurrent at $E_1 = E_2$.

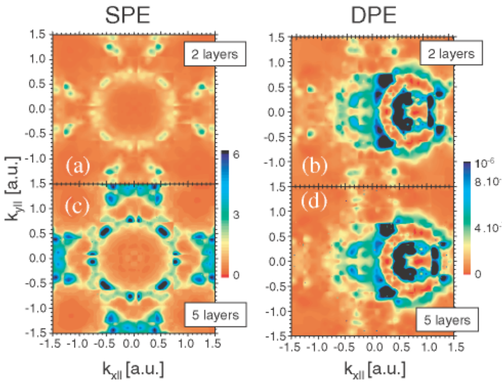

FIG. 2 (color online). Surface sensitivity of SPE [(a) and (c)] and DPE [(b) and (d)] from Cu(001). The setups are chosen as in Figs. 1(b) and 1(d), respectively, but the photoelectron energies are increased to 36 eV. The photon energy is 41 eV for SPE and 82 eV for DPE. In (a) and (b) [(c) and (d)] the contributions to the photocurrent from the two (five) outermost surface layers are depicted.

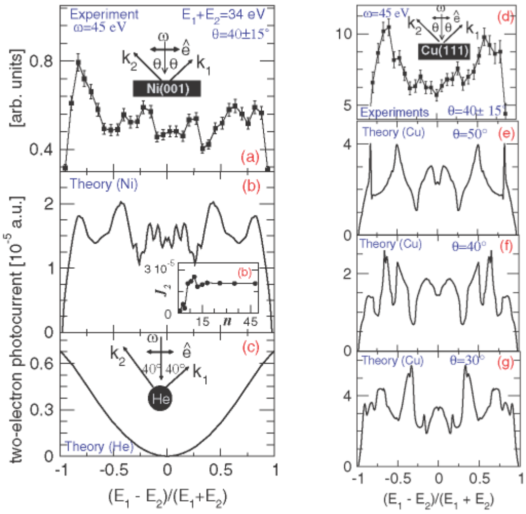

FIG. 3 (color online). (a) Experimental DPE intensity from Ni(001) [14]. The wave vectors $\boldsymbol{k}_1$ and $\boldsymbol{k}_2$ of the emitted electrons and the linear polarization vector of the light $\hat{\boldsymbol{e}}$ are coplanar (cf. inset). The total energy of the electron-pair is fixed as $E = E_1 + E_2 = 34 \pm 1$ eV with $\omega = 45$ eV. The DPE current is scanned as a function of the energy sharing $(E_1 - E_2)/E$. The electron detectors are fixed at symmetric positions (40° polar angle) and have an angular resolution of $\pm 15°$. (b) Theoretical results corresponding to case (a), with account for the experimental angular resolution. Inset: DPE current $J^{(2)}$ (at $E_1 = E_2$) vs number $n$ of plane waves included in the expansion of the photoelectron wave. (c) As in (b), but for a single He atom in state $^1S^e$; $\omega$ is adjusted to compensate for the double ionization threshold of He. For the ground state the two-electron wave function of Ref. [24] is employed. (d) As in (a), but for Cu(111). (e)–(g) Theoretical results corresponding to (d) but with varying escape angles $\theta_1 = \theta = \theta_2$ [$\theta = 50°$ (e), $\theta = 40°$ (f), $\theta = 30°$ (g)].

*Density-of-states effect.*—Assuming parabolic dispersion of the photoelectron states in the vacuum (which means $dE_j = k_j\,dk_j$; $j = 1, 2$), one obtains for the fully resolved DPE current in spherical coordinates $J^{(2)}(\theta_1, \varphi_1, E_1; \theta_2, \varphi_2, E_2) = CJ^{(2)}(\boldsymbol{k}_1, \boldsymbol{k}_2)$, where $C = k_1 k_2$, and $\varphi_1$ as well as $\varphi_2$ are azimuthal angles [9,12]. In the atomic case, the density of states (DOS) for one photoelectron in the field of the residual ion behaves as $1/k_j$ for $k_j \longrightarrow 0$ (and $k_i \gg k_j$) [25]; i.e., for one electron the DOS diverges at the ionization threshold. This DOS effect combined with the kinematical factor $C = k_1 k_2$ leads, in general, to a finite DPE current from atoms when the energy of one of the electrons diminishes. In contrast, for surfaces, the DOS is finite at the vacuum level ($\boldsymbol{k}_j \approx 0$) and, hence, the DPE current $[k_1\, k_2\, J^{(2)}(\boldsymbol{k}_1, \boldsymbol{k}_2)]$ vanishes if $E_1$ or $E_2$ is very small. This profound difference between atoms and solids is confirmed by our calculations: In contrast to DPE from surfaces (Fig. 3), for He($^1S^e$) the DPE current is finite for $E_1 \longrightarrow 0$ or $E_2 \longrightarrow 0$ [Fig. 3(c)].

*Band-structure effect.*—In Fig. 3, both the photon energy $\omega$ and the electron-pair energy $E = E_1 + E_2$ are fixed. This specifies the initial binding energy of the electron pair as $\epsilon = \omega - E$. For atoms, $\epsilon$ pins down the initial state to a specific, discrete level. For surfaces, the electronic structure is dependent not only on the energy $\epsilon_i$, but also on the Bloch wave vectors $\boldsymbol{q}_{i\|}$. When varying $(E_1 - E_2)/E$ (for fixed $E$, $\omega$, and hence fixed $\epsilon$), one scans through different $\boldsymbol{k}_{i\|}$ [Figs. 3(e)–3(g)]. Therefore, the relevant $\boldsymbol{q}_{i\|}$ and the associated electronic levels appear as sharp peaks in $J^{(2)}$ at certain $(E_1 - E_2)/E$ [16]. A similar effect arises due to the energy integration in Eq. (2) which involves several single-particle levels. In consequence, the structure of the initial-state spectral density is reflected as pronounced maxima and minima in the DPE spectra. In contrast, the smooth spectral density of the jellium model results in smooth DPE spectra [9].

Concerning the comparison with experiments, it should be remarked that the shape of the DPE spectrum changes substantially within the experimental angular resolution [Figs. 3(e)–3(g)]. This is due to the fact that, with increasing polar angles, the allowed range for the initial $\boldsymbol{k}_{i\|}$ is stretched and different initial states contribute to the photocurrent. For $\theta \longrightarrow 0$, the DPE current vanishes at $E_1 = E_2$ due to the electron-electron repulsion, whereas for $\theta \longrightarrow \pi/2$, it decreases due to the weakening of the electron-electron interaction [cf. also Figs. 1(c) and 1(d)].

In conclusion, we present pilot results to highlight the general aspects and the power of DPE from surfaces as a novel tool for electronic-correlation imaging.

We thank J. Kirschner, S. Samarin, A. Morozov, R. Dörner, M. Hattas, G. Stefani, R. Gotter, A. Ernst, R. Feder, and H. Gollisch for enlightening discussions.

---

*Electronic address: jber@mpi-halle.de

[1] S. Hüfner, *Photoelectron Spectroscopy* (Springer, New York, 1995).
[2] A. Lanzara *et al.*, Nature (London) **412**, 510 (2001).
[3] T. Yokoya *et al.*, Science **294**, 2518 (2001).
[4] Y. D. Chuang *et al.*, Science **292**, 1509 (2001).
[5] P. Segovia *et al.*, Nature (London) **402**, 504 (1999).
[6] S. Maekawa *et al.*, Rep. Prog. Phys. **64**, 383 (2001).
[7] A. Marini *et al.*, Phys. Rev. Lett. **88**, 016403 (2002).
[8] L. Hedin, J. Phys. Condens. Matter **11**, R489 (1999).
[9] J. Berakdar, Phys. Rev. B **58**, 9808 (1998).
[10] P. Selles *et al.*, Phys. Rev. A **65**, 032711 (2002); A. S. Kheifets and I. Bray, *ibid.* **65**, 012710 (2002); S. Senz and N. Chandra, *ibid.* **652**, 052702 (2000); A. Knapp *et al.*, Phys. Rev. Lett. **89**, 033004 (2002); J. Colgan *et al.*, J. Phys. B **34**, L457 (2001); M. Walter *et al.*, *ibid.* **33**, 2907 (2000).
[11] J. B. West *et al.*, J. Phys. B **34**, 4169 (2001); C. Dawson *et al.*, *ibid.* **34**, L525 (2001); P. Bolognesi, *ibid.* **34**, 3193 (2001); M. Achler *et al.*, *ibid.* **34**, 965 (2001); T. Masuoka, J. Chem. Phys. **115**, 264 (2001); S. A. Collins *et al.*, Phys. Rev. A **64**, 062706 (2001); S. Rioual *et al.*, Phys. Rev. Lett. **86**, 1470 (2001); A. Huetz *et al.*, *ibid.* **85**, 530 (2000).
[12] J. S. Briggs and V. Schmidt, J. Phys. B **33**, R1 (2000); G. C. King and L. Avaldi, *ibid.* **33**, R215 (2000); J. Berakdar and H. Klar, Phys. Rep. **340**, 473 (2001).
[13] P. Fulde, *Electron Correlation in Molecules and Solids* (Springer, Berlin, 1991).
[14] R. Herrmann *et al.*, Phys. Rev. Lett. **81**, 2148 (1998); J. Phys. IV (France) **9**, 127 (1999); H. W. Biester *et al.*, Phys. Rev. Lett. **59**, 1277 (1987).
[15] J. Kirschner and M. Hattas (private communication).
[16] N. Fominykh *et al.*, Solid State Commun. **113**, 665 (2000).
[17] N. Fominykh *et al.*, in *Correlations, Polarization and Ionization in Atomic Systems*, AIP Conf. Proc. No. 604 (AIP, New York, 2002), p. 210.
[18] A. Gonis *et al.*, Phys. Rev. B **56**, 9335 (1997); Phys. Rev. Lett. **77**, 2981 (1996).
[19] P. Ziesche, Int. J. Quantum Chem. **60**, 1361 (1996); Phys. Lett. A **195**, 213 (1994).
[20] C. Caroli *et al.*, Phys. Rev. B **8**, 4552 (1973).
[21] A. Gonis, *Theoretical Materials Science* (Materials Research Society, Pittsburgh, 2000).
[22] J. Berakdar *et al.*, Solid State Commun. **112**, 587 (1999).
[23] Th. Straub *et al.*, Phys. Rev. B **55**, 13 473 (1997).
[24] R. Bonham and D. Kohl, J. Chem. Phys. **45**, 2471 (1966).
[25] J. Berakdar *et al.*, J. Phys. B **26**, 3891 (1993).

## P.4. Spinabhängiger ballistischer Transport

**11 (S. P112ff)** J. Henk.
*Integration over two-dimensional Brillouin zones by adaptive mesh refinement.*
Physical Review B **64** (2001) 034512.

**12 (S. P118ff)** H. F. Ding, W. Wulfhekel, J. Henk, P. Bruno, J. Kirschner.
*Absence of zero-bias anomaly in spin-polarized vacuum tunneling in Co(0001).*
Physical Review Letters **90** (2003) 116603.

**13 (S. P122ff)** J. Henk, P. Bose, Th. Michael, P. Bruno.
*Spin motion of photoelectrons.*
Physical Review B **68** (2003) 052403.

## Publikation 11

# Integration over two-dimensional Brillouin zones by adaptive mesh refinement

J. Henk*
*Max-Planck-Institut für Mikrostrukturphysik, Weinberg 2, D-06120 Halle (Saale), Germany*

(Received 25 January 2001; revised manuscript received 9 April 2001; published 25 June 2001)

Adaptive mesh-refinement (AMR) schemes for integration over two-dimensional Brillouin zones are presented and their properties are investigated in detail. A salient feature of these integration techniques is that the grid of sampling points is automatically adapted to the integrand in such a way that regions with high accuracy demand are sampled with high density, while the other regions are sampled with low density. This adaptation may save a sizable amount of computation time in comparison with those integration methods without mesh refinement. Several AMR schemes for one- and two-dimensional integration are introduced. As an application, the spin-dependent conductance of electronic tunneling through planar junctions is investigated and discussed with regard to Brillouin zone integration.

DOI: 10.1103/PhysRevB.64.035412 PACS number(s): 71.15.Dx, 73.40.Gk, 02.60.Jh

## I. INTRODUCTION

The computation of physical quantities often requires integration over the Brillouin zone (BZ). Standard methods to obtain BZ integrals are special-point (SP) schemes[1] and tetrahedron methods.[2] Since both methods rely on equally spaced grid points, they may be regarded as inefficient if there are small regions in the BZ that give a sizable contribution to the integral, while large regions give almost no contribution: Either the number of grid points may be too small to sample the ''important regions'' with high accuracy, or the number of grid points may be too high and the ''unimportant regions'' are sampled with a dispensable high accuracy, thus leading to an unnecessarily large computation time. An integration method that automatically adapts the grid to the integrand's structure would overcome this problem. Such an adaptive mesh refinement (AMR) would find the important regions with high accuracy demand and sample them with high resolution, while the unimportant regions with low accuracy demand are sampled by a few points. Consequently, discretization on a very fine grid covering the entire BZ is avoided.

Bruno and Ginatempo proposed as an AMR scheme for *n*-dimensional integrals a cascade of adaptive integration techniques for one-dimensional integrals.[3] In this paper, further adaptive integration schemes based on the partitioning of the integration domain by simplexes will be introduced and investigated, with a focus on the computation of physical quantities of layered systems, e.g., the magnetic anisotropy energies of ultrathin films (see Refs. 4 and 5) and magnetoresistances of planar tunnel junctions (for a few recent publications see Refs. 6–9).

Coherent tunneling of electrons through planar magnetic junctions provides a test for the proposed AMR's. The computation of the spin-dependent conductance requires the integration of the transmission of Bloch electrons through the junction over the two-dimensional BZ. This transmission can depend strongly on $\boldsymbol{k}^{\parallel}$ (cf. Ref. 10). First, for increasing spacer thickness, the transmission at large $|\boldsymbol{k}^{\parallel}|$ becomes suppressed, leaving a sizable contribution to the conductance only near the BZ center. Second, electronic states localized at the lead/spacer interfaces can dominate the transmission in very small regions of the BZ (''hot spots''), not necessarily near the BZ center. In both cases, the regions with high accuracy demand are small in comparison with the area of the BZ and their locations are *a priori* unknown. While special-point schemes appear inefficient, an AMR provides a method of choice since it can efficiently treat both large- and small-scale variations of the integrand.

This paper is organized as follows. After having illustrated the basic idea and the main features of AMR's by means of one-dimensional integration (Sec. II), adaptive mesh refinements for two-dimensional integration are introduced in Sec. III. Exemplary results for the spin-dependent tunneling conductance for planar junctions are presented in Sec. IV in order to show the properties of the various proposed AMR's.

## II. ADAPTIVE MESH REFINEMENT FOR ONE-DIMENSIONAL INTEGRALS

Adaptive mesh refinements aim to integrate numerically a function $f(x):\mathbb{R}\rightarrow\mathbb{R}$ over the interval $[x_{\rm i},x_{\rm f}]$ with a given accuracy $\epsilon$ but with the number $n(\epsilon)$ of function evaluations as small as possible. They rely on three main ingredients:[11] (i) a crude approximation $I_{\rm ap}(x_{\rm i},x_{\rm f})$ to the exact integral $I_{\rm ex}(x_{\rm i},x_{\rm f})=\int_{x_{\rm i}}^{x_{\rm f}}f(x)dx$ [gray area in Fig. 1(a)] that uses only the interval boundaries $x_{\rm i}$ and $x_{\rm f}$, (ii) a fine approximation $I_{\rm ap'}(x_{\rm i},x_{\rm f})$ that uses (at least) one inner point $x_{\rm m}$ in addition, and (iii) a refinement rule that in dependence on $I_{\rm ap}$, $I_{\rm ap'}$, and $\epsilon$ determines whether the interval has to be refined.

A crude approximation $I_{\rm ap}(x_{\rm i},x_{\rm f})$ is for example given by the trapezoidal rule [the area hatched with thin lines in Fig. 1(a)].[12] For a fine approximation $I_{\rm ap'}(x_{\rm i},x_{\rm f})$, $f(x)$ is integrated by Simpson's rule, which uses the inner point $x_{\rm m}=(x_{\rm i}+x_{\rm f})/2$. Instead, one could also use the simpler but less accurate $I_{\rm ap''}(x_{\rm i},x_{\rm f})=I_{\rm ap}(x_{\rm i},x_{\rm m})+I_{\rm ap}(x_{\rm m},x_{\rm f})$ [the area hatched with thick lines in Fig. 1(a)]. The refinement rule states that $I_{\rm ap'}(x_{\rm i},x_{\rm f})$ is accepted as an approximation for $I_{\rm ex}(x_{\rm i},x_{\rm f})$ if $|I_{\rm ap'}(x_{\rm i},x_{\rm f})-I_{\rm ap}(x_{\rm i},x_{\rm f})|<\epsilon$ (absolute error) or $|I_{\rm ap'}(x_{\rm i},x_{\rm f})-I_{\rm ap}(x_{\rm i},x_{\rm f})|<\epsilon|I_{\rm ap'}(x_{\rm i},x_{\rm f})|$ (relative error). Otherwise the mesh is refined by applying the above scheme to the intervals $[x_{\rm i},x_{\rm m}]$ and $[x_{\rm m},x_{\rm f}]$ [an analog can be for-

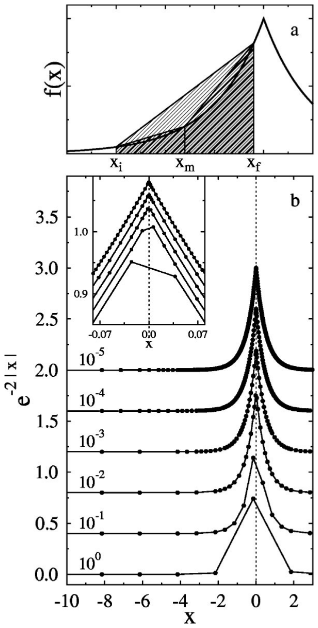

FIG. 1. Adaptive mesh refinement for one-dimensional integrals. (a) The integral of the function $f(x)$ (thick line) over the interval $[x_\mathrm{i},x_\mathrm{f}]$ is given by the gray area. A crude approximation uses only $x_\mathrm{i}$ and $x_\mathrm{f}$ and results in the area hatched with thin lines. A fine approximation uses $x_\mathrm{m}$ in addition and leads to the area hatched with thick lines. (b) Adapted meshes $[x,f(x)]$ (dots) of $f(x)=\exp(-2|x|)$ for absolute accuracies $\epsilon$ ranging from $10^0$ down to $10^{-5}$ (bottom to top, as indicated on the left of each curve). The inset shows the same data but in a small interval around $x=0$ for $\epsilon=10^{-2},\dots,10^{-6}$ (bottom to top). The curves are shifted with respect to each other for clarity. Vertical dashed lines emphasize the mirror symmetry of $f(x)$ at $x=0$.

mulated with $I_{\mathrm{ap}''}(x_\mathrm{i},x_\mathrm{f})$ instead of $I_{\mathrm{ap}'}(x_\mathrm{i},x_\mathrm{f})$].

The main properties of this AMR are revealed by considering the function $f(x)=\exp(-2|x|)$ with $I_\mathrm{ex}(-\infty,\infty)=1$ [see Fig. 1(b)]. It has been integrated numerically via the above AMR (using trapezoidal and Simpson's rules) from $-20.15$ to 19.85 with an initial grid of 11 points. (The large interval $[-20.15,19.85]$ is first partitioned into 10 equally large subintervals which are then treated by the AMR. This initial partitioning determines the large-scale resolution of the adaptive scheme. The small-scale resolution is determined by $\epsilon$.) Whether the AMR is able to recognize the cusp can be tested by choosing the interval asymmetrical with respect to $x=0$. In this case, the cusp is not hit directly by the initial grid and its first refinement. For large $|x|$, $f(x)$ is rather flat and hence $I_\mathrm{ap}$ and $I_{\mathrm{ap}'}$ do not differ significantly. In this unimportant region the demand of accuracy is low and therefore a coarse grid can be maintained. The cusp, however, represents an important region with high accuracy demand and thus requires a fine grid [see the inset in Fig. 1(b)].

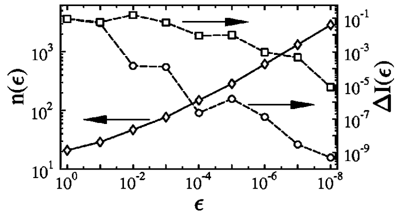

FIG. 2. Numbers $n(\epsilon)$ of mesh points (diamonds) and integration errors $\Delta I(\epsilon)$ (circles) of the AMR for $f(x)=\exp(-2|x|)$ in dependence on the absolute accuracy $\epsilon$. Squares give errors $\Delta I_{\mathrm{ap}'}(n(\epsilon))$ of a Simpson integration with the same numbers $n(\epsilon)$ of points as determined by the AMR.

In Fig. 2, the numbers $n(\epsilon)$ of grid points are shown (diamonds). An increase of accuracy by one order of magnitude requires an increase of $n(\epsilon)$ by a factor of about 2.15. The integration error $\Delta I(\epsilon)=|I(\epsilon)-I_\mathrm{ex}|$ (circles) is always less than $\epsilon$. The efficiency of the AMR becomes evident if one considers the integrals $I_{\mathrm{ap}'}(n(\epsilon))$ of $f(x)$ by Simpson's rule with the same number $n(\epsilon)$ of grid points as used by the AMR. For comparably large $n(\epsilon)$, the integration error $\Delta I_{\mathrm{ap}'}(n(\epsilon))=|I_{\mathrm{ap}'}(n(\epsilon))-I_\mathrm{ex}|$ (squares) is about four orders of magnitude larger than $\Delta I(\epsilon)$. Thus, in order to achieve an accuracy of $\epsilon=10^{-9}$ in the Simpson integration, a grid of about 32 000 points is needed. This corresponds to an increase in speed by a factor of about 5 in favor of the AMR.

### III. ADAPTIVE MESH REFINEMENTS FOR TWO-DIMENSIONAL INTEGRALS

An obvious generalization of the above AMR to integration in $n$ dimensions was proposed by Bruno and Ginatempo.[3] The integral $I_\mathrm{ex}^{(n)}=\int_{[\mathbf{x}_\mathrm{i},\mathbf{x}_\mathrm{f}]} f(\mathbf{x})\,d^n\mathbf{x}$ of $f(\mathbf{x}):\mathbb{R}^n\to\mathbb{R}$ over the interval $[\mathbf{x}_\mathrm{i},\mathbf{x}_\mathrm{f}]$ is decomposed into successive one-dimensional integrals, the AMR of Sec. II being applied to each of them. In a computer program, one would deal with a cascade of AMR's for linear meshes, and hence the name cascading linear mesh refinement, CLMR($n$) where $n$ indicates the dimension. To give an explicit example, e.g., a CLMR(2) scheme, for the integral $I_\mathrm{ex}^{(2)}=\int_\mathrm{BZ} f(\mathbf{k}^\|)\,d^2\mathbf{k}^\|$ of the function $f(\mathbf{k}^\|):\mathbb{R}^2\to\mathbb{R}$, $\mathbf{k}^\|=(k^x,k^y)$, over the two-dimensional BZ $[\mathbf{k}_\mathrm{i}^\|,\mathbf{k}_\mathrm{f}^\|]$, the cascade is given by $I_\mathrm{ex}^{(2)}=\int_{k_\mathrm{i}^y}^{k_\mathrm{f}^y} I_\mathrm{ex}^{(1)}(k^y)\,dk^y$, $I_\mathrm{ex}^{(1)}(k_y)=\int_{k_\mathrm{i}^x}^{k_\mathrm{f}^x} f(k^x,k^y)\,dk^x$.

Another type of AMR is based on the refinement of simplexes. A simplex in $\mathbb{R}^n$ is a geometrical object that consists of $n+1$ points and all its constituents (which are themselves simplexes) with dimensions $m$ $(0\leqslant m<n)$, e.g., corners ($m=0$), line segments ($m=1$), triangular surfaces ($m=2$), etc. Since a simplex is uniquely defined by its corners $\mathbf{x}_1,\mathbf{x}_2,\dots,\mathbf{x}_n,\mathbf{x}_{n+1}$ it can for short be denoted $\langle 1\,2\cdots n\,(n+1)\rangle$. The central point of a simplex, i.e., $\sum_{i=1}^{n+1}\mathbf{x}_i/(n+1)$, will be denoted as $\overline{\langle 1\cdots(n+1)\rangle}$. For example, the center $\mathbf{x}_4=(\mathbf{x}_1+\mathbf{x}_2+\mathbf{x}_3)/3$ of a triangle $\langle 1\,2\,3\rangle$ can be written as $\langle 4\rangle=\overline{\langle 1\,2\,3\rangle}$. Further, lengths, areas, or volumes will be written as $|\langle 1\cdots n\rangle|$.

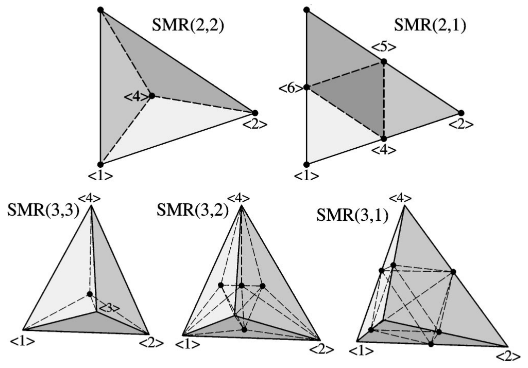

FIG. 3. Simplex mesh refinements SMR$(n,m)$ for triangular ($n=2$, top row) and tetrahedral ($n=3$, bottom row) grids. The mesh refinements are illustrated by dashed lines. Top row: The initial triangle $\langle 1\,2\,3\rangle$ is refined using as additional points the center of the triangle $\langle 4\rangle$ [left, SMR(2,2)] or the edge centers $\langle 4\rangle$, $\langle 5\rangle$, and $\langle 6\rangle$ [right, SMR(2,1)]. Bottom row: The initial tetrahedron $\langle 1\,2\,3\,4\rangle$, with corner $\langle 3\rangle$ lying behind the front surface $\langle 1\,2\,4\rangle$, is refined using the central point [left, SMR(3,3)], the centers of the surfaces [middle, SMR(3,2)], or the edge centers [right, SMR(3,1)].

Any simplex can be partitioned into smaller simplexes by adding points that are the centers of the $m$-dimensional constituents of the initial simplex $(1\leqslant m\leqslant n)$. These new points in conjunction with the initial points serve as corners of the new (smaller) simplexes, which have to be disjunct and space filling. Consequently, the simplex mesh refinements introduced below can be labeled SMR$(n,m)$.

Suppose we want to integrate numerically a function $f(\boldsymbol{x})\colon\mathbb{R}^2\to\mathbb{R}$ over a triangle $\langle 1\,2\,3\rangle$. A crude approximation to the exact integral $I_{\mathrm{ex}}(\langle 123\rangle)$ is the volume $I_{\mathrm{ap}}(\langle 1\,2\,3\rangle) = [f(\langle 1\rangle)+f(\langle 2\rangle)+f(\langle 3\rangle)]|\langle 1\,2\,3\rangle|/3$ of the prism. For the mesh refinement SMR(2,2) the center $\langle 4\rangle=\overline{\langle 1\,2\,3\rangle}$ is chosen as an additional point (see Fig. 3), and thus $I_{\mathrm{ap}'}(\langle 1\,2\,3\rangle)=I_{\mathrm{ap}}(\langle 1\,2\,4\rangle)+I_{\mathrm{ap}}(\langle 2\,3\,4\rangle)+I_{\mathrm{ap}}(\langle 3\,1\,4\rangle)$ is taken as a fine approximation. Or one might utilize for SMR(2,1) the edge centers $\langle 4\rangle=\overline{\langle 1\,2\rangle}$, $\langle 5\rangle=\overline{\langle 2\,3\rangle}$, and $\langle 6\rangle=\overline{\langle 3\,1\rangle}$ with the fine approximation $I_{\mathrm{ap}''}(\langle 1\,2\,3\rangle) =I_{\mathrm{ap}}(\langle 1\,4\,6\rangle)+I_{\mathrm{ap}}(\langle 2\,5\,4\rangle)+I_{\mathrm{ap}}(\langle 3\,6\,5\rangle)+I_{\mathrm{ap}}(\langle 4\,5\,6\rangle)$.

As for one-dimensional integration, $I_{\mathrm{ap}'}(\langle 1\,2\,3\rangle)$ is accepted in the case of SMR(2,2) if $|I_{\mathrm{ap}'}(\langle 1\,2\,3\rangle) -I_{\mathrm{ap}}(\langle 1\,2\,3\rangle)|<\epsilon$ (absolute error) or $|I_{\mathrm{ap}'}(\langle 1\,2\,3\rangle) -I_{\mathrm{ap}}(\langle 1\,2\,3\rangle)|<\epsilon\,|I_{\mathrm{ap}'}(\langle 1\,2\,3\rangle)|$ (relative error). Otherwise the AMR is applied to the refined triangles, namely, to $\langle 1\,2\,4\rangle$, $\langle 2\,3\,4\rangle$, and $\langle 3\,1\,4\rangle$. An analog can be formulated for the SMR(2,1) scheme.

It is straightforward to extend the above mesh refinements to three-dimensional integrals (Fig. 3). Using the center of the initial tetrahedron [SMR(3,3)] the centers of its four surfaces [SMR(3,2)] or the centers of its six edges [SMR(3,1)] yield 4, 11, or 8 small tetrahedra, respectively.

Note that the accuracy $\epsilon$ is directly related to the integrals over a simplex but only indirectly related to the accuracy of the integral over the complete domain $[\boldsymbol{x}_{\mathrm{i}},\boldsymbol{x}_{\mathrm{f}}]$. In the case of the refinement rule based on absolute accuracy, the total absolute error can roughly be estimated as $\epsilon\,N(\epsilon)$ where $N(\epsilon)$ is the number of simplexes used in the evaluation of the integral over the domain.

The AMR schemes are not restricted to integration of real-valued functions. Even matrix-valued functions $f(\boldsymbol{x})\colon\mathbb{R}^n\to\mathbb{R}^{r\times c}$ can be integrated, the integrals being themselves matrices. As a distance in matrix space $\mathbb{R}^{r\times c}$ one could use the matrix norm $||A||=\sqrt{\mathrm{tr}(AA^{\dagger})}$. An example for operating with matrix-valued functions is a multiple-scattering calculation which takes into account substitutional disorder within the coherent potential approximation.[13] There, one has to average the scattering-path operator $\tau(E,\boldsymbol{k})$ over the BZ, the latter being represented in angular-momentum space.[14]

## IV. APPLICATION TO THE SPIN-DEPENDENT CONDUCTANCE OF PLANAR TUNNEL JUNCTIONS

We now apply the AMR schemes for two-dimensional integration to the computation of the spin-dependent conductance of planar tunnel junctions.[9] The conductance is calculated for parallel or antiparallel alignment of the magnetic moments of the semi-infinite ferromagnetic leads which are separated by an insulating spacer. If the layer unit cells of the leads and the spacer are commensurable, the in-plane wave vector $\boldsymbol{k}^{\parallel}=(k^x,k^y)$ is conserved in the scattering process (coherent tunneling). According to Landauer and Büettiker,[15] the conductance $G$ at the Fermi energy can then be expressed as $G=(e^2/h)\int_{\mathrm{BZ}}T(\boldsymbol{k}^{\parallel})\,d^2\boldsymbol{k}^{\parallel}$. The transmission is given by $T(\boldsymbol{k}^{\parallel})=\Sigma_{m,n}|S_{m_{\mathrm{L}}\to n_{\mathrm{R}}}(\boldsymbol{k}^{\parallel})|^2$, where $S$ is the scattering matrix of the spacer expressed in terms of lead Bloch states. The sums run over all incoming Bloch states $m_{\mathrm{L}}$ of lead $L$ which are scattered into those outgoing in lead $R$ $(n_{\mathrm{R}})$. Computation of the conductance by means of a layer Korringa-Kohn-

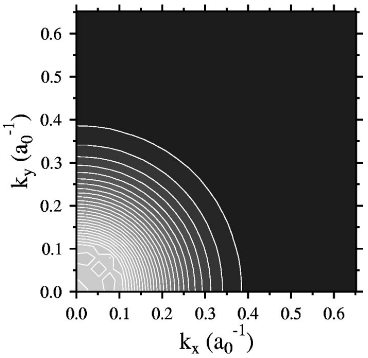

FIG. 4. Transmission $T(\boldsymbol{k}^{\parallel})$ of Ni(001)/vacuum/Ni(001) for three spacer layers of vacuum and parallel alignment of the lead magnetizations. In the gray-scale contour plot covering one-quarter of the Brillouin zone, zero transmission corresponds to black, while maximum transmission (0.036) corresponds to light gray. Equally spaced contour lines are displayed in white ($\boldsymbol{k}^{\parallel}=(k^x,k^y)$ with respect to [110] and $[\bar{1}10]$, respectively).

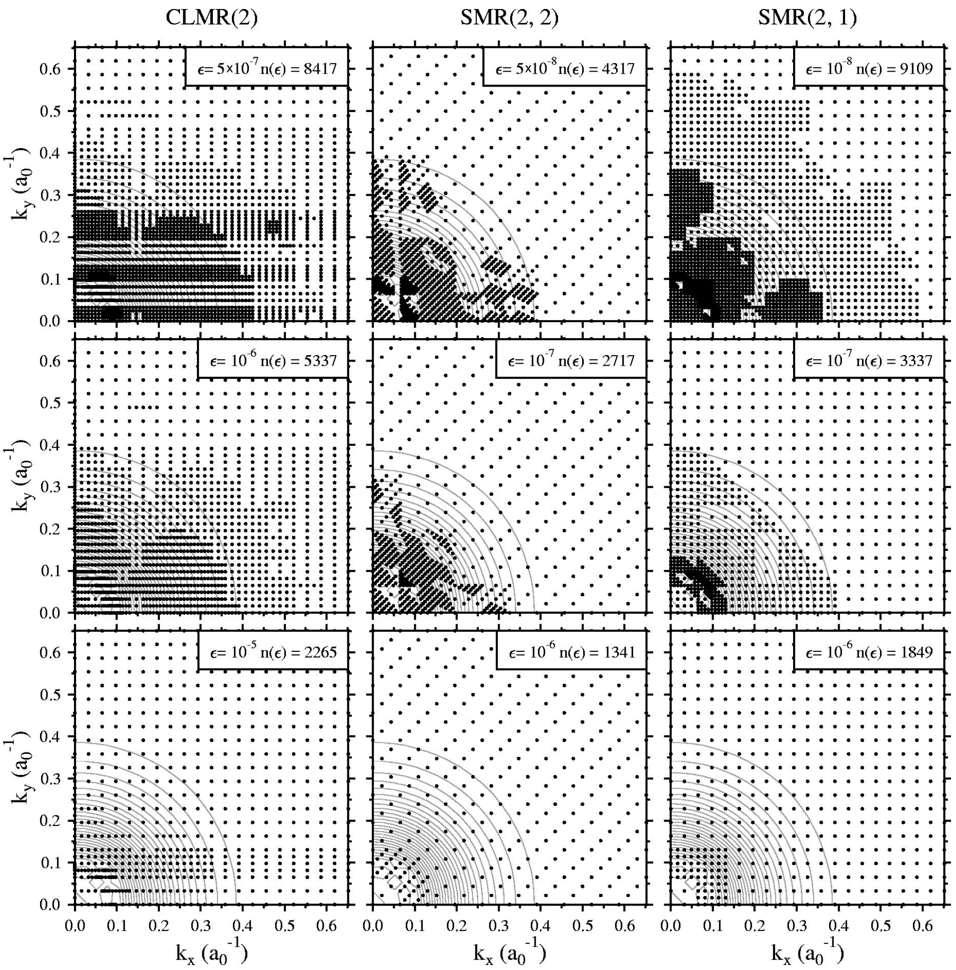

FIG. 5. Adapted meshes (dots) obtained by the CLMR(2) (left column), SMR(2,2) (middle), and SMR(2,1) (right) schemes for the transmission shown in Fig. 4. In the top right corner of each panel, the absolute accuracy $\epsilon$ and the number $n(\epsilon)$ of mesh points in the entire Brillouin zone are given. The transmission is displayed in addition by gray contour lines.

Rostoker (KKR) calculation closely follows the work by MacLaren and co-workers.[10]

For the purpose of this paper, we focus in the following on the system Ni(001)/vacuum/Ni(001) with the magnetic moments in the leads aligned along the [001] direction. Because $T(\boldsymbol{k}^{\parallel})$ shows the symmetry of the point group $4mm$, it is sufficient to present results for a quarter of the two-dimensional BZ. The wave vector components $k^x$ and $k^y$ are chosen with respect to [110] and $[\bar{1}10]$, respectively.

Due to the insulating spacer, the conductance $G$ decreases exponentially with spacer thickness. Further, the transmission $T(\boldsymbol{k}^{\parallel})$ gets focused at the BZ center. For three spacer layers of vacuum and parallel alignment of the lead magnetizations, most of the contributions to $G$ come from the region with rather small $|\boldsymbol{k}^{\parallel}|$, say, $|\boldsymbol{k}^{\parallel}|<0.25a_0^{-1}$ (Fig. 4). Note that due to the band structure of Ni $T(\boldsymbol{k}^{\parallel})$ has a plateau-shaped local minimum at $\boldsymbol{k}^{\parallel}=(0,0)$ which is surrounded by small ''ridges.''

Adapted meshes obtained by the CLMR(2), SMR(2,2), and SMR(2,1) schemes for selected absolute accuracies $\epsilon$ are shown in Fig. 5. The quarter of the BZ was initially partitioned by a $10\times10$ grid for all three schemes. As expected, the density of mesh points is rather low for small $\epsilon$ (bottom row in Fig. 5). A decrease of $\epsilon$ leads to a high sampling density of the region with small $|\boldsymbol{k}^{\parallel}|$, in accordance with the transmission shown in Fig. 4. A slightly increased point density is observed at $|\boldsymbol{k}^{\parallel}|\approx0.1a_0^{-1}$, just where the abovementioned plateau has its boundary. The local minimum at

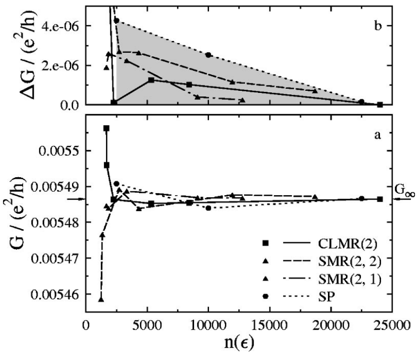

FIG. 6. Conductance $G$ of Ni(001)/vacuum/Ni(001) for three spacer layers of vacuum and parallel alignment of the lead magnetizations in dependence on the number $n(\epsilon)$ of mesh points. (a) Conductance as obtained by the three adaptive mesh refinements CLMR(2) (squares, solid lines), SMR(2,2) (triangles, dashed lines), and SMR(2,1) (triangles, dash-dotted lines), as well as by a special-point scheme (SP, circles, dotted lines). The arrows mark the converged value of the conductance $G_\infty$. (b) Same data as in (a), but displayed as the absolute deviation from $G_\infty$, $\Delta G = |G(n(\epsilon)) - G_\infty|$.

the BZ center requires a lower density than the surrounding ridge, as can be seen best for SMR(2,1). In other words, the meshes are adapted to the integrand $T(\boldsymbol{k}^{\parallel})$.

The convergence behavior of the conductance $G$ with decreasing $\epsilon$, and hence increasing number $n(\epsilon)$ of mesh points, is displayed in Fig. 6(a). For small $n(\epsilon)$, the conductance is far from being converged since it shows a significant variation for the CLMR(2) and SMR(2,2) schemes. The SMR(2,1) scheme instead appears to converge faster. For grids of about 5000 to 10 000 points, however, the conductances obtained by all three schemes are almost converged. A further increase of $n(\epsilon)$ reveals that the AMR's are robust, i.e., the conductance shows no considerable oscillations. Since the transmission shows a shape rather similar to that of the function $f(x) = \exp(-2|x|)$ one finds a similar general convergence behavior (cf. Sec. II). The AMR's have been investigated for both a variety of test functions and conductances of other systems (changing lead and spacer materials as well as spacer thicknesses): in all cases, these adaptive integration methods were robust and led to rapid convergence.

In addition to the AMR schemes, the conductance has been calculated with a special-point scheme.[16] The number of mesh points in the entire BZ ranged from 2500 up to 160 000. The conductance $G_\infty$ obtained from the largest number of points represents the converged value of $G$ and can hence be regarded as a reference. For all calculated values, the error $\Delta G = |G(n(\epsilon)) - G_\infty|$ of the AMR's is less than that of the SP scheme, i.e., the AMR points lie within the gray area in Fig. 6(b). Thus, AMR schemes can outperform SP schemes if the integrand shows unimportant regions of considerable size (here, $|\boldsymbol{k}^{\parallel}| > 0.3 a_0^{-1}$).

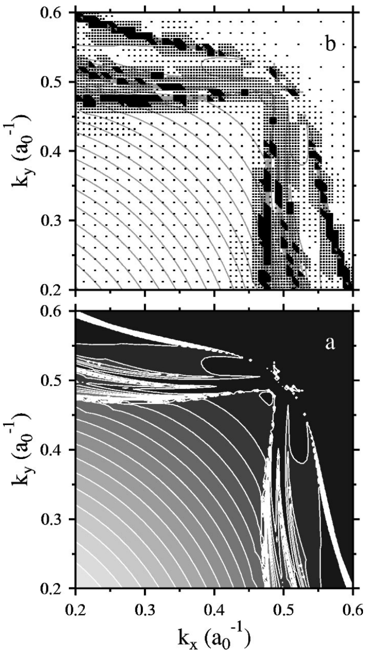

FIG. 7. Transmission $T(\boldsymbol{k}^{\parallel})$ of Ni(001)/vacuum/Ni(001) for one vacuum layer as spacer and antiparallel alignment of the lead magnetizations. (a) $T(\boldsymbol{k}^{\parallel})$ is shown as gray-scale contour, with black for zero transmission and light gray for maximum transmission (0.857). Equally spaced contour lines are displayed in white. (b) Adapted mesh (dots) as obtained by the SMR(2,1) scheme. The contour lines of (a) are shown in gray.

A particularly interesting case is tunneling through one spacer layer for antiparallel alignment of the magnetizations. The transmission for this system decays smoothly with increasing $|\boldsymbol{k}^{\parallel}|$, thus leading to a rather large region with almost zero contribution to the conductance [say $|\boldsymbol{k}^{\parallel}| > 0.5 a_0^{-1}$; black area in Fig. 7(a)]. Consequently, the adapted mesh [Fig. 7(b)] as obtained by SMR(2,1) with $\epsilon = 10^{-6}$ and a 10×10 initial grid is coarse in this area. However, interface resonances produce ''hot ridges'' with a large transmission (see Sec. I; cf. also Fig. 5 in Ref. 10). The AMR leads to a fine mesh right at these ridges [similar meshes were obtained by both the CLMR(2) and the SMR(2,2) schemes]. This clearly proves that the AMR's discussed in this paper are capable of finding even tiny important regions and therefore may considerably reduce the computation time.

## V. CONCLUDING REMARKS

Adaptive mesh-refinement schemes for Brillouin zone integration provide robust numerical methods which automatically find regions with a high accuracy demand. These regions are sampled with high density, while the other regions are sampled with low density. This salient feature may save a considerable amount of computational time as compared to integration methods that rely on equally spaced mesh points, regardless of the particular AMR used (cascading linear or simplex mesh refinement).

In our computer code for electron spectroscopies which is based on the layer-KKR method, a special-point scheme as well as three AMR's (the cascading linear and two simplex mesh refinements) for integration over the two-dimensional Brillouin zone were implemented. Since it is written in C++, the recursive algorithms of the AMR's could easily be implemented. The nesting is terminated if either the integration error is smaller than the prescribed accuracy or a maximum recursion level is reached. One minor disadvantage of the AMR's might be that the execution time of a calculation is hard to estimate since the number of mesh points is unknown *a priori*.

Adaptive mesh-refinement schemes, like other grid techniques, are of course not restricted to Brillouin zone integrations (for application of grid techniques in density-functional theory see Ref. 17). We suggest considering the implementation of AMR's in computer codes for electronic-structure calculations.

---

*Electronic address: henk@mpi-halle.mpg.de

[1] R. Evarestov and V. Smirnow, Phys. Status Solidi B **119**, 9 (1983).

[2] P.E. Blöchl, O. Jepsen, and O.K. Andersen, Phys. Rev. B **49**, 16 223 (1994).

[3] E. Bruno and B. Ginatempo, Phys. Rev. B **55**, 12 946 (1997).

[4] B. Heinrich and J.F. Cochran, Adv. Phys. **42**, 523 (1993).

[5] M. Johnson, P. Bloemen, and J. de Vries, Rep. Prog. Phys. **59**, 1409 (1996).

[6] J.C. Slonczewski, Phys. Rev. B **39**, 6995 (1989).

[7] E.Y. Tsymbal and D.G. Pettifor, J. Phys.: Condens. Matter **9**, L411 (1997).

[8] J. Mathon, Phys. Rev. B **55**, 960 (1997).

[9] W.H. Butler, X.-G. Zhang, T.C. Schulthess, and J.M. MacLaren, Phys. Rev. B **63**, 054416 (2001).

[10] J.M. MacLaren, X.-G. Zhang, W.H. Butler, and X. Wang, Phys. Rev. B **59**, 5470 (1999).

[11] C.W. Ueberhuber, *Numerical Computation 2* (Springer, Berlin, 1997).

[12] W.H. Press, B.P. Flannery, S.A. Teukolsky, and W.T. Vetterling, *Numerical Recipes. The Art of Scientific Programming* (Cambridge University Press, Cambridge, 1989).

[13] J. Henk, J. Phys.: Condens. Matter **13**, 833 (2001).

[14] P. Weinberger, *Electron Scattering Theory of Ordered and Disordered Matter* (Clarendon Press, Oxford, 1990).

[15] M. Büettiker, Phys. Rev. Lett. **57**, 1761 (1986).

[16] H.J. Monkhorst and J.D. Pack, Phys. Rev. B **13**, 5188 (1976).

[17] T.L. Beck, Rev. Mod. Phys. **72**, 1041 (2000).

## Publikation 12

# Absence of Zero-Bias Anomaly in Spin-Polarized Vacuum Tunneling in Co(0001)

H. F. Ding, W. Wulfhekel, J. Henk, P. Bruno, and J. Kirschner
*Max-Planck Institut für Mikrostrukturphysik, Weinberg 2, D-06120 Halle, Germany*

(Received 23 September 2002; published 20 March 2003)

In a joint experimental and theoretical study, we investigate the bias-voltage dependence of the tunnel magnetoresistance (TMR) through a vacuum barrier. The TMR observed by spin-polarized scanning tunneling microscopy between an amorphous magnetic tip and a Co(0001) sample is almost independent of the bias voltage at large tip-sample separations. Whereas qualitative understanding is achieved by means of the electronic surface structure of Co, the experimental findings are compared quantitatively with bias-voltage dependent first-principles calculations for ballistic tunneling. At small tip-sample separations, a pronounced minimum in the experimental TMR was found at +200 mV bias.

DOI: 10.1103/PhysRevLett.90.116603 PACS numbers: 72.25.Mk, 68.37.Ef, 85.75.–d

Nowadays, spin-polarized tunneling (SPT) is of particular interest due to its applications in magnetic tunnel devices and in magnetic imaging [1–3]. The field of SPT was opened in the early 1970s, when Tedrow and Meservey studied electron tunneling between a ferromagnet and a superconductor through an amorphous barrier [4] and Müller *et al.* analyzed the spin polarization of field-emitted electrons from EuS coated W tips through vacuum [5]. After Jullière had found the tunnel magnetoresistance (TMR) effect, i.e., the dependence of the tunneling resistance on the relative orientation of the lead magnetizations [6], SPT was studied intensively. Recently, magnetic tunnel junctions with reproducible characteristics at room temperature were fabricated, allowing one to elucidate the underlying physical mechanisms [3,7–15].

However, SPT is still far from being completely understood. Because of its importance for applications, a large number of studies were devoted to the so-called zero-bias anomaly, i.e., the decrease of the TMR with increasing bias voltage in planar junctions [9,16–21]. Junctions made of the same electrodes but with different insulating spacer materials or even with identical but differently prepared insulators vary considerably concerning the voltage dependence of the TMR [6,7,12,20]. With the advances in sample preparation, especially of the barriers, the bias voltage which is sufficient to halve the TMR increased from 3 mV [6] to 500–700 mV [12,20].

To explain this still puzzling behavior, several models were proposed, which have in common that they relate the TMR to the spin polarization. First, biasing of the metal-insulator-metal junctions at finite temperature leads to elastic tunneling of electrons mostly from the Fermi energy of the negative electrode into unoccupied states of the positive electrode [22,23]. The energy dependence of the density of states (DOS) in the positive electrode causes variations of the spin polarization that translate into TMR variations [24]. This DOS effect was observed in crystalline junctions [10]. Second, hot electrons from the positive electrode might be scattered in a spin-dependent way by local magnetic moments at the interfaces [9] or might create magnons [17]. Both effects reduce the spin polarization and, consequently, lower the TMR. Finally, Zhang and White suggested that incoherent tunneling due to scattering at impurities or defects located in the barrier reduces the spin polarization because the electrons tunnel via trap states [16]. This model was supported by both experiment and theory [12,18,21].

Until now, a consistent picture of the zero-bias anomaly has not been achieved. The difficulties are partly related to the complex structure of the tunnel junctions which often comprise poorly characterized amorphous barriers that bring about higher-order SPT effects [16,19,20] and complicate the theoretical treatment. However, by replacing the insulator barrier by vacuum, one can rule out defects in the spacer. Because the DOS effect, spin scattering at the interfaces, and magnon creation remain, SPT through a vacuum barrier allows one to identify the responsible mechanisms for the bias-voltage dependence.

In this Letter, we report on a joint experimental and theoretical investigation of the TMR between a Co(0001) sample and an amorphous CoFeSiB tip through a vacuum barrier as a function of bias voltage. By means of a spin-polarized STM (SP-STM), a strong drop of the experimental TMR with bias voltage is not found. To explain qualitatively this absence of the zero-bias anomaly, we performed first-principles calculations of the electronic structure of semi-infinite Co(0001). Calculations for ballistic tunneling through planar Co(0001) junctions, which take into account the bias voltage, corroborate our experimental findings quantitatively. To summarize at this point, the zero-bias anomaly can be attributed to scattering of electrons at defects in amorphous barriers. Magnon creation appears to be less important.

*Experimental.*—All experiments were performed in an ultrahigh vacuum chamber ($p = 5 \times 10^{-11}$ mbar) equipped with a SP-STM and standard surface characterization techniques [2,25,26]. The single-crystalline Co(0001) sample and the magnetic tip were cleaned *in situ* by $Ar^+$ sputtering. During scanning, the longitudinal magnetization of the tip was switched periodically. The resulting variations of the tunneling current were detected with a phase-sensitive lock-in amplifier, allowing one to map the magnetic structure of the sample. Measuring this way the average tunneling current and its modulation between opposite tip magnetizations, the TMR was determined *directly*, in analogy to the experiments by Jullière. This approach differs from recent SP-STM experiments by Bode *et al.* [1], in which the differential conductance was measured. Their $dI/dV$ spectra contain information on the spin polarization as well as on the local DOS and stress the role of spin-polarized surface states in vacuum tunneling.

Tunneling images of both the topography and the magnetic structure were recorded simultaneously at room temperature. The typical dendriticlike perpendicular domain pattern of Co(0001) was observed, similar to that seen with standard magnetic-imaging techniques [27–29]. Applying an external magnetic field, the domain pattern could be displaced while the topography image did not move, thus proving the magnetic origin of the contrast. Magnetic contrast due to mechanisms similar to magnetic force microscopy was ruled out [28] and changes of the tip-sample distance due to magnetostriction were experimentally and theoretically shown to be less than 0.1 pm [30]. Exposure of a few Langmuir of oxygen or deposition of a few monolayers of Au on Co(0001) caused a fading of the magnetic contrast, as was observed for SPT in Au seeded planar tunnel junctions [31].

To study the TMR as a function of the applied bias voltage, we zoomed into a small area and recorded the magnetic contrast (which is proportional to the TMR). In each pixel of the images, the feedback loop was opened for a short time such that the tip position was fixed. The bias-voltage $U$ was ramped while measuring the averaged and the modulated tunneling currents $I_t(U)$ and $\Delta I(U)$, respectively. The TMR, defined as the asymmetry $\delta$ of the tunneling currents for opposite tip magnetizations ($\uparrow$ and $\downarrow$), was calculated from the ratio of these two currents averaged over about 1000 pixels,

$$\delta(U) = \frac{I_\uparrow(U) - I_\downarrow(U)}{I_\uparrow(U) + I_\downarrow(U)} = \frac{\Delta I(U)}{2 I_t(U)}. \qquad (1)$$

Since the TMR is proportional to the scalar product of the tip and the sample magnetizations [32,33], the relative change of the magnetic contrast in small-scale images fully reflects the TMR obtained from parallel (P) and antiparallel (AP) magnetic configurations, although the sample magnetization is oriented only slightly out of the surface plane (typically 10°) [27,29].

*Theoretical.*—To explain qualitatively and quantitatively the experimental results, we performed first-principles relativistic Korringa-Kohn-Rostoker (KKR) calculations for bulk Co and semi-infinite Co(0001). Besides band structures and layer-resolved spectral densities that provide qualitative insight, we obtained quantitative support by TMR calculations for a planar junction of two Co(0001) surfaces. Conductances $G$ for P and AP magnetic configurations were computed within the layer-KKR scheme of tunneling proposed by MacLaren and co-workers [34]. The time-consuming Brillouin-zone integration of the transmission was carried out by adaptive mesh refinement [35]. In order to treat a bias voltage between the leads in a simple model, the inner potentials of the leads were kept fixed but differed by the voltage drop $\Delta E$. The potential of the tunnel barrier was taken as a superposition of two surface barriers [36]. Hence, this barrier interpolates smoothly between the respective surfaces. Note that the height of the tunnel barrier is determined by the distance $d$ between the leads and by the bias-voltage $\Delta E$. This model should be valid in first approximation for small $\Delta E$ and for large $d$. The TMR is defined in analogy to Eq. (1) in terms of the averaged conductances $G_{\mathrm{av}} = \int_{\Delta E} G(E) dE / \Delta E$. Note that the theoretical TMR is symmetric with respect to the bias voltage due to identical leads, in contrast to the experiment (surface vs STM tip).

*Results and discussion.*—The measured TMR [37] [Fig. 1(a)] obtained with the tip stabilized at 1 V, 1 nA ($\approx$ 7 Å above the sample surface) appears to be almost constant for bias voltages up to ±1 V. This absence of the zero-bias anomaly is in clear contrast to the case of planar tunnel junctions with insulating spacers. If spin-dependent scattering at the interface magnetic moments and at magnons were the prominent mechanisms for the decrease of the TMR, the latter should also be present in our case. Its absence, however, indicates that these mechanisms are not dominant.

The probability for an electron to tunnel coherently through a barrier with height $V_b$ is proportional to $\exp(-2d\sqrt{2V_b + \vec{k}_\parallel^2})$ [23,38]. Because it decays stronger with tip-sample distance $d$ for large transverse crystal momentum $\vec{k}_\parallel$ than for a small one, it gets "focused" at the Brillouin-zone center for large $d$. Therefore, we concentrate in the following on the electronic structure of the $\Gamma$–$\Delta$–A direction ($\vec{k}_\parallel = 0$). The band structure [Fig. 2(a)] shows two very close but spin-orbit

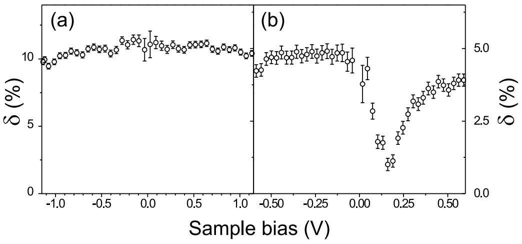

FIG. 1. Tunnel magnetoresistance $\delta$ and its error of a clean Co(0001) surface vs bias voltage $U$, obtained with a magnetic tip stabilized at 1 V, 1 nA (a) and at 100 mV, 1 nA (b).

split minority bands (white) ranging from slightly below the Fermi energy (0 eV) up to about 1 eV. Since their spin polarization $P$ is almost constant ($P \approx -0.99$ with variation less than 0.01), an almost constant TMR is expected, in agreement with the experimental findings. For negative bias, the TMR is expected constant as well because the electrons tunnel into the amorphous tip, the spectral density of which should possess no sharp features. Summarizing, the bulk electronic structure corroborates qualitatively our experimental findings for large $d$.

To support quantitatively the experimental finding, we present in Fig. 3(a) the calculated averaged tunneling conductances $G_{\mathrm{av}}$ integrated over the whole Brillouin zone. As expected for a symmetric junction, these are larger for the P than for the AP configuration. Further, they decrease by almost 2 orders of magnitude when increasing $d$ from $2d_0 = 4.07$ Å to $3d_0 = 6.11$ Å ($d_0 = 2.035$ Å, the Co interlayer distance). In agreement with the preceding arguments, the TMR is almost constant [Fig. 3(b)].

The TMR can be considerably changed for small barrier widths because electronic states with large $\vec{k}_{\parallel}$ can contribute significantly to the tunneling current (cf. the argument above) and tunneling via surface states can become important also (for STM experiments, see, e.g., Ref. [38]). Figure 1(b) presents the experimental TMR vs bias voltage obtained with the same tip as used for large separations, but at a smaller tip-sample separation ( ≈ 5 Å; feedback conditions: 100 mV, 1 nA). In this case, the bias voltage was limited to a smaller range (from −600 mV up to +600 mV) to avoid saturation of the $I(V)$ spectra. For negative bias, a constant TMR was still observed, in agreement with the expected tip electronic structure. For positive bias, however, the TMR showed a strong minimum at 200 mV and was reduced above 400 mV. As the bulk states along the Γ–Δ–A direction ($\vec{k}_{\parallel} = 0$) are mostly of minority character, one can speculate whether the dip is related to majority states with large $\vec{k}_{\parallel}$ or to a majority surface state reducing the TMR. Indeed, inverse photoemission measurements revealed a surface state in Co(0001) at about 200 meV [39,40] which is also found in our calculations [black arrow in Fig. 2(b)] [41]. At small tip-sample separations, the tunneling probability through this surface state might be enhanced, so as to decrease significantly the TMR. This mechanism could qualitatively explain the constant TMR for large tip-sample separations and the minimum at small tip-sample separations. Our tunneling calculations cannot provide direct support because surface states lie in a bulk band gap and, therefore, do not contribute to the ballistic conductance. Nevertheless, it is conceivable that the surface state contributes via scattering at steps or other defects at the surface which breaks the $\vec{k}_{\parallel}$ conservation in ballistic tunneling [42] and by this reduce the TMR. We note in passing that the TMR dip reported here is not related to a drop in the TMR asymmetry between forward and backward biasing observed by LeClair *et al.* for a Co tunnel junction with insulating spacer [43]. That feature was related to bulk states and not to a

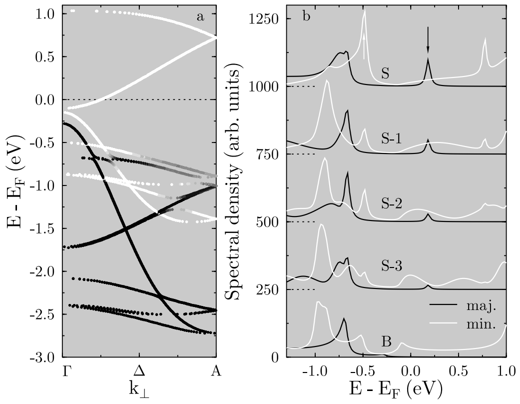

FIG. 2. (a) Spin-resolved relativistic band structure of bulk hcp Co along the Γ–Δ–A direction (i.e., $\vec{k}_{\parallel} = 0$). The sliding grey scale of the filled circles reflects the spin polarization $P$: "majority" ($P \approx 1$) black; "minority" ($P \approx -1$) white. (b) Spin- and layer-resolved spectral density of Co(0001) at $\vec{k}_{\parallel} = 0$ for the first four surface layers (S, S-1, …, S-3) and a bulk layer (B). The arrows mark surface states.

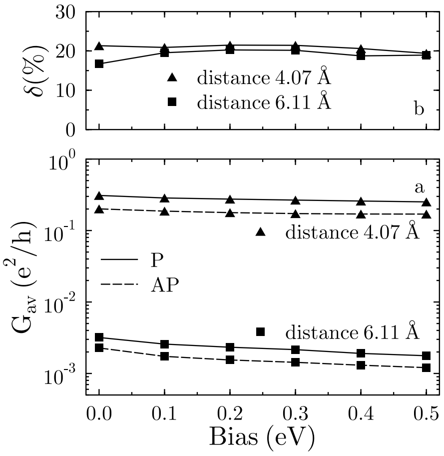

FIG. 3. Theoretical spin-dependent tunneling through Co(0001) planar junctions. (a) Averaged conductances $G_{\mathrm{av}}$ in logarithmic scale for P (solid lines) and AP (dashed) configurations at various barrier widths $d$ (triangles: $d = 2d_0$, squares: $d = 3d_0$; in units of the Co interlayer distance $d_0$) vs bias voltage. (b) Tunnel magnetoresistance $\delta$ obtained from the data shown in (a).

surface state. Eventually, the minority surface state at about $-430\,\mathrm{meV}$ which accounted for a considerable increase of the TMR in spin-polarized scanning tunneling spectroscopy [44] is not expected to change significantly the TMR of the total tunneling current because its spin polarization is similar to that in the bulk states [white arrow in Fig. 2(b)]. This is a striking difference to the surface state at 200 meV.

*Conclusions.*—Investigating the electron tunneling between a Co(0001) surface and an amorphous tip across a vacuum barrier with a spin-polarized STM, we observed an almost constant tunneling magnetoresistance with bias voltage for large tip-sample separations, i.e., no zero-bias anomaly. Thus, the zero-bias anomaly in planar tunnel junctions with insulator barriers can be attributed to defect scattering in the barrier, rather than to magnon creation or spin excitations at the interfaces. First-principles calculations for the electronic structure and for ballistic tunneling including the bias voltage corroborate our experimental finding qualitatively and quantitatively. For small barrier width, a drop in the TMR occurred at $+200$ mV bias voltage, which is likely related to a majority surface state of Co(0001).

[1] M. Bode, M. Getzlaff, and R. Wiesendanger, Phys. Rev. Lett. **81**, 4256 (1998).

[2] W. Wulfhekel and J. Kirschner, Appl. Phys. Lett. **75**, 1944 (1999).

[3] J. S. Moodera and G. Mathon, J. Magn. Magn. Mater. **200**, 248 (1999).

[4] P. M. Tedrow and R. Meservey, Phys. Rev. Lett. **26**, 192 (1971).

[5] N. Müller, W. Eckstein, W. Heiland, and W. Zinn, Phys. Rev. Lett. **29**, 1651 (1972).

[6] M. Jullière, Phys. Lett. **54A**, 225 (1975).

[7] J. S. Moodera, L. R. Kinder, T. M. Wong, and R. Meservey, Phys. Rev. Lett. **74**, 3273 (1995).

[8] Y. Lu, R. A. Altman, A. Marley, S. A. Rishton, P. L. Trouilloud, G. Xiao, W. J. Gallagher, and S. S. P. Parkin, Appl. Phys. Lett. **70**, 2610 (1997).

[9] S. Zhang, P. M. Levy, A. C. Marley, and S. S. P. Parkin, Phys. Rev. Lett. **79**, 3744 (1997).

[10] J. M. De Teresa, A. Barthélémy, A. Fert, J. P. Contour, F. Montaigne, and P. Seneor, Science **286**, 507 (1999).

[11] M. Sharma, S. X. Wang, and J. H. Nickel, Phys. Rev. Lett. **82**, 616 (1999).

[12] S. Yuasa, T. Sato, E. Tamura, Y. Suzuki, H. Yamamori, K. Ando, and T. Katayama, Europhys. Lett. **52**, 344 (2000).

[13] P. LeClair, J. T. Kohlhepp, H. J. M. Swagten, and W. J. M. de Jonge, Phys. Rev. Lett. **86**, 1066 (2001).

[14] S. Yuasa, T. Nagahama, and Y. Suzuki, Science **297**, 234 (2002).

[15] R. Meservey and P. M. Todrow, Phys. Rep. **238**, 173 (1994).

[16] J. Zhang and R. M. White, J. Appl. Phys. **83**, 6512 (1998).

[17] J. S. Moodera, J. Nowak, and R. J. M. van de Veerdonk, Phys. Rev. Lett. **80**, 2941 (1998).

[18] E. Y. Tsymbal and D. G. Pettifor, Phys. Rev. B **58**, 432 (1998).

[19] E. Y. Tsymbal and D. G. Pettifor, J. Appl. Phys. **85**, 5801 (1999).

[20] H. Boeve, E. Girgis, J. Schelten, J. De Boeck, and G. Borghs, Appl. Phys. Lett. **76**, 1048 (2000).

[21] R. Jansen and J. S. Moodera, Phys. Rev. B **61**, 9047 (2000).

[22] J. Frenkel, Phys. Rev. **36**, 1604 (1930).

[23] E. L. Wolf, *Principles of Electron Tunneling Spectroscopy* (Oxford University Press, New York, 1985).

[24] D. A. Papaconstantopoulos, *Handbook of the Band Structure of Elemental Solids* (Plenum, New York, 1986).

[25] W. Wulfhekel, H. F. Ding, and J. Kirschner, J. Appl. Phys. **87**, 6475 (2000).

[26] W. Wulfhekel, H. F. Ding, W. Lutzke, G. Steierl, M. Vàzquez, P. Marìn, A. Hernando, and J. Kirschner, Appl. Phys. A **72**, 463 (2001).

[27] J. Unguris, M. R. Scheinfein, R. C. Celotta, and D. T. Pierce, Appl. Phys. Lett. **55**, 2553 (1989).

[28] H. F. Ding, W. Wulfhekel, C. Chen, J. Barthel, and J. Kirschner, Mater. Sci. Eng. B **84**, 96 (2001).

[29] H. F. Ding, W. Wulfhekel, and J. Kirschner, Europhys. Lett. **57**, 100 (2002).

[30] W. Wulfhekel, R. Hertel, H. F. Ding, G. Steierl, and J. Kirschner, J. Magn. Magn. Mater. **249**, 368 (2002).

[31] J. S. Moodera, M. E. Taylor, and R. Meservey, Phys. Rev. B **40**, 11 980 (1989).

[32] J. C. Slonczewski, Phys. Rev. B **39**, 6995 (1989).

[33] T. Miyazaki and N. Tezuka, J. Magn. Magn. Mater. **139**, L231 (1995).

[34] J. M. MacLaren, X.-G. Zhang, W. H. Butler, and X. Wang, Phys. Rev. B **59**, 5470 (1999).

[35] J. Henk, Phys. Rev. B **64**, 035412 (2001).

[36] R. O. Jones, P. J. Jennings, and O. Jepsen, Phys. Rev. B **29**, 6474 (1984).

[37] To present the full TMR between P and AP magnetic configurations, the contrast was scaled by $1/\cos\theta$, where $\theta$ is the angle between sample magnetization and surface normal.

[38] J. A. Stroscio, D. T. Pierce, A. Davies, R. J. Celotta, and M. Weinert, Phys. Rev. Lett. **75**, 2960 (1995).

[39] C. Math, J. Braun, and M. Donath, Surf. Sci. **482–485**, 556 (2001).

[40] J. Braun and M. Donath, Europhys. Lett. **59**, 592 (2002).

[41] This surface state was recently observed in scanning tunneling spectroscopy experiments on standing waves on thick hcp Co(0001) films. K. Kern (private communication).

[42] O. Wunnicke, N. Papanikolaou, R. Zeller, P. H. Dederichs, V. Drchal, and J. Kudrnovský, Phys. Rev. B **65**, 064425 (2002).

[43] P. LeClair, J. T. Kohlhepp, C. H. van de Vin, H. Wieldraaijer, H. J. M. Swagten, W. J. M. de Jonge, A. H. Davis, J. M. MacLaren, J. S. Moodera, and R. Jansen, Phys. Rev. Lett. **88**, 107201 (2002).

[44] S. N. Okuno, T. Kishi, and K. Tanaka, Phys. Rev. Lett. **88**, 066803 (2002).

## Publikation 13

# Spin motion of photoelectrons

J. Henk,* P. Bose, Th. Michael, and P. Bruno
*Max-Planck-Institut für Mikrostrukturphysik, Weinberg 2, D-06120 Halle (Saale), Germany*

(Received 16 May 2003; published 12 August 2003)

*Ab initio* and model calculations demonstrate that the spin motion of electrons transmitted above the vacuum energy through ferromagnetic films can be investigated by means of angle- and spin-resolved core-level photoelectron spectroscopy. The motion of the photoelectron spin polarization can be regarded as a combination of a precession around and a relaxation towards the magnetization direction. For ultrathin Fe films on Pd(001), its dependence on the Fe film thickness and on the Fe electronic structure is studied systematically. In addition to elastic and inelastic scattering, the effect of band gaps on the spin motion is addressed in particular.

DOI: 10.1103/PhysRevB.68.052403 PACS number(s): 75.70.Ak, 79.60.−i, 73.40.Gk, 75.50.Bb

Taking advantage of the spin in electronic devices, in order to form new ‘‘spintronic’’ devices, is currently in progress worldwide. This goal challenges both applied and basic physics, the latter being mostly concerned with model systems of spin-dependent transport.[1] Aiming at very small devices, the properties of magnetic nanostructures become increasingly important. In particular, spin-dependent scattering in ultrathin films and at interfaces may have a profound effect on the transport properties[2,3]: the electronic spins start to precess and the spin current applies a spin-transfer torque on the magnetization in the ferromagnet. To understand in detail the spin motion in electron transmission through magnetic films, one obviously needs a microscopic probe.

Ferromagnetic resonance, used successfully to study the magnetic properties of multilayer systems,[4] cannot deal with electron transmission. However, spin- and time-resolved photoelectron spectroscopy was employed to investigate directly spin filtering in the time domain.[5] Spin motion, which can be regarded as a combination of a precession of the electron spin polarization (ESP) $\vec{P}$ around the magnetization direction and as relaxation of $\vec{P}$ towards the magnetization $\vec{M}$, is interesting in its own right.[6,7] A successful method which addresses the spin motion of electrons above the vacuum level is the transmission of spin-polarized electrons (usually produced with a GaAs source) through freestanding ferromagnetic films.[8] Further, spin motion was recently observed in spin-resolved low-energy electron diffraction (SPLEED).[9]

The purpose of this paper is twofold. First, we propose to apply angle- and spin-resolved photoelectron spectroscopy from core levels to access directly the spin motion of electrons transmitted through an ultrathin ferromagnetic film (Fig. 1). Therefore, it is proved by means of *ab initio* calculations that precession and relaxation can be observed in experiments. We are not aware of other first-principles investigations of spin motion in electron transmission. Beyond that, it is shown that spin motion can serve as a tool for obtaining information on the electronic and magnetic structure of the system.

Our approach relies in particular on the possibility to orient the spin polarization of the incoming photoelectrons by the incident light, an effect due to spin-orbit coupling. In the following, the basic ideas are described for the chosen systems $n$ monolayer (ML) Fe/Pd(001), $n=1, \ldots ,6$ (for details, see Ref. 10).

(i) The incident light excites electrons from Pd $3d_{3/2}$ core levels of the Pd(001) substrate into a state above the vacuum level $E_{\mathrm{vac}}$.

(ii) Choosing linearly $p$-polarized light with incidence direction given by $\vartheta_{\mathrm{ph}}=45°$ polar angle and variable azimuth $\varphi_{\mathrm{ph}}$, the ESP in the substrate can be aligned to any desired direction in the $xy$ surface plane (Cartesian coordinates are defined in Fig. 1). It was theoretically and experimentally shown for nonmagnetic layered systems with fourfold rotational symmetry that an ESP perpendicular to the scattering plane (spanned by the surface normal and the incidence direction; see Ref. 11 and references therein) is produced: $\vec{P}^{\mathrm{in}} \propto (-\sin\varphi_{\mathrm{ph}}, \cos\varphi_{\mathrm{ph}}, 0)$. For $\varphi_{\mathrm{ph}}=0°$ and 180°, $\vec{P}^{\mathrm{in}}$ is perpendicular to the magnetization $\vec{M}$ (which is parallel to $x$). Hence, the commonly used external GaAs source for spin-polarized electrons is, so to speak, replaced by an internal one, with the advantage of easy orientation of $\vec{P}^{\mathrm{in}}$.

(iii) During the transmission through the Fe film, the photoelectron is subject to elastic and inelastic scattering processes. Both can simply be modeled by spin-dependent scattering at an asymmetric quantum well which comprises the substrate-film and film-vacuum interfaces. The transmitted ESP $\vec{P}^{\mathrm{tr}}$ reads

$$\vec{P}^{\mathrm{tr}} \propto \begin{pmatrix} |T^{\uparrow}|^2 - |T^{\downarrow}|^2 + P_x^{\mathrm{in}}(|T^{\uparrow}|^2 + |T^{\downarrow}|^2) \\ P_y^{\mathrm{in}}\mathrm{Re}(T^{\uparrow\star}T^{\downarrow}) - P_z^{\mathrm{in}}\mathrm{Im}(T^{\uparrow\star}T^{\downarrow}) \\ P_z^{\mathrm{in}}\mathrm{Re}(T^{\uparrow\star}T^{\downarrow}) + P_y^{\mathrm{in}}\mathrm{Im}(T^{\uparrow\star}T^{\downarrow}) \end{pmatrix}, \qquad (1)$$

where the spin-dependent transmission coefficients $T^{\uparrow(\downarrow)}$ take into account multiple reflection. Considering elastic scattering, the dependence of $\vec{P}^{\mathrm{tr}}$ on the film thickness $d$ shows two oscillation periods. The precession of the transversal components $P_y^{\mathrm{tr}}$ and $P_z^{\mathrm{tr}}$ around $\vec{M}$ (Refs. 12 and 13) has a longer period with wavelength $2\pi/(k_z^{\uparrow} - k_z^{\downarrow})$, $k_z^{\uparrow(\downarrow)}$ being the electron wave numbers in the film. Multiple reflection at the interfaces results in a short-period oscillation with wavelength $2\pi/(k_z^{\uparrow} + k_z^{\downarrow})$ and much smaller amplitude. The longitudinal component $P_x^{\mathrm{tr}}$ remains constant on average.

Inelastic scattering leads to spin-dependent attenuation within the film. Simulated by multiplying the propagators between the interfaces by $\exp(-d/\lambda^{\uparrow(\downarrow)})$, this spin-filter effect relaxes $\vec{P}^{\mathrm{tr}}$ towards $\vec{M}$ (i.e., $\lim_{d\to\infty} P_x^{\mathrm{tr}} = 1$ for $\lambda^{\uparrow} > \lambda^{\downarrow}$). It

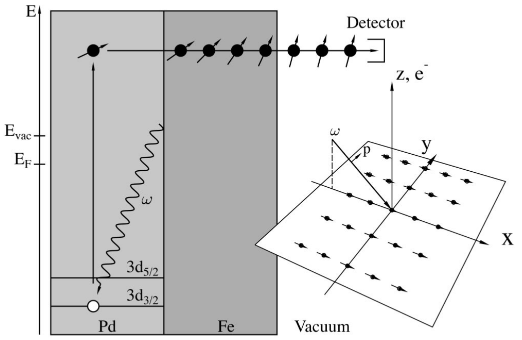

FIG. 1. Spin motion in electron transmission through a ferromagnetic film accessed by photoelectron spectroscopy. Left: a core electron is excited by the incident radiation (wavy line, photon energy $\omega$) in the Pd substrate (light gray). The spin polarization (arrow) of the photoelectron (solid circle) is oriented due to spin-orbit interaction. During the transmission through the magnetic Fe film (dark gray), the spin polarization rotates further (spin motion) but stops rotating in the vacuum. $E_{\mathrm{F}}$ and $E_{\mathrm{vac}}$ are the Fermi and vacuum levels, respectively. Right: setup of normal photoemission from a ferromagnetic surface (with magnetization along $x$) and $p$-polarized light incident in the $xz$ plane.

was successfully used to determine the attenuation lengths $\lambda^{\uparrow(\downarrow)}$ (Refs. 14 and 15) and to obtain the spin-resolved electronic structure of Fe.[16] There is no spin motion in nonmagnetic regions (e.g., vacuum).

(iv) The photoelectrons are eventually detected as spin resolved in normal emission ($\vec{k}_{\parallel}=0$). The electron energies are considerably larger than those in spin-dependent transport measurements. To come closer to the Fermi level one might use threshold photoemission (PE) or deposit a work-function-reducing adlayer onto the surface.

The small photoelectron escape depth[17,18] restricts $d$ to a few ML. This implies for ultrathin films that the short-period oscillation might dominate the spin motion, a complete precession cannot be observed, and the relaxation limit ($\vec{P}\parallel\vec{M}$) cannot be reached in practice. The present approach is not restricted to linearly polarized light. Spectra for circularly polarized light (not reported here), for which one can produce $\vec{P}^{\mathrm{in}}$ with a component along the surface normal,[19] agree qualitatively with those discussed here.

*Theoretical.* To obtain reliable results, we rely on a computational scheme which proved to be successful in describing qualitatively and quantitatively PE from nonmagnetic and ferromagnetic surfaces in the valence-band and core-level regimes (Ref. 20 and references therein). Starting from first-principles electronic-structure calculations for 0–6 ML fcc Fe/Pd(001) [Ref. 10, local spin-density approximation of density-functional theory, screened Korringa-Kohn-Rostoker (KKR) method; for details, see Ref. 21], spin- and angle-resolved constant-initial-state PE spectra were computed within the relativistic one-step model (layer-KKR method; cf. Ref. 22). The latter describes PE correctly as a coherent process (in contrast to the three-step model which treats excitation, propagation towards the surface, and transmission into the vacuum separately). The applicability of the initial-state picture of core-level PE (see, e.g., Ref. 20) was checked by comparing theoretical with experimental spectra. Here, a poor description would affect mainly the size of the incoming ESP. The general results on spin motion, however, would still be valid. Within the KKR method, the semi-infinite systems (Pd substrate/Fe film/vacuum) were treated with the correct boundary conditions. Reasonable values were chosen for the free parameters[10]; e.g., the first 30 layers contributed to the photocurrent.

The structure of Fe on Pd(001) depends on the preparation conditions and can show disorder and imperfections at the surface.[23] Since the present investigation focuses on the basic spin-motion effects, we deliberately choose ideal fcc Fe films instead. Consequently, a perfect agreement with future experiments is not expected.

We choose Fe/Pd(001) due to the large magnetic moment of Fe and the strong spin-orbit coupling in Pd which results in a sizable $\vec{P}^{\mathrm{in}}$. The covering Fe induces a magnetic moment of about $0.24\mu_{\mathrm{B}}$ in the Pd layer close to the Fe/Pd interface.[10] Hence, $\vec{P}^{\mathrm{in}}$ originates from the induced exchange splitting and from spin-orbit coupling. That the spin motion is dominantly due to the Fe magnetism was checked by considering several "artificial" magnetic configurations and by variation of the azimuth of light incidence. Further, changing the inverse photoelectron lifetime in the Fe film allowed us to differentiate between elastic (precession around $\vec{M}$) and inelastic processes (relaxation towards $\vec{M}$).

*Elastic and inelastic processes.* Inelastic processes can be simulated in calculations by adding an imaginary self-energy to the potential (see, e.g., Ref. 24). To unveil the influence of these processes, the inverse photoelectron lifetime in the Fe film was reduced to 0.001 eV ("elastic" case), as compared to the otherwise chosen 1.8 eV ("inelastic" case). Being rather small and almost constant in the elastic case, $P_x^{\mathrm{tr}}$ in-

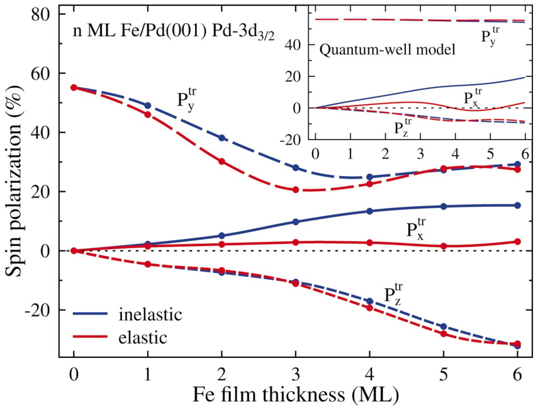

FIG. 2. (Color) Elastic and inelastic effects in spin motion for 0–6 ML Fe on Pd(001) at 17.5 eV kinetic energy and azimuth of light incidence $\varphi_{\mathrm{ph}}=0°$. The transmitted electron-spin polarization $\vec{P}^{\mathrm{tr}}$ is shown vs Fe-film thickness $n$ (in ML) for the inelastic (blue) and elastic (red) cases. The inset shows corresponding results of a model calculation.

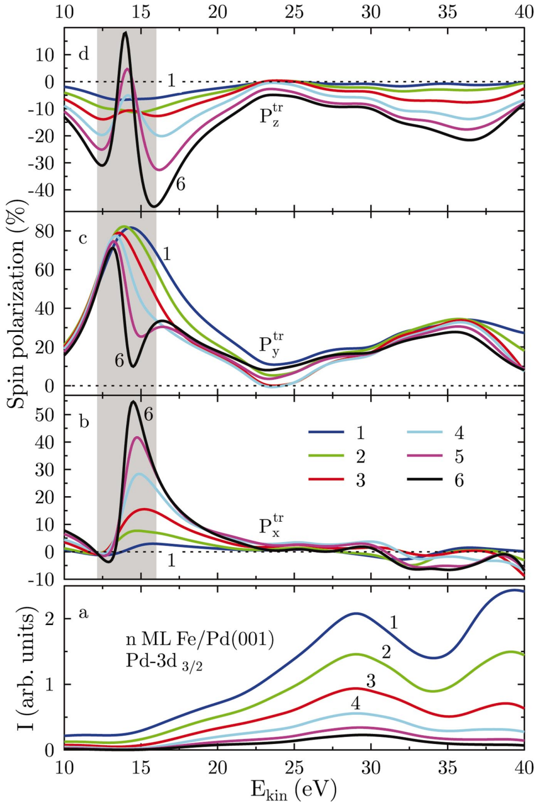

FIG. 3. (Color) Energy dependence of the spin motion for 1–6 ML Fe on Pd(001). (a) Spin-averaged constant-initial-state photoemission intensities $I$ vs kinetic energy $E_{\mathrm{kin}}$ of the photoelectrons. (b)–(d) Transmitted electron-spin polarization $\vec{P}^{\mathrm{tr}}$. The Fe-film thickness $n$ (in ML) is indicated by numbers and color coding. The gray area highlights a prominent feature discussed in the text.

creases with Fe coverage in the inelastic case (Fig. 2), i.e., $\vec{P}^{\mathrm{tr}}$ starts to relax towards $\vec{M}$. Because the short-period oscillation is relevant for ultrathin films, the precession of $\vec{P}^{\mathrm{tr}}$ around $\vec{M}$ (which shows the long wavelength) cannot be clearly observed. To corroborate these findings, we calculated $\vec{P}^{\mathrm{tr}}$ within the quantum-well model sketched preceding, with parameters obtained from the Pd and Fe bulk-band structures (inset in Fig. 2). The resulting wavelengths of about 200 ML (precession) and 3.9 ML (multiple reflection) lead to reasonable agreement concerning $P_x^{\mathrm{tr}}$ and $P_z^{\mathrm{tr}}$. However, $P_y^{\mathrm{tr}}$ does not show such a pronounced minimum at 3–4 ML. The differences between model and *ab initio* calculations can be attributed to the number of transmission channels: a single one in the model but several channels (with different wavelengths) in the *ab initio* calculations.

*Effects of the electronic structure.* To show how the spin motion depends on details of the electronic structure, we address constant-initial-state PE spectra. In contrast to SPLEED experiments in which $\vec{P}^{\mathrm{in}}$ is typically parallel or antiparallel to the magnetization,[25,26] a transverse $\vec{P}^{\mathrm{in}}$ ($\varphi_{\mathrm{ph}} = 0°$) is chosen. For clarity reasons, the following discussion rests upon the complex bulk-band structure, rather than on layer-resolved spectral densities. The "pure" effect is worked out by a model calculation, rather than complicating the discussion by complex-band structures.

The spin-averaged intensities [Fig. 3(a)] decrease significantly with Fe coverage, caused by the small photoelectron escape depth. The global shape of the spectra, however, remains almost unaffected. Changes of the slopes, best to be seen for 1 ML Fe but present for all Fe-film thicknesses, can be traced back to the Fe electronic structure (not shown): an increase of the slope is associated with the onset of additional transmission channels, i.e., dispersive Fe bands. In particular, one pair of spin-split bands provides efficient transmission, which leads to the intensity increase at about 15 eV. A Pd-band gap, which reduces the number of channels in the substrate, causes the pronounced minimum at about 34 eV kinetic energy.

At low energies where the number of transmission channels is small, the evolution of $\vec{P}^{\mathrm{tr}}$ with Fe coverage is almost monotonous [Figs. 3(b)–3(d)]. The most significant structures show up between 12 eV and 16 eV (gray area): $P_x^{\mathrm{tr}}$ and $P_y^{\mathrm{tr}}$ display $-/+$ and $+/-$ modulations, respectively, accompanied by a maximum in $P_z^{\mathrm{tr}}$. A detailed analysis corroborates their relation to the Fe electronic structure, in particular to exchange-split band gaps in conjunction with the onset of additional transmission channels in that particular energy range.

To provide direct evidence that band gaps manifest themselves pronounced in spin motion, the ESP is calculated in an inelastic three-band nearly-free-electron model. The substrate is taken as semi-infinite free space (with zero potential), whereas a nonzero scattering potential in the magnetic film gives rise to exchange-split band gaps [Figs. 4(a) and 4(b)]. There, the transmission of one spin channel is reduced

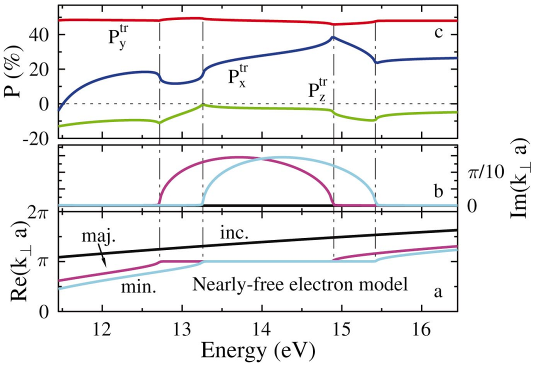

FIG. 4. (Color) Effect of exchange-split band gaps in the film electronic structure on the spin motion. (a) and (b) Complex band structure of the substrate ("inc.," black) and the magnetic film (majority, "maj.," magenta; minority, "min.," cyan) in the extended zone scheme. (c) Electron spin polarization of the transmitted electrons. Vertical dash-dotted lines serve as guides to the eye.

due to evanescent states [nonzero Im($k_z$) in Fig. 4(b)]. Since incoming transverse spinors are weighted sums of spin-up (“maj.”) and spin-down (“min.”) Pauli spinors ($P_y^{\mathrm{in}} = 50\%$), $P_x^{\mathrm{tr}}$ and $P_y^{\mathrm{tr}}$ show a $-/+$ and a small $+/-$ modulation, respectively, whereas $P_z^{\mathrm{tr}}$ increases in the band-gap middle [Fig. 4(c)]. Although the Fe-band structure is much more complicated, the structures in the model calculation have counterparts in Figs. 3(b)–3(d) (gray area). Distinct band-gap related features do not show up at higher kinetic energies due to the onset of several efficient transmission channels just at about 15 eV.

*Conclusions.* First-principles “theoretical experiments” demonstrate that the spin motion in electron transmission through ferromagnetic films can be analyzed in detail by angle- and spin-resolved photoelectron spectroscopy. Calculations for Fe films on Pd(001), which are to be confirmed experimentally, suggest promising analyses of spin-dependent transport through magnetic layers. In particular, information on the electronic and magnetic film structure is obtained since intensities and spin polarizations depend significantly on the film thickness. Beyond that, one can speculate to use the approach for investigating magnetic configurations, with the possibility of analyzing noncollinear magnetism. The main advantages appear to be that the preparation of freestanding films is avoided and that the spin polarization of the incoming electrons can easily be oriented.

---

*Corresponding author. Electronic address: henk@mpi-halle.de

[1] *Spin Dependent Transport in Magnetic Nanostructures*, edited by S. Maekawa and T. Shinjo (Taylor & Francis, London, 2002).

[2] S.S.P. Parkin, J. Appl. Phys. **79**, 6078 (1996).

[3] P. Zahn, J. Binder, I. Mertig, R. Zeller, and P.H. Dederichs, Phys. Rev. Lett. **80**, 4309 (1998).

[4] J.A.C. Bland and B. Heinrich, *Ultrathin Magnetic Structures* (Springer, Berlin, 1994).

[5] M. Aeschlimann, R. Burgermeister, S. Pawlik, M. Bauer, D. Oberli, and W. Weber, J. Electron Spectrosc. Relat. Phenom. **88-91**, 179 (1998).

[6] D. Oberli, R. Burgermeister, S. Riesen, W. Weber, and H.C. Siegmann, Phys. Rev. Lett. **81**, 4228 (1998).

[7] W. Weber, D. Oberli, S. Riesen, and H.C. Siegmann, New J. Phys. **1**, 9.1 (1999).

[8] Y. Lassailly, H.-J. Drouhin, A.J. van der Sluijs, and G. Lampel, Phys. Rev. B **50**, 13 054 (1994).

[9] W. Weber, S. Riesen, C.H. Back, A. Shorikov, V. Anisimov, and H.C. Siegmann, Phys. Rev. B **66**, 100405(R) (2002).

[10] J. Henk and A. Ernst, J. Electron Spectrosc. Relat. Phenom. **125**, 107 (2002).

[11] J. Henk, T. Scheunemann, and R. Feder, J. Phys.: Condens. Matter **9**, 2963 (1997).

[12] M.D. Stiles and A. Zangwill, J. Appl. Phys. **91**, 6812 (2002).

[13] M.D. Stiles and A. Zangwill, Phys. Rev. B **66**, 014407 (2002).

[14] D.P. Pappas, K.-P. Kämper, B.P. Miller, H. Hopster, D.E. Fowler, C.R. Brundle, A.C. Luntz, and Z.-X. Shen, Phys. Rev. Lett. **66**, 504 (1991).

[15] M.P. Gokhale and D.L. Mills, Phys. Rev. Lett. **66**, 2251 (1991).

[16] W. Kuch, M.-T. Lin, K. Meinel, C.M. Schneider, J. Noffke, and J. Kirschner, Phys. Rev. B **51**, 12 627 (1995).

[17] M.P. Seah and W.A. Dench, Surf. Interface Anal. **1**, 2 (1979).

[18] A. Jablonski and C.J. Powell, Surf. Sci. Rep. **47**, 33 (2002).

[19] J. Henk, T. Scheunemann, S.V. Halilov, and R. Feder, J. Phys.: Condens. Matter **8**, 47 (1996).

[20] J. Henk, A.M.N. Niklasson, and B. Johansson, Phys. Rev. B **59**, 13 986 (1999).

[21] A. Ernst, M. Lüders, W.M. Temmerman, Z. Szotek, and G. van der Laan, J. Phys.: Condens. Matter **12**, 5599 (2000).

[22] J. Henk, in *Handbook of Thin Film Materials*, edited by H.S. Nalwa (Academic Press, San Diego, 2001), Vol. 2, Chap. 10, p. 479.

[23] S.-K. Lee, J.-S. Kim, B. Kim, Y. Cha, W.K. Han, H.G. Min, J. Seo, and S.C. Hong, Phys. Rev. B **65**, 014423 (2002).

[24] J. Rundgren, Phys. Rev. B **59**, 5106 (1999).

[25] T. Scheunemann, R. Feder, J. Henk, E. Bauer, T. Duden, H. Pinkvos, H. Poppa, and K. Wurm, Solid State Commun. **104**, 787 (1997).

[26] S. Egger, C.H. Back, J. Krewer, and D. Pescia, Phys. Rev. Lett. **83**, 2833 (1999).